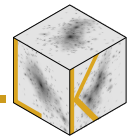


Rise and Shine – The Formation of Structures from Cosmic Dawn to Present Day

Lucas C. Kimmig



Munich 2026

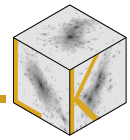


Strukturentstehung vom Beginn des Universums bis heute

Lucas C. Kimmig



München 2026



Rise and Shine – The Formation of Structures from Cosmic Dawn to Present Day

Lucas C. Kimmig

PhD Thesis

at the University Observatory Munich

Ludwig Maximilian University

Submitted by

Lucas C. Kimmig

born in Wiesbaden

Munich, 18. 02. 2026

Erstgutachter: Appl. Prof. Klaus Dolag

Zweitgutachter: Prof. em. Rolf-Peter Kudritzki

Tag der mündlichen Prüfung: 14. 04. 2026

Abstract

Through the use of state-of-the-art hydrodynamical cosmological simulations, we explore three fundamental questions on the growth of structure in the Universe. We begin by uncovering how the first massive galaxies formed their stars, why many of them quenched rapidly, and why a number of simulations have failed to reproduce these observations from the James Webb Space Telescope. We demonstrate that differentiating cold and hot gas flows onto the central black holes is crucial, and gives rise not only to early quenching but also a later rejuvenation of the star formation in massive galaxies. Furthermore, we find that the morphology of the first galaxies does not yet correlate with their environment or their star formation, and predict the presence of massive quenched slowly rotating galaxies by $z > 3$, which has since been confirmed by observations.

Prompted by the unexpected rejuvenating nature of early galaxies, we then analyze how galaxies grow their stellar mass through time. We construct a semi-empirical model of galaxies on the star forming main sequence, and demonstrate that this nicely predicts the mean ages and star formation histories of present day galaxies. However, we show both from simulations and observations that individual galaxies actually undergo cycles of on-off star formation around the star forming main sequence, with our own Milky Way galaxy showing evidence for a similar behavior. Stellar chemical abundances are demonstrated to be powerful tools to capture the resulting complex star formation histories of galaxies.

Finally, we consider the evolution of the most massive bound structures in the Universe, namely clusters of galaxies. While the mean growth of an ensemble follows expectations from theory, we show that the connection between the most massive systems in the early Universe and present day breaks down for individual systems. By leveraging the power of five different cosmological simulations, we determine observable tracers that allow us to re-establish the connection. At present day, the fraction of light in the diffuse halo and central galaxy is a consistent, subgrid independent tracer of the assembly time of the galaxy cluster. At high redshift, the best identifier of regions that will actually become galaxy clusters is the large-scale environment on scales of 10 cMpc.

We conclude that the analysis of structure at the extremes – the earliest galaxies, the most massive clusters, and star formation that goes in cycles instead of following the mean – is a fruitful approach toward uncovering how galaxies in our Universe formed and evolved.

Zusammenfassung

In dieser Arbeit werden mittels Nutzung hydrodynamischer kosmologischer Simulationen drei fundamentale Fragen bezüglich des Wachstums der Strukturen im Universum ergründet: Beginnend mit den ersten Galaxien wird erörtert, wie diese erst rapide ihre Sterne bilden und die Sternenstehung dann kurzfristig beenden, und warum viele gängige Simulationen daran scheitern, die neuen Beobachtungen des James Webb Space Teleskops zu reproduzieren. Hervorgehoben wird dabei die Unterscheidung zwischen der Akkretion heißen bzw. kalten Gases auf das zentrale Schwarze Loch, welche nicht nur für das Ende, sondern auch für den darauf folgenden Neustart der Sternentstehung verantwortlich ist. Es wird gezeigt, dass im frühen Universum die Morphologie der Galaxien noch nicht stark mit ihrer Umgebung oder ihrer Sternentstehungsrate korreliert, und die Existenz der ersten langsam rotierenden Galaxien bei $z > 3$ postuliert, welche seither beobachtet wurden.

Die unerwartete Wiederaufnahme der Sternentstehung massereicher Galaxien gibt Anlass zur genaueren Untersuchung ihrer Sternentstehungsgeschichten. Anhand eines semi-empirischen Models wird gezeigt, dass eine Entwicklung entlang der Hauptreihe sternbildender Galaxien die beobachtete Beziehung zwischen stellarer Masse und stellarem Alter zur Folge hat. Es wird gezeigt, dass simulierte und beobachtete Galaxien nichtsdestotrotz Zyklen in ihren Sternenstehungsraten aufweisen, unter anderem auch unsere Milchstraße. Dabei sind die chemischen Häufigkeiten der Sterne hervorragende Diagnostiken der resultierenden komplexen Sternentstehungsgeschichten der Galaxien.

Die Entwicklung der Galaxien ist intrinsisch gekoppelt an die Entwicklung ihrer Umgebungen, insbesondere die der Galaxienhaufen, den größten gebundenen Strukturen im Universum. Ihr Wachstum folgt im Mittel den Erwartungen des hierarchischen Modells, allerdings können einzelne Systeme stark davon abweichen. Anhand fünf bekannter Simulationen wird nachgewiesen, dass der Bruchteil des Intrahaufenlichts und der zentralen Galaxie an dem gesamten Licht hervorragend geeignet ist, die Aufbauzeit des Haufens vorherzusagen, unabhängig der verschiedenen Kalibrierungen der Subgrid-Modelle. Für frühe Strukturen wird gezeigt, dass die Masse in der großräumigen Umgebung auf Skalen von 10 cMpc für die Identifizierung von echten Protohaufen ausschlaggebend ist.

Es wird geschlussfolgert, dass die Analyse der extremsten Objekte, also der frühesten Galaxien, der massereichsten Galaxienhaufen, und der zyklischen Sternentstehungsgeschichten anstelle stetigen Wachstums, ein wichtiger Schritt auf dem Weg unserers Verständnisses der Entstehung und Entwicklung von Galaxien im Universum ist.

Contents

Abstract **vii**

Zusammenfassung **viii**

1 Introduction **1**
1.1 The First Galaxies . . . 2
1.1.1 The Formation of Disks and Ellipticals . . . 3
1.1.2 The Era of the James Webb Space Telescope . . . 6
1.2 Connecting Galaxies to their Progenitors . . . 10
1.3 Clusters of Galaxies . . . 11

2 Simulations **17**
2.1 Cosmology . . . 18
2.2 Gravity and Hydrodynamics . . . 19
2.3 Star Formation and Chemical Enrichment . . . 21
2.4 Supermassive Black Holes . . . 24
2.4.1 The Eddington Limit . . . 24
2.4.2 A Two-Mode Two-Phase Model for Blackholes . . . 25
2.4.3 Consequences of the Model and the Future . . . 27
2.5 Parameter Testing – The MagneticumDawn Simulation Suite . . . 29
2.5.1 The Dawn Project . . . 30
2.5.2 The Masses of the First Black Holes . . . 30
2.5.3 The Interplay between Star Formation, Black Hole Feedback, and UV Background . . . 34

3 Blowing Out the Candle: How to Quench Galaxies at High Redshift – an Ensemble of Rapid Starbursts, AGN Feedback, and Environment **41**
3.1 Introduction . . . 42
3.2 The Magneticum Simulation . . . 45
3.3 Galaxies at High Redshifts . . . 46
3.3.1 Galaxy Sample from $z = 15$ to $z = 2$ . . . 47
3.3.2 Quenched Galaxies: Selection and Statistics . . . 49
3.4 How Do Galaxies at High Redshifts Quench? . . . 53

3.4.1 Combined Stellar and AGN Feedback . . . 54
3.4.2 Massive Quiescents Quench Quickly (MQQQ) . . . 60
3.4.3 Baryon Fraction and Kinematics of Quenching . . . 64
3.5 The Role of Environment . . . 68
3.6 Predictors for Quenching . . . 70
3.7 Conclusions . . . 75

4 Relight the Candle: What happens to High Redshift Massive Quenched Galaxies 79
4.1 Introduction . . . 80
4.2 Simulations and Observations . . . 82
4.3 Quenched Galaxies at $z \approx 3.4$ . . . 84
4.3.1 Global Properties . . . 87
4.3.2 Environment . . . 90
4.3.3 Formation Redshifts - When Do the Quenched Galaxies Form? . . . 92
4.4 What Do they Become – the Multiple Pathways of Quenched Galaxies into the Future . . . 95
4.4.1 Evolution to Redshift of $z = 2$ . . . 96
4.4.2 Rejuvenation . . . 102
4.4.3 Descendant Galaxies at $z = 0$ . . . 105
4.5 Summary and Conclusions . . . 106

5 Flaring Candles: Quenched Galaxies from Simulations and Observations – A Comparison 109
5.1 Star Formation and Quenching in the High Redshift Universe in a Nutshell . 109
5.1.1 Introduction . . . 110
5.1.2 Quenching . . . 110
5.1.3 Rejuvenation . . . 112
5.1.4 Summary and Conclusions . . . 113
5.2 Observational Kinematics and Quenching Behavior at Cosmic Dawn . . . 114
5.2.1 Quenched Fractions Renewed: A Larger Observational Sample . . . 114
5.2.2 Slow Rotators at Cosmic Dawn . . . 116
5.2.3 Quenching and Formation Times from Observations . . . 117
5.3 Conclusion . . . 119

6 The Emergence of Massive Disks at Cosmic Dawn 121
6.1 Introduction . . . 121
6.2 When Do Disks Emerge . . . 122
6.3 The Impact of the Observed Wavebands . . . 124
6.4 A Simulated Big Wheel Counterpart . . . 125
6.5 Conclusion . . . 126

7 The Dawn of Puffy Galaxies 127
7.1 Introduction . . . 127
7.2 The Descendants of Puffy Galaxies at $z = 0$ . . . 128
7.2.1 Sample Selection . . . 128
7.2.2 Dark and Bright Matter . . . 129
7.2.3 Angular Momentum Distribution . . . 131
7.3 Discussion and Conclusion . . . 132

8 The Evolution of Star Forming Main Sequence Galaxies 133
8.1 Introduction . . . 134
8.2 The Model . . . 136
8.3 Results . . . 138
8.3.1 Properties of Main Sequence Galaxies . . . 138
8.3.2 Connecting Galaxies Across Cosmic Time . . . 143
8.3.3 Milky Way-like Galaxies . . . 146
8.4 Conclusion . . . 149

9 Universal Blacksmith: What Global Stellar Metal Abundances Reveal About Galaxies' Formation Histories 153
9.1 Introduction . . . 153
9.2 Sample of Galaxies and Definitions . . . 156
9.3 Evolution of Alpha-Enhancement . . . 157
9.3.1 Stellar Chemical Abundances through Cosmic Time . . . 158
9.3.2 Distinguishing Galaxies . . . 162
9.3.3 Comparison to the SAMI Survey . . . 166
9.4 Considering Specific Cases . . . 166
9.5 How Differences in Metallicity Emerge . . . 169
9.6 Milky Way Metallicity . . . 173
9.7 Conclusions . . . 176

10 To Form or Not To Form Stars – Galaxy Evolution through Cosmic Time 179
10.1 The Star Formation Histories of Galaxies Through Cosmic Time . . . 179
10.1.1 Classifying Galaxies According to their Star Formation History . . . 179
10.1.2 Connecting the Star Formation History of a Galaxy and its Stellar Metallicity . . . 180
10.1.3 Connecting the Star Formation History of Milky Way Mass Galaxies with their Merger Rates . . . 182
10.2 The Impact of a Galaxies' Environment at Cosmic Noon in Predicting its Present-Day Stellar Mass . . . 185

11 Substructures as a Dynamical Clock for Galaxy Clusters 187
11.1 Introduction . . . 187

11.2 Results . . . 190
11.2.1 The Case of Abell 2744 . . . 190
11.2.2 Accretion and Dynamical State . . . 195
11.2.3 Substructures and Centershift . . . 198
11.3 Summary and Conclusion . . . 201

12 Intra-Cluster Light as a Dynamical Clock for Galaxy Clusters: Insights from the Magneticum, IllustrisTNG, Hydrangea, and Horizon-AGN Simulations 205
12.1 Introduction . . . 206
12.2 Simulations . . . 210
12.2.1 Magneticum Pathfinder . . . 211
12.2.2 IllustrisTNG . . . 213
12.2.3 Horizon-AGN . . . 213
12.2.4 Hydrangea . . . 214
12.2.5 Property Definitions . . . 215
12.3 Results . . . 215
12.3.1 Populations of Galaxy Clusters . . . 215
12.3.2 Defining Cluster Dynamical State . . . 218
12.3.3 The Fraction of ICL+BCG and Cluster Dynamical State . . . 220
12.3.4 Halo Mass (In-)Dependence . . . 223
12.3.5 Tracing ICL+BGC through Other Observables . . . 226
12.3.6 Evolution Through Cosmic Time . . . 229
12.3.7 Rate of Satellite Shredding . . . 232
12.4 Summary and Conclusions . . . 234

13 Intra-Cluster Light as a Dynamical Clock for Galaxy Clusters II: Insights from the SLOW/LowerDecks simulations 239
13.1 Introduction . . . 239
13.2 Simulations . . . 241
13.3 Dynamical State Parameters and Mock Images . . . 241
13.4 Results . . . 245
13.4.1 Simulated Counterparts . . . 246
13.4.2 The Mass Assembly Histories of Local Galaxy Clusters . . . 248
13.4.3 The X-ray Dynamical State of Local Galaxy Clusters . . . 251
13.5 Conclusion . . . 254

14 A Whale of a Time: Cluster Evolution from Cosmic Dawn to Present Day 255
14.1 Introduction . . . 255
14.2 The Magneticum Pathfinder Box2/hr Simulation . . . 256
14.3 The Non-linear Growth of Massive Structures . . . 257
14.4 The Power of Environment . . . 261

14.5 Looking Back from $z = 0$ . . . 263
14.5.1 Introduction . . . 263
14.5.2 The Most Massive Structures . . . 264
14.5.3 Consequences for Stellar Mass . . . 266
14.5.4 Summary and Conclusions . . . 266
14.6 The Impact of Dynamical State on the Star Forming Galaxy Population in Galaxy Clusters . . . 267
14.7 Conclusion . . . 268

15 Summary and Conclusion **271**
15.1 How do the First Galaxies form? . . . 271
15.2 How Can We Connect Present Day Galaxies to Their Progenitors? . . . 273
15.3 How do the Densest Environments, Clusters of Galaxies, Evolve through Cosmic Time? . . . 274
15.4 Final Thoughts and the Future . . . 275

A Radial Profiles for High-Redshift Quenched Galaxies **277**

B Model Parameter Study for the Mass Evolution on the Main Sequence **281**
B.1 Impact of the model parameters . . . 281
B.2 Main sequence star formation history fits . . . 282
B.3 Connecting present day galaxies and their progenitors . . . 283

C Correlations and Definitions for ICL and BCG Quantities in Simulations **285**
C.1 Partial Correlations and Fitting . . . 285
C.2 Definitions for Center Shift and BCG vs ICL . . . 287

References **291**

Quotations **349**

Acknowledgments **353**

See yonder, lo, the Galaxyë
Which men clepeth the Milky Wey
For hit is whyt

Geoffrey Chaucer, *The House of Fame*, circa 1380

1 Introduction

The quest to understand the world around us has been and remains a deeply human experience. Ever since we first gazed upon the sky and wondered how the stars, how our planet and how we ourselves came into being, humans as a whole have spent enormous efforts toward uncovering answers to those questions. A particular feature of the night sky has been recorded for millennia in cultures across the world, described as a river (e.g., "Wodliparri" by the Kaurna people of Australia or 银河 in the Chinese folktale *The Cowherd and the Weaver Girl*), a "Birds' Path" in several Turkic and Baltic languages, and the "Via Lactae" or "γαλαξιαζ" in Latin and Greek: the Milky Way Galaxy. The latter two descriptions stem from its milky appearance, with the Greek word being the origin of the English "Galaxy" (Liddel & Scott, 1996; Waller & Hodge, 2003).

As we now know (e.g., Naidu et al., 2026), galaxies have illuminated the Universe for the past thirteen billion years. Containing anywhere from millions to trillions of stars, their existence as "island universes" ("Welteninsel", Kant, 1775) has only really been established for about a century (Shapley & Curtis, 1921), with remarkable progress made over that time on their formation and evolution. This deepening understanding has been driven by advances both from the observational side, with the increasing fidelity of both ground and space-based telescopes (e.g., Laureijs et al., 2011; Ivezić et al., 2019; Montes et al., 2023), as well as from the computational side, with the advent of supercomputing centers capable of running simulations with trillions of particles (see the introduction by Valentini & Dolag, 2025). Another great success has been that of the ΛCDM (Lambda Cold Dark Matter) model (e.g., Blumenthal et al., 1984), which together with observations of the cosmic microwave background (e.g., Komatsu et al., 2011; Planck Collaboration et al., 2014) has paved the way to realistic initial conditions of the Universe for these cosmological simulations.

The work throughout this thesis is based on the use of state-of-the-art hydrodynamical cosmological simulations, and what their results tell us about the evolution of structure within our Universe. It is focused on three primary questions:

- How do the first galaxies form?
- How can we connect galaxies at present day with their progenitors at earlier times?
- How do the densest environments, clusters of galaxies, evolve through cosmic time?

Consequently, this thesis itself is split into three parts. Chapters 3 to 6 discuss the emergence of the first galaxies and the challenges they have posed to theoretical models. Chapters 7 to 10 then demonstrate how the evolutionary history of galaxies imprints in their present day properties, and how that can be used to connect them to their progenitors at higher redshifts. Finally, we move on to the densest environments within which galaxies reside, namely galaxy clusters, in chapters 11 to 14. We discuss their evolution through time, and how the obstacle of non-linear growth can be overcome to identify the true protostructures of local galaxy clusters. We summarize our findings and conclude in chapter 15.

A large part of this work is already published in the papers by Kimmig et al. (2023, 2025a,b); Remus & Kimmig (2025); Gannon et al. (2025); Nanayakkara et al. (2025); Merlin et al. (2025); Forrest et al. (2025); Çakır et al. (2025); Fortuné et al. (2025) and Gao et al. (2026), to which I have contributed significantly either as the first or second author, or through data processing, plotting, discussions or scientific motivation, and which all address in some manner one of the above three questions. I additionally include two papers that are to be submitted in chapters 8 (Kimmig, to be subm., a) and 13 (Kimmig, to be subm., b), as well as other ongoing topical work from my thesis in chapters 9 and 14.

Each chapter includes its own brief, more focused introduction to the topic. The goal of this general introduction is not to provide an exhaustive overview on the matter, as there already exist excellent books/reviews written on the topics of galaxy formation and evolution (e.g., Mo et al., 2010; Conselice, 2014), their constituent stars (e.g., Kudritzki & Puls, 2000; Krumholz, 2014) and cosmological simulations (e.g., Somerville & Davé, 2015; Vogelsberger et al., 2020; Valentini & Dolag, 2025). Instead, I seek here to place my results on these three key questions into the context of the broader fields surrounding them. In addition, chapter 2 provides a similar higher-level overview of the cosmological simulations used throughout this work, including a parameter study for which I performed 44 cosmological simulations as part of the MagneticumDAWN project.

1.1 The First Galaxies

The question of how galaxies form and evolve necessarily involves the question of what types of galaxies came first. One of the most striking observations is the morphological diversity of galaxies, with descriptions of celestial bodies based on their apparent clumping differentiating them from stars as early as in the 10th century by the Persian astronomer Abd al-Rahman al-Sufi (Conselice, 2014). Classification schemes (e.g., Wolf, 1908; Hubble, 1922) evolved until the seminal work by Hubble (1926), who investigated 400 galaxies, then known as

"extragalactic nebulae", and classified them by their rotational symmetry about a dominating nuclei broadly into two groups. First, those which fade smoothly from bright nuclei to indefinite edges, termed "elliptical" galaxies and quantified by their apparent ellipticity from 0 to 7 (dropping the decimal point). Second, those with spiral arms aptly termed "spiral" galaxies, which range in how strongly they are dominated by their central nuclei, whether they host a central bar, and how tightly their arms are wound (Hubble, 1926). They are also commonly known as "disk galaxies".

We begin in Subsec. 1.1.1 therefore with a historic perspective on how our understanding of the formation of disk and elliptical galaxies has evolved through time. As we aim to show, it was the quest to explain the diversity in galaxy properties that pushed the boundaries of our physical understanding, moving the field toward now-common concepts such as star formation and active galactic nuclei (AGN) feedback, the presence of an ultraviolet (UV) background, and the role of mergers for the formation of galaxies within the ΛCDM (lambda cold dark matter) cosmogony. This brings us naturally to the state of the field prior to the launch of the James Webb Space Telescope (JWST) on the 25th of December, 2021. We discuss the impact of its observations and the new questions that have arisen in Subsec. 1.1.2, and emphasize there again the crucial role of seeking answers not only to describe the mean properties of galaxy populations, but their *scatter* as well. We turn to how our understanding of galaxy formation has informed our current methods to connect galaxies across cosmic epochs in Subsec. 1.2. Finally, we finish in Subsec. 1.3 with the largest bound structures in the Universe, galaxy clusters, and the role they too have played in the advancement of our understanding of the physical processes, such as when trying to explain the lack of star formation of their galaxy populations, and the observed dependence of other galaxy properties on environment.

1.1.1 The Formation of Disks and Ellipticals

A notable choice in terminology were the labels of "early-type" galaxy for an elliptical and "late-type" galaxy for spirals, which were originally meant to symbolize a progression from simple to complex forms (Hubble, 1926) but which naturally imply an evolutionary sequence between the types. Indeed, whether elliptical or spiral galaxies form first had been a recurring question ever since it was shown that they differ not only in shape but also in the properties of their stellar populations (e.g., Holmberg, 1958), as well as their light distributions.

Both spiral and elliptical galaxies follow the general form of a Sérsic (1963) profile,

$$I(R) = I_0 \cdot \exp\left(-kR^{1/n}\right), \tag{1.1}$$

with I_0 the intensity at projected radius $R = 0$. Disk galaxies exhibit light profiles with $n = 1$ while de Vaucouleurs (1948) found that ellipticals follow $n = 4$.

Consequently, initial theories for their formation posited two fundamentally differing pathways. For elliptical galaxies, early work by Lynden-Bell (1967) proposed a mechanism termed "violent relaxation". The distribution function describing a set of particles that

may not overlap in phase-space is of Fermi-Dirac form, but, crucially, Lynden-Bell (1967) demonstrate that the phase-space volume filled by the stellar distribution of the elliptical galaxy must be far lower than that of the initial gas prior to collapse from which the stars were born. In this non-degenerate (note that this is meant in the sense of classical mechanics, not quantum states), i.e., the Maxwellian limit, the distribution follows that of an isothermal sphere, with $\rho \propto r^{-2}$. Because the integral of this profile diverges (giving infinite mass), Lynden-Bell (1967) additionally assumes that the relaxation process is limited to a radius R_1, while the states with $R > R_1$ are strongly depopulated and comprised of weakly bound stars near escape velocity. Roughly this can be understood as the idea that stars can only be formed in the denser central regions, and thus scatter outwards only through the relaxation and only when they have high energies. From this final assumption, he shows that one can derive the resulting distribution as $\rho \propto r^{-4}$, recovering the observed de Vaucouleurs (1948) profile.

For the disk galaxies, the first convincing picture of their formation required advances on the cosmological model itself. This was achieved through the introduction of a dissipationless component called dark matter that dominated the mass budget of galaxies and other collapsed structures in the Universe. Its existence was motivated by observations such as the flat rotation curves observed in galaxies out to tens of kiloparsecs (Faber & Gallagher, 1979) and the observed high velocities of galaxies in galaxy clusters that, under the assumption of virialization, required significant amounts of non-luminous matter (Zwicky, 1933; Smith, 1936), in addition to a better formalization of how isothermal perturbations at recombination grew over time in a cold dark matter model (e.g., White & Rees, 1978; Efstathiou & Jones, 1980).

Among other similar ideas, it was then the work by Fall & Efstathiou (1980) that considered what happened to the gas forming within these dark matter halos. They assumed the gas collapsed with the same angular momentum as the halo, and further that the angular momentum remained conserved throughout the collapse. Furthermore, the observed flat rotation curves gave the constraint that the specific angular momentum of outer stars must follow as $j = r \cdot v_{\rm circ}$. These assumptions, in addition to positing a centrifugal balance between the rotating disk material and the gravitational pull of both the halo and disk mass within its orbit, allowed them to show that an exponential profile for the surface mass density of the disk would fit the resulting conservation equations. This was further refined by Mo et al. (1998), who used the new, more realistic density profile of dark matter halos by (Navarro & Steinmetz, 1997), termed the "NFW profile", in addition to the effects of adiabatic contraction (where the inner regions of the dark matter halo are pulled together by the non-negligible gravitational pull of the baryons, see Blumenthal et al., 1986) to derive the rotation curves of stellar disks in dark matter halos with NFW profiles based on the halo concentration, the fraction of total mass in the disk, and the spin parameter characterizing the total amount of angular momentum in the initial distribution (see figure 2 by Mo et al., 1998).

Interestingly, within the emerging ΛCDM framework there was a new difficulty for the elliptical galaxies. The dissipative collapse of gas within the dark matter halos made it difficult the remove the resulting angular momentum from the stars, as the violent relaxation

model by Lynden-Bell (1967) assumed a monolithic collapse scenario. In this framework, a large gas cloud rapidly collapses (fast relative to the dynamical timescale, on the order of thousands of years rather than millions), star formation happens similarly quickly, and then the system dynamically relaxes (e.g., Eggen et al., 1962). This was no longer possible in the ΛCDM, with much longer timescales and, crucially, the build up of structure through hierarchical clustering (Press & Schechter, 1974).

Thankfully, it was this very same characteristic that provided an alternative route to the formation of elliptical galaxies. Observations showing tidal tails and shells had already hinted at a less secular evolution of galaxies (e.g., Toomre & Toomre, 1972). Consequently, mergers within the cold dark matter framework now took on the crucial role of explaining the formation of ellipticals as the end result of a merger between two disk galaxies, with new simulations proving pivotal for this understanding (e.g., Toomre, 1977; Fall, 1979; Barnes, 1992).

Indeed, over the years following there were a sequence of new issues and solutions with the formation of both disks and ellipticals within the ΛCDM framework. Early comparisons of simulations and observations found that the stars needed to retain over half of the angular momentum of all the baryons, while accounting for less than half of the mass (Navarro & Steinmetz, 2000). Consequently, the simulated disks were too small, known as the "angular momentum catastrophe" (e.g., Cole & Lacey, 1996; Navarro & Steinmetz, 1997) leading to the inclusion of energy injected by supernovae, termed stellar feedback (e.g., Katz, 1992), and an ultraviolet background that delayed the gas collapse and thus preserved angular momentum (Dekel & Silk, 1986; Navarro & Steinmetz, 2000). Stronger stellar feedback also solved the problem of early bulge overgrowth and the destruction of disks in dry mergers (Robertson et al., 2006), as gas-rich mergers were able to preserve a disky morphology (Springel et al., 2005a; Springel & Hernquist, 2005).

Simultaneously, statistical surveys of galaxies such as the Sloan Digital Sky Survey (York et al., 2000) were finding the massive tail end of galaxies (typically ellipticals) to be red and dead relative to their bluer, lower mass disk galaxy counterparts (Kauffmann et al., 2003; Baldry et al., 2004), while simulations found that the more massive halos, even with stellar feedback, continued cooling and forming stars (Cole et al., 2000; Benson et al., 2003). The solution to this so-called "overcooling problem" (Somerville & Davé, 2015) was found in the supermassive black holes at the centers of galaxies and their associated AGN feedback (e.g., Springel et al., 2005b; Croton et al., 2006; Bower et al., 2006). However, observations of high redshift (i.e., early Universe) ellipticals ended up finding them much more compact than their local counterparts (Daddi et al., 2005; Trujillo et al., 2007). This culminated in the two-phase formation scenario of ellipticals, where they first evolve in-situ toward the compact massive systems seen at high redshifts, and then grow through minor mergers later (Oser et al., 2010). These minor mergers deposit their stellar material farther out, thus contributing little to the stellar mass but significantly increasing the galaxy size (e.g., Amorisco, 2015; Karademir et al., 2019).

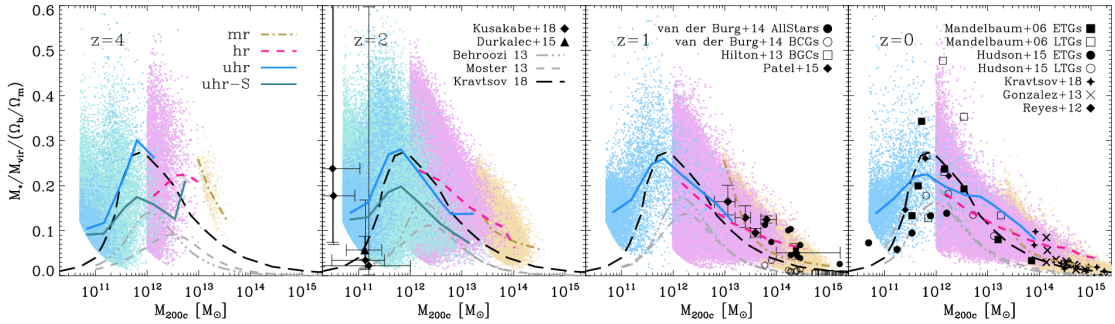


Figure 1.1. Figure 18 taken from Dolag et al. (2025) showing the fraction of stars formed from the expected amount of baryons in dark matter halos of a given mass going from the early Universe to present day (*left* to *right*), both for simulated galaxies drawn from the *Magneticum Pathfinder* simulations (colored points and lines) as well as from observations (black points and dashed curve, Mandelbaum et al., 2006; Reyes et al., 2012; Gonzalez et al., 2013; Hilton et al., 2013; van der Burg et al., 2014; Durkalec et al., 2015; Patel et al., 2015; Kusakabe et al., 2018; Kravtsov et al., 2018) and semi-empirical models (gray lines, Moster et al., 2013; Behroozi et al., 2013).

The final resulting view is that the formation of stars in galaxies is regulated by stellar feedback (galactic winds driven by supernovae) on the low mass end, and the feedback from supermassive black holes (in the form of either jets or radiation driven winds) on the high mass end, with galaxies in the middle with stellar masses of $M_* \approx 10^{10} M_\odot$ having the highest conversion efficiency. This is summarized in Fig. 1.1 taken from Dolag et al. (2025), which shows this characteristic peak across early (left panel) and late (right panel) times.

1.1.2 The Era of the James Webb Space Telescope

By the year 2020, modern cosmological simulations were finding great successes in reproducing a broad range of observations (e.g., Hirschmann et al., 2014; Dubois et al., 2014; Hopkins et al., 2014; Teklu et al., 2015; Schaye et al., 2015; Pillepich et al., 2018b; Davé et al., 2019, among others). Ellipticals were characterized by their two-phase evolution, where disk galaxies had instead evolved more secularly, with extended histories of smooth gas accretion preserving their high angular momentum and star formation rates, while irregular galaxies were those caught during or just after the time of merging.

The launch of the James Webb Space Telescope (JWST) was thus met with many predictions on what we could expect beyond the limits of the Hubble Space Telescope (HST) at redshifts of $z > 3$ (Conselice, 2014), namely a plethora of gas rich, strongly star forming galaxies with predominantly disky morphologies. We show in Fig. 1.2 the observed wavelength of optical light coming from a galaxy at redshifts $z = 0$ (today) up to $z = 10$ (when the Universe was only 500 million years old). As can be seen from the colored band, all optical light emitted from galaxies at $z > 1$ (about 8 billion years ago) has been redshifted so strongly that it must be observed in the infrared today. The shaded bands show the range in wavelengths that is detectable by the HST (light gray) and the JWST (dark gray), which

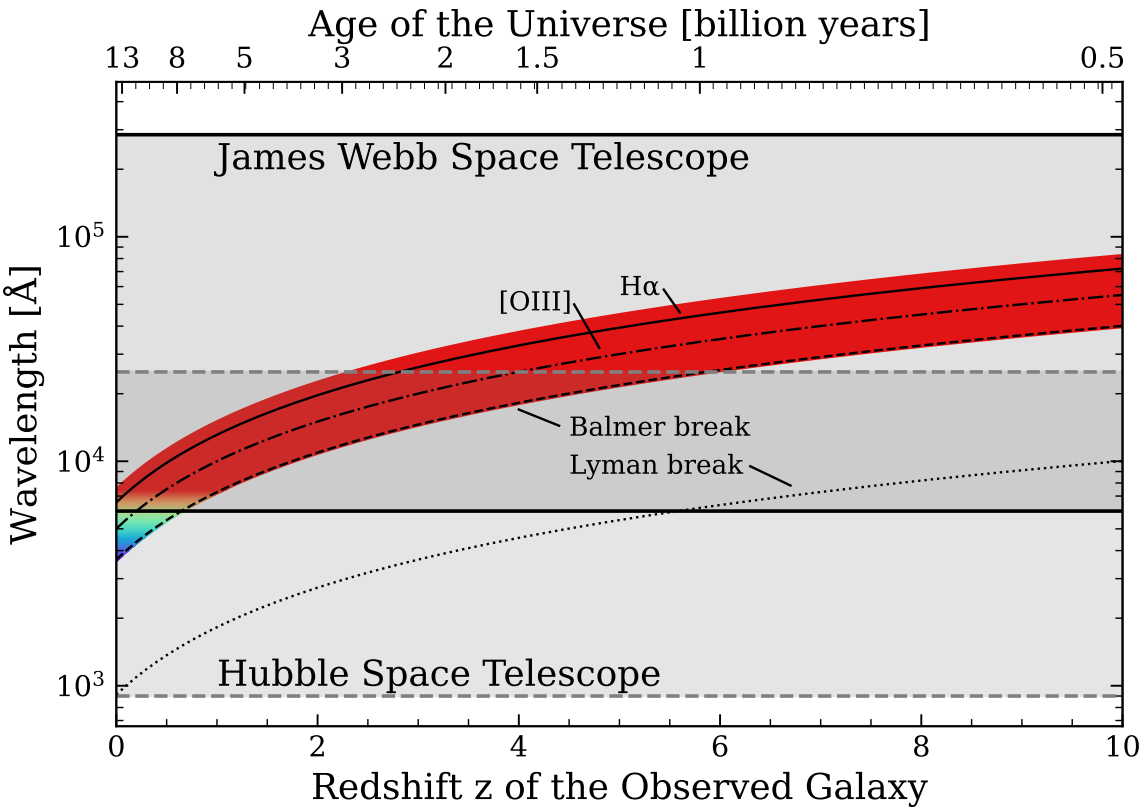


Figure 1.2. Visualization of the observed wavelengths at $z = 0$ (present day) for optical light emitted at higher redshifts (colored band)

clearly demonstrates that only the JWST is able to detect the strongly redshifted light from the earliest galaxies.

We highlight additionally some specific wavelengths used to classify galaxies (labels and black curves), such as Hα (measuring the strength of recent star formation, e.g., Kennicutt, 1998a; Brinchmann et al., 2004), the oxygen line [OIII] (used to identify supermassive black holes at the centers of galaxies, e.g., Kewley et al., 2001), the Balmer-break (with stronger breaks present in older stellar populations, e.g., Bruzual & Charlot, 2003) and the Lyman-break (which can identify high redshift galaxies, Steidel et al., 1996; Blaizot et al., 2004). Diagnostic tools such as the BPT diagram (Baldwin et al., 1981) make use of combinations of these lines and others to classify quiescent galaxies, that is galaxies that are no longer forming stars.

Therefore, the JWST was set to provide observations of the star formation, stellar masses and ages of these earliest forming galaxies, as well as the properties of their supermassive black holes, to test our understanding of galaxy formation. The expectation of for example the evolution of galaxy morphology prior to the JWST launch is nicely summarized by Fig. 1.3, where Buitrago et al. (2013) plot the fraction of disks and spheroids based on a cut in Sérsic index n. The earliest galaxies are found there to have predominantly disky stellar morphologies.

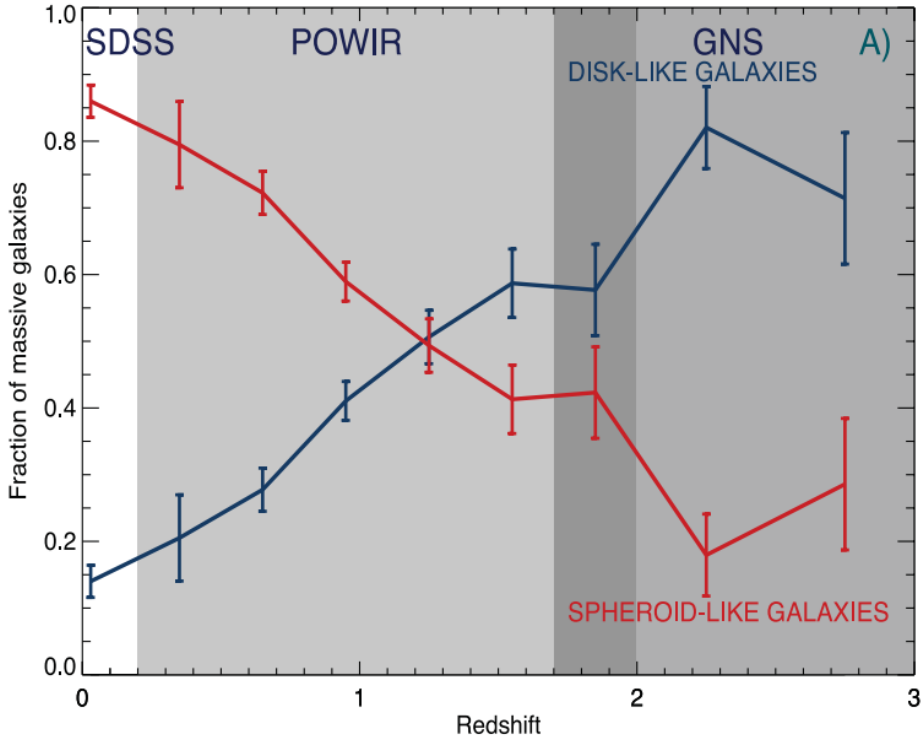


Figure 1.3. Figure 7 taken from Buitrago et al. (2013) showing the fraction of massive $M_* \geq 10^{11} M_\odot$ galaxies which are disks (Sérsic index $n < 2.5$) and spheroids ($n > 2.5$) as a function of redshift.

It was thus something of a surprise when first observations of massive quenched (i.e., not currently forming stars) galaxies were reported (Belli et al., 2023; Carnall et al., 2023b), which quickly grew from a few to hundreds (e.g., Carnall et al., 2023a; Long et al., 2023; Valentino et al., 2023; Nanayakkara et al., 2024; Baker et al., 2025b; Stevenson et al., 2026). While not unheard of in observations prior to JWST (Straatman et al., 2014; Schreiber et al., 2018; Merlin et al., 2019; Weaver et al., 2023), the number densities found with the JWST were about an order of magnitude higher than previously reported (see figure 2 by Kimmig et al., 2025b), and were thus in contention with those found from modern cosmological simulations (e.g., Remus & Kimmig, 2025; Weller et al., 2025).

These quenched galaxies were puzzling not only because they had to form up to $10^{11} M_\odot$ by $z \approx 3$, i.e., within just 2 Gyr, but they also must have shut off their star formation just as rapidly during a time when the majority of the Universe was still gas rich (Conselice, 2014). Understanding how these first galaxies at $z > 3$ formed and what becomes of them at later times were the primary questions of the works by Kimmig et al. (2025b) and Remus & Kimmig (2025), which we discuss in chapters 3 and 4, respectively.

Furthermore, if quenching in galaxies of $M_* \geq 10^{10} M_\odot$ were widespread at $z > 3$, as we know from Subsec. 1.1.1, dry merging must become a possibility, and thus potentially also the emergence of slow rotators on similar timescales. Indeed, we predicted from our simulations the presence of quiescent slow rotators already within the first 1.5 billion years ($z \approx 4.2$). Consequently, the first discovery of such an object by Forrest et al. (2025, incl. Kimmig) was

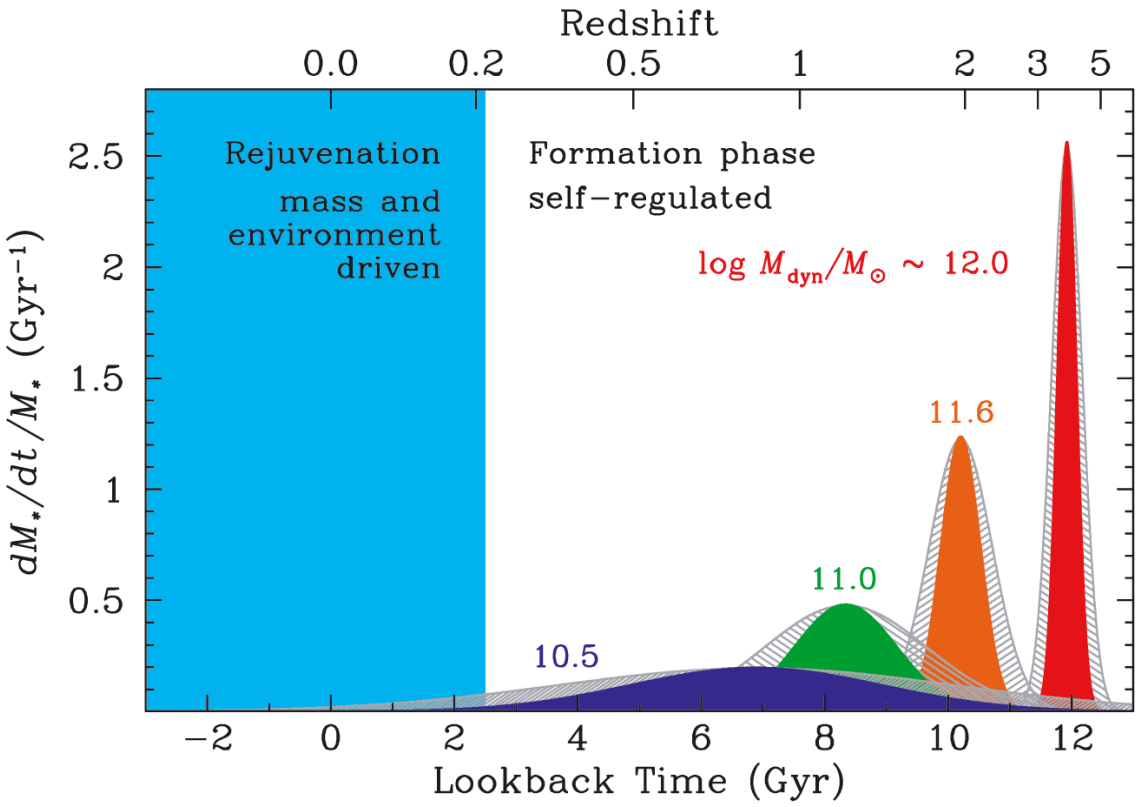


Figure 1.4. Figure 9 taken from Thomas et al. (2010), which shows the specific star formation rate of early type galaxies, based on observed stellar ages of galaxies binned into four stellar mass bins (colors). As stated by Thomas et al. (2010), this is meant as a simplified sketch showing the evolutionary trends between galaxies of different mass.

a great success, once again pushing the boundary of how quickly the diversity of galaxies in our Universe came into place. We discuss their observation, as well as other observations of high redshift quenched galaxies that we were involved with (Nanayakkara et al., 2025; Merlin et al., 2025, incl. Kimmig), and how these relate to predictions from our simulations, in chapter 5.

Returning to the question of the morphologies, then, another surprise found in observations with JWST by Kartaltepe et al. (2023) was a *decrease* in the amount of galaxies with clear disk features going from $z = 3$ to $z = 7$, while the amount of spheroidals remains approximately steady. This is also interesting when considering the results by Huertas-Company et al. (2024, 2025), who find at $z > 3$ significant amounts both of star forming spheroidals and quiescent disks in the mass range $10^{10} < M_* \, [M_\odot] < 10^{12}$. Consequently, it raises the question of when exactly the correlation between galaxy morphology and its star formation rate settled into place, and we explore this question as well as the impact of the environment on these early disks and spheroidal galaxies in chapter 6 and chapter 3, respectively.

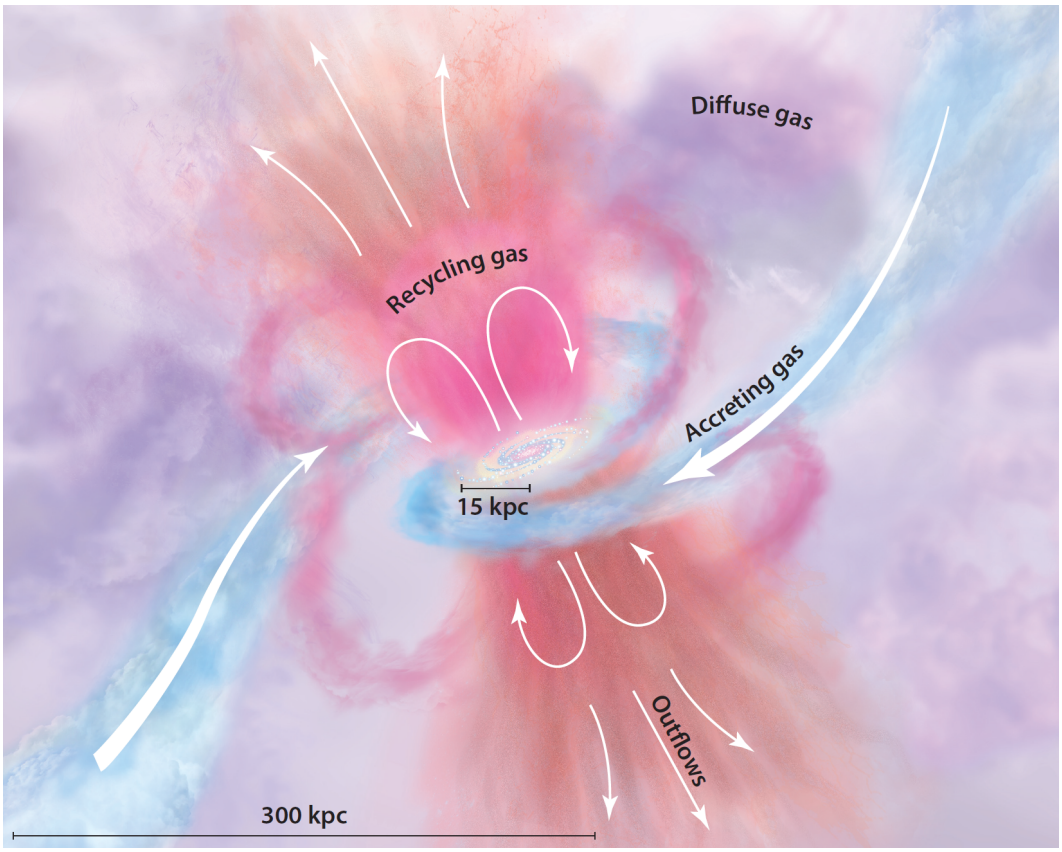


Figure 1.5. Figure 1 taken from the review by Tumlinson et al. (2017) demonstrating the in- and outflow processes that shape a star forming galaxy. The inflowing gas from the cosmic web is shown as blue filaments, and this gas is thought to be pristine and not yet metal enriched. In red, outflowing gas ejected by stellar or AGN feedback is illustrated, this metal enriched, some of which can leave the galaxy completely. Other parts rain down eventually as recycled gas, cooling down and rejoining the star formation processes, self-enriching the galaxy. Overall, the ejected gas also contributes to the diffuse hot halo of the galaxy, which is more and more dominant the more massive the galaxy and its host halo become.

1.2 Connecting Galaxies to their Progenitors

These findings from the JWST observations have opened questions on the exact formation histories of galaxies, and in particular how they regulate the in and outflow of their gas (which is the fuel of the star formation). If they can quench earlier than expected, even in gas-rich conditions, could they not also then re-accrete some of this ejected gas and begin star formation anew?

This idea again stands in contrast with the common view on the formation of galaxies, where there is a hierarchy of the most massive galaxies forming all their stars early while the lower mass galaxies begin comparably late and then form their stars over an extended period of time. A good overview of this idea is shown in Fig. 1.4 taken from Thomas et al. (2010), with a clear segregation in the age distributions based on the final galaxy stellar mass. Only the lowest mass galaxies are expected to be able to rejuvenate, and only at later times.

An example for this late rejuvenation is the idea of galactic fountains, with a sketch of the idea shown in Fig. 1.5 taken from Tumlinson et al. (2017), whereby the gas comes in along

filaments in plane with the stellar disk of the galaxy (blue gas). There it cools and condenses to form stars (see also Section 2.3), with the resulting galactic winds from the explosions of stars as supernovae driving gas back out of the galaxy (red gas). This can then rain back down onto the disk to begin this cycle again.

However, this is commonly thought of as a longer-term process, and only for lower mass galaxies at later times in the Universe (Thomas et al., 2010; Tumlinson et al., 2017). Based on the earlier than expected formation of galaxies seen with the JWST, we consider the evolution of the star formation in galaxies through cosmic time. We therefore begin in chapter 7 by studying a class of galaxies that clearly do not follow the normal star formation behavior, namely the ultra diffuse galaxies with particularly large sizes and low stellar masses (van Dokkum et al., 2015), and what their likely progenitors must have looked like (Gannon, Kimmig, et al., 2025).

More broadly, a typical method to connect galaxies through cosmic time, is to assume that galaxies of a given comoving number density at high redshifts will evolve into galaxies with that same number density at present day (van Dokkum et al., 2013; Papovich et al., 2015). Given the new measurements of the number density of galaxies of a given stellar mass (Weaver et al., 2023), as well as the star forming main sequence of galaxies (star formation rate versus stellar mass) now extending all the way from $z = 0$ to $z = 6$ (Popesso et al., 2023), we consider in chapter 8 a model that compares the growth in stellar mass expected from the fixed number density assumption, to the actual growth of galaxies evolving along the star forming main sequence (Kimmig, to be subm., a). Going beyond this theoretical model, we then consider the results from cosmological simulations on whether galaxies can be connected through their number densities (Gao et al., 2026, incl. Kimmig) or whether they evolve along the star forming main sequence (Fortuné et al., 2025, incl. Kimmig) in chapter 10.

Finally, when it comes to connecting galaxies with their progenitors, the most well studied galaxy in our Universe is the Milky Way. Measurements of individual stars in their kinematics and chemical compositions have enabled a wealth of information to be derived (Gaia Collaboration et al., 2023), from identifying progenitor remnants (Chiba & Beers, 2000; Helmi et al., 2018; Belokurov et al., 2018; Naidu et al., 2020) up to reconstructing the star formation history of the Milky Way galaxy (Haywood et al., 2016). Given the crucial role that chemical metal abundances of the stars have played in constraining the past history, we present an analysis on the stellar chemical abundances within simulated galaxies in chapter 9, in particular highlighting how the different sources of metals (supernovae of Type Ia and Type II, as well as from winds of stars on the asymptotic giant branch, Kobayashi, 2025) can be used to date the stellar age and time of assembly of a given galaxy.

1.3 Clusters of Galaxies

When discussing how extreme objects have shaped our understanding of the physical processes underlying the formation and evolution of structure in the Universe, it is difficult to

overstate the impact of galaxy clusters. These systems of up to thousands of galaxies are the largest bound structures in existence (Libeskind et al., 2018), and they are host to a particularly extreme environment found nowhere else (Sarazin, 1988). The intra-cluster medium (IGM) that fills the space between the galaxies is comprised of incredibly hot gas 10^8 K that simultaneously is at incredibly low densities of $\approx 10^{-3}$atoms/cm^3, which is about twenty four (!) orders of magnitude less dense than the air we breathe. Put another way, a gram of IGM material fills the equivalent volume of the whole of the Earth, while being hotter than the core of the Sun ($\approx 10^7$ K).

Consequently, it is perhaps unsurprising that reproducing the properties of these systems has significantly advanced the field of astrophysics. As already discussed in Subsec. 1.1.1, observations of the velocities of galaxies in clusters provided crucial evidence for the existence of a dark matter component (Zwicky, 1933; Smith, 1936), while the fact that the massive galaxies at their centers formed little to no stars was a key indication for the need of AGN feedback (Navarro & Steinmetz, 2000; Croton et al., 2006). Similarly, the question of why the gas at the center of galaxy clusters was not cooling and condensing to form stars was intriguing, given the large X-ray luminosities which indicated short cooling times (Croton et al., 2006). This cooling flow puzzle ended up being a strong indicator for the presence of a regulatory process at the core of galaxy clusters, which was given by the presence of a supermassive black hole at the center of the brightest cluster galaxy (BCG). The energy released from this black hole, through either jets or radiation, is then enough to replace the thermal energy lost to X-ray emission (Binney & Tabor, 1995; Churazov et al., 2002).

Since then, the impact of galaxy clusters both on their surroundings (Sarron et al., 2019; Vernstrom et al., 2023) as well as the galaxies within their potential well has been increasingly established, with for example Dressler (1980) noting as early as the year 1980 a difference in the amount of elliptical galaxies depending on the environment. This is now known as the morphology-density relation (e.g., Postman & Geller, 1984), where with increasing density the fraction of ellipticals goes up, and the fraction of disk galaxies goes down. This is thought to be driven by interactions with the hot cluster atmosphere which both strips the cold gas of the galaxies (Gunn & Gott, 1972), as well as prevents any new gas from being accreted onto the disk (starvation, Peng et al., 2015), in addition to tidal interactions that heat the galaxy.

Through these processes the galaxy cluster builds up its intra-cluster medium mentioned prior, but also the intra-cluster light (ICL). This diffuse mass of stars from shredded galaxies extends hundreds of kiloparsecs outside the BCG, and has been observed to increase in clusters of equal mass toward lower redshifts (Burke et al., 2015; Montes & Trujillo, 2018). The implication is that the ICL must first be built up over time as clusters grow and assemble their material, which then would make the ICL a tracer of the current dynamical state of the galaxy cluster (Montes, 2019).

Dynamically active clusters are then those that have recently undergone significant mergers, and which have not yet had time to disrupt the many new satellite galaxies. An example of such a cluster is Abell 2744, known as “Pandora’s cluster”, which we show on the left of Fig. 1.6. These massive merger events, which represent the most energetic processes taking



Figure 1.6. Images of galaxy clusters Abell 2744 (left panel, non-relaxed cluster) and Abell 383 (right panel, relaxed cluster). X-ray measurements from Chandra in red are overlaid with optical images, and in blue for Abell 2744 dark matter inferred from strong lensing measurements. Image credit for Abell 2744: X-ray: NASA/CXC/Ecole Polytechnique Federale de Lausanne, Switzerland/D.Harvey & NASA/CXC/Durham Univ/R.Massey; Optical & Lensing Map: NASA, ESA, D. Harvey (Ecole Polytechnique Federale de Lausanne, Switzerland) and R. Massey (Durham University, UK). Image credit for Abell 393: X-ray: NASA/CXC/Cinestav/T.Bernal et al.; Optical: NASA/STScI.

place in our Universe, also distort the shape of the X-ray halo (plotted in red) as the IGM from both clusters collides. On the other side is then a dynamically relaxed cluster such as Abell 383 plotted on the right of Fig. 1.6, characterized by a strong central concentration of both its ICL and ICM, resulting in a smooth profile for both the light as well as the X-ray halo.

Thus, both the distribution of the diffuse stars and gas are thought to serve as tracers of the dynamical state (Biffi et al., 2016; Haggar et al., 2024), which is to say of the assembly history of the galaxy cluster. Generally, in the ΛCDM framework of hierarchical growth, the most massive structures are those that have most recently formed, as structure merges bottom-up (Press & Schechter, 1974; Allen et al., 2011). While this may be the case on average (Allen et al., 2011), the diversity in dynamical state seen for these most massive structures is the first indication that the story is not quite as simple for individual galaxy clusters. Whether or not the most massive structures today can be linked one-to-one to the most massive structures that are now being observed with the JWST (see Subsec. 1.1.2), or if individual structures may break this mold as shown in Fig. 1.7, is therefore a crucial question, with far reaching implications for the evolution of their constituent galaxy populations.

We thus explore this question in the final third of this thesis, beginning with an example for a particularly strongly merging cluster in our simulations that well matches the observed Abell 2744 in chapter 11 (based on Kimmig et al., 2023). In chapter 12 we then measure dynamical properties of simulated galaxy clusters drawn from four different state-of-the-art

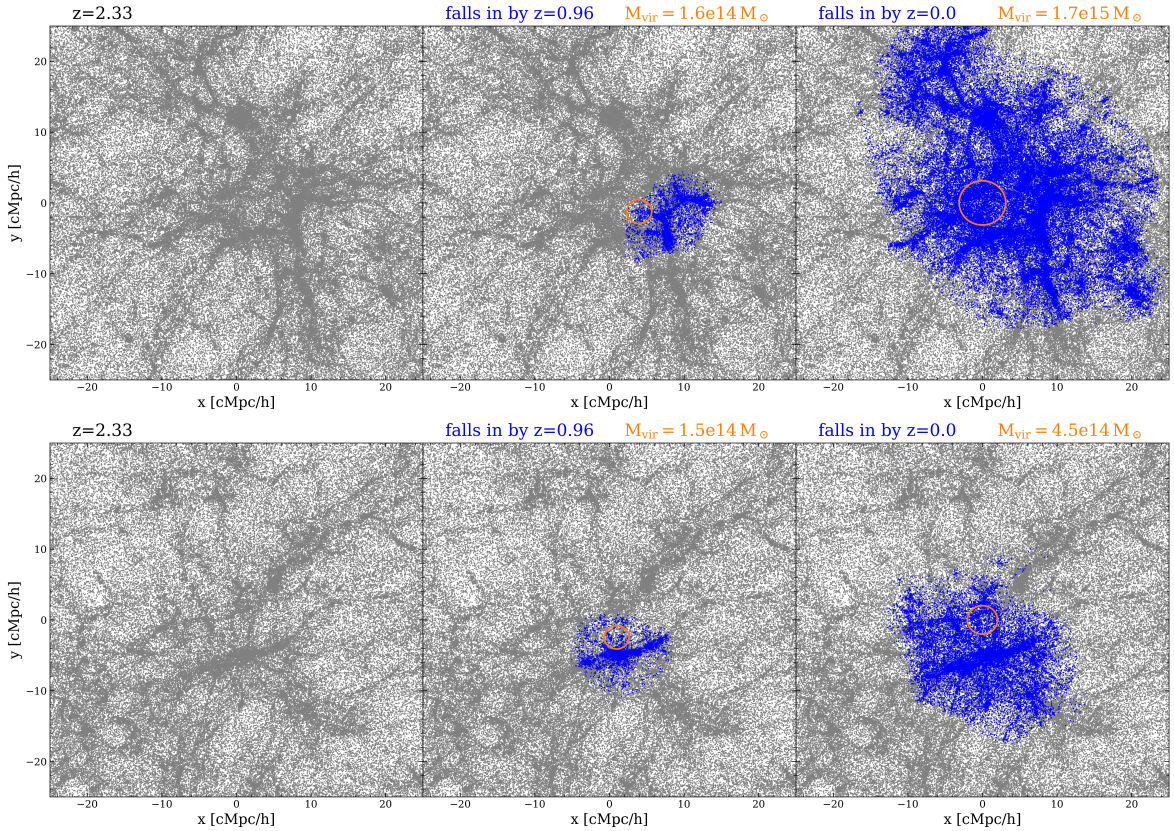


Figure 1.7. A $(50\,\mathrm{cMpc})^2$ slice through the *Magneticum Pathfinder* Box2/hr at $z = 2.3$ (early in the Universe). The mass distribution of these two regions collapses to similarly massive structures by $z = 1$ (*middle panel*, colored in blue), even though the top galaxy cluster ends up being more than twice as massive as the bottom one at $z = 0$ (*right panel*, present day). These large areas at high redshift (early in the Universe), when the clusters are not yet fully assembled, are called protocluster regions, or protoclusters.

cosmological simulations, with a particular focus on the ICL and BCG, to see whether the assumption that the diffuse light traces galaxy cluster assembly is sensitive to the implemented physics (which differ somewhat between the four cosmological simulations), with the results published by Kimmig et al. (2025a). We go a step further to consider additionally dynamical tracers based on X-ray maps for simulated clusters from the new Lower Decks suite of simulations (Seidel et al., in prep.) in chapter 13, before finally addressing the question of whether individual galaxy clusters can be traced through cosmic time and linked to their protocluster regions, or if it is only possible to connect these structures on average, in chapter 14.

As a last note, an overview of the various topics addressed in this work is given in Fig. 1.8. The overall leitmotif is the question of how galaxies evolve from cosmic dawn to present day, which we explore by considering 1) their internal processes (blue arrow), such as how they feed their central black hole and cycle their gas; 2) external processes, that is to say interactions with their environment, such as being disrupted within a galaxy cluster to build up the ICL, which can then in turn be used to predict the assembly of the galaxy cluster itself; and finally 3) in what manner individual structures at early and later times can be

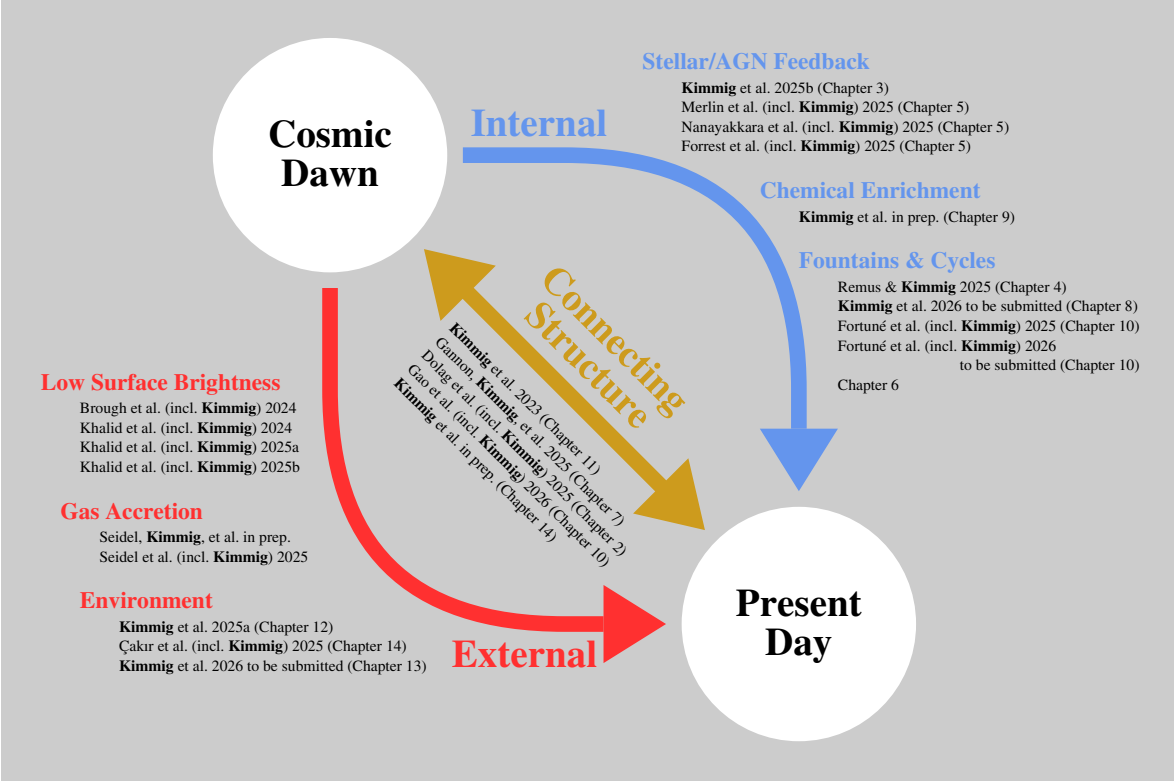


Figure 1.8. This work in a nutshell.

linked, and in particular whether this is possible for the most massive systems at every epoch. Every subsequent chapter after the next is given a pictogram that depicts where in this trinity of approaches the work can be characterized (with some cases addressing two, or all three approaches).

The fault, dear Brutus, is not in our stars,
But in ourselves

William Shakespeare, *Julius Caesar*, circa 1599

2 Simulations

Simulations have proven an invaluable tool in the quest to understand how structure in the Universe forms and evolves. From isolated merger simulations unveiling the origin of elliptical galaxies (Toomre, 1977, e.g.,), to the first cold dark matter simulations demonstrating the hierarchical build up and resulting properties of dark matter halos (White & Rees, 1978), to the modern cosmological simulations today (e.g., Vogelsberger et al., 2020; Valentini & Dolag, 2025, for an overview). These now include sophisticated models of for example gas cooling (Wiersma et al., 2009; Ploeckinger et al., 2025), accounting for the effects of a UV background (e.g., Wiersma et al., 2009; Haardt & Madau, 2012; Faucher-Giguère, 2020), to then form stellar particles (e.g., Springel & Hernquist, 2003; Tornatore et al., 2004, 2007; Stinson et al., 2013; Nobels et al., 2024), which evolve through time and via their winds and supernovae explosions chemically enrich the intragalactic medium (e.g., Wiersma et al., 2009; Chaikin et al., 2023), as well as including the seeding, growth of and feedback from central supermassive blackholes (e.g., Croton et al., 2006; Hirschmann et al., 2014; Steinborn et al., 2015) and their dynamical friction (Damiano et al., 2024), with specific models extending this set to include dust (e.g., Grudić et al., 2021; Trayford et al., 2026), magnetic fields (Dolag et al., 2008; Steinwandel et al., 2024; Hopkins et al., 2024) and cosmic rays (Böss et al., 2023; Ramesh et al., 2025; Hopkins, 2025).

As throughout the work of this thesis we make use of these cosmological simulations, it is worthwhile here to present the basic ingredients. These are crucial to understanding for example why some models succeed and others fail to match the early quenched galaxies (Kimmig et al., 2025b, see chapter 3), as well as why some characteristic correlations are shared among all of them, such as the fraction of diffuse stellar light and the assembly time of galaxy clusters (Kimmig et al., 2025a, see chapter 12). Note that we present here the

implementations in the *Magneticum Pathfinder* suite of cosmological simulations and their spin-offs. For other implementations, see the great overviews by Somerville & Davé (2015); Vogelsberger et al. (2020); Valentini & Dolag (2025).

We begin with the assumed cosmology that dictates the initial conditions of the simulation in Sec. 2.1, before covering (in broad strokes) the basic SPH code in Sec. 2.2, the stellar formation model in Sec. 2.3 and in more detail the black hole model in Sec. 2.4. In Sec. 2.5 we conclude by showing the results from a suite of cosmological boxes run as parameter tests for the new MagneticumDAWN simulation (Remus et al., in prep.).

2.1 Cosmology

Before discussing specific implementations, the framework within which the simulation is run must be established. Most all modern cosmological simulation codes assume a ΛCDM cosmogony, with minor variations on the parameters chosen. In the case of simulations used at some point throughout this work, *Magneticum Pathfinder* (Dolag et al., 2025) and *Horizon-AGN* (Dubois et al., 2014) assume a WMAP-7 cosmology (Komatsu et al., 2011), Hydrangea (Bahé et al., 2017) assumes (Planck Collaboration et al., 2014) while IllustrisTNG uses those by (Planck Collaboration et al., 2016). Note that these are all based on measurements from the cosmic microwave background (CMB), which in recent times has been shown to differ from local measurements of cosmological parameters (Riess et al., 2022).

From the measurements of the CMB temperature powerspectrum, it is possible to first convert these into a powerspectrum of density fluctuations. As inflation predicts Gaussian perturbations, the resulting density field is entirely defined by this powerspectrum (Vogelsberger et al., 2020). However, we do not initialize the simulation already at the redshift of recombination, as the growth of density perturbations progresses approximately linearly (Zel'dovich, 1970) until the density contrast of the perturbation reaches a critical threshold (Gunn & Gott, 1972). This means that the mass resolution of the simulation dictates an earliest sensible time to begin the simulation, such that the initial density field from the CMB is convolved with a transfer function (e.g., Eisenstein & Hu, 1998) to get the initial conditions at the actual starting redshift of the simulation (Vogelsberger et al., 2020).

In the specific case of the *Magneticum Pathfinder* simulation suite, initial conditions are generated via the N-GenIC code (Springel et al., 2005c; Angulo et al., 2012). For the *SLOW* cosmological simulation, the CMB powerspectrum is convolved not with a Gaussian random field, but rather with a density field constructed via measurements of local peculiar velocities from surveys such as CosmicFlows-2 (Tully et al., 2013), which was then integrated back in time, as discussed in more detail by Sorce (2018). Consequently, the large scale density fluctuations within that simulation mimic those of our local environment. The *Lower Decks* suite of zoom-in simulations, where a high-resolution region is enclosed in shells of increasingly coarsely resolved particles and baryonic effects are then simulated only in the central region (which still feels the gravitational effects of the surrounding larger scale environment), which we use in chapter 13, are therefore also constrained by local observations.

	Box0	*Box1a*	*Box2b*	*Box2*	*Box3*	*Box4*	*Box5*
Volume [Gpc^3]	56.35	2.06	0.75	0.125	0.006	0.00032	0.000017
Boxlength [Mpc]	3820	1300	910	500	180	68	26
Boxlength [h^{-1}Mpc]	2688	896	640	352	128	48	18
mr	2×4536^3	2×1512^3		2×594^3	2×216^3	2×81^3	
hr			2×2880^3	2×1564^3	2×576^3	2×216^3	2×81^3
uhr					2×1536^3	2×576^3	2×216^3
xhr							2×576^3

Table 2.1. Table 1 taken from Dolag et al. (2025) listing for simulations from the *Magneticum Pathfinder* suite their volumes and initial particle numbers. We employ here the Box4/uhr, Box3/uhr, Box2/hr and Box2b/hr simulations, in addition to zoom-in simulations taken from the *Lower Decks* suite.

2.2 Gravity and Hydrodynamics

The fundamental ingredients within any astrophysical code is that of the implemented gravity and hydrodynamical equations. Generally the stellar and dark matter particles are treated as collisionless while the gas content (representing the majority of the baryons) is treated as an ideal fluid subject to the Euler equations (Valentini & Dolag, 2025). Their integration through time requires both discretizations in time as well as either mass or volume. Depending on the latter, codes fall into two primary groups, namely the particle codes (e.g., smoothed particle hydrodynamics, SPH, Gingold & Monaghan, 1977; Lucy, 1977; Monaghan, 1992) and grid-based codes (Cen, 1992; Pen, 1998).

For the collisionless stellar and dark matter particles, the set of governing equations for a collisionless fluid are the Boltzmann equation (the requirement that local phase-space density is conserved, i.e., Liouville's theorem) and the Poisson's equation, which gives the collective gravitational potential (Vogelsberger et al., 2020). How the Poisson's equation is solved varies by the discretization choice, where the types of codes solve either the integral or differential version:

$$\Phi(\vec{r}) = -G \int \mathrm{d}\vec{r}' \frac{\rho(\vec{r}')}{|\vec{r} - \vec{r}'|} \qquad \text{or} \qquad \nabla^2 \Phi(\vec{r}) = 4\pi G \rho(\vec{r}). \tag{2.1}$$

The former can be solved by a direct summation over particle-particle interactions, but a tree approach is more commonly employed (Barnes & Hut, 1986) due to its lower complexity (Vogelsberger et al., 2020). The tree method splits particles into a hierarchy of nodes, and then computes the gravitational force either for each particle or for each node that is felt from all other nodes (using increasingly high-level nodes with increasing distance). For the later differential version instead the problem is translated into Fourier space (Hockney & Eastwood, 1981), with the determined potential field then differentiated via a finite difference approximation to obtain the forces, which can be interpolated to the positions of individual mesh cells (Vogelsberger et al., 2020). There exist also codes which represent a hybrid between the two methods, as shown in Fig. 2.1 taken from Hopkins (2015).

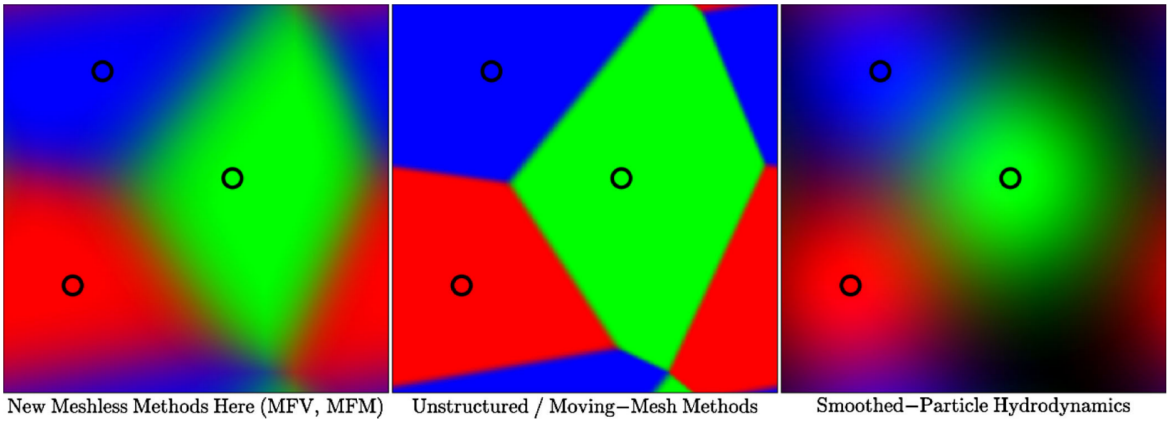


Figure 2.1. Figure 1 taken from Hopkins (2015) showing a comparison of different methods, which follow either an unstructured mesh that partitions the fluid volume (*middle*), particles that partition the fluid mass and represent kernel-smoothed regions of space (*right*), and hybrid methods (*left*).

Most of the baryonic mass is present in the form of the gas particles (from which the stellar particles are born, anyway), for which deflections in their motion through interactions with other gas particles are significant and which therefore cannot be considered collisionless (Valentini & Dolag, 2025). Typically, cosmological codes assume the gas to be inviscid and ideal, which then follows the Euler equations. These are the continuity equation, momentum equation, and the first law of thermodynamics (Vogelsberger et al., 2020; Valentini & Dolag, 2025). With ρ the density, P the pressure, $e = u + \vec{v}^2/2$ the total specific energy and u the internal energy, and defining the Lagrangian derivative as $\mathrm{d}/\mathrm{d}t \equiv \partial/\partial t + \vec{v} \cdot \nabla$, these are

$$\frac{\mathrm{d}\rho}{\mathrm{d}t} = -\rho \nabla \cdot \vec{v} \qquad \frac{\partial \rho}{\partial t} + \nabla \cdot (\rho \vec{v}) = 0 \tag{2.2}$$

$$\frac{\mathrm{d}\vec{v}}{\mathrm{d}t} = -\frac{1}{\rho} \nabla P \qquad \frac{\partial \rho \vec{v}}{\partial t} + \nabla \cdot (\rho \vec{v} \times \vec{v} + P) = 0 \tag{2.3}$$

$$\frac{\mathrm{d}e}{\mathrm{d}t} = -\frac{1}{\rho} \nabla \cdot P\vec{v} \qquad \frac{\partial \rho e}{\partial t} + \nabla \cdot (\rho e + P)\vec{v} = 0 \tag{2.4}$$

where the first column is the Lagrangian formulation employed in particle codes while the second is the Eulerian formulation used for mesh-based codes (Vogelsberger et al., 2020; Valentini & Dolag, 2025). The equations can be understood equivalently as three conservation laws, namely the conservation of mass, momentum and energy (including internal energy). They must be closed by an equation of state for the gas $P = P(\rho, u)$, which for the case of an ideal gas with the polytropic index $\gamma = 5/3$ takes the form $P = (\gamma - 1)\rho u$.

In the case of the *Magneticum Pathfinder* suite, the simulations were run with a significantly updated version of the GADGET-2 SPH code Springel (2005). Because the discretized mass elements in SPH (the particles) represent partitions in mass of the fluid, their properties are only valid across a given volume (as discretizing the fluid into zero-volume points would reduce the actual density field into an array of delta peaks). In this formulation, the true fluid density $\rho(\vec{x}_i)$ felt by particle i at position $\vec{x}_i$ is estimated as $\langle \rho_i \rangle$ from the masses m_j and

positions $\vec{x}_j$ of all particles following:

$$\rho(\vec{x}_i) \approx \langle \rho_i \rangle \equiv \sum_j m_j W(\vec{x}_i - \vec{x}_j, h_i) \tag{2.5}$$

where h_i is the smoothing scale of particle i and $W(\vec{x}, h)$ the smoothing kernel (Dehnen & Aly, 2012). For *Magneticum Pathfinder* simulations the employed SPH kernel is a Wendland C^6 (Dehnen & Aly, 2012) with 295 neighbors (Dolag et al., 2025). Note that this is not the same as the softening length ϵ applied to the gravitational force law to smooth out close particle-particle interactions (as again the SPH particles technically represent a sampling of the density field and not single points that would strongly scatter from small-scale interactions). Updates further include the improved artificial viscosity that results in better mixing (where SPH historically struggles with shearing flows, Beck et al., 2016), with the most recent formulation (Marin-Gilabert et al., 2022) included only for the newest simulations in the suite.

Finally, post-processing of the simulation is done with the structure finder code SUBFIND Springel et al. (2001a); Dolag et al. (2009). A halo is first identified through a Friends-of-Friends linking algorithm, before subhalos are determined within that halo by finding saddle-points in the potential. All particles assigned to the these subhalos undergo an iterative unbinding procedure, removing particles that are not gravitationally bound until either the galaxy remains or the subhalo vanishes (Dolag et al., 2009, 2025). In the case that it is a real subhalo, additional properties such as the galaxy stellar mass or star formation rate are calculated from all particles linked to the subhalo.

2.3 Star Formation and Chemical Enrichment

The gas in the simulation can cool through radiative processes following the prescription by Wiersma et al. (2009), where the contributions from 11 elements (H, He, C, N, O, Ne, Mg, Si, S, Ca, Fe) are included, using pre-tabulated cooling rates assuming an optically thin gas in photo-ionization equilibrium calculated via CLOUDY Ferland et al. (1998). Additionally, heating from the CMB and UV backgrounds (coming from background galaxies) are accounted for following Haardt & Madau (2001). Never versions include an updated UV background (e.g., from Khaire & Srianand, 2019; Faucher-Giguère, 2020).

Star formation from gas particles is modeled following the basic implementation by Springel & Hernquist (2003). Below an effective density threshold ρ_{thresh} (modified by Tornatore et al. 2007 to be dependent on various other model properties, such as the gas metallicity) the gas behaves as a single-phase fluid, while above the threshold it is instead treated as a multi-phase medium as observed in the inter-stellar medium (ISM, see McKee & Ostriker, 1977). In this latter case, each gas particle consists of a mass of cold clouds entrained within a hot ambient medium (denoted by subscripts c and h), where the two phases are in pressure equilibrium. The fraction of gas in the cold phase $x = \rho_c/\rho$ is regulated here by star formation, cloud evaporation from the energy injected by supernovae, and cloud growth

through cooling (Springel & Hernquist, 2003). As the density grows so does the pressure (recall that $P = (\gamma - 1)\rho u$, where here the effective pressure of the multi-phase medium is given by $P_{\rm eff} = (\gamma - 1)\rho \cdot [(1 - x)u_h + xu_c]$). This continues until eventually the amount of energy released by supernovae Type II from formed massive stars serves to self-regulate the gas particle, resulting in a characteristic shape of the star forming branch in the plot of temperature versus density (Springel & Hernquist, 2003; Tornatore et al., 2007).

For gas above the density threshold $\rho_{\rm thresh}$, stars are then formed from the cold gas following a Schmidt (1959) law,

$$SFR = \frac{xm}{t_*} \tag{2.6}$$

where xm is the total mass in cold clouds while $t_* = t_*(\rho) = t_0^*/\sqrt{\rho/\rho_{\rm thresh}}$ is the star formation timescale (proportional to the local dynamical time of the gas), with the model parameter $t_0^* = 1.5\,{\rm Gyr}$ chosen by Tornatore et al. (2007) such that the model reproduces the observed relation between gas mass and star formation surface density (Kennicutt, 1998b).

Note crucially that the total gas mass m in Eq. 2.6 is *actually* of the form $m - m_*$, as any amount of stellar mass produced by the gas particle is *not* available to produce more stars in the future. Consequently, for the expected amount of stellar mass M_* formed over time Δt (assuming a constant fraction of cold gas x) we have

$$\begin{aligned}
SFR = \frac{{\rm d}m_*}{{\rm d}t} &= \frac{x(m - m_*)}{t_*} \\
\int_0^{M_*} \frac{{\rm d}m_*}{m - m_*} &= \frac{x}{t_*} \int_0^{\Delta t} {\rm d}t \\
[-\ln(m - m_*)]_0^{M_*} &= \frac{x}{t_*}[t]_0^{\Delta t} \\
\ln(m - M_*) - \ln(m) &= -\frac{x\Delta t}{t_*} \\
\frac{m - M_*}{m} &= \exp\left(-\frac{x\Delta t}{t_*}\right) \\
M_* &= m \cdot \left[1 - \exp\left(-\frac{x\Delta t}{t_*}\right)\right].
\end{aligned}$$

However, to instead form stars stochastically (i.e., either form one with a given stellar mass of m_* or not) instead a random number is drawn from the interval [0,1], and if it falls below the probability

$$p_* = \frac{m_g}{m_*} \cdot \left[1 - \exp\left(-\frac{x\Delta t}{t_*}\right)\right] \tag{2.7}$$

then a stellar particle is formed from the gas particle of total mass m_g. Note that for the *Magneticum Pathfinder* simulations each gas particle can spawn up to four generations of stars (so the pre-factor in Eq. 2.7 is ≈ 4), which better matches observations that find that giant molecular clouds (the birthplace of stars) do not convert 100% of their mass into stars Chevance et al. (2023).

The stellar particles formed in this manner represent a population of stars, as opposed to an individual star. This population shares the same time of formation and metallicity

(derived directly from the spawning gas particle), and is characterized by the stellar initial mass function (IMF) which gives the number of stars of given stellar mass. The *Magneticum Pathfinder* simulations assume a Chabrier (2003) IMF, with the lifetimes of stars in the population modeled following Padovani & Matteucci (1993).

Depending on their starting mass, stars may explode as supernovae Type II ($m_* > 8\,M_\odot$), as supernovae Type Ia ($0.8\,M_\odot < m_* < 8\,M_\odot$ and they must be in a binary system, where the fraction is assumed to be 7% following Greggio & Renzini, 1983), or may go through the asymptotic giant branch phase (AGB, stars of $0.8\,M_\odot < m_* < 8\,M_\odot$ that are not binaries), all of which produce characteristic amounts of metals (Kobayashi, 2025) that then enrich the surrounding gas (Tornatore et al., 2007). We assume as chemical yields for supernovae Type II those by Woosley & Weaver (1995), for Type Ia those by Thielemann et al. (2003), and for AGB stars those by van den Hoek & Groenewegen (1997). The most recent simulations assume the same Type Ia yields, but Type II as given by Kobayashi et al. (2020) and AGB yields by Karakas (2010). Metals ejected into the surrounding ISM are distributed in a weighted fashion given by the Wendland C^6 kernel (Dehnen & Aly, 2012) with 295 neighbors, see Sec. 2.2.

Beyond metals, the supernovae (but not the AGB winds) also inject energy into the surrounding ISM. The more rapidly acting supernovae Type II are treated with an instantaneous recycling approximation, meaning that the more massive stars explode on small enough timescales that their energy works to heat their parent gas particle and can thus self-regulate the star formation by evaporating the cold clouds (Springel & Hernquist, 2003; Tornatore et al., 2007). Note that the amount of stars produces is thus reduced through the fraction of mass instantly recycled in this manner, β, which is determined by the amount of massive stars, i.e., by the IMF (Springel & Hernquist, 2003).

Together with the Type Ia supernovae, these explosions are assumed to drive a galactic wind as

$$\dot{M}_{\mathrm{wind}} = \eta \cdot \dot{M}_*, \tag{2.8}$$

so proportional via the mass loading factor η to the star formation rates (more stars formed, more mass in wind driven out). Note that the mass outflow rate itself is related to the amount of energy released by the supernovae ϵ_{SNe} under the instant recycling approximation as

$$E_{\mathrm{kin,wind}} = \frac{1}{2}\dot{M}_{\mathrm{wind}} v_{\mathrm{wind}}^2 = \chi \epsilon_{\mathrm{SNe}} \dot{M}_*, \tag{2.9}$$

where χ is the fraction of the supernovae energy powering the galactic wind (Tornatore et al., 2007). Together, these equations reduce to the form $v_{\mathrm{wind}}^2/\chi = 2 \cdot \epsilon_{\mathrm{SNe}}\eta$. For the simulations of the *Magneticum Pathfinder* suite we set $v_{\mathrm{wind}} = 350\,\mathrm{km/s}$ as a model parameter, with χ and the mass loading fraction η as an outcome. Individual supernovae are assumed to inject 10^{51} erg.

2.4 Supermassive Black Holes

Supermassive black holes are now thought to play a key role in the regulation of the star formation within the most massive galaxies (Springel et al., 2005a; Croton et al., 2006; Hirschmann et al., 2014; Steinborn et al., 2015). A significant fraction η of the mass they accrete through their accretion disks is converted into feedback energy (known as active galactic nuclei feedback, or AGN feedback), which can be released either through radiation and winds (Silk & Rees, 1998) or via relativistic jets (McNamara & Nulsen, 2012) depending on how high the mass accretion rate of the black hole is (Churazov et al., 2005).

2.4.1 The Eddington Limit

When the accretion is significant, the primary mode of feedback is radiation driven. In this case, an upper limit can be derived from the balance of forces between the radiation and gravity (Eddington, 1926), where a shell of mass m at radius r feels the gravitational force of the central black hole with mass $M_{\rm bh}$ as

$$F_G = \frac{G M_{\rm bh}\, m}{r^2}. \tag{2.10}$$

Acting against gravity is the rate of momentum deposition onto the shell. For photons of energy $E = pc$, with p their momentum and c the speed of light, we can derive that the momentum per time is given by $p/t = E/(ct) = L/c$, where L is the luminosity (energy per time). However, only a fraction of the photon will exchange momentum with the electrons of the ionized hydrogen from the accretion disk via Thomson scattering. Given the surface density of the shell of $m/(4\pi r^2)$ and the opacity $\kappa = \sigma_T/m_p$, where σ_T is the Thomson cross-section and m_p is the proton mass, we thus derive for the momentum deposition per time:

$$F_\gamma = \frac{L}{c}\frac{\kappa m}{4\pi r^2}. \tag{2.11}$$

Setting $F_G = F_\gamma$, we finally get:

$$L_{\rm Edd} = \frac{G M_{\rm bh}\, m}{r^2}\frac{4\pi r^2 \cdot c m_p}{m\sigma_T} = \frac{4\pi G M_{\rm bh}\, c m_p}{\sigma_T}. \tag{2.12}$$

This luminosity is related to the accreted mass via the conversion factor of mass into feedback energy η, where for a black hole accretion at the Eddington limit then:

$$\dot{M}_{\rm Edd} = \frac{L_{\rm Edd}}{\eta_{\rm Edd} c^2} = \frac{4\pi G M_{\rm bh}\, m_p}{\eta_{\rm Edd}\, \sigma_T\, c}. \tag{2.13}$$

The efficiency η technically depends on the innermost stable orbit (ISCO, see e.g., Sala et al., 2024), but simulations typically approximate this by a fixed value of $\eta \approx 0.1$ (e.g., Springel et al., 2005a), which is the mean value of a Schwarzschield black hole that is accreting radiatively efficiently (Shakura & Sunyaev, 1973).

2.4.2 A Two-Mode Two-Phase Model for Blackholes

To account for this dependence, Steinborn et al. (2015) model the efficiency based on observational data (Davis & Laor, 2011; Chelouche, 2013) as a function of the black hole mass and current accretion rate relative to the Eddington limit, $\eta(M_{\rm bh}, f_{\rm Edd})$, with $f_{\rm Edd} \equiv \dot{M}_{\rm bh}/\dot{M}_{\rm Edd}$. They split the AGN feedback into an outflow component $P = \epsilon_o \dot{M}_{\rm bh} c^2$ that acts primarily at low accretion rates, and a radiative component $L = \epsilon_r \dot{M}_{\rm bh} c^2$ as we discussed. Then η is the total efficiency, $\eta = \epsilon_o + \epsilon_r$.

Based on the work by Churazov et al. (2005), for the radiative regime (also known as the quasar regime) Steinborn et al. (2015) use the parametric form of

$$\epsilon_r(M_{\rm bh}) = \eta A \left(\frac{\dot{M}_{\rm bh}}{\dot{M}_{\rm Edd}}\right)^{\beta}, \tag{2.14}$$

where $A \equiv \left(10^{-4} \cdot 0.05^{-2.8431-\beta}\right)$ and β is a free slope that they choose as $\beta = 0.5$. Based on observational data, Steinborn et al. (2015) further parametrize the total efficiency at the Eddington limit, which is then essentially the radiative efficiency (because radiation dominates at $f_{\rm Edd} \approx 1$), as,

$$\eta_{\rm Edd,M_{bh}} \equiv \eta_{\rm Edd}(M_{\rm bh}) \approx \epsilon_{r,\rm Edd}(M_{\rm bh}) = 0.089 \left(\frac{M_{\rm bh}}{10^8 M_\odot}\right)^{0.52}, \tag{2.15}$$

with the upper limit given by $\eta_{\rm max} = 0.42$ as the theoretical maximum efficiency of a rotating black hole (Steinborn et al., 2015; Sala et al., 2024).

For the outflow regime (also known as the radio regime), Steinborn et al. (2015) set the limit as $\epsilon_o = 0.1$ based on the work by Churazov et al. (2005), and finally then interpolate between these two limits. They choose a threshold between the two at $f_{\rm Edd} = 0.05$, such that finally:

$$\epsilon_r = \begin{cases} A \eta_{\rm Edd,M_{bh}} f_{\rm Edd}^{\beta} & \text{if } f_{\rm Edd} < 0.05 \\ \eta_{\rm Edd,M_{bh}} - 10^{-4}\, \eta_{\rm Edd,M_{bh}} f_{\rm Edd}^{-2.8431} & \text{otherwise,} \end{cases} \tag{2.16}$$

and

$$\epsilon_o = \begin{cases} 0.1 - 0.1 \cdot A f_{\rm Edd}^{\beta} & \text{if } f_{\rm Edd} < 0.05 \\ 10^{-5} f_{\rm Edd}^{-2.8431} & \text{otherwise.} \end{cases} \tag{2.17}$$

The resulting total feedback energy injected back into the surrounding gas is then given by a fraction ϵ_f of the total energy as,

$$\dot{E} = \epsilon_f \eta \dot{M}_{\rm bh} c^2, \tag{2.18}$$

where for Box3/uhr $\epsilon_f = 0.03$, with other typical values around $\epsilon_f = 0.1$. The distribution of the energy is done in a kernel weighted manner.

The above parameterizations all concern how the central supermassive black hole processes the accreted material, but we lack still the actual accretion rate from the surrounding

gas. This is commonly parametrized by the Bondi-Hoyle-Littleton accretion rate (Hoyle & Lyttleton, 1939; Bondi & Hoyle, 1944; Bondi, 1952), which assumes for the surrounding matter spherical symmetry, a lack of perturbations and magnetic fields, adiabaticity, steady initial conditions, and the absence of self-gravity and feedback (Gaspari et al., 2013). Under these (restrictive) conditions, and ignoring that in most cases the actual region of influence of the accreting black hole (given by the Bondi radius, $r_B = GM_{\rm bh}/c_s^2$, with c_s the speed of sound of the gas) is not actually resolved, the accretion rate follows as:

$$\dot{M}_B = \frac{4\pi G^2 M_{\rm bh}^2 \rho}{\left(c_s^2 + v^2\right)^{3/2}}, \tag{2.19}$$

where ρ is the gas density and v is the velocity of the gas relative to the black hole (Steinborn et al., 2015).

For the actual implementation instead the formula is

$$\dot{M}_B = \frac{4\pi \alpha G^2 M_{\rm bh}^2 \langle\rho\rangle}{\left(\langle c_s\rangle^2 + \langle v\rangle^2\right)^{3/2}}, \tag{2.20}$$

where $\langle\rho\rangle$, $\langle v\rangle$ and $\langle c_s\rangle$ are computed via kernel-weighted estimates from the gas particles (dictated by their SPH kernel size). Of note is further the boost factor α, added due to the resolution limitations (as for accurate density, velocity and speed of sound estimations those within the Bondi radius would have to be computed, which is unresolved in the simulation for hot gas or low mass black holes).

An additional key difference to common implementations (e.g., Springel et al., 2005a) is that the black hole accretion rates are determined *separately* for the hot and cold gas phases, with a temperature cut of $T = 5 \times 10^5$ K. Cold gas below that temperature threshold is boosted by $\alpha = 100$, while hot gas has $\alpha = 10$, following the results by Gaspari et al. (2013), who found that cold turbulent streams are more efficient at feeding the black hole than the Bondi-Hoyle-Littleton accretion rate predicts. Note that the total resulting accretion rate (hot + cold) is capped at the Eddington limit (Eq. 2.13).

Finally, black holes are seeded as sink particles at masses of around 10^{-4} times the stellar mass of their host galaxy at the time of seeding, which for the *uhr* resolution comes to around $M_{\rm bh} = 7 \times 10^5 M_\odot$. Note that the seeding of Box3/uhr, which was run with the Steinborn et al. (2015) model, is higher than the *Magneticum Pathfinder* default by a factor of ten, with consequences that we discuss in the next subsection and chapter 3. This seeding mass still lies below the observed stellar mass-black hole mass relation (Kormendy & Ho, 2013), making its resulting emergence a prediction of the simulation.

When seeded, black hole particles are given a separate dynamical mass equal to that of a dark matter particle (so around 100 times larger than their true mass), to allow them to remain more steady at the center of the galaxy during the early phase of their growth. This is necessary as we do not pin them to the center of the galaxies, as is often done (Vogelsberger et al., 2020). In reality, the supermassive black holes (even at low mass) are far more

massive than any individual stars and gas particles around them, and would thus sink toward the center naturally due to dynamical friction (Chandrasekhar, 1943). However, due to the comparatively coarse resolution of the simulation stellar and gas particles, interactions with particles of comparable mass could heat the black hole orbit through scattering. As such, the black hole sink particle is given this enhanced dynamical mass (which is not used for purposes of calculating any of the above introduced accretion rates and feedback efficiencies), in addition to the implementation of a subgrid model for its dynamical friction. The newest versions of the *Magneticum Pathfinder* simulation code include an updated prescription to this dynamical friction, as detailed by Damiano et al. (2024).

2.4.3 Consequences of the Model and the Future

Given the key role the Steinborn et al. (2015) model plays in the success of the *Magneticum Pathfinder* Box3/uhr simulation in matching the observed quenching rates of massive galaxies at cosmic dawn (see chapter 3 and 4), it is worthwhile to briefly consider some consequences of the parametrization.

We first note that the black hole accretion rate from Eq. 2.20 can be rewritten as:

$$\dot{M}_B = \frac{4\pi G^2 (10^8 M_\odot)^2 \, (m_H/\mathrm{cm}^3)}{(10\mathrm{km/s})^2} \times \alpha \left(\frac{\rho}{m_H/\mathrm{cm}^3}\right) \left(\frac{v_\mathrm{eff}}{10\mathrm{km/s}}\right)^{-3} \left(\frac{M_\mathrm{bh}}{10^8 M_\odot}\right)^2 \tag{2.21}$$

$$\approx 4.679 \, [M_\odot/\mathrm{yr}] \times \alpha \left(\frac{\rho}{m_H/\mathrm{cm}^3}\right) \left(\frac{v_\mathrm{eff}}{10\mathrm{km/s}}\right)^{-3} \left(\frac{M_\mathrm{bh}}{10^8 M_\odot}\right)^2 \tag{2.22}$$

$$= 4.679 \, [M_\odot/\mathrm{yr}] \times (\alpha \hat{\rho} \hat{v}_\mathrm{eff}^{-3}) \left(\frac{M_\mathrm{bh}}{10^8 M_\odot}\right)^2 \tag{2.23}$$

where we have defined the effective velocity $v_\mathrm{eff} \equiv \sqrt{c_s^2 + v^2}$ and the unitless variables $\hat{\rho} = \rho/(m_H/\mathrm{cm}^3)$ and $\hat{v}_\mathrm{eff} = v_\mathrm{eff}/(10\,\mathrm{km/s})$. This allows us to summarize the gas conditions surroundings the black hole into the factor $(\alpha \hat{\rho} \hat{v}_\mathrm{eff}^{-3})$, where we have chosen the normalizations such that they are comparable to the density and temperature (and resulting speed of sound) of star forming gas (Schaye et al., 2025).

We plot the resulting relation between the black hole accretion rate $\dot{M}_\mathrm{bh}$ and the black hole mass M_bh for different values of $\log(\alpha \rho v_\mathrm{eff}^3)$, as shown by the colorbar, in the first panel of Fig. 2.2. As is apparent, lines of equal color rise sharply with increasing black hole mass, because Eq. 2.23 is $\propto M_\mathrm{bh}^2$, until they reach the Eddington limit (Eq. 2.13). This means that more massive black holes need less favorable conditions in the surrounding gas to hit their Eddington limit, although they are also less likely to be surrounded by dense, cold gas because they reside in more massive galaxies (Kormendy & Ho, 2013) which build up a hot halo (Dekel & Birnboim, 2006). We can further see how the mass dependence of the total efficiency at the Eddington limit (Eq. 2.15) alters the slope of the relation, in between the minimum ($\eta_\mathrm{min} = 0.057$) and maximum ($\eta_\mathrm{max} = 0.42$) values.

The dash-dotted, dashed and dotted black lines in this panel equate to values of $\log(\alpha \rho v_\mathrm{eff}^3) = 2, 0$ and -2.5, respectively. These are similar to the expected conditions of a boosted cold gas

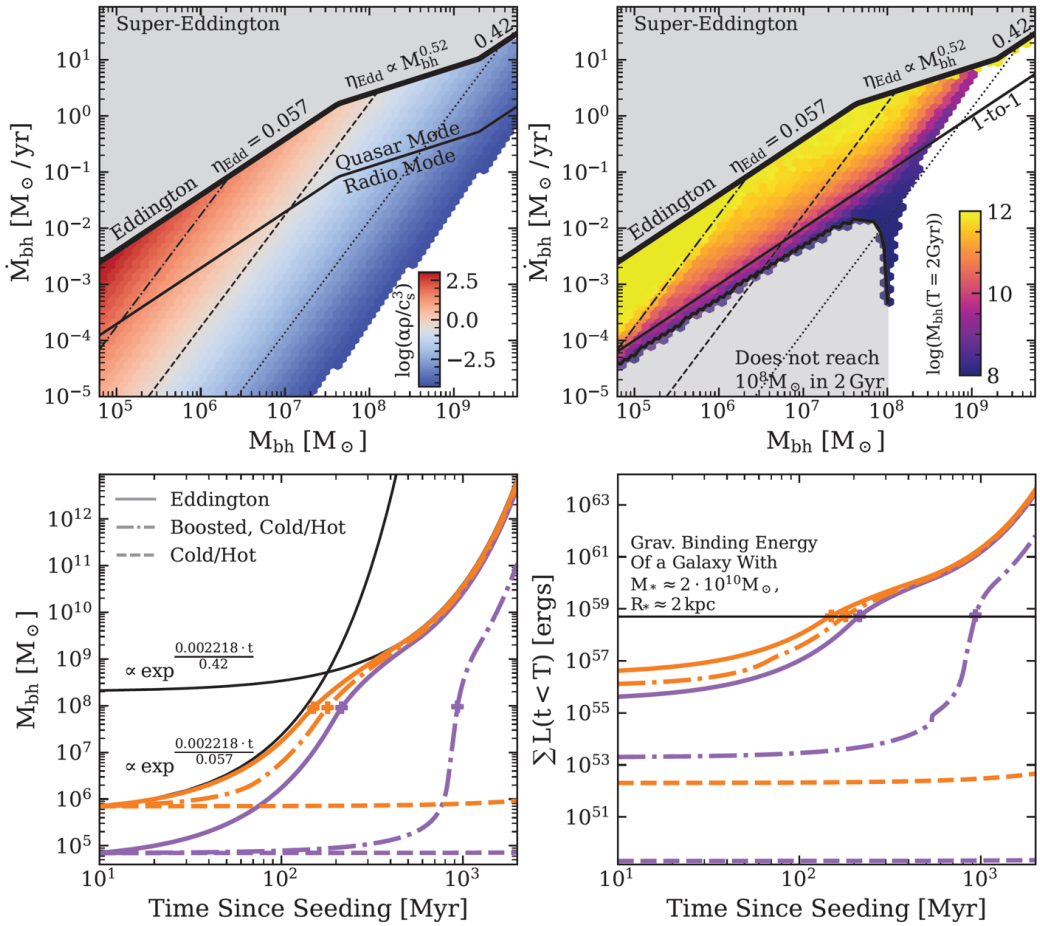


Figure 2.2. *Top row:* The black hole accretion rate $\dot{M}_{bh}$ as a function of black hole mass M_{bh}. We plot the relation for different values of $\log(\alpha\rho v_{eff}^3)$ (colorbar) in Eq. 2.23 in the *left panel*, while we color by the final black hole mass after 2 Gyr of accreting with that $\log(\alpha\rho v_{eff}^3)$ in the *right panel*. The light gray shaded area denotes super-Eddington accretion. We further plot in the *bottom row* the resulting black hole mass (*left*) and cumulative feedback energy (*right*) versus time for two different seeding masses (orange versus purple), and for different values of $\log(\alpha\rho v_{eff}^3)$, as given in the legend. The solid black (*left*) curves show the exponential limits that black holes accreting at the Eddington limit converge to, while the horizontal black line (*right*) shows the gravitational binding energy of an example galaxy.

accretion ($\alpha = 100$, $\rho = 10\, m_H/\mathrm{cm}^3$, $v_{eff} = 20\,\mathrm{km/s}$), just cold gas ($\alpha = 1$, $\rho = 10\, m_H/\mathrm{cm}^3$, $v_{eff} = 20\,\mathrm{km/s}$) and just hot gas ($\alpha = 1$, $\rho = 10\, m_H/\mathrm{cm}^3$, $v_{eff} = 150\,\mathrm{km/s}$). We see that for the first case already low mass black holes ($M_{bh} \approx 10^6 M_\odot$) can reach the Eddington accretion rate, while for the last case only the very most massive black holes do so ($M_{bh} \approx 10^9 M_\odot$).

To more clearly demonstrate the consequences, we plot in the second panel of Fig. 2.2 the same relation but with a colormap based on the final black hole mass after accreting for 2 Gyr in fixed conditions (given by the starting point $\log(\alpha\rho v_{eff}^3)$ in the diagram). This time period is comparable to that of a black hole seeded at $z = 10$ evolving until $z = 3$, when a plethora of massive quenched galaxies are observed (see chapter 3 and chapter 4). We find that only black holes growing in favorable conditions ($\log(\alpha\rho v_{eff}^3) \approx 2$) or seeded at high initial masses reach the threshold of $M_{bh} = 10^8 M_\odot$, above which the simulated galaxies in Box3/uhr typically quench.

We can see that this is because at that time the cumulative energy released by the AGN is approximately equal to the binding energy of the galaxy, $U = 3GM_*/5R_* \approx 5 \times 10^{58}$erg for $M_* = 2 \times 10^{10} M_\odot$ and $R_* = 2$ kpc in the fourth panel of Fig. 2.2. We plot there the evolution in cumulative energy against time for the dashed and dash-dotted models (cold gas without and with boost) at two different seeding masses (colors), in addition to the evolution if the black hole had grown entirely at the Eddington limit (solid line). In the third panel we do the same but for the black hole mass against time.

For this simplified model (lacking feedback and with a fixed type of environment around the black hole), we see that without the high boost factor (dash dotted), in addition to the high seeding mass of the black hole particles (orange), the black holes would not grow fast enough to reach the required amount of energy to quench the galaxies on timescales of 200 Myr (the quenching timescale we find for galaxies of Box3/uhr, see chapter 3).

Note further that black holes at the Eddington limit grow exponentially. This can be simply derived, as,

$$\frac{\mathrm{d}M}{\mathrm{d}t} = \dot{M}_{\mathrm{Edd}} \overset{Eq.\ 2.13}{=} \frac{4\pi G M}{\eta_{\mathrm{Edd}} \sigma_T c} \approx \frac{1}{450\,\mathrm{Myr}} \frac{M}{\eta_{\mathrm{Edd}}}, \tag{2.24}$$

$$\int \mathrm{d}M \frac{\eta_{\mathrm{Edd}}}{M} = \frac{1}{450\,\mathrm{Myr}} \int \mathrm{d}t, \tag{2.25}$$

$$(\ln(M) - \ln(M_0)) \cdot \eta_{\mathrm{Edd}} = \frac{t - t_0}{450\,\mathrm{Myr}}, \tag{2.26}$$

$$M(t) = M_0 \cdot \exp\left(\frac{(t - t_0)/\eta_{\mathrm{Edd}}}{450\,\mathrm{Myr}}\right) \tag{2.27}$$

where in the integral over black hole mass we have assumed a fixed η_{Edd}. In the case of the Steinborn et al. (2015) model, the value of η_{Edd} transitions from 0.057 to 0.42 going from lower to higher black hole mass, which are the values used for the two black curves plotted in the third panel Fig. 2.2. The η_{Edd} for the mass range in between is $\propto M^{0.52}$, resulting in a slope of $M(t) \propto t^{1/0.52}$.

2.5 Parameter Testing – The MagneticumDawn Simulation Suite

As discussed in Subsec. 1.1.2, the formation of early massive quiescent galaxies is a particular challenge of modern cosmological simulations. The success of the Box3/uhr simulation in reproducing those number densities (see chapters 3 and 4) has prompted the follow-up project MagneticumDAWN. In this section we discuss the new simulations of the MagneticumDAWN suite (Subsec. 2.5.1), the modified black hole seeding (Subsec. 2.5.2), and finish by presenting the results of our parameter tests from running a set of 44 simulations of $(68\,\mathrm{cMpc})^3$ size each (Subsec. 2.5.3).

Table 2.2. Overview of the simulation technical parameters for the two flagship simulations and the test suite of the MagneticumDAWN project. A breakdown of the 44 test simulations is given in Tab. 2.3 below, showing that some DawnBox4 are finished while others are still ongoing.

Sim	Boxsize $[h^{-1}\mathrm{cMpc}]$	N_{parts}	m_{gas} $[h^{-1}M_{\odot}]$	#cores	#runs	status
Box2/uhr	352	2×4276^3	7.3×10^6	147456	1	ongoing
Box4/uhr	48	2×576^3	7.3×10^6	3072	13	mostly completed
Box3/xhr	128	2×4078^3	3.9×10^5	147456	1	granted since Nov.2025

2.5.1 The Dawn Project

The MagneticumDAWN suite consists of two flagship simulations, DawnBox2 and DawnBox3, which are calibrated based on the results from a set of 44 Box4/uhr test simulations, which we term here DawnBox4. An overview of the MagneticumDAWN simulations is given in Tab. 2.2. These parameter tests cover the star formation threshold ρ_{thresh}, the wind velocity v_{wind}, a novel black hole seeding scheme, and the choice of UV background. DawnBox4 is large enough to test the impact of these parameters with a statistical set of galaxies at high redshifts, while simultaneously allowing enough resolution for an early onset of star formation. Simulations were performed with the most up-to-date developer version of the OpenGadget3 code, building on the version discussed in the prior sections here but with added improvements concerning the dynamical friction of the black holes (Damiano et al., 2024), the tracking of their spin (Sala et al., 2024), an improved viscosity scheme (Marin-Gilabert et al., 2022), as well as updated tables for the UV background which have been extended up to $z = 15$ (Di Federico et al., in prep.).

The full set of 44 simulations and their key parameters is given in Tab. 2.3. Several of these are still running until around $z \approx 2$, where the stellar mass function and quenching fractions used to calibrate our high redshift performance become less sensitive to the exact timing of the onset of quenching. The setup for the flagship simulations, including the currently ongoing DawnBox2, follows that of DawnBox4-L, which will be run until $z = 0$ to test the low-redshift development.

As a first indication of the significant impact from the new subgrid choices, we plot the gas distribution of the cosmic web in Fig. 2.3 going from high ($z = 7$) to low ($z = 0.8$) redshift for *Magneticum Pathfinder* Box4/uhr (top row) and for DawnBox4-L (bottom row). We see that already at $z = 7$ there are differences, which grow by $z = 3.4$ to the clear signal of increased temperatures in the collapsing nodes and filaments. This is because of the earlier and more rapid black hole growth that injects additional feedback energy (thus increasing the temperature) into the gas of the cosmic web, as we discuss next.

2.5.2 The Masses of the First Black Holes

Beyond the overabundance of massive quiescent galaxies, JWST observations have also found particularly massive black holes at the centers of early galaxies. These deviate quite significantly from the the local relation between black hole mass and stellar mass (Kormendy

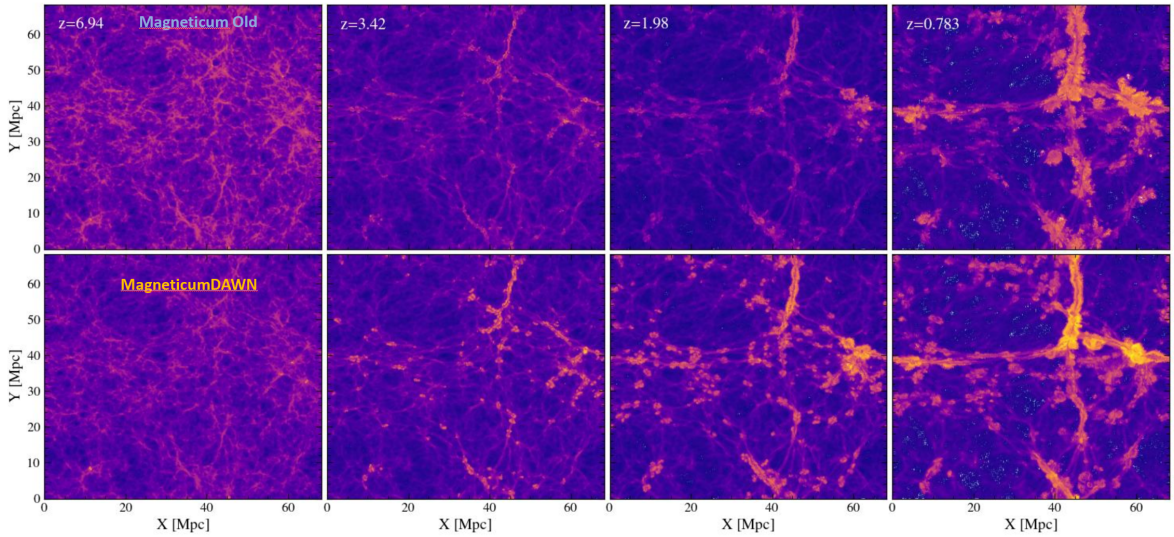


Figure 2.3. Distribution of gas in the cosmic web colored by temperature (cold to hot as lilac to yellow) from high (*left*) to low (*right*) redshift. The *top row* show a slice from the *Magneticum Pathfinder* Box4/uhr simulation, while the bottom shows the same for DawnBox4-L.

& Ho, 2013), reaching an order of magnitude higher black hole masses than expected (Farina et al., 2022; Pacucci et al., 2023; Harikane et al., 2023c; Übler et al., 2023; Maiolino et al., 2024; Hoshi et al., 2024). We collect these observations into five redshift bins (including the local $z = 0$ data) and plot the median ratio of $M_{\rm bh}/M_{\rm star}$ across cosmic time in Fig. 2.4. There is a weak evolution between $z = 2$ and $z = 0$, explaining why prior to JWST the local relation was found also at higher redshifts. Above $z = 2$, however, there is a significant evolution.

As normally we seed the black holes below the black hole-stellar mass relation, to allow them to grow naturally up to their expected mass and inject the energy through that process into their surroundings (Dolag et al., 2025), this has resulted in the *Magneticum Pathfinder* Box4/uhr black hole masses at high redshift lying well below the expected values. We note, however, that this is due to two reasons: 1) the lack of separating cold and hot gas accretion, leading to an underestimation of the density and overestimation the velocity relative to the pure cold gas accretion at high redshifts when smoothing over both phases (and thus suppressed growth following Eq. 2.23); 2) the low seeding mass, which requires particularly favorable conditions to grow initially before relaxing those conditions, as we discussed for Fig. 2.2.

Previous discussions by Steinborn et al. (2015) have already highlighted the importance of point 1), i.e., separating the cold and hot gas phases into two distinct accretion rates, which is particularly important at high redshifts when there is abundant cold gas available. However, as we show in Fig. 2.2, another key ingredient for the rapid growth of the black holes in *Magneticum Pathfinder* Box3/uhr is the high black hole seeding mass. This has the unwanted consequence of later black holes growing rapidly as well, even when there is less cold gas available (Steinborn et al., 2015), leading to overmassive black holes at later times.

Table 2.3. The suite of DawnBox4 test simulations. Under status we list those that are currently ongoing (r) and those that have finished (f). For the other columns from left to right, the wind velocity is given in km/s, the star formation threshold $\rho_{\rm thresh}$ is in internal units (where 0.5 is the fiducial *Magneticum Pathfinder* Box4/uhr value), the growth is the cold gas boost factor α as in Eq. 2.20, seeding denotes fixed or modified seeding (in the form KA, with A the prefactor in Eq. 2.28) as discussed in Subsec. 2.5.2, the UV backgrounds are WSS08 (Wiersma et al., 2009), FG20 (Faucher-Giguère, 2020), and KS19 Khaire & Srianand (2019), while $z_{\rm final}$ is the current simulation redshift. *S15* denotes feedback according to Steinborn et al. (2015), while all other runs use feedback adapted from Sala et al. (2024).

Simulation	Wind velocity	SF threshold	Growth BH	Seeding BH	UV backgr.	$z_{\rm final}$	CPU-h (millions)	Status (r/f)	Notes -
Box4-A	450	0.1	100	fixed	WSS08	1.8	1.2	f	-
Box4-B	450	0.1	50	fixed	WSS08	2.1	1.6	f	-
Box4-C	450	2	50	fixed	WSS08	2.9	1.5	f	-
Box4-D	550	5	50	fixed	WSS08	1.9	1.5	f	-
Box4-E	350	0.5	50	fixed	WSS08	3.2	1.0	f	-
Box4-F	350	0.5	10	fixed	WSS08	2.0	0.9	f	-
Box4-G	400	2.0	10	fixed	WSS08	2.9	1.0	f	-
Box4-H	400	0.2	10	fixed	WSS08	2.1	1.3	f	-
Box4-I	400	0.2	10	K100	WSS08	1.0	0.9	f	-
Box4-J	400	0.2	10	K10	WSS08	1.6	0.9	f	-
Box4-K	400	0.2	10	K10	FG20	1.5	1.0	f	-
Box4-L	500	0.2	10	fixed, 1e-4	WSS08	2.9	0.7	f	-
Box4-M	350	0.1	100	fixed	WSS08	3.2	0.7	f	-
Box4-N	350	0.1	100	fixed	WSS08	2.9	0.4	f	S+15 feedback
Box4-AA	450	0.1	50	fixed	KS19	2.6	0.3	f	-
Box4-AB	450	0.1	50	fixed	KS19	2.7	0.3	f	$\epsilon_{\rm f}$ high
Box4-AC	450	0.1	50	fixed	KS19	2.4	0.4	f	$\epsilon_{\rm f}$ low
Box4-AD	450	0.1	50	fixed	KS19	2.4	0.4	f	$\epsilon_{\rm f}$ spin
Box4-AE	450	0.1	50	fixed	KS19	2.0	0.5	f	$\mathrm{eps}_{\rm gas}$ =1.4
Box4-AF	450	0.1	50	fixed, 5e-5	KS19	1.2	0.6	f	-
Box4-AG	450	0.1	50	fixed, 5e-5	FG20	3.8	0.2	f	-
Box4-AH	450	0.1	50	K10, 10%	KS19	1.8	0.6	f	-
Box4-AI	450	0.05	50	fixed	KS19	2.4	0.4	f	-
Box4-AJ	550	0.1	50	fixed	KS19	1.3	0.6	f	-
Box4-AK	550	0.1	50	fixed	FG20	3.8	0.2	f	-
Box4-AL	550	0.1	50	fixed, 1e-4	KS19	1.8	0.5	f	-
Box4-AM	550	0.1	50	K10, 10%	KS19	1.7	0.6	f	-
Box4-AN	550	0.1	50	K5, 5%	KS19	1.5	0.6	f	-
Box4-AO	700	0.1	50	fixed, 1e-4	KS19	3.4	0.1	f	-
Box4-BA	500	0.1	50	fixed, 1e-4	KS19	1.5	0.6	f	$\mathrm{eps}_{\rm gas}$ =2.25
Box4-BB	500	0.1	50	fixed, 1e-4	KS19	1.8	0.5	f	$\mathrm{eps}_{\rm gas}$ =2.25
Box4-BC	500	0.1	50	fixed, 5e-5	KS19	2.0	0.5	f	$\mathrm{eps}_{\rm gas}$ =2.25
Box4-BD	500	0.1	100	fixed, 5e-5	KS19	2.0	0.5	f	$\mathrm{eps}_{\rm gas}$ =2.25
Box4-BE	550	0.1	50	fixed, 1e-4	KS19	3.1	0.2	f	$\mathrm{eps}_{\rm gas}$ =2.25
Box4-BF	550	0.1	50	fixed, 1e-4	KS19	3.2	0.2	f	$\mathrm{eps}_{\rm gas}$ =1.4
Box4-D1	500	0.1	50	K5, 5%	KS19	0.5	0.6	r	-
Box4-D2	500	0.1	50	fixed, 1e-4	KS19	2.9	0.2	r	-
Box4-D3	500	0.1	50	K5, 5%	KS19	3.4	0.2	r	No BH spin
Box4-D4	500	0.1	50	K5, 5%	KS19	4.0	0.2	r	SnII=5e51 erg
Box4-D5	500	0.05	50	K5, 5%	KS19	4.2	0.2	r	-
Box4-D6	400	0.05	50	K5, 5%	KS19	2.8	0.2	r	-
Box4-D7	400	0.01	50	K5, 5%	KS19	3.4	0.2	r	-
Box4-D8	400	0.05	100	K5, 5%	KS19	2	0.4	r	-
Box4-D9	400	0.05	100	fixed, 5e-5	KS19	4.5	0.1	r	-

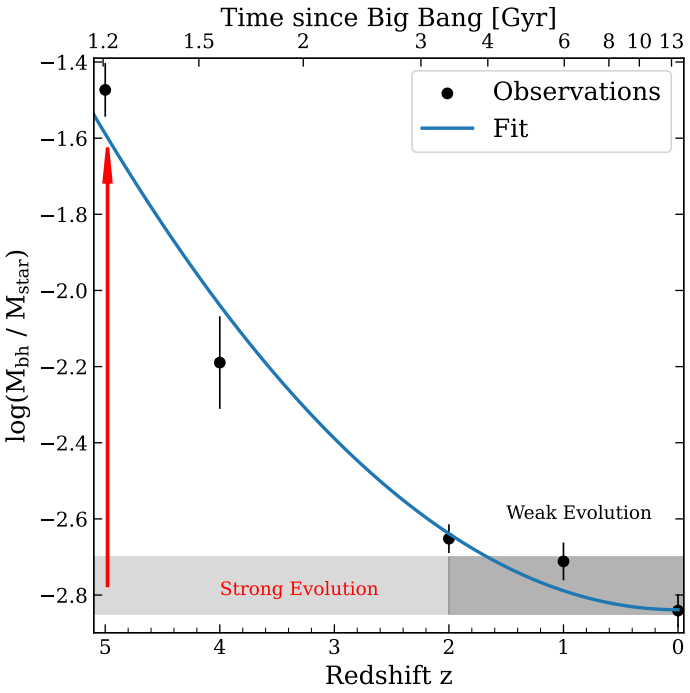


Figure 2.4. Ratio of black hole mass to stellar mass plotted against redshift, both for binned observational data (black points) and our best-fit (blue line). The observations at high redshifts of $z > 2.5$ are by Farina et al. (2022); Harikane et al. (2023c); Übler et al. (2023); Maiolino et al. (2024); Hoshi et al. (2024), while the included lower redshift observations are discussed in more detail by Dolag et al. (2025).

To remedy this, we implement a redshift dependent black hole seeding, following the fit (blue line) from Fig. 2.4 as a baseline:

$$\left(\frac{M_{\rm bh}}{M_{\rm star}}\right)(z) = A \cdot 0.00145 \times 10^{0.05 z^2}, \tag{2.28}$$

with A a free model parameter. We have tested seeding on ($A = 1$) and below the relation ($A < 1$), and have found the best results when seeding at $A = 5\%$ of the observed relation. Note that because observations above $z > 5$ are sparse, and with large uncertainties (e.g., Farina et al., 2022), we further limit the maximum seeding fraction to $\min(M_{\rm bh}/M_{\rm star}, 5\%)$, as otherwise early black holes can begin rivaling the host galaxy in total stellar mass very quickly because of the squared dependence of the accretion rate on black hole mass $\dot{M}_{\rm bh} \propto M_{\rm bh}^2$ (see Eq. 2.20).

At low redshifts this relation essentially behaves like a fixed seeding mass of $M_{\rm bh,seed} = 3.5 \times 10^5 M_\odot$ for galaxies of stellar mass $M_* = 5 \times 10^9 M_\odot$, around a factor two lower than the value of $M_{\rm bh,seed} = 7 \times 10^5 M_\odot$ used for the *Magneticum Pathfinder* Box3/uhr simulation.

The seeding of more massive black holes at higher redshifts is motivated through theory, which finds at earlier times higher possible black hole seeds as a result of either the death of massive Population III stars, or by forming them through a direct collapse (Jeon et al., 2025a,b). We have extensively tested other parameters, such as altering the stellar winds or star formation threshold, as shown in Tab. 2.3, as well as altering the black hole itself through its feedback coupling factor η (see Sec. 2.4), which we set high, low, or couple directly to the

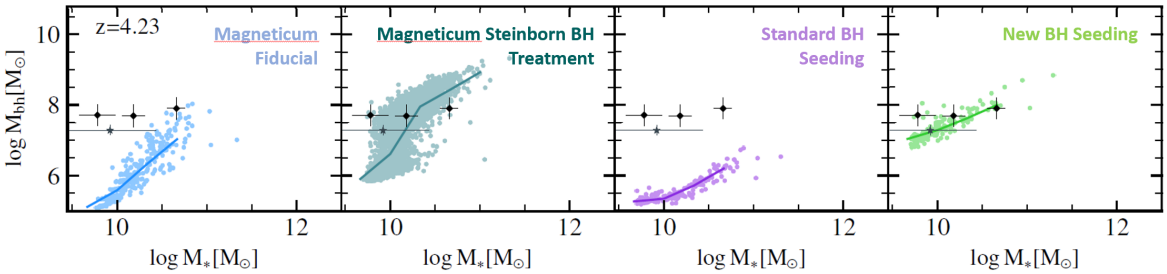


Figure 2.5. The black hole mass-stellar mass relation at $z = 4.2$, going from *left* to *right* for the *Magneticum Pathfinder* simulation Box4/uhr (lacking cold/hot separation), Box3/uhr (including cold/hot and high fixed seeding following Steinborn et al., 2015), our standard seeding (including cold/hot but at low fixed seeding) and our new modified redshift-dependent seeding model in the Dawn-Box4 simulation (including cold/hot accretion). Observations by Harikane et al. (2023c); Maiolino et al. (2024) are shown as black points.

black hole spin following Sala et al. (2024). In all cases, we find that only the runs with the modified black hole seeding mass reach the observed black hole mass-stellar mass relation at high redshifts, as we plot for $z = 4.2$ in Fig. 2.5.

2.5.3 The Interplay between Star Formation, Black Hole Feedback, and UV Background – a Parameter Study

The comparison of simulation results with observed scaling relations is a powerful tool to constrain the subgrid model parameters (e.g., Dolag et al., 2025). Having discussed the need for a higher black hole seeding to reproduce the observed black hole masses, we turn here to consider four other relations under the aspect of varying only parameters of the star formation model (see 2.3). We test in particular the star formation (SF) threshold ρ_{thresh} and wind velocity v_{wind}. For the first, we use the test simulations "a50t2w450" ($\rho_{\mathrm{thresh}} = 2$, purple), "a50t01w450" ($\rho_{\mathrm{thresh}} = 0.1$, red), and "$\mathrm{D_{sf}}$" ($\rho_{\mathrm{thresh}} = 0.05$, gold), which all have a fixed wind velocity of $v_{\mathrm{wind}} = 450\,\mathrm{km/s}$. For the second set, we again use "a50t01w450" ($v_{\mathrm{wind}} = 450\,\mathrm{km/s}$, red), in addition to "$\mathrm{D_{wind}}$" ($v_{\mathrm{wind}} = 550\,\mathrm{km/s}$, dark blue) and "$\mathrm{D_{w700}}$" ($v_{\mathrm{wind}} = 700\,\mathrm{km/s}$, orange), which all have a star formation threshold of $\rho_{\mathrm{thresh}} = 0.1$, as well as the original *Magneticum Pathfinder* Box4/uhr simulation "M4" ($v_{\mathrm{wind}} = 350\,\mathrm{km/s}$, light blue) for comparison (but note that it has a higher threshold of $\rho_{\mathrm{thresh}} = 0.5$).

We begin with the cosmic star formation rate density (SFRD), which is known to peak at $z \approx 2$ (e.g., Madau & Dickinson, 2014) and was previously assumed to strongly decrease toward both lower and higher redshifts but is now shown to flatten at $z > 8$ (Harikane et al., 2023b). As shown in Fig. 2.6, our simulations well reproduce the behavior at $z < 2$, though they tend to lie above the observed values between $z = 2$ and $z = 8$, albeit being closer than the previous results from *Magneticum Pathfinder* Box4/uhr. We further find that a lower SF threshold or higher wind velocity both reduce the total amount of SF, with the former doing so at all redshifts while the later impacts $z < 7$. Note that neither parameter has increased the amount of energy injected by supernovae. However, they do alter when and how this feedback is injected, with a lower SF threshold making SF take place in lower mass halos that

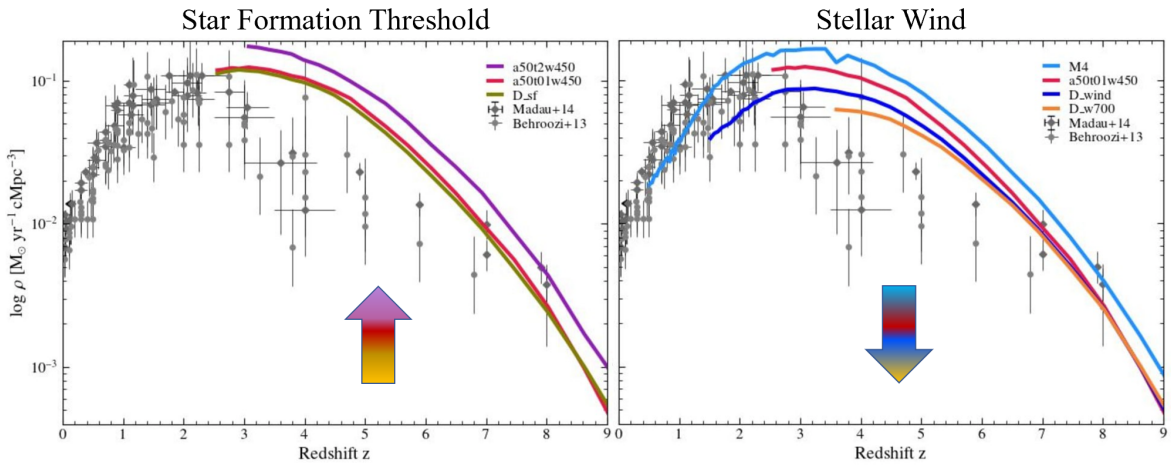


Figure 2.6. The cosmic star formation rate density of galaxies with $M_* \geq 10^8 M_\odot$ for our test sets with varying SF threshold (*left*) and wind velocity (*right*), with the arrows showing the direction the relation moves when increasing the respective parameter. We plot also observations compiled by Moster et al. (2013) and Behroozi et al. (2013) as black points.

are more vulnerable to galactic winds (Bland-Hawthorn et al., 2015), while a higher wind velocity results in less individual gas particles being kicked, but those that are kicked are done so with greater velocities and can thus leave the higher mass galaxies that are forming later. Interestingly, we have tested a change in UV background and found nearly no impact on the SFRD, indicating that this only marginally alters the cooling rate of the early gas (and perhaps the very first galaxies, or those of even lower mass than we can reasonably resolve in these test simulations).

Another important scaling relation is the stellar mass function through cosmic time, which shows the number of galaxies of a given stellar mass per comoving volume and logarithmic bin in stellar mass. We plot this in Fig. 2.7 for the set with varying SF threshold (top two rows) and varying wind velocity (bottom two rows), each going from $z = 12.5$ (top left) to $z = 2.75$ (bottom right), and include observational data as black points (Ilbert et al., 2013; Stefanon et al., 2021; Weaver et al., 2023; Navarro-Carrera et al., 2024; Harvey et al., 2025).

We find that increasing the SF threshold both increases the amount of massive galaxies while lowering the amount of lower mass galaxies. This is because the star formation is delayed, moving it farther into the center, where for massive galaxies this means that the stellar feedback is less effective at quenching them while for lower mass galaxies it can entirely suppress them from forming. By contrast, increasing the wind velocity only suppresses the number of higher mass galaxies $M_* \geq 10^{10} M_\odot$. It is interesting that there is little effect at intermediate masses of $M_* \approx 10^9 M_\odot$, where the amount of stellar feedback is thought to regulate their formation. This implies that for those galaxies it is not the ejection velocity that limits their suppression, but the total energy injected (which is not altered by changing the wind velocity, see Sec. 2.3).

In Fig. 2.8 we then consider the stellar mass-size relation, again plotting the set with varying SF threshold in the first two rows, and the varying wind velocity in the bottom two. We find that the SF threshold does not significantly alter the sizes of massive galaxies, but

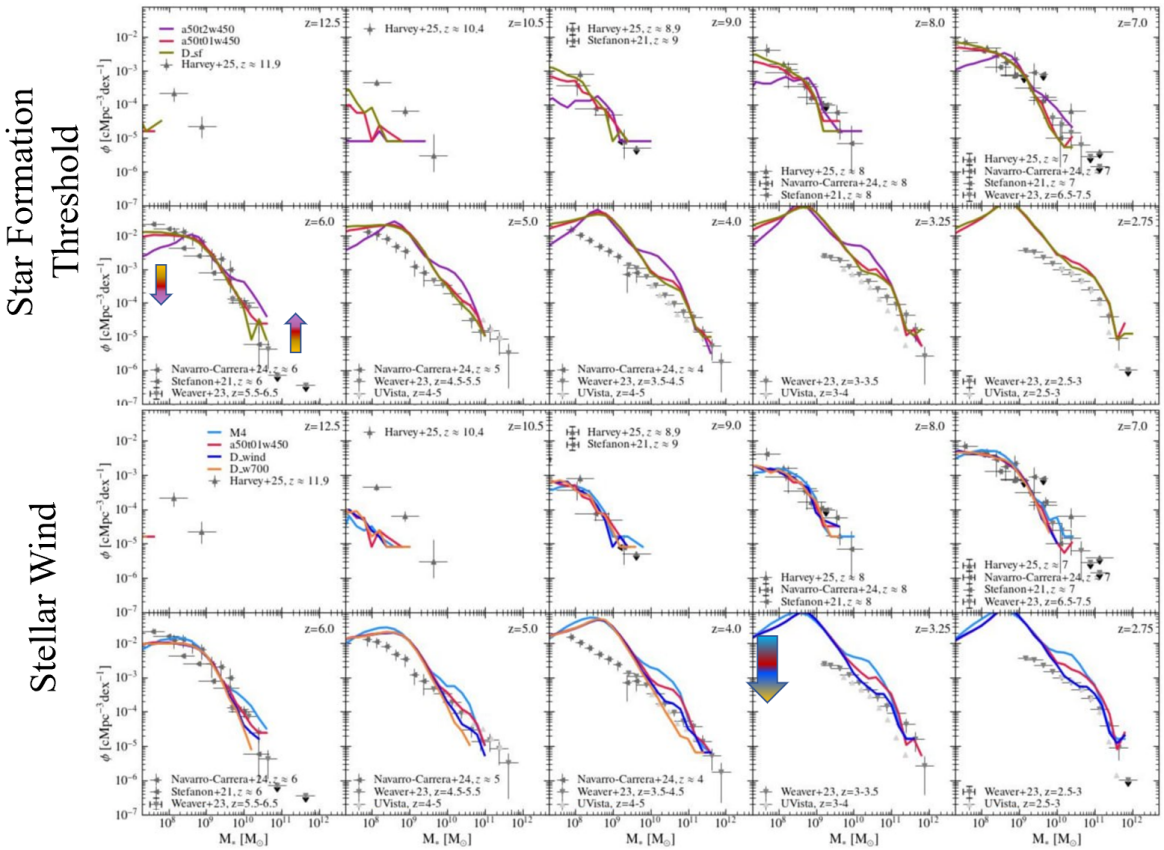


Figure 2.7. The stellar mass function of galaxies in our two sets of test simulations, where we vary the SF threshold (*top two rows*) or galactic wind velocity (*bottom two rows*). We indicate the direction that an increase in the respective parameter alters the relation with colored arrows. Included are observations (black points) from UltraVista by Ilbert et al. (2013), as well as newer observations by Stefanon et al. (2021); Weaver et al. (2023); Navarro-Carrera et al. (2024) and Harvey et al. (2025).

does have a strong impact on galaxies of $M_* < 5 \times 10^{10} M_\odot$, with a higher threshold leading to more compact galaxies, as expected. Conversely, the wind velocity has no impact on these lower mass galaxies (as expected from the results of Fig. 2.7), but does make the massive galaxies more puffy if it is higher.

We then turn to the number density of galaxies across cosmic time in Fig. 2.9, plotting them for different limiting stellar masses (columns) and for our two sets of simulations (top and bottom row). We find that the highest mass galaxies are the most insensitive to both SF threshold and wind velocity, unsurprisingly. For lower mass galaxies $M_* < 10^{11} M_\odot$, an increasing SF threshold increases the number density as well as shifts the emergence of the first galaxies to earlier times, while increasing wind velocity decreases the number density and shifts the first galaxies to later times.

What is apparent when comparing with the observations (pink data points) is that, while there are models which well capture the total number densities given by Chworowsky et al. (2023) and Brammer et al. (2011) for the intermediate and high mass galaxies, they all fail to capture the early rise of quiescent galaxies with $M_* > 10^{10} M_\odot$ as observed by Valentino et al. (2023) and Baker et al. (2025a). Indeed, while the original *Magneticum Pathfinder* Box4/uhr

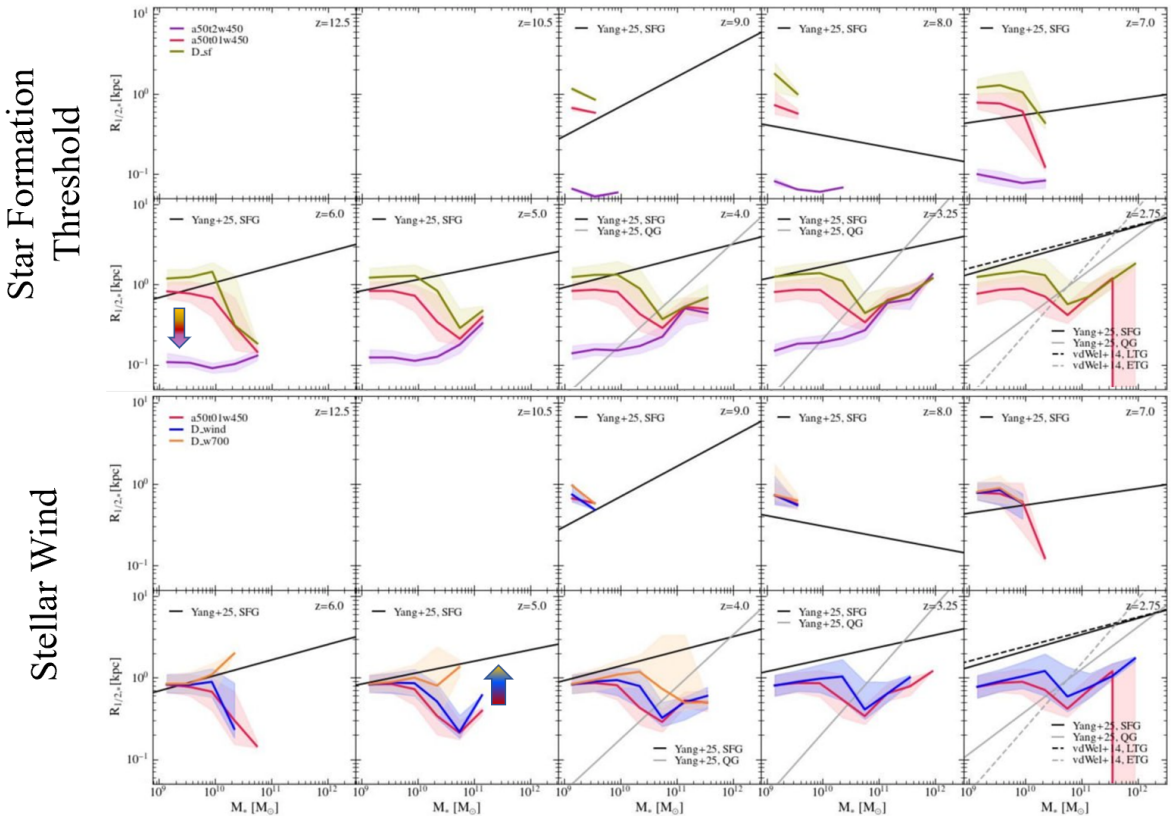


Figure 2.8. The mean and 1σ-scatter in the stellar mass-size relation of simulated galaxies from our two sets of test simulations, where we vary the SF threshold (*top two rows*) or galactic wind velocity (*bottom two rows*). We plot the observational relations by van der Wel et al. (2014) and Yang et al. (2025) as solid and dashed lines, respectively.

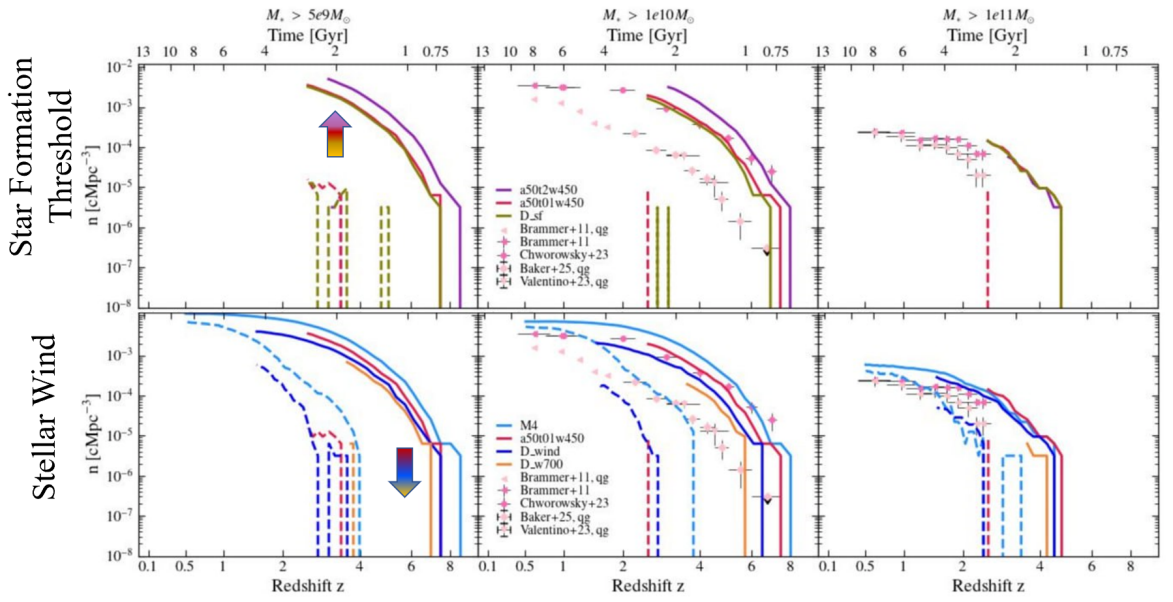


Figure 2.9. The number density of all (solid) and quenched (dashed) simulated galaxies with $M_* > 5{\times}10^9 M_\odot$ (*left column*),$M_* > 10^{10} M_\odot$ (*middle column*) and $M_* > 10^{11} M_\odot$ (*right column*), as drawn from our two sets of test simulations, where we vary the SF threshold (*top row*) or galactic wind velocity (*bottom row*). We plot observations of the total number density (bright pink points) by Brammer et al. (2011) and Chworowsky et al. (2023), as well as the quiescent number densities by Brammer et al. (2011); Valentino et al. (2023) and Baker et al. (2025a).

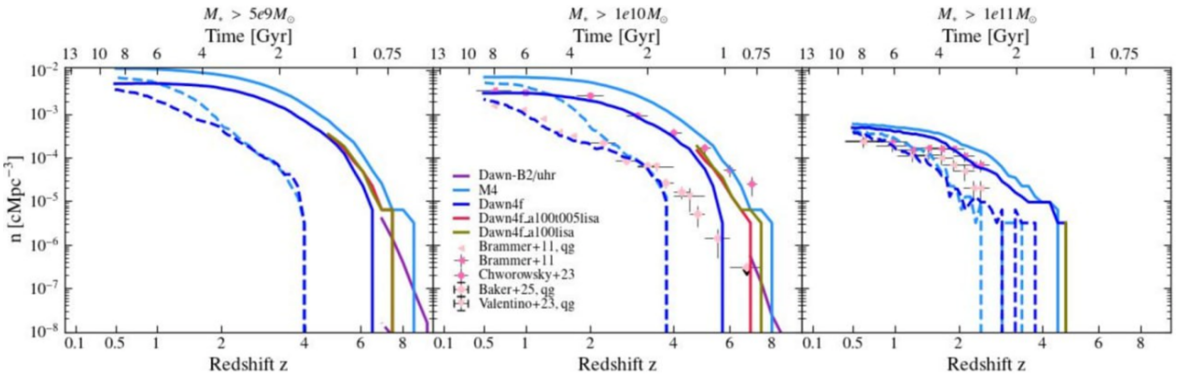


Figure 2.10. As Fig. 2.9 but with a DawnBox4 simulation that includes the modified black hole seeding (dark blue). This much better captures the early rise in quiescent galaxies, without overshooting their number (and the total number of galaxies) at later times.

simulation does overshoot the total number density somewhat, it at least produces early $z \approx 4$ quiescent galaxies.

We therefore plot the same figure also for a set of simulations including a DawnBox4 run with our redshift dependent black hole seeding with $A = 0.05$ (dark blue), as described in Subsec. 2.5.2. As is apparent for galaxies with $M_* > 10^{10} M_\odot$ (middle panel), this model now captures both the observed total and quiescent number densities. In particular the early rise, plateau, and then late rise in quiescent galaxies is reproduced remarkably well. The very earliest quiescent galaxies at $z > 4$ likely require larger simulation volumes to correctly capture, as we discuss in chapters 3 and 4.

Finally, we consider a scaling relation that the original *Magneticum Pathfinder* suite of simulations captured particularly well, namely that of the stellar angular momentum versus stellar mass (van de Sande et al., 2019; Dolag et al., 2025). The stellar angular momentum is an excellent tracer for the morphology of galaxies, as found both for observations (e.g., Romanowsky & Fall, 2012) and simulations (e.g., Teklu et al., 2015). We therefore choose four DawnBox4 simulations (top to bottom rows) and plot in Fig. 2.11 the relation of stellar angular momentum to stellar mass for the simulated galaxies from $z = 6.9$ (left column) to $z = 2.8$ (right column). The first two simulations vary only in their SF threshold, while the latter two include our redshift dependent black hole seeding (with the final one additionally having a different UV background). We find that the difference in varying the SF threshold to 2 (second row) has a far more significant impact on the galaxy angular momentum than the black hole seeding does, with the first, third and fourth simulations all showing comparable relations. Crucially, they are similar not only in median behavior (solid colored line) but also in their scatter, and manage to reach the high angular momentum observed in late type galaxies (Fall & Romanowsky, 2013) – where the second simulation with high SF threshold fails to do so.

In summary, we find that our redshift-dependent black hole seeding model efficiently solves the current challenges to cosmological simulations of the observed early rapid growth of black holes, as well as the high number densities of quiescent galaxies, without altering the existing scaling relations. This supports the idea that the earliest black hole seeds have a

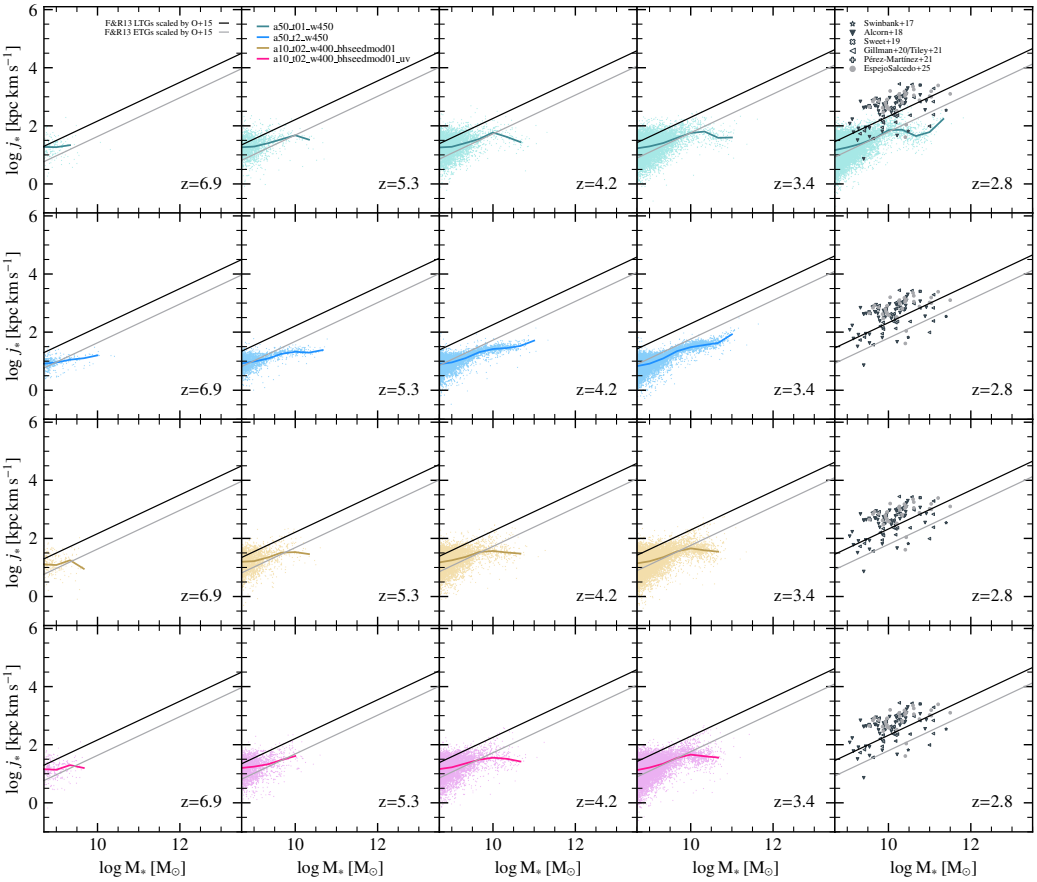


Figure 2.11. The stellar mass-angular momentum relation at $z = 6.9$ (*left column*) to $z = 2.8$ (*right column*) for simulated galaxies with $M_* > 3 \times 10^8 M_\odot$ drawn from four DawnBox4 simulations (*top to bottom row*), with their median relation plotted as solid colored lines. The top two rows vary only in their SF threshold, while the bottom two include the modified black hole seeding prescription described in Subsec. 2.5.2, with $A = 0.1$. Note that the simulation plotted in the last row additionally includes a different UV background, namely that by Faucher-Giguère (2020). The observed relations by Fall & Romanowsky (2013) for late and early type galaxies are plotted as solid lines.

different origin than those formed at later times, perhaps indeed coming from Population III or formed in a direct collapse (Jeon et al., 2025a,b).

παντὶ γάρ μοι δοκεῖ δῆλον ὅτι αὕτη [ἀστρονομίας] γε ἀναγκάζει
ψυχὴν εἰς τὸ ἄνω ὁρᾶν καὶ ἀπὸ τῶν ἐνθένδε ἐκεῖσε ἄγει.

Plato, *The Republic*, Book VII, circa 375 BCE

3

Blowing Out the Candle: How to Quench Galaxies at High Redshift – an Ensemble of Rapid Starbursts, AGN Feedback, and Environment

This chapter was published as Kimmig et al., 2025, ApJ 979, 15.

Recent observations with JWST and ALMA have revealed extremely massive quiescent galaxies at redshifts of $z = 3$ and higher, indicating both rapid onset and quenching of star formation. Using the cosmological simulation suite Magneticum Pathfinder we reproduce the observed number densities and stellar masses, with 36 quenched galaxies of stellar mass larger than $3 \times 10^{10} M_\odot$ at $z = 3.42$. We find that these galaxies are quenched through a rapid burst of star-formation and subsequent AGN feedback caused by a particularly isotropic collapse of surrounding gas, occurring on timescales of around 200Myr or shorter. The resulting quenched galaxies host stellar components which are kinematically fast rotating and alpha-enhanced, while exhibiting a steeper metallicity and flatter age gradient compared to galaxies of similar stellar mass. The gas of the galaxies has been metal enriched and ejected. We find that quenched galaxies do not inhabit the densest nodes, but rather sit in local underdensities. We analyze observable metrics to predict future quenching at high redshifts, finding that on shorter timescales < 500 Myr the ratio $M_{\rm bh}/M_*$ is the best predictor, followed by the burstiness of the preceding star-formation, $t_{50} - t_{90}$ (time to go from 50% to 90% stellar mass). On longer timescales, $>$ 1Gyr, the environment becomes the strongest

predictor, followed by $t_{50} - t_{90}$, indicating that at high redshifts the consumption of old and lack of new gas are more relevant for long-term prevention of star-formation than the presence of a massive AGN. We predict that relics of such high-z quenched galaxies should best be characterized by a strong alpha enhancement.

3.1 Introduction

In the last few years, the high redshift universe beyond $z = 2$ has become increasingly accessible to observations due to instruments like ALMA and JWST. The detection of galaxies already massive at redshifts beyond $z = 6$ (e.g., Finkelstein et al., 2015; Oesch et al., 2018; Bouwens et al., 2020; Adams et al., 2023; Curtis-Lake et al., 2023; Donnan et al., 2023; Labbé et al., 2023) has challenged our current understanding of structure formation, as models and simulations struggle to reproduce and predict the properties of such galaxies at high redshifts (e.g. Harikane et al., 2022b; Kakimoto et al., 2024). This has led to the question whether these galaxies could feasibly exist within the framework of ΛCDM, as the measured masses were larger than what models predicted to be allowed (e.g., Behroozi & Silk, 2018; Tacchella et al., 2022b; Boylan-Kolchin, 2023; Lovell et al., 2023a). However, these early JWST observations were usually obtained using photometry, and spectroscopic follow-ups have found several of them to reside at lower redshifts (Harikane et al., 2023a) or to be less massive than originally assumed (e.g., Desprez et al., 2023). Furthermore, high-redshift properties may be particularly challenging for current generation spectral energy distribution (SED) codes (Wang et al., 2023).

Beyond the existence of particularly massive galaxies, the detection of quiescent galaxies at high redshift provides another challenge to our understanding of galaxy and structure formation (e.g., Nanayakkara et al., 2024; Carnall et al., 2023a; Long et al., 2023; Carnall et al., 2023b; Glazebrook et al., 2023; Ito et al., 2024). At low redshifts, several different mechanisms to quench a galaxy are known: Most prominently, mergers between massive galaxies involving little gas are a common cause for quenching (e.g., Barnes, 1988, 1992; Barnes & Hernquist, 1996; Bois et al., 2011; Dekel & Cox, 2006). In such cases, the feedback from central supermassive black holes (SMBH), so called active galactic nucleus (AGN) feedback, is thought to be an important contributor to the quenching (e.g., Combes, 2017; Man & Belli, 2018). However, also stellar feedback has been shown to be efficient in supressing star formation (e.g., Feldmann & Mayer, 2015). Another established quenching mechanism for galaxies beyond $M_{\rm vir} \approx 10^{12} M_{\odot}$ is mass quenching, as a galaxy that reaches such large halo masses inhabits a hot gas halo that cannot be penetrated by cold inflowing streams, cutting the galaxy off from the continuous inflow of cold gas from the cosmic web (Birnboim & Dekel, 2003; Dekel & Birnboim, 2006). Finally, the hot gas environment of galaxy groups and particularly galaxy clusters prohibit cold gas supply to their member galaxies, independent of the galaxies' mass, and thus all galaxies in such environments eventually run out of gas and quench. This family of processes acting in a cluster environment

is known as environmental quenching (e.g., Gabor & Davé, 2015; Zinger et al., 2016; Lotz et al., 2019).

However, all of these processes work on timescales larger than those available to the quenched galaxies found when the Universe was not even 1 Gyr old. Even in the quenched galaxy population observed at low redshifts, some galaxies are found to have quenched at very early times, while for many others the quenching occurred on longer timescales more recently (Carnall et al., 2018; Tacchella et al., 2022a). So the question arises how such galaxies can effectively quench at such early times.

Observations report evidence for the quenching at cosmic noon to be rapid in nature, especially before $z \approx 2$, preceded by a rapid and massive starburst (Carnall et al., 2018; Tacchella et al., 2023; Kakimoto et al., 2024). The star formation timescales of these galaxies are found to be on the order of 150 – 300 Myr. For example, Belli et al. (2023) report a galaxy at $z \approx 2.5$ with a starburst time of less than 300 Myr, while Carnall et al. (2023b) find a quenched galaxy at $z = 4.658$ with a stellar mass of $M_* \approx 3.8 \times 10^{10} M_\odot$ which was formed in a starburst event lasting around 200 Myr. At low redshifts, such a massive starburst followed by rapid quenching is usually only known for Post-Starburst (PSB) galaxies (e.g., Wild et al., 2016), caused either by rapid AGN quenching due to merging in case of field-PSBs, or by the cluster environment (e.g., Lotz et al., 2021). Overall, observations indicate that rapid quenching is increasingly more common at higher redshifts than at lower redshifts (Belli et al., 2019; Park et al., 2023), most likely caused by efficient gas funneling to the galaxy centers.

Evidence for a co-evolution of starbursts and AGN feedback through cosmic time has been reported from the GAMA/DEVILS survey by D'Silva et al. (2023a), with the star formation rate density and the AGN density rising until $z \approx 2$, before declining again. Similarly, Tozzi et al. (2023) found a co-evolution between star formation and black hole accretion activity, albeit not all galaxies that show AGN activity are found to be quenched, indicating that AGN feedback does not always lead to immediate quenching of the star formation in a galaxy. Similarly, in their review on black holes at cosmic noon, Fan et al. (2023) also report on the co-evolution of star formation and black hole properties. For redshifts between $z = 1$ to $z = 5$, Ito et al. (2022) also report low luminosity AGN to be present in star forming and quiescent galaxies, although the luminosity of the AGN is larger for the quiescent galaxies.

Furthermore, while usually strong outflows are associated with AGN driven quasars (e.g., Vayner et al., 2023), there are also outflows detected in galaxies without direct evidence for an AGN to be responsible (Wylezalek et al., 2020). This implies either that the outflows originate from a different source, or that the outflows are more long lasting than the AGN activity itself. Similarly, neutral outflows are reported by Belli et al. (2023) for a rapidly quenching galaxy at $z = 2.445$ which exhibits neither X-ray nor radio emissions, and only gas emission lines might indicate an AGN as the source of these outflows. In fact, JWST observations by Veilleux et al. (2023) recently showed detailed imaging of an active AGN outflow at $z = 1.6$ that burns a channel into the surrounding medium. This indicates that it is not the mechanical feedback that is impacting the galaxy but rather the combination of

radiative feedback and heating from the outflow which could contribute to the lack of gas in the galaxy. Nevertheless, it is possible that the gas could also have already been driven out previously. A complete picture of the interplay between star formation, AGN feedback, and quenching at high redshifts has yet to be established. Nonetheless, it is becoming apparent that AGN activity and massive rapid starbursts are coupled and connected to the process that quenches galaxies at high redshifts.

Simulations and models that have been able to reproduce the observed overall star formation rate density have found particularly the number density of quenched galaxies to depend on the included AGN feedback. In the family of IllustrisTNG and MilleniumTNG models, MilleniumTNG is large enough to successfully reproduce star formation rate densities and number densities of high redshift galaxies (Kannan et al., 2023). However, the quenching solely depends on the onset of the AGN feedback (Park et al., 2023). As shown by Hartley et al. (2023) and Kurinchi-Vendhan et al. (2023), as soon as the kinetic feedback kicks in the galaxies are quenched. This directly correlates the possible quenching times with the timescales implemented for the onset of AGN feedback, which vary strongly between simulations. In this framework, however, the observed extremely early quenching times found for example by Nanayakkara et al. (2024), Glazebrook et al. (2023), or Carnall et al. (2023a,b) cannot successfully be reproduced, as shown by Hartley et al. (2023), and the number densities of quiescent galaxies at $z = 4 - 5$ are noticeably lower than observed. This is true also for other cosmological simulations including EAGLE (Schaye et al., 2015), IllustrisTNG (Pillepich et al., 2018b), Astrid (Ni et al., 2022) and FLARES (Lovell et al., 2021) as shown by Weller et al. (2025), Long et al. (2023) and Gould et al. (2023), which are compiled by Remus & Kimmig (2025). Furthermore, Tollet et al. (2019) found for the NIHAO simulations that stellar feedback from supernovae can generate outflows that reach beyond the virial radius, and therefore can have non-negligible impact on the feedback energy budget. That quenching can potentially also occur due to stellar feedback alone was also found by Merlin et al. (2012). Nevertheless, feedback from AGN plays an important role in the quenching of galaxies at cosmic noon: as shown by Lovell et al. (2023b) for the FLARES zoom simulations, comparing runs with and without AGN feedback, quenching does not occur if the AGN feedback is not included.

On the modeling side, D'Silva et al. (2023b) compared high-redshift quenching from the cosmological simulation FLARES with predictions from the semi-analytic model SHARKS, and found the onset of quenching to be earlier in FLARES than in SHARKS due to stronger feedback. Lagos et al. (2024) showed that SHARK 2.0, with a new AGN model that accounts for angular momentum transfer to the black hole spin as well as angular momentum transfer from the intergalactic medium to stars, can now successfully reproduce the observed fractions of quenched galaxies. Using the semi-analytic model on the Uchuu simulations, Houston et al. (2023) reported a trend for galaxies with masses below $\log(M_*/M_\odot) = 9$ and above $\log(M_*/M_\odot) = 11.5$ to spend the longest overall time as quenched galaxies, with the low mass galaxies switching star formation on and off, while the high mass galaxies tend to quench more permanently. This is similar to the results by Merlin et al. (2012) who also

found massive galaxies to be quenched by short powerful starburst, while small mass galaxies switch on and off due to small starbursts. The latter was also reported by Dome et al. (2023) for the small mass haloes in IllustrisTNG.

To disentangle the contributions of stellar feedback from the starbursts and the SMBHs, but also address the question of the importance of the environment on quenching of galaxies at high redshifts, we study the processes that lead to the quenching of galaxies at high redshifts using the Magneticum[1] pathfinder simulation suite, reviewed shortly in Sec. 3.2. In Sec. 3.3, we analyze the global properties of the simulated galaxies in comparison to high-redshift observations, demonstrating that the simulation is well suited for this study. Furthermore, the sample of quenched galaxies is introduced, where for more details on the overall properties of the quenched galaxy sample we refer the reader to the companion paper of this study by Remus & Kimmig (2025). Sec. 3.4 then analyzes in detail the processes that lead to quenching, including quenching timescales and angular momentum properties. We focus on the impact of the environment for the quenching of galaxies in Sec. 3.5. Finally, we discuss possible observable indicators to predict quenching on a longer timescale, disentangling the relative importance of star formation, AGN feedback, and environment on the quenching at high redshifts in Sec. 3.6, before we conclude our paper in Sec. 3.7. As mentioned above, this paper is the companion paper to a second study by Remus & Kimmig (2025), where we study the properties of the quenched galaxies and their future evolution and rejuvenation in more detail.

3.2 The Magneticum Simulation

As we will show in Sec. 3.3.1, a simulation requires both a large volume as well as a high particle resolution to sufficiently reproduce the observed massive quiescent galaxies at high redshifts. To this end, we employ Box3 uhr of the hydrodynamical cosmological simulation suite Magneticum Pathfinder (www.magneticum.org), which has a volume of $(128\mathrm{Mpc}/h)^3$ and particle masses of $m_{\mathrm{dm}} = 3.6 \times 10^7 M_\odot/h$ and $m_{\mathrm{gas}} = 7.3 \times 10^6 M_\odot/h$, for dark matter and gas, respectively. As every gas particle can spawn up to four stellar particles, their mass resolution is $m_* \approx 1/4^{\mathrm{th}} m_{\mathrm{gas}} \approx 1.8 \times 10^6 M_\odot/h$, such that galaxies of $M_* \approx 3 \times 10^{10} M_\odot$ are well resolved. The softening lengths for every component are $\epsilon_{\mathrm{dm}} = \epsilon_{\mathrm{gas}} = 1.4\ \mathrm{kpc}/h$ and $\epsilon_* = 0.7\ \mathrm{kpc}/h$. The assumed cosmology is that of WMAP-7, with $h = 0.704$, $\Omega_m = 0.272$, $\Omega_b = 0.0451$, $\Omega_\lambda = 0.728$, $\sigma_8 = 0.809$ and $n_s = 0.963$ as given by Komatsu et al. (2011).

The code employed for the simulation is a modified version of GADGET-2 (Springel, 2005), with upgrades to the implementation of the smoothed particle hydrodynamics (SPH), covering thermal conduction (Dolag et al., 2004) and artificial viscosity (Dolag et al., 2005b), as well as other improvements (Donnert et al., 2013; Beck et al., 2016). The included baryonic physics are described in detail by Teklu et al. (2015) and Steinborn et al. (2015), but we will give a short description of the included physics important for this study in the following.

[1] www.magneticum.org

Star formation and stellar feedback is based on Springel & Hernquist (2003), with feedback and metal enrichment from supernovae type Ia and II as well as from stars on the asymptotic giant branch (AGB) based on Tornatore et al. (2004, 2007). The treatment of the cooling is extended to including the contribution of various metal species (see Wiersma et al., 2009), background radiation from UV/X-rays as well as the cosmic microwave background included as given by Haardt & Madau (2001). The assumed initial mass function is that by Chabrier (2003). Black hole (BH) seeding, evolution and feedback are implemented based on (Springel et al., 2005a), with improvement of the model regarding BH seeding and internal consistencies as described by Hirschmann et al. (2014), which includes also the treatment of the radio mode feedback as described by Fabjan et al. (2010).

The improvements by Steinborn et al. (2015) concern BH accretion and feedback. For the former, the rate of BH mass growth is given by the Bondi accretion $\dot{M}_{\mathrm{B}} \propto \alpha\rho/(c_{\mathrm{s}}^2 + v^2)^{3/2}$, where to account for limited resolution and thus densities a boost factor α is applied. The model differentiates cold and hot gas, applying a weaker boost factor of 10 for the hot gas, as it more closely follows the assumptions for Bondi accretion in an adiabatic isotropic sphere, and a stronger boost factor of 100 for the cold gas, as cold streams feed the BH more efficiently (Gaspari et al., 2013). This allows regulation of the BH mass growth both in a hot adiabatic medium present in massive galaxies as well as for star forming galaxies with cold, thin and rapidly rotating disks.

Changes in the BH feedback include a smoother transition between quasar and radio mode feedback efficiency, as well as a radiative efficiency that increases with the BH mass according to observational findings. These combined changes result in a more rapid growth of the high-redshift BHs while simultaneously reproducing low redshift scaling relations, as shown by Steinborn et al. (2015).

Identification of galaxies is done via the structure finder SUBFIND (Springel et al., 2001a; Dolag et al., 2009). Structure is linked by a friends-of-friends algorithm, and saddlepoints in the potential of such a linked 'halo' are used to identify separate 'subhalos', which represent individual galaxies. The most massive galaxy within a given halo is termed the 'central', with all other galaxies present within the halo being 'satellite' galaxies. The tracing of galaxies through time is performed via L-BaseTree (Springel et al., 2005c), allowing us to track the individual assembly history of galaxies in our study down to $z = 2$ where the simulation Box3 uhr stopped. The range up to $z \approx 15$ is covered via nine snapshots with full particle data in spacing of $\approx 400\,\mathrm{Myr}$, with one in particular at $z = 3.42$. This is comparable to the average redshift of observed quenched galaxies from Nanayakkara et al. (2024) or Long et al. (2023).

3.3 Galaxies at High Redshifts

The detection of galaxies at high redshifts had already been done in the last few years by HST, and for those that contain large gas fractions also by ALMA, but with the advent of JWST we have now reached the ability to also statistically probe the properties of galaxies at

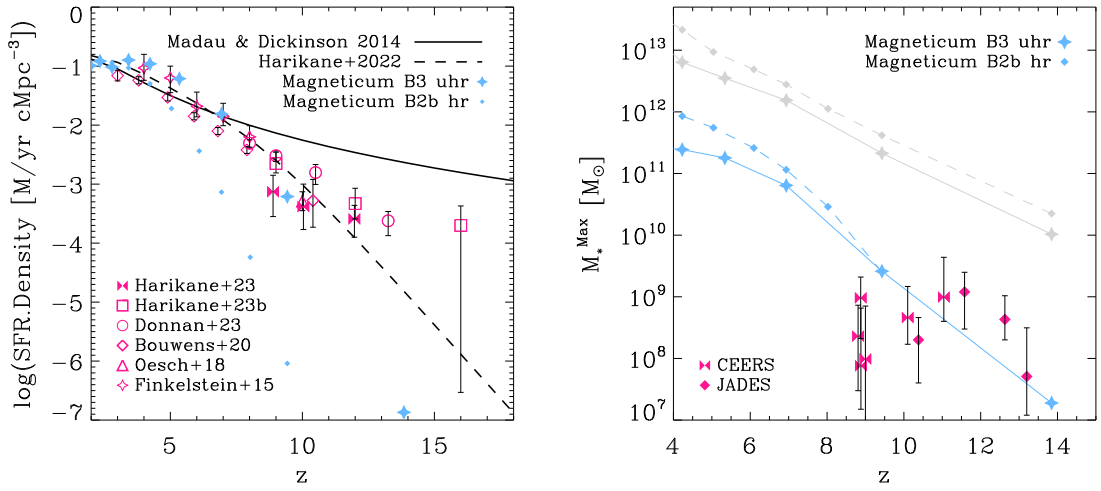


Figure 3.1. *Left:* Star formation rate density as a function of redshift for Magneticum Box3 uhr (large blue stars) and Box2b hr (small blue stars). Model predictions from Madau & Dickinson (2014) and Harikane et al. (2022b) are included as solid and dashed lines, respectively. Observational data from different methods are included: Spectroscopic data from JWST by Harikane et al. (2023a) is shown as solid pink bow-ties, while photometric JWST data is included as open pink squares (Harikane et al., 2023b) and open pink circles (Donnan et al., 2023). The UV-based measurement from HST by Oesch et al. (2018) at $z \approx 10$ is marked as open pink star. For a larger redshift range, ALMA-based measurement by Bouwens et al. (2020) and UV-based measurements sampled over different instruments by Finkelstein et al. (2015) are included as open pink triangles and diamonds, respectively. We clearly see that the higher resolved simulation reproduces the star formation rate density up to much larger redshifts than the lower resolution simulation. *Right:* Maximum stellar mass of a galaxy within the simulation at a given redshift, for Box3 uhr (large blue stars and solid line) and Box2b hr (small blue stars and dashed line). Observed galaxies with spectroscopic redshifts from the JWST programs CEERS and Jades, taken from Harikane et al. (2023a), are included as pink bow-ties and diamonds, respectively. The gray lines show the maximum dark matter mass at these redshifts in Box3 uhr (solid gray) and Box2b hr (dashed gray).

high redshifts in unprecedented detail. However, simulations still struggle to reproduce and understand many of the observed properties of galaxies at cosmic dawn, as this requires large simulation volumes while simultaneously also providing high resolutions. This is particularly challenging, and only few simulations that are currently available are capable of fulfilling this criterion. Thus, we will introduce the global properties of the galaxies found in our simulation in more detail in this section.

3.3.1 Galaxy Sample from $z = 15$ to $z = 2$

The ability of a simulation to answer the questions of how and why massive quiescents formed and quenched is closely related to its size and resolution. To demonstrate this, the left panel of Fig. 3.1 shows the star formation rate density as a function of redshift for two simulations of the Magneticum Suite, the larger but less resolved Box2b hr (small blue stars, see Lotz et al.; Kimmig et al. for more details on this simulation), and the better resolved but smaller Box3 uhr that is used throughout this study (large blue stars).

We find that at redshifts below $z < 4$ both simulations agree with the observational results by Finkelstein et al. (2015) and Bouwens et al. (2020), as well as with the relations found by Madau & Dickinson (2014) and Harikane et al. (2022b). At higher redshifts than $z = 4$, however, the star formation rate density of Box2b hr noticeably falls below that of Box3 uhr and the observed values. The star formation rate density of the higher resolved Box3 uhr still agrees well with the observations from different instruments up to $z \approx 10$, including UV-based observations by Oesch et al. (2018) from HST and Finkelstein et al. (2015) from different instruments, ALMA observations from Bouwens et al. (2020), and JWST observations from photometry (Harikane et al., 2023b) and spectroscopy (Harikane et al., 2023a). It also agrees with the fit by Harikane et al. (2022b), however, it does not agree with the prediction from Madau & Dickinson (2014), which also diverts from the observed results as already discussed by Harikane et al. (2022b) and Harikane et al. (2023b). Unfortunately, at even higher redshifts the resolution of our simulation becomes too small such that we cannot statistically probe galaxies beyond $z \approx 10$. We furthermore caution the use of the smallest mass bin due to the stellar resolution, and include it primarily to get an impression of the expectations at this lowest mass range.

When instead we consider the maximum stellar mass as a function of redshift, as shown in the right panel of Fig. 3.1, we find that the larger simulation volume of Box2b hr generally contains more massive galaxies at a given redshift, which is caused by the bigger box containing more massive nodes of the cosmic web. This can also be seen when looking at the total maximum mass at a given redshift for both simulations, which are included as gray lines in the right panel of Fig. 3.1. However, while we find constantly larger values in total mass for the larger volume simulation, we again see the effect of resolution on the baryonic component at higher redshifts. At about $z \approx 8$ the lower resolution box produces no galaxies with larger stellar masses than those in the higher resolution volume, while for $z > 8$ there are no galaxies which contain the minimum number of 20 stellar particles identified in the box. For the higher resolution volume, we find that galaxies are already present with masses above $M_* > 10^7 M_\odot$ at $z \approx 14$. Nevertheless, if the simulation with the larger simulation volume would have better resolution, it would also contain more massive galaxies at high redshifts as the halo masses are accordingly larger. This mirrors the results by Remus et al. (2023), who discuss the consequences of box volume on finding massive structures at high redshift in more detail. It is also in good agreement with the results found for the MilleniumTNG and IllustrisTNG Simulations by Kannan et al. (2023), who have the same problems in obtaining massive galaxies at high redshifts, albeit they get closer to observations at $z \approx 12$ as their box volume is large and their resolution relatively high.

Overall, we see from the right panel of Fig. 3.1 that the massive galaxies observed at particularly high redshifts of $z > 8$ are generally covered well by the predictions from the Box3 uhr simulation, albeit some observed galaxies are more massive than those predicted by the simulation at $z \approx 12$. Note that we here only include galaxies that have been spectroscopically confirmed, and not those that are currently debated from photometric redshift to challenge ΛCDM. As discussed above, we expect these to be reproducible within

the standard framework of ΛCDM for an even larger simulation volume on the given resolution level. Nevertheless, such a simulation would prove highly computationally expensive and consequently does not exist to our knowledge. We conclude that our simulation Box3 uhr successfully reproduces the star formation rate density and hosts galaxies of comparable stellar masses to those observed at high redshifts, providing us with a galaxy sample that can be used to study the evolution and formation of galaxies at cosmic dawn.

3.3.2 Quenched Galaxies: Selection and Statistics

The recent observations of very massive quiescent galaxies at redshifts of $z \approx 3-4$ by for example Nanayakkara et al. (2024) and Long et al. (2023) raise crucial questions to how they could have formed and why they quenched. However, before we can address these particular questions, we must define quiescence and compare the overall quenched fractions found at different redshifts to observations.

Based on the observed stellar masses of the quiescent galaxies (Nanayakkara et al., 2024; Carnall et al., 2023a), we require for this study that $M_* \geq 3 \times 10^{10} M_\odot$, which equates to around 11000 stellar particles per galaxy and results in sufficient resolution to study their properties in detail. This cut leaves us with 1309 galaxies at $z = 3.42$, the snapshot that most closely resembles the redshift at which quenched galaxies are currently observed, of which 1217 are centrals. It is equivalent to the cut of level II from the companion study to this work by Remus & Kimmig (2025).

The definition of what differentiates quenched versus non-quenched galaxies is crucial when comparing to the number densities found by observations. We consider here multiple approaches and definitions and compare the resulting quenched number densities to values from the literature.

We begin by employing the criterion by Franx et al. (2008) based on the specific star formation rate (sSFR = SFR/M$_*$). Quenched galaxies are then defined by sSFR $< 0.3/t_{\rm hub}$. This cosmic-time dependent cut has been used in various prior works to delineate star forming and quiescent populations through time (e.g., Tacchella et al., 2019; Carnall et al., 2020; Bluck et al., 2024), and in particular by Remus et al. (2023) to predict the fraction of quiescent galaxies for different halo masses up to high redshifts comparable to those in this work, but also to study the quiescent populations of galaxies at $z = 2.7$ in comparison to observations (Lustig et al., 2023) and the overall quiescent stellar mass function at different redshifts (Steinborn et al., 2015).

When using this criterion we find 352 quenched galaxies with $M_* \geq 3 \times 10^{10} M_\odot$ at $z = 3.42$, of which 315 are central galaxies and 37 are satellite galaxies of more massive galaxies. Using instead the cutoff value of $0.2/t_{\rm hub}$ following Carnall et al. (2020) we find 301 quenched galaxies (270 centrals, 31 satellites). It is interesting to note here that already at this redshift we find massive yet quenched galaxies that are *satellites* to another more massive galaxy, and in some cases we find indications that the quenching (or at least lack of

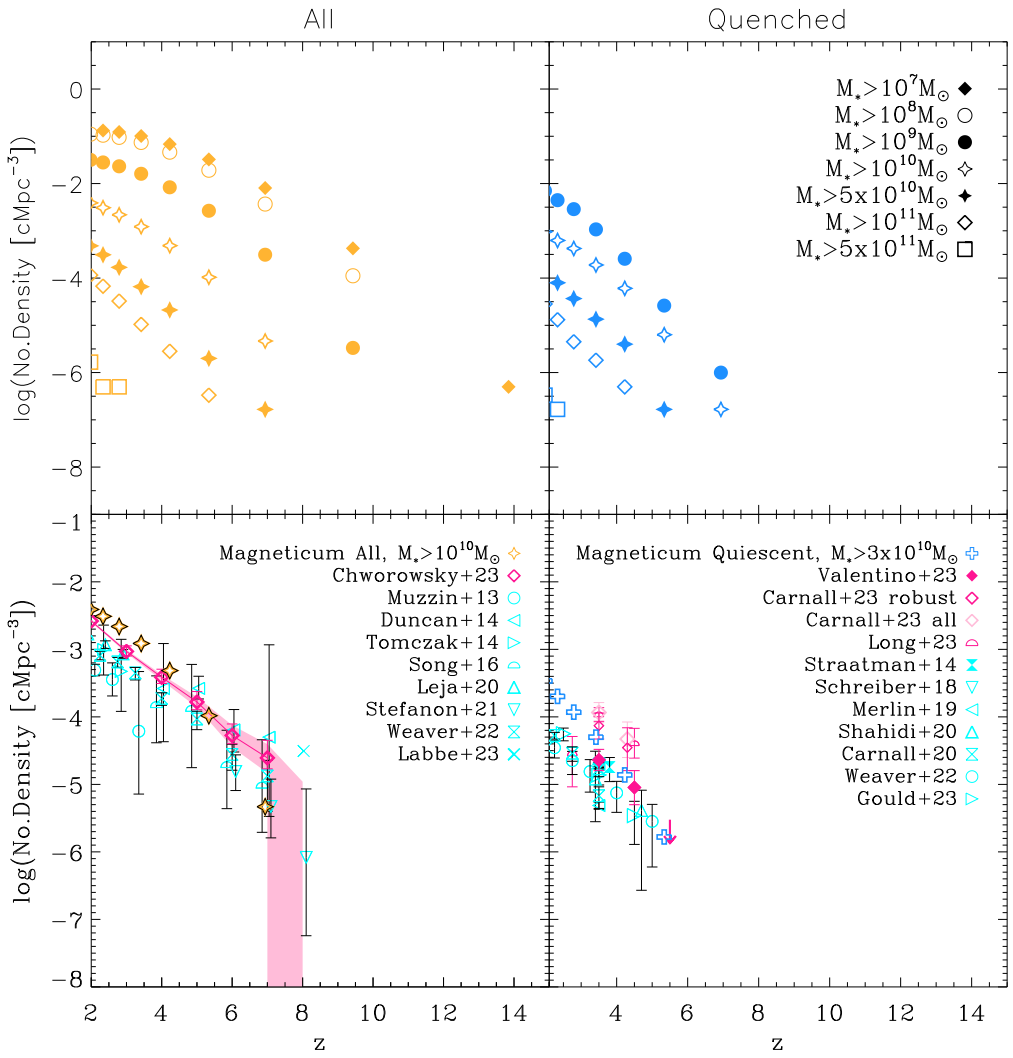


Figure 3.2. *Top row*: Number density of simulated galaxies above a given mass cut from $z = 2$ to $z = 15$. Different symbols mark the different lower mass limits applied, as indicated in the legend. We show both all galaxies (*left*), regardless of their star formation properties, and only galaxies that are quenched (*right*). The quenched number densities do not include the two lowest mass cuts, as below $M_* < 10^9 M_\odot$ we cannot reasonably distinguish between quenched and non-quenched galaxies due to resolution limitations. *Bottom row*: Comparison of the simulated number densities (yellow stars or blue pluses) with observations (JWST spectroscopy in pink, others in cyan), both for total numbers above $M_* > 10^{10} M_\odot$ (*left*) and quiescent galaxies above $M_* > 3 \times 10^{10} M_\odot$ (*right*). Observed total values are taken from Chworowsky et al. (2023); Muzzin et al. (2013); Duncan et al. (2014); Tomczak et al. (2014); Song et al. (2016); Leja et al. (2020); Stefanon et al. (2021); Weaver et al. (2022); Labbé et al. (2023), while quiescent values are from Long et al. (2023); Carnall et al. (2023a); Valentino et al. (2023); Straatman et al. (2014); Schreiber et al. (2018); Merlin et al. (2019); Shahidi et al. (2020); Carnall et al. (2020); Weaver et al. (2022); Gould et al. (2023).

rejuvenation) may have been assisted by being within range of the more massive host galaxy (see also Remus & Kimmig, 2025).

The top row of Fig. 3.2 shows the resulting number densities in the simulation for all galaxies (left panel) and quenched galaxies only (right panel), for different redshifts from $z = 15$ to $z = 2$, for different stellar mass cuts from $M_* > 10^7 M_\odot$ (filled diamonds) to $M_* > 5 \times 10^{11} M_\odot$ (open squares). Quiescence here is determined via the criterion by Franx

et al. (2008), which provides the highest number of quiescent galaxies from all the criteria and is the one most commonly used. As expected, we find that small galaxies assemble the earliest, while the really massive galaxies with $M_* > 5 \times 10^{11} M_\odot$ only appear at around $z = 3 - 4$. This overall trend is also seen for the quenched galaxies, just with a delayed onset at a fixed stellar mass compared to the general number densities.

In the lower left panel of Fig. 3.2 we show the number densities of galaxies with $M_* > 1 \times 10^{10} M_\odot$ from various observations from JWST spectroscopy by Chworowsky et al. (2023) in pink, and other observations in cyan (Muzzin et al., 2013; Duncan et al., 2014; Tomczak et al., 2014; Song et al., 2016; Leja et al., 2020; Stefanon et al., 2021; Weaver et al., 2022; Labbé et al., 2023), in comparison to our simulation (yellow stars). We find that the number densities from our simulation match the observations very nicely up to a redshift of $z = 5$, and within the error bars even up to $z = 7$, which is the highest redshift for which galaxies with masses larger than $M_* > 1 \times 10^{10} M_\odot$ are found in the simulation. This is in agreement with the results presented by Steinborn et al. (2015), who showed that the stellar mass functions from the Magneticum simulations agree well with observations over a large range of redshifts.

Going to the quenched number densities in the right panels of Fig. 3.2, we do not consider galaxies below $M_* < 10^9 M_\odot$, as for those galaxies quenching might be arbitrary due to resolution issues (where they would have less than 1000 baryonic particles). Nevertheless, it is very clear from the top panel that quenched galaxies of a given mass appear later than their non-quenched counterparts of the same mass, showing that the quenching process requires a certain amount of time to act on our galaxies. As can also be seen from the top right panel of Fig. 3.2, the most massive galaxies at a given redshift are not among the quenched ones, as for example the non-quenched galaxies with $M_* > 1 \times 10^{11} M_\odot$ and $5 \times 10^{11} M_\odot$ are present in the simulation one snapshot, so around 400 Myrs, before their quenched counterparts.

When comparing the quenched fractions from the simulations to JWST observations by Long et al. (2023), Valentino et al. (2023) and Carnall et al. (2023a) (in pink) as well as other observations (in cyan, see caption), we find good agreement, indicating that the timescales of quenching in our simulation act on comparable scales to the real Universe. Remus & Kimmig (2025) further compile the results from several cosmological simulations including EAGLE (Schaye et al., 2015), IllustrisTNG (Pillepich et al., 2018b), Astrid (Ni et al., 2022) and FLARES (Lovell et al., 2021), which are shown to struggle to reproduce these quenched number densities. This is true particularly beyond $z > 3$, with common simulated values of $n_q \approx 10^{-7}\mathrm{cMpc}^{-3}$ compared to the observational values of $n_q \approx 3 \times 10^{-6}\mathrm{cMpc}^{-3}$ at $z = 5$. Therefore, being able to reproduce the quenched number densities to redshifts as high as $z = 5.5$ with our simulation is very promising for the endeavour of understanding the origin of quenching at high redshifts.

Given that our simulation is capable of reproducing the observed number densities of quenched galaxies up to redshifts as high as $z = 5.5$ using the commonly used definitions of quenching, we also briefly consider what happens when defining quenched via a smoothed SFR by summing the total stellar mass produced within a time window dT = 300Myr prior to $z = 3.42$ based on the stellar birth redshifts. Using the condition

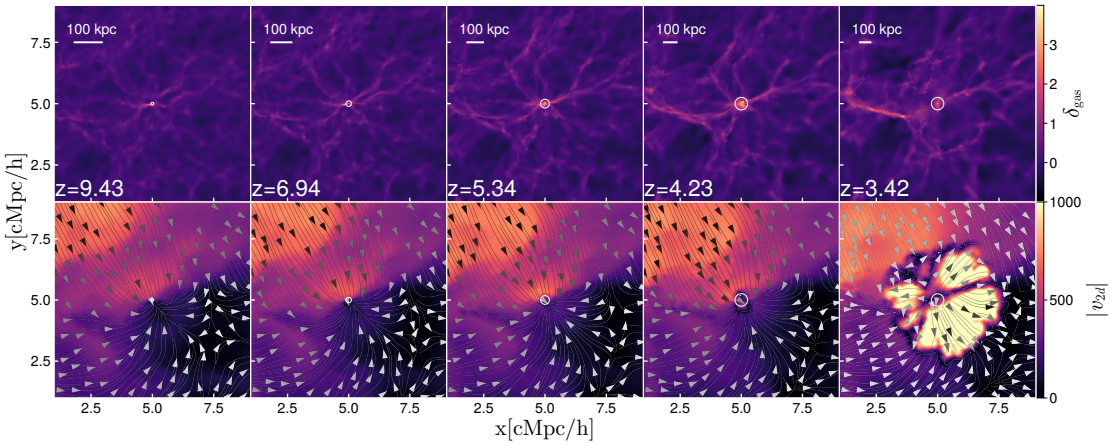


Figure 3.3. Projected gas density (*top row*) and velocity (*bottom row*) of example quenched galaxy ID16396 at redshifts from $z = 9.43$ down to $z = 3.42$ (*columns, left to right*), the moment when it is identified as quenched. Redshifts are given in the lower left corner of each upper panel. Each box has a comoving side length of 10cMpc$/h$ and a depth of ±500ckpc$/h$, with the physical size that corresponds to 100kpc denoted in the upper left corner of each of the upper panels. In all panels, the white circle marks the virial radius of the galaxy at the given redshift. Arrows in the lower panel mark the directions of the gas flow.

of sSFR $\equiv$ (M$_{*,\rm new}$/dT)$/M_{*,\rm tot} < 0.3/t_{\rm hub}$ or $< 0.2/t_{\rm hub}$, we find 180 or 137 quiescent galaxies, respectively. This results in quenched number densities of 3.04×10^{-5}cMpc^{-3} or 2.31×10^{-5}cMpc^{-3}, which is a bit lower than with the non-smoothed criterion but still in good agreement within the bounds of the results by Carnall et al. (2023a) and Valentino et al. (2023). Thus, even with a smoothed quiescent criterion our simulation is capable of reproducing the observed number densities of quenched galaxies at high redshifts.

Summarizing, we have found good agreement with observed number densities of quenched galaxies both when using the criterion by Franx et al. (2008) or by Carnall et al. (2020), as well as when considering quenching over extended periods of time. However, it is clear that there are differences of up to a factor two depending on the parameters used. This is indicative of the difficulty of separating distinct classes of galaxies at high redshift, as star formation is increasingly found to be on-off in nature at cosmic dawn.

In the following we are interested in those galaxies which have completely ceased their star formation, so where there are no star forming gas particles with SFR > 0. These galaxies allow us to effectively isolate the processes which led to the decline of star formation. This reduces the larger quenched sample, which includes galaxies that may be going through on-off star formation episodes or mini-quenching (Looser et al., 2024; Endsley et al., 2023), or which are 'smouldering' (Trussler et al., 2025), down to those which fully quench and will likely remain quenched for some time. This criterion should also result in galaxies more comparable to those observed by Nanayakkara et al. (2024), which show no rekindled star formation over some time.

We thus restrict our analysis to those 36 galaxies that are found to be quenched with SFR = 0 at $z = 3.42$, 28 of which are centrals at that redshift, and 22 of those stay central galaxies until $z = 2$. Whenever galaxy properties are traced through time, these 22 galaxies



are considered unless stated otherwise. They represent the core sample of this study, with a few special cases introduced specifically. All galaxies that are not quenched at $z = 3.42$ and remain central galaxies until $z = 2$ are used as non-quenched control sample throughout. In particular, the sample of galaxies at $z = 3.42$ consists of 1217 galaxies which are centrals, with 1189 of them that are not quenched. Throughout this study we refer to the 28 quenched central galaxies at $z = 3.42$ as 'quenched', and the remaining centrals as 'non-quenched', and note that this does not refer to their current state at all redshifts but rather to what they eventually are at $z = 3.42$.

3.4 How Do Galaxies at High Redshifts Quench?

Having seen that the global population of massive galaxies is well reproducing the observations at high redshifts, we turn here to the central question of how massive quiescents form and quench. A first indication can be gained from Fig. 3.3, which shows the projected gas density (top) and velocity (bottom) of the surroundings of one of our quenched galaxies, galaxy ID16369. It is one of the most massive central galaxies which quenches by $z = 3.42$, reaching a stellar mass of $M_* \approx 5.6 \times 10^{10} M_\odot$.

Going from left to right we find that galaxy ID16369 collapsed as one of the earliest structures in its surroundings, present as an overdensity already at $z = 9.43$ (leftmost column). Consequently, the surrounding gas is primarily flowing toward it. Interestingly, the gas inflow is largely isotropic with the exception of the bottom right, where there is a noticeable underdensity. As discussed further in Sec. 3.5, we find that lying in or near an underdense region is actually not unusual for the quenched galaxies, but rather a requirement.

This accretion continues until $z = 4.23$, which is the last moment prior to the galaxy quenching. We note that a few minor filaments have formed by this point through which gas is flowing, while to the left another overdensity is beginning to collapse. A small outflow can already be seen to emerge from the galaxy in the flow field, although no impact on the gas density is yet visible.

It is then in between $z = 4.23$ and $z = 3.42$ where the galaxy quenches. This process is rapid and violent, resulting in a massive expulsion of gas away from the galaxy (bottom right panel). We find this expulsion to be sufficiently powerful to disrupt the thin connecting filaments in the gas (top right panel), which become much more diffuse. Furthermore, the ejected gas can be driven out particularly far into the aforementioned underdensity located in the lower right, reaching well beyond the virial radius indicated by the white circle. Virial radius and virial mass are defined via the redshift-dependent homogeneous top-hat overdensity criterion given by Bryan & Norman (1998), see Ragagnin et al. (2021) for more details. Though this is just an example of one of the quenched galaxies, it illustrates the process found for all of them, as we will quantify more in the following.

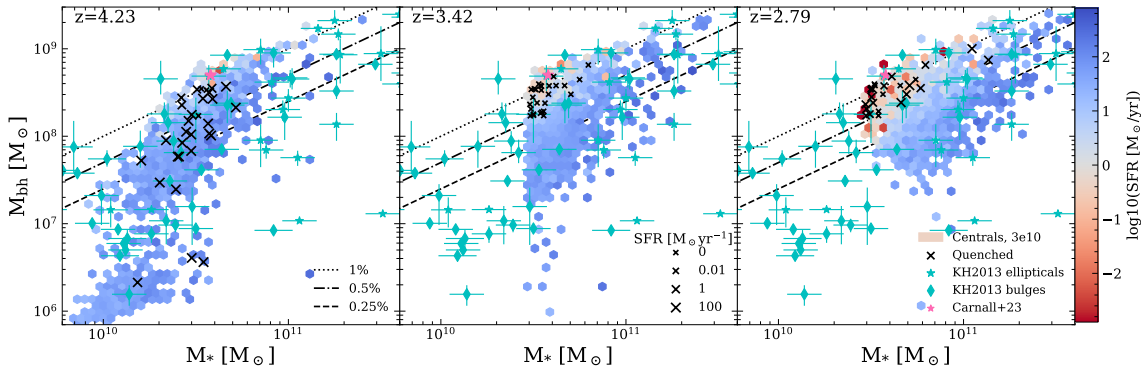


Figure 3.4. Black hole mass versus stellar mass of the central galaxies in our sample at a redshift of $z = 4.23$ (*left*), 3.42 (*middle*) and 2.79 (*right*), colored by star formation rate. Quenched galaxies are plotted as black crosses with the size increasing with star formation rate, while black lines show different mass fractions of the black hole relative to the stellar mass as indicated by the legend. Observed galaxies at $z = 0$ by Kormendy & Ho (2013) are in cyan, while the quenched galaxy at $z = 4.658$ by Carnall et al. (2023b) is shown in pink for comparison (where the errors are small in relation to the marker size).

3.4.1 Combined Stellar and AGN Feedback

As discussed in the introduction, the actual quenching mechanisms at high redshifts are still under debate. While by construction the IllustrisTNG model causes massive galaxy quenching to result solely from AGN feedback (Hartley et al., 2023; Kurinchi-Vendhan et al., 2023), models and observations are not as set on the AGN scenario as the sole reason for quenching; they rather find a co-evolution between high star formation rates in short bursts and evidence of AGN activity (Tacchella et al., 2016; Tozzi et al., 2023; D'Silva et al., 2023a; Fan et al., 2023). Furthermore, simulations from NIHAO have shown that supernova feedback is also able to generate strong outflows that even reach beyond the virial radius (Tollet et al., 2019). Given the strong nature of the observed starbursts, the feedback from supernovae expected at high redshifts is most likely non negligible.

Conversely, the co-evolution of M_{bh} and the bulge mass, often traced by the central velocity dispersion, is well established observationally (Kormendy & Ho, 2013), and inclusions of preventative feedback through AGNs have been important in regulating the star formation in simulations (Bower et al., 2006; Fabian, 2012; Steinborn et al., 2015; Remus et al., 2017b). Depending on the implementation, this may result in the AGN playing the dominant role in the quenching of massive galaxies (Piotrowska et al., 2022; Bluck et al., 2024). Interestingly, using SDSS at $z = 0$ Bluck et al. (2016) also find a correlation of quenching with the black hole mass traced through the central velocity dispersion. Crucially, however, they also report at a fixed black hole mass a trend with bulge-to-total ratio in the quenched fractions, indicating that more extended star formation may survive the integrated feedback from massive central AGNs even at z=0.

This raises the question whether the feedback from the central black hole is sufficient by itself to explain the quenching of galaxies at high redshifts, or if other components such as the rapid depletion of gas through star formation also play a crucial role. To answer

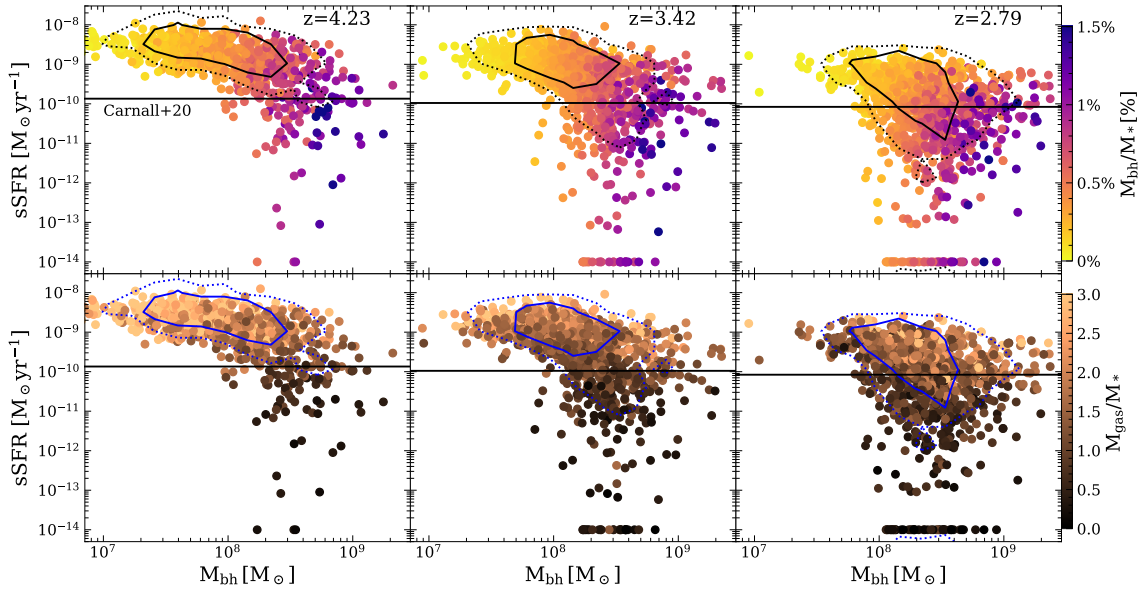


Figure 3.5. Specific star formation rate versus black hole mass of the central galaxies in our sample at a redshift of $z = 4.23$ (*left*), 3.42 (*middle*) and 2.79 (*right*), colored by the black hole mass fraction of the stellar mass (*top row*) and the gas mass divided by the stellar mass (*bottom row*). Galaxies with sSFR = 0 are set to sSFR = $10^{-14} M_{\odot} yr^{-1}$ so as to be visible in the plot. The black solid line shows the criterion employed by Carnall et al. (2020) to define quiescence. Contours enclose 50% (solid lines) and 80% (dotted lines) of the galaxies.

this question, we first consider the well-known black-hole-to-stellar-mass relation at redshifts from $z = 4.23$ (pre-quenching) to $z = 2.79$ (post-quenching) in Fig. 3.4. We plot here only central galaxies to avoid including additional effects from the environment, and only those which have a stellar mass of $M_* > 3 \times 10^{10} M_{\odot}$ at $z = 3.42$ to be comparable with the observed quenched galaxies.

We find that the simulated high redshift galaxies overall follow the relation found in observations at $z = 0$ (Kormendy & Ho, 2013). This is in agreement with observations by Ding et al. (2022) who found a black hole in a quasar at $z \approx 6$ to already reside on the black-hole-to-stellar-mass relation observed at present day, and the JWST observation of a black hole in a quiescent galaxy detected at $z = 4.658$ by Carnall et al. (2023b). However, recently Pacucci et al. (2023) and Harikane et al. (2023c) presented evidence from JWST observations at $z = 4$ to 7 for this relation to be shifted towards higher black hole masses, although these observations are for galaxies with lower stellar masses than probed here. Note that, as our model seeds central black holes at masses below the relation (which can be seen for some of the galaxies at $z = 4.23$, which are gathering in a cloud in the lower left of Fig. 3.4), this implies that the SMBHs first rapidly grow until they reach the relation, after which they evolve according to it.

When coloring by star formation rate we find that galaxies hosting more massive black holes at equal stellar masses generally have a lower star formation rate (redder color). However, the correlation does not hold for all galaxies, with numerous galaxies lying at the highest black hole masses and yet still exhibiting significant star formation.

The quenched galaxies (black crosses) host particularly massive SMBH by the time they are identified as quenched ($z = 3.42$), but they do not represent significant outliers. It should be noted that AGN feedback scales not only with the absolute mass but also with the recent mass accretion (Steinborn et al., 2015). However, also in terms of SMBH mass growth there are 197 centrals which grow more significantly than the median growth of quenched galaxies (both in absolute mass as well as mass ratio between $z = 4.23$ to $z = 3.42$). This means that the pure growth of a massive central black hole by itself is insufficient to cause a complete stop of star formation. This is in agreement with the observation of active AGN in galaxies with ongoing star formation for example by Tozzi et al. (2023).

To see the impact of the black hole on the star formation rate more directly, we plot the specific star formation rate against the black hole mass in Fig. 3.5. Going from left to right shows $z = 4.23$ (pre-quenching) to $z = 2.79$ (post-quenching), as with Fig. 3.4. The top row shows the central galaxies colored by the fraction of mass of the black hole relative to the stellar mass, while the bottom row is colored by the fraction of gas mass relative to the stellar mass. As can be seen from the contours, there is a clear trend of declining specific star formation rate with increasing black hole mass, as expected. Furthermore, the total sample of galaxies moves toward higher black hole masses and lower sSFRs as time passes.

We first consider the top row. There is a color gradient present, where at a given black hole mass those with relatively less stellar mass (so higher $M_{\rm bh}/M_*$ or more purple color) lie at a lower sSFR. Indeed, most of the galaxies which fall below the quiescent cut used by Carnall et al. (2020) have black hole masses larger than $M_{\rm bh} > 10^8 M_\odot$, which is around 0.5% or more of the total stellar mass. Comparing to Fig. 3.4, we see that this corresponds to the dash-dotted line and lies well within the black-hole-stellar-mass relation.

However, the reverse is not true. There are numerous galaxies which have $M_{\rm bh} > 10^8 M_\odot$ and high black hole mass fractions but which are not quenched, neither fully (SFR = 0) nor when using the definition by Carnall et al. (2020). This can be understood when considering the lower row of Fig. 3.5, where the color shows the gas mass relative to the stellar mass. We find that a higher sSFR corresponds to a higher amount of gas still present. Critically, the galaxies with high black hole masses but which are not quiescent have retained or newly accreted significant amounts of gas, generally in excess of the total stellar mass present.

In these cases the AGN was either unable to eject the gas or the gas has been re-accreted on extremely short timescales. This could be due to multiple factors: Firstly, the AGN may have grown rapidly, ejected its current but then re-accreted new gas (replenishment). Secondly, the galaxy may have been in such an overdense environment that the same feedback energy was unable to fully eject all the gas (retainment). Thirdly, the gas in the galaxy may have been nearly entirely distributed in a disk. As the implemented AGN feedback is isotropic, a majority of the feedback energy would not be pointed toward this disk, but would instead mostly go into a small amount of gas being ejected *perpendicularly* to the disk. This would allow most of the gas to remain in the galaxy. We would expect then galaxies with accretion along a dominant plane, for example through massive filaments, to continue to be star forming,



while those fed isotropically would be more efficiently quenched by the feedback (see also Fig. 3.10).

At any rate, the degree of isotropy in the accretion has an impact on the resulting AGN feedback due to the distinction made in the AGN model between hot and cold accretion. The black hole accretion is proportional to the density and inverse of the relative velocity between gas and the black hole. Hot gas typically has lower density, so even when the relative velocity is low enough to be easily accreted the total mass growth (and thus feedback energy) of the black hole is low. By contrast the cold gas is denser, and thus can cause massive growth spikes. These require low relative velocities, however, and if the cold gas instead is accreted with high angular momentum or settles into a disk the total growth of the black hole can remain low. This allows for situations where a galaxy experiences high cold gas inflow onto a central star forming disk *without* triggering a major feedback event from the AGN. Consequently, the model allows for different black hole growth and feedback based on the mode (temperature and orientation) of accreted gas, as opposed to averaged total gas quantities, which creates the greater diversity in behavior seen in Fig. 3.5.

This is interesting when contrasted with the results found by Zinger et al. (2020) for IllustrisTNG, whereby the threshold mass of the black hole transitioning between radiative and kinetic feedback results in a step-function like behavior in the surrounding gas. Above $log(M_{bh}\,[M_\odot]) = 8$ the entropy of galactic gas jumps by nearly three orders of magnitude, rapidly shutting down the star-formation (Zinger et al., 2020).

Thus, if the AGN feedback alone is not the sole reason for quenching, the question remains what else contributes. Therefore, we turn to analyze what happens to the gas within a galaxy during the process of quenching. Due to the limited time resolution of the stored simulation outputs we cannot follow a single galaxy through the process from start to finish, despite the original simulation of course performing all this in detail. We can, however, quantify how far along the quenching of a given galaxy is by using t_{90}, the time since a galaxy made 90% of its final stellar mass at $z = 3.42$. A negative t_{90} implies that the galaxy has yet to make 90%. To follow an evolutionary sequence we order galaxies by both their fraction of stars made at $z = 4.23$ as well as t_{90}, going from a low fraction and recent t_{90} to a high fraction and older t_{90}.

The top set of panels of Fig. 3.6 shows the phase space diagram of the gas within the virial radius at $z = 4.23$ for five centrals which will quench by $z = 3.42$. Going from left to right they are sorted from lowest to highest t_{90}, and the gas particles are colored by star formation rate (upper panel, in $M_\odot \mathrm{yr}^{-1}$) and total metallicity (lower panel, defined as total mass in metals divided by the total hydrogen mass). We find that around 200 Myr before reaching t_{90} the galaxy is undergoing a massive starburst, with a prominent star forming branch. This results in a noticeable cloud of particularly cold and dense gas particles, so-called wind particles. They are the result of gas particles being subjected to stellar feedback and winds.

As the starburst progresses (moving toward the right panels) the star-forming branch begins to be disrupted, with gas particles being heated due to the feedback processes. In particular we note multiple metal rich gas particles which start being found at lower densities

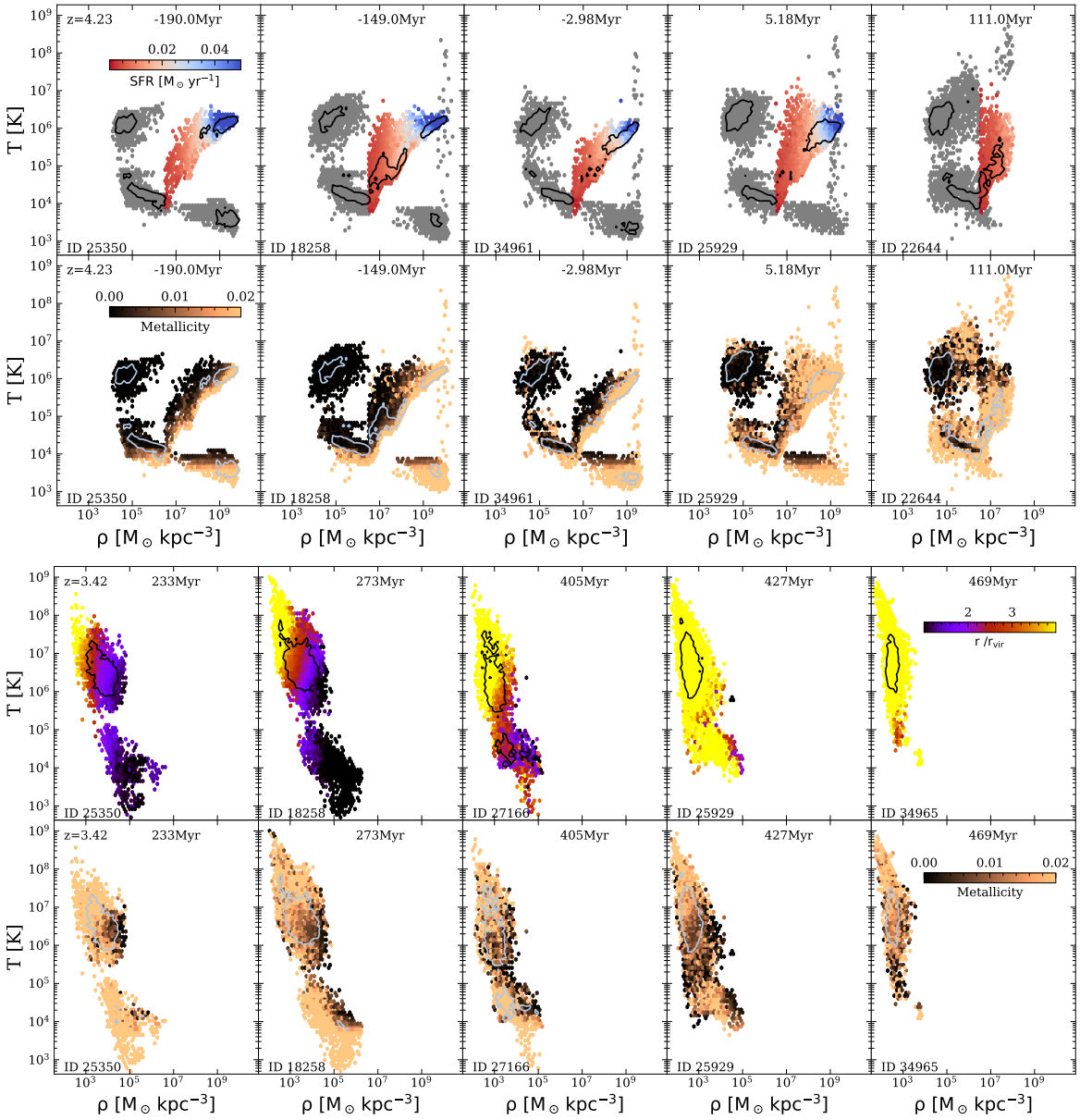


Figure 3.6. Phase space evolution of quenched galaxies' gas prior to (*top*, $z = 4.23$) and post quenching (*bottom*, $z = 3.42$). Galaxies shown from left to right are sorted based on their t_{90} (given in the top left corner), with negative values implying that they have yet to form 90% of their final stellar mass present at $z = 3.42$. Contours enclose half of the total gas mass. IDs of the galaxies are given in the bottom left. Colored from top to bottom by the star formation rate in $M_{\odot}\mathrm{yr}^{-1}$, the metallicity (total mass in metals divided by total hydrogen mass), the distance from the galaxy center in units of the virial radius, and the metallicity.

of $\rho \approx 10^5 M_{\odot}\mathrm{kpc}^{-3}$. At $t_{90} = -2.98$ Myr this ejected metal rich gas appears also in the region of phase space occupied by the IGM (thin and hot). The fact that this gas is metal enriched indicates that it has been subject to stellar feedback, either through SN or AGB stellar winds.

At $t_{90} = 5$ Myr the star forming branch is now significantly disrupted, until finally at $t_{90} \approx 100$ Myr all gas has been removed from the most dense central regions, either by being used up for star formation or by being ejected. We note also the presence of a cloud of hot and metal rich gas which is in the process of being ejected.

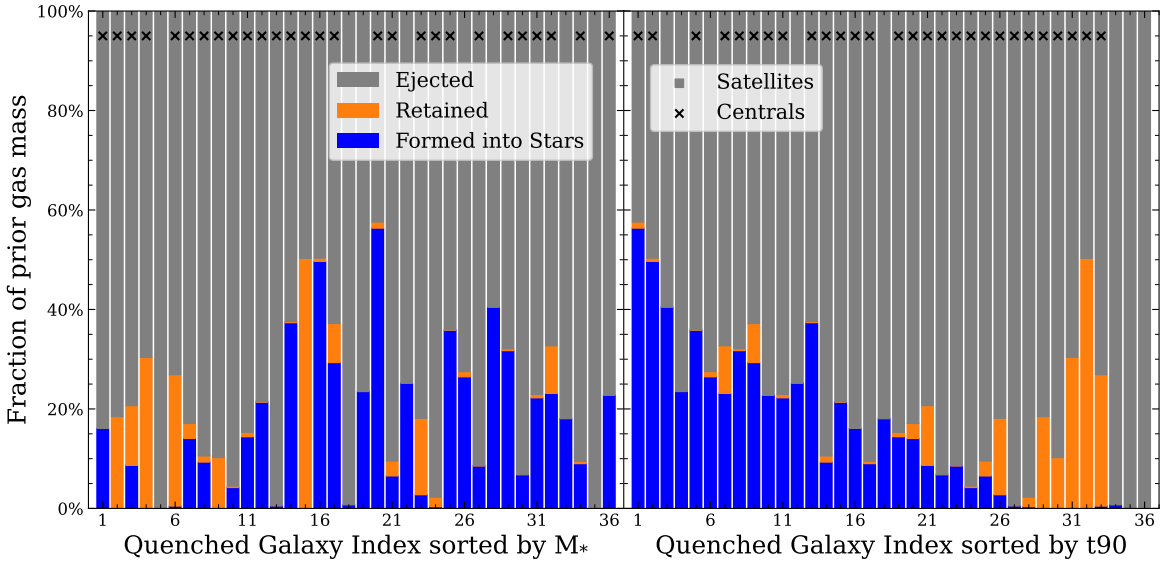


Figure 3.7. Fraction of the gas mass present in the 36 quenched galaxies at $z = 4.23$ (prior to quenching) which is ejected (gray), retained in the galaxy (orange) or formed into stars (blue) by $z = 3.42$. Central galaxies are marked with a cross. The *left* panel shows the galaxies sorted from highest to lowest final stellar mass at $z = 3.42$. On the *right* they are instead sorted by t_{90} determined at $z = 3.42$, such that the farthest left has most recently formed 90% of its stars while the right has done so long ago.

Tracing the gas which was present within the galaxy forward to times post quenching (bottom set of panels), we find two main properties: the ejected gas is noticeably metal enhanced (bottom row) and reaches out to significant radii in excess of $r > 3 \times r_{\rm vir}$ (top row). At $t_{90} > 400\,$Myr all gas which was present pre-quenching has been fully removed from the galaxy. This is vastly different from the non-quenched galaxies, where the gas stays much closer to the central parts of the galaxy. We discuss the exact radial profiles of the gas pre- and post-quenching in more detail in the Appendix with Fig. A.1.

This again is in good agreement with what we found for our example halo in Fig. 3.3, where we saw the gas being driven outwards after quenching. However, the fact that the gas that is being ejected is already metal enriched clearly shows that the starburst precedes the ejection of the gas through feedback during quenching, clearly indicating that the stellar feedback from the supernovae Type II adds to the energy budget of the quenching process, and that a massive starburst is required preceding the quenching.

This raises the question of how much of the gas is actually ejected. Fig. 3.7 shows the fraction of gas mass that was present in these galaxies prior to quenching at $z = 4.23$ and ejected (gray), retained within the virial radius (orange) or formed into stars (blue) by $z = 3.42$ when the galaxies are identified as quenched. The left panel is sorted from left to right by decreasing stellar mass. Galaxies which have retained a greater fraction of their gas tend also to be more massive, though there is considerable variation. We further find that most of the mass in gas is ejected, with retained gas typically at less than 30% and often down to zero. Most galaxies still transform some amount of that gas into stars, though the range in values is large and does not depend on their total stellar mass.

When the galaxies are sorted instead by t_{90} in the right panel of Fig. 3.7, so by how far along in their starburst they are, we find a much clearer signal. Galaxies which have retained a lot of their gas generally have already experienced their starburst. This means that the quenching process likely also ejected practically all of their gas, but that they have since accreted new gas which they are *not* ejecting. This crucially implies that the AGN is not permanently regulating them to quiescence, and that they may rejuvenate (Remus & Kimmig, 2025). The three galaxies with the oldest t_{90} show no such retained gas, but all three of them have since become satellites (marked by their lack of black cross). This may imply that while the environment of the more massive host is insufficient to quench the satellites themselves (as they quenched prior to falling in), it plays a critical role in *preventing rejuvenation*.

3.4.2 Massive Quiescents Quench Quickly (MQQQ)

In the previous section we have shown how quenched galaxies exhibit a starburst preceding the enrichment and ejection of all gas which ultimately results in a stop to all star formation (i.e., quenching). We turn here to the question on which timescales this occurs and whether there is any signature left behind in the quenched galaxy which could be observed.

The left panel of Fig. 3.8 shows star formation histories (SFH) for the quenched centrals (thin blue lines). There emerges a characteristic 'S'-shape, with an initial period of low star formation, followed by a burst producing around 80% of the final stellar mass and subsequent rapid quenching (flattening) of the SFH. The difference to the non-quenched galaxies can be seen clearly by comparing the mean of the quenched centrals (thick blue line) to the mean of the non-quenched centrals (thick sand line).

To characterize how rapidly this starburst occurs, we consider for a galaxy the elapsed time between forming 50% and 90% (horizontal black lines in the left panel) of its final stellar mass at $z = 3.42$, $t_{50} - t_{90}$. The resulting times are shown in the middle panel of Fig. 3.8. We find that most of the quenched galaxies (blue histogram) have $t_{50} - t_{90} < 170\,\mathrm{Myr}$. Four quenched galaxies of the sample even reach times around 100 Myr.

These values agree well with comparable timescales found in observations of massive quiescent galaxies, both for individual (Kakimoto et al., 2024; de Graaff et al., 2024a), as well as sets of multiple galaxies (Forrest et al., 2020; Nanayakkara et al., 2024), as marked in the middle panel of Fig. 3.8 in pink and cyan. We note that the given times from observations are between the formation time (50% stars formed) and 80% (t_{58}), 90% (t_{59}) or the quenching time (t_{5q}). At these scales, however, we expect little difference in these times. For one particular example, Carnall et al. (2023b) observe a galaxy which formed practically all of its stellar mass on timescales of just around 200 Myr.

This differs clearly from the non-quenched galaxies, for which the mean $t_{50} - t_{90}$ is nearly at 300 Myr. There is a noticeable scatter in range for the non-quenched galaxies, with some reaching $t_{50} - t_{90} \approx 150\,\mathrm{Myr}$. This is expected as the non-quenched galaxies at $z = 3.42$ studied here are also fairly massive and had to form stars in a rather short period of time. Nonetheless, it is still apparent that the quiescent galaxies generally went through a shorter

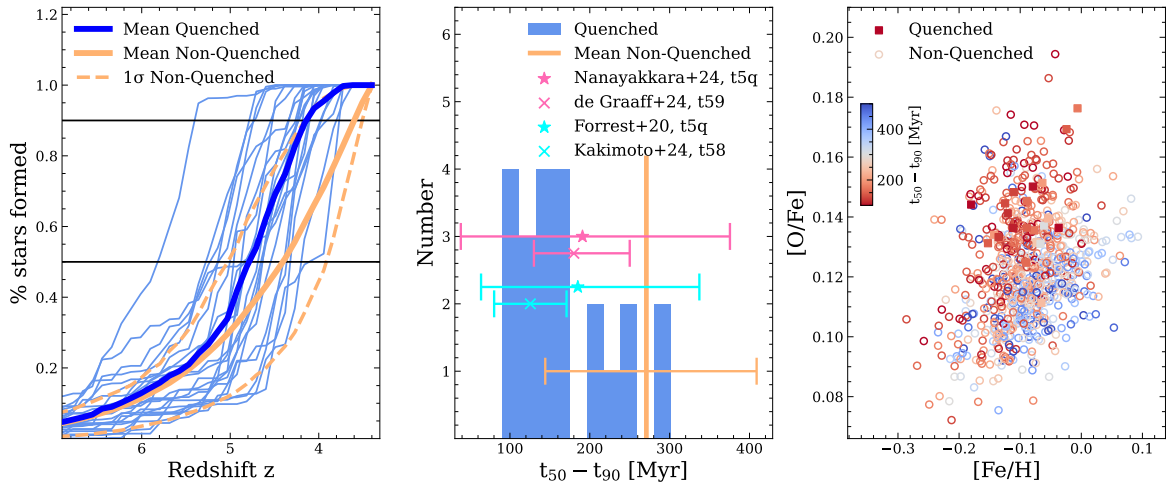


Figure 3.8. *Left:* Star formation history of quenched centrals (thin blue lines) as well as their mean (thick blue line) and the mean of non-quenched centrals (thick sand line). *Center:* Distribution of the quenching times $t_{50} - t_{90}$ for quenched centrals (blue bars), as well as the mean time and 1σ bounds for non-quenched (sand color line). Observational data of individual galaxies given by de Graaff et al. (2024a) and Kakimoto et al. (2024) are plotted as crosses, while data for multiple galaxies is given by Nanayakkara et al. (2024) and Forrest et al. (2020) and plotted as stars. In the latter case, the error range represents the 1σ bounds of the set of quenching times. Colors distinguish observations performed with JWST/NIRSpec (pink) and Keck/MOSFIRE (cyan). *Right:* Alpha enhancement given by [O/Fe] versus metallicity [Fe/H] for all centrals colored by $t_{50} - t_{90}$, with redder colors indicating a more rapid burst. Quenched centrals are plotted as filled squares.

burst than their average non-quenched counterparts. Interestingly, the starburst timescales found in our simulation are similar or even slightly shorter than those found for the quenched galaxies from the FLARES simulations at high redshifts by Lovell et al. (2023b).

Alternatively, we can determine the time between the last formed stellar particle and the highest peak in SFR, termed t_q. We bin the stellar formation times in steps of equal time and define t_q then as the time between the bin with the highest formed mass and the last bin containing any mass. Note that this definition is dependent on the chosen size of bin, so we test for bins of time 10 Myr to 100 Myr.

We find that t_q ranges from 30 Myr to 560 Myr. The mean lies at $t_q \approx 183$ Myr, and is largely stable for different sizes of bin (lying between 160 Myr and 200 Myr). Due to the more sporadic shape of individual bursts in SFR, we choose here to focus on the time characterizing the more smooth build up of stellar mass, $t_{50} - t_{90}$, instead.

Returning then to $t_{50}-t_{90}$, we found that the quenched galaxies experience a generally more rapid burst (which also enhanced the central stellar density, see Fig. A.1 in the Appendix). The rapidity of this process should result in a stellar population which is enriched primarily through the faster SNII compared to SNIa. This enhances alpha elements such as oxygen faster than iron.

We define $[X/Y] = \log_{10}(M_X/M_Y) - \log_{10}(M_X/M_Y)_\odot$, with solar values given by Wiersma et al. (2009). The right panel of Fig. 3.8 shows the locations of the stellar populations for all central galaxies in the [O/Fe]-[Fe/H] plane at $z = 3.42$, colored by the rapidity of the

star formation given by $t_{50} - t_{90}$. As is expected, we find that galaxies which underwent more rapid star formation (shorter $t_{50} - t_{90}$) lie at higher [O/Fe] compared to those of equal [Fe/H] which exhibit a more prolonged, continual star formation. The quenched galaxies (filled squares) reside in the area of highest alpha enhancement with comparable [Fe/H] to the non-quenched centrals. Consequently, the observed relation between alpha enhancement and central surface mass density in early type galaxies (ETGs) at lower redshifts (Barone et al., 2018) may well in part result from galaxies quenched via the mechanism described here, producing compact and strongly alpha enhanced galaxies. Interestingly, this does not mean that the *total* metallicity of the quenched galaxy stars is enhanced, which we discuss further in Fig. A.2 in the Appendix. We conclude that using the [O/Fe]-[Fe/H] plane as a diagnostic for the recent star formation history is feasible also at redshifts $z > 3$.

However, there are a few notable outliers with enhanced [O/Fe] yet particularly large $t_{50} - t_{90}$. We identify six such galaxies which have [O/Fe]> 0.13, [Fe/H]< -0.09 and $t_{50} - t_{90} > 500\,\mathrm{Myr}$. The star formation histories of these six outliers down to $z = 3.42$ are shown as solid gray lines in the top panel of Fig. 3.9, with the mean trends of quenched (blue) and non-quenched (sand) centrals for comparison. Five of the outliers show the same characteristic 'S'-shape of the quenched galaxies, but shifted to earlier times. They indeed undergo a rapid phase of star formation (hence the enhanced [O/Fe]) but stop just short of forming 90% of their stars. Instead, they transition into a more gradual phase of star formation which results in a high $t_{50} - t_{90}$. This post starburst phase, however, is not extended enough to significantly enhance [Fe/H].

The last of the six galaxies, galaxy *G*7854, is a particularly interesting case. Its SFH shows that it underwent *two* separate star formation bursts, with a prolonged period of relative quiescence in between. In fact its first burst is so early that, were it observed at $z = 5.5$, its formation redshift would be $z_{\mathrm{form}} \approx 8$ (dashed gray line), and it would appear both quiescent and massive ($M_* > 1{\times}10^{10} M_\odot$), making it comparable to all but the earliest forming quiescent galaxy from Nanayakkara et al. (2024), similar to the results for the quenched galaxy reported by Glazebrook et al. (2023).

It follows that the original assumption that enhanced [O/Fe] is the result of a phase of rapid star formation holds also for these outliers. It is through the peculiar shape of their SFH that they posses unusually large $t_{50} - t_{90}$. This can be seen further in the bottom panel of Fig. 3.9, where we show [O/Fe] as a function of the variance in stellar age. Low variance indicates that most of the stars were formed in a single star formation event and correlates with enhanced [O/Fe]. On the other hand, high variance indicates more prolonged star formation, and subsequently more iron enrichment through SNIa, which reduces [O/Fe]. The six outliers inhabit here the region of particularly high [O/Fe] and high age variance, with the most extreme outlier with the highest variance being galaxy *G*7854.

Furthermore, we find that the scatter in [O/Fe] at a given variance in stellar age is driven by different total metallicities [Fe/H]. Interestingly, higher [O/Fe] are found for galaxies with higher [Fe/H]. We interpret this as a result of the amount of self enrichment which occurs within a galaxy. As star formation at high redshift is primarily bursty, metal enrichment is

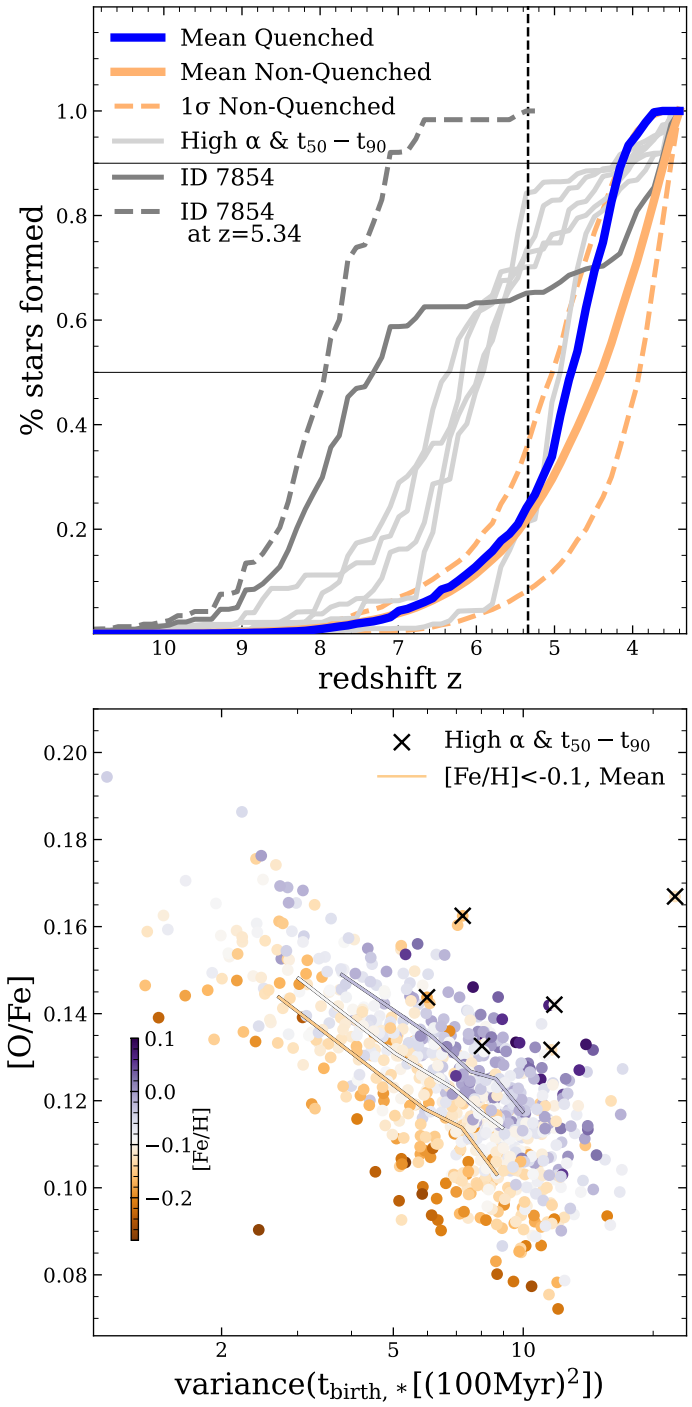


Figure 3.9. *Top:* Star formation histories for the six outliers (gray), with one particular case highlighted in a darker gray. For this galaxy the SFH is shown also at $z = 5.34$ (gray dashed). Mean SFH for the quenched (thick blue) and non-quenched (thick sand) are shown for comparison. *Bottom:* Stellar alpha enhancement [O/Fe] versus the variance in birth times of stellar particles, colored by metallicity [Fe/H]. Mean trends for low, intermediate and high [Fe/H] are given as colored lines (orange, silver, purple). The six outliers are indicated by black crosses.

driven by the SNII. Consequently, a galaxy which manages to enrich its star-forming gas more efficiently in [Fe/H] will be doing so mostly through SNII, thus driving [O/Fe] even higher.

This imprint of the metal enrichment in the alpha elements should, if a galaxy is quenched at high redshifts and does not undergo either merging or rejuvenation, still be measurable in the galaxy if observed at present day. Thus, if relic galaxies like those found by INSPIRE (Spiniello et al., 2021, 2023) and Comerón et al. (2023) really are the remnants of quenched galaxies at cosmic dawn, they should not only be rather compact and have extremely old stellar ages, they should also show strong alpha enhancements in their metal composition.

3.4.3 Baryon Fraction and Kinematics of Quenching

We have shown that the radial profiles of the stars and dark matter of quenched versus non-quenched galaxies at $z = 5-2$ do not differ strongly in their overall behavior. However, it has been claimed that quenched galaxies reside in comparatively overmassive halos and could have enhanced baryon fractions. We do not find our quenched galaxies to live in particularly massive halos (see Remus & Kimmig (2025) for more details), in fact the most massive halos at $z = 3.42$ all host star forming central galaxies. This is vastly different from the results found for IllustrisTNG by Hartley et al. (2023) and Kurinchi-Vendhan et al. (2023), where the quenched galaxies only reside in the most massive halos, as only in such halos the AGN has already switched to kinetic feedback which in their simulation is essential for quenching. In our simulation, the quenched galaxies are not solely quenched by the AGN feedback alone, as shown before, and thus we also find them in a different kind of environment. This environment in fact plays an important role, as we will see in more detail in Sec. 3.5.

We begin with the question whether the quenched galaxies have enhanced baryon fractions or even lower baryon fractions compared to their halo mass, something that is currently debated in the literature for most of the massive galaxies observed at high redshifts (e.g., Boylan-Kolchin, 2023; Harikane et al., 2023a). The top row of Fig. 3.10 shows the baryon fraction f_b and star formation rate of the quenched (blue) and non-quenched (sand) galaxies at different redshifts, filled symbols marking central galaxies and open symbols those that are satellite galaxies of a more massive galaxy. f_b is defined within the virial radius for centrals, and for all bound particles in the case of satellites.

Generally, we find that galaxies at higher baryon fractions can reach higher star formation rates on average, independent of the redshift. However, overall a significant fraction of the progenitors of both non-quenched and quenched galaxies lie at the cosmic baryon fraction of 16.8% within the simulation, marked by the dashed line. Central galaxies tend to have lower baryon fractions, while galaxies with larger baryon fractions than the cosmic one tend to be satellite galaxies. For those, this enhancement in baryon fraction is clearly driven by the onset of stripping of the dark matter in their outskirts in the larger potential of the host, and as such this behavior is expected.

For our quenched galaxies identified at $z = 3.42$, we do not find that they are overly baryon dominated prior to quenching when tracing them back in time, they rather behave exactly the same as the non-quenched sample. We find a slight tendency for those galaxies

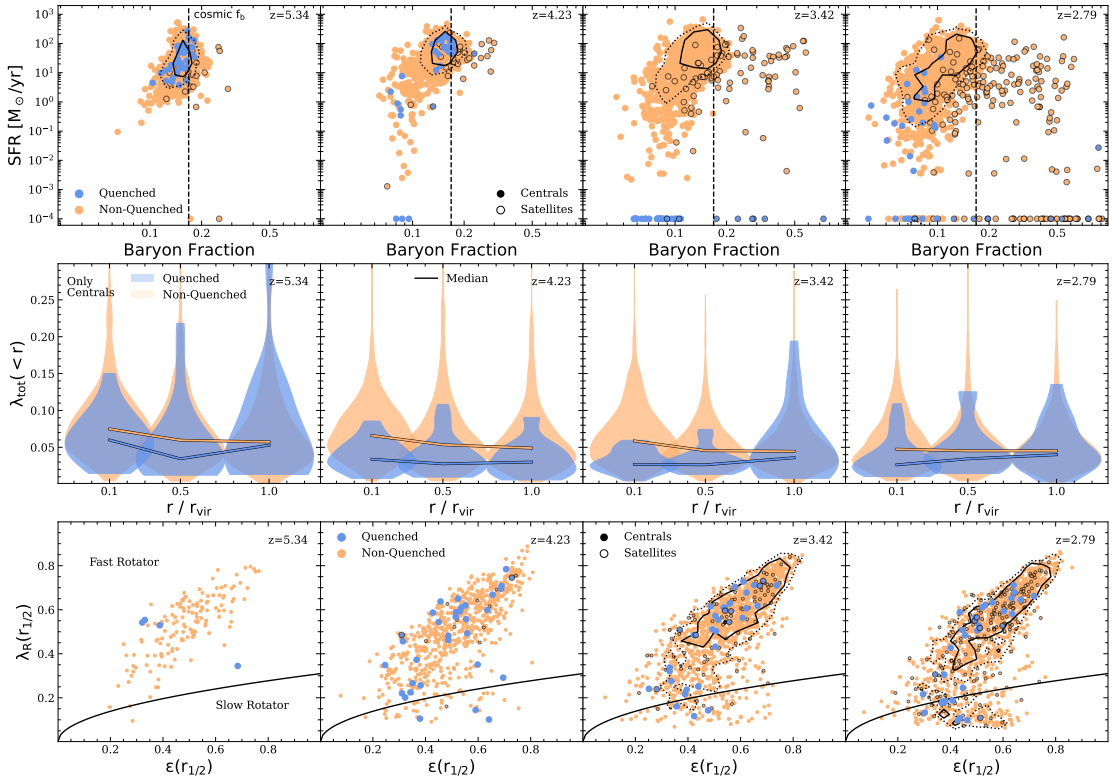


Figure 3.10. Various galaxy properties of the traced galaxy population going from high (z = 5.34, left column) to intermediate redshift (z = 2.79, right column). The quenched sample is defined by its SFR at z = 3.42. *Top row:* Star formation rate of traced quenched (blue) and non-quenched (sand) satellites (black outline) and centrals (no outline) as a function of the baryon fraction (for centrals defined as within the virial radius). The cosmic baryon fraction is indicated by vertical dashed line, while the contours enclose 80% (dotted) or 50% (solid) of all galaxies. *Middle row:* Distribution of total spin within different radii for the quenched (blue) and non-quenched (sand) centrals. Colored lines give the median. *Bottom row:* λ_R versus ϵ for the stars within one stellar half-mass radius. The solid line defines the split between fast and slow rotators given by Emsellem et al. (2011), with the fast rotators lying above the line. Contours enclose 80% (dotted) or 50% (solid) of all galaxies.

where their star formation has already declined but is not yet fully quenched to have lower baryon fractions

After quenching at z = 3.42, there is a very clear separation between quenched centrals and satellites. The centrals all lie far below the cosmic f_b as they have ejected practically all of their gas but not their DM. On the other hand, the satellites mostly lie at or above the cosmic f_b, indicating that they have had significant amounts of their DM stripped away through interactions with their host, a behavior that is also seen for the non-quenched sample.

Going to z = 2.79, we see that some of the quenched centrals actually rekindle their star formation even though they all remain noticeably below the cosmic f_b. They have yet to accrete significant amounts of gas, but what they have is sufficient to slowly begin forming stars again. To conclude, we find that quenched galaxies lie in halos of high dark matter fraction as a result of the quenching process, as opposed to quenching occurring due to the galaxies residing in overly massive halos.

Given how strongly the quenching process changes the baryon fraction throughout the entire halo, it is interesting to ask if it also imprints in the kinematics. To answer this we consider the dimensionless total spin $\lambda_{\rm tot}$ within a radius r as defined by Bullock et al. (2001):

$$\lambda_{\rm tot}(r) = \frac{J(r)}{\sqrt{2}M(r)V_{\rm circ}(r)r}, \tag{3.1}$$

where $J(r)$ is the total angular momentum within r, $M(r)$ the total mass within r, and $V_{\rm circ}(r) = \sqrt{GM(r)/r}$ is the circular velocity. This form is based on the initially introduced spin parameter by Peebles (1969). For a thorough study of the properties of $\lambda_{\rm tot}$ within the Magneticum simulations, see Teklu et al. (2015).

The central row of Fig. 3.10 shows the total spin measured within different radii around the galaxies at different times. Again, the sample of galaxies that are identified to be quenched at $z = 3.42$ is shown in blue, while the results for the total galaxy population are shown in sand. Since it is unclear what a halo total spin should be for a satellite galaxy, we only include those galaxies that are centrals in this figure.

At $z = 5.34$ the total spin for the quenched galaxies is equal to the non-quenched sample in the outskirts, and largely similar in the center (see Fig. 3.10). Both show slightly increasing rotation toward the center. However, it is already apparent that the peak total spin of the soon to be quenched galaxies is *decreasing* toward the center.

At $z = 4.23$ (prior to quenching) this signal becomes significant, with noticeably reduced total spin throughout the entire galaxy, which is not the case for the comparison sample of non-quenched galaxies. At scales of the galaxy ($\approx 0.1 r_{\rm vir}$) the $1\,\sigma$ range of the spin $\lambda_{\rm tot}$ of the quenched centrals lies entirely below the mean of the non-quenched population, with the two populations distinct at the $p < 10^{-4}$ level under a one sample t-test. This means that immediately prior to quenching the galaxies show surprisingly little rotation, even though they are undergoing a large starburst. This may indicate that the accretion of mass is happening isotropically, as the total halo spin is lowered on all radial scales prior to quenching. While tidal torque interactions usually enhance the halo spin (e.g., Peebles, 1969), the spin of the dark matter is usually removed through strong isotropic accretion or a major merger event on a counter-rotating orbit (Cervantes-Sodi et al., 2010); however, we tested the latter and found that all of our quenched halos show multiple gas-rich merger events from multiple directions, and only two exhibit a major merger going from $z = 5.34$ to $z = 4.23$ (with zero major mergers going from $z = 4.23$ to $z = 3.42$).

Indeed, post quenching ($z = 3.42$ and $z = 2.79$) the central region containing the galaxy shows the lowest amount of total spin, while in the outskirts we already find the spin starting to build up again to values comparable with the non-quenched sample. A positive total spin gradient with radius may then point toward the type of self-quenching burst found here, correlating with a preceding phase of isotropic infall. This matches the picture discussed for Fig. 3.5, where the isotropic accretion both more efficiently feeds the central AGN and is more easily disrupted by the consequent feedback. We also find an increased concentration of both the stellar density and dark matter halo compared to non-quenched galaxies, which



we discuss in the Appendix with Fig. A.1, and which may be a result of this differing mode accretion.

But does this large scale transformation of the galactic halo's spin also imprint on the stellar angular momentum within the central galaxy? To answer this we use the λ_R-parameter, a proxy for the projected angular momentum that can be measured from observations, introduced by Emsellem et al. (2007) and adapted for cosmological simulations assuming a constant mass-to-light ratio (e.g., Jesseit et al., 2009; Bois et al., 2011):

$$\lambda_R = \frac{\sum_i R_i M_i |V_i|}{\sum_i R_i M_i \sqrt{|V_i|^2 + \sigma_i^2}}, \tag{3.2}$$

where the sums $\sum_i$ run over the Voronoi tessellation cells (Cappellari & Copin, 2003), R_i is the projected distance of the Voronoi cell center, M_i is the total mass, V_i is the mean line-of-sight velocity, and σ_i is the line-of-sight velocity dispersion, each as measured within the ith Voronoi cell. For a detailed study on the properties of λ_R in the Magneticum simulations from $z = 2$ to $z = 0$, see Schulze et al. (2018).

The bottom row of Fig. 3.10 shows λ_R versus the ellipticity ϵ within the stellar half-mass radius for the sample of traced galaxies. Here we only plot a galaxy starting from when it reaches $M_* > 3 \times 10^{10} M_\odot$ to ensure a good resolution of the central kinematics. The solid black line indicates the separation between fast and slow rotators, as determined by Emsellem et al. (2011), with the fast rotators lying above the line.

For all galaxies (sand color), we find the vast majority to be fast rotating independent of the redshift, but we also see the onset of the formation of a slow rotating population towards lower redshifts, emerging at $z > 4$. Interestingly, this does not correlate at all with our population of quiescent galaxies (blue color). In fact, the majority of the quenched galaxies identified at $z = 3.42$ retain their rotation and remain fast rotators after quenching, clearly indicating that for the high-redshift galaxies the quenching process is not coupled to an increase in dispersion and a decrease in rotational velocity. This is in excellent agreement with observations by Newman et al. (2018), who reported their four lensed quenched galaxies at $z = 2 - 2.5$ to all be fast rotators.

The origin of the emerging slow rotating population is thus not the mechanism that quenches galaxies, as most of the slow rotating galaxies at these high redshifts are still star forming. This is different from observations of low-redshift slow rotating galaxies, which are usually quiescent elliptical galaxies (e.g., Emsellem et al., 2007; Falcón-Barroso et al., 2015; Cortese et al., 2016), as the origin of these slow rotating galaxies is found to be mostly merger driven (e.g., Bois et al., 2011; Schulze et al., 2018; Lagos et al., 2022). However, Lagos et al. (2022) also report from the EAGLE simulation a population of slow rotating galaxies at $z = 0$ which have not been formed through merger events. They find these non-merger-quenched galaxies to be more compact and more recently quenchend, i.e., they retained star formation while possibly already being slowly rotating. This is in good agreement with the properties of our slow rotating galaxy population emerging between $z = 4$ and $z = 2$. However, the

process that leads to the formation of these slow rotating galaxies at high redshifts is beyond the scope of this work and will be addressed in a future study.

We conclude for the population of quenched galaxies at high redshifts that on the one hand an isotropic infall of both gas and dark matter is essential, resulting in the total halo spin being significantly lowered compared to other galaxies. On the other hand, the isotropically infalling gas has time to redistribute its angular momentum into a disk-like configuration to make stars before the actual quenching occurs, as we find the quenched galaxies to be predominantly fast rotating with no clear offset to the total sample. Nevertheless, the imprint in the total halo spin clearly shows evidence for an isotropic accretion of matter onto the galaxy prior to quenching, and hints at the environment being an important aspect for the quenching to be successful which we explore in the following.

3.5 The Role of Environment

Having noted the curious dip in total spin prior to quenching, we move here to analyze the surrounding environment of these galaxies. However, the multi-scalar nature of the cosmic web makes the task of linking the large-scale environment to galaxy properties an inherently difficult one, as a given galaxy might inhabit one environment (e.g., a 1-dimensional filament) at a certain scale, but a different one (e.g., a void) at another scale (Rieder et al., 2013). Modern structure finders like the Hessian-based NEXUS (Cautun et al., 2013) respect this multi-scalar nature by applying a spherical filter of different radii and then combining structural elements identified at different scales. For flexible case-by-case galaxy environment studies, however, these algorithms remain cumbersome.

Instead, we consider the environment around the galaxies here in two ways. Firstly, by considering whether they live in generally over or underdense environments as given by the density contrast δ. Secondly, by the geometric dimensionality parameter (hereafter referred to as D) as suggested by Sarkar & Bharadwaj (2009). As this section of the analysis focuses on the intermediate-to-large scale environments, all quantities computed in this section are in comoving units. We start with the density contrast δ, defined as

$$\delta(< R) = \frac{\rho(< R) - \bar{\rho}}{\bar{\rho}} \tag{3.3}$$

with $\rho(< R)$ the density within a sphere of radius R around a galaxy and $\bar{\rho}$ the mean density at the current redshift. In order to be able to fully capture the morphology of the forming cosmic web around these galaxies, we choose an upper filter radius of 10 Mpc/h. This value is motivated by previous studies on the characteristic sizes of network components such as by Aragón-Calvo et al. (2010).

To better quantify the difference between the quenched and non-quenched centrals, we then define

$$\delta_{\sigma,\mathrm{rel}}(< R) = \frac{\delta(< R) - \bar{\delta}(< R)}{\sigma_{\delta,R}} \tag{3.4}$$

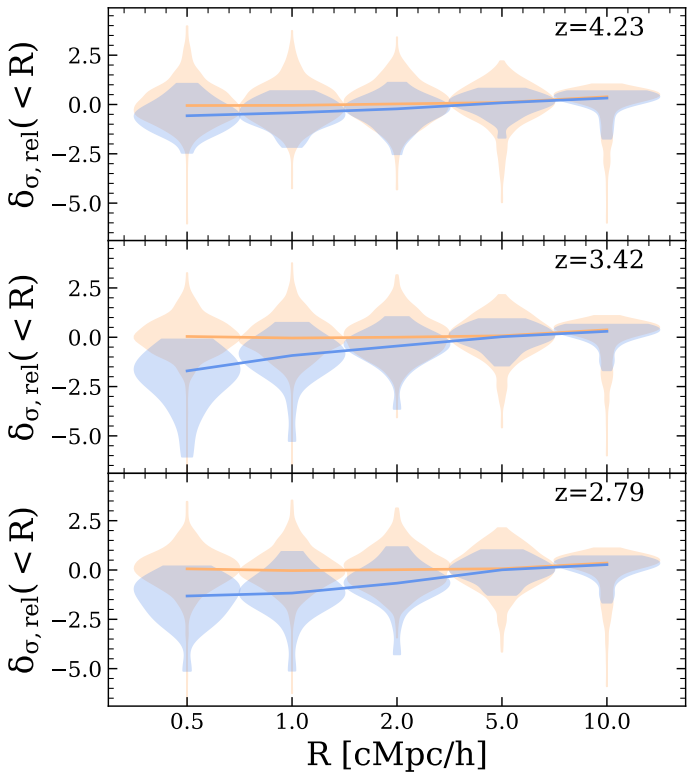


Figure 3.11. The deviation from the median density $\delta_{\sigma,\mathrm{rel}}$ within a sphere of radius R for quenched (blue) and non-quenched (sand) centrals at three redshifts (*top* to *bottom*, $z = 4.23$ to $z = 2.79$).

with $\bar{\delta}(< R)$ the mean density contrast within a sphere of radius R for the galaxies in our sample and $\sigma_{\delta,R}$ the standard deviation of the distribution of density contrasts.

By this definition $\delta_{\sigma,\mathrm{rel}}(< R)$ quantifies how strongly a galaxy's density contrast is an outlier compared to all the other galaxies within our sample. For example, $\delta_{\sigma,\mathrm{rel}}(< 1\,\mathrm{Mpc}) = +1$ would imply that the environment within 1 Mpc around the galaxy is denser compared to the total sample, being a $1\,\sigma$ outlier. If we assume the overdensities of our sample are distributed normally this is equivalent to being denser than around 84% of other galaxies.

Fig. 3.11 shows $\delta_{\sigma,\mathrm{rel}}(< R)$ for the quenched (blue) and non-quenched (sand) centrals for different radii. On the largest scales $R > 5\,\mathrm{cMpc/h}$ the quenched galaxies lie in comparable environments to the rest of the sample, both before ($z = 4.23$, top panel) and after quenching ($z = 3.42$ and $z = 2.79$, middle and bottom panels).

However, the more locally we consider the environment around the galaxy, the more the quenched centrals deviate from those which do not quench. Interestingly, they inhabit comparably underdense regions (note that this does not mean underdense compared to the full simulation volume, but rather compared to galaxies of similar stellar mass).

Prior to quenching they lie on average at $\delta_{\sigma,\mathrm{rel}} = -0.5$ for $R = 0.5\,\mathrm{cMpc/h}$, while immediately post quenching this drops to $\delta_{\sigma,\mathrm{rel}} = -1.7$. This means that the galaxies which fully quench lie in more underdense regions than 96% of galaxies of comparable stellar mass. Fascinatingly this signal is present even on larger scales of up to $2\,\mathrm{cMpc/h}$, and also at $z = 2.79$.

We then move on to the dimensionality parameter D (Sarkar & Bharadwaj, 2009). It is built on the simple assumption that the number of density tracers within a spherical filter scales with $N_{\text{tracer}} \propto R_{\text{filter}}^{D}$ in a D-dimensional spatial configuration. This means that $D = 1$ is equivalent to the geometry of a filamentary structure, $D = 2$ to a sheet and $D = 3$ to a node (cluster) or antinode (void). It should be noted that intermediate values do not offer a clear interpretation as to the density structure, as the information is heavily convolved with the precise radial profile of the environment. This is why this parameter should be used only in joint analysis with the overdensity information itself, as is done within this section.

D can be computed by

$$D \propto \frac{d\log(N)}{d\log(R_{\text{filter}})} \tag{3.5}$$

with N the number of dark matter particles. We determine D within 100 logarithmically spaced ($\Delta \log(R[\text{cMpc/h}]) = 1.05$) spherical filters with radii ranging from 0.1 cMpc/h to 10 cMpc/h.

Fig. 3.12 shows the distribution of dark matter around the centrals as a function of radius (left panels) as well as the resulting dimensionality D (right panels). At $z = 4.23$ (top row) we find the quenched galaxies to behave similar to the non-quenched sample in terms of total mass as expected from Fig. 3.11. However, we find that D drops noticeably below a value of 1 at around 0.2 cMpc/h, and here the median of the quenched galaxies lies even outside the 1σ bounds of the non-quenched sample. This implies a local shell of nearly null density (which shows up in the left panel as a region of nearly flat N).

Comparing the profiles $N(R)$ between $z = 4.23$ and $z = 3.42$ for the quenched centrals, we find that they remain remarkably similar. Where the non-quenched galaxies have accreted additional dark matter towards their centers (thus generally reaching higher amounts of dark matter N at < 1 cMpc), the quenched halos have not.

Combined with the results seen in Fig. 3.11, we conclude that the galaxies which quench did not start out themselves being in severely underdense regions. Rather, they *develop* into underdense regions coinciding with the time of quenching. This may be due either to other structures growing to become the locally dominant node or because there was always a region of low density nearby (or both, as for example seen in Fig. 3.3).

3.6 Predictors for Quenching

Throughout the prior sections we have shown the quenching process to correlate with a diverse set of galactic properties. We here quantify which parameters best predict future quenching, preferring observable quantities to best enable predictions for observed galaxies.

Firstly, as discussed in Sec. 3.4, quenched galaxies possess particularly massive black holes compared to their stellar mass (so have high M_{BH}/M_*). We further find that they funnel significant amounts of gas towards their centers prior to quenching, which results in a large growth of their SMBH mass (high ΔM_{BH}). Aside from their SMBH properties, however, we

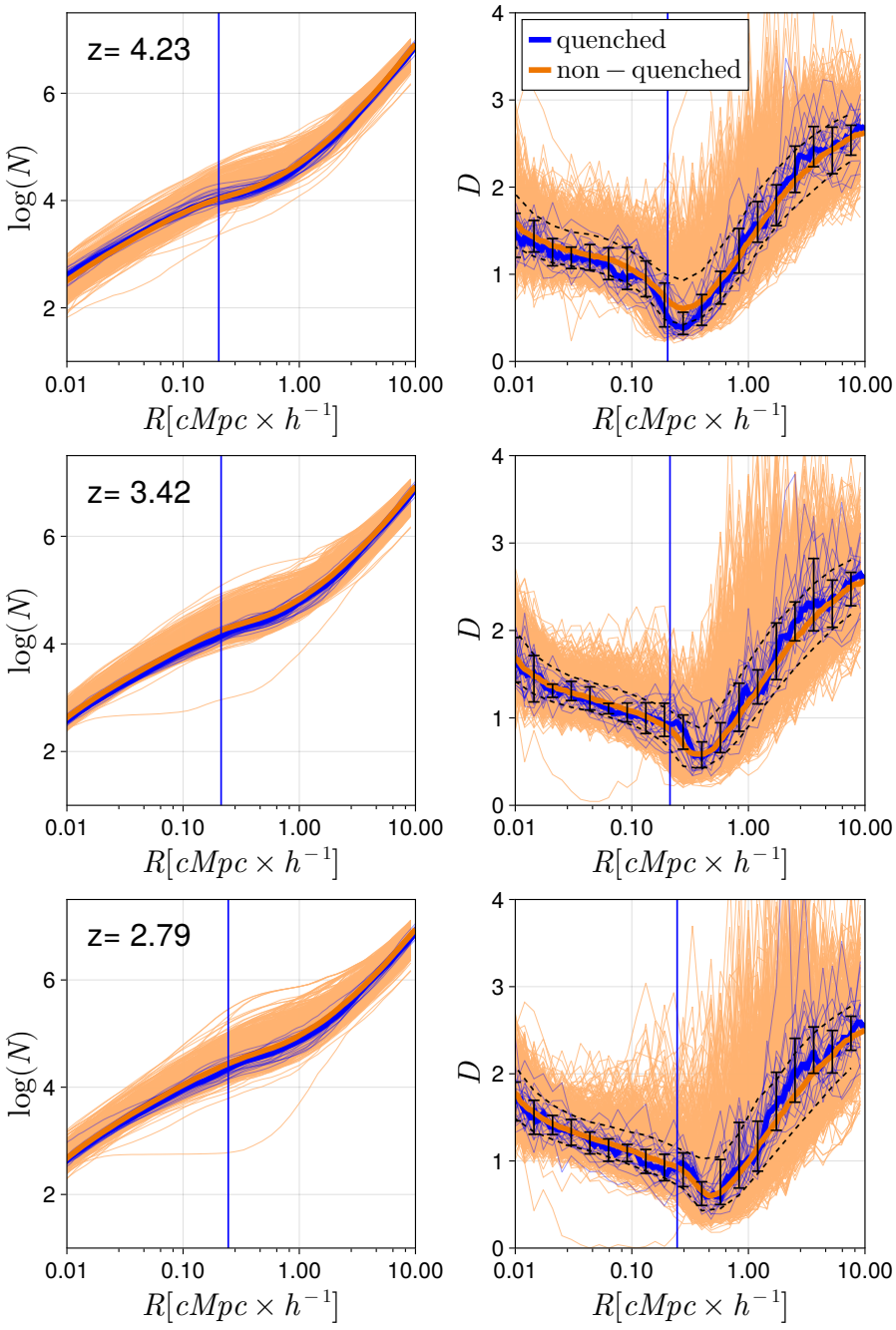


Figure 3.12. Number of dark matter particles N (*left panels*) and resulting dimensionality parameter D (*right panels*) as a function of radius around the quenched (blue lines) and non-quenched (sand lines) centrals, for three redshifts ($z = 4.23$ to $z = 2.79$, top to bottom). Median behaviors are given by the fat solid lines. In the right panels the thin dashed lines show the 1σ bounds of the non-quenched sample, while the quenched samples 1σ bounds are shown as black errorbars. Also shown are the median virial radii of the quenched centrals (vertical blue line).

find that the funneling of gas also results in a massive starburst (low $t_{50} - t_{90}$, see Sec. 3.4.2). Finally, Sec. 3.5 showed that they lie in generally underdense regions.

We thus have four parameters to predict the future quenching (or lack thereof) for a given galaxy at high redshift. These are the black hole properties, $M_{\rm BH}/M_*$ and $\Delta M_{\rm BH}$, the star formation history quantified by the timescale $t_{50} - t_{90}$ on which stars are formed, and finally

Table 3.1. Fraction (number) of central galaxies that lie in the upper third for a given property/combination of properties which become quenched at $z = 2.79$, $z = 1.98$ or at some point by $z = 1.98$. The right-most column is the probability $P_{\rm rand}$ of randomly drawing the fraction of quenched galaxies given by the constraint of all properties excluding the recent mass growth of the SMBH (labeled "Ex. $\Delta M_{\rm bh}$")

Constraint	None	$M_{\rm bh}/M_*$	$\Delta M_{\rm bh}$	$t_{50} - t_{90}$	d_5	BH	t+d	Ex. $\Delta M_{\rm bh}$	Combined	$P_{\rm rand}$
$N_{\rm galaxies}$	839	280	280	280	280	170	102	52	32	-
	Fraction [%] (Number) Which Fully Quench									
At z=2.79	5.1 (43)	8.2 (23)	7.9 (22)	8.2 (23)	7.1 (20)	9.4 (16)	9.8 (10)	17.3 (9)	18.8 (6)	7.6e-4
At z=1.98	6.8 (57)	10 (28)	11.1 (31)	13.2 (37)	13.6 (38)	11.1 (19)	18.6 (19)	25 (13)	28.1 (9)	1.4e-5
By z=1.98	13.3 (112)	19.6 (55)	18.9 (53)	23.2 (65)	21.1 (59)	21.8 (37)	31.4 (32)	44.2 (23)	53.1 (17)	<1e-6

the environment quantified by the parameter d_5. As opposed to the tracers of the environment used in Sec. 3.5 (measuring *all* mass), we use here instead d_5, which is the minimum radius required to contain within it five other galaxies of total mass $M_{\rm all} \geq 1 \times 10^{11} M_\odot$, aside from the galaxy in question. This is a much more reasonable characterization in terms of observability. Remus & Kimmig (2025) show this parameter to be correlated nicely with the final halo mass at $z = 0$, and that the quenched galaxies are also predominantly underdense by this definition of environment.

In the following, we will now quantify the importance of all four parameters with respect to a long lasting quenching of a galaxy at high redshifts. We therefore take the sample of 1217 central galaxies at $z = 3.42$ with a stellar mass of $M_* > 3 \times 10^{10} M_\odot$, and keep only the 839 which remain centrals until $z = 2$ for this comparison, to exclude for example galaxies that merge onto more massive galaxies.

For every property we split the sample into three nearly equal groups (of around 280 galaxies each) going from galaxies with values which should result in the lowest chance of quenching to those with the highest. For example, $M_{\rm BH}/M_*$ goes from lowest to highest (as the quenched galaxies have massive black holes) while $t_{50} - t_{90}$ goes from highest to lowest values (as the quenched galaxies show more rapid bursts of star formation).

Every group of galaxies has their median specific star formation rate determined for the three redshifts of $z = 2.79$, $z = 2.33$ and $z = 1.98$ (equivalent to times of around 0.5, 1 and 1.5 Gyr from when the properties are determined at $z = 3.42$). This tells us if a subset has enhanced or decreased star formation activity relative to the total sample of galaxies traced forward in time.

Fig. 3.13 shows the resulting median sSFR for the 839 centrals, with individual properties (red to orange) and combinations of properties (brown to black). For combinations we determine the intersect, so the galaxies which are *simultaneously* in the upper/middle/lower third of two, three or all four parameters. Galaxies which are spread in properties (for example upper third in black hole mass and middle third in d_5) are thus not included in the combined property constraints.

When using a single property to determine whether a central galaxy will be starforming or quenched within the next 0.5 Gyr, we find the strongest dependence on $M_{\rm BH}/M_*$. The galaxies with the lowest mass ratio (red open diamond) exhibit a noticeably enhanced sSFR

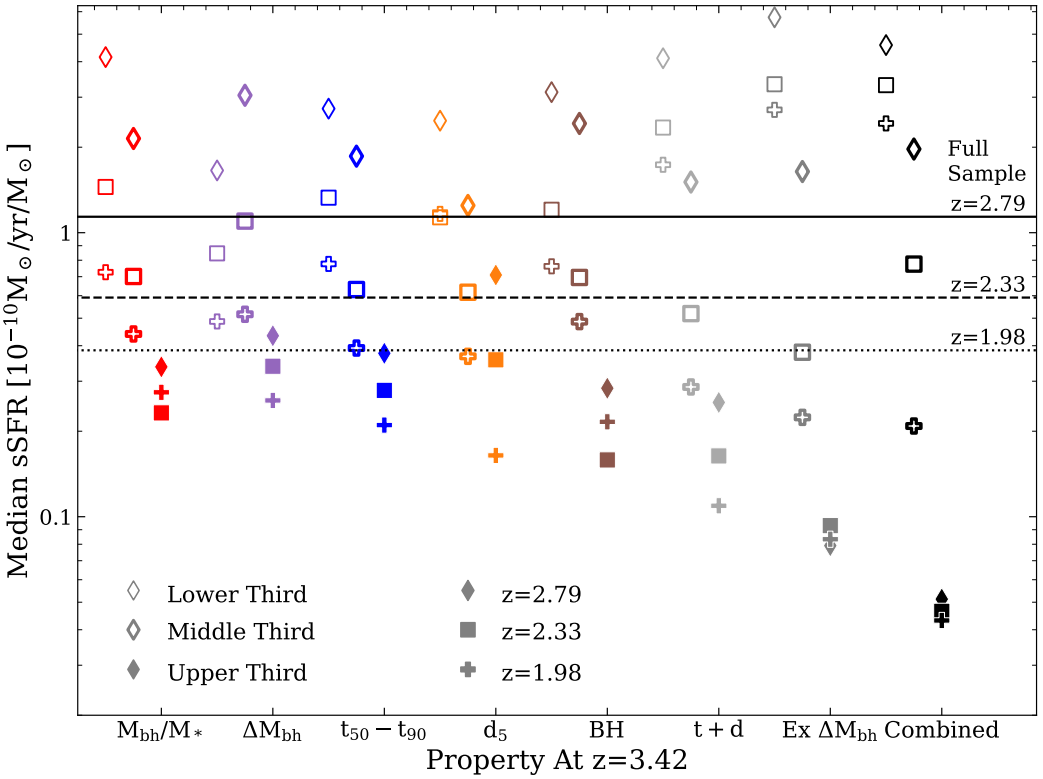


Figure 3.13. Median sSFR of 839 centrals traced forward in time to $z = 2.79$, $z = 2.33$ and $z = 1.98$ (diamond, square and plus markers). They are split into three groups based on whether they are in the lower, middle or upper third (open, semi-filled and filled symbols) of different parameters (colors) at $z = 3.42$. Median sSFR for the full 839 centrals are shown as horizontal black lines for the three redshifts. Combinations of parameters (brown, light gray, dark gray and black) show galaxies which lie in the lower/middle/upper third for all properties in the combination given on the x-axis, with the combinations being: "BH" for both black hole related properties, "t+d" for $t_{50} - t_{90}$ and d_5, "No $\Delta M_{\rm BH}$" for all properties excluding the SMBH mass growth and "All" for all properties combined.

of around 4.2×10^{-10}/yr, while those with the highest ratio (red filled diamond) have only around 3.3×10^{-11}/yr compared to the total samples' average of 1.1×10^{-10}/yr.

Only marginally less significant is the correlation with $t_{50} - t_{90}$ (blue), where galaxies which exhibit more prolonged star formation histories will likely continue forming more stars, while those which recently underwent a rapid burst are prone to find strongly reduced star formation compared to the total sample.

When determining the star formation up to $z = 1.98$, the picture changes. Both tracers for the SMBH perform more poorly than the other tracers, and in particular the tracer for environment (orange markers) becomes the most significant. On longer timescales the future of a galaxy is therefore most determined not by its internal properties, but rather the surrounding matter which may fall in. Even if a galaxy becomes quenched for some time along the way, if there is sufficient surrounding gas it may well rekindle its star formation (a point which Remus & Kimmig (2025) discuss in more depth). Conversely, the galaxy may itself house the ideal conditions for a star formation burst (little SMBH feedback, no other recent burst) but if there is insufficient gas to fuel it, the burst will not happen.

For the combined properties (brown to black markers) we note first that the number of galaxies per group is reduced. For a given combination (for example $t_{50} - t_{90}$ and $d5$) the "upper third" would be the subset of galaxies which lie in the highest third of values for both properties *simultaneously* (so for example galaxies which have the fastest $t_{50} - t_{90}$ *and* largest d_5).

Fascinatingly, we find that at all redshifts the combination of star formation history and environment ($t_{50} - t_{90}$ and $d5$, light gray "t+d") more significantly splits up the sample than the combined SMBH properties ($M_{\rm BH}/M_*$ and $\Delta M_{\rm BH}$, brown "BH").

The difference is most pronounced when predicting the star formation rate up to 1.5 Gyr in the future. Galaxies which have the most prolonged SFH and lie in the densest environments will retain a comparably high specific star formation rate of 1.7×10^{-10}/yr (light gray open diamond), while galaxies which have undergone recent bursts of star formation and which lie in underdense regions will on average exhibit very little star formation (around 1.1×10^{-11}/yr).

That is not to say that the SMBH does not impact the significance of the prediction. When we further add $M_{\rm BH}/M_*$ to the SFH and environmental tracers, the split up becomes even more noticeable. On shorter timescales of 0.5 Gyr in particular, isolated galaxies which host massive central black holes and had a rapid burst of star formation exhibit a reduced specific star formation rate by over an order of magnitude compared to the total sample (8×10^{-12}/yr versus 1.7×10^{-10}/yr).

Including also the recent growth of the SMBH mass, so all tracers considered here simultaneously (black points), produces the strongest prediction towards low star formation rates. This, however, also represents the most stringent constraint, with just 32 of 839 central galaxies lying in the highest third for black hole mass, growth, fastest star formation burst and most underdense environment at the same time.

This is interesting when comparing with the results found by Bluck et al. (2024), who find using a random forest analysis that in EAGLE and TNG the black hole mass is of larger relative importance to quenching than halo mass, stellar mass, or half mass radius. This matches what we find here, that compared to other tracers the black hole mass is most significant for the short term ($t = 500$Myr) impact on future star formation. Our findings, that for longer term quiescence the environment becomes more significant, can serve to inform future interpretations of observed galaxies, to identify those which will likely become or remain quiescent.

Bluck et al. (2024) also show that the stellar potential ϕ_* performs better in terms of quenching importance compared to stellar mass or size, both from the simulations as well as observations from JWST-CEERS. It would be interesting to extent their analysis to include for example $t_{50} - t_{90}$ as a tracer of the immediate impact from star formation, and likewise to consider whether the stellar potential ϕ_* also has predictive power for long term quiescence. The latter would inform whether the assumptions of using ϕ_* as a tracer of black hole mass, which in turn should provide an estimation of the amount of preventative feedback that is found from lower redshifts to be crucial in stopping rejuvenation (Bower et al., 2006; Fabian, 2012), is indeed feasible.

It would be further intriguing to test their conclusions also for the case of a simulation which reproduces the observed high number densities of quiescent galaxies at high redshifts, as discussed here with Fig. 3.2 and by Remus & Kimmig (2025), to understand whether the distinction of cold and hot accretion implemented by Steinborn et al. (2015) allows for more fluid transitions into and out of quiescence compared to the rapid decline at a specific threshold mass as seen for example by Zinger et al. (2020) or Piotrowska et al. (2022) in the case of IllustrisTNG.

Finally, we consider also which properties predict the future complete shut-down of star formation the best (galaxy reaches sSFR= 0/yr). To do so, we determine the number and fraction of galaxies within the "upper third' samples for each property (and combination of properties) which become quenched. We consider three times, namely if they are quenched at $z = 2.79$, at $z = 1.98$, or if they were ever quenched between $z = 3.42$ and $z = 1.98$. The results are shown in Tab. 3.1.

Generally we find comparable behavior to that seen in Fig. 3.13. If a property results in a more reduced median sSFR, it also results in a higher fraction of quenched galaxies. We find that if a galaxy lies in the upper third for either massive $M_{\rm BH}/M_*$ or rapid $t_{50} - t_{90}$ compared to galaxies of like stellar mass, the probability that it will fully quench its star formation within 0.5 Gyr is around 8% (compared to a base probability of 5% for all galaxies).

Combinations of properties provide more stringent conditions but also significantly increase the probability of the galaxy quenching. The combination of the observable quantities, so if a galaxy has a particularly massive black hole, a rapid burst of star formation and lies in a comparatively underdense region, results in a 17% probability that the galaxy will fully quench within the next 0.5 Gyr (9 of the 52 galaxies fulfilling the combined constraints). This chance is further enhanced to 44% (23 galaxies) that it will be quenched at some point within the next 1.5 Gyr. To confirm that this result is not a statistical outlier, we determine the probability of randomly selecting a subsample of 52 galaxies from the full sample of 839 and finding at least 23 galaxies which fully quench. From a million random draws, not a single one finds 23 or more quenched galaxies.

3.7 Conclusions

Massive quiescent galaxies at cosmic dawn pose an interesting challenge to our understanding of the processes which occur at high redshift to build and transform galaxies. They must have undergone significant accretion and star formation on short timescales to reach the observed stellar masses, while simultaneously quenching it fully by the time they are observed. To explore how exactly these galaxies form and quench, we have employed Box3 uhr of the Magneticum Pathfinder suite of cosmological simulations, which we have shown to fulfills both the requirements of high resolution (to resolve early bursty star formation) as well as box size (to contain more significant overdensities which can collapse early).

We find that quenched galaxies undergo a noticeable starburst prior to quenching, resulting in some of the most peaked star formation histories even compared to other massive

galaxies at high redshift. The rapid growth required to trigger such a large starburst means that they start out as *local* attractors, quickly rising to become some of the most massive galaxies. Importantly, the influx of matter occurs rather isotropically compared to other massive galaxies at the same redshifts, and not directional along big filaments which is more common at lower redshifts.

Simultaneously, the internal processes of stellar and AGN feedback triggered by the preceding generally isotropic influx of massive amounts of gas have served to eject most gas far outside of the galaxy at the moment of quenching. Important for a successful quenching is hereby that the galaxies were only *local* and not *global* nodes of the cosmic web, and in fact reside in a globally underdense region of the web. The surrounding relative underdensity equates to weak feeding filaments, which on one hand allow for the gas to be ejected farther out, while on the other hand are themselves more easily disrupted. With all of its own gas consumed or ejected and no new gas streaming in, the galaxy is quenched. Whether it remains quenched or rejuvenates is discussed in greater depth by Remus & Kimmig (2025). However, here we have shown an underdense environment to be the best indicator for a long-term quenching to be successful.

To summarize, we conclude that massive quenched galaxies at high redshifts generally

- lie in significant *local underdensities* compared to galaxies of similar stellar mass.
- *have a phase of strong isotropic accretion prior to quenching.*
- went from 50% to 90% of their stellar mass in a *fast starburst* usually in less than 200 Myr, comparable to recent observations (e.g., Carnall et al., 2023b; Kakimoto et al., 2024; de Graaff et al., 2024a).
- host *massive central black holes*, but not more excessive than other galaxies of the same mass.
- have *enhanced* $[O/Fe] \approx 0.14$ compared to non-quenched galaxies of the same stellar mass.
- have similar kinematic properties to non-quenched galaxies, mostly being *fast rotators*, in agreement with observations (Newman et al., 2018).
- are surrounded by *metal-rich ejected gas*.

We also investigate which quantities are most indicative of the future evolution of a given galaxy, especially with regards to observable quantities. For predicting whether a massive galaxy will be quenched in the future, we find that

- on short timescales a high black hole to stellar mass ratio $M_{\rm BH}/M_*$ is the best predictor, followed by a rapid starburst with short timescales of $t_{50} - t_{90}$, both of which are caused by the same infall of low angular momentum gas.
- on longer timescales it is instead the environment which becomes most significant, with less dense environments leading to the highest quenching likelihood due to the limited gas reservoir.
- on all timescales the combination of stellar and environmental properties is more relevant than the mass or recent growth of the SMBH.



- but including the requirement of a high SMBH mass further enhances the probability of a galaxy quenching within the next 1.5 Gyr to 44%.

To conclude, we find evidence that quenching at high redshifts depends on more than just the AGN feedback, although the AGN feedback is a crucial component. In fact, the overall process of quenching is connected to a massive and rapid starburst event, caused by a fast isotropic accretion of gas that triggers both the starburst and also the growth of the SMBH. This ultimately leads to an alpha-enhancement of the stellar and gas metallicity through the short nature of the starburst and then full gas removal by the AGN feedback out to several virial radii in some cases. However, we find galaxies with similarly massive BHs, strong AGN feedback or short starbursts which do not quench.

In fact, we conclude that quenching tends to depend on the infall of gas being rather isotropic and the environment being underdense. These conditions may be uniquely prevalent in the early universe, where strong feeding filaments have yet to form. *We suggest that this rapid starburst quenching (RSQ) mechanism is the dominant mode of quenching down to a redshift of about* $z = 2$, however, further studies on the efficiency of this type of quenching at different redshifts are required to confirm this in the future.

Preso dall'operazione del lume del Sole, il quale, mentre attrae quei vapori o riscalda quella pianta, gli attrae e la riscalda in modo, come se altro non avesse che fare; anzi nel maturar quel grappolo d'uva, anzi pur quel grapello solo, vi si applica che piu efficacemente applicar non vi si potrebbe quando il termine di tutti i suoi affari fusse la sola maturazione di quel grano.

Galileo Galilei, *Dialogo sopra i due massimi sistemi del mondo*, 1632

4

Relight the Candle: What happens to High Redshift Massive Quenched Galaxies

This chapter was published as Remus & Kimmig 2025, ApJ 982, 30.
Both authors contributed equally to this paper.

A puzzling population of extremely massive quiescent galaxies at redshifts beyond z=3 has recently been revealed by JWST and ALMA, some of them with stellar ages that show their quenching times to be as high as z=6, while their stellar masses are already above $5 \times 10^{10} M_\odot$. These extremely massive yet quenched galaxies challenge our understanding of galaxy formation at the earliest stages. Using the hydrodynamical cosmological simulation suite Magneticum Pathfinder, we show that such massive quenched galaxies at high redshifts can be successfully reproduced with similar number densities as observed. The stellar masses, sizes, formation redshifts, and star formation histories of the simulated quenched galaxies match those determined with JWST. Following these quenched galaxies at $z = 3.4$ forward in time, we find 20% to be accreted onto a more massive structure by $z = 2$, and from the remaining 80% about 30% rejuvenate up to $z = 2$, another 30% stay quenched, and the remaining 40% rejuvenated on a very low level of star formation. Stars formed through rejuvenation are mostly formed on the outer regions of the galaxies, not in the centres. Furthermore, we demonstrate that the massive quenched galaxies do not reside in the most massive nodes of the cosmic web, but rather live in side-nodes of approximately Milky-Way halo mass. Even at $z = 0$, only about 10% end up in small-mass galaxy clusters, while most of the quenched galaxies at $z = 3.4$ end up in group-mass halos, with about 20% actually not even reaching $10^{13} M_\odot$ in halo mass.

4.1 Introduction

The high-redshift Universe has become available to observations in the last year thanks to JWST in unprecedented detail, revealing star forming galaxies to exist at redshifts as high as $z = 13$ or possibly higher from photometry (e.g. Adams et al., 2023; Harikane et al., 2023b), and despite some of them having shown to be at lower redshifts by spectroscopic follow up, several of them have been confirmed at redshifts as high as $z = 13$ (e.g. Harikane et al., 2023a; Arrabal Haro et al., 2023). Furthermore, ALMA has added to the zoo of high redshift galaxies observations of low-turbulence but dust-obscured disk galaxies that cannot be detected by JWST due to their high dust content (e.g. Lelli et al., 2023; Rizzo et al., 2023). Such dust obscured galaxies with average star formation rates have been found even up to $z = 7$ (Fudamoto et al., 2021). Massive galaxies with disk morphologies have been resolved at redshifts up to at least $z = 4$ (e.g., Tsukui & Iguchi, 2021; Roman-Oliveira et al., 2023), with star formation rates of more than $1000 M_{\odot}/yr$ and strong AGN activity (Tsukui et al., 2023), but also some spiral galaxies have been reported at those redshifts that show signs of their star formation being shut off (Fudamoto et al., 2022; Nelson et al., 2023). All of these observations challenge our understanding of galaxy formation and the overall structure formation and cosmology when the Universe was very young, and are the perfect testbed for theoretical models and simulations to probe our grasp on the underlying physics.

To this zoo of extraordinary galaxies at high redshift also belong massive quenched galaxies, that is galaxies at redshifts as high as $z = 4$ with stellar masses of $M_* > 3 \times 10^{11} M_{\odot}$ (Schreiber et al., 2018; Nanayakkara et al., 2024; Carnall et al., 2023a; Long et al., 2023), for which spectroscopically their formation times, i.e. the time at which half of their stars have been formed, were confirmed to be as high as $z = 6 - 7$ (Nanayakkara et al., 2024; Carnall et al., 2023a), in one case even as high as $z = 11$ (Glazebrook et al., 2023). These quiescent galaxies are found in significant numbers at high redshift, unexpectedly, as with the overall gas content in these galaxies much higher than at present day, it is still a matter of debate how these galaxies have come to be quenched at such early times, but also how they evolve after they were quenched, and what they become at $z = 0$.

Quenched, or quiescent, galaxies at high redshifts are known to be more compact than their present-day counterparts of the same stellar mass, more so the higher the redshift (e.g. van der Wel et al., 2014; Ito et al., 2024). Such compact quiescent galaxies are not observed at low redshifts, at least not in quantities that can account for the numbers of compact quenched galaxies now reported at high redshifts. Multiple dry minor mergers have been proposed as a possible formation pathway for such quenched galaxies (Bournaud et al., 2007; Bezanson et al., 2009; Naab et al., 2009), as such small mergers deposit most of their stellar mass at larger radii and as such enhance the radial growth compared to normal major merger events (Hilz et al., 2012; Karademir et al., 2019). However, dry mergers are known to be more common the lower the redshift (e.g. Bell et al., 2006), and rather rare at high redshifts before $z = 2$, where the gas fractions are generally much higher. Thus, other additional evolution pathways for such high redshift quenched galaxies are required. One possible evolution pathway is for

the compact quenched galaxy to merge into another, more massive (and possibly still star forming) galaxy as the minor progenitor.

Another suggested pathway is so-called rejuvenation, that is re-accretion of gas from either the cosmic web or through gas-rich mergers onto the central galaxy, thereby reforming a disk and re-starting star formation, Indications for such a process have been found imprinted in observed quiescent galaxies at present-day (e.g. Yi et al., 2005), clearly showing that the simple assumption that once a galaxy has been quenched it stays quenched is not valid. Similarly, about 16% of the quiescent galaxies found at $z \approx 0.8$ in the LEGA-C survey show signs of rejuvenation (Chauke et al., 2019). Models predict a range of 10% to 70% of all massive galaxies to have lived through a rejuvenation phase (Zhang et al., 2023), and even the possibility of multiple rejuvenation events for a galaxy throughout its life (Tanaka et al., 2023). The exact conditions under which some quenched galaxies can revive through accretion of new gas and others do not are yet not well understood. However, observations of local galaxies that host AGN show signs of their last massive star burst event to have occured at the same time as the last AGN activity, indicating that both AGN activity and the massive starburst might have been triggered by the same event (Martín-Navarro et al., 2022).

Using the Illustris-TNG300 simulation, Hartley et al. (2023) identified 5 quenched galaxies emerging at $z = 4.2$, which were all quenched by the implemented AGN feedback and ended up as the most massive nodes of the box at $z = 0$. However, their predicted number densities of quenched galaxies is significantly lower[1] than what has been observed by Long et al. (2023); Carnall et al. (2023a). More problematic, observations also report some of the quenched galaxies to have been quenched since $z = 5$ or earlier (Nanayakkara et al., 2024; Carnall et al., 2023a), which is higher than found for any quenched galaxy in that simulation (Kakimoto et al., 2024). Thus, many questions are actually still open, which we will address in this study together with its companion study by Kimmig et al. (2025b), hereafter K25 .

This paper will focus on the properties and future evolution pathways of quenched galaxies found in the Magneticum simulations, and compare the properties of those galaxies to observations. The companion paper K25 focuses on the mechanisms and environmental conditions that lead to the quenching, discussing how the feedback both from the stars and the central supermassive black hole combined are responsible. The paper is structures as follows: Sec. 4.2 will introduce the simulation suite used to study quenched galaxies at high redshifts. Sec 4.3 presents the sample of quiescent galaxies, and compares global properties between quenched simulated and observed galaxies, including the formation redshifts obtained from stellar populations. Sec. 4.4 focuses on the different pathways galaxies follow after they have been quenched at high redshifts. In particular, we discuss the process of rejuvenation, with an outlook to the halo properties of the quenched galaxies at $z = 0$. Finally, Sec. 4.5 will summarize the results and discuss them in the global context of galaxy evolution since cosmic dawn.

[1]The value calculated by Hartley et al. (2023) is given in physical units, however, all observations are given in comoving units. Therefore, the number density obtained by Hartley et al. (2023) in comoving units (with $5/(302.6\text{cMpc})^3 \approx 1.8 \times 10^{-7}[\text{cMpc}^{-3}]$) is about 2 orders of magnitude smaller than the observations.

4.2 Simulations and Observations

Finding quenched galaxies at high redshifts requires a box volume large enough to encompass all potential environments while at the same time the simulation needs to have high enough resolution to properly resolve galaxies with stellar masses larger than $1 \times 10^{10} M_{\odot}$ to capture the observed mass ranges of quiescent galaxies. We use Box3 with a volume of $(128 Mpc/h)^3$ from the fully hydrodynamical cosmological simulation suite Magneticum Pathfinder (www.magneticum.org), in the ultra-high resolution uhr, with dark matter, gas, and stellar particles masses of $m_{\rm dm} = 3.6 \times 10^7 M_{\odot}/h$, $m_{\rm gas} = 7.3 \times 10^6 M_{\odot}/h$, and $m_* \approx 1/4^{\rm th} m_{\rm gas} \approx 1.8{\times}10^6 M_{\odot}/h$, respectively, as every gas particle spawns up to 4 stellar particles. Gravitational softening for the three components is included as $\epsilon_{\rm dm} = \epsilon_{\rm gas} = 1.4\,{\rm kpc}/h$ and $\epsilon_* = 0.7\,{\rm kpc}/h$. The simulation uses a WMAP-7 cosmology following Komatsu et al. (2011), with $h = 0.704$, $\Omega_m = 0.272$, $\Omega_b = 0.0451$, $\Omega_\lambda = 0.728$, $\sigma_8 = 0.809$, and an initial slope of the power spectrum of $n_s = 0.963$.

The simulation was performed with an updated version of GADGET-2 (Springel, 2005), with modifications to smoothed particle hydrodynamics (SPH), including artificial viscosity and thermal conductivity, according to (Dolag et al., 2004, 2005b; Donnert et al., 2013; Beck et al., 2016). It includes full baryonic physics as described in detail by Teklu et al. (2015). Star formation and stellar feedback are implemented based on the model by Springel & Hernquist (2003). Stellar feedback encompasses feedback from SN-I, SN-II, and AGB stars, with metal enrichment and cooling from all three sources are implemented according to Tornatore et al. (2004, 2007) and Wiersma et al. (2009). The assumed initial mass function is given by Chabrier (2003). In addition, UV/X-ray background and CMB background radiation are computed according to Haardt & Madau (2001).

Black hole treatment and feedback is included as described by Steinborn et al. (2015) based on the model by Fabjan et al. (2010) and Hirschmann et al. (2014). Typically, AGN are seeded in lower mass galaxies and then grow through accretion or mergers with other black holes. This mass growth is dependent on the surrounding gas density and velocity relative to the black hole, with higher density and lower velocity resulting in higher accretion following the Bondi prescription of $\dot{M}_{\rm B} \propto \alpha \rho / (c_{\rm s}^2 + v^2)^{3/2}$. Limited resolution reduces the efficiency of the mass accretion, such that a boost factor α is usually applied. The implemented changes by Steinborn et al. (2015) concern both the accretion and feedback. For the former, instead of determining the density ρ and relative velocity v of the total gas present, the model differentiates cold and hot gas into two separate accretion rates with their own boost factors.

The boost factor for the hot phase is 10, as hot gas generally more closely follows the assumptions used for the Bondi model of a hot isothermal medium. For cold gas, the boost factor is 100 due to their more efficient feeding as shown by high resolution simulations (Gaspari et al., 2013). This means that even when the galaxy is generally dominated by a hot phase, cold streams can still efficiently grow the black hole, resulting in a faster growth at higher redshifts while reducing the accretion at intermediate redshifts. Steinborn et al. (2015) show that this more accurately reproduces observed scaling relations.

Finally, the feedback itself is changed by Steinborn et al. (2015), with a smoother transition between quasar and radio mode efficiencies as well as making the radiative feedback efficiency increase with black hole mass following observational findings. This results in lower feedback of highly accreting low mass black holes.

Galaxies are identified using SUBFIND (Springel et al., 2001a; Dolag et al., 2009). In a nutshell, SUBFIND identifies structure linked by a friends-of-friends algorithm. It then detects saddlepoints in the potential of these linked "halos", which are then used to identify separate "subhalos", which represent individual galaxies. Galaxies that SUBFIND identifies as the most massive galaxy in a given halo are called "central" galaxies, while we call all galaxies that are not the centrals of their host halo "satellite" galaxies. Galaxies are traced forward and backwards in time using L-BaseTree (Springel et al., 2005c). Towards higher redshifts, the most massive galaxy at each snapshot is used as the main progenitor, and that branch of the merger tree is followed. Tracing forward, we mark those galaxies that merge with a larger galaxy, i.e. that are the smaller partner in the merger event, as "central subs", since the remnant galaxy after the merger is still a central, but the galaxy we were tracing was the minor contributor to the mass growth and thus not the main branch itself. This procedure works until the last high-resolution snapshot at $z \approx 2$.

The simulation Box3 uhr ran until $z \approx 2$, covering the redshift evolution with outputs since $z \approx 15$. Most importantly, it provides a snapshot with full particle information at $z = 3.4$, which is comparable to the average redshift at which the quenched galaxies presented by Nanayakkara et al. (2024) and Long et al. (2023) are observed. At $z = 3.4$, 2903 galaxies are found with stellar masses above $M_* > 2 \times 10^{10} M_\odot$, above which we consider galaxies to be resolved well enough to be included in this study for more than pure number counting aspects.

To trace halos at redshifts below $z \approx 2$, we match halos at the last available snapshot to the halos in the simulation Box3 hr, which ran until $z = 0$ with the same initial conditions but a lower resolution, and track those forward to $z = 0$. The hr resolution simulations have dark matter, gas, and stellar particles masses of $m_{\rm dm} = 6.9 \times 10^8 M_\odot/h$, $m_{\rm gas} = 1.4 \times 10^8 M_\odot/h$, and $m_* \approx 1/4^{\rm th} m_{\rm gas} \approx 3.5 \times 10^7 M_\odot/h$, respectively, and gravitational softening of $\epsilon_{\rm dm} = \epsilon_{\rm gas} = 3.75$ kpc$/h$ and $\epsilon_* = 2$ kpc$/h$. Note that all simulations in Magneticum with the same box size have the same initial conditions (ICs), and the lower resolution initial conditions were generated through downsizing of the higher resolution ICs.

Matching was done by taking all galaxies in the hr box within 500 ckpc ($\approx$ 100 physical kpc) around the original galaxy location in the uhr box. Of these, we match to the galaxy with the most similar total subhalo mass M_{tot} (baryonic plus dark matter). Note that we also compared what happens when matching to the *halo* with the most similar total halo mass $M_{200crit}$ (instead of using the galaxies themselves), which produced identical matches for 98% of the galaxies. Generally, we find that for 92% of matched galaxies the comoving separation is less than 200 ckpc and the total halo mass $M_{200crit}$ is within 0.1 dex ($\approx$ 25%).

Due to the lower resolution of the hr simulations compared to the uhr simulation, we only use global information like total galaxy (or halo) mass to track down to $z = 0$. While

overall at redshifts below $z < 5$, global properties like star formation rate densities, halo mass functions and stellar mass functions converge between the simulation runs within the mass ranges that the resolution allows (see Hirschmann et al., 2014; Kimmig et al., 2025b), on an individual galaxy basis this might differ strongly. This may be due to differences in feedback or the timing of star formation events, as well as the larger smoothing in the hr simulations, which all impact parameters such as star formation rate, stellar size or stellar mass. Therefore, we do not attempt to compare these properties between the two simulation runs, but only use the halo properties to track down the evolution of the total halo mass and the environment at the end of this work.

4.3 Quenched Galaxies at $z \approx 3.4$

Observed quiescent galaxies with full spectra have recently been reported by Nanayakkara et al. (2024) and Carnall et al. (2023a) using JWST NIRIS spectra at redshifts of $z \approx 3-4$, enabling examination of the stellar age distributions and thus the quenching and formation times of these galaxies. In the following, we identify quenched quiescent galaxies at a redshift of $z = 3.4$ in the simulations and compare their global properties to their observed counterparts.

Throughout this work we consider galaxies with 3 different stellar mass cuts: I) a stellar mass of $M_* \geq 2 \times 10^{10} M_\odot$, for which star formation properties are well enough resolved to safely identify quiescent galaxies; II) a stellar mass of $M_* \geq 3 \times 10^{10} M_\odot$, where these are well resolved with more than 10000 stellar particles; III) a stellar mass of $M_* \geq 5 \times 10^{10} M_\odot$, encompassing the best resolved and most massive galaxies at the given redshift. At $z = 3.42$, this encompasses 2903 galaxies in cut I), and 1309 galaxies above the most important cut level II) of which 1217 are centrals and 92 are satellite galaxies. Above the third cut range, cut III), we find 395 galaxies.

We define galaxies as "fully quenched" if their current star-formation rate is in fact zero, which means given the resolution of our simulation that it is below $10^{-3} M_\odot/yr$. At $z = 3.4$, for our three mass cuts this leads to 109 quenched galaxies in cut I) of stellar mass larger than $M_* \geq 2 \times 10^{10} M_\odot$, and 36 quenched galaxies of cut II) with $M_* \geq 3 \times 10^{10} M_\odot$, being 28 centrals and 8 satellites. In our highest mass cut III), we find 6 quenched galaxies with $M_* \geq 5 \times 10^{10} M_\odot$, two of which are satellites and four are centrals. This is the sample we study here in detail, see also the according discussion on that by K25.

However, observationally measuring zero star formation is not actually zero but limited by what can still be detected. Therefore, "quenched" is usually defined using the specific star formation rate sSFR, i.e., galaxies with sSFR $< 0.3 \times t_{\mathrm{Hub}}$ are defined as quiescent (Franx et al., 2008)[2]. Alternatively, at high redshifts a slightly adapted version of this is used as introduced by Carnall et al. (2020), where quiescence is defined as sSFR $< 0.2 \times t_{\mathrm{Hub}}$. At $z = 3.4$, for our three mass cuts this leads to 722 (620) quenched galaxies in cut I) of

[2]This is also the method that was used by Remus et al. (2023) to predict quiescent fractions for different halo masses through cosmic time up to $z = 4.2$.

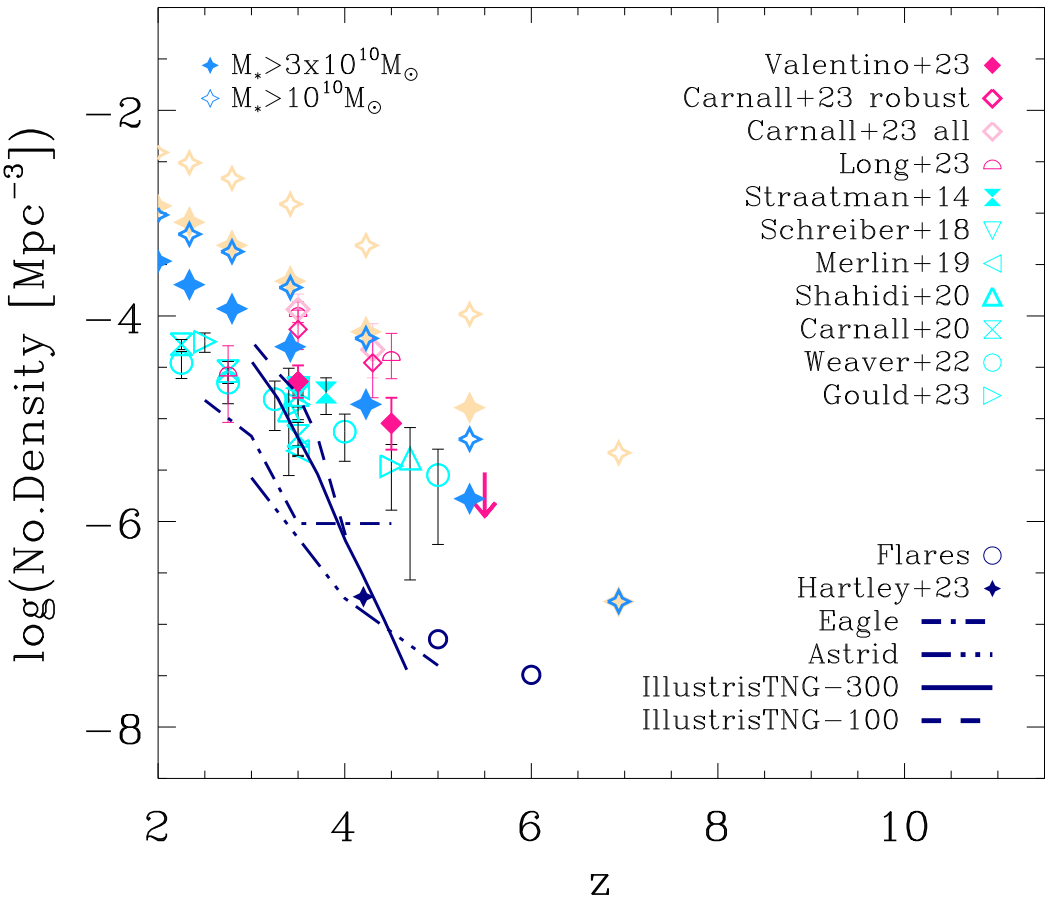


Figure 4.1. Number densities of quenched (blue) and non-quenched (sand) galaxies with stellar masses above $3\times10^{10}M_{\odot}$ (filled) and $1\times10^{10}M_{\odot}$ (open), as a function of redshift. Pink symbols show the observed number densities of quenched galaxies with $M_* > 3\times10^{10}M_{\odot}$ obtained with JWST from Valentino et al. (2023) (filled diamonds and downward pink arrow), Long et al. (2023) (open half circle), and Carnall et al. (2023a) (open diamonds, dark pink for their robust sample, light pink for all). Cyan data points present pre-JWST measurements of quenched number densities from Straatman et al. (2014, filled hourglas), Schreiber et al. (2018, downward triangles), Merlin et al. (2019, leftward triangles), Shahidi et al. (2020, upward triangles), Carnall et al. (2020, open hourglas), Weaver et al. (2023, open circles), and Gould et al. (2023, rightward triangles). The number densities reported for different simulations in comparable mass cuts are shown in dark blue, i.e., IllustrisTNG-300 (solid line), IllustrisTNG-100 (dashed line) and Astrid (dash-dot-dot-dotted line) from Weller et al. (2025), Eagle (dash-dotted line) from Long et al. (2023), IllustrisTNG-300 (filled diamond) from Hartley et al. (2023), and Flares (open circles) from Gould et al. (2023).

stellar mass larger than $M_* \geq 2\times10^{10}M_{\odot}$, and 352 (301) quenched galaxies of cut II) with $M_* \geq 3\times10^{10}M_{\odot}$, being 315 (270) centrals and 37 (31) satellites. In our highest mass cut III), we find 97 (81) quenched galaxies with $M_* \geq 5\times10^{10}M_{\odot}$, of which 11 (9) are satellites and 86 (72) are centrals, using the criterion by Franx et al. (2008) (Carnall et al. (2020)).

Before we study the details of our fully quenched galaxy sample, we first test if the number densities of quenched galaxies in the simulation is in agreement with observations. Here, we use the criterion of Franx et al. (2008) as this is most commonly used in the literature to which

we compare here, but we note that the differences between the results using the Franx et al. (2008) or the Carnall et al. (2020) criterion are so small they the data points for the number densities actually overlap, which is why we chose to show the results from the more commonly used Franx et al. (2008) criterion. Fig. 4.1 shows the number densities of quenched (blue) and non-quenched (sand) galaxies from $z = 2$ to $z = 10$, for two different stellar mass cuts (open symbols: $M_* > 1 \times 10^{10} M_\odot$, filled symbols: $3 \times 10^{10} M_\odot$). Generally, the number density of both quenched and all galaxies increases similarly with redshift. Quenched galaxies appear later than non-quenched galaxies of similar mass, with the first quenched galaxies with stellar masses above $M_* > 1 \times 10^{10} M_\odot$ appearing around $z = 5.5$. This does not imply that there are no quenched galaxies at higher redshift, but rather that the simulated volume with $128 Mpc/h$ box length is still too small to have massive galaxies appear at redshifts as high as $z = 8$, as discussed in more detail in the companion paper K25. In addition, there are a few massive galaxies in our simulation that are quenched at higher redshifts, but rejuvenate until the point of measurement at $z = 3.4$. One of these galaxies is shown in K25 in more detail, and we will come back to this point later in this study.

Furthermore, Fig. 4.1 also provides a comparison to current observed quenched number densities from JWST (filled pink diamonds: Valentino et al. (2023); open pink diamonds: Carnall et al. (2023a); pink half circles: Long et al. (2023)) using NIRCam imaging and a lower mass cut of about $3 \times 10^{10} M_\odot$ comparable to the filled blue symbols from the simulation. We find overall very good agreement, in particular we see the same increase in the number density when going from a redshift of around $z = 5$ to $z = 3.4$. We do not find as decrease to $z = 2.8$ as reported by Long et al. (2023), however, this could also be due to non-completeness in that measurement. JWST measurements of quenched number densities at lower redshifts are yet missing, but generally, it can be seen that the number densities of quenched galaxies increase in the JWST measurements compared to the pre-JWST measurements of quenched number densities that are included in the figure as cyan symbols. Note that we only included the spectroscopic JWST measurements, as for the photometric measurements contamination from dusty galaxies at $z \approx 2$ is still a matter of concern (Forrest et al., 2024). Compared to the pre-JWST, our simulation tends to produce slightly larger number densities of quenched galaxies at redshifts below $z = 3$, however, going down from $z = 4$ to $z = 0$, Steinborn et al. (2015) have show in a previous study using the same physics as the simulation used in this work that the number densities end up matching those from observations quite well again at the lowest redshifts.

While it remains to be seen whether follow up JWST observations also find enhanced quenched number densities at lower redshifts or if the AGN feedback should be further refined, or both, it is clear that our simulation manages to capture the JWST observations at high redshift, in particular above $z = 4$, where it has been reported previously that simulations struggle to reproduce these high number densities (Long et al., 2023). To demonstrate this issue, the number densities of quenched galaxies of different known simulations from the literature are also included in Fig.4.1 as dark blue lines and symbols, if comparable stellar mass cuts were available. More explicitly, values are included for Astrid, IllustrisTNG-300

and IllustrisTNG-100 from Weller et al. (2025), and for Eagle (Long et al., 2023) and Flares (Gould et al., 2023). In addition, we included the quenched galaxy number density reported for the IllustrisTNG-300 simulation by Hartley et al. (2023) at $z \approx 4.2$ as dark blue diamond[3].

The differences between the simulations originate from the different subgrid physics implementations, most likely the AGN feedback. For example, for IllustrisTNG both Hartley et al. (2023) and Kurinchi-Vendhan et al. (2023) show that quenching is due to the implemented AGN feedback as soon as the kinetic feedback kicks in. This kinetic feedback and its efficiency are coupled to the black hole mass, which itself correlates with the stellar mass of the galaxies, and thus quenching is inevitable by construction for galaxies above a given stellar mass in these simulations. In Magneticum, the main driver of the difference is that the prescription differentiates accretion onto the black hole in terms of cold or hot gas, as described in more detail in Sec. 4.2 and by Steinborn et al. (2015). By using different boost factors for these two accretion modes, Magneticum allows for more diverse black hole mass histories. A stream of cold gas can still be accreted efficiently (and thus result in a large black hole growth and subsequent feedback event) even if the surrounding gas is hot, as we do not smooth over both modes. Simultaneously, if the cold gas forms a disk, the high relative velocity will naturally reduce the amount of accretion, even if the surrounding hot gas has lower relative velocities (again, because we do not smooth over the two modes).

Overall, the similarity in quenched number densities from observations and the Magneticum simulations is promising, so we will now study the properties of the simulated quenched galaxies at a representative redshift of $z = 3.4$, the snapshot closest to the redshifts of the observed samples of quiescent galaxies from JWST (Long et al., 2023; Nanayakkara et al., 2024; Carnall et al., 2023a) in more detail.

4.3.1 Global Properties

First, we test the general properties of the quenched galaxies compared to the non-quenched galaxies from our simulations and compare with the available observations from the literature. Fig. 4.2 shows the star formation rate of the galaxies against stellar mass, the so called star formation main sequence, at three different redshifts of $5 > z > 4$, $4 > z > 3$, and $3 > z > 2$ for all galaxies in the simulation (sand color). We find that most of the galaxies lie around the star-forming main sequence, as observed by Salmon et al. (2015) at $z \approx 4$ from the CANDELS survey or by Pearson et al. (2018) at $z \approx 2$.

As expected, there are, however, some galaxies which scatter down towards lower star formation rates, and the commonly used cuts for what is called quiescence by Franx et al. (2008) and Carnall et al. (2020) are shown as dashed and dashed-dotted lines, respectively. All galaxies with star formation rates below the Franx et al. (2008) criterion are shown in light blue. Those galaxies with no ongoing star formation at all, that are therefore classified as fully quenched, are shown in blue (with their logarithmic star formation rate artificially

[3]Note that we adapted the data point from the paper to comoving units, as the value presented by Hartley et al. (2023) was given in physical units (see also Weller et al., 2025, for this point), while all the observations are given in comoving units

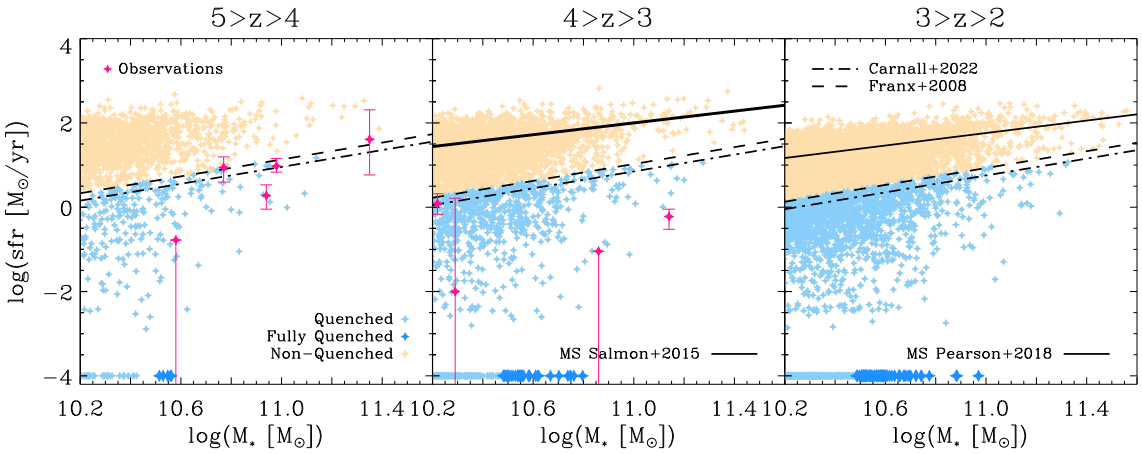


Figure 4.2. The star formation rate (sfr) of Magneticum galaxies at different redshifts as a function of stellar mass. From left to right: $5 > z > 4$, $4 > z > 3$, and $3 > z > 2$. Galaxies with sfr = 0 are placed at $\log(sfr[\mathrm{M}_\odot/\mathrm{yr}]) = -4$ and defined as " fully quenched" (dark blue). Galaxies with star formation rates below the Franx criterion of sSFR $< 0.3 \times t_{\mathrm{Hub}}$ are defined as "quenched" (light blue). All other galaxies have ongoing star-formation and are defined as "non-quenched" (sand). The black solid line represents the observed star-forming main sequence at $z = 4$ from Salmon et al. (2015) and at $z \approx 2$ from Pearson et al. (2018). The black dashed lines mark the criterion by Franx et al. (2008), while the black dash-dotted lines mark the adapted criterion from Carnall et al. (2020). Observations of quenched galaxies from the literature are included as magenta diamonds, compiled from Antwi-Danso et al. (2023); de Graaff et al. (2024b); Kakimoto et al. (2024); Urbano Stawinski et al. (2024).

set to -4 so that they can be included in the figure despite their real star formation rate being 0). The galaxies that are targeted in this work are those shown in blue in the middle panel. This visualizes our selection criterion while also showing that the simulations successfully reproduce the star formation main sequence and thus can be utilized for this study. For comparison, we also included several data compiled from observations by Antwi-Danso et al. (2023); Carnall et al. (2024); de Graaff et al. (2024b); Kakimoto et al. (2024); Urbano Stawinski et al. (2024) as pink diamonds. As can clearly be seen, our simulation captures all of the observed quenched galaxies in its range.

Interestingly, none of the quenched galaxies from the simulations is among the most massive galaxies at $z = 3.4$. Even more so, most of the massive galaxies are actually on the main sequence, heavily forming stars. This already indicated that the quenched galaxies are, in fact, not hosted by the most massive nodes in the cosmic web at that redshift, but we will return to this in more detail soon. Note that we here already see a difference to the results reported for the IllustrisTNG simulations by Hartley et al. (2023) and Kurinchi-Vendhan et al. (2023), as in these simulations the quenched galaxies are the most massive ones in the sample.

Before we look at the host halo masses of the quenched galaxies, we study the mass-size relation of the simulated galaxies at the same three different redshifts of $5 > z > 4$, $4 > z > 3$, and $3 > z > 2$ $z = 3.4$ as in Fig. 4.2, in Fig. 4.3. The simulated galaxies (sand diamonds) clearly lie within the observed range of sizes for a given mass that are found at high redshifts,

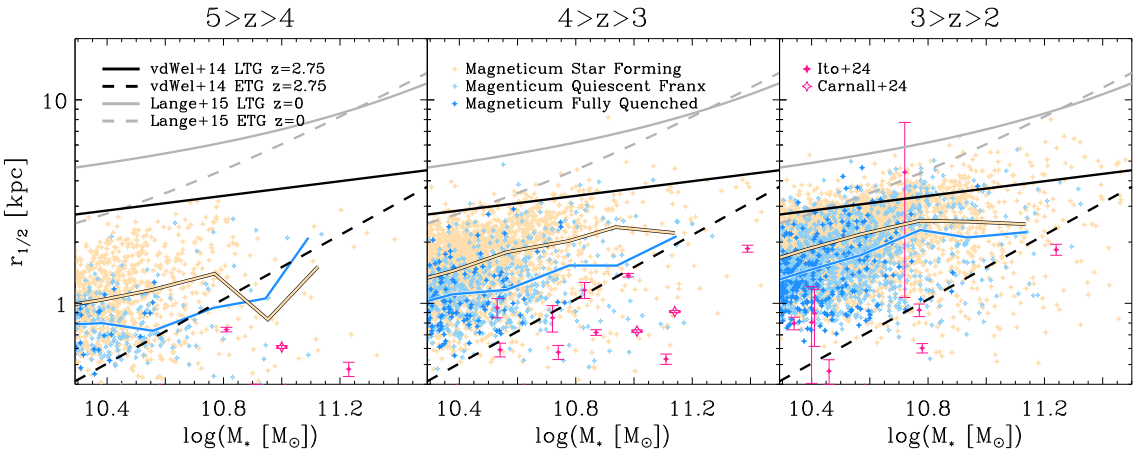


Figure 4.3. Stellar mass-size relation of all Magneticum galaxies (sand diamonds), with the quenched galaxies according to Franx et al. (2008) shown in light blue and the fully quenched galaxies shown in blue. Sand and blue solid lines mark the median values for the non-quenched and quenched galaxies. Black lines mark the relations found for early-type (dashed) and late-type (solid) galaxies at $z = 2.75$ from van der Wel et al. (2014), while gray lines mark early-type (dashed) and late-type (solid) relations at $z = 0$ from Lange et al. (2015) from the GAMA survey for comparison. From left to right: $5 > z > 4$, $4 > z > 3$, and $3 > z > 2$. Observations from Carnall et al. (2024) and Ito et al. (2024) are included as open and filled pink diamonds, respectively.

indicated by the black lines from van der Wel et al. (2014) for galaxies at $z = 2.75$, and not within the size range observed at $z = 0$ marked in gray (GAMA survey, Lange et al., 2015). As shown already by Schulze et al. (2018), the Magneticum simulation in the uhr resolution successfully reproduce the mass-size relation of galaxies at $z = 0$, and they also reproduce the change in mass-size relation with redshift from $z = 2$ to $z = 0$ for early-type galaxies (Remus et al., 2017b). From Fig. 4.3 we clearly see from the left to the right panel that this trend of generally having smaller galaxy sizes for a given stellar mass at higher redshifts continues to even higher redshifts than $z = 2$, in good agreement with the observed trends by van der Wel et al. (2014) and also with size evolution trends reported from JWST up to $z \approx 5$ from Ito et al. (2024) and Carnall et al. (2024).

Fig. 4.3 also reveals that the quenched galaxies (blue diamonds) in our sample on average have smaller sizes at a given stellar mass than the overall sample (sand diamonds), albeit the scatter is similarly large. We do not find a correlation between the stellar mass of the quenched galaxies and their formation redshift, but there is a slight tendency for quenched galaxies that have formed earlier to be larger in size than those that have formed more recently at a fixed stellar mass. We also included in the figure as pink data points the observed quenched galaxies from Ito et al. (2024) and Carnall et al. (2024). While the overall behavior is, as mentioned above, in qualitative agreement, we also note that the actual sizes of the observed quiescent galaxies are generally smaller than those reported from the simulation. This is due to the limitations of our softening, which prevents sizes to be smaller than its value by smearing out the distribution of the matter in this region. Thus, capturing the size evolution

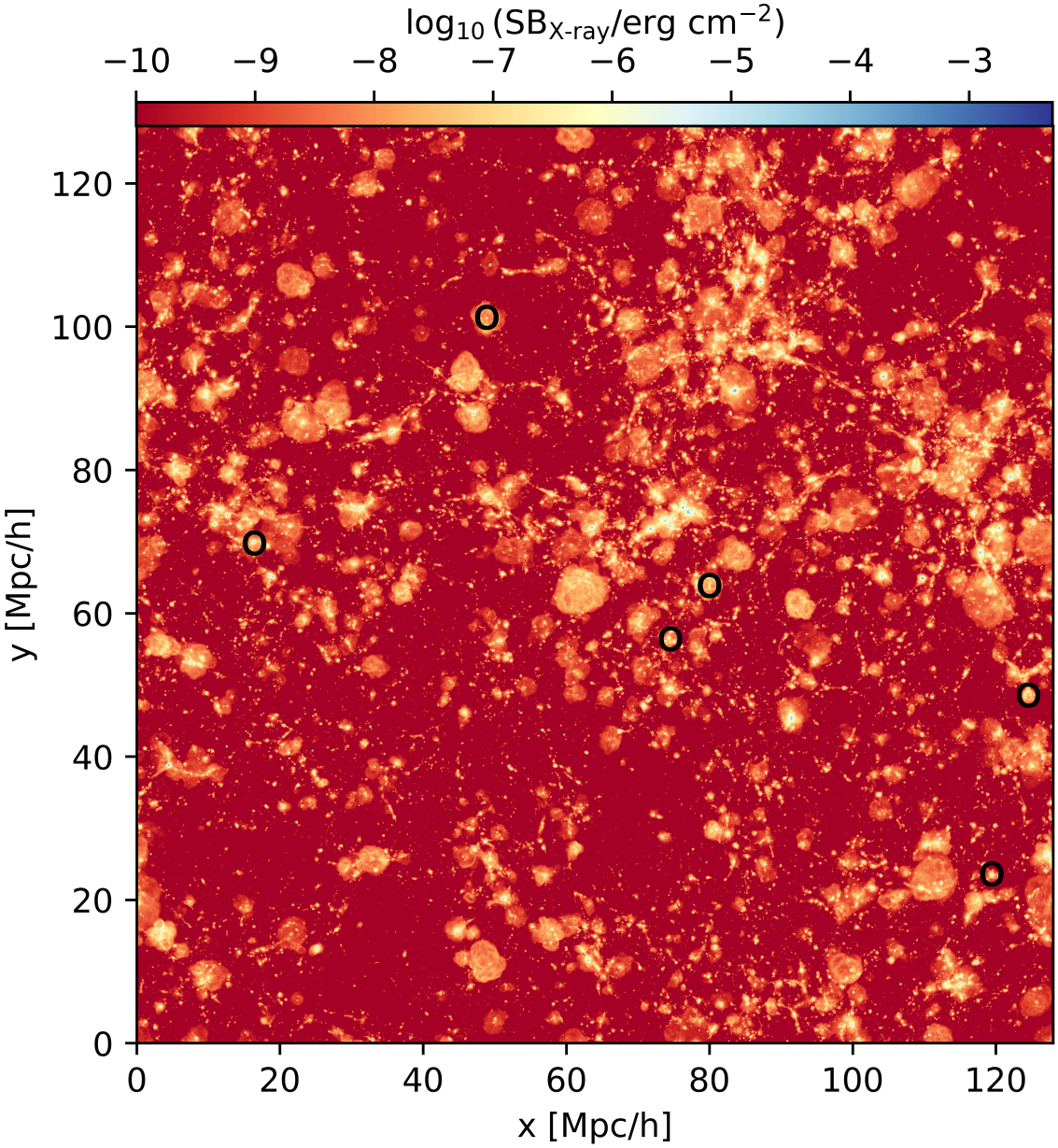


Figure 4.4. Projected surface brightness of the gas of the full Box3/uhr at $z = 3.4$. Black circles mark the six most massive quenched galaxies. This is actually a measure for the temperature of the gas, as the surface brightness is brighter the hotter the gas.

despite the limitations of the resolution is promising, but also highlights the need for even better resolved simulations in the future to study the radial properties of galaxies.

4.3.2 Environment

Coming back to the question of the environment of the quenched galaxies, Fig. 4.4 depicts the projected surface brightness of the gas in Box3 (uhr) at $z = 3.4$, that is a measure for the temperature of the gas as brighter surface brightness corresponds to higher temperatures of the gas. The positions of the six most massive quenched galaxies are marked by black circles. They appear to inhabit diverse regions of the cosmic web, though none of them lie at

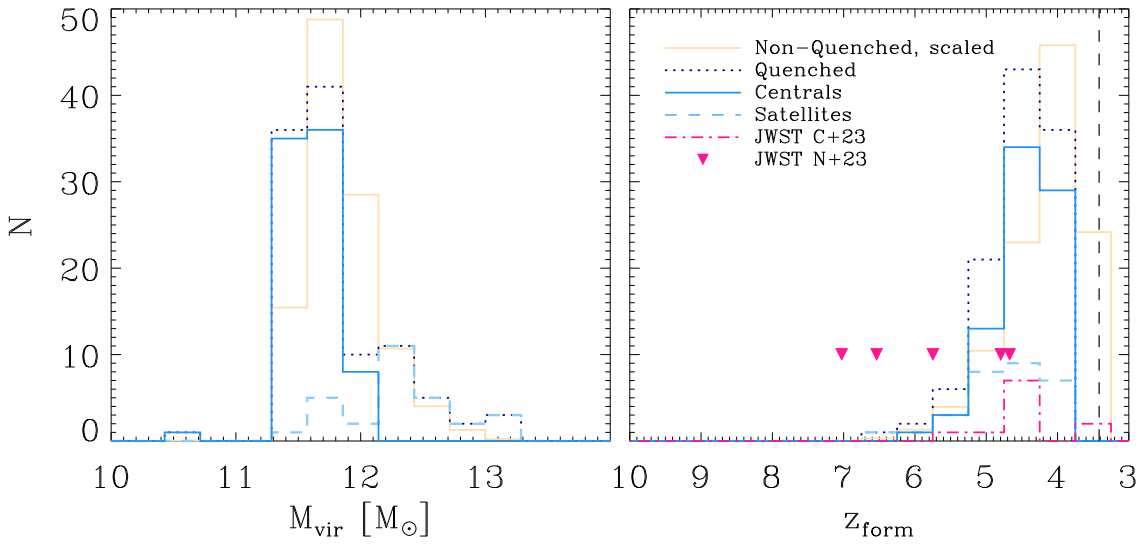


Figure 4.5. *Left:* Histogram of the virial masses of the host haloes of the quenched galaxies (blue dotted) and non-quenched galaxies (sand solid line, scaled down to match) with stellar masses above $2 \times 10^{10} M_{\odot}$. The solid blue and dashed blue lines denote quenched galaxies which are centrals and satellites, respectively. *Right:* Histogram of the formation redshifts $z_{\rm form}$, colored as in the left panel. In addition, observations from JWST are included in pink: the dash-dotted line marks the formation redshift distribution of JWST CEERS quenched galaxies observed between $z = 4$ and $z = 3$ from Carnall et al. (2023a). The solid triangles mark the formation redshifts of the five galaxies from Nanayakkara et al. (2024) with spectroscopic NIRSpec data.

the centers of the hottest, most dense regions. Instead, they lie adjacent (left-most and central two), removed (two right-most) or even entirely isolated (top most) from the more pronounced filaments of the cosmic web. We tested this for all 28 quenched galaxies above a stellar mass of $M_* \geq 3 \times 10^{10} M_{\odot}$, and found all of them to live in rather remote or adjacent regions of the developing cosmic web, never in the main nodes. This suggests that quenching at high redshifts is not efficient in the densest environments albeit the AGN feedback is strongest for the most massive galaxies, indicating that the processes that lead to quenching of galaxies at high redshifts are more complicated than the simple picture of AGN feedback quenching the galaxy.

Despite not being the most massive structures in the simulation, all of the quenched halos exhibit a bubble of heated gas surrounding them, reaching out to several virial radii. Note that this is difficult to see for some of these halos in Fig. 4.4 as the figure shows the whole box volume and therefore the individual halos are actually small. The fact that the bubbles can be clearly seen for some of the marked halos (for example the uppermost quenched halo) demonstrates how large these bubbles can become. The origin of these bubbles is discussed in the companion paper K25 to be the result of their rapid quenching process, driven outward by the feedback from the AGN.

This is in agreement with what we had seen before already, namely that the quenched galaxies are not among the most massive galaxies. The left panel of Fig. 4.5 further strengthens this point: Shown is a histogram of the virial masses of the quenched (dark blue, dotted) and

all (sand, solid) galaxies with stellar masses above $M_* > 2\times10^{10}M_\odot$, albeit the latter is scaled to match the numbers of the quenched galaxies for better comparison of the distributions. On first glance, both distributions appear to be similar, with a tendency for the quenched galaxies to be overly common at small virial masses around $M_{\rm vir} \approx 5 \times 10^{11}M_\odot$, that is around the Milky-Way mass range.

However, this picture changes once we split the quenched sample into central galaxies (solid blue line) and satellite galaxies (dashed light blue line). The quenched sample clearly divides in halo mass, with all quenched galaxies in halos of virial masses above $M_{\rm vir} \approx 2 \times 10^{12}M_\odot$ being satellites, i.e. they were accreted onto a more massive dark matter halo, and they are not the central galaxies of the massive nodes. Those quenched galaxies that are central galaxies all live in smaller mass halos, clearly supporting the idea that the environment of a galaxy is crucial for quenching to happen at high redshifts.

4.3.3 Formation Redshifts - When Do the Quenched Galaxies Form?

Given that the quenched galaxies are already rather massive at $z = 3.4$, the question arises when they had actually formed their stars, and whether or not they already differ from non-quenched massive galaxies with respect to their formation times. To this end we define $z_{\rm form}$ here as the redshift at which half of a galaxy's total stellar mass at $z = 3.4$ has been formed. The right panel of Fig. 4.5, shows a histogram of the formation redshifts of all galaxies (sand) and the quenched galaxies (blue). As can be seen most galaxies have formed their stars around a redshift of $z_{\rm form} \approx 4$, though there is some scatter towards formation redshifts as high as $z_{\rm form} \approx 7$. The quenched galaxies, both centrals and satellites, have on average formed earlier than the non-quenched galaxies, with the satellites having even earlier formation redshifts than the centrals. These high formation redshifts found for the quenched galaxies are in broad agreement with those found in observed quenched galaxies by Nanayakkara et al. (2024, magenta triangles) and Carnall et al. (2023a, magenta line). It should be noted, however, that the only quenched galaxy which matches the earliest two times of $z_{\rm form} \approx 7$ found by Nanayakkara et al. (2024) ends up being a satellite galaxy at $z = 3.4$.

Nevertheless, we do not have a quenched galaxy with a formation redshift larger than $z = 7$, and thus no counterpart for the quenched galaxy reported by Glazebrook et al. (2023) to exhibit a formation redshift around $z = 11$. However, earlier formation redshifts can be found in our sample of galaxies if we identify quenched galaxies at $z \approx 5$. Observed at that redshift, we even have a quenched galaxy with a formation redshift before $z = 8$, as shown by K25. Interestingly, that galaxy rekindles its star formation at about $z \approx 4$, and is no longer quiescent at $z = 3.4$.

All observed quenched galaxies at around $z = 3.4$ are rather massive in stellar mass, so the question arises if the formation redshift is connected to the stellar mass. Fig. 4.6 shows the stellar mass against the formation redshift for the quenched (blue) and non-quenched galaxies (sand) for the simulations, including the observed quenched galaxies (magenta). There is

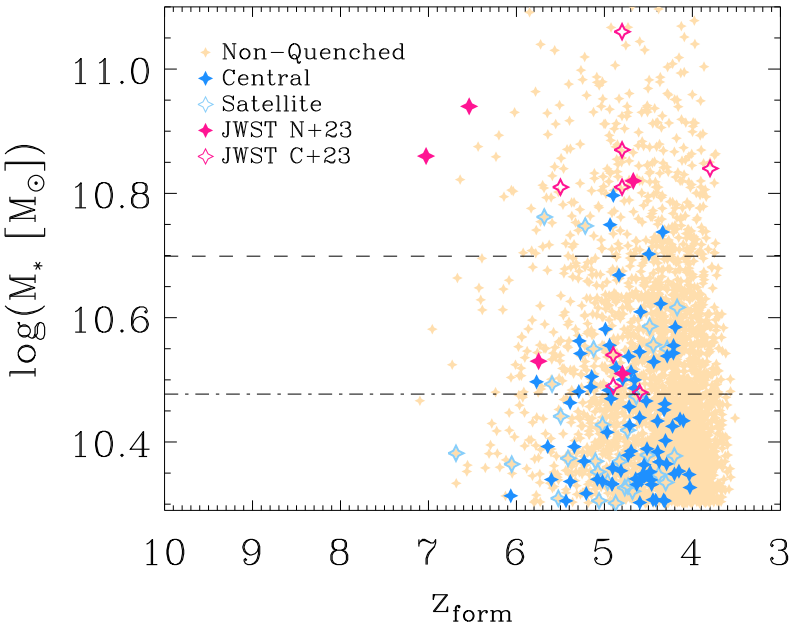


Figure 4.6. Stellar mass as a function of the formation redshift for the star forming (sand) and quenched galaxies (blue stars), with the latter further differentiated between centrals (filled) and satellites (open) defined at redshift $z = 3.4$. Also plotted are observed quenched galaxies from Nanayakkara et al. (2024) and Carnall et al. (2023a) (filled and open pink symbols, respectively). The black horizontal lines indicate stellar masses of 5 (dashed) and $3 \times 10^{10} M_{\odot}$ (dash dotted).

no apparent correlation between the stellar mass either of the quenched or non-quenched galaxies, neither in the simulations nor the observations.

However, while the simulation includes quenched galaxies with masses and formation redshifts comparable to the observations by Nanayakkara et al. (2024) and Carnall et al. (2023a) at the mass range from $3 \times 10^{10} M_{\odot}$ to $6 \times 10^{10} M_{\odot}$, we also clearly see that we do not recover the extremely massive quenched galaxies that are part of the observed sample. The most extreme stellar masses around $10^{11} M_{\odot}$ are found only for galaxies which are actively forming stars. There are, however, six quenched galaxies with masses which are in excess of $5 \times 10^{10} M_{\odot}$, with ids as ID4180, ID5058 (for the two satellites) and ID16396, ID18258, ID20633 and ID22007 (for the four centrals).

Fig. 4.7 shows the fraction of stars which are formed at a given redshift for these six most massive quenched galaxies (solid lines) as well as their formation redshifts $z_{\rm form}$ (vertical dash-dotted lines). They exhibit diverse stellar formation histories, with galaxy ID5058 (purple) in particular having formed most of its stars very early on. This galaxy is also quenched at an earlier time, with only around 5% of its stars formed after $z = 5$ and practically none after $z = 4$. Although it is a satellite at $z = 3.4$, it was still a central at $z = 4.2$ and thus the quenching did not occur due to the environment of the host. In fact, it is quenched in a similar process like the other central galaxies and afterwards accreted by the more massive structure that also prevents any kind of rejuvenation.

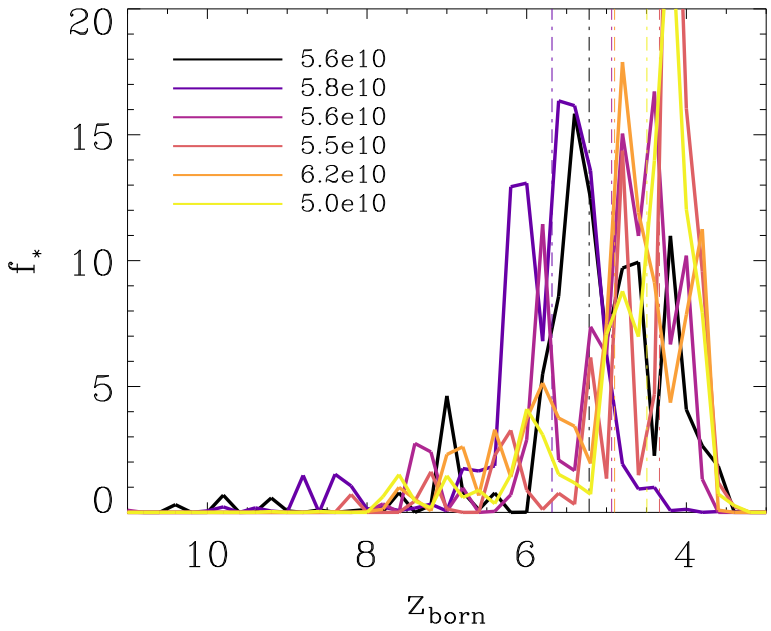


Figure 4.7. The fraction of stars in % formed at a given redshift for each of the six most massive quenched galaxies. Vertical colored dash-dotted lines denote their z_{form}, while the label denotes their stellar mass at $z = 3.4$ (sorted in order of their ids).

By contrast, galaxies ID18258 and ID22007 (salmon and yellow) exhibit a strong starburst right around $z = 4$, resulting in a much more recent z_{form}. The former in particular has an interesting stellar build up, with three distinct peaks of star formation in sequence at $z \approx 5.2$, 4.8 and then the final at $z = 4$.

All six galaxies show generally bursty star formation, with significant fractions (> 10%) of their final stellar mass formed in these short peaks, usually then followed by dips. As these are the binned formation redshifts of individual stellar particles, this burstiness is not a result of a lack of temporal resolution of snapshot outputs but rather physical in origin. Strong star formation results in higher stellar feedback, which in turn can then briefly inhibit the formation of new stars thus causing a dip.

It is interesting to note that although this interplay of star formation and feedback had been active in all six galaxies from around $z = 6$, they retain significant star formation also during the dips and it is not until close to $z = 3.4$ that they fully quench. The final mechanism required to result in a full stop of their star formation is the feedback from the central supermassive black hole, in combination with their environment, which is discussed in more detail in the companion paper K25.

The time of quenching, z_{quench}, is defined as the redshift at which the last star in the galaxy as seen at $z = 3.4$ has formed. The top panel in Fig. 4.8 shows z_{quench} as a function of M_* for all quenched galaxies with $M_* > 3 \times 10^{10} M_\odot$ (light blue symbols), and the fully quenched galaxies (blue). We find z_{quench} between $z = 3$ to $z = 6.5$, similar to the observed values of Nanayakkara et al. (2024) aside from their most striking outlier. Most of the galaxies from Carnall et al. (2024) and the galaxy from de Graaff et al. (2024b) have earlier quenching



times, but are also generally more massive than the bulk of our sample of quenched galaxies, which is most likely a result of our simulated box volume still being to small to reproduce the most massive galaxies at these redshifts in a statistically representative matter as discussed by K25. There is no clear additional trend with stellar mass visible, neither in the simulation nor the observations, indicating that the process that quenches galaxies at high redshifts in fact is not directly correlated to the galaxy mass but rather other effects come to play. As discussed by K25, these are a combination of the feedback from the stars, the AGN feedback, and the environment being underdense; this is different than what has been found by Hartley et al. (2023) and Kurinchi-Vendhan et al. (2023) for IllustrisTNG, where the quenching is correlated with the mass of the galaxies due to the implemented feedback.

Interestingly, the formation redshift z_{form} and the quenching redshift z_{quench} are correlated, as shown in the lower panel of Fig. 4.8. Galaxies with younger formation redshifts also have lower quenching redshifts, meaning that more recent quenching also implies that half the total stellar mass was formed more recently. This is in agreement with the result that the quenching of the galaxies is preceded by a spike in star formation that forms most of the stars in the galaxy. And while the simulation does not recover the high formation and quenching redshifts of the most extreme outlier from the observations by Nanayakkara et al. (2024) (which is also the galaxy discussed in more detail by Glazebrook et al. (2023)), we clearly see that it lies around where one would expect from the simulated sample when extending the correlation to higher formation redshifts.

This clearly indicates that the quenched galaxies form most of their stars both in simulations and observations rather quickly in a short time period prior to the very quick quenching event, in agreement with what is discussed by K25. It also shows that this process of quenching must be similar also at higher redshifts, as the behavior of the galaxy from Glazebrook et al. (2023) agrees well with the other galaxies. A larger simulation volume of the same resolution would however be needed to test this hypothesis with respect to the most extreme observed outlier quenched galaxy, which unfortunately is not available at the moment.

4.4 What Do they Become – the Multiple Pathways of Quenched Galaxies into the Future

As we have shown our simulated quenched galaxies to have similar properties as the observed quenched galaxies at high redshifts, we will now study their evolution forward in time to see if they stay quenched or rekindle their star formation. In the following we consider the evolution of the sample of galaxies, both quenched and star forming. As the simulation only evolved in the high resolution down to $z \approx 2$, we can only trace the individual galaxy properties down to this redshift, but the overall properties can be followed in lower resolution down to $z = 0$.

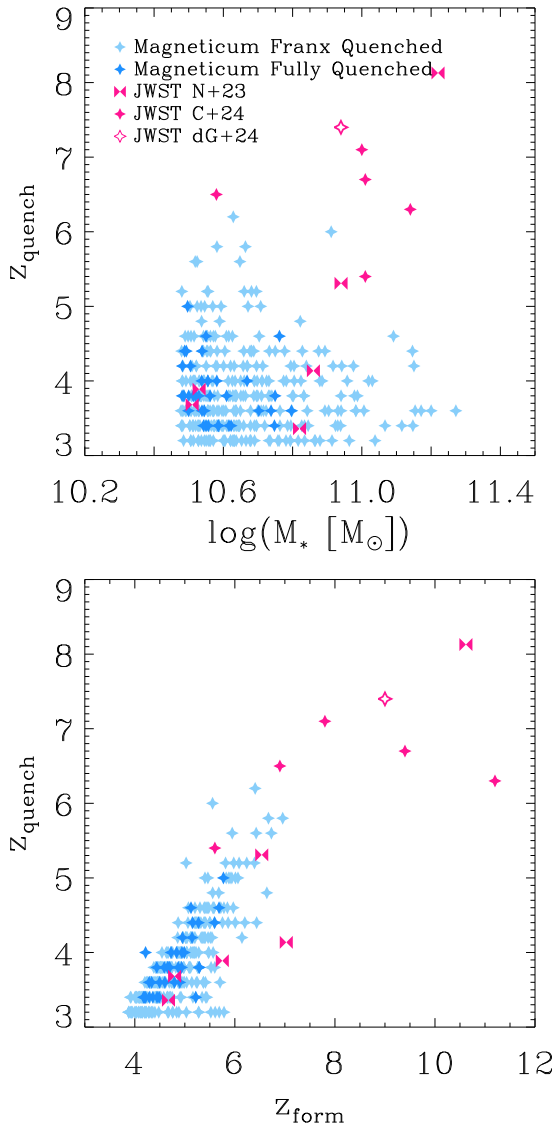


Figure 4.8. z_{quench} versus M_* (*top*) and z_{form} (*bottom*) for all simulated quenched galaxies (light blue), the fully quenched sample (blue), and the values of observed galaxies from Nanayakkara et al. (2024) (pink bowties), de Graaff et al. (2024b) (pink open diamond), and Carnall et al. (2024) (pink filled diamonds).

4.4.1 Evolution to Redshift of $z = 2$

For the six most massive galaxies Fig. 4.9 shows their star formation histories down to $z = 2$, going from top to bottom in order of the galaxies ids. For comparison, the dotted lines of the same color show the star formation histories of the same galaxies when observed at $z = 3.4$, as shown in Fig.4.7, with all dotted lines reaching zero star formation before $z = 3.4$.

We find that for three of the central galaxies (ID16396 in pink, ID18258 in salmon, and ID22007 in yellow) there is practically no new stellar mass present at $z = 2$, neither accreted nor formed. That is to say they remain quenched down to $z = 2$. However, the fourth central quenched galaxy (ID20633 in orange) gained stellar mass, as there are more stars present with formation times $z_{form} > 3.4$ compared to what was present in the main progenitor (dotted

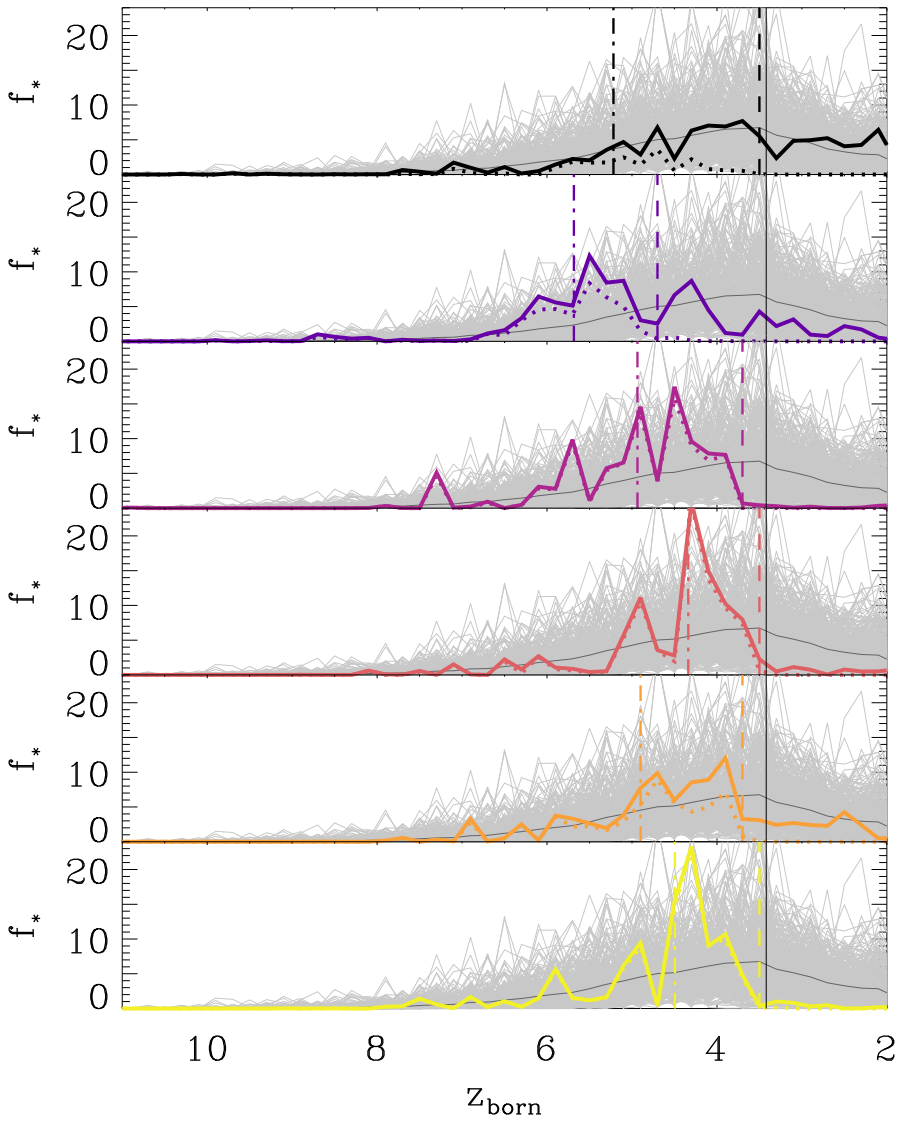


Figure 4.9. The fraction of stars in % within the galaxy at $z = 2$ as a function of their formation redshift for each of the six most massive quenched galaxies (plotted in order of their ids from top to bottom, ID4180, ID5058, ID16396, ID18258, ID20633 and ID22007). Plotted as colored dotted lines are the fractions at $z = 3.4$ when the galaxies are identified as quenched, as shown in Fig. 4.7, re-scaled to the total stellar mass at $z = 2$. The light gray lines show the formation histories of all galaxies with $M_* > 5 \times 10^{10} M_\odot$, with their mean in dark gray. The black vertical line denotes $z = 3.4$, with the colored vertical lines denoting $z_{\rm form}$ (dash-dotted) and $z_{\rm quench}$ (dashed) when observed at $z = 3.4$.

line). It is however not clear from this figure if the galaxy itself has rejuvenated or if it has only accreted matter. Nevertheless, while the largest peak of star formation for this galaxy before quenching produced about 20% of its stars as shown in Fig. 4.7, the contribution of this peak only account for about $10 - 12\%$ with respect to the stellar mass of that galaxy at $z = 2$ as shown in Fig. 4.9.

The first of the two satellites (ID4180 in black) eventually merges with its central which is still actively forming stars, thereby significantly increasing its total stellar mass (hence the noticeable deviation to the dotted line also for $z_{\rm form} > 3.4$). At $z = 2$ the resulting

galaxy is actively forming stars. However, this quenched galaxy was not rejuvenated but rather was the smaller member in a merger event and not the main progenitor of the resulting galaxy at $z = 2$. Interestingly, the galaxy that has consumed our quenched galaxy shows a star formation history very similar to the main star formation history of all galaxies above $M_* > 5 \times 10^{10} M_\odot$ shown as gray line.

Finally, galaxy ID5058 (lilac) first merges with its central, and thus shows very similar behavior to ID4180 for $z_{form} > 3.4$. Towards $z = 2$, however, the newly formed galaxy shows very little ongoing star formation, in stark contrast to galaxy ID4180. This is because after merging with its central, ID5058 then falls onto an even larger nearby galaxy group becoming a satellite again at $z = 2$. Here, the second galaxy also experiences quenching after it has consumed our quenched galaxy, this time, however, the quenching is a slow process as it is due to the new hosts environment. It is the only case of environmental quenching that we found in our sample of quiescent galaxies at high redshifts.

Compared to the mean of the total sample of galaxies plotted in gray, the three which remain fully quenched naturally deviate most strongly toward earlier formation times. Interestingly, the two satellites which merge however show largely different behavior from one another, with ID4180 even exceeding the total sample's average fraction of stars formed at later times $z \approx 2$, while ID5058 suffers a second quenching event.

To see how other properties of the quenched galaxies evolve with time compared to like galaxies, we consider the broader sample of the II) mass cut. We reduce the sample to galaxies which are centrals at $z = 4.2$ and remain centrals until $z = 2$ to avoid including galaxies which may have quenched environmentally as opposed to internally. This results in 817 non-quenched and 22 quenched centrals, with their evolution of galactic properties shown in Fig. 4.10.

The top left panel depicts the star formation rate of the sample. We find that the quenched galaxies all spike in their star formation rate in either of the two snapshots ($z = 4.2$ or $z = 5.3$) immediately before being quenched by $z = 3.4$. All but one exception reach star-formation rates in excess of the median of non-quenched centrals (sand color line), with half exceeding the median by more than $1\,\sigma$ at either $z = 4.2$ or $z = 5.3$ (gray shaded area).

It is interesting to note here that the non-quenched sample of galaxies already more massive than $M_* > 3 \times 10^{10} M_\odot$ (sand line and gray shade) at $z = 3.4$ also strongly drops in star formation rate toward $z = 2$, with the peak of its median at $z = 4.2$. This drop is much stronger than the slight decline found if all centrals with $M_* > 3 \times 10^{10} M_\odot$ at a given redshift are included, as shown by the black lines, which include also those which only recently rose above the stellar mass cut (median black dash-dotted, $1\,\sigma$ bounds black dashed). Consequently, if one were to observe all central galaxies at $z = 2$ those which have been massive centrals since $z = 4.2$ (around 2 Gyr) will generally have lower star formation rates. This also indicates that those galaxies that newly cross the mass threshold are still evolving due to ongoing star formation more strongly than those galaxies that have already formed stars early on.

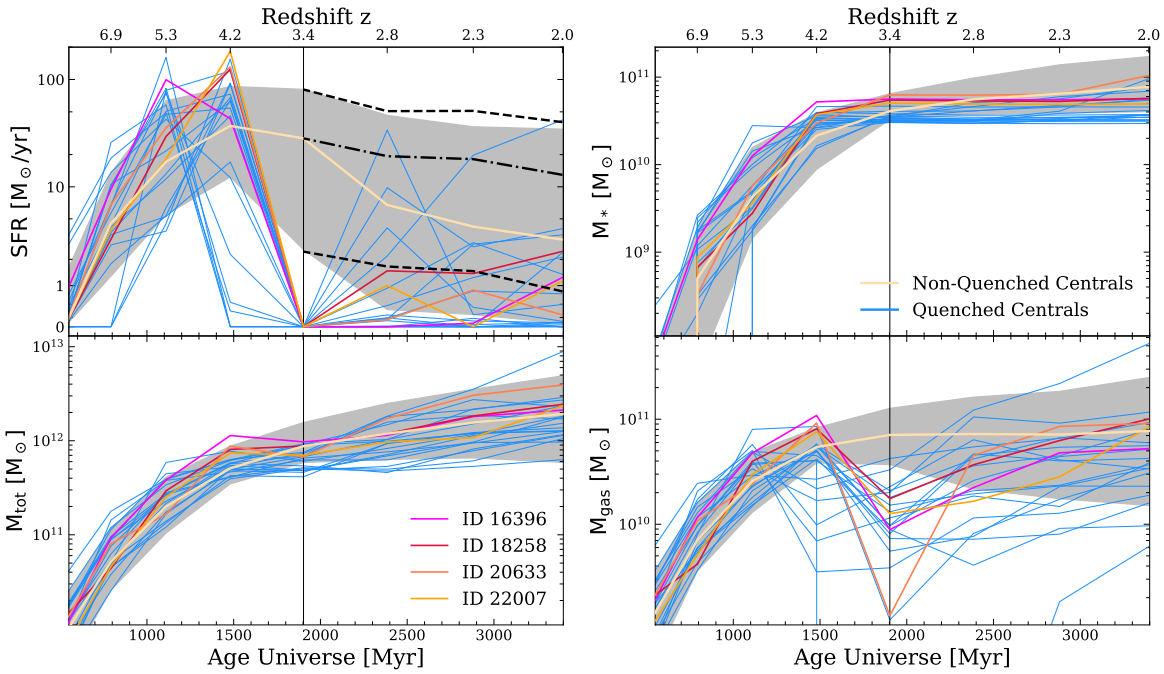


Figure 4.10. Redshift evolution of the star-formation rate (*upper left*), stellar mass (*upper right*), the total mass (*lower left*) and gas mass (*lower right*) of centrals within the II) mass cut which remain centrals down to $z = 2$. For the 817 non-quenched galaxies the median is shown as sand color line, with 1 σ as gray shaded. The individual evolutionary tracks of the 22 quenched galaxies are in blue, with the four most massive main galaxies at $z = 3.4$ as colored lines as in Fig. 4.9. For the star-formation rate the $y-$axis is scaled with asinh. The black dash dotted line shows the mean SFR of all centrals (also including galaxies which fulfilled the mass cut only after $z = 3.4$), with the dashed black lines showing the 1 σ range of this larger sample.

The excess in star formation rate at early times correspondingly leads to the quenched galaxies lying at the higher end of stellar mass at $z > 4$, as can be seen in the top right panel of Fig. 4.10. All but two of the 22 quenched centrals lie above the median stellar mass at $z = 4.2$ (sand color line). As all galaxies (quenched and non-quenched) are selected based on their stellar mass at $z = 3.4$ this means that the quenched galaxies generally formed their stellar mass earlier compared to like galaxies. Following their evolution forward in time most remain quenched, forming (or accreting) little to no additional stellar mass over a time of around $t \approx 1.5$ Gyr. However, there are a few which gain sufficient amounts of new stars to reach the median of the total sample.

Interestingly, the total mass of the galaxies dips below the median for most quenched centrals at $z = 3.4$ (lower left panel of Fig. 4.10). This is largely due to the significant ejection of gas which occurs during quenching (lower right panel of Fig. 4.10). The gas is then replenished less quickly compared to the accretion of dark matter, resulting in the descendants at $z = 2$ of quenched centrals having average to slightly reduced total masses but significantly less gas and stellar mass. This means that the reduction in baryon fraction caused by the quenching process as described by K25 remains in place for most cases up to a time of 1.5 Gyr.

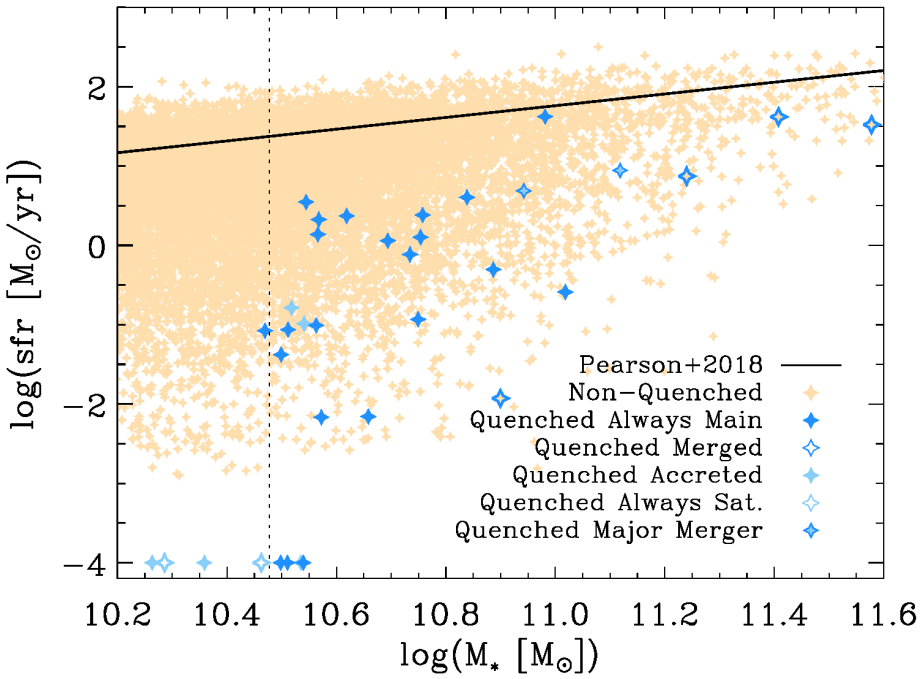


Figure 4.11. Star formation rate versus stellar mass at $z = 2$ of the descendants of our sample of galaxies with mass cut II), with the observed main sequence from Pearson et al. (2018) shown as a black line. Tan symbols are galaxies which were forming stars at $z = 3.4$, while blue symbols were quenched. We differentiate the second group into five subgroups, depending on their merger history post-quenching.

As we saw in the top left panel of Fig. 4.10, the quenched centrals do not necessarily remain quenched. To define then whether a quenched galaxy has rejuvenated at some point after $z = 3.4$, we must consider what we mean by *rejuvenation*. It is for example possible that the quenched galaxy merges with a larger other galaxy which has ongoing star formation, as noted earlier for the cases of ID4180 and ID5058.

We begin first by considering the sample at $z = 2$, simply asking whether the quenched galaxies' descendants have rekindled their star formation to become normal main-sequence galaxies. Fig. 4.11 shows the star forming main sequence at $z = 2$, with the blue stars being the traced descendants of the quenched galaxies and sand color points being all non-quenched galaxies (not only traced galaxies).

The quenched galaxies are split into five groups. First, those which were a satellite at the time of quenching at $z = 3.4$ and have remained a satellite down to $z = 2$ ("always sat"). Second, those which were centrals at $z = 3.4$ but were accreted onto another larger halo but have not yet merged ("accreted"). Third, quenched galaxies which merged with another more massive structure, where the original quenched galaxy cannot be separated anymore ("merged"). Fourth, there are two cases where at the time of quenching the galaxy is closely interacting with another galaxy of comparable mass, and merges by $z = 2$ ("major merger"). Finally, those which remained centrals without ever merging with a larger galaxy ("always main").



Group one contains three galaxies (open light blue symbols). They all remain fully quenched, and the hot halo of their host galaxies (two of which become groups by $z = 2$) is thus efficient enough to suppress any rejuvenation of the star formation within the massive quenched galaxies already at $z > 2$. They also experience stripping, as their mass now is below our original stellar mass cut of $M_* = 3 \times 10^{10} M_\odot$, as marked by the dashed black line.

There are five quenched galaxies which are accreted onto other structures post-quenching (filled light blue symbols). Their star formation rates are very low, with two fully quenched. However, unlike the "always sats", they are not entirely shut-down with three retaining very low residual star formation that they rekindled prior to infall in the more massive structure. Here, we see environmental quenching at work as these galaxies slowly loose their star formation abilities. They highlight that even for how massive the quenched galaxies are at $z = 3.4$, they do not necessarily remain the locally dominant node.

Four quenched galaxies merge (open dark blue symbols) with a more massive system to become a central by $z = 2$ (including ID4180). They contribute between $1/10$ to $1/3$ of the stellar mass at $z = 2$, and the descendant galaxy has high mass and star forming activity. These are curious cases then where a quiescent galaxy is assembled onto a more massive star forming galaxy, and the star formation is not quenched, opposite to the common pathway found at low redshift. Such remnant galaxies have extensive stellar bulges and are closer to S0 galaxies than typical disk galaxies.

Then we have two galaxies undergoing a major merger around the time of quenching (two-color symbols), one of which is ID5058. Both show a large growth in stellar mass and high star forming activity, being very comparable to the behavior seen for the "merged" category. It follows that so long as the galaxy with which the quenched one merges is of equal or greater mass, the odds are it will become a "normal" sub-main sequence galaxy.

The final group are the 22 quenched centrals which remained centrals and never merged with any larger galaxy down to $z = 2$ (filled dark blue symbols). They represent the largest group, as well as the one with the most scatter in resulting star formation rates. These are the ones which we are most interested in for considering how many galaxies can rejuvenate from internal quenching through gradual feeding from the cosmic web.

Of these 22, we find a few which lie near the main sequence, with one in particular fully rejuvenating to lie on the relation. The majority lie at middling to low star formation rates, while three are still fully quenched. None have grown to stellar masses $M_* > 1 \times 10^{11} M_\odot$, with about half growing by less than 10%. Nonetheless, we find that star formation is not permanently shut off even for central galaxies which undergo violent quenching, eject their gas and which subsequently have a large SMBH at their core. These are not rejuvenated via major mergers bringing in significant gas, or by merging themselves with a more massive starforming galaxy, but rather through accretion of gas from the cosmic web, and we will study this process in more detail in the following.

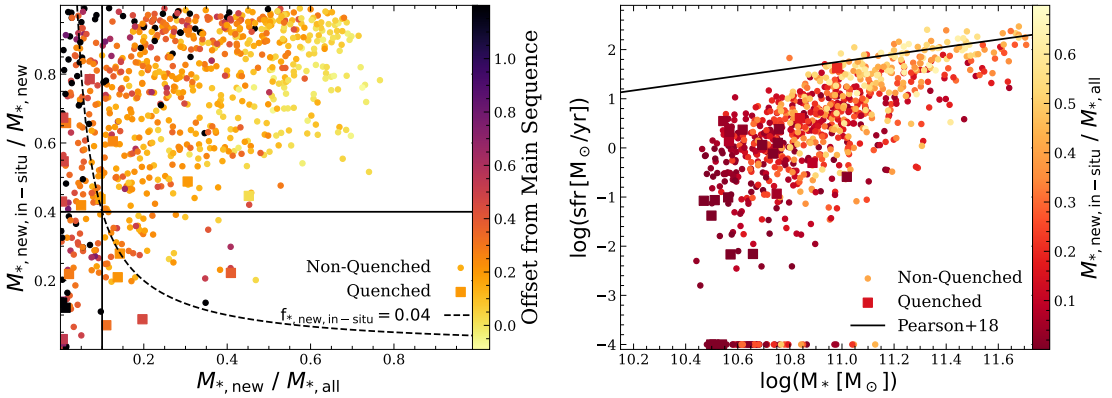


Figure 4.12. *Left:* Fraction of young stars which are self-made versus fraction of total stars which are young for traced centrals at $z = 2$, defined as non-quenched (dots) or quenched (square) based on the SFR at $z = 3.4$. Colored by a galaxy's perpendicular offset from the $z = 2$ main-sequence, normalized between 0 (lies on MS, yellow) and 1 (farthest offset to MS, purple), with starburst galaxies lying above the MS at < 0 (yellow) and galaxies with $SFR = 0$ in black. The black dashed line denotes a fraction of young in-situ stars $f_{*,new,in-situ} = M_{*,\mathrm{new,in-situ}}/M_{*,\mathrm{all}} = 0.04$. *Right:* As Fig. 4.11, but only galaxies which remained centrals from $z = 3.4$ to $z = 2$. Colored by the fraction of total stellar mass contained in young in-situ stars.

4.4.2 Rejuvenation

We differentiate between stars formed in other galaxies and are then accreted versus those which are formed within the galaxy itself, so in-situ. To consider a newly formed star as in-situ made, we require the progenitor gas particle to be within the virial radius of the central galaxy, and the resulting star to be bound to the central immediately afterwards. This gives four categories of stars in a given galaxy at $z = 2$: the initial old component which was in the galaxy at $z = 3.4$ ("Old, In Halo"), old stars which were formed elsewhere and accreted sometime after $z = 3.4$ ("Old, Accreted"), and younger stars (formed after $z = 3.4$) either made in-situ ("New, In-Situ") or accreted ("New, accreted").

In the left panel of Fig. 4.12 we show the mass fraction of in-situ formed younger stars, $M_{*,\mathrm{new,in-situ}}/M_{*,\mathrm{new}}$ as a function of the fraction of total stellar mass contained in younger stars, $M_{*,\mathrm{new}}/M_{*,\mathrm{all}}$ for central galaxies at $z = 2$ traced from $z = 3.4$. We find that galaxies which have formed a significant fraction of their final mass recently tend also to have formed most of that mass in-situ. This is because high-redshift galaxies contain significant fractions of gas, such that any accretion event involving young stars will also involve bringing in a lot of gas, enabling in-situ star formation. Consequently, there emerges a lower bound to the fraction of young stars made in-situ with a slope of around 1. Put another way, if x% of all stars in a traced galaxy at $z = 2$ are young (< 1.5 Gyr old), then at least x% of these young stars were made in-situ (though the range can go up to 100% made in-situ for any given x).

For the quenched galaxies this trend is largely absent, as there are multiple quenched galaxies with many young stars but few of which are in-situ made. This indicates that galaxies which have quenched previously are better at prohibiting rekindling of their own



star-formation even when they accrete significant amounts of new matter compared to other non-quenched galaxies.

However, we also find that prior quenching of a galaxy does not mean that it cannot rejuvenate. Indeed, there are six galaxies which post-quenching end up making at least 4% of their total stellar mass in-situ afterwards. Three of them simultaneously grow by more than 10% while making at least 40% of these new young stars in-situ (lie in the upper right quadrant). Nine exhibit some lesser degree of star-forming activity, with five in the upper left (little new stars but mostly made in-situ) and four in the lower right (many new stars but few of them self made), while seven remain effectively quenched (lower left). This means we find that around 30% rejuvenate, 40% rekindle some residual star forming activity and 30% remain quenched throughout.

The location in the $M_{*,\mathrm{new,in-situ}}/M_{*,\mathrm{new}} - M_{*,\mathrm{new}}/M_{*,\mathrm{all}}$ plane gives the *integrated* star-forming activity, but how does it compare to the *instantaneous* star forming rate? To see this we color the points by their perpendicular distance to the star-forming main sequence at $z = 2$ as given by Pearson et al. (2018), normalized from 0 (on the MS, dark yellow) to 1 (far below, dark purple), with > 1 being quenched (black) and < 0 being star-bursting galaxies above the MS (yellow).

Interestingly, galaxies which end as quenched at $z = 2$ (black points) preferentially stick towards the perimeter, having either very little young stars (lie far left) or having formed practically all younger stars in-situ (lie at the top). We interpret this as them quenching either through starvation caused by lack of accretion (low $M_{*,\mathrm{new}}/M_{*,\mathrm{all}}$) or through the rapid starburst quenching (RSQ) mechanism described by K25, with a collapse of significant gas followed by a massive starburst (high $M_{*,\mathrm{new,in-situ}}/M_{*,\mathrm{new}}$) and combined stellar and AGN feedback which quenches the star formation.

Generally, we find that when comparing galaxies which made a similar fraction of new stars in-situ, those which show a higher instantaneous SFR (closer to main sequence, more yellow) lie farther right (have a higher total fraction of younger stars). This also implies a higher total fraction of new in-situ formation (an *integrated* quantity) based on the current SFR (an *instantaneous* quantity). To validate this we plot the star formation rate versus stellar mass in the right panel of Fig. 4.12 and color by the total fraction of young in-situ formed stars $M_{*,\mathrm{new,in-situ}}/M_{*,\mathrm{all}}$. We indeed find that galaxies lying closer to the MS show higher $M_{*,\mathrm{new,in-situ}}/M_{*,\mathrm{all}}$, though there is some scatter which warrants a closer look in the future.

Having seen that around 30% of the quenched galaxies rejuvenate we consider now where they make these new in-situ stars, in particular when compared to galaxies which were not quenched at $z = 3.42$. We find in the left panel of Fig. 4.13 that the new in-situ stars in the six quenched descendants (blue color) which rejuvenated significantly ($M_{*,\mathrm{new,in-situ}}/M_{*,\mathrm{all}} > 0.4$) lie at noticeably farther radii than in the non-quenched galaxies (sand color), indicating that the most central region does not experience significantly rekindled star formation once a galaxy has been quenched. This may also in part be caused by the comparatively more compact central bulges formed from the starburst which precedes the quenching (see also

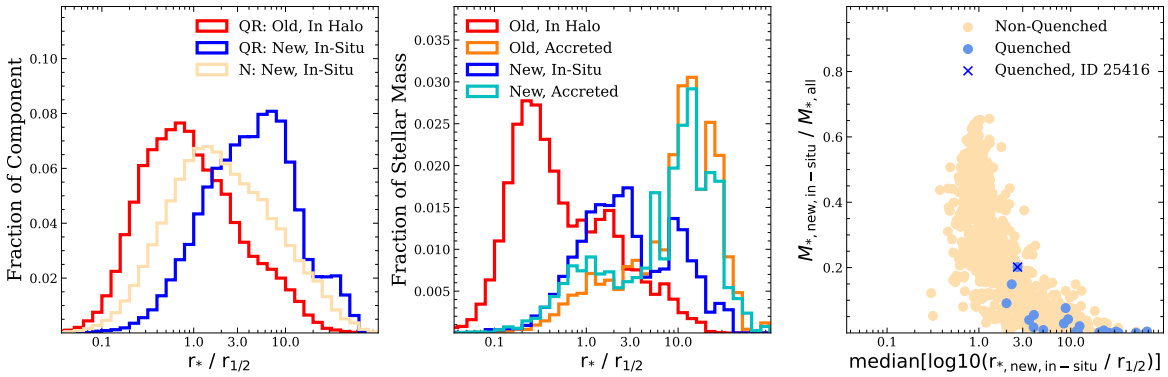


Figure 4.13. *Left:* Radial distributions of the young in-situ formed stars for the descendants of rejuvenated quenched (blue) and non-quenched (sand) galaxies at $z = 2$. The old component which was in the halo prior is also shown for the quenched descendants (red). *Middle:* The radial total mass fraction of different components (legend) for the quenched galaxy ID25416 which rejuvenates the strongest. *Right:* Fraction of total stellar mass which is young and in-situ made versus the its median radial position. All radii are given relative to the stellar half mass radius.

Fig. 4.2), where at $z = 2$ the non-quenched sample have $r_{1/2}^{-} \approx 3.1$kpc while the quenched have $r_{1/2}^{-} \approx 1.8$kpc.

Taking the descendant of the quenched galaxy which has rejuvenated the most, galaxy ID25416, we plot the origin of its stellar component in the middle panel of Fig. 4.13. The most central region within $1\,r_{1/2}$ is dominated by the original stars formed in the burst prior to quenching (red line). The stars which are formed in-situ post quenching primarily reside between $1\,r_{1/2}$ and $3\,r_{1/2}$, where they also are the dominant component. Beyond around $5\,r_{1/2}$ the accreted components begin dominating, with comparable mass contained in younger versus older stars.

Finally we show the fraction of total stellar mass in young in-situ stars as a function of their median radius for all individual galaxies. We find that galaxies with little recent in-situ star formation also tend to have this formation occurring farther out. As the fraction of in-situ formed stars increases they begin to dominate the total stellar mass budget, until eventually the stellar half mass radius coincides with their median radius.

We then ask whether the degree of rejuvenation can be predicted from observables at the time of quenching already. Fig. 4.14 shows the fraction of young in-situ formed stars versus the surrounding gas within three virial radii, split by outflowing and inflowing components defined by $\vec{v}\cdot\vec{r} > 0$ and < 0 (crosses and dots, respectively). The amount of mass is comparable in both components, and we find the outflowing gas to be generally hot ($> 10^{5.4}$K) while the inflowing gas is colder. We further see that a larger amount of inflowing cold gas (blue) results in a higher amount of rekindled in-situ star formation, while there is no such correlation with the amount of outflow.

This dependence of rejuvenation on the inflowing gas mass indicates that it is the environment which ultimately determines the fate of high-z quenched galaxies as opposed to for example the mass of their AGN. Indeed, we find no correlation between the amount of rejuvenation $M_{*,\mathrm{new,in-situ}}/M_{*,\mathrm{all}}$ and the relative mass fraction of the black hole M_{BH}/M_{*} at

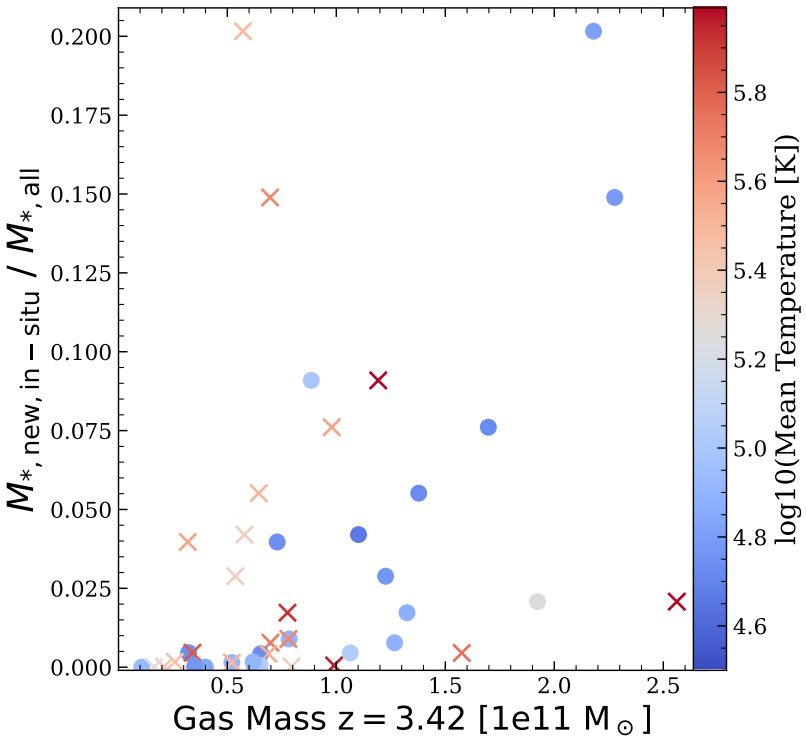


Figure 4.14. The fraction of stellar mass at $z = 2$ which was formed in-situ post-quenching (after $z = 3.4$) versus the gas mass within three virial radii around the galaxy immediately following quenching (at $z = 3.4$). Gas is split into inflowing (dots) and outflowing components (crosses), and colored by the mean temperature.

$z = 3.4$ for the quenched galaxies. This mirrors the results by K25, where the long-term evolution of the star formation is most tightly correlated with the environment.

4.4.3 Descendant Galaxies at $z = 0$

Finally, we want to see where the quenched galaxies end up at present day. As the higher resolution Box3 uhr ran until $z \approx 2$, we match at the last snapshot the galaxies to their counterparts in the lower resolution version of the same box, Box3 hr, which ran until $z = 0$. Note that exact matches are difficult in the case of satellites. However, as we care only about the final halo in which they end up in, it matters only that we can match the correct larger halo, which is generally possible.

The right panel of Fig. 4.15 shows the histogram of the total mass of the host halo M_{all} at $z = 0$ for the descendants of the quenched (blue lines) and the non-quenched galaxies (tan lines). We find that the quenched galaxies generally end up in galaxy groups of a total mass around $M_{\mathrm{all,z=0}} \approx 10^{13.5} M_\odot$. This is particularly true for the galaxies which were centrals at $z = 3.4$ (dashed blue line), with only three of 28 ending in galaxy clusters with $M_{\mathrm{all,z=0}} \geq 10^{14} M_\odot$.

This means that on average they end in less massive halos compared to the total sample. The median mass of the final halo for non-quenched galaxies (sand lines) is $6.6 \times 10^{13} M_\odot$, while for quenched galaxies it is $4.4 \times 10^{13} M_\odot$. This difference is even more significant

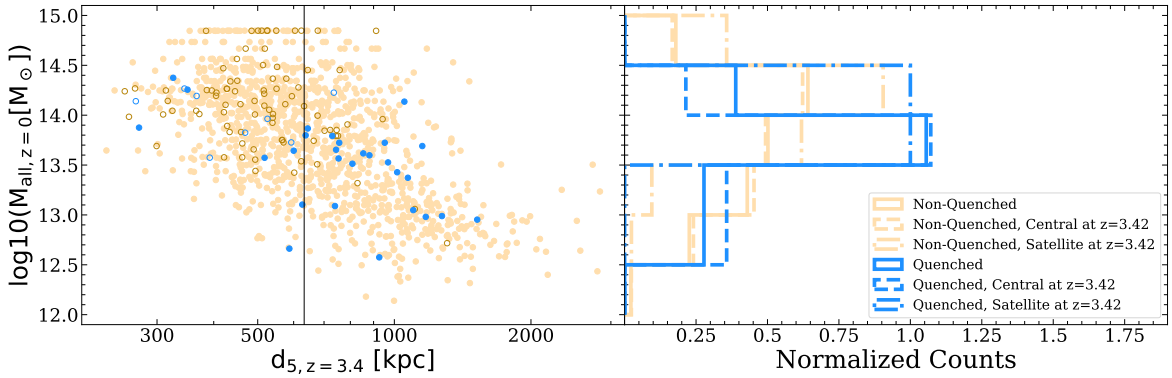


Figure 4.15. *Left:* Total halo mass at $z = 0$ plotted against a tracer for the environment at $z = 3.4$, d_5 (in physical kpc), for quenched (blue) and non-quenched (sand) centrals (filled symbols) and satellites (open symbols), defined at $z = 3.4$. The median d_5 for all galaxies is given by the vertical black line. *Right:* Binned total halo mass at $z = 0$.

for centrals, with $5.8 \times 10^{13} M_\odot$ versus $3.8 \times 10^{13} M_\odot$, while for satellites the final halos are similar ($1.3 \times 10^{14} M_\odot$ versus $1.2 \times 10^{14} M_\odot$). That is to say we find that a massive central galaxy at $z = 3.4$ will on average end up in a halo of 50% higher mass at $z = 0$ if it is forming stars versus if it is fully quenched.

This imprint of the eventual halo mass is also present in the environment at higher redshifts. As an environmental tracer we define here d_5 as the radius of the sphere required to include five neighboring galaxies with total masses $M_{\rm all} \geq 10^{11} M_\odot$. The final halo mass at $z = 0$ is then plotted against this radius calculated at $z = 3.4$ in the left panel of Fig. 4.15.

We find that there is a diffuse correlation between a more dense environment at $z = 3.4$ (lower d_5) and a higher final halo mass at $z = 0$. This is overall to be expected as Remus et al. (2023) find that the environment is the best tracer for the $z = 0$ mass of protoclusters. What is striking, however, is that of the 28 quenched centrals (blue filled dots) 75% lie above the median separation of all galaxies (vertical black line), so lie in underdense environments.

This may mean that a specific type of environment is required to fully self-quench through combined stellar and AGN feedback. Indeed, it is reasonable to assume that denser environments are more proficient at replenishing lost gas. To remove enough gas to completely cease star formation requires so little gas accretion that the feedback can overpower the inflow. This idea is explored further in K25 and explains why here the quenched galaxies are found predominantly in underdense environments.

4.5 Summary and Conclusions

We studied quenched galaxies identified at $z = 3.4$ in the Magneticum Pathfinder large high-resolution Box3 uhr and compared their properties to observations of quenched galaxies from JWST by Valentino et al. (2023), Nanayakkara et al. (2024) and Carnall et al. (2023a), and also to pre-JWST observations of quenched number densities. We show that the Magneticum simulation can successfully reproduce similar quenched fractions for comparable stellar

masses to those observed, albeit we cannot reproduce the most massive of the quenched galaxies as the box volume of the simulation is still too small to capture these biggest nodes. We also compared the observations and the Magneticum number densities to those of other simulations like IllustrisTNG, Eagle, Astrid, and Flares, that struggle to capture the quenched fractions at $z > 3.5$ as shown also by Weller et al. (2025). As discussed in more detail by K25, it is likely that these differences originate from differing implementations of the AGN feedback schemes. The Magneticum simulations used here differentiate between hot and cold gas accretion onto the black hole, allowing for increased accretion rates at higher redshifts while simultaneously dampening them at intermediate redshifts (Steinborn et al., 2015). By contrast, other models typically couple to the total gas reservoir, which may be underestimating variability in the black hole mass accretion and thus feedback, resulting in both less quenched galaxies at high redshifts and subsequently also less rejuvenation.

We find the quenched galaxies to be rather compact in size compared to non-quenched galaxies, in good agreement with recent observations by Ito et al. (2024) and Carnall et al. (2024), albeit being generally a bit larger than observed due to the limiting softening length of the simulation. Furthermore, the formation redshifts of the simulated quenched galaxies are in good agreement with the observed formation redshifts, with some reaching up to $z_{\rm form} \approx 6$, aside from the observation of a peculiar quenched galaxy reported by Glazebrook et al. (2023) which is older than any formation redshift we can produce here. However, our full simulation sample contains at least one galaxy that is quenched at about $z = 5$ and which has a formation redshift beyond $z = 8$ but which rejuvenated afterwards, as shown in the companion study to this work by K25.

All our quenched galaxies experience a fast period of star formation followed by a rapid decline that leads to quenching, resulting in similar quenching redshifts as observed. In fact, we find that the quenching redshifts and formation redshifts of the quenched galaxies are correlated, with galaxies with higher formation redshifts also having higher quenching redshifts. This is found for both simulations and observations to be the case, and the outlier quenched galaxy from the observed sample by Glazebrook et al. (2023) actually follows the same trend as the simulations predict if extrapolated to higher redshifts. This indicates that quenching at high redshifts proceeds generally in a similar manner, that is quenching at high redshifts occurs on a very short timescale after a massive star formation event, in agreement with what is discussed by K25.

We follow the quenched galaxies forward in time, and find that by $z = 2$, that is within 1.5Gyr after being fully quenched, about 20% of the galaxies that are centrals at $z = 3.4$ are accreted onto a more massive structure by $z = 2$, and are either still satellites of that structure or have merged with the more massive central galaxy. Of the remaining 80% of quenched galaxies, 30% rejuvenate, 30% remain fully quenched, and 40% develop some residual star formation. Those galaxies that rejuvenate can even reach the star formation main sequence and appear at a later time to be normal star-forming galaxies.

For those quenched galaxies that rejuvenate, we find the star formation to primarily occur on the outskirts between $1\,r_{1/2}$ and $3\,r_{1/2}$, not reaching the central regions. This is different

the non-quenched comparison sample of galaxies that are already massive at $z = 3.4$, where star formation can still occur at the center even down to $z = 2$. Furthermore, we find that the amount of newly formed stars post-quenching primarily correlates with the amount of cold gas that has been inflowing, while there is no correlation to the outflowing hot gas component, clearly showing that the rejuvenation only depends on new inflowing gas reaching the galaxy, independent of the mass of the AGN that drives the hot wind outwards.

Finally, we find that quenched galaxies at $z = 3.4$ tend to end up in less massive final halos at $z = 0$ compared to non-quenched massive galaxies at $z = 3.4$. This difference is negligible for galaxies that become satellites by $z = 2$, but significant for galaxies that stay centrals, with the final mass deviating on average by 50%. This is because whether a galaxy is star forming or not at high redshift correlates with the environment, where we showed that quenched galaxies tend to lie in underdense regions. We conclude that the environment of a galaxy at high redshift is not only important for it being quenched as shown by K25, but that it also plays a crucial role for the future development of the quenched galaxies at low redshifts. Thus, we suggest that relics of galaxies quenched at high redshifts can best be found in low mass group environments or isolated fields, albeit it might be possible for a high redshift quenched galaxy to be accreted onto a cluster and still remain as a compact quenched galaxy. As the quenched galaxies at high redshifts are very compact, relics of such galaxies should also still be significantly more compact than other quenched galaxies of comparable mass at present day. Nevertheless, as some quenched galaxies also merge with other, still star forming galaxies prior to $z = 2$, it is also possible to find contributions of the quenched galaxies distributed in other galaxies, however, detecting those might be extremely difficult.

Sól þat né vissi hvar hon sali átti,
stjörnur þat né vissu hvar þær staði áttu,
Máni þat né vissi hvat hann megins átti.

Völuspá, *Codex Regius*, Ancient Norse poem, circa 1270

5

Flaring Candles: Quenched Galaxies from Simulations and Observations – A Comparison

This Chapter provides an overview of additional high-redshift work I have done or to which I contributed. Each Section is marked with the relevant information at the beginning.

5.1 Star Formation and Quenching in the High Redshift Universe in a Nutshell

This section was published as IAU proceedings for symposium 369 by Kimmig & Remus.

This study expands on the findings presented by Kimmig et al. (2025b), Remus & Kimmig (2025), and Fortuné et al. (2025) on the quenching and rejuvenation cycles of galaxies from the Magneticum simulations. We find that the quenching of massive galaxies at cosmic dawn is the result of an isotropic influx of gas, triggering rapid star-formation and then the central active galaxy nucleus (AGN), where resulting feedback quenches the galaxy by evacuating gas out to three virial radii with outflows of maximally 1000km/s. Whether a galaxy remains quiescent depends on the environment, with galaxies in gas-rich regions rejuvenating while gas-poor regions starve, thus being possible progenitors of observed

low-redshift relic galaxies. This on-off-cycle of star-formation is common at cosmic noon, occurring also at lower redshifts, with at least one period of quiescence experienced by most main-sequence galaxies. Finally, we demonstrate that higher mass quiescent galaxies have typically quenched earlier.

5.1.1 Introduction

Surprisingly large amounts of massive quiescent galaxies have been detected with JWST in the last few years (e.g., Nanayakkara et al., 2024; Ito et al., 2024), which have proven challenging to reproduce in simulations (e.g., Remus & Kimmig, 2025; Weller et al., 2025; Chittenden et al., 2025). The Magneticum Simulations, however, successfully reproduce both the total and the quenched number densities of galaxies at $z = 3 - 7$ (Kimmig et al., 2025b; Dolag et al., 2025; Merlin et al., 2025), making it possible to study the processes that lead to the quenching of galaxies at cosmic dawn, as done by Kimmig et al. (2025b) and Remus & Kimmig (2025). They find a complex interplay between rapid starbursts, feedback from the central black hole (AGN feedback), and crucially also the environment to be responsible for quenching and remaining quenched. Interestingly, they also report that quenching at high redshifts is often followed by a rejuvenation event due to the large amounts of gas still present in the early Universe. As also demonstrated by Fortuné et al. (2025), these cycles of quenching and rejuvenation are common for all galaxies especially before cosmic noon, but also at lower redshifts and even present-day. In this work, we review the findings of these studies, providing a comprehensive overview especially in regards to the importance of the environment in quenching as rejuvenating star formation at cosmic dawn, and finally consider also the low-mass end of quenched galaxies at high redshifts.

We use the Magneticum Pathfinder simulation suite for this work (Dolag et al., 2025; Teklu et al., 2015), in particular the simulation volume Box3 uhr which employs an AGN model as described by Steinborn et al. (2015). This simulation has been shown to be able to reproduce the observed quiescent fractions at cosmic dawn (Kimmig et al., 2025b; Remus & Kimmig, 2025; Dolag et al., 2025). The simulation has a volume of $(128\mathrm{Mpc/h})^3$ with dark matter, gas, and stellar particles masses of $m_{\mathrm{dm}} = 3.6\times10^7\mathrm{M}_\odot/\mathrm{h}$, $m_{\mathrm{gas}} = 7.3\times10^6\mathrm{M}_\odot/\mathrm{h}$, and $m_* \approx 1/4^{\mathrm{th}} m_{\mathrm{gas}} \approx 1.8\times10^6\mathrm{M}_\odot/\mathrm{h}$, respectively. The underlying cosmology uses the WMAP-7 parameters $h = 0.704$, $\Omega_m = 0.272$, $\Omega_b = 0.0451$, $\Omega_\lambda = 0.728$, and $\sigma_8 = 0.809$. The lower mass cut for galaxies included in this study is $M_* > 5\times10^9 M_\odot$. Galaxies are defined as quenched if their star formation rate at a given mass, i.e., their specific star formation rate sSFR is lower than $sSFR < 0.2\times t_{\mathrm{Hub}}$ following the criterion introduced by Carnall et al. (2020).

5.1.2 Quenching

For all our quenched galaxies selected at $z = 3.4$, we find the same general process of quenching as demonstrated by Kimmig et al. (2025b), which is summarized schematically in Fig. 5.1: These galaxies initially form in some of the most massive nodes in the young

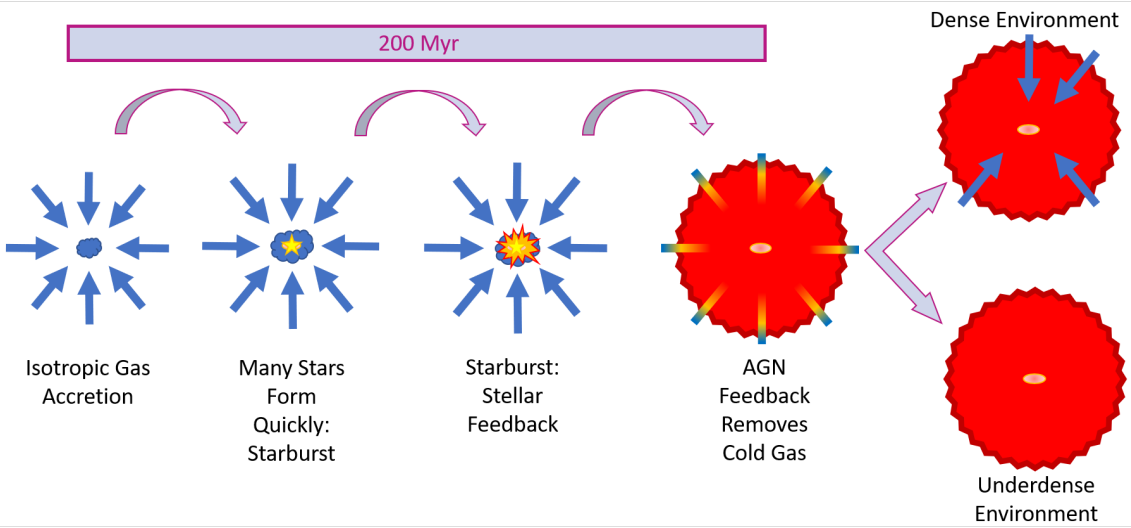


Figure 5.1. Quenching process at high redshifts, illustrating the findings by Kimmig et al. (2025b) and Remus & Kimmig (2025). We find quenching to occur following an isotropic gas accretion onto the halo, triggering a rapid starburst that generates stellar feedback, and eventually igniting the AGN feedback to blow out the gas, effectively leading to quenching of the galaxy. The timescale of this process is 200Myr or less. The subsequent evolution then depends on the environment. For dense environments, the gas is reaccreted through mergers and the cosmic web, reigniting star formation and thus rejuvenating the galaxy. In comparatively more underdense environments, such as adjacent nodes to the dense environments, no re-accretion of gas occurs and the galaxy remains quiescent.

Universe, with isotropic influx onto them flowing from all directions. This is visible in an overall lower halo spin compared to non-quenching galaxies. From this isotropic influx of gas originates a rapid starburst that is continuously fed from new infalling gas until stellar feedback from the first massive dying stars starts to lower the star formation rate. In total, this process takes only 200Myr or less, in agreement with observations (e.g. Forrest et al., 2020; Kakimoto et al., 2024; Nanayakkara et al., 2024). Therefore, the stars made in this starburst are alpha-element enriched but not iron enriched (Kimmig et al., 2025b), since the only enrichment originates from core collapse supernovae (SNII), and not from Supernova Type Ia which originate from lower mass stars that need longer times than 200Myr to explode and enrich the gas. This initial enrichment mirrors that of the oldest stars seen in the Milky Way with APOGEE (Imig et al., 2023), equivalent to a single stellar population star formation event given the rapid nature of the event. Eventually, the AGN feedback grows to then eject the gas from the galaxy, reaching velocities of up to 1000km/s, similar to observational results of outflows at $z = 3.064$ by D'Eugenio et al. (2024). The gas that is removed from the galaxy has been enriched in metallicity, and can reach distances of three times the virial radius of the galaxy.

To quantify the time at which quenching took place, we calculate the time at which a galaxy has formed 90% of its stars, i.e., t_{90}. This is done for all galaxies that are found to be quenched at a given redshift in the simulation. Fig. 5.2 shows t_{90} for all quenched galaxies at their given redshift, split into four different stellar mass bins. At all redshifts, we find more

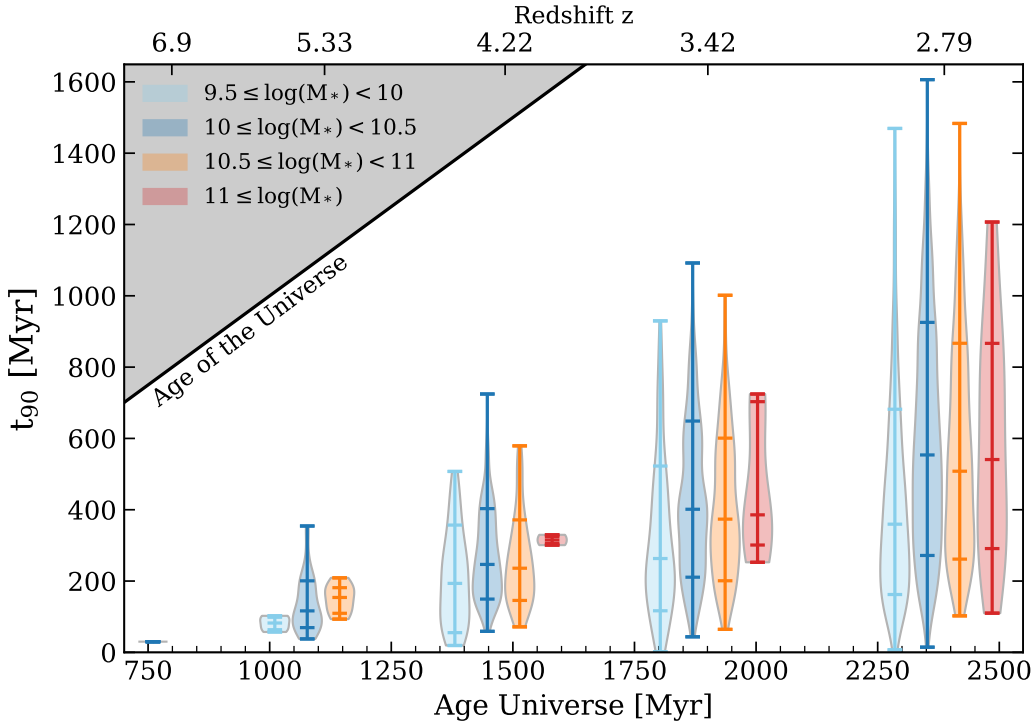


Figure 5.2. For quenched galaxies above a stellar mass of $3 \times 10^9 M_\odot$ at five redshifts, the time at which the galaxy has formed 90% of its stars, t_{90}, is plotted split into four stellar mass bins as given in the legend. For each redshift and mass bin, the violin shows the overall distributions of t_{90}. Each block of four mass bins belongs to the redshift given in the upper x-axis legend. Lower values of t_{90} indicate a generally more recent cessation of star formation than larger values, with the age of the Universe shown as black line providing an upper possible bound for the stellar ages. Generally, t_{90} is larger for more massive galaxies, indicating an earlier onset of quenching for those than for the smaller galaxies, as discussed in more detail by Merlin et al. (2025).

massive galaxies to be quenched earlier than lower mass galaxies on average, albeit the scatter is generally large between individual galaxies. This is in agreement with results presented by Merlin et al. (2025) from an observational sample of quenched galaxies observed with JWST, and results by Nanayakkara et al. (2025). Note that the quenched galaxies at higher redshift are not necessarily a subset of those at lower redshifts, as rejuvenation is a common occurrence at high redshifts as will be discussed in the following.

5.1.3 Rejuvenation

We tracked the evolution of the quenched galaxies identified at $z = 3.4$ down to $z = 2$, and found that most of these galaxies had rekindled some kind of star formation (Remus & Kimmig, 2025). In fact, for the massive quenched galaxies which did not merge onto larger structures by $z = 2$, 70% of them rekindle their star formation, with 30% rejuvenating onto the main sequence and 40% rejuvenating onto a lower level of star formation but still above the criterion for quenching. Only 30% of the galaxies remained fully quenched. Whether rejuvenation occurs or not depends on the environment: if the galaxy resides in a denser environment, inflow from the cosmic web and gas rich mergers are able to reach the galaxy



and restart star formation, and only those quenched galaxies that are not the main nodes of the cosmic web can stay quenched, as schematically shown in Fig. 5.1. Therefore, the environment is the most important predictor of long term quenching at high redshifts, as demonstrated by Kimmig et al. (2025b). We find this process of rejuvenation to occur not only at high redshifts, but in fact to be a common occurrence for all galaxies. In fact, Fortuné et al. (2025) showed from the Magneticum simulations that only about 14% of all galaxies always stay on the main sequence, with all other galaxies going through on-off cycles of star formation and quenching, making this the dominant star formation process in galaxy evolution. Indications are recently also seen from observations, with Muñoz López et al. (2025) finding multiple star formation episodes for their sample of more than 300 galaxies at $z = 0.1 - 0.9$.

5.1.4 Summary and Conclusions

In these proceedings we summarize and illustrate the findings of Kimmig et al. (2025b), Remus & Kimmig (2025), and Fortuné et al. (2025) from the Magneticum Pathfinder simulations on the quenching processes and rejuvenation cycles of galaxies from cosmic dawn to present day. We find quenching at cosmic dawn to be driven by rapid isotropic gas inflow, leading to a massive starburst and a subsequent AGN feedback episode that drives the gas out to several times the virial radius of the galaxy. However, such quenched galaxies do not need to remain quenched till present day, with the majority (70%) of these galaxies rejuvenating by cosmic noon. This rejuvenation depends on their cosmic environment, with galaxies in the densest environments rekindling star formation due to influx of gas and gas-rich mergers from the cosmic web, while those galaxies remain quenched that live in adjacent nodes of the cosmic web. This cycle of rejuvenation and quenching is found to be common through cosmic time for all galaxies with stellar masses $M_* > 1 \times 10^{10} M_\odot$, with galaxies that always live on the main sequence representing only about 14% of all galaxies. These always-main-sequence growing galaxies are more common at the higher stellar masses, matching the masses of present-day super spirals, with low mass galaxies typically showing episodes of quiescence.

5.2 Observational Kinematics and Quenching Behavior at Cosmic Dawn

This section summarizes three observational publications to which I contributed and for which I am a co-author, which take inspiration from the work presented in Chap. 3 and Chap. 4.

5.2.1 Quenched Fractions Renewed: A Larger Observational Sample

The results presented here are part of the publication by Merlin et al. (incl. Kimmig), 2025, OJAp 8, 170, for which I provided simulation comparison data.

With the increasing abundance of massive quiescent galaxies observed with the James Webb Space Telescope at high redshifts (e.g., Carnall et al., 2023a; Valentino et al., 2023; Pérez-González et al., 2023; Long et al., 2023; Baker et al., 2025b; Stevenson et al., 2026), understanding their formation has become a central question (Kurinchi-Vendhan et al., 2023; Kimmig et al., 2025b). By compiling around half a million sources from various JWST observations (Treu et al., 2022; Eisenstein et al., 2023; Oesch et al., 2023; Bagley et al., 2024; Bezanson et al., 2024; Morishita et al., 2025; Finkelstein et al., 2025), in addition to the hydrodynamical cosmological simulations *Magneticum Pathfinder* (Dolag et al., 2025, see also chapter 2), IllustrisTNG (Pillepich et al., 2018b), Eagle (Schaye et al., 2015) and Simba (Davé et al., 2019), Merlin et al. (2025) analyzed the emergence of lower and higher mass quiescent galaxies at $z \geq 3$, as well as considered on which timescales they are found to quench.

In Fig. 5.3, we show their compilation of quiescent number densities for galaxies with $M_* \geq 10^{10.5} M_\odot$ (left) and $M_* \geq 10^{9.5} M_\odot$ (right), with observations as data points and the

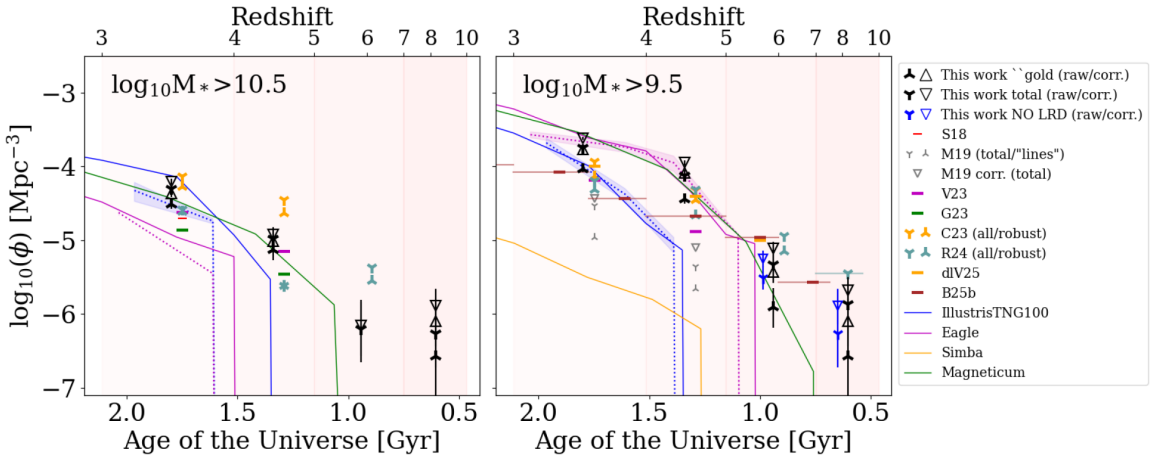


Figure 5.3. This figure has been published as Fig. 9 by Merlin et al. (2025), and shows the quiescent number densities of $M_* \geq 10^{10.5} M_\odot$ (*left*) and $M_* \geq 10^{9.5} M_\odot$ (*right*) galaxies both from observations (points) and simulations (lines).

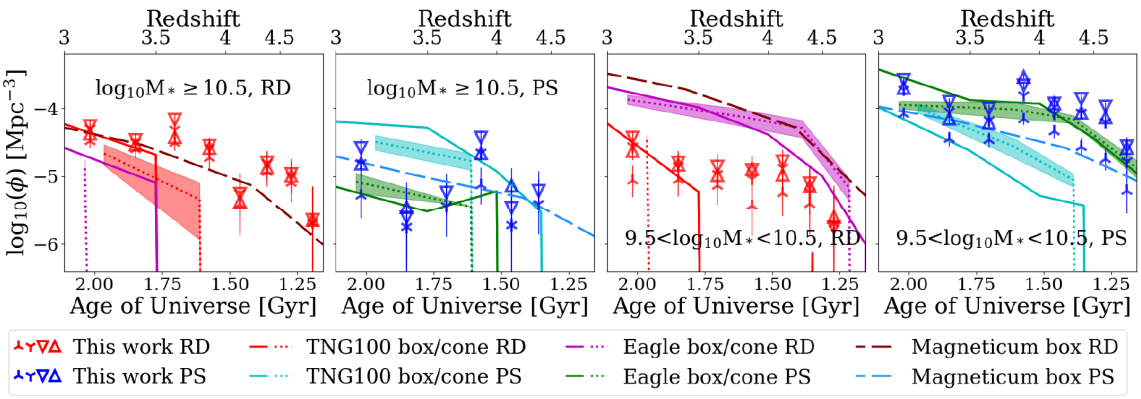


Figure 5.4. This figure has been published as Fig. 10 by Merlin et al. (2025), and plots the quiescent number density for RD (*first* and *third* panel) and PS galaxies (*second* and *fourth* panel).

simulations plotted as lines. They find that most simulations at high redshifts underproduce the amount of quenched galaxies relative to observations, where *Magneticum Pathfinder* Box3/uhr shows the overall best performance, in agreement with Kimmig et al. (2025b). Interestingly, Merlin et al. (2025) find that it is in particular the higher mass end that is underproduced, with less of a disagreement to observations at $M_* \geq 10^{9.5} M_\odot$ for simulations such as Eagle.

They then split their quiescent galaxies by the time of quenching, defining those that have recently quenched ($t_q \leq 150$ Myr) as "post-starburst" (PS) while older quiescent galaxies are "red and dead" (RD). We show in Fig. 5.4 the resulting comoving number density against time split by mass (left two vs right two) and type (RD first and third panel, PS second and fourth). Doing so, Merlin et al. (2025) find that in particular the massive RD quenched galaxies are entirely absent at $z \geq 3.7$ from the included cosmological simulations other than *Magneticum Pathfinder*, which manages to match the number densities of both the massive RD and PS galaxies. Interestingly, the lower mass galaxies show a predominance of PS quenched galaxies, with very few RD lower mass galaxies. While *Magneticum Pathfinder* well matches the PS low mass number densities, both it and Eagle overproduce the number of low mass RD galaxies, while IllustrisTNG underproduces them at $z \geq 3.5$.

The consistently higher number of PS quenched galaxies compared to RD imply that these PS must rejuvenate (Remus & Kimmig, 2025), else they would become RD quenched galaxies. These findings show that, while there have been successes in reproducing the quenched galaxy population in general (Kimmig et al., 2025b), there is additional work to be done for the lower mass galaxies (Merlin et al., 2025).

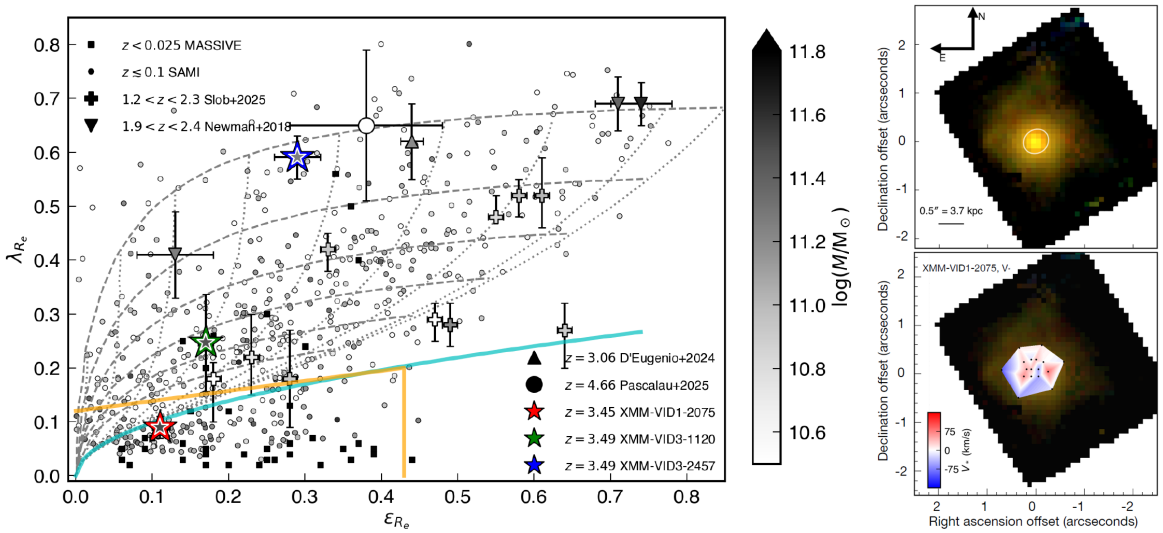


Figure 5.5. The left figure has been published as Fig. 4 by Forrest et al. (2025), while the right figure is a mixture of Fig. 2 and Fig. 3 from that work.

5.2.2 Slow Rotators at Cosmic Dawn

The results presented here are part of the publication by Forrest et al. (incl. Kimmig), 2025, submitted to Nature Astronomy, arXiv:2508.10987, who observed the first slow rotator at cosmic dawn in agreement with the prediction from Kimmig et al. (2025b). I contributed to the discussion of the findings.

Kinematic slow rotators are defined as galaxies showing little to no rotation in their stellar bodies, and are known in the $z = 0$ Universe to be more massive than their fast rotator counterpart (Emsellem et al., 2011; van de Sande et al., 2021). This is commonly attributed to mergers, and in particular major dry mergers because they do not rekindle star formation (Jesseit et al., 2007; Naab et al., 2014). Residing in denser environments (Brough et al., 2017), these galaxies are thought to represent the final phase of the hierarchical growth of galaxies. As such, it stands to reason that they would emerge later in cosmic time, needing sufficient time for the formation of many dry galaxies that then merge to disrupt the rotation of their respective stellar disks.

However, there is an alternative formation scenario at high redshifts (Naab et al., 2014), where the initial formation is the result of a more isotropic collapse of gas, and thus the resulting body of stars is also not as strongly rotating. Kimmig et al. (2025b) demonstrated that for galaxies within the *Magneticum Pathfinder* Box3/uhr simulation (Dolag et al., 2025) massive, quiescent slow rotator galaxies can emerge as early as $z = 4.2$ (and star forming slow rotators already by $z = 5.3$), much earlier than previously assumed (Khochfar et al., 2011). Given that the few observational kinematic studies had found only fast rotators until this point (e.g., Newman et al., 2018; D'Eugenio et al., 2024; Pascalau et al., 2025), it was the observations by Forrest et al. (2025) that for the first time demonstrated that, also in the real Universe, massive quiescent slow rotator galaxies do indeed form already by $z = 3.45$.

We show the observed slow rotator galaxy XMM-VID3-2075 in Fig. 5.5 in the right panels, both as an RGB image (top) as well as the kinematic fitting to Voronoi binned data (bottom). The velocity structure clearly exhibits a lack of rotation, which is captured in the plot on the right of Fig. 5.5 showing the λ_{R_e} parameter (Emsellem et al., 2007) against the ellipticity. Empirical cuts separating fast and slow rotators are given by the cyan (Emsellem et al., 2011) and gold lines (van de Sande et al., 2021). The galaxy XMM-VID3-2457 is therefore a slow rotator under both criterion, and Forrest et al. (2025) measure it to be additionally quiescent (SFR $< 1\,M_\odot$/yr) and massive ($M_* \approx 3.3 \times 10^{11} M_\odot$). Furthermore, XMM-VID3-2075 is compact at $R_e \approx 1.95 \pm 0.15$ kpc, and therefore closely follows the predictions by Kimmig et al. (2025b), where quenching follows a starburst caused by a particularly isotropic collapse that both drives up the mass in the central supermassive black hole as well as makes the resulting galaxy more compact. This observation has again pushed the boundary for common assumptions of hierarchical formation ever earlier, with the $z = 3$ Universe already hosting massive disks (Wang et al., 2025), quenched galaxies (Carnall et al., 2023a; Valentino et al., 2023), and now also slow rotators (Forrest et al., 2025).

5.2.3 Quenching and Formation Times from Observations

The results presented here are part of the publication by Nanayakkara et al. (incl. Kimmig), 2025, ApJ 981, 78, for which I provided simulation comparison data.

Beyond the statistics of quenched galaxies (e.g., Merlin et al., 2025), it is useful to consider smaller samples that can then be dissected galaxy by galaxy for their stellar formation histories. This was the goal of the work by Nanayakkara et al. (2025), who selected 19 massive ($\geq 3\times10^{10} M_\odot$) galaxies at $z = 3$ to $z = 4.5$ with negligible amounts of ongoing star formation (sSFR = SFR/$M_* < 0.15$/Gyr) observed by JWST/NIRSpec.

In the left panel of Fig. 5.6 we show the stellar mass assembly histories of these galaxies as tracks (lines), and mark the time when they reach 50% of their final stellar mass (blue stars), when they quenched (red diamonds) in addition to the time of observation (black dots). The galaxy sample of Nanayakkara et al. (2025) show a remarkable diversity in formation histories, with some such as ID 35168 forming among the earliest but quenching quite late, while others such as ID 8192 quench within 100 Myr of reaching 50% of their stellar mass. A particularly early forming and early quenching galaxy is ZF-UDS7329, as first observed by Glazebrook et al. (2023).

We plot in the right panel of Fig. 5.6 equivalent tracks for a select subset of massive quenched galaxies from the *Magneticum Pathfinder* Box3/uhr simulation. The spread in formation histories, with some forming and quenching rapidly while others take longer, mirrors that seen in the observations. While the simulation hosts galaxies with formation and quenching times that are similar to that of ZF-UDS7329 (marked within the panel, but without a formation line to differentiate it from the simulated galaxies), as well as those with similarly extreme stellar masses, we do not find any individual object with the two of these

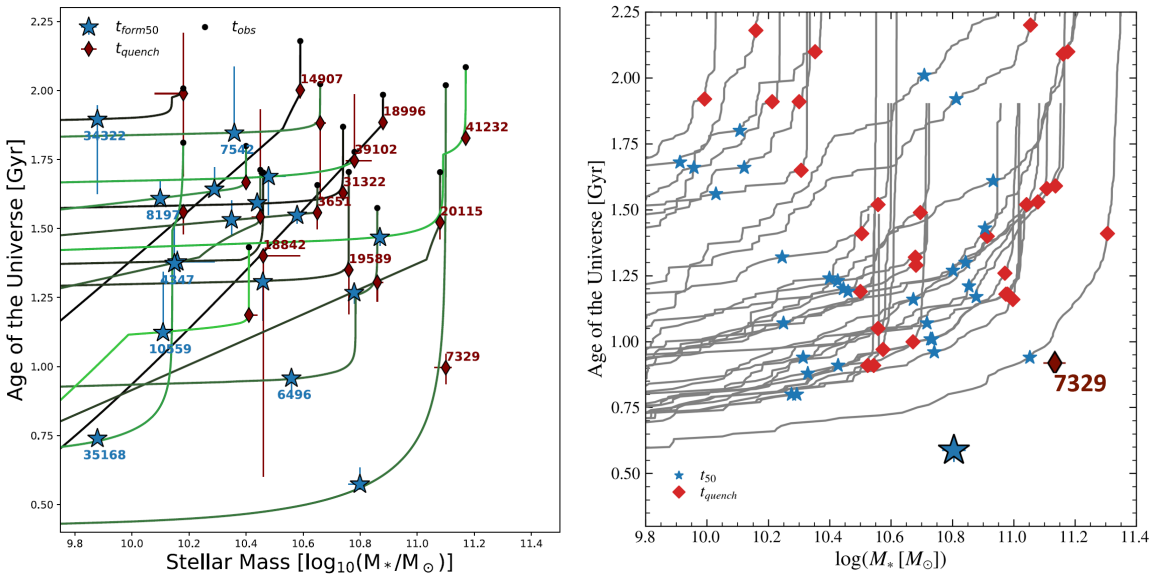


Figure 5.6. The *left* figure has been published as figure 6 by Nanayakkara et al. (2025), while the *right* figure is a version of that figure based purely on quenched galaxies from the *Magneticum Pathfinder* Box3/uhr simulation. The two symbols without a track in the *right* panel are the observed galaxy ZF-UDS7329 (Glazebrook et al., 2023).

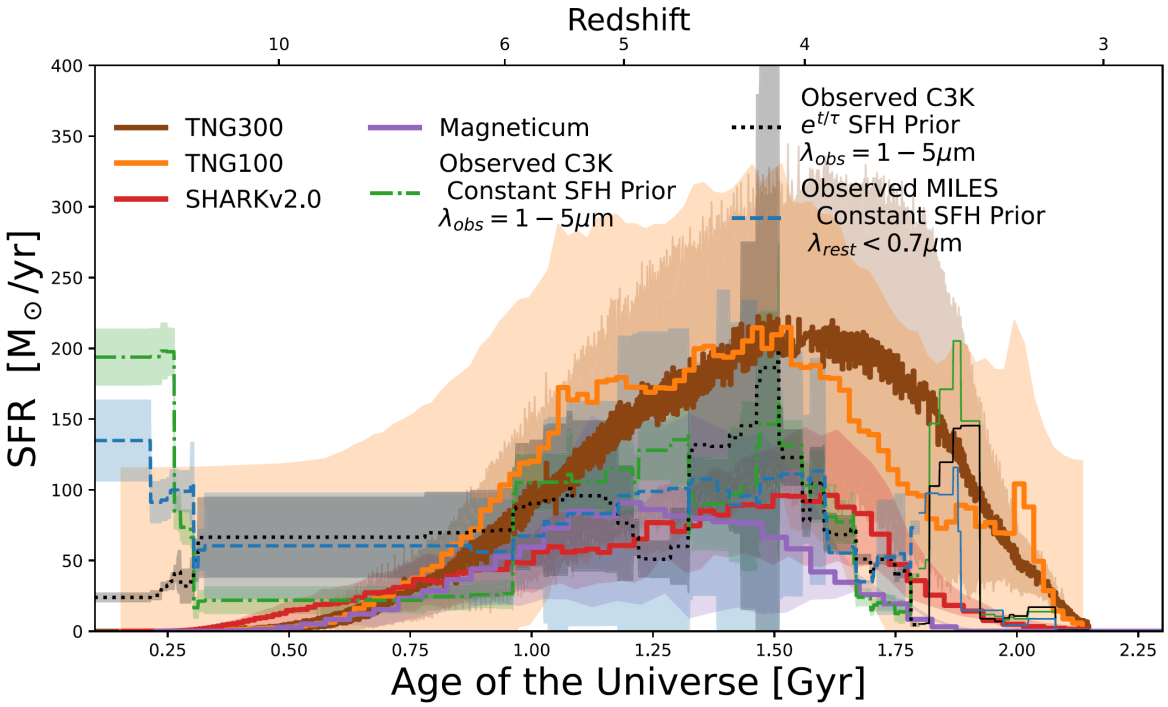


Figure 5.7. The left figure has been published as figure 17 by Nanayakkara et al. (2025), which shows the mean star formation history of quenched galaxies at $z \approx 3$ for the observed sample (black dotted, blue dashed and green dash-dotted lines) in addition to simulated galaxies drawn from a diverse set of hydrodynamical simulations and semi-analytical models (colored lines).

properties combined. This may be a result of the limited simulation box volume (Kimmig et al., 2025b), or requires an improvement to the implemented physics, as currently being run for the MagneticumDAWN suite of simulations (Remus et al., in prep.).

In Fig. 5.7 we show figure 17 by Nanayakkara et al. (2025), which plots the star formation histories of observed (dashed, dotted and dash-dotted lines) and simulated galaxies (colored lines). It is apparent that the fitted models for the observed galaxies all produce star formation histories which begin incredibly early, as well as steeply terminate between $t = 1.5$ Gyr and $t = 1.75$ Gyr. While the former is not captured by any of the theoretical models, there is a similarly steep decline found in the quenched galaxies from *Magneticum Pathfinder* Box3/uhr (Dolag et al., 2025; Kimmig et al., 2025b) and SHARKv2.0 (Lagos et al., 2024). This, similar to the findings by Forrest et al. (2025), provide further evidence for an earlier onset of star formation in the history than assumed prior.

5.3 Conclusion

This chapter has provided an overview of various follow-up works on high redshift galaxy formation that build on the foundations of the papers discussed in chapters 3 and 4. We began with an improved overview of the formation mechanism of early massive quenched galaxies in Sec. 5.1, and showed that more massive quenched galaxies tend to be older than less massive ones, a trend which is already in place as early as $z = 5$.

In Sec. 5.2, we placed our theoretical predictions into the context of three observational studies of high redshift galaxies where we contributed both simulation data and discussions of their results. First, Merlin et al. (2025) compiled a large set of observations from $3 \leq z \leq 5$ to determine the ages of quenched galaxies. Matching our simulations, they find consistently younger ages for lower mass quenched galaxies than for older ones. This necessarily implies that a majority of these galaxies rejuvenate, in agreement with our theoretical predictions (Remus & Kimmig, 2025), as otherwise the stellar populations of these galaxies would grow older going from $z = 5$ to $z = 3$, and would thus increase the number of older lower mass quenched systems toward lower redshifts.

In Subsec. 5.2.2 we then discussed the observation by Forrest et al. (2025) of the first observed galaxy with a stellar body that is kinematically slowly rotating at $z \geq 3$. This result is particularly exciting given that our simulation predicts the emergence of such systems as early as $z \approx 5$ (Kimmig et al., 2025b), and opens the door for future spatially resolved studies of high redshift galaxies. It remains an open question whether these earliest forming slow rotators form via the typical pathway of multiple dry mergers (Jesseit et al., 2009), which would require the unique circumstance of two quiescent systems merging within the first billion years of the Universe, or whether they instead form through a different type of more isotropic collapse (Naab et al., 2014), reminiscent of the formation pathway for the fully quenched galaxies that we identified in our simulations (Kimmig et al., 2025b).

Remaining on the topic of quenched galaxy formation pathways, we presented in Subsec. 5.2.3 the great diversity found both in the observations by Nanayakkara et al. (2025) as well as within our simulations. Although the majority of these galaxies form and quench rapidly on the timescale of 100 Myr (Kimmig et al., 2025b), there exist outliers with a more extended formation, such as those red and dead galaxies found by Merlin et al. (2025). It

will be interesting in future work to distinguish these types of galaxies not only in their star formation history, but also through their stellar chemical abundances, an idea that we discuss in a more general context in chapters 9 and 10.

Wenn eine solche Welt von Fixsternen [wie die Milchstraße] in einem so unermesslichen Abstand ... angeschaut wird, so wird dieselbe unter einem kleinen Winkel als ein mit schwachem Lichte erleuchtetes Räumchen erscheinen, dessen Figur zirkelrund sein wird, wenn seine Fläche sich dem Auge gerade zu darbietet, und elliptisch, wenn es von der Seite gesehen wird.

Immanuel Kant, *Allgemeine Naturgeschichte und Theorie des Himmels, erster Theil*, 1755

6

The Emergence of Massive Disks at Cosmic Dawn

This section summarizes ongoing analyses on simulated high redshift disk galaxies, which complement the work presented in Chap. 3 and Chap. 4.

6.1 Introduction

With the wealth of data from the James Webb Space Telescope, the formation of the first massive galaxies has been pushed to ever higher redshifts. A great deal of work has been focused on the emergence of such galaxies which have already ceased their star formation by the time of observation, so-called quiescent galaxies (Carnall et al., 2023a; Valentino et al., 2023; Long et al., 2023; Nanayakkara et al., 2025; Baker et al., 2025b). These galaxies challenge our theoretical models (Weller et al., 2025), as they require both a rapid progression as well as shutdown of their star formation. There is by now extensive work showing that various theoretical models are well able to reproduce key characteristics of the quiescent population (e.g., De Lucia et al., 2024; Lagos et al., 2024; Kimmig et al., 2025b; Chandro-Gómez et al., 2025). Beyond quiescent galaxies has emerged another notable set of observations, which is the presence of massive disk galaxies already by $z \geq 3$ (e.g., Jain & Wadadekar, 2025; Rowland et al., 2024; Umehata et al., 2025b; Shapley et al., 2025; Wang et al., 2025; Xiao et al., 2025).

At high redshifts, the morphology of observed galaxies does not appear to necessarily correlate with the star formation properties. For example, using JWST and COSMOS-Web

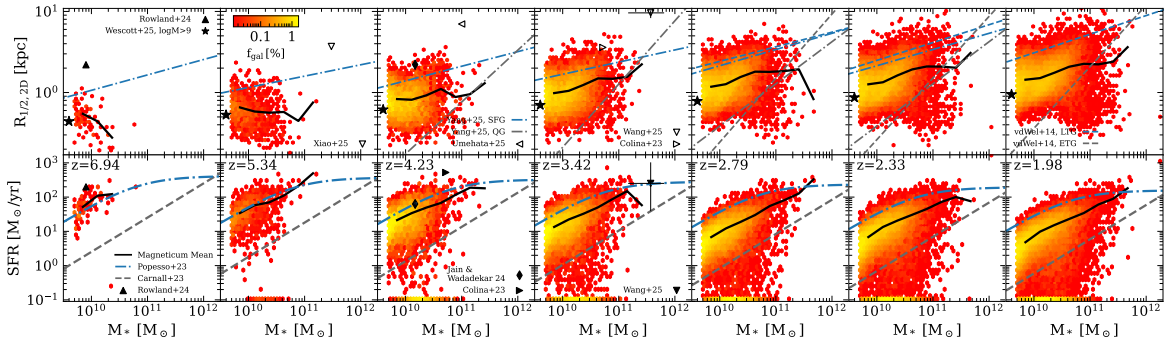


Figure 6.1. The stellar mass-size (*top row*) and star forming main sequence (*bottom row*) from $z = 7$ to $z = 2$ (*left to right*) for galaxies from the *Magneticum Pathfinder* Box3/uhr simulation (histogram, with median lines in black), as well as observations of individual disk galaxies (Colina et al., 2023; Rowland et al., 2024; Xiao et al., 2025; Wang et al., 2025; Umehata et al., 2025b; Jain & Wadadekar, 2025) and relations (van der Wel et al., 2014; Popesso et al., 2023; Carnall et al., 2023a; Westcott et al., 2025; Yang et al., 2025).

data, Huertas-Company et al. (2024) and Huertas-Company et al. (2025) report a large fraction of the disk galaxies to be red and quiescent, and a significant amount of the spheroidal galaxies to be blue and star forming. This is in agreement with observations at cosmic noon, where star formation in massive galaxies is reported to be centered on the cores of those galaxies, causing them to be more compact than expected (e.g., Tadaki et al., 2017).

We employ here the *Magneticum Pathfinder* Box3/uhr cosmological simulation (Dolag et al., 2025) to explore massive disk galaxies in the context of their environments in Subsec. 6.2, discuss the impact of the chosen waveband when determining their sizes in Subsec. 6.2, and finish with the example of a particularly large disk galaxy in Subsec. 6.4.

6.2 When Do Disks Emerge

We first explore the population of galaxies from $z = 7$ to $z = 2$ in Fig. 6.1, plotting the stellar half-mass size (top row) and star formation rate (SFR, bottom row) against the stellar mass. The distribution of simulated galaxies is shown with a 2D histogram, with the mean size and SFR plotted as thick black lines. We include various observations of disk galaxies (Colina et al., 2023; Rowland et al., 2024; Xiao et al., 2025; Wang et al., 2025; Umehata et al., 2025b; Jain & Wadadekar, 2025), as well as fits to the observed mass-size relation (van der Wel et al., 2014; Westcott et al., 2025; Yang et al., 2025), the star forming main sequence (Popesso et al., 2023), as well as the cutoff criterion for quiescent galaxies by Carnall et al. (2023a).

The simulated galaxies overall well reproduce the observations, with increasing sizes and lower star formation rates for a given stellar mass toward lower redshifts. The first quiescent galaxy appears already at $z = 7$ with $M_* \approx 2\times10^{10} M_\odot$, while at the same redshift starbursting galaxies can reach SFR $\approx 300 M_\odot$/yr. We find that the largest disks at each redshift can be somewhat larger than our simulated galaxies, although there may be an impact from using

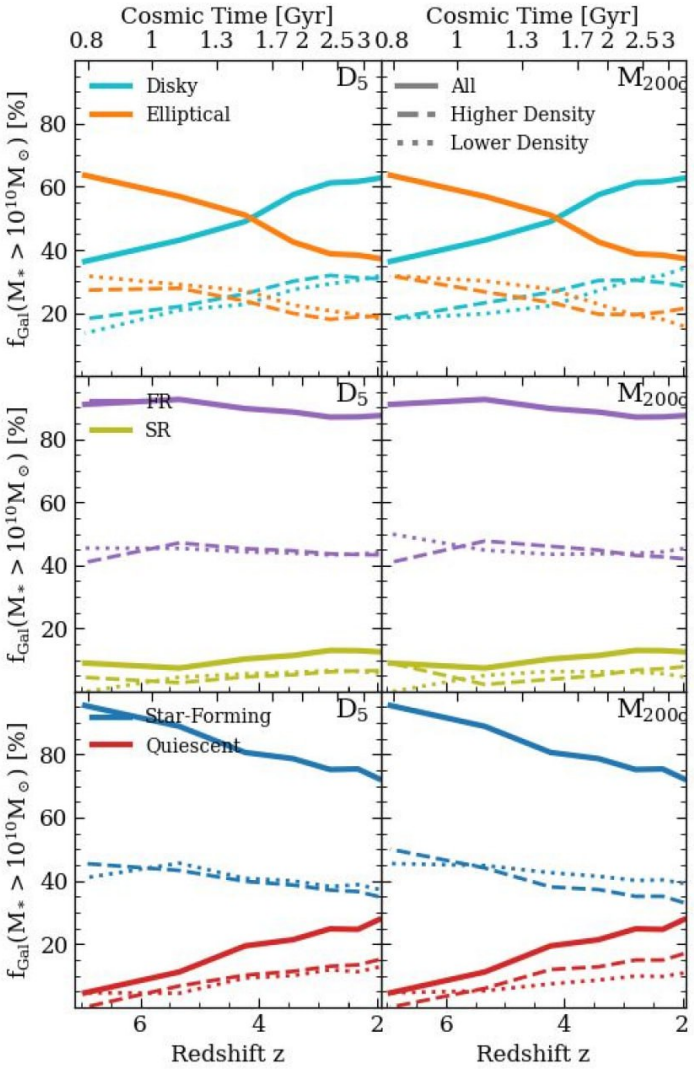


Figure 6.2. The evolution of massive galaxies ($M_* \geq 1 \times 10^{10} M_\odot$) for simulated galaxies split by their morphology (*top row*), kinematic rotation (*middle row*) and star formation (*bottom row*). We further distinguish galaxies by their environments (line styles), employing as environmental tracers the distance to the nearest five galaxies with the same mass cut D_5 (*left column*) and the halo mass M_{200c} (*right column*).

light-weighted radii and Sersic (1968) fits to the profiles to determine the radii, while we plot here the projected stellar half-mass radius.

In Fig. 6.2 we then consider the evolution of the split in galaxy types for galaxies with $M_* \geq 1 \times 10^{10} M_\odot$ at high redshifts. Beginning with the top row, we see that the earliest forming galaxies are predominantly morphologically elliptical, with b-values $\leq$ (Teklu et al., 2015). Unexpectedly, morphological disks appear to form later, likely because the require gas with larger angular momentum to infall while the earliest galaxy formation is more isotropic.

The second row of Fig. 6.2 shows the fraction of fast and slow rotators defined using the split by Emsellem et al. (2007), where at early times fast rotators are the great majority of all galaxies. However, there are slow rotators already at $z = 7$, which are entirely within the most massive halos (see the right column), but show no split in clustering D_5. Finally, we

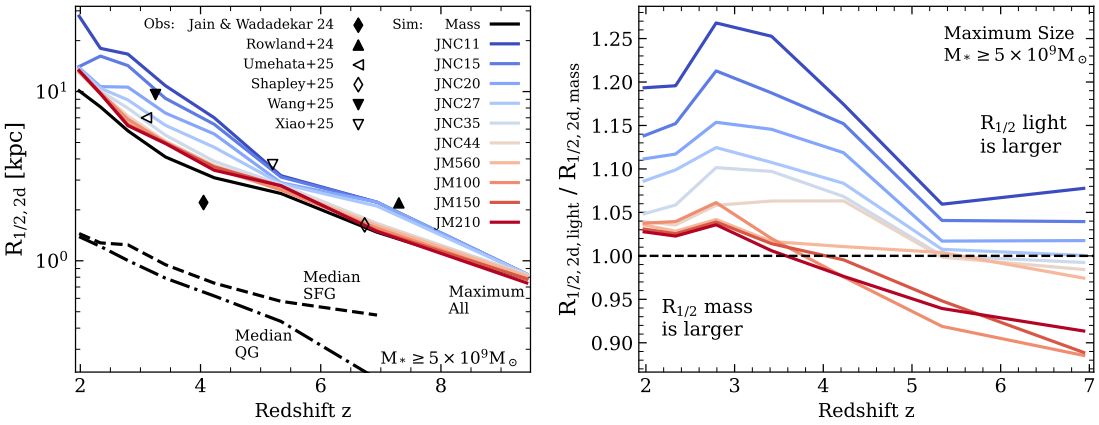


Figure 6.3. *Left:* The maximum stellar half mass (solid black line) and half light radii (colored lines) for galaxies with $M_* \geq 5 \times 10^9 M_\odot$ for our simulated galaxies, as compared to observed massive disks (black markers). We further plot the median half mass radius of star forming and quiescent galaxies as black dashed and dash-dotted lines. *Right:* The ratio of the maximum half light to maximum half mass radius, with the horizontal black dashed lines showing equality.

plot the split by star formation rate, using the criterion by Carnall et al. (2023a), and find that the fraction of quiescent galaxies is increasing with time.

6.3 The Impact of the Observed Wavebands

Having seen the difference in the mass size, it is worthwhile to consider the impact of determining mass-weighted versus light-weighted radii. We calculate projected light-weighted radii for all galaxies with $M_* \geq 5 \times 10^9 M_\odot$ for JWST bands ranging from NIRCam F115W to MIRI F2100W and plot the resulting maximum sizes (colored lines) in the left panel of Fig. 6.3. We find that light-weighted radii, aside from the longest wavelength band at the highest redshift, on average result in larger maximum sizes. This is likely driven by younger stellar populations in the stellar disks farther out, indicating inside-out growth, as is also found from observations at high redshifts (Baker et al., 2025a) and for simulations at lower redshifts (Teklu et al., 2023). We plot the ratio of the maximum light-weighted to mass-weighted radii in the right panel of Fig. 6.3 for a clearer visualization.

Observations of disks at high redshifts are plotted as points in the left panel of Fig. 6.3. We find that particularly large galaxies like those observed by Wang et al. (2025) and Rowland et al. (2024) are rare, but are not impossible to be found within cosmological simulations. We further split our sample into star forming and quiescent galaxies, with the former defined here by a star formation rate within 0.3 dex of the star forming main sequence by Popesso et al. (2023) while for the latter we use the criterion by Carnall et al. (2023a), and find that at all redshifts quiescent galaxies are more compact. However, their median radii are not as strongly different as expected from lower redshifts (van der Wel et al., 2014), in agreement with the larger amount of red and quiescent disks (e.g., Jones et al., 2025) or star forming

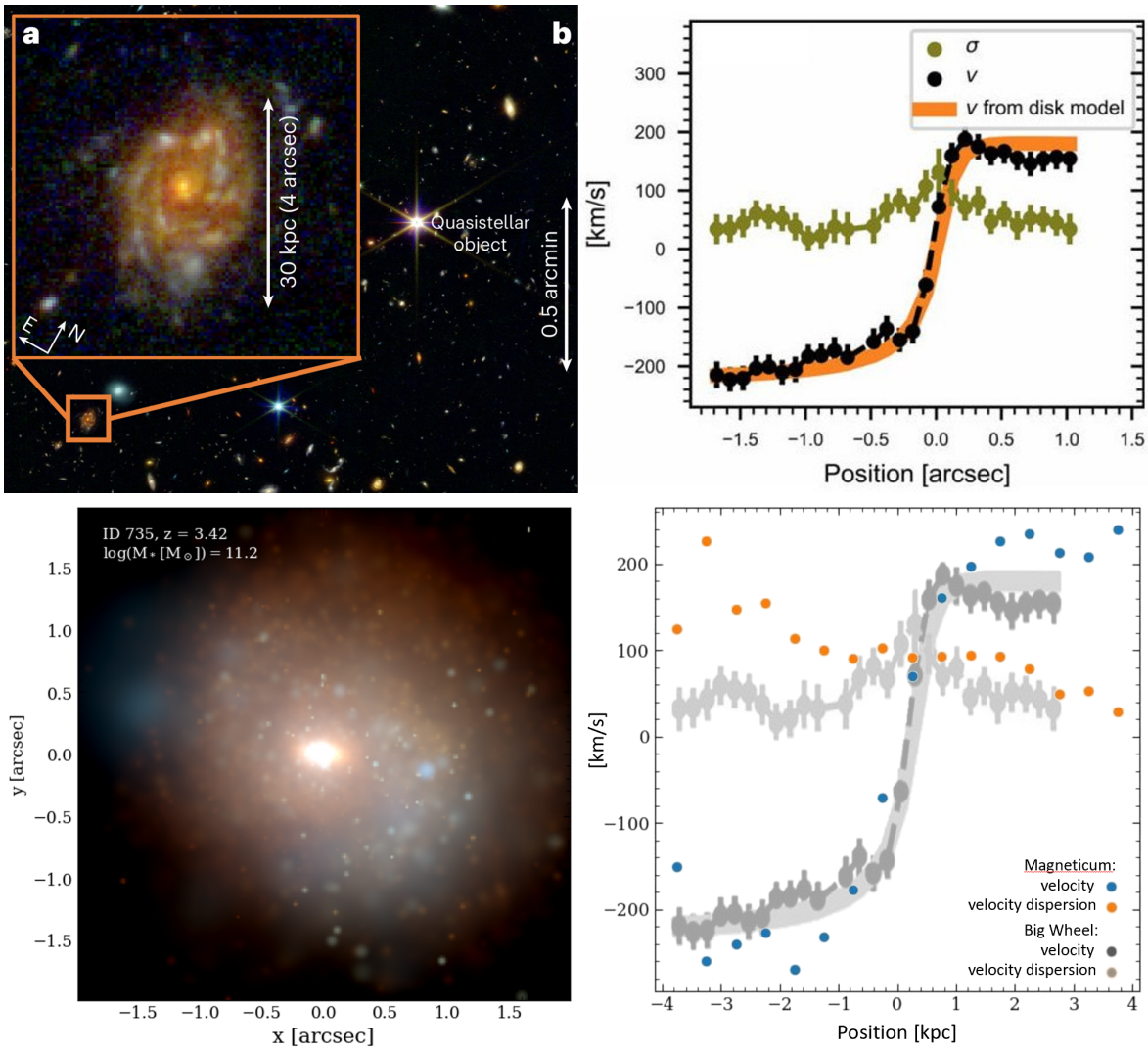


Figure 6.4. *Upper panels:* This is a compilation of the big wheel galaxy from figure 1 and extended data figure 2 from Wang et al. (2025). *Lower panels:* A simulated big wheel galaxy counterpart from the *Magneticum Pathfinder* Box3/uhr simulation.

spheroidals (e.g., Lee et al., 2025) seen in observations at these redshifts (Huertas-Company et al., 2024, 2025).

6.4 A Simulated Big Wheel Counterpart

Finally we turn to the so-called "Big Wheel" galaxy, a massive spiral observed at $z = 3.25$ by Wang et al. (2025) reaching $M_* = 3.7 \times 10^{11} M_\odot$ with size $r_{\mathrm{halflight}} = 9.6\,\mathrm{kpc}$. Interestingly, it is located within a large overdensity, matching our findings from Fig. 6.2 that disks appear frequently also in high density environments at high redshifts. Furthermore, their high resolution data allowed them to determine a rotation curve, which we show in the top right panel of Fig. 6.4.

We identify a disk galaxy of similar mass $M_* = 1.6 \times 10^{11} M_\odot$ at $z = 3.42$, which we plot in the lower left panel of Fig. 6.4. This disk is also large at $r_{\mathrm{halfmass}} = 2.3\,\mathrm{kpc}$, albeit a fair

bit less compared to their deduced radius. We plot its rotation curve in the lower right panel, finding remarkable agreement with the observed galaxy. It will be worthwhile in the future to consider extraordinary objects like these as testbeds of early galaxy formation physics, with this example perhaps indicating the need for more extended star formation (where younger stars farther out might be strongly enhancing the observed galaxy size as well).

6.5 Conclusion

We discussed the other side of the coin of early galaxy formation, namely the plethora of observations of massive disk galaxies that are now being found at $z \geq 3$ (e.g., Jain & Wadadekar, 2025; Rowland et al., 2024; Umehata et al., 2025b; Shapley et al., 2025; Wang et al., 2025; Xiao et al., 2025). We showed that comparable systems emerge at similar times within our simulations and highlighted that there is a surprising lack of an environmental dependence, whether splitting galaxies by their morphology, rotation, or star formation properties. These results indicate that typical low redshift correlations of galaxy formation, such as the morphology-density relation (Dressler, 1980; Postman & Geller, 1984), are not yet in place at $z \geq 3$. Finally, we discussed the particular observation of a massive disk by Wang et al. (2025), finding a simulated galaxy that matches the rotation curve and mass but is a fair bit more compact.

We conclude here the chapters 3, 4, 5, and 6, which focused on the formation and evolution of the earliest galaxies. The advent of the James Webb Space Telescope has revolutionized our view on galaxies, and it is in the combination of the extreme objects now being observed – quenched galaxies both old and massive or young and of lower mass, as well as disks already formed by $z = 3$ (Wang et al., 2025) that rival the super spirals seen today (Ogle et al., 2019b,a; Lisenfeld et al., 2023) – where we can hope to push our understanding of the underlying physical drivers in the early Universe.

First, it is allowed . . . by all modern Philosophers, that the Sun and Stars are all of the same or like Nature; consequently, that the Stars are all Suns, and that the Sun himself is a Star.

Thomas Wright, *An Original Theory or New Hypothesis of the Universe, 6th Letter*, 1750

7

The Dawn of Puffy Galaxies

This chapter summarizes the results published by Gannon, Kimmig, et al., 2025, OJAp 8, 150, for which I provided the complete simulation analysis.

7.1 Introduction

The advent of detailed observations of the high redshift Universe, in particular with the James Webb Space Telescope, has pushed the boundary of our understanding of structure formation (Oesch et al., 2018; Finkelstein et al., 2024). We have discussed the emergence of the first galaxies (Kimmig et al., 2025b) and their unexpected star formation behavior (Remus & Kimmig, 2025) with regards to lower redshift analogues in chapters 3 and 4, but there is another class of galaxies observed at $z = 0$ which have challenged models of galaxy formation: ultra diffuse galaxies (van Dokkum et al., 2015). In the case of "failed galaxy" types of UDGs (van Dokkum et al., 2015; Peng & Lim, 2016; Danieli et al., 2022; Forbes & Gannon, 2024), their progenitor galaxies are expected to undergo a rapid burst of star formation before immediately quenching at high redshifts (Forbes et al., 2020), and must do so in a manner that results in their puffy, diffuse stellar structure seen at $z = 0$ (Gannon et al., 2025).

As we also discuss (Gannon et al., 2025), indications for this scenario are 1) the enhanced number of globular clusters (GCs) in these UDGs, which imply a massive dark matter halo (Burkert & Forbes, 2020; Forbes et al., 2020), 2) stellar velocity dispersion measurements that match the halo mass expectations from GCs (van Dokkum et al., 2019; Gannon et al., 2023),

3) their star formation histories showing rapid quenching ≥ 8 Gyr ago (Ferré-Mateu et al., 2023), 4) an enhanced α-abundance in their stars supporting this quick formation (Ferré-Mateu et al., 2023; Kimmig et al., 2025b), and 5) their stellar mass-metallicity following higher redshift relations (Buzzo et al., 2022). This scenario is different from that of UDG formation from a "puffed up" dwarf, where the dark matter content is as expected for the stellar mass, but the stars are heated (e.g., tidal heating or stellar feedback, mergers) into a more diffuse distribution (Gannon et al., 2025).

The lack of these "failed galaxy" UDGs in cosmological simulations at $z = 0$ makes it worthwhile to identify whether at least their possible progenitors at higher redshifts can be found in the simulations, or whether the necessary properties based on the observations at $z = 0$ are already absent from simulated galaxies at $z = 2$. If plausible progenitors cannot be identified, this implies that their initial formation itself is missing in models of galaxy formation, while if the progenitors are present but the simulations lack $z = 0$ UDGs this instead implies that it is the evolution post-formation that is still not captured (Gannon et al., 2025). As such, we employed the Box3/uhr simulation from the *Magneticum Pathfinder* suite to identify candidate progenitors of "failed galaxy" UDGs at $z = 2$. We summarize here the results presented by Gannon et al. (2025), including our sample selection from the simulation and how UDG progenitor candidates differ from the global galaxy population already at $z = 2$ in Sec. 7.2, before discussing the results in context of this unique class of observed galaxies in Sec. 7.3.

7.2 The Descendants of Puffy Galaxies at $z = 0$

One of the hallmarks of "failed galaxy" UDGs is their large halo mass for their stellar mass. Given that they represent extreme outliers in this regard, it follows that any simulation wishing to match their progenitors must be sufficiently large in volume to include them. This need is further emphasized by their common presence within massive galaxy clusters (van Dokkum et al., 2015; Yagi et al., 2016). We thus use the *Magneticum Pathfinder* Box3/uhr simulation (see chapter 2 and Dolag et al., 2025), with volume of $(128\mathrm{Mpc}/h)^3$, and particle masses of $m_{\mathrm{dm}} = 3.6 \times 10^7 M_\odot/h$, $m_{\mathrm{gas}} = 7.3 \times 10^6 M_\odot/h$, and $m_* \approx 1/4^{\mathrm{th}} m_{\mathrm{gas}} \approx 1.8 \times 10^6 M_\odot/h$ for dark matter, gas, and stellar particles, respectively, with $h = 0.703$ the reduced Hubble parameter of the WMAP-7 cosmology (Komatsu et al., 2011). This is highly resolved enough to capture the UDG progenitors of $M_{200\mathrm{c}} \approx 10^{11} M_\odot$ with $\geq 10^3$ particles.

7.2.1 Sample Selection

Halos and subhalos are identified via the SUBFIND structure finder (Springel et al., 2001b; Dolag et al., 2009), from which we then select central galaxies at $z = 2$. We plot the stellar (left) and total baryonic (right) mass as a function of halo mass in Fig. 7.1. Crucially, we see that the scatter around the median stellar mass reaches over an order in magnitude. To compare the properties of potential UDG progenitors, we select three samples. Within a

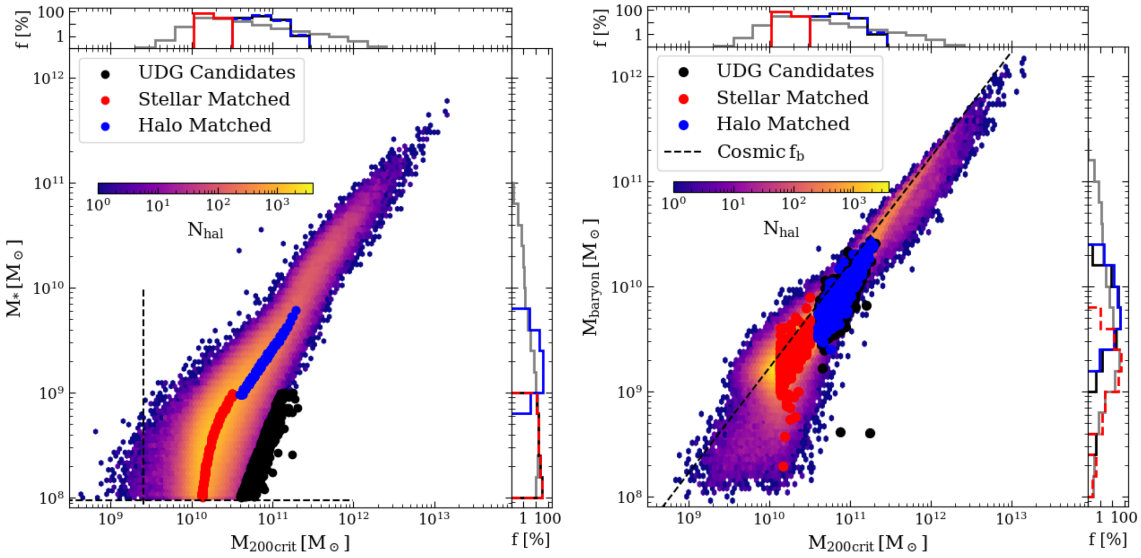


Figure 7.1. Figures 2 and 3 taken from Gannon et al. (2025), showing the stellar (*left*) and baryon (*right*) mass as a function of halo mass for all Box3/uhr galaxies at $z = 2$ (histogram), as well as the UDG candidates (black), stellar mass matched (red) and halo mass matched (blue) galaxies.

stellar mass range of $M_* = 10^8$ to $10^9 M_\odot$ we select the 443 galaxies with the highest halo masses for their given stellar mass as UDG candidates (black points), with a cutoff criterion of

$$\log_{10}(M_{200\mathrm{crit}}[M_\odot]) - 0.5 \cdot \log_{10}(M_*[M_\odot]) > 6.59. \tag{7.1}$$

By splitting these candidates into 15 equal bins in stellar or halo mass, we then identify in each bin an equal number of galaxies lying at the median halo or stellar mass for all galaxies in the simulation, respectively. The former, stellar mass matched sample is plotted in red, while the halo mass matched sample is in blue.

As we see from the right panel of Fig. 7.1, all three samples follow the same baryon mass to halo mass relation, even though the UDG candidates are significantly undermassive in terms of stellar mass. This means they these galaxies assembled the same amount of gas as others of their halo mass, but have converted about an order in magnitude less of that gas into stars – matching expectations from the observed UDGs (van Dokkum et al., 2019; Gannon et al., 2023). In addition, matching the UDG candidates into a lower resolution version of the Box3/uhr simulation that was run until $z = 0$, we find that about 5% end up in galaxy clusters ($M_{200c} \geq 10^{14} M_\odot$), where the observed "failed galaxy" UDGs are commonly found (Yagi et al., 2016; Gannon et al., 2025).

7.2.2 Dark and Bright Matter

With this sample of galaxies, we can now work toward understanding why the UDG progenitor candidates are comparatively inefficient at converting their gas. As a first indication, we plot in Fig. 7.2 the absolute (top row) and normalized (bottom row) density profiles of their total mass, dark matter, stars and gas (left to right). The UDG candidates by necessity match the

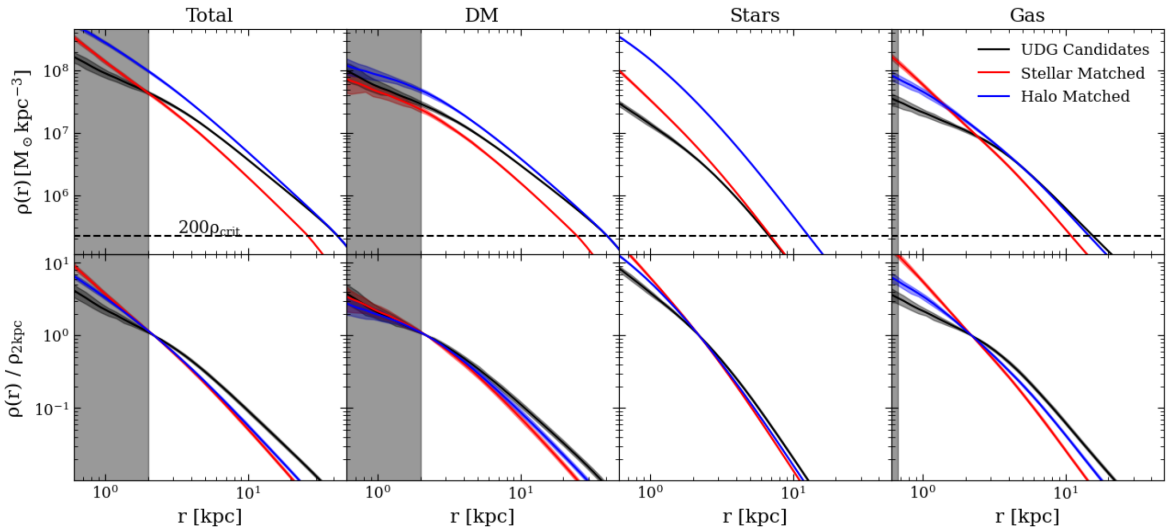


Figure 7.2. Figure 4 from Gannon et al. (2025), plotting the absolute (*top row*) and normalized (*bottom row*) density profiles of UDG candidate galaxies (black) and their stellar mass (red) and halo mass matched (blue) samples. The gray shaded areas show the softening lengths of each particles, while the colored regions around each profile are generated from boostrapping the sample's particles 100 times.

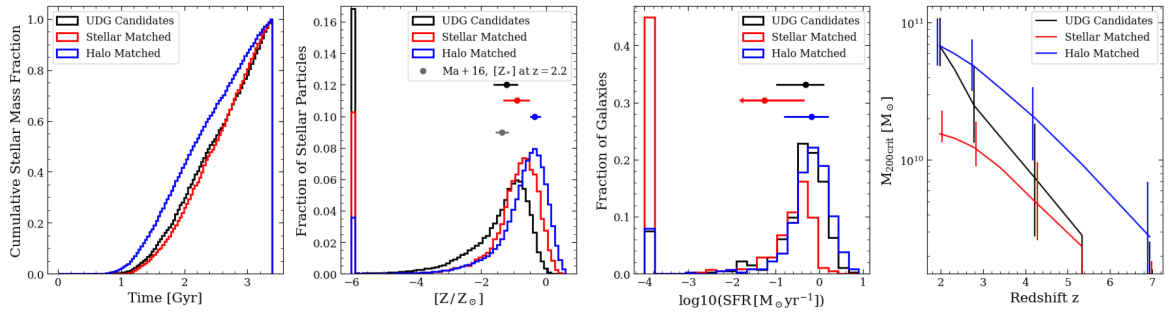


Figure 7.3. Figure 5 from Gannon et al. (2025) showing from *left* to *right* the cumulative star formation history, the distribution of stellar metallicity and gas particle star formation rates, and finally the halo mass assembly history.

outer density of the halo matched sample, but interestingly flatten significantly toward the center in total density, becoming even less dense than galaxies of the stellar mass matched sample which are around an order in magnitude less massive.

We find that while the central dark matter density matches that of the stellar matched sample, the baryons (both stars and gas) lie well below. This is surprising given that the stellar mass matched sample has, by definition, the same mass in stars as the UDG candidates, but the latter must have had a far more clumpy star formation history that resulted in a diffuse body of stars (matching density with the stellar matched sample only at $r \approx 10\,\mathrm{kpc}$). The picture remains the same for the gas, which is also significantly less dense at the center of the UDG candidate halos, as has also been seen in the UDGs from the NIHAO simulations (Di Cintio et al., 2017). This suppressed central density provides a first indication as to their inefficiency in forming stars.

In Fig. 7.3 we plot various galactic properties for the three samples. Beginning with the first panel, we find that the cumulative star formation history of the UDG candidates pretty

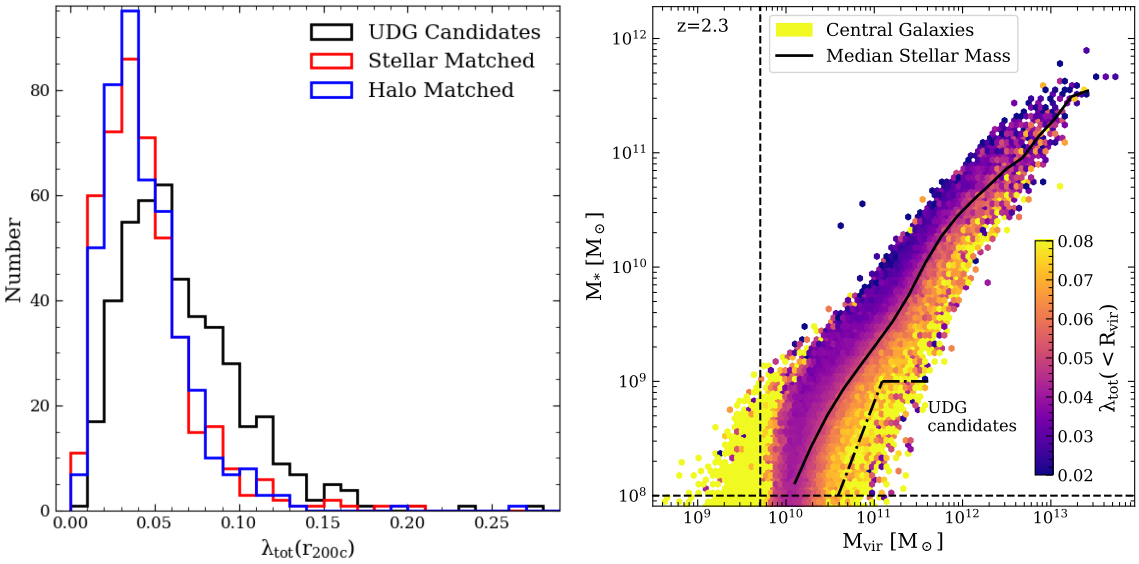


Figure 7.4. The left panel of this Figure is included as Figure 7 in the paper by Gannon et al. (2025), and shows the distribution in total halo spin (Bullock et al., 2001) of the halos in each sample. The right shows the stellar mass-halo mass relation colored by the total halo spin (note, at $z = 2.3$).

much exactly matches that of the stellar mass matched sample, meaning they have formed their stars in a similar manner up until $z = 2$. This later formation of their stars relative to the halo matched sample is mirrored in the right panel of Fig. 7.3, which shows the halo mass assembly. The UDG candidates are therefore not only forming stars later than their halo mass matched equivalents, but have also assembled their halo mass later – again matching expectations from other simulations (Rey et al., 2020).

We show in the second panel of Fig. 7.3 the distribution of stellar metallicity, and find the surprising result that even though the stellar formation history of the UDG candidates matches that of the stellar matched sample, their metallicities are lower. This means that the star formation must have been occurring at different sites spatially, so as to avoid enriching the star-forming gas, which is again indicative of the more clumpy star formation expected from Fig. 7.2. It also matches the low stellar metallicites found in the $z = 0$ observed UDGs (Buzzo et al., 2022; Ferré-Mateu et al., 2023).

Finally, we plot the star formation rates in the third panel of Fig. 7.3, finding that the UDG candidates match those of the halo matched sample. This star burst reaches SFRs comparable to those expected from the fitted star formation histories of observed UDGs (Ferré-Mateu et al., 2023), and may be what drives the formation of the high GC numbers in "failed galaxy" UDGs (Pfeffer et al., 2024; Valenzuela et al., 2025; Gannon et al., 2025).

7.2.3 Angular Momentum Distribution

We then explored the angular momentum of these halos to understand why they may be showing this delayed formation of stars, and lower central densities. In Fig. 7.4 we show the histogram of total halo spin calculated following Bullock et al. (2001) within $R \leq R_{200c}$ as plotted by Gannon et al. (2025). It is apparent that the UDG candidates have significantly

higher angular momentum in their halos, which may be preventing the matter from collapsing into the center and reaching the high densities (and thus more stars formed) seen for the galaxies of the halo matched sample. In the right panel of Fig. 7.4 we additionally plot the full stellar mass-halo mass relation colored by the total halo spin for central galaxies one snapshot prior at $z = 2.3$, where it should be noted that this calculation is done within $R_{\rm vir}$ although these radii are only about 2% different. We find a striking dependence of the stellar mass at a given halo mass on the total halo spin, with a higher spin resulting in a lower stellar mass. This is likely because the higher spin prevents the gas from reaching the center to form stars, matching the findings by Kimmig et al. (2025b) for high redshift massive galaxies, where those that formed most rapidly had the lowest halo spin.

7.3 Discussion and Conclusion

We have presented here an abridged version of the results by Gannon et al. (2025), which drew on the power of the large volume *Magneticum Pathfinder* Box3/uhr simulation to identify plausible progenitors of an elusive class of ultra diffuse galaxies – so-called "failed galaxies" (van Dokkum et al., 2015; Peng & Lim, 2016; Danieli et al., 2022; Forbes & Gannon, 2024). By considering three samples of galaxies at $z = 2$, namely the "failed galaxy" candidates as well as two control samples following the mean of the stellar mass-halo mass relation and matching either the candidates' stellar or halo mass, we determined how these progenitors differ from typical galaxies. We determine that the "failed galaxy" progenitors

- follow the baryonic mass-halo mass relation,
- possess more cored density profiles than both control samples,
- have star formation histories similar to those of the lower halo mass sample,
- have particularly low stellar metallicites, indicative of unusually clumpy star formation,
- assembled their halo mass particularly late, and
- lie at the upper tail of the halo spin distribution.

These findings together provide a plausible picture for the formation of a "failed galaxy" ultra diffuse galaxy. In this view, their progenitors are particularly late assembling halos, where stars are formed in a clumpy manner already in smaller substructures prior to merging together. These substructures arrive with high angular momentum, resulting in a high halo spin and more cored central density profiles. It is at this point that our simulations eventually cool the gas to the point of forming stars similar to a normal galaxy, where there may be processes missing from the simulations to prevent them from doing so. At any rate, it appears clear that halos of low spin, with their more cored density profiles that allow for stellar feedback to be more effective, present an interesting case for being the progenitors of present day "failed galaxy" ultra diffuse galaxies.

Περισκοπεῖν ἄστρων δρόμους ὥσπερ συμπεριθέοντα καὶ τὰς τῶν στοιχείων εἰς ἄλληλα μεταβολὰς συνεχῶς ἐννοεῖν: ἀποκαθαίρουσι γὰρ αἱ τούτων φαντασίαι τὸν ῥύπον τοῦ χαμαὶ βίου.

Marcus Aurelius, *Meditationes*, circa 161–180

8

The Evolution of Star Forming Main Sequence Galaxies

This chapter is to be submitted to ApJ as Kimmig et al., 2026.

The star forming main sequence of galaxies has now been observed out to redshifts of $z = 6$ and beyond. However, it remains unclear if it represents a true evolutionary sequence or an ensemble relation of individual histories. We construct an analytical model to evolve galaxy properties along the star forming main sequence through time and determine the resulting star formation histories. Our model galaxies reproduce observations of star formation histories and mean stellar ages as a function of current day stellar mass remarkably well, with older and more peaked histories arising naturally for more massive galaxies. Simultaneously, we demonstrate that low-mass ($M_* \approx 10^8 M_\odot$) early ($z > 3$) progenitors that remain on the star forming main sequence must evolve into massive ($M_* > 10^{11} M_\odot$) galaxies today, placing stringent constraints of either suppressed star formation rates (0.3 dex below the star forming main sequence) or late formation ($z < 2$) on the progenitors of less massive galaxies of $M_* = 10^{11} M_\odot$ today. We provide finding charts to connect galaxies from $z = 6$ to $z = 0$ by their star forming behavior above or below the main sequence. By applying number density arguments to construct updated evolutionary histories for Milky Way-mass galaxies, we find that they must on average undergo a significant phase of suppressed star formation, nearing quiescence. This is particularly true for the Milky Way itself, where we show that the presence of a large amount of old stars directly implies a departure from the star forming main sequence over the majority of its history.

8.1 Introduction

Galaxies over all ranges of masses are known to grow either by forming stars themselves, i.e. in-situ, or through mergers with another galaxy (e.g., Oser et al., 2010; Remus & Forbes, 2022). Those galaxies which are actively forming stars are found to do so in a manner that establishes a relation between their star formation rates and their current stellar masses, resulting in the so-called star formation main sequence (SFMS) of galaxies. This star formation main sequence can be observed at redshifts as high as $z = 6$ and down to $z = 0$, with the relation evolving with decreasing redshift toward lower star formation rates at a given stellar mass (e.g., Speagle et al., 2014; Pearson et al., 2018; Leslie et al., 2020; Popesso et al., 2023). However, while this behavior of the relation is consistently observed, the normalization and slopes of the relation deviate between observational campaigns (e.g., Popesso et al., 2023; Fortuné et al., 2025), and precisely which physical processes dominate in establishing this correlation are still debated to date.

Disk galaxies are known to populate the star formation main sequence over a large range of stellar masses at $z = 0$, from galaxies as small as M33 and NGC 300 with about $M_* \approx 1 \times 10^9 M_\odot$ (e.g., Argudo-Fernández et al., 2025, for galaxies in the local volume) to the most massive disk galaxies in the present-day Universe, the Super Spirals with masses that can even reach $M_* \approx 1 \times 10^{12} M_\odot$ (Di Teodoro et al., 2021; Ogle et al., 2019b). The scatter of the main sequences given in the literature usually amounts to about 0.3 dex (Noeske et al., 2007; Whitaker et al., 2012; Speagle et al., 2014; Pearson et al., 2018). Deviations of the star formation main sequence towards higher star formation rates are usually correlated to (gas-rich) merger events (e.g., Genzel et al., 2010; Gómez-Guijarro et al., 2022), while deviations towards lower star formation rates are thought to be indicative of ongoing quenching either through mergers (e.g., Ellison et al., 2022) or other mechanisms like starvation due to halo mass quenching (e.g., Birnboim & Dekel, 2003; Dekel & Birnboim, 2008) or feedback from stars and black holes (e.g. Kimmig et al., 2025b).

The question remains whether the SFMS is an ensemble relation (i.e., results from galaxies moving in and out of the relation but with enough statistically present at all times to define its presence) or represents a true evolutionary pathway (i.e., galaxies evolve steadily along this main sequence until their star formation is quenched). In the latter case, the main sequence could indicate the balance between the average amount of gas accreted onto a galaxy of a given mass and the star formation that is fueled by this gas. This accretion rate decreases with decreasing redshift (e.g. Seidel et al., 2025), explaining the decline on the SFMS with redshift. In addition, the amount of angular momentum in the galaxy disks impacts the radial distribution of star formation in a galaxy, with star formation at larger radii being less efficient due to the relatively lower gas densities (e.g., Noeske et al., 2007; Teklu et al., 2023). An evolution along the main sequence for a given galaxy would then equate to a continuous accretion of gas from the cosmic web that is balanced by continuous star formation in the galaxy, a model commonly referred to as the "bathtub model" (e.g., Bouché et al., 2010; Lilly et al., 2013; Burkert, 2017). In this simple picture, the galaxy grows continuously through



in-situ star formation in this equilibrium state until its star formation is terminated through, for example, a merger event.

However, recent results from simulations have started to report a different, more complicated picture, in which galaxies do not live continuously on the main sequence but rather are moving on and off in a cycle of quenching and rejuvenation (Fortuné et al., 2025). In this case, feedback from within the galaxy can quench the star formation for a short time period before accretion from the cosmic web or merging can then reignite the star formation, even back onto the main sequence (Remus & Kimmig, 2025). In fact, Fortuné et al. (2025) find that such cycles are rather common events for more than half of the galaxies at $z = 0$ with stellar masses above $10^{10} M_{\odot}$, with some galaxies running through 6 such cycles in their evolution. Interestingly, despite being difficult to measure, observations are also finding indications of such on-off episodes of star formation. For example, Muñoz López et al. (2025) find multiple star formation cycles for about 85% of a set of 393 galaxies from CANDELS/GOOD-S and CANDELS/COSMOS. Similarly, Trussler et al. (2025) find indications for such on-off cycles in galaxies at high redshifts before cosmic noon. Previously, Chauke et al. (2019) had already reported rejuvenation indications in the galaxies from the Lega-C survey at $z \approx 0.8$.

Answering whether there exists a preferred star formation history for galaxies of a given mass, or if there are various star formation cycles, would require accurate measurements of the exact distribution in stellar ages, which are notoriously difficult to measure. Instead, when working on the average stellar age of galaxies, Mattolini et al. (2025) report a positive correlation with the stellar mass of SDSS galaxies, especially for $\mathrm{M}_{*} > 10^{10}\mathrm{M}_{\odot}$. A similar trend was already reported for early-type galaxies for example by Thomas et al. (2010) and McDermid et al. (2015), with average ages older than 10 Gyrs for early-type galaxies with more than $\mathrm{M}_{*} > 10^{11}\mathrm{M}_{\odot}$.

Resolved stellar population ages can, as of yet, only be obtained for galaxies close to our own Milky Way galaxy, and best for the Milky Way itself. Haywood et al. (2016) found, based on APOGEE data, that our own Milky Way has formed a significant amount of its stellar mass already prior to $z = 2$, and had a rather low star formation rate ever since, with a dip in star formation between $z = 1 - 2$ indicative of even a period of quenching. This change in star formation behavior coincides with the age-dating of the last major merger event of our Milky Way galaxy, Gaia Enceladus, as reported by Helmi et al. (2018) and Belokurov et al. (2018). Additional evidence for such an evolutionary scenario was reported based on O-stars by Xiang & Rix (2022) as well. However, with only a small sample of galaxies close enough for detailed measurements of stellar ages and thus star formation histories, it is unclear if such an on-off growth scenario is actually common for galaxies of Milky Way mass, or if this is a rather special case.

Under the assumption that Milky Way-mass galaxies underwent coherent assembly histories, such that the number density of their progenitors through cosmic time should be conserved, van Dokkum et al. (2013) and Papovich et al. (2015) determined the resulting stellar mass growth history. They predict that Milky Way-mass galaxies should have had masses of $M_{*} > 10^{9} M_{\odot}$ already at $z \approx 3$, somewhat below the results by Haywood et al.

(2016), with even larger masses at high redshift for Andromeda galaxy mass counterparts. It is as of yet unclear if these massive progenitors, such as the barred galaxy CEERS-2112 at $z \approx 3$ with a stellar mass larger than $M_* > 10^9 M_\odot$ observed by Costantin et al. (2023), could have evolved along the SFMS to become galaxies like the Milky Way today, or if they would have necessarily grown more massive.

As the number of massive disks at high redshifts of $z > 2$ steadily increases, the question of their possible present-day descendants only grows in importance. Beyond CEERS-2112, Rowland et al. (2024) for example report REBELS-25, a dynamically cold disk at $z = 7.3$ with $M_* \approx 8 \times 10^9 M_\odot$, while Wang et al. (2025) and Umehata et al. (2025a) reported two different massive disks at $z \approx 3$ with $M_* > 10^{11} M_\odot$. Even more extreme, Xiao et al. (2025) find a star forming disk galaxy at $z = 5.2$ from the JWST-Panoramic survey with $M_* = 2 \times 10^{11} M_\odot$. These galaxies are so massive already at high redshifts that they could be potential progenitors to the super spiral galaxies reported today.

In this study we address how the formation pathways, average stellar age distributions, and final stellar masses of galaxies look like if they evolved entirely on the main sequence throughout their life, based on a model we developed. We introduce the model in Sec. 8.2, and present the resulting properties of main sequence galaxies in Sec. 8.3.1. In Sec. 8.3.2, we discuss how to connect galaxies through cosmic time, including finding charts for present-day stellar masses expected for different stellar masses observed at $z = 6, 5, 4, 3, 2, 1$ in Fig. 8.4 and the appendix Fig. B.2. In Sec. 8.3.3, we apply our model to the Milky Way and discuss the resulting implications. Finally, we conclude the paper with a discussion in Sec. 8.4.

8.2 The Model

To evolve the stellar masses and star formation rates of model galaxies there are four important criteria to consider:

1. The chosen star forming main sequence (SFMS).
2. The chosen initial mass function (IMF).
3. The timestep size of the iteration δt.
4. The initial progenitor galaxy properties.

For our SFMS we select the one given by Popesso et al. (2023) due to their range in redshift ($0 < z < 6$), stellar mass ($M_* = 10^{8.5}$ to $10^{11.5} M_\odot$) and SFR (0.01 to $500 M_\odot \mathrm{yr}^{-1}$). In addition, they fit the functional form of their SFR dependent on both the stellar mass and, crucially, the cosmic time directly. This is necessary to smoothly integrate our model galaxies along the SFMS as opposed to redshift bins with discontinuous jumps in SFR. Specifically then, we chose the turnover mass parametrization by Popesso et al. (2023), where

$$\log \mathrm{SFR}_{\mathrm{SFMS}}(M_*, t) = (a_0 + a_1 t) - \log\left(1 + \left(\frac{M_*}{10^{a_2 + a_3 t}}\right)^{-1}\right) \tag{8.1}$$

with $a_0 = 2.71$, $a_1 = -0.186$, $a_2 = 10.86$ and $a_3 = -0.0729$ (their Eq. 14). The term $10^{a_2+a_3 t}$ works as a turnover mass $\mathrm{M_T}(t)$, above which the SFMS flattens, while $10^{a_0+a_1 t}$ is the maximum $\mathrm{SFR_{max}}(t)$ reached for $\mathrm{M_*} \to \infty$. This can be seen directly when re-writing Eq. 8.1 as:

$$\mathrm{SFR_{SFMS}}(\mathrm{M_*}, t) = \frac{\mathrm{SFR_{max}}(t)}{1 + M_\mathrm{T}(t)/M_*}. \tag{8.2}$$

For our IMF we use a Chabrier (2003) mass function, which dictates the fraction and timescale of the formed stellar mass that is lost to winds and supernovae. In particular, we use the parametrization of the fraction of stellar mass loss as a function of time given by Leitner & Kravtsov (2011),

$$f_\mathrm{ml}(t) = C_0 \cdot \ln(t/\lambda + 1), \tag{8.3}$$

with $C_0 = 0.046$ and $\lambda = 2.76 \times 10^5$ yr. As only the high-mass slope really alters the loss rate (Leitner & Kravtsov, 2011), our findings hold true for IMFs with similar slopes in that regime such as the Kroupa (2001) IMF. Conversely, a Salpeter (1955) IMF would result in a significantly lower stellar mass loss rate, which would consequently accelerate the evolution of our model galaxies toward higher stellar masses. Our model stellar masses can thus be understood as lower limits for IMFs with steeper high-mass slopes.

The timestep size refers here to how often the stellar mass and SFR of our model galaxies are updated, where we choose $\delta t = 100\,\mathrm{Myr}$. We have tested values from $\delta t = 5\,\mathrm{Myr}$ to 1 Gyr, and find that the results converge within 5% for $\delta t < 200\,\mathrm{Myr}$ when the galaxy remains at a fixed logarithmic separation to the star forming main sequence through cosmic time (i.e., $\log \mathrm{SFR}(\mathrm{M_*}, t) = \log \mathrm{SFR_{SFMS}}(\mathrm{M_*}, t) + \Delta_\mathrm{SFMS}$, with Δ_SFMS fixed). Differences between the shorter timesteps become more pronounced (though remain at $< 15\%$) when allowing for a lognormal random scatter around the SFMS (i.e., $\Delta_\mathrm{SFMS} = \Delta_\mathrm{SFMS}(t)$), which we discuss in more detail in the appendix B.1. As we mostly assume a consistent separation from the SFMS throughout this work we chose $\delta t = 100\,\mathrm{Myr}$, which is also the age of the stellar populations that contribute 90% of the emission to most SFR tracers except Hα (Kennicutt & Evans, 2012).

Finally, the progenitor galaxy of stellar mass M_1 at cosmic time t_1 (or equivalently redshift z_1) should itself be attributed an age, so that it also experiences mass loss with time, as opposed to having a "static" core of mass M_1. This choice of age is a priori arbitrary, with the only requirement being that the original mass M_0 seeded at time $t_0 \leq t_1$ results in the "observed" mass M_1 at t_1, i.e., $M_1 = M_0 \cdot [1 - f_\mathrm{ml}(t_1 - t_0)]$. For example, if $t_0 = t_1$ then $M_0 = M_1$ as $f_\mathrm{ml}(0) = 0$. We chose $t_0 = 917\,\mathrm{Myr}$ for all progenitors, equivalent to $z_0 = 6$ in the 0.3/0.7 cosmology. To mitigate the impact of the unavoidable discontinuity in the star formation history at whichever chosen z_0, we set our progenitor stellar masses low at $\mathrm{M_*}(t = t_1) = M_1 = 1 \times 10^8 \mathrm{M_\odot}$. This is low enough to be just 1% of the final mass for galaxies with $\mathrm{M_*} > 1 \times 10^{10} \mathrm{M_\odot}$, while remaining near the $\mathrm{M_*} \approx 3 \times 10^8 \mathrm{M_\odot}$ lower bound of the SFMS fit by Popesso et al. (2023).

Our final algorithm then looks as follows:

1. Input the progenitor stellar mass of M_1 at time t_1 and determine its age relative to $z = 6$.

2. Iteration from timestep $n = 1$ to $n = N$:
   - Apply mass loss to stellar mass bins m_i from $i = 1$ to $i = n$ according to $f_{\rm ml}(t_n - t_i)$
   - Determine total current mass $M_n = \sum_{i=1}^{n} m_i$ and resulting $\mathrm{SFR}_n(M_n, t)$
   - Add next stellar mass bin $m_{n+1} = \mathrm{SFR}_n(M_n, t_n) \times \delta t$ with birth time $t = t_{n+1}$
3. Output list of total masses M_n, star formation rates SFR_n, and corresponding steps in cosmic time t_n

Note that at timestep n the stellar mass that was just formed m_n is taken to have a mean stellar age of half of the timestep size $\delta t/2$, which effectively means that the stellar mass is added at the middle of the timestep. This choice means that a portion of the just formed stellar mass is immediately lost to supernovae, as for our timestep size $\delta t/2 = 50\,\mathrm{Myr}$ we have $f_{\rm ml} = 0.24$ with a Chabrier IMF. This is very close to the mean mass loss that would result from subdividing each 100 Myr timestep into 1 Myr blocks, which gives $f_{\rm ml} = 0.23$, meaning that our choice well approximates a steady formation of stars over 100 Myr. The minor difference grows even smaller with increasing age of the stars.

Finally, all our calculations assume a 0.3/0.7 ΛCDM concordance cosmology, with $\Omega_m = 0.3$, $\Omega_\Lambda = 0.7$ and $h_0 = 0.7$.

8.3 Results

8.3.1 Properties of Main Sequence Galaxies

First, we consider how a broad range of galaxies would evolve if they remain fixed on the SFMS. To this end, we seed progenitors with $M_{*,\mathrm{z}} = 1 \times 10^8 \mathrm{M}_\odot$ from $z = 0.5$ to $z = 6$ in 150 equal steps in cosmic time (a spacing of 50 Myr) and plot the evolution of their stellar mass (top, M_*), star formation rate (middle, SFR), and specific star formation rate (bottom panel, $\mathrm{SFR}/\mathrm{M}_*$) as a function of cosmic time in Fig. 8.1. We color each line by the final stellar mass, as indicated in the colorbar. As expected, seeding the progenitor at earlier times results in larger stellar masses at $z = 0\,\mathrm{M}_{*,z=0}$, following a linear relation as $\log \mathrm{M}_{*,0} = 11.43 - 0.36 \cdot t$, where t is the cosmic time in Gyr of the progenitor. This relationship is remarkably tight, with a median absolute deviation in $\log \mathrm{M}_{*,0}$ of just 0.023 dex (≈ 5.4%).

As can be seen from the lower panel, at a given redshift the Popesso et al. (2023) SFMS finds more massive galaxies to have lower sSFR, but notably also that galaxies of equal stellar mass decrease their sSFR with increasing cosmic time. This is apparent from the upper bound of the curves, which represents the sSFR of the progenitor galaxies that all start with $\mathrm{M}_{*,\mathrm{z}} = 1 \times 10^8 \mathrm{M}_\odot$ and which follows a slope of $\mathrm{sSFR} \propto 10^{-0.113 \cdot t}$, indicated by the upper dashed line.

This slope directly follows from the turnover mass parametrization of the Popesso et al. (2023) SFMS. For low stellar masses $\mathrm{M}_* \ll \mathrm{M}_\mathrm{T}(\mathrm{t})$ (i.e., $1 \ll \mathrm{M}_\mathrm{T})(\mathrm{t})/\mathrm{M}_*$, Eq. 8.2 becomes

$$\begin{aligned} \mathrm{SFR}(\mathrm{low\,M}_*, t) &\approx \mathrm{M}_* \cdot \mathrm{SFR}_{\max}(t)/\mathrm{M}_\mathrm{T}(t) \\ &= \mathrm{M}_* \cdot 10^{a_0 + a_1 t - (a_2 + a_3 t)} = \frac{\mathrm{M}_*}{10^{a_2 - a_1}} \cdot 10^{(a1 - a3) \cdot t} \end{aligned}$$

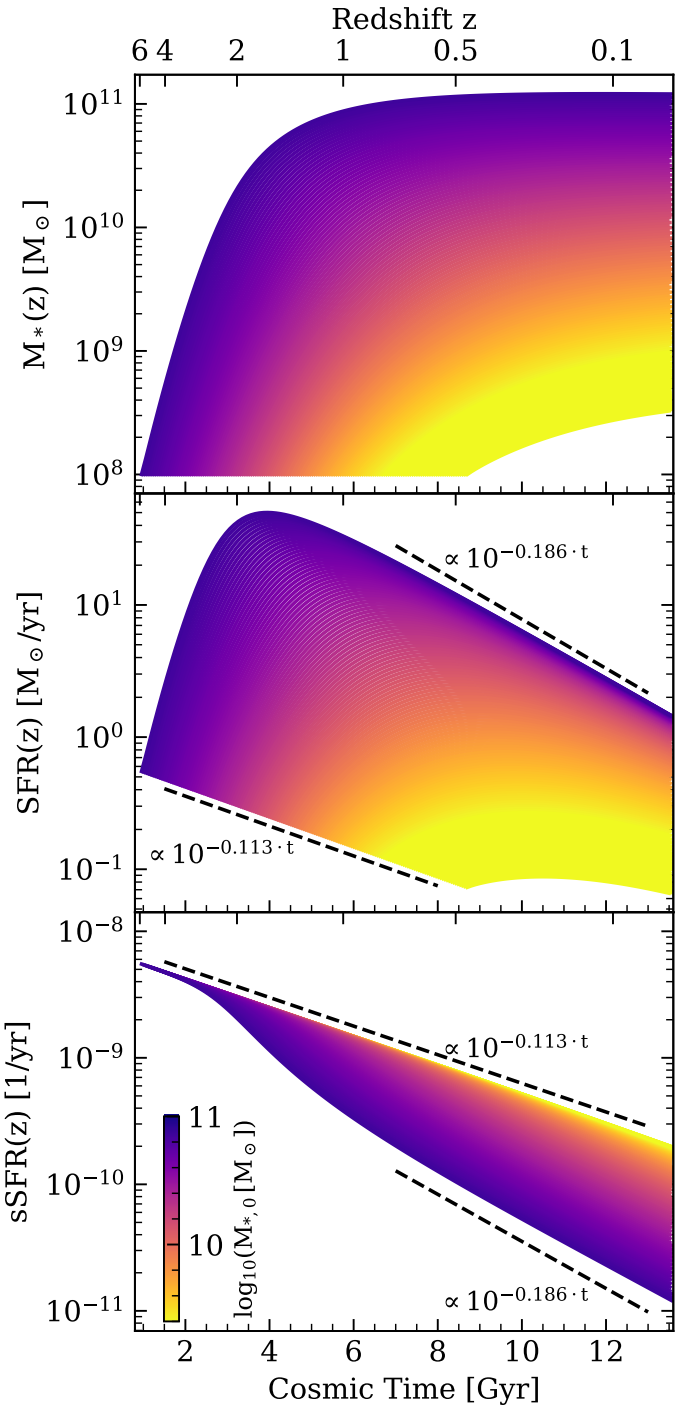


Figure 8.1. Stellar mass (M_*, **top**), star formation rate (SFR, **middle**), and specific star formation rate (sSFR, **bottom**) against cosmic time for galaxies evolving along the Popesso et al. (2023) main sequence. Progenitors are seeded between $z = 6$ and $z = 0.5$ at $M_* = 10^8 M_\odot$, while lines are colored by their final $z = 0$ stellar mass, $M_{*,z=0}$. We find that with increasing $M_{*,z=0}$ the peak SFR shifts to earlier times and higher values. At any redshift, the sSFR of more massive galaxies is lower, as expected, while for a given stellar mass the sSFR decreases with time.

$$= \frac{M_*}{1.4 \times 10^8} \cdot 10^{-0.113 \cdot t}.$$

It follows that the sSFR for main sequence galaxies with low stellar masses (well below $M_T(t)$) does not effectively depend on their concrete stellar mass, but instead only on cosmic time $\text{sSFR}\,[1/\text{yr}] = \text{SFR}/M_* = 7 \times 10^{-9} \cdot 10^{-0.113 \cdot t}$. This implies that the steady state for star

formation in low mass galaxies ($M_* < 10^9 M_\odot$) becomes increasingly inefficient toward lower redshifts (matching findings for example by Ilbert et al., 2015), even though their total gas content does not significantly decrease (Mérida et al., 2024). Furthermore, the metallicity of the gas in these galaxies increases toward lower times (Maiolino et al., 2008; Curti et al., 2024), which would imply faster, more efficient cooling (Wiersma et al., 2009). Instead, this may be due to an increase in the angular momentum of the infalling gas (seen for more massive galaxies in cosmological simulations by Teklu et al., 2023 and Fortuné et al., 2025), which would depress the central gas density and thus SFR.

For large stellar masses $M_* \gg M_T(t)$ the fraction $M_T(t)/M_*$ tends toward zero, such that

$$\begin{aligned} \mathrm{SFR}(\text{high } M_*, t) \approx \mathrm{SFR}_{\max}(t) &= 10^{a_0 + a_1 t} \\ &= 512.9 \cdot 10^{-0.186 t}, \end{aligned}$$

which means that, unlike low mass galaxies, massive galaxies retain a $1/M_*$ dependence for their sSFR. However, as their sSFR is so low and thus their stellar mass does not noticeably increase at later times (see the top panel of Fig. 8.1), effectively their sSFR again mostly depends on the cosmic time.

Finally, we see that more massive galaxies peak in their SFR earlier in time and at higher values, and in particular that they form the majority of their stars faster than lower mass galaxies. To quantify this, we plot in the top panel of Fig. 8.2 the formed stellar mass as a function of lookback time, normalized by the total formed stellar mass (note that this is not equal to the final, i.e., remaining stellar mass). Here we seed progenitors with stellar masses between 1×10^8 and $1 \times 10^9 M_\odot$ and redshift bins from $z = 0.5$ to $z = 6$, but keep only those models where the progenitor mass never accounts for more than 1% of the final stellar mass (i.e., the evolution on the SFMS dominates the stellar ages).

We see from the top panel of Fig. 8.2 that for purely main sequence-evolved galaxies there naturally emerges a more peaked, early star formation history (SFH) in more massive galaxies, while lower mass galaxies have broader distributions and peak later toward $t = 6$ Gyr. To quantify the behavior more clearly, we fit a Gaussian function of the form $y = 1/(\sqrt{2\pi}\sigma_{\mathrm{SFH}}) \cdot \exp^{-((x-\mu)/\sqrt{2}\sigma_{\mathrm{SFH}})^2}$ to the SFHs, and plot the location of the peaks μ (in lookback time) against the final stellar mass in the bottom panel of Fig. 8.2. We find a very tight relation that we fit (blue line) as $m = 0.9408 \cdot T^2 - 15.88 \cdot T + 69.18$, with $T \equiv \mu_{\mathrm{peak}}$ [Gyr] and $x = \log(M_{*,z=0}\,[M_\odot])$.

Our behavior found for SFMS evolved galaxies is very similar to the distribution of stellar ages found by Thomas et al. (2010) in early type galaxies (colored stars), where those with $M_{*,z=0} = 10^{10.5} M_\odot$ peak at $T \approx 6.9$ Gyr compared to our later $T \approx 6.2$ Gyr. This is likely due to quenching, as model SFMS galaxies of $M_{*,z=0} = 10^{10.7} M_\odot$ have the same peak location such that, if we cut their later evolution short through quenching, they would end up at lower mass where Thomas et al. (2010) find their ETGs. This agreement persists also for galaxies of $M_{*,z=0} = 10^{11} M_\odot$, which have identical peak ages of $T \approx 8.3$ Gyr for both our model SFMS galaxies and their SDSS ETGs.

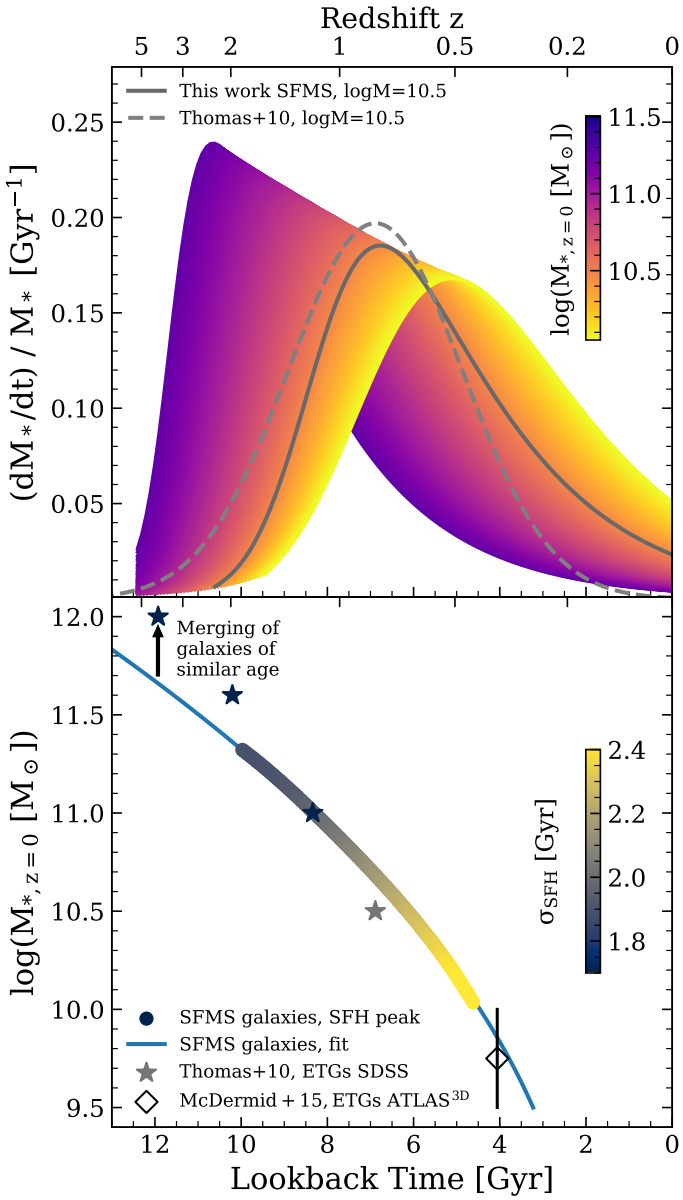


Figure 8.2. Top: The specific star formation rate history of massive galaxies that fully evolved along the SFMS, colored by their final stellar mass $M_{*,z=0}$. Plotted are only models where the progenitor galaxy accounts for less than 1% of $M_{*,z=0}$. **Bottom:** The peak location of best-fit gaussians to each SFH versus $M_{*,z=0}$, colored by the width of the gaussian. From observations of early type galaxies we include the fits of Thomas et al. (2010) for SDSS galaxies, and the peak location of the SFH for lower mass galaxies in ATLAS^{3D} by McDermid et al. (2015).

For those of $M_{*,z=0} > 10^{11} M_{\odot}$, forming that many stars along the SFMS becomes increasingly difficult (due to the flattening in SFR at high M_*) and requires starting well before $z > 6$ where the fit by Popesso et al., 2023 does not apply any longer. This simply indicates that such galaxies must be formed either through particularly strong starbursts, or more likely through the merging of multiple old, massive galaxies. Such merging increases the mass without altering the peak ages, as indicated by the arrow in the bottom panel of Fig. 8.2. Nevertheless, the fact that the model predicts a very similar relation to observations even of ETGs highlights the self-similarity of the galaxy growth for a given stellar mass until the moment of dry merging and quenching.

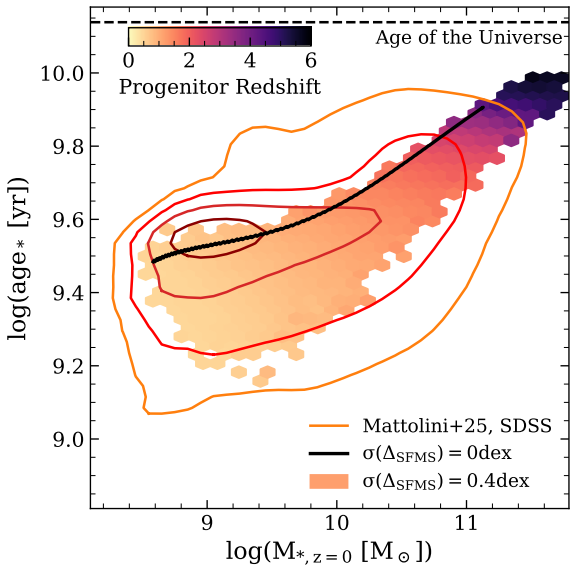


Figure 8.3. Mass weighted mean stellar age plotted versus stellar mass at $z = 0$. The black solid line shows the ages for galaxies evolving exactly along the SFMS, while the heatmap is the distribution when including a lognormal scatter in SFR with $\sigma = 0.4$dex. Contour lines are from observed SDSS galaxies by Mattolini et al. (2025). Interestingly, the observed ages very closely follow the expectations from the SFMS evolution, in particular when we allow for some scatter about the main sequence.

To further emphasize this point, we consider the remaining stellar mass at $z = 0$ (instead of the total formed mass through time), and determine the mass-weighted ages as a function of the total $M_{*,z=0}$. We then obtain the solid black line in Fig. 8.3, which follows the age distribution of a large sample of SDSS galaxies by Mattolini et al. (2025) as indicated by the orange contour lines remarkably well. However, the requirement that our model galaxies formed their stars exactly along the SFMS necessarily leads to a lack of the range of scatter seen in the observations.

Therefore, we allow for a lognormal scatter around the SFMS with a standard deviation of 0.4 dex to obtain the heatmap (with the color being the redshift of the progenitor galaxy). We find that this fills out the range in contours by Mattolini et al. (2025) very well. Naturally, the extreme cases of very young (recent starbursts) and very old (quenched and/or dry merged galaxies) are not captured, but the overall behavior is. Consequently, we conclude that for the majority of stars in present day galaxies, their age distribution is essentially as would be expected if the host had evolved with some scatter around the SFMS. Intriguingly, this is true even for the more massive galaxies that are known to grow primarily through accretion at later times (Oser et al., 2010; Remus et al., 2023), which we do not include in the model at all. However, the good agreement in the ages imply that the amount of younger stars brought in during these merging events is comparable to the amount of stars the galaxy would have formed in-situ if the baryons had come in as gas instead (in which case it could have remained on the SFMS down to $z = 0$). This is likely because the young stars in massive galaxies contribute so little that possible differences in late in-situ vs merging activity makes no discernible difference for the average age of stars in the galaxy.

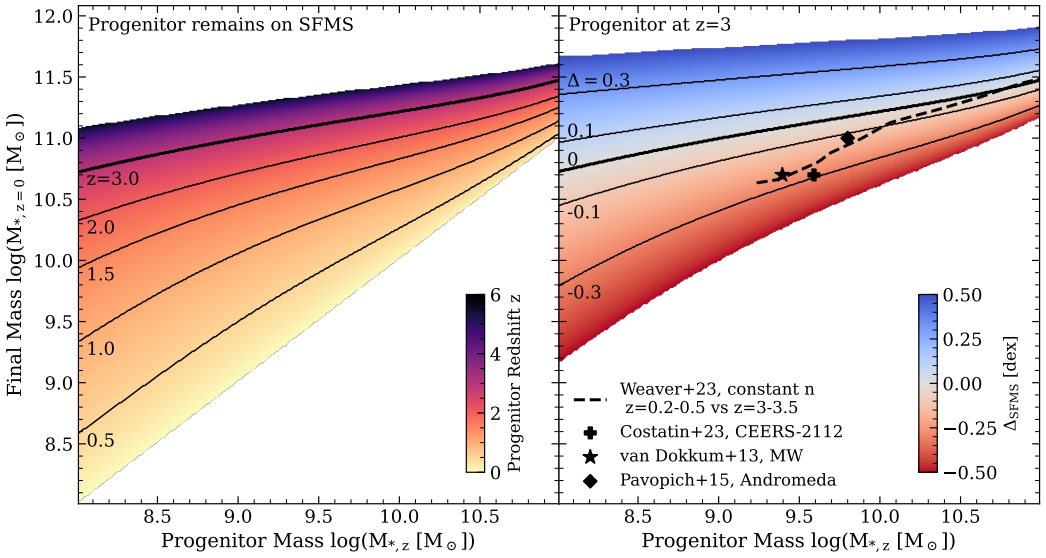


Figure 8.4. The final stellar mass of a given galaxy plotted against its progenitor mass. On the **left** we vary the redshifts of the progenitor galaxies (given by the color) and then evolve them precisely on the SFMS. On the **right** the progenitors are fixed at $z = 3$ while the SFR of the galaxies may lie consistently above (blue) or below (red) the expected SFR from the SFMS. The thick solid black line is identical for both panels (SFMS evolved galaxies with progenitors at $z = 3$). In the right panel, we additionally plot progenitor stellar masses of the MW and Andromeda galaxies from van Dokkum et al. (2013) and Papovich et al. (2015), as well as the possible MW progenitor CEERS-2122 by Costantin et al. (2023). It follows that the MW and Andromeda must have either undergone cycles of bursty and then suppressed star formation, or instead formed stars since $z = 3$ at a rate consistently below the SFMS by 0.3 and 0.1 dex, respectively.

8.3.2 Connecting Galaxies Across Cosmic Time

Finally, we then consider the relation between the progenitor galaxies and the final stellar mass. This relation is crucial when connecting high redshift and low redshift galaxies, both from the perspective of present day main sequence galaxies and understanding what type of galaxies at high redshifts are possible progenitors, as well as to see which stellar masses would be expected if the observed massive star forming galaxies at high redshifts (e.g., Wang et al., 2025) could remain on the SFMS down to $z = 0$ or would then produce too many stars.

To this end, we construct a grid of models with progenitor masses between $M_* = 1{\times}10^8 M_\odot$ and $M_* = 1 \times 10^{11} M_\odot$, with redshifts from $z = 0$ to $z = 6$, and plot their final $z = 0$ stellar mass assuming they evolve entirely along the Popesso et al. (2023) SFMS in the left panel of Fig. 8.4. The colorbar indicates the redshift of the progenitor, with the solid black lines highlighting particular redshifts. We see that varying the mass of the progenitor galaxy does not strongly impact the resulting final mass if it is seeded at high redshifts (purple region), because in all cases the galaxies reach the turnaround mass before $z = 0$, above which the sSFR becomes too low to significantly grow the galaxies any further (as discussed also for Fig. 8.1).

We find that even a low mass progenitor of $M_* = 1{\times}10^8 M_\odot$ reaches $M_{*,z=0} = 1{\times}10^{11} M_\odot$ by $z = 0$ if it evolves along the SFMS from $z = 6$ onward. Conversely, because the high

redshift lines lie at very high final stellar masses for the whole range of progenitor masses, galaxies today with $M_{*,z=0} = 10^{10} M_\odot$ or lower either had their progenitor emerge particularly late in cosmic time, past the peak of the cosmic star formation rate density (Madau & Dickinson, 2014) at $z = 1.5$ even for a dwarf of $M_* = 1 \times 10^8 M_\odot$, or they must have undergone phases of suppressed star formation or even quiescence. Two interesting examples for this can be found directly in the local Universe: M33, the third most massive galaxy in our local group, has a stellar mass of $4.8 \times 10^9 M_\odot$ (Corbelli et al., 2014). With respect to many of its properties, NCG 300 with a stellar mass of $2 \times 10^9 M_\odot$ (Muñoz-Mateos et al., 2007) is often treated as its analogue, with the difference that NGC 300 lives within a cosmic void. Both galaxies are close enough that stars can be resolved observationally. Based on such a study, Gogarten et al. (2010) find that NCG 300 had formed about 70% of its stars, that is $1.4 \times 10^9 M_\odot$, already at $z = 2$, while M33 has formed only about 20-30% at $z \approx 2$, i.e., $1.4 \times 10^9 M_\odot$. While M33 after $z = 2$ can have continued to form stars on the main sequence, albeit with a SFR continuously about -0.5dex below the main sequence, NGC 300 must have gone through a period of relative quiescence with SFR more than -0.5dex below the SFMS (see Fig. B.2 in the Appendix for the finding chart). Indeed, for M33 Williams et al. (2009) find indications for a rather low-star formation period 8-10Gyrs ago, with the more recent star formation taking place mostly in the outskirts. This clearly demonstrates that significant amounts of old stars detected in low mass galaxies is a smoking gun for a period of quiescence in the galaxy's lifetime.

Furthermore, cycles of rejuvenation and quiescence are indeed found from cosmological simulations both at later times (Fortuné et al., 2025) as well as already at high redshifts (Remus & Kimmig, 2025), with indications for rejuvenation also seen from observations (e.g., Peletier et al., 2007; Muñoz López et al., 2025). Any amount of ex-situ stars (i.e., mergers), which we do not consider here, would only exacerbate the need for such suppressed phases by decreasing the amount of time allowed on or near the SFMS.

For the case of super spirals with $M_{*,z=0} \approx 10^{12} M_\odot$ (Ogle et al., 2019b), we find there to be no way to produce their stellar mass in-situ while evolving entirely on the SFMS, even for extreme progenitors of $M_* = 10^{11} M_\odot$ at $z = 6$ like the disk galaxy reported by Xiao et al. (2025). This implies that they must have either undergone significant amounts of merging or evolved consistently above the main sequence. To test the second possibility, we again construct a grid of progenitors but fix their redshift at $z = 3$, and instead allow their SFR to evolve at a fixed offset $\Delta_{\rm SFMS}$ from the SFMS going from -0.5 dex (red) to $+0.5$ dex (blue) in the right panel of Fig. 8.4. The solid black lines here denote particular values of $\Delta_{\rm SFMS}$, while the thick solid black line is the same in both panels (SFMS evolved galaxies seeded at $z = 3$).

We find for the case of $\Delta_{\rm SFMS} = 0.5$ dex, so if the galaxy has consistently been above the SFMS since $z = 3$, that in-situ formation of enough stars to match the observed super spirals by Ogle et al. (2019b) is possible, though it is doubtful whether galaxies can remain so far above the SFMS over the majority of the age of the Universe. Given their largely undisturbed morphologies in observations, this points toward very significant contributions

from (gas-rich) minor mergers that can be accreted without destroying the disk structure of a galaxy (Karademir et al., 2019), or progenitors in excess of $M_* = 10^{11} M_\odot$ by $z = 3$.

Generally for galaxies with progenitors $M_* > 10^8 M_\odot$ present by $z = 3$, we find that they must either end up being very massive at $z = 0$ or have spent a majority of their time with SFRs well below the SFMS mean. In particular, we highlight here the cases of Milky Way- and Andromeda-mass galaxies. Under the assumption that the present day number density of galaxies of a given stellar mass is comparable to the number density of their progenitors, van Dokkum et al. (2013) and Papovich et al. (2015) determine the expected progenitor galaxy stellar masses at $z = 3$ of the Milky Way and Andromeda galaxies to be $M_* \approx 2.5 \times 10^9 M_\odot$ and $M_* \approx 6.3 \times 10^9 M_\odot$, respectively. We plot those points, as well as the potential Milky Way progenitor CEERS-2112 with $M_* \approx 3.9 \times 10^9 M_\odot$ from Costantin et al. (2023), in the right panel of Fig. 8.4.

The plot shows that Milky Way-mass galaxies must have formed stars at a rate nearly 0.3 dex below the SFMS value since $z = 3$ if they are to end up with their current day stellar mass of $M_{*,z=0} \approx 5 \times 10^{10} M_\odot$, and that is under the assumption of no additional merging. Indeed, there are well known indications from the ages of stars in the Milky Way itself that indicate a low star formation rate after $z < 1$ (Haywood et al., 2016). In contrast, the Andromeda galaxy at $M_{*,z=0} \approx 1 \times 10^{11} M_\odot$ is massive enough that, while still suppressed, it could have evolved from $z = 3$ progenitors of the same number density with a SFR just 0.1 dex below the SFMS value.

Going one step further, we have applied a similar number density methodology to the more recent census of the galaxy stellar mass function from $z = 6$ to $z = 0.1$ on the COSMOS2020 catalog done by Weaver et al. (2023). We interpolate between their data points in log-log space to produce the smooth black dashed line in the right panel of Fig. 8.4, which shows the relation between $z = 3$ and $z = 0$ galaxy stellar masses of constant number density. Naturally, the values by van Dokkum et al. (2013) for the Milky Way and Papovich et al. (2015) for Andromeda lie near this line, while the potential Milky Way progenitor from Costantin et al. (2023) has a somewhat higher stellar mass. We find, if the number density connection is correct, that galaxies of $M_{*,z=0} = 3 \times 10^{10} M_\odot$ must have spent the majority of their evolution below the SFMS, while, curiously, more massive galaxies of $M_{*,z=0} > 2 \times 10^{11} M_\odot$ could have remained entirely on the SFMS ($\Delta_{SFMS} = 0$) down to $z = 0$. As those more massive ones are instead expected to grow primarily through mergers at later times, the accreted stellar mass must approximately equal the expected in-situ formed amount if they retained a SFR on the SFMS.

This plot is particularly useful for constraining possible star formation histories of galaxies evolving near the SFMS over cosmic time, and connecting possible past progenitors with present day galaxies. As it is limited by the choice of progenitor redshift, we include six versions with progenitors at redshifts $z = 6$ to $z = 1$ in the Appendix B.3.

8.3.3 Milky Way-like Galaxies

Having seen that galaxies of Milky Way mass, $M_{*,z=0} = 5 \times 10^{10} M_\odot$, appear to require a suppressed late time SFR to match expectations from number density arguments, it is worthwhile to consider a more detailed look at model star formation histories. We show in Fig. 8.5 the stellar mass against cosmic time, in the top panel for a $M_* = 1 \times 10^8 M_\odot$ progenitor galaxy set at $z = 4.4$ based on the van Dokkum et al. (2013) fit for the Milky Way's evolution, and in the bottom panel for a set of model galaxies that all end at $M_{*,z=0} = 5 \times 10^{10} M_\odot$.

Beginning with the top panel of Fig. 8.5, we find that the progenitor would noticeably overshoot the MW if it evolved along the SFMS, ending with $M_{*,z=0} = 1 \times 10^{11} M_\odot$. This is particularly interesting, as the early growth of the van Dokkum et al. (2013) evolution (dash-dotted black line) actually exceeds the expected SFMS evolution (solid black line) of the progenitor by around +0.3 dex until $z = 3$, when it nears the stellar mass of the possible MW progenitor observed by Costantin et al. (2023). At that point, the growth slows significantly relative to the SFMS curve, very closely matching a suppressed SFR with $\Delta_{SFMS} = -0.3$ dex (dotted black line) until $z = 0$. The same holds true for the predictions (diamonds) by Papovich et al. (2015), which lie near the SFMS line at $z = 2$ but afterward deviate toward negative Δ_{SFMS} values.

The same holds true for the data points (crosses) we derive from the COSMOS2020 galaxy stellar mass function by Weaver et al. (2023). To do so, we first determine the number density of Milky Way mass galaxies ($M_{*,z=0} = 5 \times 10^{10} M_\odot$) at $z = 0.2$ to $z = 0.5$ as $n_{MW} = 2.2 \times 10^{-3} \mathrm{cMpc}^{-3}$, and then find the stellar mass that matches this number density at higher redshifts by linearly interpolating in log-log space between the Weaver et al. (2023) data points. Furthermore, we fit an orthogonal distance regression to these new data points with the same function form as that by van Dokkum et al. (2013), and obtain for the galaxy stellar mass evolution of Milky Way-mass galaxies:

$$M_{*,MW}(z) = 10^{10.74 - 0.007 \cdot z - 0.17 \cdot z^2}. \tag{8.4}$$

This fit is largely similar to that determined by van Dokkum et al. (2013), though with a stronger decrease in stellar mass at higher redshifts.

It is further striking that our integration of the SFR(t) determined by Haywood et al. (2016), which they derived from chemical abundances of Milky Way stars following Snaith et al. (2015), results in a particularly early star formation history, with a stellar mass of $M_* = 1 \times 10^{10} M_\odot$ by $z = 3.6$. We note that, to obtain a final mass $M_{*,z=0} \approx 5 \times 10^{10} M_\odot$ it was necessary to assume a steep Chabrier IMF, which is more akin to the Kroupa et al. (1993) IMF (Leitner & Kravtsov, 2011). If we instead assume a normal Chabrier as done for our SFMS models (and which is also closer to the Kroupa, 2001 IMF used by Haywood et al., 2016), we obtain a final stellar mass of $M_{*,z=0} \approx 3.6 \times 10^{10} M_\odot$. While this does reduce the early stellar mass by the same fraction, $M_* = 1 \times 10^{10} M_\odot$ is still reached much earlier (by $z = 3.1$) than found by the curves from number density arguments.

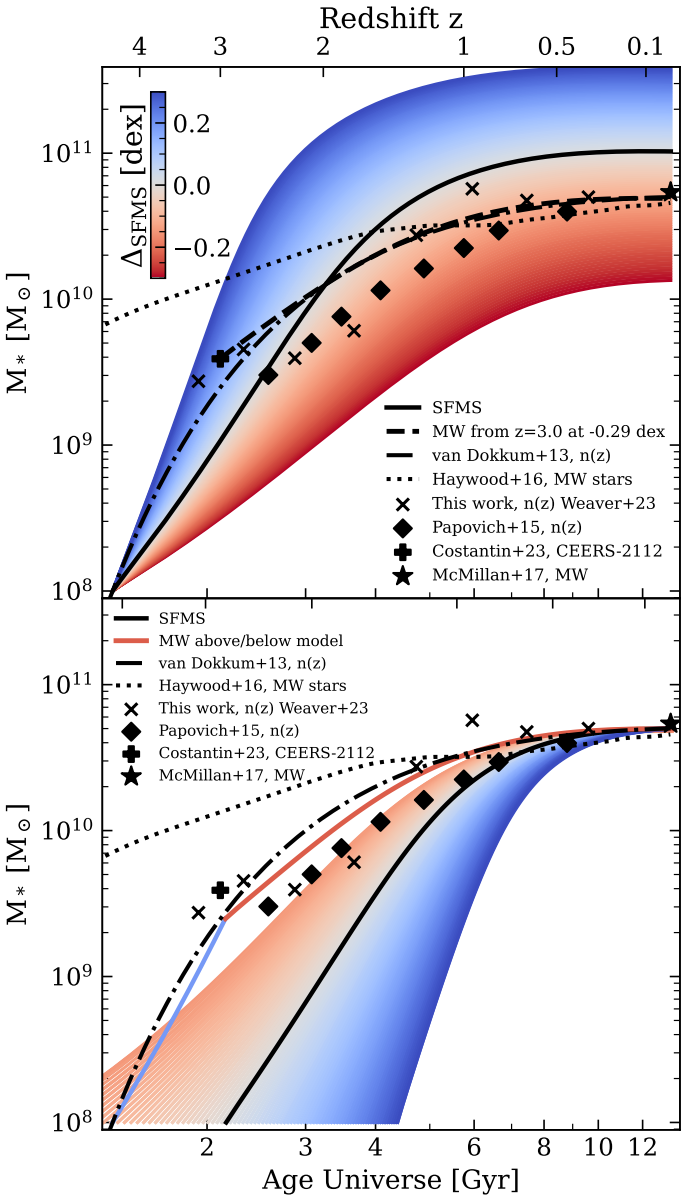


Figure 8.5. The evolution of the stellar mass of Milky Way-like galaxies that formed stars along (solid black line), above (blue) or below (red) the SFMS, plotted against time. The **top** panel shows expectations for a progenitor galaxy with $M_* = 1 \times 10^8 M_\odot$ at $z \approx 4.4$, following the prediction from van Dokkum et al. (2013) made on the basis of number density arguments (dash dotted line). Also plotted are the data by Papovich et al. (2015) obtained in a similar manner (diamonds), our own version obtained from the Weaver et al. (2023) COSMOS2020 data (crosses), the integrated stellar mass from the SFRs (dotted line) by Haywood et al. (2016), the potential MW progenitor CEERS-2112 (plus sign) by Costantin et al. (2023), and the $z = 0$ MW mass (star) determined by McMillan (2017). The **bottom** panel shows instead the possible galaxy stellar mass tracks that obtain a MW-like stellar mass at $z = 0$ $M_{*,0} = 5 \times 10^{10} M_\odot$, and a model that closely resembles the van Dokkum et al. (2013) predictions (two-colored solid line).

For the bottom panel of Fig. 8.5, we see that if the Milky Way had evolved entirely on the SFMS, its progenitor would fall below a stellar mass of $M_* = 1 \times 10^8 M_\odot$ above $z = 2.8$. Given the observational evidence for significant amounts of older stars from directly within the Milky Way itself (Haywood et al., 2016; Imig et al., 2023; Leung et al., 2023) this is clearly not the case. Consequently, our Milky Way galaxy must have followed a SFH which

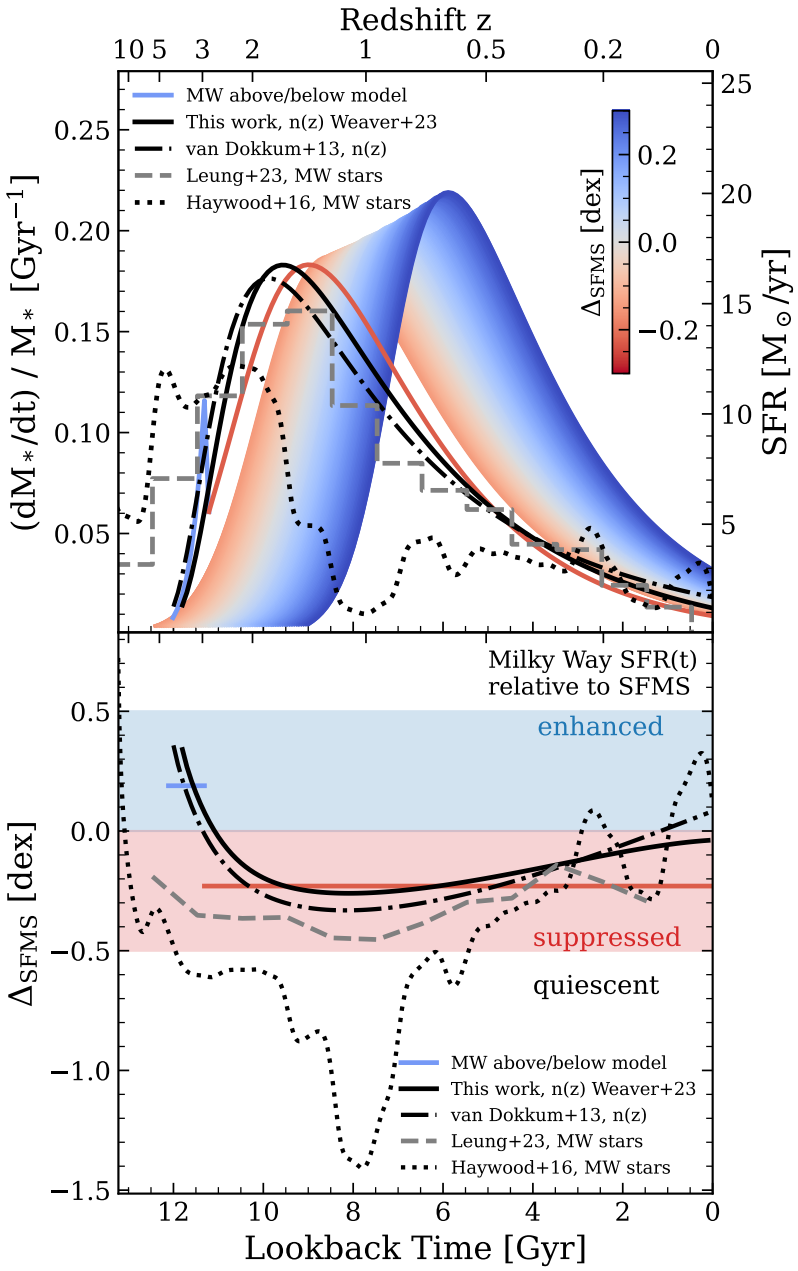


Figure 8.6. The normalized star formation histories of galaxies with a Milky Way-like $z = 0$ stellar mass $M_{*,0} = 5 \times 10^{10} M_\odot$ that evolved consistently on (solid black line), above (blue) or below (red) the SFMS. Because the total mass for all curves is the same, the y-axis translates directly to a SFR. We plot also the SFH which we derive from van Dokkum et al. (2013), the age distribution by Leung et al. (2023) based on APOGEE data of Milky Way stars, and the SFR against time derived by Haywood et al. (2016) through the alpha abundances of Milky Way stars via the method from Snaith et al. (2015).

sees an early, bursty rise in stellar mass, after which its SFR was strongly suppressed well below the SFMS. Indeed, this is the scenario derived by Haywood et al. (2016) from the alpha abundances of stars in the Milky Way. We find that a model with $\Delta_{SFMS} = 0.189$ dex for $z > 3$ and $\Delta_{SFMS} = -0.23$ dex after provides a good representation of the evolution by van Dokkum et al. (2013).

From the mass evolution, we can plot also the resulting sSFR history in the top panel of Fig. 8.6, which can be directly converted to the SFR because the final stellar mass

$M_{*,z=0} = 5 \times 10^{10} M_\odot$ is approximately the same for all curves. By necessity, models which grow later but with higher SFRs (positive Δ_{SFMS}, blue) show more peaked SFHs, while allowing for a more suppressed SFR (negative Δ_{SFMS}, red) broadens the SFH but crucially also shifts the peak toward earlier times. This better matches expectations for the Milky Way itself, as can be seen from the SFH by van Dokkum et al. (2013), as well as the age distribution and SFR derived from Milky Way stars directly by Haywood et al. (2016) and Leung et al. (2023), respectively. Note that for the van Dokkum et al. (2013) curve we have converted their fit of the observed stellar mass $M_*(t)$ (equal to the formed minus lost mass) into an SFR $SFR(t)$ (which is just the formed mass) by splitting the evolution into timesteps and accounting for stellar mass loss following a Chabrier IMF.

Finally, the combination of $SFR(t)$ and $M_*(t)$ allows us to directly compare the Milky Way SFR with the expectation SFR from the Popesso et al. (2023) SFMS through cosmic time, which we plot in the bottom panel of Fig. 8.6. All methods find that the Milky Way begins its star formation particularly early and bursty, lying around 0.3 dex above the SFMS for the number density based models and 0.5 dex for the Haywood et al. (2016) data. We note that for both cases this occurs at a stellar mass within the bounds of the Popesso et al. (2023) main sequence fit $M_* > 3 \times 10^8 M_\odot$, but for the latter at earlier redshifts than their fits. It is thus possible that the extrapolation is incorrect here, and the early Milky Way could still have evolved along the SFMS. Then, between a redshift of $z = 3$ and $z = 2$, all models find the Milky Way SFR to decrease relative to the SFMS, dropping down to $\Delta_{SFMS} = -0.4$ dex for the number density models and even farther below for those based on Milky Way stars. The SFR remains suppressed until very late times, when in the last gigayear it lies on the main sequence again.

We note that this rise toward the SFMS at later times is actually driven entirely by the SFMS itself coming down, as can be seen from the absolute SFR in the top panel of Fig. 8.6. The SFRs at later times of our Milky Way galaxy are flat (Haywood et al., 2016) or decreasing (van Dokkum et al., 2013; Leung et al., 2023), but the SFMS sinks rapidly enough that they still meet by $z = 0$. This matches the behavior of the "caught" type of galaxies defined by Fortuné et al. (2025) within cosmological simulations, which exhibit also other properties that are similar to those of the Milky Way. They are found there to be more common than galaxies that evolved entirely on the SFMS, though the most common type are rejuvenating galaxies that go through cycles of SF and quiescence on timescales $t > 1$ Gyr. For the case of the Haywood et al. (2016) SFH, the Milky Way galaxy would actually fall under this latter category.

8.4 Conclusion

We have made a model that allows us to trace the evolution of galaxy stellar masses and star formation rates (SFR) through cosmic time in relation to their position on the star forming main sequence of galaxies (SFMS) described by Popesso et al. (2023). With this model, we explored the star formation histories and stellar mass growth of galaxies of differing masses,

their resulting age distributions and in particular highlighted the example of the Milky Way galaxy.

We found that the observed difference in age distributions between galaxies of lower and higher stellar masses, with the former being younger and more extended while the latter are earlier and more bursty (Thomas et al., 2010; Mattolini et al., 2025), naturally arises from the evolution of the star forming main sequence through cosmic time in Fig. 8.2 and Fig. 8.3. Indeed, galaxies that evolved entirely along that sequence match the observed age distributions for galaxies from $M_* = 1 \times 10^9 M_\odot$ up to $M_* = 3 \times 10^{11} M_\odot$ remarkably well, with only a slight tendency toward younger ages due to the lack of quenching.

Based on our model, we provided figures relating present day stellar masses with possible progenitors at redshifts from $z = 1$ up to $z = 6$, accounting also for scatter above/below the star forming main sequence of up to ±0.5 dex. These figures can be used to inform current observations of high redshift galaxies about the expected stellar masses should they continue to evolve along, above or below the star forming main sequence down to $z = 0$. Based on the COSMOS2020 galaxy stellar mass function (Weaver et al., 2023), and under the assumption that galaxies of the same number densities may be connected through cosmic time, we showed that present day high mass galaxies ($M_* \geq 1 \times 10^{11} M_\odot$) grew their stellar mass exactly in the manner as expected if they had evolved along the star forming main sequence. As these more massive galaxies are known to grow secularly (Oser et al., 2010), this indicates that they end up with the same growth in stellar mass regardless of whether the baryons come in as gas and are then formed into stars in-situ or if they are primarily brought in as stars through merging.

We then applied our model to the Andromeda and Milky Way galaxies. As Andromeda is more massive ($M_* \approx 1 \times 10^{11} M_\odot$) we find that the predicted growth history by Papovich et al. (2015) matches the expectations from an evolution along the SFMS (lying on average at $\Delta_{SFMS} = -0.1$ dex). By contrast, we show that galaxies which end up with a present day Milky Way stellar mass ($M_* \approx 5 \times 10^{10} M_\odot$) must have evolved with star formation rates well below the SFMS ($\Delta_{SFMS} \approx -0.3$ dex) since = 3, if they are to remain at the same comoving number density through cosmic time. Any additional contributions from mergers only further reduce the allowed SFR. However, before $z = 3$ this trend is reversed, and they would have had to evolve significantly *above* the SFMS. Indeed, the lowest point of their expected SFRs relative to the SFMS is found to be around $z = 1$, after which the distance shrinks and they approach the SFMS again. We additionally provide a fit for the growth of Milky Way-mass galaxies as $M_{*,MW}(z) = 10^{10.74 - 0.007 \cdot z - 0.17 \cdot z^2}$, based on the updated data by Weaver et al. (2023).

For the particular case of the Milky Way itself, we demonstrate that data based on chemical abundances in stars in the Milky Way (Haywood et al., 2016; Leung et al., 2023) imply that our Galaxy effectively quenched ($\Delta_{SFMS} < -0.5$ dex) around $z = 1$, very similar to the time of the dip in galaxies of comparable mass. The scenario of rejuvenated star formation is increasingly found also for other galaxies of similar mass, both from observations (Muñoz López et al., 2025) and simulations (Fortuné et al., 2025; Remus & Kimmig, 2025), and may



warrant further exploration, in particular with regard to the assumed shapes of SFHs used in SED fitting codes (Carnall et al., 2018).

In all cases, whether by arguments based on number densities of galaxies through cosmic time (van Dokkum et al., 2013; Papovich et al., 2015 or our own determination from Weaver et al., 2023), by chemical abundance models from Milky Way stars (Snaith et al., 2015; Haywood et al., 2016) or machine learning extrapolations (Leung et al., 2023), it is apparent that the Milky Way had a particularly early rise and then subsequent fall in SFR.

Veritatem inquirenti, semel in vita de omnibus,
quantum fieri potest, esse dubitandum.

Rene Descartes, *Principles of Philosophy*, 1643.

9

Universal Blacksmith: What Global Stellar Metal Abundances Reveal About Galaxies' Formation Histories

The research described in this chapter is planned to be published as independent papers in the future as Kimmig et al.

9.1 Introduction

The field of elemental abundances in stars has undergone an immense transformation in the past years, going from measured chemical abundances of hundreds of thousands of Milky Way stars (e.g., RAVE, Steinmetz et al., 2006; GALAH, Martell et al., 2017; and APOGEE, Majewski et al., 2017) to the around 200 million stars with low-resolution "XP" prism spectroscopy from the Gaia space mission (Gaia Collaboration et al., 2023; Chandra et al., 2024). This plethora of data from long-lived stars represents a treasure trove of fossil records, the kind that has already been employed in the past to great effect to uncover how our Galaxy formed (Freeman & Bland-Hawthorn, 2002; Bland-Hawthorn & Gerhard, 2016). The Gaia data has significantly strengthened the case for a particularly early formation of our Milky Way galaxy (Belokurov & Kravtsov, 2022; Conroy et al., 2022), something which we already discussed from the perspective of the evolution of the star forming main sequence in chapter 8.

The power of chemical abundances stems from the different modes of productions and their timescales, as shown schematically in Fig. 9.1. Core collapse supernovae (SNe) of massive stars, known as Type II supernovae, occur relatively quickly after the star was formed ($t < 100\,\mathrm{Myr}$), while thermonuclear explosions known as supernovae Type Ia happen for lower mass stars ($M_* < 8\,M_\odot$) and on longer timescales ($t > 100\,\mathrm{Myr}$). Importantly, the chemical elements produced during these processes differ significantly in their amount and type, with Type II producing primarily α elements (O, Ne, Mg, Si, S, Ar, Ca, e.g., Woosley & Weaver, 1995) while Type Ia produce significant amounts of iron-peak elements (Cr, Mn, Fe, and Ni, e.g., Nomoto et al., 1984).

Beyond a core collapse or thermonuclear explosion, intermediate mass stars ($0.8 < M_* < 8\,M_\odot$) on the asymptotic giant branch (AGB) also enrich their surroundings through their dust-driven stellar winds (Herwig, 2005). During this phase, mixing of the nuclearly processed core and its envelope can be driven by the thermally unstable He-burning shell (Kobayashi, 2025), enriching the stars surface in particular with carbon. This carbon is converted into nitrogen through the CNO cycle (e.g., Bethe, 1939), thus leading to large amounts of both carbon and nitrogen being produced and ejected (Karakas, 2010). The resulting production through cosmic time of the elements of the periodic table is nicely shown in Fig. 9.2, with the colors showing the different sources. We see how α-elements are primarily produced by exploding massive stars (Type II SNe, blue), iron-peak elements mostly come from exploding white dwarfs (Type Ia SNe, orange) while carbon and nitrogen primarily come from the ejecta of dying low mass stars (AGB, green), respectively. It should be noted that all groups of elements are not exclusively injected into the IGM from one source, however, as can be seen for example for carbon, where there is also a significant amount hailing from Type II SNe.

Recently, discussions have arisen on the predictive power of elements heavier than iron, such as those produced in the slow neutron capture process (s-process, e.g., Eu) in AGB stars (Busso et al., 1999), as well as the rapid neutron capture process (r-process, e.g., Ba, Pb) in neutron rich environments (Cameron, 1973; Kobayashi et al., 2020). As their sites and exact production is as-of-yet still debated (Kobayashi, 2025), we focus here on the more common ratios used to constrain the formation histories of galaxies, namely the α-elements abundance ratio to iron [α/Fe] and the iron abundance [Fe/H] (e.g., Fuhrmann, 1998; Mackereth et al., 2018; Hamadouche et al., 2026). As α-elements come primarily from Type II SNe, they are enriched into the surrounding intergalactic medium on rapid timescales, down to the tens of megayears. Consequently, any star formation event that takes longer than that amount of time will find the newly forming generation of stars strongly enriched in α-elements. The longer timescale for the explosion of the white dwarfs that produce the iron-peak elements (including Fe itself) is delayed enough that the newly formed stars are not yet enriched. Consequently, stars produced in a short burst will show an enhancement in [α/Fe].

We explore here how the imprint of chemical abundances frozen into stars can provide a look into the past formation history of their host galaxy as a whole by drawing on the power of cosmological simulations, because of their ability to trace the formation and evolution of galaxies through cosmic time. In Sec. 9.2 we briefly discuss the simulations and our selection

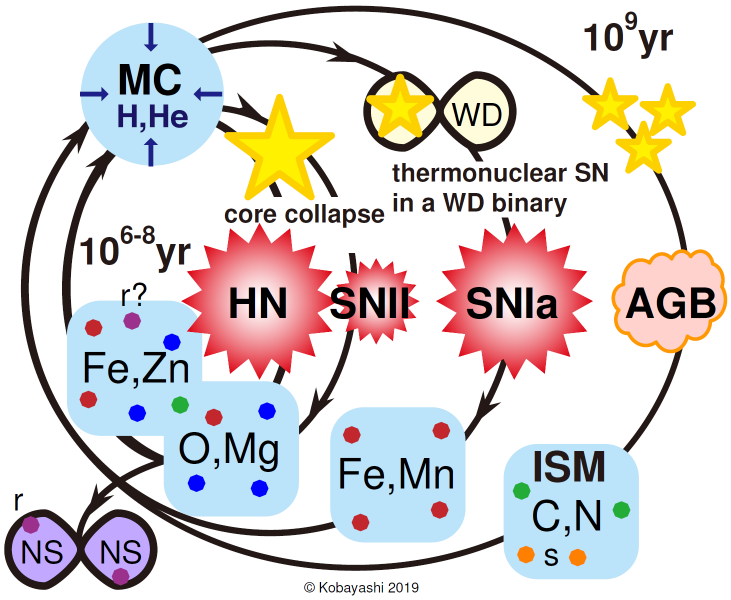


Figure 9.1. This figure has been published as Fig. 1 of Kobayashi (2025). It shows how different elements are produced, going from rapid (megayears to hundreds of megayears) to slow processes (gigayears and longer). The α elements (O, Ne, Mg, Si, S, Ar, Ca) are mainly produced by core-collapse supernovae (hypernovae and supernovae Type II), while thermonuclear explosions observed as supernovae Type Ia produce primarily iron-peak elements (Cr, Mn, Fe, and Ni). Stars on the asymptotic giant branch (AGB) eject carbon and nitrogen through their winds, primarily produced via helium burning (for carbon) and the CNO cycle (for nitrogen) (Kobayashi, 2025).

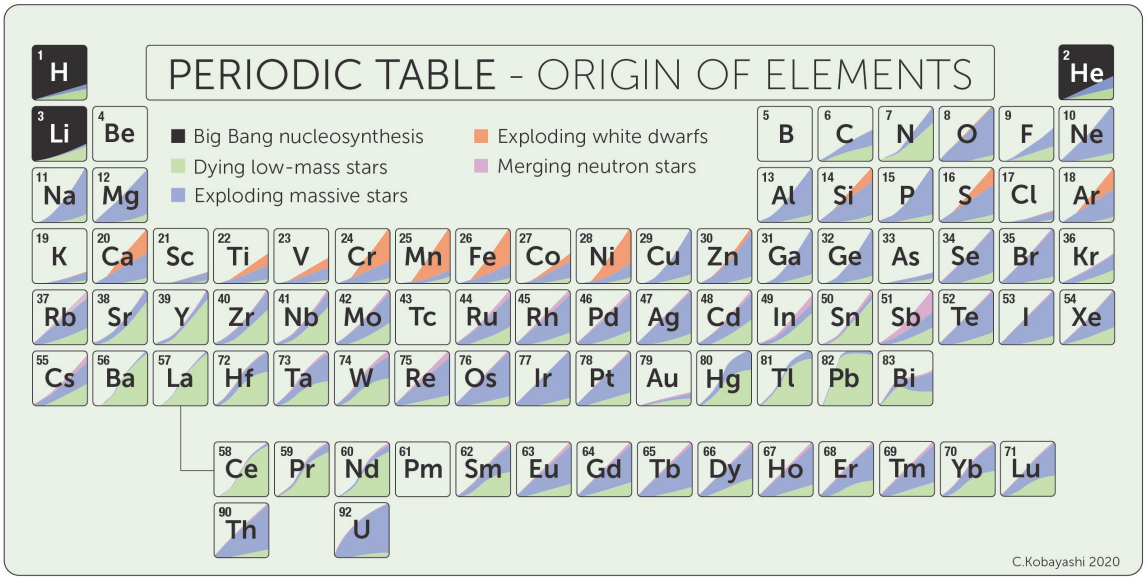


Figure 9.2. This figure is a press-release version of Fig. 39 published by Kobayashi et al. (2020). Its shows the source of each element through cosmic time as colored regions changing from left to right (high redshift to present day) in each tile.

of galaxies, as well as our definitions for chemical abundance. We show in Sec. 9.3 how various stellar chemical abundances in galaxies evolve through cosmic time, and demonstrate that the [O/Fe] abundance ratio in particular tightly predicts the assembly history of the host

galaxy, as well as compare our results with those from the SAMI galaxy survey (Croom et al., 2012; van de Sande et al., 2017). In Sec. 9.4 we consider specific cases to illustrate how abundances evolve, before summarizing our understanding of chemical evolution in galaxies in Sec. 9.5. We finish with exciting results of the first Milky Way-like galaxy in terms of chemical abundances found within a cosmological simulation in Sec. 9.6, before presenting our conclusions in Sec. 9.7

9.2 Sample of Galaxies and Definitions

We select galaxies from the *Magneticum Pathfinder* simulation (Dolag et al., 2025), specifically from Box4/uhr and Box3/uhr, as described in more detail in Chap. 2. These galaxies are traced back in time using L-BaseTree (Springel et al., 2005c), where the main progenitor branch is typically defined by following at every split the progenitor which in the snapshot prior had the highest number of particles. We use here a minor alteration, where we choose the progenitor branch which over a depth of three prior snapshots has the highest average stellar mass. This method largely matches the typical version at the depth of only one snapshot, with identical tracks up until $z = 4.2$ for 94% of the set of galaxies. In some cases, however, the higher depth chosen here successfully avoids following a track which strongly drops in mass over a few snapshots, and which would bias our results.

Generally, we consider either SUBFIND (Springel et al., 2001b; Dolag et al., 2009) or particle properties. The former are given directly by the structure finder SUBFIND and include the total stellar ($M_{\rm str}$) and baryonic (stellar+gas) mass ($M_{\rm b}$) assigned to the central galaxy, as well as the virial mass of the halo ($M_{\rm vir}$).

For the other set of properties, including our stellar chemical abundances, we directly read in the particles assigned to the central galaxy by SUBFIND and cut them down to only those within $0.1 r_{\rm vir}$ from the center. This avoids including diffuse stellar material in the far outskirts, and the resulting stellar mass function, stellar mass-halo mass and stellar mass-size relation of our simulated galaxies well capture the observational relations (Dolag et al., 2025). The stellar mass within this radius is defined as $M_{\rm gal}$. Throughout this work, we will primarily consider a set of 1208 central galaxies with $M_{\rm gal} > 10^{10}\,M_\odot$ at $z = 0$.

With this cut, we then determine the stellar center-of-mass via a shrinking-sphere method with shrinking factor of 5% per iteration (Power et al., 2003), and shift all particles onto the new center. This ensures that we center on the stellar body as opposed to the point of deepest potential used by SUBFIND to define the center of the subhalo, which may diverge in disturbed systems (even if the offset is typically negligible). From the newly shifted set of particles we then determine the stellar half-mass radius $r_{1/2,\rm str}$ as described by Valenzuela et al. (2024). All our particle properties beyond the galaxy stellar mass $M_{\rm gal}$ are calculated within $3\,r_{1/2,\rm str}$. These include the star-formation rate (by summing up the SFR of all gas particles), the b-value (see e.g. Teklu et al., 2015), and the mass-weighted mean stellar age $\langle age \rangle_{str}$.

Chemical properties are also determined within $3\,r_{1/2,\mathrm{str}}$. Abundance ratios such as [O/Fe] are defined as the total mass of oxygen in stars divided by the total mass of iron in stars. Note that we use stellar instead of gas abundances, unless explicitly stated otherwise. We use square brackets to denote that we have normalized by the corresponding value for the Sun. That is to say, for two elements A and B:

$$\begin{aligned}[A/B] &\equiv \log_{10}\left(\frac{n_\mathrm{A}}{n_\mathrm{B}}\right) - \log_{10}\left(\frac{n_\mathrm{A,Sun}}{n_\mathrm{B,Sun}}\right), \\ &= \log_{10}\left(\frac{m_\mathrm{A}}{m_\mathrm{B}}\right) - \log_{10}\left(\frac{m_\mathrm{A,Sun}}{m_\mathrm{B,Sun}}\right),\end{aligned}$$

where n_A and m_A are the total number density and mass of element A within $3 \cdot r_{1/2,\mathrm{str}}$, while the solar values are denoted with subscript “Sun". We use solar mass fractions given by Wiersma et al. (2009). This normalization ensures comparability with abundances ratios measured in number density as the division by the solar value in either case removes the unit dependence.

The star formation and chemical enrichment follows the model by Tornatore et al. (2007), which we describe in more detail in chapter 2, with yields for our SNe Type II by Woosley & Weaver (1995), Type Ia by Thielemann et al. (2003), and AGB stars by van den Hoek & Groenewegen (1997). We note here that because *Magneticum Pathfinder* was run with the yield tables by Woosley & Weaver (1995) for Type II SNe, which are known to overproduce Fe (Kobayashi, 2025), our absolute values of [α/Fe] will be somewhat lower than expected in cases where the primary source of Fe is not yet Type Ia SNe. However, as Type II SNe remain the primary source for α-elements, this does not alter the relative trends among our simulated galaxies in the [α/Fe] versus [Fe/H] plane, as we show in Fig. 9.3. There we plot the direction traveled in the [O/Fe]-[Fe/H] plane for a given enrichment event, split by type (top to bottom going from Type II SNe of increasing initial masses, with Type Ia at the bottom) as well as by the amount of metals added in the event relative to the existing amount present (left to right, going from an event that adds little new metals to one that dominates the new chemical composition). Arrows of different color are for stars of different starting metallicities for the Type II SNe (Woosley & Weaver, 1995), while our Type Ia SNe yields are metallicity independent (Thielemann et al., 2003).

We find that the Type II SNe with higher initial mass of the star strongly enhance the [O/Fe] abundance ratio, while adding little Fe – in the case of $M_{*,\mathrm{ini}} = 40 M_\odot$ with low stellar metallicity even tending toward sub-solar [Fe/H]. By contrast, lower mass Type II SNe actually decrease the [O/Fe] ratio, in much a similar manner to the Type Ia SNe.

9.3 Evolution of Alpha-Enhancement

We first consider the evolution of metal ratios within galaxies through time to see if there are fundamental differences in the metal distributions of galaxies of comparable mass at high redshift versus low redshift. We will use the [O/Fe] abundance in place of the full [α/Fe], as

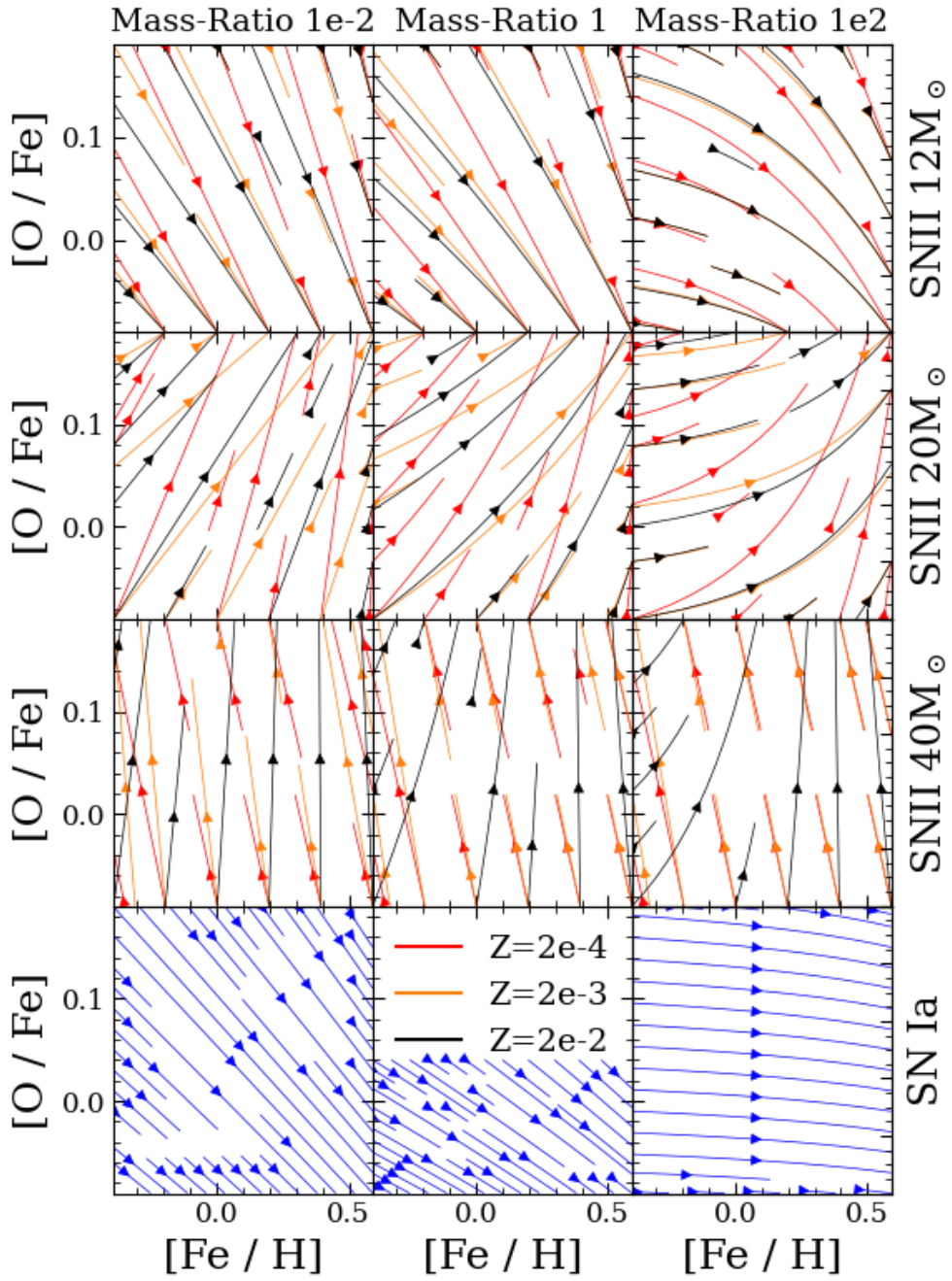


Figure 9.3. Direction in the [O/Fe]-[Fe/H] plane for a single enrichment event from a SNe Type II (*top three rows*) and Type Ia (*bottom row*). Columns go from enrichment events adding only 1% mass, to enrichment events that dominate over the previous enrichment (*left* to *right*).

the Woosley & Weaver (1995) magnesium yield is also underestimated compared to newer yields (Kobayashi, 2025).

9.3.1 Stellar Chemical Abundances through Cosmic Time

Fig. 9.4 shows the stellar [O/Fe] versus [Fe/H] within $3 \cdot r_{1/2,\mathrm{str}}$ of all central galaxies of stellar mass $M_{gal} > 10^{10} M_{\odot}$ at different redshifts within the simulation (panels). Beginning at the top left and a redshift of $z = 5.3$, we find that all galaxies exhibit a noticeable alpha enhancement of [O/Fe]≈ 0.15 while having sub-solar iron abundance [Fe/H]< 0. As time

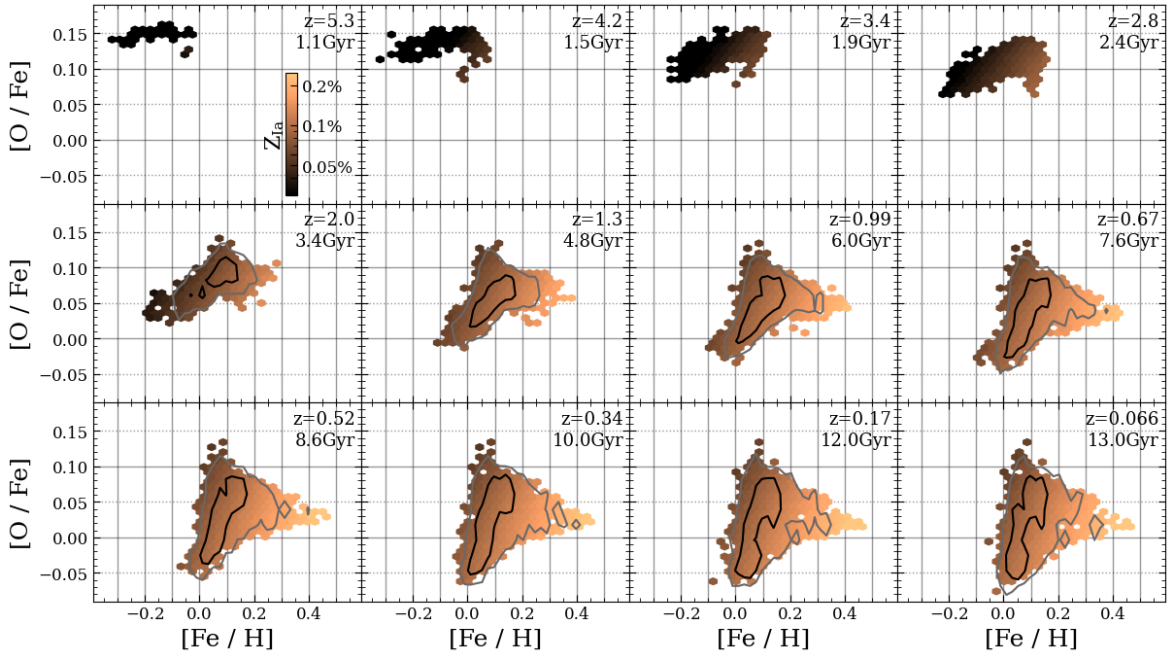


Figure 9.4. [O/Fe] versus [Fe/H] as a function of redshift (top left to bottom right panels). Plotted are all central galaxies with stellar masses $M_{\rm gal} > 10^{10} M_\odot$ at the given redshift (i.e., not traced), colored by the mass fraction of total metallicity which comes from SN type Ia. Contours enclose 50% (black) and 90% (gray) of these galaxies, respectively. Solid gridlines indicate multiples of 0.1 dex (≈ 25% change), while dotted give 0.05 dex.

progresses the distribution of galaxies travels down and to the right, reaching an average stellar [O/Fe]≈ 0.1 while [Fe/H] has been enhanced to around 0.1 at $z = 2.8$ (top right panel).

As we apply the same stellar mass cut throughout, this implies that the general pathway to reaching $M_{gal} > 10^{10} M_\odot$ *changes* with time. In the early Universe the more rapid star-formation is chemically enriched primarily by the faster acting Type II SNe, so by the core collapse supernovae of massive stars. These strongly enrich alpha elements such as oxygen, magnesium and silicon, while comparatively more weakly enriching iron (Kobayashi et al., 2020, see also Fig. 9.3). Thus a galaxy formed by $z = 5.3$ has very little iron relative for its given stellar mass. With time, the slower acting Type Ia begin enriching the gas within the galaxies as well, providing a significant source of iron while contribution negligible amounts of oxygen and other alpha elements. Thus SN Ia reduce [O/Fe] while increasing [Fe/H], pushing the distribution of stars in galaxies farther down and to the right, following the Type Ia arrows in Fig. 9.3.

We additionally color the galaxies by the fraction of mass contributed by Type Ia SNe to the total metals locked in stars ($Z_{\rm Ia}$), where black equates to less than 0.05% of the total metallicity coming from Type Ia SNe. When comparing galaxies at $z = 5.3$ versus $z = 2$ we find that, at a given iron abundance [Fe/H], the $Z_{\rm Ia}$ has increased while [O/Fe] has correspondingly decreased. Note that the fraction of total metals from Type Ia SNe is very low, but they do contribue a significant fraction of the iron-peak elements (see Fig. 9.2).

To emphasize this point, we plot in Fig. 9.5 the median mass fraction of stellar iron, calcium and oxygen which originate from Type Ia SNe as a function of cosmic time. We find

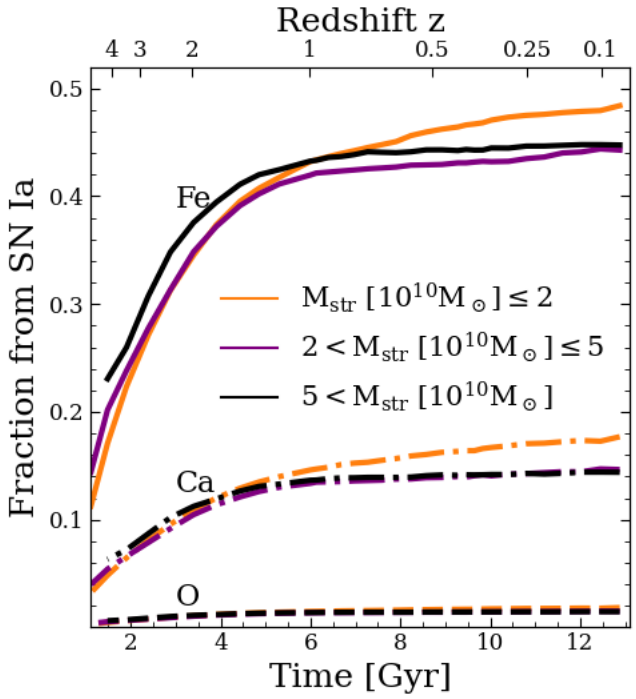


Figure 9.5. The median mass fraction of specific metals in stars which comes from SN type Ia as a function of time. At every redshift central galaxies are split into three stellar mass bins (colored lines) for the metals Fe (solid), Ca (dash-dotted), and O (dashed).

that oxygen shows little evolution, remaining at a low contribution from Type Ia SNe (< 5%). Calcium rises somewhat before leveling out at around $z = 2$ with a contribution of 15%, while we see that iron ends at nearly 50% coming from Type Ia SNe. There is little dependence of these fractions on the galaxy mass (different colored lines), with only the lowest mass bin increasing the contribution of Type Ia enrichment up until $z = 0$. This is likely because it contains the greatest number of disk galaxies, which have ongoing star formation and thus continually add more iron from Type Ia into newly formed stars. Quiescent galaxies naturally also continually enrich their gas through Type Ia SNe, but do not form any new stars, so their fraction stays relatively flat.

Having seen the global behavior of galaxies in the stellar [O/Fe] verus [Fe/H] abundance plane, it is interesting to ask how individual galaxies end up at their final position seen at $z = 0$. We split our galaxies by the redshift z_0 when they first reached $M_{\rm gal} > 5 \cdot 10^9 M_\odot$ and plot their tracks in [O/Fe]-[Fe/H] in Fig. 9.6. We see that the earliest forming galaxies end up with supersolar [O/Fe] by $z = 0$, though interestingly enough they do not represent the galaxies with the highest [O/Fe]. Those we find to have $z_0 = 4.2$ or $z_0 = 3.42$. This may be because the oldest galaxies tend to be the most massive, and thus by $z = 0$ have undergone extensive merging (O'Leary et al., 2021). The lower mass galaxies would then bring in younger, more iron enriched stars, thus lying at lower $z = 0$ [O/Fe] relative to galaxies which formed similarly early and bursty but did not merge quite as much.

When we consider the galaxies that form at $z_0 < 3$, we note that they no longer come from the upper left region of strongly enhanced [O/Fe]. Instead, by the time they have reached

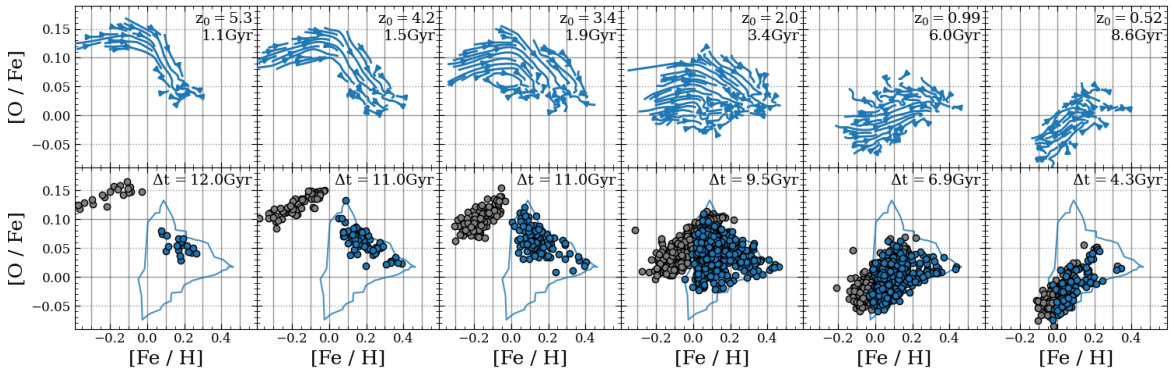


Figure 9.6. We split the sample of traced galaxies by the moment in time z_0 when they first reached $M_{\rm gal} > 5 \cdot 10^9 M_\odot$, with the earliest on the left and latest on the right (indicated in the top right of each panel). *Top Row:* Traced path of those galaxies in the [O/Fe]–[Fe/H] plane. *Bottom Row:* Starting (gray) and ending points (blue) of the galaxies in the plane. The blue line gives the outline of the total sample of all galaxies at $z = 0$. Solid gridlines indicate multiples of 0.1 dex ($\approx 25\%$ change), while dotted give 0.05 dex.

$M_{\rm gal} = 1 \times 10^{10} M_\odot$, which is when they are included in the plot, their stellar [O/Fe] already has had significant contributions from Type Ia SNe. Naturally, the oldest stars of the galaxy would have still formed with the same enhanced [O/Fe] as those with $z_0 > 3$, but they then went on to have more extended star formation histories, which means more enrichment into the gas from Type Ia SNe before it was locked into the stars.

We can see this disconnect between the gas and stars by plotting the relative difference of the stellar versus gas [O/Fe] abundance, which we do in Fig. 9.7 against the mean stellar age converted into a mean stellar formation redshift. As expected, we find a strong correlation, with older galaxies showing strongly enhanced stellar [O/Fe] relative to the [O/Fe] abundance within the gas. For the youngest galaxies this ratio becomes unity, because the gas within the galaxy is the same gas from which stars are still being actively formed – hence they share similar abundance ratios.

However, there remains a difference between the star forming gas (and thus stellar abundances) relative to the intergalactic medium, which we can see in the bottom panel of Fig. 9.7. We plot there the ratio between the total metallicity [Z/H] of the stars and gas, and find that the gas is generally more metal rich than the stars across all galaxies. This demonstrates that the equality seen in the stellar and gaseous [O/Fe] for the young galaxies is a result of our yields converging at maximum Type Ia contribution toward a fixed [O/Fe] of around solar (see Fig. 9.4). In truth, the gas is still being enriched until $z = 0$ by both Type II and Ia SNe, thus reaching an overall higher metallicity $[\mathrm{Z/H}]_{\rm gas} > [\mathrm{Z/H}]_{\rm str}$ while having similar [O/Fe]. We also find rare cases of old galaxies with higher stellar metallicity compared to their gas, which we find to be the case for quiescent galaxies. The majority of the total metallicity from SNe comes from Type II (see Fig. 9.5), so if the gas of this first starburst is ejected and new, pristine gas replaces it, then even though this new gas is continually enriched by AGB winds and Type Ia SNe, the lack of the Type II enrichment will result in a relatively lower metallicity.

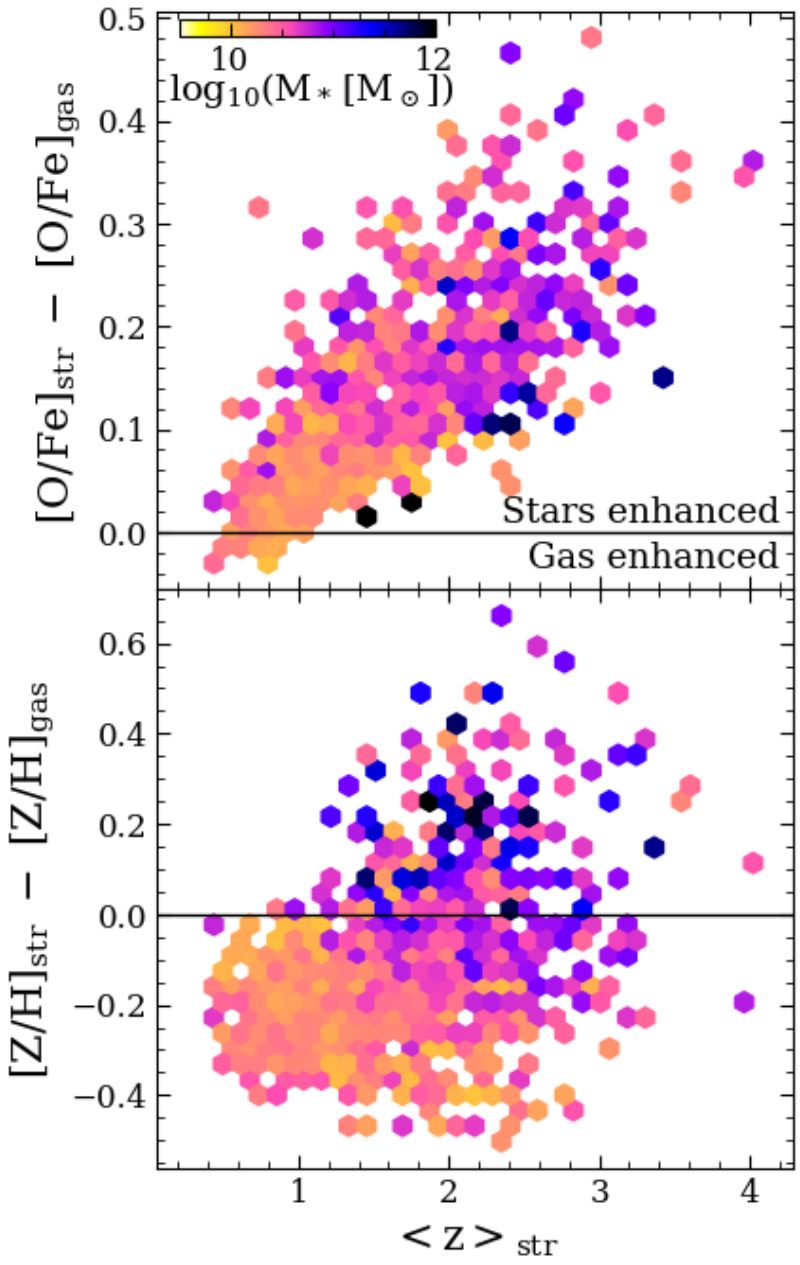


Figure 9.7. *Top:* Difference in [O/Fe] between the stellar and gas phase within $3 \cdot r_{1/2,\mathrm{str}}$ plotted as a function of the mass-weighted formation redshift of the stars. Points are colored by the stellar mass. The horizontal black line splits galaxies where either the stars (above) or the gas (below) have higher [O/Fe]. *Bottom:* As above but for total metallicity [Z/H] instead of [O/Fe].

9.3.2 Distinguishing Galaxies

We then turn to the question whether stellar metals can assist in distinguishing galaxy evolutionary histories. To this end, in Fig. 9.8 we split the 1208 galaxies in our sample at $z \approx 0$ by their stellar half-mass radius (top row) and stellar mass (middle row) into five bins of at least 180 galaxies each. Within each bin we then plot $z_{1/2,\,\mathrm{stars}}$, defined as the redshift when the galaxy first reached half of its final stellar mass, against the alpha-enhancement [O/Fe].

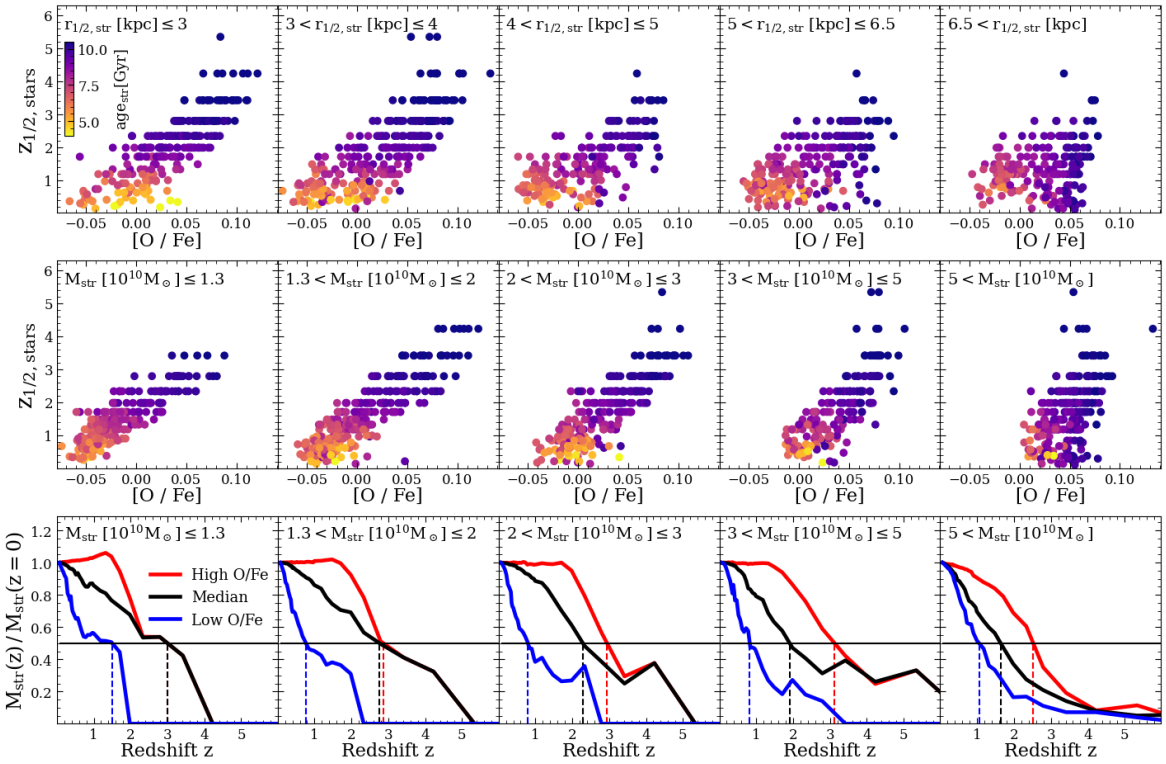


Figure 9.8. *Top Row:* Redshift when the main progenitor galaxy first reached 50% of its final stellar mass as a function of the alpha enhancement [O/Fe]. From left to right galaxies are binned by their half mass radii $r_{1/2,\mathrm{str}}$. Colored by the mass-weighted average age of the stars. *Middle Row:* As the top row but with galaxies binned by their stellar mass. *Bottom Row:* The median stellar mass accretion histories of all galaxies in the five stellar mass bins (thick black line) as well as the galaxies with final [O/Fe] within the upper (red) and lower (blue) $1\,\sigma$ of their mass bin.

For the smaller galaxies there is a clear correlation, consistent with our findings from Sec. 9.3. This demonstrates that the abundances locked in the stars directly dates when the galaxy itself was formed. An early, bursty formation results in a high [O/Fe] abundance ratio, while later, more extended formation histories result in a lower [O/Fe]. It is nonetheless remarkable how tight the relation is for compact galaxies with half-mass radii of $R \leq 4\,\mathrm{kpc}$, where for example a measured stellar [O/Fe]> 0.06 guarantees that the galaxy had assembled half of its final stellar mass into a single progenitor galaxy by $z \geq 2$.

For the bin with the largest galaxies (right-most column of the top row) the correlation disappears. This can be understood when considering the mean stellar age $\langle age \rangle_{str}$ of these galaxies, as given by the color. The galaxies retain a correlation between the stellar age and [O/Fe] abundance, where increasing [O/Fe] (left to right) still correlates with increasing age (orange to purple). However, those with the highest [O/Fe]≈ 0.05 now exhibit a diverse behavior for when the galaxy first reached half its stellar mass, ranging from $z_{1/2,\,\mathrm{stars}} = 4$ all the way down to $z_{1/2,\,\mathrm{stars}} \approx 0.2$. It follows then that this bin contains many galaxies which have undergone significant merging, where multiple older stellar populations (with correspondingly higher [O/Fe], see Fig. 9.4) only merge together at later times. The formation redshift $z_{1/2,\,\mathrm{stars}}$ is then low while the stars and their metals indicate an older age.

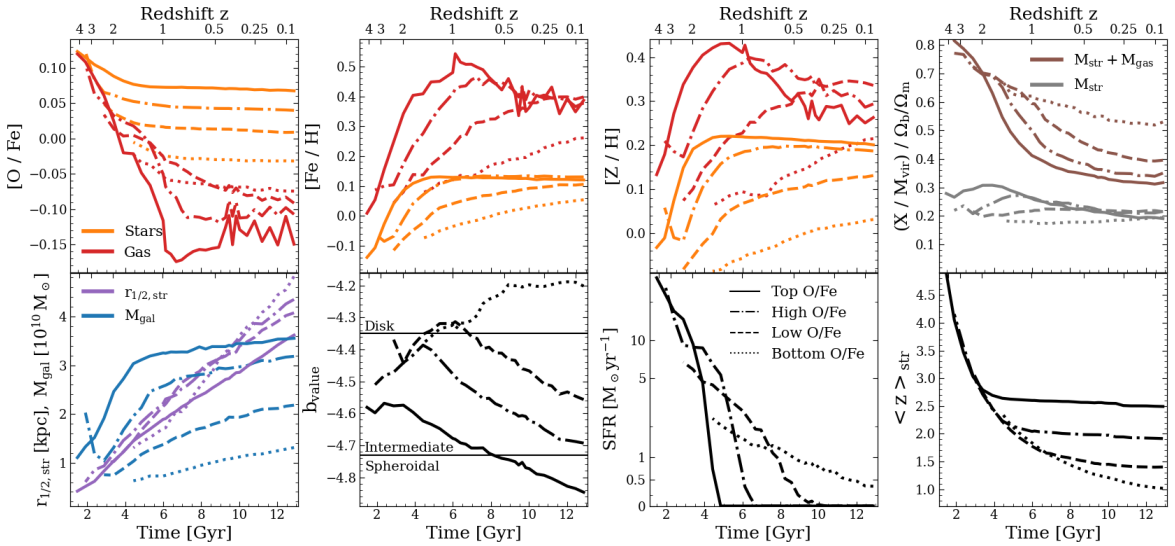


Figure 9.9. Traced median properties of our sample of galaxies split by their final [O/Fe] into four groups (highest to lowest, solid to dotted lines). Lines are only drawn when the main progenitors of at least 50 galaxies in the bin have $M_{\rm gal} > 5 \cdot 10^9 M_\odot$ at the given time. *Top Row:* The first three panels show the evolution of stellar (red) and gas phase (yellow) [O/Fe], [Fe/H] and total metallicity [Z/H] within $3 \cdot r_{1/2,\rm str}$. The baryon conversion efficiency (gray) and baryon fraction relative to cosmic (brown) are shown in the fourth panel. *Bottom Row:* The first panel shows stellar mass (blue) and stellar half-mass radius (purple) as a function of time, while the second to fourth panel plot the b-value, star formation rate and average stellar age, respectively.

When splitting the sample of galaxies instead by the stellar mass, the correlation now persists within all bins. From left to right, the Pearson correlation coefficient between [O/Fe] and $z_{1/2,\,\rm stars}$ is $\rho = 0.86, 0.88, 0.85, 0.79$ and 0.55, respectively. The highest mass bin thus still retains the relation, where the largest radial bin did not. This may be because the split by stellar mass also includes an implicit split by morphology, with the highest radius bin including 81 disks where the highest mass bin has only 17. At any rate, we find that an accurate measure of stellar mass and [O/Fe] allows for a reliable prediction of the formation redshift of the galaxy.

To finish this point, we plot as the last row of Fig. 9.8 the median stellar mass accretion histories for the galaxies within the five stellar mass bins (black solid line), as well as for those with [O/Fe] values in the top/bottom 1σ of the bin (red/blue solid lines). We find that galaxies which end with comparable stellar masses but higher [O/Fe] will have accreted their masses much earlier than those with lower [O/Fe]. In particular for galaxies with $M_{\rm gal} < 5 \cdot 10^{10} M_\odot$, we find that most galaxies with the 1σ-lowest [O/Fe] of their respective mass bin were not yet present at a redshift of $z > 3$.

To see whether these different formation histories manifest themselves in other properties of the galaxies, we split our $z = 0$ sample into four equal bins in stellar [O/Fe] and trace them back trough time, plotting their properties in Fig. 9.9. Galaxies with the highest to lowest [O/Fe] are plotted as solid to dotted lines, as indicated in the legend.

Beginning with the top left panel, we plot the evolution in [O/Fe] for the gas and stars in the main progenitor branch of each galaxy. We find that all four bins begin with similar stellar



and gas [O/Fe] which decreases steadily with time. For the earliest forming galaxies of the highest [O/Fe] bin, the gas is already significantly sub-solar in [O/Fe] abundance while the stars freeze at a super-solar [O/Fe]= 0.06. For galaxies with low [O/Fe] at $z = 0$, there is less of a difference in the gas and stellar abundances. We plot the same for the [Fe/H] abundance in the second panel of the top row, finding that the gas [Fe/H] is always higher than that of the stars. The top bin plateaus in stellar iron abundance by $z = 2$ and in gas iron abundance by $z = 1$, with the lower [O/Fe] bins exhibiting the same behavior at later times.

In the third panel of the top row we plot the total metallicity, and find that this actually decreases for the gas over time for the two bins with highest [O/Fe] (corresponding to the bins with the oldest two galaxies). This implies that there is either some amount of pristine gas inflow at later times which lowers the mean metallicity of the gas, or that the metal enriched gas is ejected with time. We find the former to be more likely when considering the mass in baryons that is bound to the galaxy relative to the expected cosmic mean, which we plot in the fourth panel of the top row of Fig. 9.9. For the galaxies of highest [O/Fe] this fraction decreases significantly toward $z = 0$, indicating the presence of many satellites (where likely some amount would also merge into the central galaxy, thus lowering its average gas metallicity), as the alternative would require nearly 60% of the baryons in the galaxy to be ejected between $z = 2$ and $z = 0$.

We then consider in the first panel of the lower row of Fig. 9.9 the evolution in stellar mass and size. The galaxies of highest [O/Fe] grow the fastest and become the most massive, plateauing in $M_{\rm gal}$ by around $z = 1$, while galaxies in the other bins more continually grow in mass, and do so at later times. The galaxy sizes show the exact opposite behavior, where the galaxies of lowest [O/Fe] grow the largest. Together with their relatively lower stellar masses, this implies that this bin contains a significant amount of disks. We can confirm this hypothesis by plotting the b-value (Teklu et al., 2015) in the second panel of the bottom row. Indeed, the galaxies in with lowest [O/Fe] retain a high b-value, which traces the amount of ordered angular momentum of the stellar distribution and thus correlates with the diskiness of the galaxy. By contrast, the galaxies with highest [O/Fe] show the most spheroidal stellar distributions, with the other bins in between.

In the third panel of the lower row of Fig. 9.9 we see that this matches the behavior in star formation rate, as the disky low [O/Fe] galaxies retain some amount of their star formation, while the spheroidals with the highest [O/Fe] peak earlier and at much higher star formation rates before rapidly quenching by $z = 2$, not unlike the recently observed massive quiescent galaxies (Hamadouche et al., 2026). Indeed, we already discussed how simulated quenched galaxies at high redshifts have enhanced stellar [O/Fe] relative to their star forming counterparts (see chapter 3, Kimmig et al., 2025b). The consequence of this lack of star formation is apparent in the mean stellar ages, which we plot in the bottom right panel of Fig. 9.9. The high [O/Fe] galaxies plateau at a stellar age of around $z = 2.5$, while galaxies of low [O/Fe] continue forming new stars until $z = 0$.

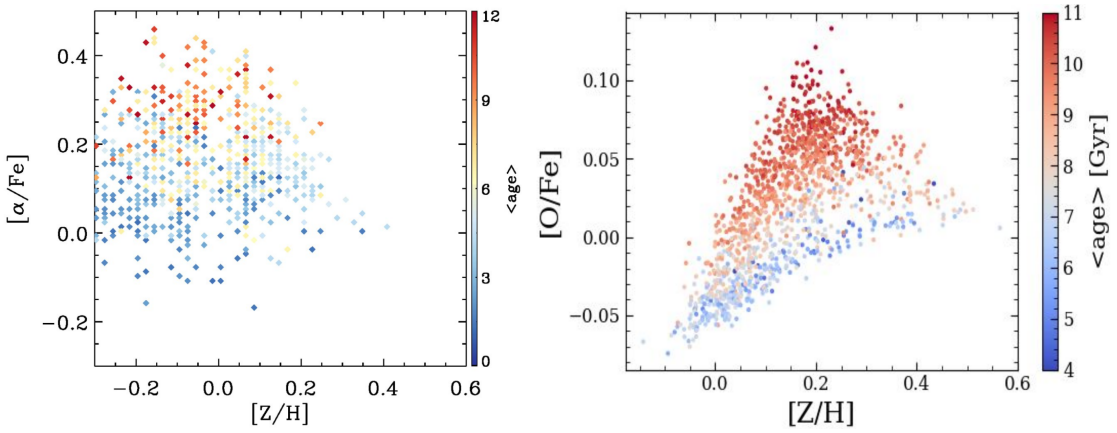


Figure 9.10. Relation between stellar [α/Fe] to [Z/H] for observed (*left*) and simulated (*right*) galaxies, colored by their mean stellar age. Observed data are determined by Scott et al. (2018) for SAMI galaxies via Lick absorption line strength indices (Faber, 1973; Trager et al., 1998).

9.3.3 Comparison to the SAMI Survey

Given the clear correlations that we find for our simulated galaxies, it is prudent to compare this result to observed galaxies. We do so with data from the SAMI galaxy survey (Croom et al., 2012; van de Sande et al., 2017), where Scott et al. (2018) determined stellar chemical abundances such as [α/Fe] as well as mean stellar ages via Lick absorption line strength indices (Faber, 1973; Trager et al., 1998). We plot [α/Fe] versus metallitcity [Z/H] in the left panel of Fig. 9.10, with our simulated galaxies on the right. In both cases we find the mean stellar age (color) to be largely independent of metallicity and instead to correlate strongly with [α/Fe].

We note that the metallicities [Z/H] of our simulated galaxies are higher by around 0.2 dex. This is intriguing given other findings by Kudritzki et al. (2021) and Dolag et al. (2025) that the *Magneticum* galaxies closely follow the stellar mass-metallicity relation, which may be because the observed metallicities there were not computed through Lick indices. Similarly, the range in [α/Fe] is much broader, which may be driver either by the inclusion of other α-elements beyond oxygen for the observed galaxies, or again by a larger scatter when using the Lick absorption line strength indexes to determine chemical abundances. A more thorough, apples-to-apples comparison is necessary in the future, but at the very least the SAMI galaxies appear to follow the same behavior in the relation between stellar age and [α/Fe] as what we find here for our simulated galaxies.

9.4 Considering Specific Cases

We turn to consider in more detail the evolution in stellar chemical abundances of individual systems, as opposed to population statistics. To this end, we choose six galaxies from the sample at $z = 0$, consisting of three disks and three spheroids. Fig. 9.11 shows g-band mock images generated via the method by Martin et al. (2022) of the galaxies as well as their line-of-sight velocity.

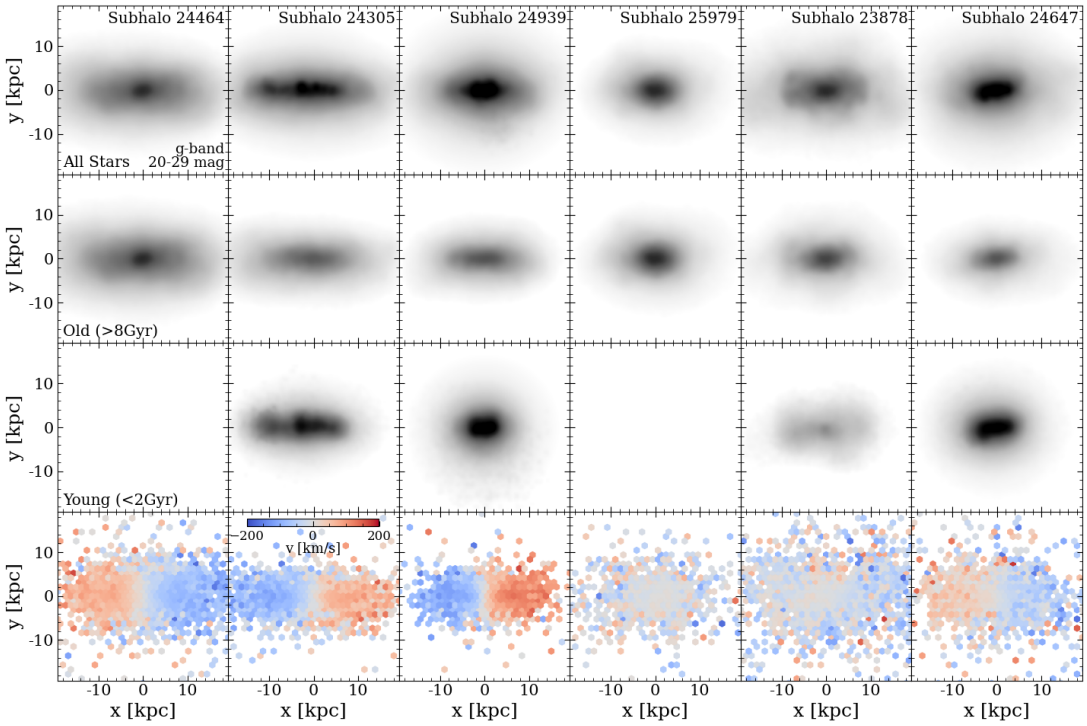


Figure 9.11. *First Row:* G-band mock images of a choice of galaxies at $z \approx 0$. The visualization is done via the method by Martin et al. (2022) and color-scaled from 20 to 29 mag (black to white). *Second* and *Third Row:* As the first, but only for the light from stars older than 8 Gyr ($z > 1.3$) or younger than 2 Gyr ($z < 0.25$). *Fourth Row:* Binned line-of-sight velocity of all star particles. The first three chosen galaxies are classified as disks by their b-value and the last three are spheroidals (where the last is fast rotating), while all galaxies have total stellar masses between $1 < \log_{10}(M_{\rm gal}[10^{10}\,M_\odot]) < 2$.

Beginning with the three disks, all of them have stellar masses of around $M_{\rm gal} \approx 2{\cdot}10^{10} M_\odot$. As can be seen from the young stars, however, the galaxies G24305 and G24939 had an extended star formation history where galaxy G24464 is particularly old. This is despite galaxy G24464 having the highest stellar half-mass radius at $r_{1/2,\rm str} = 5.5$kpc, where it is typically expected that later star formation occurs farther out in the disk and thus increases the half-mass radius (Teklu et al., 2023). By contrast, the youngest disk G24939 is also the most compact at $r_{1/2,\rm str} = 3$kpc and shows a prominent bulge which is younger than the surrounding disk ($\langle age \rangle_{\rm str} = 4.8$ Gyr at $0.5\,r_{1/2,\rm str}$ versus $\langle age \rangle_{\rm str} = 6.2$ Gyr at $3\,r_{1/2,\rm str}$).

This result for our example disk galaxies complicates the use of stellar mass and size as predictors of assembly history. To see that this is also the case for spheroidal galaxies, we again choose three with nearly identical masses of $M_{\rm gal} \approx 1.4 \cdot 10^{10} M_\odot$. In this case, the oldest galaxy G25979 ($\langle age \rangle_{\rm str} = 11.8$ Gyr) and the youngest G24647 ($\langle age \rangle_{\rm str} = 6.6$ Gyr) are both of similar size $r_{1/2,\rm str} = 2.3$kpc, where the largest G23878 is instead the one of intermediate age.

This diverse behavior makes it difficult from general properties such as mass and size to distinguish the evolutionary histories of galaxies. Earlier formation times are generally correlated with more compact sizes (van der Wel et al., 2014; Yang et al., 2025), but later accretion can strongly increase the half-mass radius (Oser et al., 2010). At the same time,

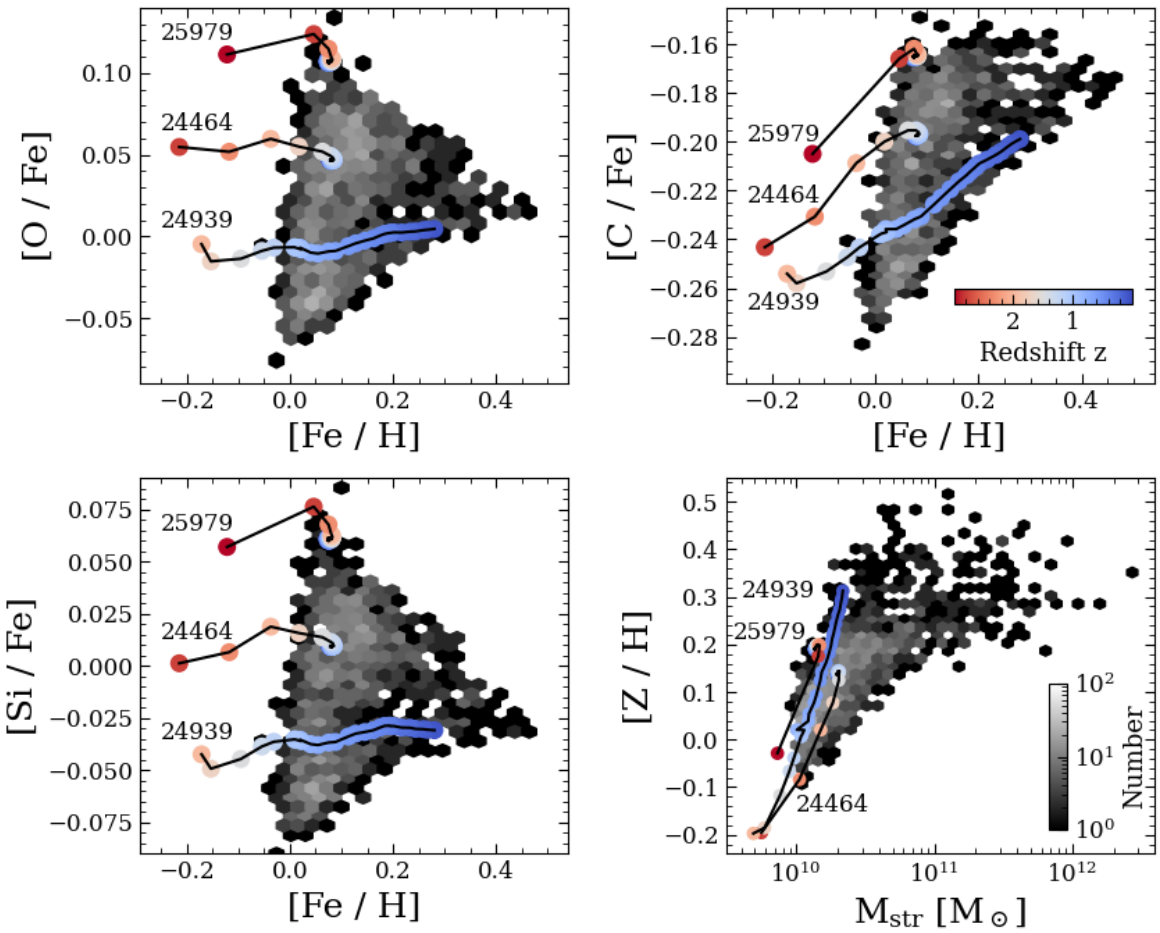


Figure 9.12. [O/Fe], [C/Fe] and [Si/Fe] versus [Fe/H] (*first* to *third* panels) and mass versus metallicity [Z/H] (*fourth* panel) of central galaxies with $M_{\rm gal} > 10^{10} M_{\odot}$ at z=0 (gray 2d-histograms). Also plotted are the tracks of two disk galaxies and one spheroidal shown in Fig. 9.11 (black lines), with the color of the dots corresponding with the redshift.

a rapid starburst at later times can work to reduce the stellar half-mass radius. Thus, it is once again through the [O/Fe] of these galaxies that their ages and formation can better be constrained, where for example from oldest to youngest spheroid G25979, G23878 and G24647, they also go from the highest to lowest [O/Fe]= 0.1, −0.02 and −0.05, matching expectations from Fig. 9.4.

We can plot how three of our galaxies evolved in terms of their stellar chemical abundances in Fig. 9.12, plotting them there from the moment they first reached $M_{\rm gal} \geq 5 \times 10^{10} M_{\odot}$. For all three galaxies, their stellar iron-abundance steadily increases with time, with the oldest G25979 reaching just over solar before it quenched, i.e., ceased forming new stars. By contrast, G24939 continues forming stars over an extended period of time, reaching [Fe/H]= 0.3. Interestingly, the abundance ratio to iron of both α-elements oxygen and silicon remained essentially flat in time, indicating that their evolution prior to crossing our stellar threshold of $M_{\rm gal} \geq 5 \times 10^{10} M_{\odot}$ already differed significantly, and dictated their final abundance ratio. Finally, we note that although G25979 is the oldest, because it is more massive it still reached a higher total stellar metallicity than G24464.

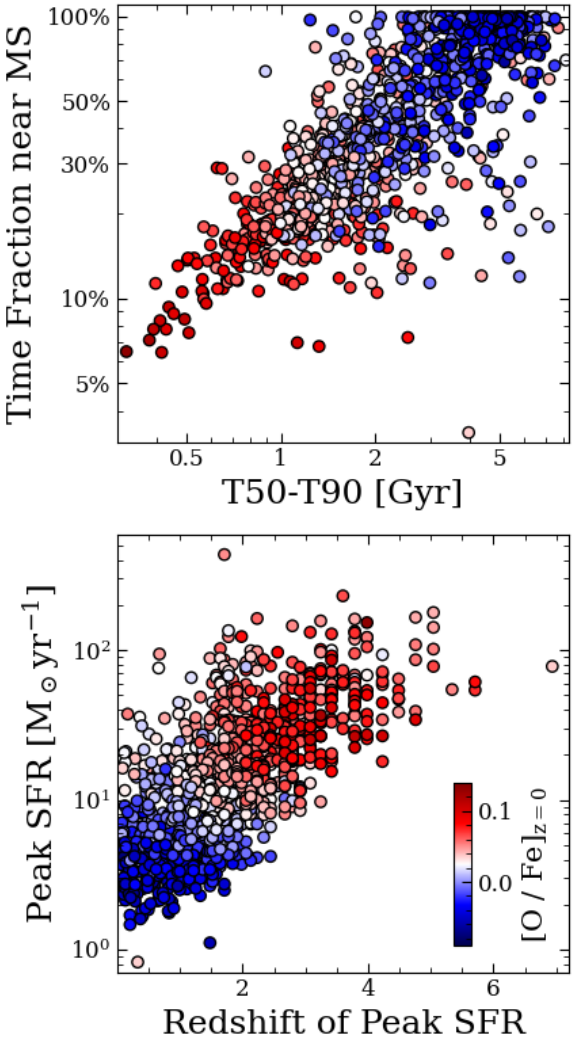


Figure 9.13. *Top:* The fraction of time spent within 1 dex of the main sequence as a function of the time between reaching 50% and 90% of the final stellar mass for all central galaxies with $M_{\rm gal} > 10^{10} M_{\odot}$ at z=0. Colored by the stellar [O/Fe] within $3 \cdot r_{1/2,\rm str}$. *Bottom:* The peak SFR reached by a galaxy versus the redshift when it reaches it, colored as above.

9.5 How Differences in Metallicity Emerge

We have demonstrated the power of the [O/Fe] versus [Fe/H] abundance plane in constraining galaxy evolution. Here we seek to link this result more explicitly to the star formation history of the galaxy. We can define the time a galaxy has spent having a star formation rate that is within 1 dex of the expected value from the Pearson et al. (2018) star forming main sequence given the galaxy stellar mass. Note that we begin counting this time from the point when the galaxy first reached $M_{\rm gal} \geq 5 \times 10^{10} M_{\odot}$. Based on our work on high redshift galaxies (see chapter 3, Kimmig et al., 2025b), we further quantify how extended the star formation was by determining $T50 - T90$. Tx is defined here as the stellar formation time of the oldest x-percent of the stellar mass in the galaxy, so $T50$ is the minimum age of 50% of the stellar mass in the galaxy.

Plotting the time fraction near the star forming main sequence as a function of $T50 - T90$ in the top panel of Fig. 9.13, we find as expected a tight correlation. This is because galaxies with short star formation histories (low $T50 - T90$) can by definition only have spent a short time with SFRs comparable to those of the star forming main sequence, while those with extended histories must also have spent significant time with elevated SFRs. Outliers are likely the result of galaxy mergers, which can alter the age distribution of stars (and thus $T50 - T90$) but cannot alter the amount of time the main progenitor had spent prior to the merger near the star forming main sequence. Those cases would scatter to high $T50 - T90$ and low fractions, which is precisely where we see some clustering in the top panel of Fig. 9.13.

We find that the position of a galaxy in this plot is also strongly correlated with its stellar [O/Fe] as given by the color, with short, bursty star formation histories resulting in high [O/Fe] while galaxies with extended histories have lower [O/Fe]. In the bottom panel of Fig. 9.13 we then plot the peak SFR that the galaxy achieved throughout its history against the redshift of that peak SFR, finding again a tight relation which correlates also with the stellar [O/Fe]. Overall, we find here that galaxies with extended star formation histories and low [O/Fe] tend to have formed later and at lower peak SFRs, while simultaneously spending a greater amount of their history on or near the star forming main sequence.

The fact that galaxies which formed early also formed in a more bursty manner, with shorter histories and higher peak SFRs (as is also found in observations, e.g., Popesso et al., 2023), gives the first insight into why, physically, the stellar [O/Fe] so well distinguishes old from young galaxies. It is because the physical conditions of star formation have changed through cosmic time. We show this in Fig. 9.14, where we plot the conversion, containment and amount of cycling for our galaxies at $z = 4.2$, $z = 2$ and $z = 0.066$ (top to bottom).

We note that the expected amount of baryons within each halo is given by the cosmic baryon fraction $f_\mathrm{b} = 16.8\%$ times the virial mass, so $M_{\mathrm{b,\,exp}} = M_\mathrm{vir} \cdot f_\mathrm{b}$. This gives us the stellar conversion efficiency $M_\mathrm{str}/M_{\mathrm{b,\,exp}}$ and the baryon fraction $M_\mathrm{b}/M_{\mathrm{b,\,exp}}$. Plotting the conversion efficiency against the baryon fraction in the first column of Fig. 9.14, we find that both values decreases for our galaxies with time. Put another way, high redshift galaxies both have more gas, as well as convert more of that gas into stars, the latter of which has been similarly found by both observations (Scoville et al., 2016) as well as models and simulations (Behroozi et al., 2013; Ceverino et al., 2024; Andalman et al., 2025).

Because of the unique implementation of our star formation model, which allows each gas particle to spawn up to four generations of stars (Dolag et al., 2025), we can actually trace whether the stars in a galaxy are the first generation (i.e., come from gas that has never formed another star before) or if their gas was pre-processed. We use this to define the fraction of stars which have previously formed a star (so are second to fourth generation) as $f_{\mathrm{str,\,2^{nd}\,Gen}}$, given as the colorbar in the first column of Fig. 9.14. There is a clear dependence where, for a given baryon fraction, galaxies that formed more stars did so not by converting a greater number of gas particles, but by converting the same gas multiple times (redder colors).

We plot $f_{\mathrm{str,\,2^{nd}\,Gen}}$ as a function of the galaxy stellar mass in the second column of Fig. 9.14, and color by the central stellar density. Across all redshifts, more massive galaxies

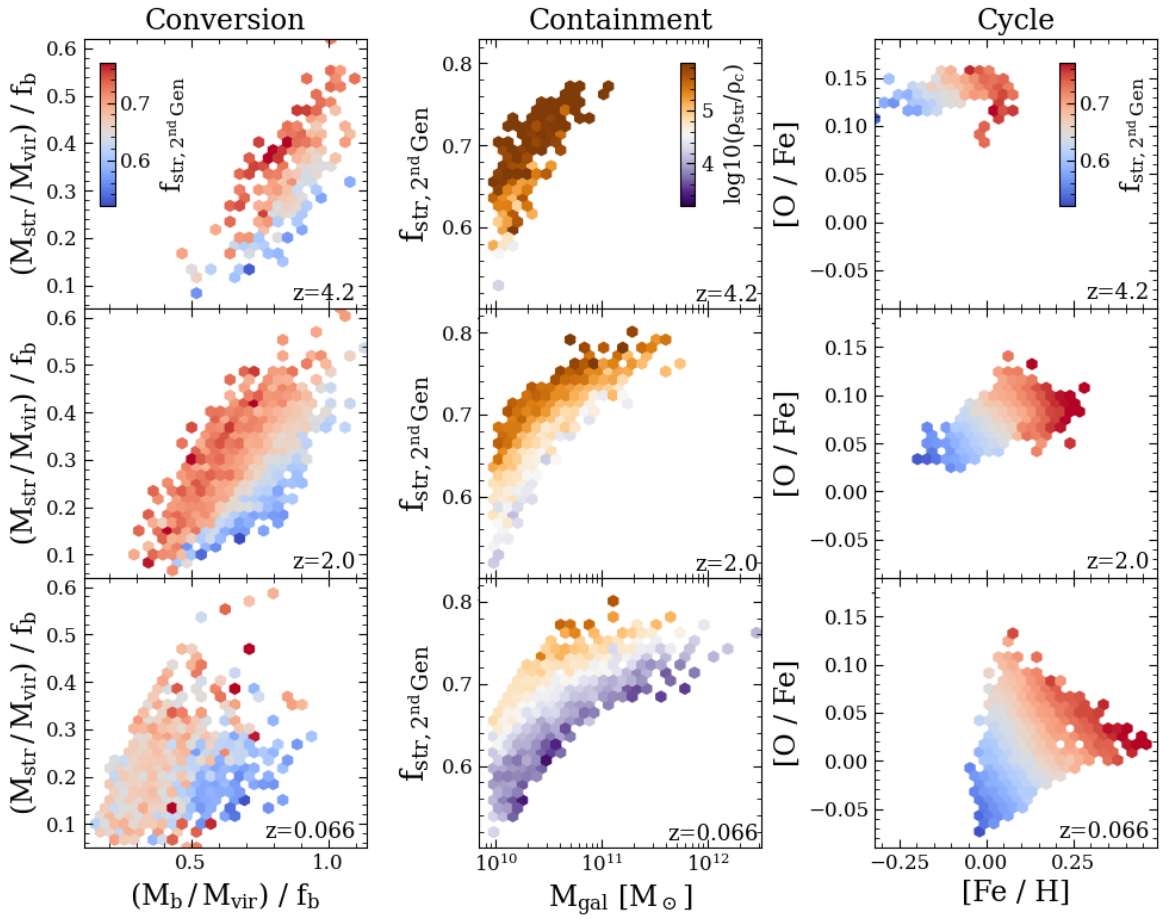


Figure 9.14. *Left Column:* Baryon conversion efficiency as a function of the baryon fraction for central galaxies with $M_{\rm gal} > 10^{10} M_{\odot}$, colored by the fraction of stars that are of 2nd generation and above, denoted as $f_{\rm str,2^{nd}Gen}$. Plotted at a redshift of $z = 4.2$, $z = 2$ and $z \approx 0$ (top to bottom). *Middle Column:* $f_{\rm str,2^{nd}Gen}$ versus the stellar mass $M_{\rm gal}$, colored by the stellar density (normalized by the critical density $\rho_{\rm c}$ at the given redshift). *Bottom Column:* [O/Fe] versus [Fe/H] colored by $f_{\rm str,2^{nd}Gen}$.

have cycled their gas more often and thus show higher amounts of second to fourth generation stars. This fact also naturally explains the emergence of the stellar mass-stellar metallicity relation. Because the stellar population birthed from a given gas particle will include some amount of massive stars, as dictated by the stellar initial mass function for our simulation (Chabrier, 2001), these rapidly enrich their surroundings with metals when they explode as Type II SNe. The timescale ($\approx 10\,$Myr) is short enough that this self-enriches the gas particle from which they came, thus driving up the metallicity in gas particles which have already formed a star before. Thus, galaxies with higher $f_{\rm str,\,2^{nd}\,Gen}$ also have higher stellar metallicities.

For a given stellar mass, we find that higher redshift galaxies tend toward higher $f_{\rm str,\,2^{nd}\,Gen}$. This can be understood when we color by the central stellar density, where we see that galaxies which are more compact for a given mass have a higher $f_{\rm str,\,2^{nd}\,Gen}$, and that higher redshift galaxies are more compact (van der Wel et al., 2014; Yang et al., 2025).

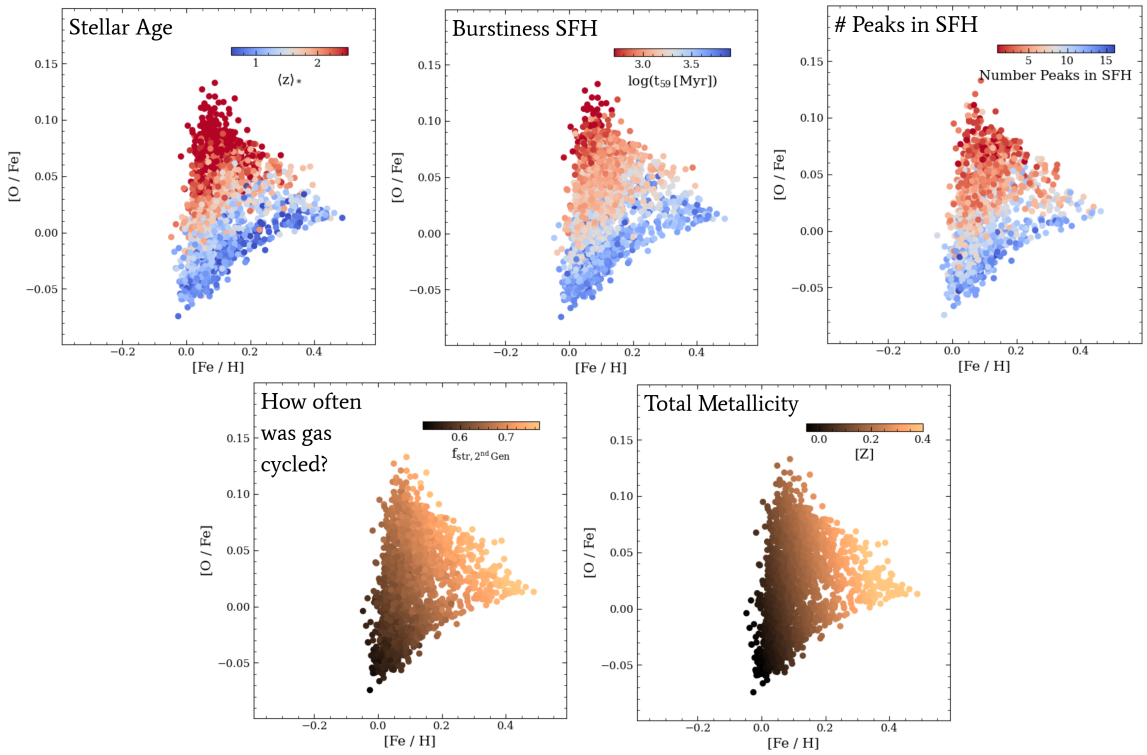


Figure 9.15. The stellar [O/Fe] versus [Fe/H] plane for simulated galaxies with $M_{\rm gal} \geq 10^{10} M_{\odot}$ at $z = 0$, colored in the upper row from left to right by their mean stellar formation redshift, $T50 - T09$, and the number of peaks of their star formation history, while in the bottom row they are colored by the fraction of second to fourth generation stars $f_{\rm str,\,2^{nd}\,Gen}$ and their total stellar metallicity.

Finally, we tie this result back to chemical abundances by plotting the stellar [O/Fe] versus [Fe/H] colored by $f_{\rm str,\,2^{nd}\,Gen}$ in the right column of Fig. 9.14. We see a clear trend with $f_{\rm str,\,2^{nd}\,Gen}$ going up and to the right, or equivalently toward higher oxygen abundance, as [O/Fe]/[Fe/H] = [O/H]. Because [O/H] is commonly understood as a tracer of overall metallicity (Kewley & Ellison, 2008; Kewley et al., 2019), this means that $f_{\rm str,\,2^{nd}\,Gen}$ indeed strongly correlates with the total metallicity, as could be expected from its positive trend with increasing mass that we discussed prior (middle column of Fig. 9.14).

It is interesting to note that the color-trend for $f_{\rm str,\,2^{nd}\,Gen}$ in the [O/Fe]-[Fe/H] plane goes almost perpendicular to the trend with mean stellar age that we saw in Fig. 9.10. We show this difference more clearly in Fig. 9.15, where we plot the stellar [O/Fe]-[Fe/H] plane for our simulated galaxies at $z = 0$ colored by two sets of properties. The upper row shows the first group, being the mass-weighted mean stellar formation redshift, the extendedness of the star formation history $T50 - T90$, and its number of peaks. Note that before counting the number of peaks in the SFR versus time plot for a given galaxy, we first LOESS smooth with a width of 100 Myrs. This first group of properties shows a clear trend with [O/Fe], while showing very little trend with [Fe/H].

Plotted in the lower row of Fig. 9.15 is the second group of properties, consisting of the fraction of second to fourth generation stars and the total stellar metallitic. Here we find instead a trend in color going up and to the right. We can summarize this differing behavior

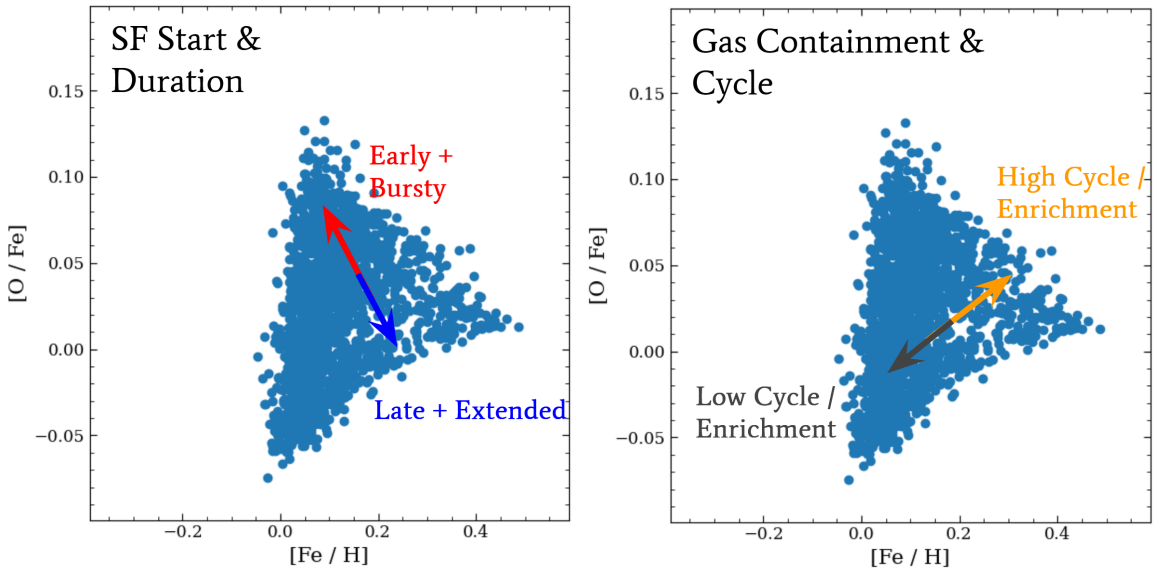


Figure 9.16. What the location of a galaxy in the stellar [O/Fe] versus [Fe/H] plane reveals about its star formation history (left) and the amount of cycling its gas underwent (right).

in Fig. 9.16. The history of the star formation within a galaxy is tightly encoded in the stellar [O/Fe] versus [Fe/H], with early and bursty formation resulting in strongly enhanced [O/Fe] with only slightly decreased [Fe/H] relative to the mean $z = 0$ galaxy, while late and extended star formation places a galaxy in the lower right of the diagram. By contrast, how the galaxy cycled its gas is strongly correlated with [Fe/H] and only subtly with [O/Fe]. A stronger containment and thus repeated cycling of the same gas results in strongly enhanced [Fe/H] and only marginally enhanced [O/Fe], while galaxies fed more with pristine gas lie in the lower left of the diagram.

9.6 Milky Way Metallicity

In the field of stellar chemical abundances, the best studied objects due to their proximity are the stars of the Milky Way (Steinmetz et al., 2006; Martell et al., 2017; Majewski et al., 2017; Gaia Collaboration et al., 2023), Andromeda (Escala et al., 2020) and their satellites (Hasselquist et al., 2021). For other galaxies, baring some exceptions such as direct measurements of blue supergiant stars in NGC 4258 (Kudritzki et al., 2024), single stellar population models are fitted to the integrated light instead (Tinsley, 1972; Vazdekis et al., 2010; Leja et al., 2017), which come with their own significant challenges (Kewley & Ellison, 2008; McDermid et al., 2015; Jofré et al., 2019). One of the most notable features found within the chemical abundances of the Milky Way stars is the existence of a high-α and low-α sequence in the [α/Fe] versus [Fe/H] diagram (Fuhrmann, 1998; Hayden et al., 2015). This origin of this bimodality has been extensively discussed, with common models to explain it being radial migration (Sellwood & Binney, 2002; Schönrich & Binney, 2009), where stars born in different radial zones and thus with differing abundance patterns are mixed radially, and that of a two-phase model (Chiappini et al., 1997; Grisoni et al., 2017), where the high-α

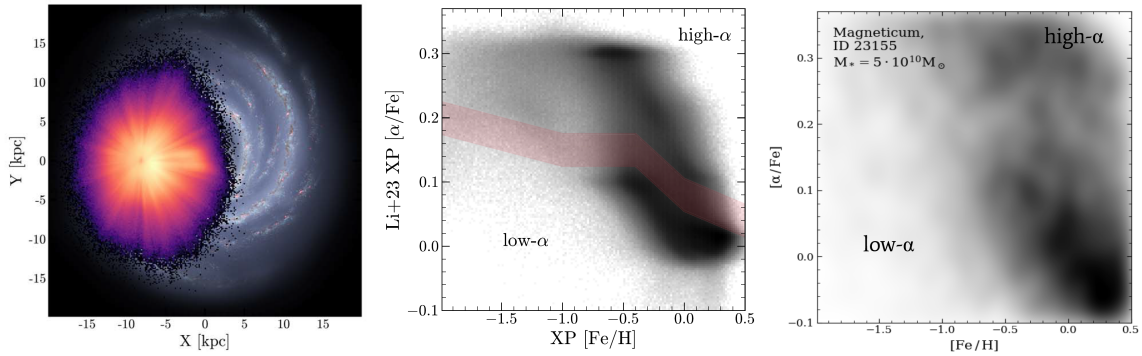


Figure 9.17. *Left:* Figure 1 from Chandra et al. (2024), showing the galactocentric distribution of their sample of stars laid over an artist's rendering of the Milky Way disk (NASA/JPL-Caltech/R. Hurt). *Center:* Figure 3 from Chandra et al. (2024) plotting the resulting [α/Fe] versus [Fe/H] abundances. *Right:* Our Milky Way-like galaxy which is of both comparable mass and with a comparable chemical abundance.

sequence was born first, after which a second, more extended star formation formed the low-α sequence.

We briefly consider here the case of the Milky Way-like galaxy which we identified in a newly run version of the *Box4/uhr* simulation from the *Magneticum Pathfinder* suite (Dolag et al., 2025), which crucially for our purposes was run with the updated metal yields by Nomoto et al. (2013) for Type II SNe. By selecting for galaxies of similar stellar mass to the Milky Way of $M_{\rm gal} = 5 \times 10^{10} M_\odot$, we could then identify those with particularly high dispersion in [α/Fe] at fixed [Fe/H] abundance. Note that here we define our α abundance with the three alpha elements of oxygen, magnesium and aluminum, as opposed to just oxygen as done prior.

In Fig. 9.17, we show the spatial distribution (left) and resulting chemical abundance pattern (center) for observed stars in the Milky Way as presented by Chandra et al. (2024). In the right panel we plot for our simulated Milky Way analogue the [α/Fe] versus [Fe/H] distribution of stellar particles within 15 kpc of the galaxy center of mass. We find that this simulated galaxy shows a remarkable agreement in chemical abundance to the stars of the Milky Way galaxy, with the same high-α and low-α sequences at comparable absolute abundances, and with a majority of the stellar mass being in the low-α stars – as is also the case for the Milky Way itself.

We can see the similarity of the bimodality even more strikingly when we split it into bins in height relative to the galactic disk and radius. This has been done by Imig et al. (2023) for observations of red giants stars within the Milky Way, where we show their figures 8 and 9 in Fig. 9.18. These show a clear bimodality in all radial bins within $R < 9$ kpc of the galactic center, with a tendency toward more low-α stars in the disk itself (bottom row) and high-α stars above (upper row). Note that they use magnesium as their alpha element here. They find the split in [Mg/Fe] to correlate strongly with the stellar ages, with an old high-α and a much younger low-α sequence, and conclude that their findings necessitate a two-infall

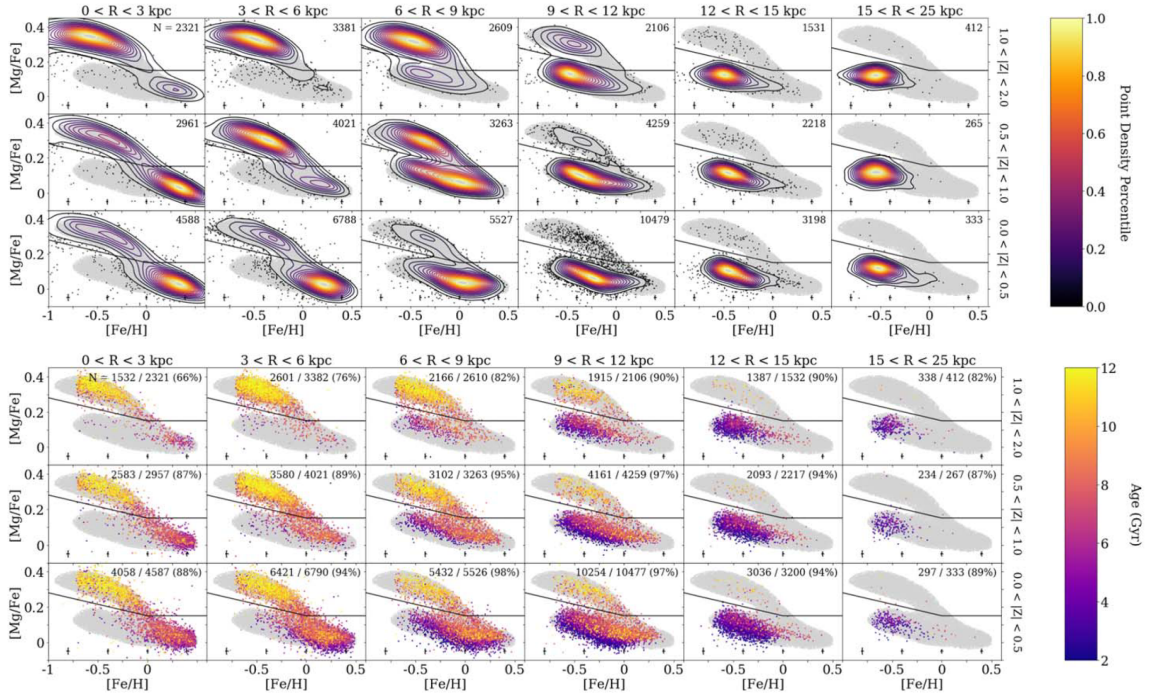


Figure 9.18. Figure 8 and Figure 9 from Imig et al. (2023), showing the point density (*top*) and stellar age (*bottom*) of their sample of red giants stars in the Milky Way, split into bins in radius and height above the stellar disk (columns and rows). The number of stars per bin is shown in the upper right.

scenario (Chiappini et al., 1997) or clumpy star formation as opposed to pure radial migration (Sellwood & Binney, 2002).

In Fig. 9.19 we plot the distribution of stellar particles within our Milky Way-like galaxy with the same kind of radial and height bins, rotating our galaxy edge-on based on the method by Valenzuela et al. (2024) to determine a height above the disk. We find again a very similar bimodality for this galaxy, with two distinct peaks in [Mg/Fe] for a given [Fe/H]. There are slight differences to the observations of the Milky Way itself, with less of a trend in disk height and instead more of a trend in radius, where most of the stars in the central region of our disk ($R < 3\,\mathrm{kpc}$) are low-α and iron enhanced. Our absolute [Mg/Fe] abundance of the high-α sequence is also lower. We thus modify their split (black line in Fig. 9.18) and decrease the cutoff by 0.1 dex, separating the two sequences by the line:

$$[\mathrm{Mg/Fe}] = \begin{cases} 0.05 - 0.13 \cdot [\mathrm{Fe/H}] & \text{if } [\mathrm{Fe/H}] \leq 0 \\ 0.05 & \text{otherwise.} \end{cases} \tag{9.1}$$

We plot the resulting age histograms in Fig. 9.20, finding somewhat surprisingly that the simulated galaxy has been quiescent for about 8 Gyr, and has formed most of its stars in a short 3 Gyr burst. Even still it exhibits the same age bimodality, where the high-α sequence (red lines) is consistently older than the low-α sequence (blue lines) across all radial bins, resulting in a clear bimodality of stellar ages (black line) in some of the bins. We have traced the formation history of the galaxy and confirmed that the stars formed in two distinct

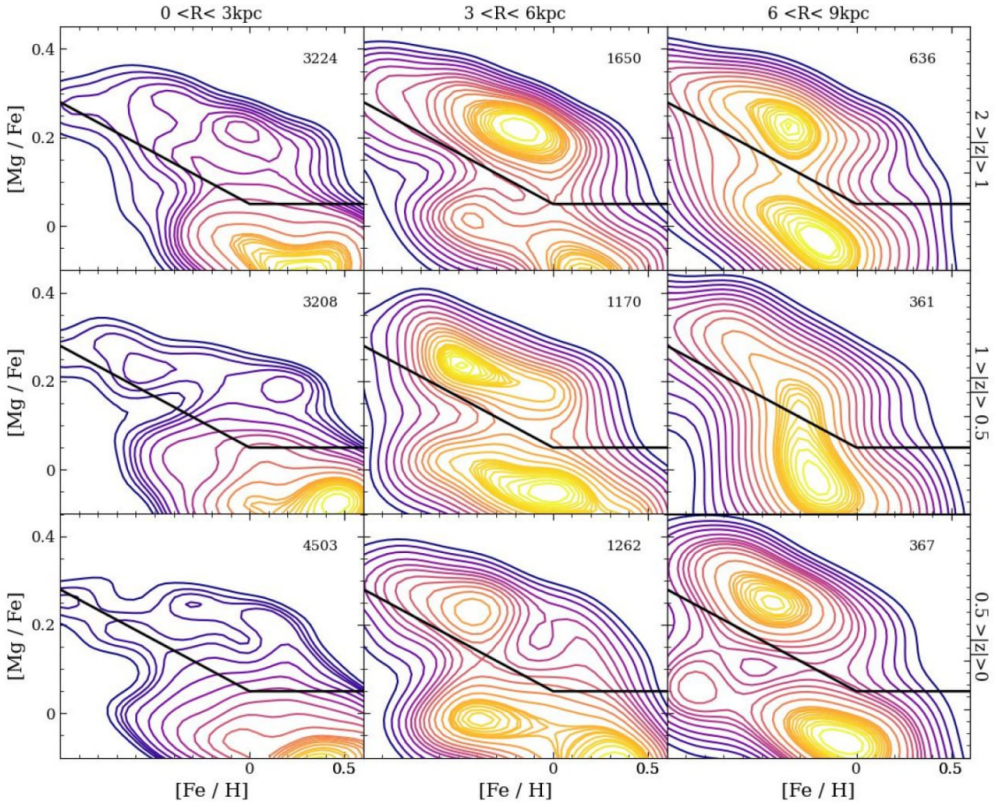


Figure 9.19. Point density of stellar particles in the [Mg/Fe] versus [Fe/H] plane for our Milky Way analogue, split into bins in radius and height above the stellar disk (columns and rows). The number of particles per bin is shown in the upper right.

bursts, with the second generation of low-α and high metallicity stellar particles born during a merger event that triggered a starburst at a lookback time of around 12 Gyr.

This result emphasizes that, so long as there is enough time since the formation of the first generation of high-α stars for Type Ia SNe to enrich the intergalactic medium, the next stars may already lie at significantly lower [Mg/Fe] abundances. Nonetheless, even in these cases the spread in stellar chemical abundance is a smoking gun for a two-infall type of formation, as argued by Imig et al. (2023) to occur also for the Milky Way galaxy. In future work we will search for similar Milky Way-analogues in the new MagneticumDAWN simulations (Remus et al., in prep.), which preliminary tests have already shown well reproduce the high redshift Universe. These simulations also include updated yield tables, and additionally trace the contribution from Type Ia SNe, Type II SNe, and AGB stars separately, allowing future studies to better distinguish the sources of metals in cosmological simulations.

9.7 Conclusions

By drawing on a sample of 1208 central galaxies with stellar masses of $M_* \geq 1 \times 10^{10} M_\odot$ from the *Magneticum Pathfinder* Box4/uhr simulation, we have explored here the evolution of their stellar chemical abundances through cosmic time. In Sec. 9.3, we showed how the stellar population of early galaxies are strongly enhanced in their α-abundance, because their

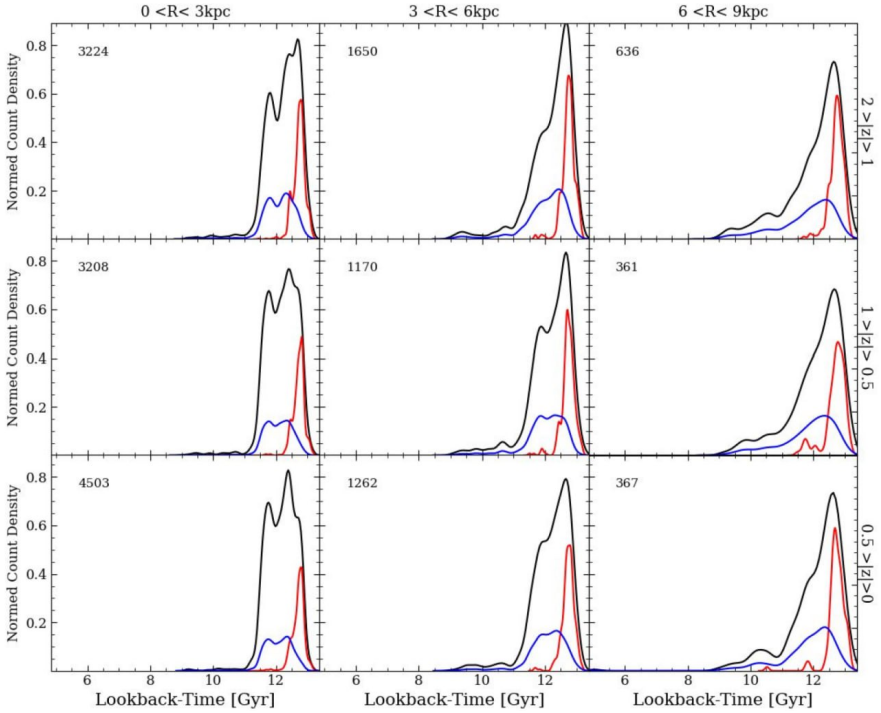


Figure 9.20. Age histograms of stellar particles in our simulated Milky Way analogue, split into radial and height bins (columns and rows). Plotted are the total age distribution (black) and the split by high-α (red) and low-α (blue) stellar particles. The number of particles per bin is shown in the upper right.

enrichment stems primarily from the quick explosions of massive stars as Type II supernovae. We characterize this abundance by [O/Fe], the ratio of the α-element oxygen over iron. Going toward lower redshifts [O/Fe] strongly decreases as [Fe/H] increases, driven by increasing contribution from slower acting Type Ia supernovae. By $z = 2$, almost half of the iron locked in the stars of galaxies comes from these Type Ia supernovae.

We then demonstrate that the differing timescales of Type Ia and Type II supernovae, and the fact that they enrich the intragalactic medium with different elements, allows both the mean stellar age as well as the redshift when a galaxy first assembled half its stars to be tightly predicted by its stellar [O/Fe]. This split works for all galaxies except those where the stellar mass from ex-situ sources, i.e., from merging, becomes significant. In those cases, which tend to be the most massive galaxies and the largest in size, a high [O/Fe] still implies a high mean stellar age, but the stars can have assembled from various progenitors at later times. Observed galaxies from the SAMI galaxy survey (Croom et al., 2012; van de Sande et al., 2017) also show the same correlation between [O/Fe] and stellar age, with little to no correlation to [Fe/H], though it has to be explored further to what degree this results from the Lick indices used to derive the properties (Scott et al., 2018).

We additionally find that the gas phase [O/Fe] is correlated with the stellar [O/Fe] via the stellar age, where older galaxies exhibit greater discrepancies between the two. Furthermore, galaxies of different morphologies tend to have different stellar [O/Fe], with spheroids having the highest while disks have the lowest [O/Fe].

In Sec. 9.4 we show that how long a galaxy evolved near the star forming main sequence (Popesso et al., 2023) correlates with the stellar [O/Fe], as does the peak star formation rate it reached. Earlier formed galaxies spend less time on the SFMS, reach higher peak SFRs, and consequently have higher [O/Fe].

We demonstrate that this has to do with the central stellar density reached in Sec. 9.5, finding that early forming galaxies reach higher central densities, and simultaneously convert a greater fraction of their gas into stars. Because gas particles in the simulation can spawn up to four stellar particles, we can additionally deduce that these high redshift galaxies are cycling the same gas particles multiple times. This indicates that the higher central density allows these galaxies to more efficiently retain their gas even during rapid bursts of star formation, thus strongly enriching it with α-elements through Type II supernovae. We identify two axes within the [O/Fe] versus [Fe/H] plane, where the begin and duration of star formation for a given galaxy most strongly correlate with [O/Fe], while the amount of gas cycling and overall enrichment correlates with both [O/Fe] and [Fe/H].

Finally, we examine the case of a Milky Way-like galaxy within a newly run version of *Magneticum Pathfinder* Box4/uhr that includes the updated Type II supernovae yield tables by Nomoto et al. (2013). This simulated galaxy shows the same type of bimodal distribution in the [O/Fe] versus [Fe/H] plane as observed for the Milky Way galaxy, with an older high-α branch and a younger low-α branch. Crucially, however, the simulated galaxy has been quiescent for over 8 Gyr, demonstrating that these bimodal distributions can emerge already on shorter timescales than are found for the Milky Way galaxy, with the only condition being that they are sufficiently long to incorporate enrichment slower acting Type Ia supernovae. Overall, stellar chemical abundances are a powerful tool to constrain both the formation of observed galaxies, as well as their enrichment cycles.

天の川　流れてぞありし　夏の月

Matsuo Bashō, circa 1660–1694

10

To Form or Not To Form Stars – Galaxy Evolution through Cosmic Time

This Chapter provides an overview of additional work on galaxy formation to which I contributed. Each Section is marked with the relevant information at the beginning.

10.1 The Star Formation Histories of Galaxies Through Cosmic Time

This Section summarizes findings from two publications by Fortuné et al., for which I am the third author and that directly connect to the work I presented in Chap. 8 and Chap. 9. The first paper has been published as Fortuné et al. (incl. Kimmig), 2025, A&A 704, 185. The second paper is submitted.

10.1.1 Classifying Galaxies According to their Star Formation History

As demonstrated in chapter 8, the high star formation rate (SFR) of galaxies on the star forming main sequence (SFMS) implies that any sufficiently massive progenitor ($M_* \geq 1 \times 10^9 M_\odot$) which forms early enough ($z \geq 2$) must either grow into a very massive ($M_* \geq 1 \times 10^{11} M_\odot$) galaxy by $z = 0$, or undergo cycles of star formation and quenching (Kimmig et al., in prep.). As such, it is worthwhile to consider the behavior of galaxies through cosmic time

with regards to their star formation rate, and how often – if indeed they do – they undergo such cycles. That was the goal of the work by Fortuné et al. (2025), where we employ the *Magneticum Pathfinder* Box4/uhr to trace all central galaxies with $M_* \geq 1 \times 10^{10} M_\odot$ at $z = 0$.

We proceed as follows: for every galaxy we determine SFR and stellar mass at every snapshot, and apply a 1 Gyr running median to determine a smoothed SFR. This avoids spurious phases of quiescence to reveal instead longer term trends. The smoothed SFR is compared against that of the Pearson et al. (2018) SFMS for the given stellar mass of the galaxy, and quantified as quiescent if it lies 0.5 dex below. This gives a flag for every snapshot of either quiescent or star forming, but to ensure that we uncover stable rejuvenation cycles we only consider the galaxy as quenched if it keeps the flag over a 1 Gyr time period.

With this method, Fortuné et al. (2025) were able to define four types of general behavior of the star formation histories of galaxies.

- Main-sequence evolved galaxies, which remain on the SFMS throughout their entire history.
- Quenched galaxies, where their SFR falls of the SFMS and does not go back up by $z = 0$.
- Rejuvenating galaxies, which go through one or more cycles on and off the SFMS.
- Caught galaxies, an unusual case where, because the SFMS lowers with time (Pearson et al., 2018; Popesso et al., 2023), galaxies with SFRs just below it can end up back on the SFMS without actually increasing their SFR.

These cases are illustrated in Fig. 10.1 from Fortuné et al. (2025), where we plot the specific star formation rate (sSFR = SFR/M_*) of an example galaxy from each class against cosmic time.

Remarkably, of the sample of 1282 central galaxies, only 22 ($\approx$ 2%) of them are main-sequence evolved galaxies, comparable in number to the unique case of caught galaxies (20 or 2%), while the majority quench (833 or 64%) and the rest undergo rejuvenation cycles (407 or 32%). We further split our quenched galaxies by those which quenched early ($z_q \geq 1$, abbreviated QE) or late ($z_q < 1$, abbreviated QL), and the rejuvenators by whether they end up on the SFMS at $z = 0$ (rejuvenator main sequence, RM) or end us quenched (rejuvenator quenched, RQ).

10.1.2 Connecting the Star Formation History of a Galaxy and its Stellar Metallicity

Based on our findings in chapter 9, we expect the star formation history of a galaxy to imprint within the stellar chemical abundances. In brief, more extended star formation allow for more enrichment from Type Ia supernovae that explode some time after formation ($\approx$ 1 Gyr), while a more bursty star formation results in the stars being chemically enriched through the faster Type II supernovae from massive stars (Kobayashi, 2025). Because the former primarily enriches the iron-peak elements (Cr, Mn, Fe, and Ni, e.g., Nomoto et al., 1984) where the latter produces a large amount of lighter α-elements (O, Ne, Mg, Si, S, Ar, Ca,

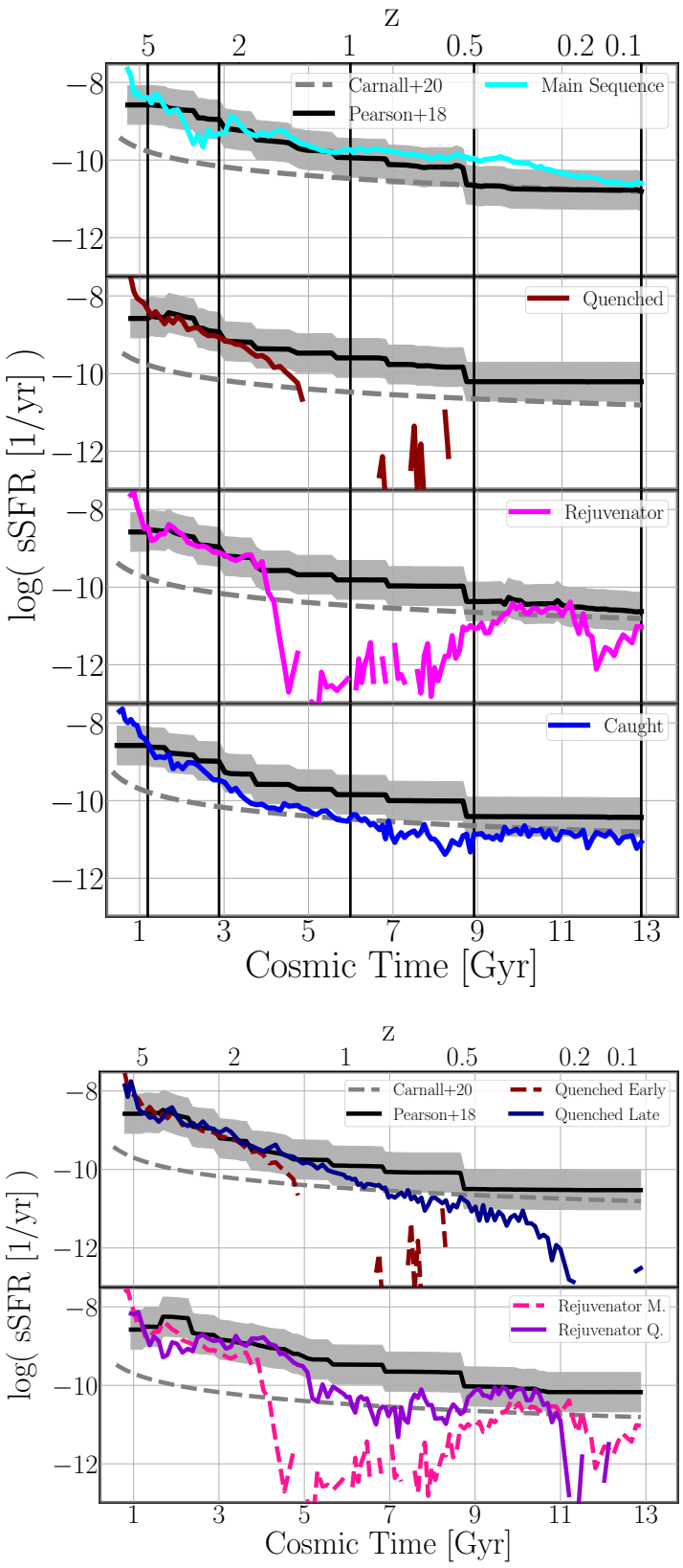


Figure 10.1. Figures 2 (*top*) and 4 (*bottom*) taken from Fortuné et al. (2025), showing the different types of star formation history of a sample of 1282 simulated galaxies. The *top four* panels show the general classes of main-sequence evolved, quenched, rejuvenated and caught galaxies, while the *bottom two* show our different definitions between quenched early and quenched late, and rejuvenated main sequence and rejuvenated quenched galaxies.

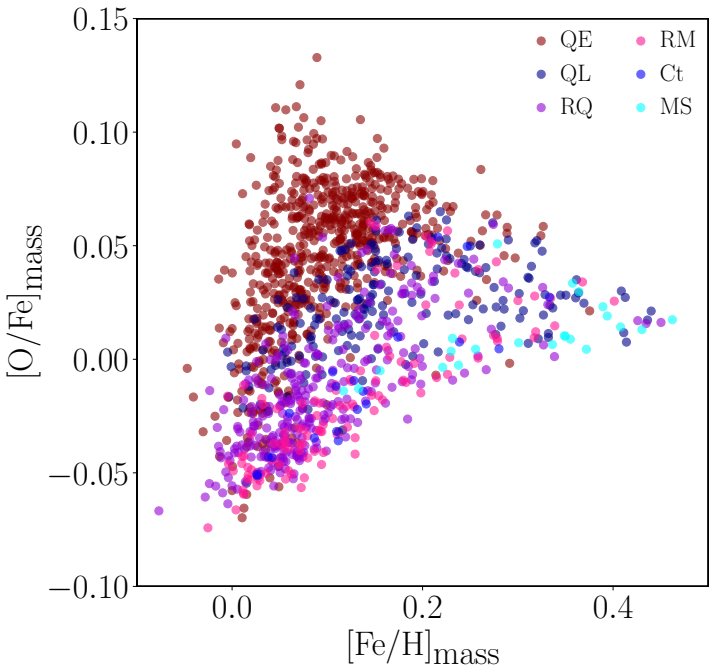


Figure 10.2. Figure 8 taken from Fortuné et al. (2025), plotting the stellar chemical abundance ratio [O/Fe] versus the iron abundance [Fe/H] for each galaxy class.

e.g., Woosley & Weaver, 1995). Consequently, extended star formation histories result in a low α-elemental abundance ratio over iron, [O/Fe], while burst histories do the opposite.

Using the class definitions, Fortuné et al. (2025) plot the [O/Fe] versus [Fe/H] stellar abundance ratios, which we show in Fig. 10.2. There emerges a clear gradient between the classes, going from the early quenched galaxies occupying the top right (enhanced [O/Fe], low [Fe/H]) down to the main-sequence evolved galaxies at the bottom right (low [O/Fe], high [Fe/H]). The gradient is roughly given by QE-QL-RQ-Ct-RM-MS, showing that early and bursty formation with subsequent quenching results in the expected high [O/Fe] ratio, while a galaxy that spent its entire formation history residing on the SFMS necessarily enriches its intragalactic medium with many Type Ia SNe and thus reaches the highest overall iron abundances.

10.1.3 Connecting the Star Formation History of Milky Way Mass Galaxies with their Merger Rates

Building on the findings by Fortuné et al. (2025), we have explored the galaxy classes farther in another work (Fortuné et al., subm.) focusing on a subset of galaxies with the same stellar mass range of those from the Geckos survey (van de Sande et al., 2024), $10^{10.3} M_\odot \leq M_* \leq 10^{11.1} M_\odot$, comparable to that of the Milky Way galaxy. The great diversity in the star formation histories gives rise to the question of physical drivers, i.e., which processes are responsible for some galaxies undergoing rejuvenation cycles, where others simply quench. A natural assumption is that these galaxies underwent different

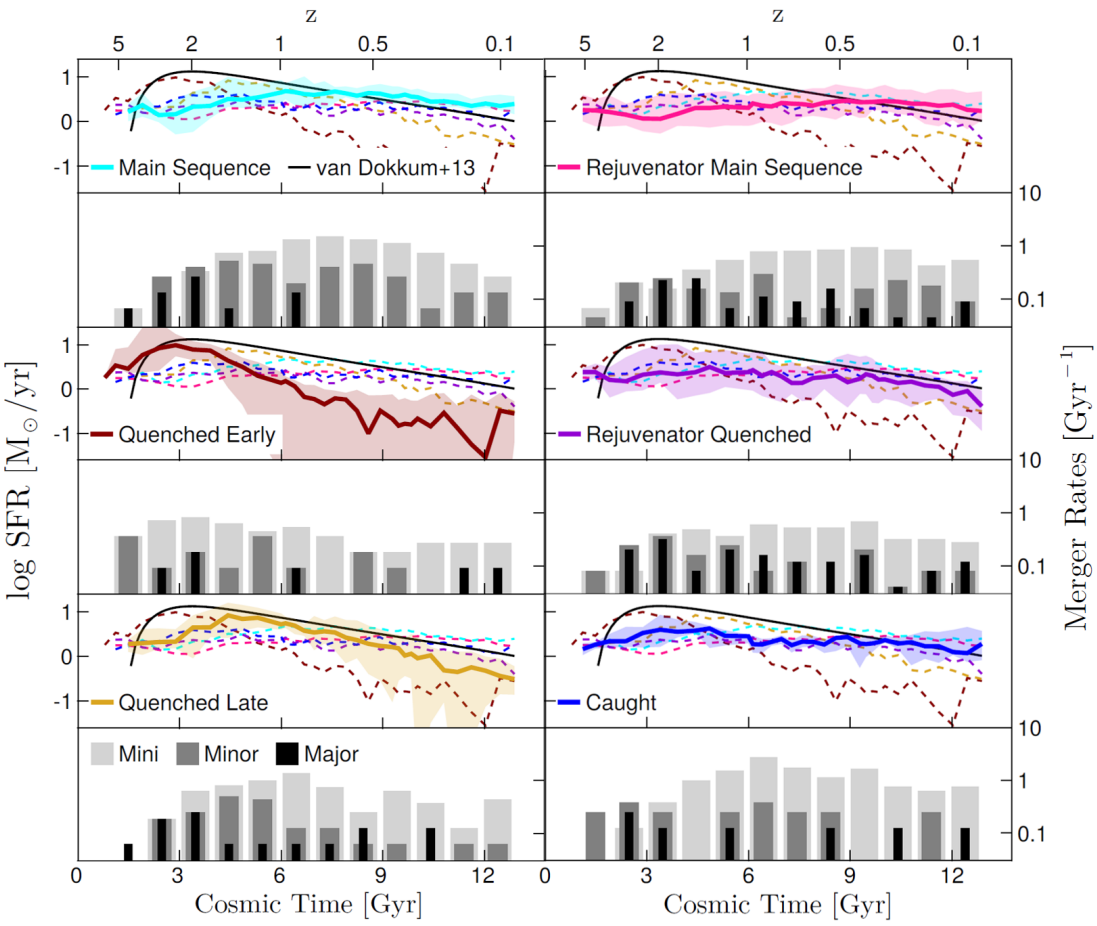


Figure 10.3. Alternative version of figure 5 by Fortuné et al. (subm.). For the galaxies from each class we plot in two panels the median evolution of in-situ star formation (*upper*, with colored lines) as well as the histogram of the number of major (black), minor (gray) and mini (light gray) mergers across cosmic time (*lower panels*). The solid black lines in the upper panels is the derived star formation history for Milky Way-like galaxies by van Dokkum et al. (2013).

assembly histories, where a merger with another galaxy could either trigger rejuvenation (if gas-rich) or quiescence (Gómez-Guijarro et al., 2022).

Therefore, in the work by Fortuné et al. (subm.), we consider the evolution of the SFR of galaxies within each class, and compare it to the merger rates of these galaxies, which we plot in Fig. 10.3. For each class, the upper panels show the median in-situ star formation rate across cosmic time, while the lower panels show the merger rates, split by the stellar mass ratio of the merging galaxies as major (1:3, black), minor (1:10, gray) and mini (1:100, light gray). We find that main sequence-evolved galaxies lack major mergers past $z < 1$ and instead, along with rejuvenated main sequence galaxies, show the highest rate of late-time mini and minor mergers. We demonstrate that this is because the lower mass galaxies tend to be more gas rich, thus triggering renewed star formation.

As a whole, the group of rejuvenating galaxies have the highest rate of major mergers, which may indicate that these types of mergers play a role both for the quenching (Gómez-Guijarro et al., 2022) as well as the rejuvenation (Remus & Kimmig, 2025). It is interesting

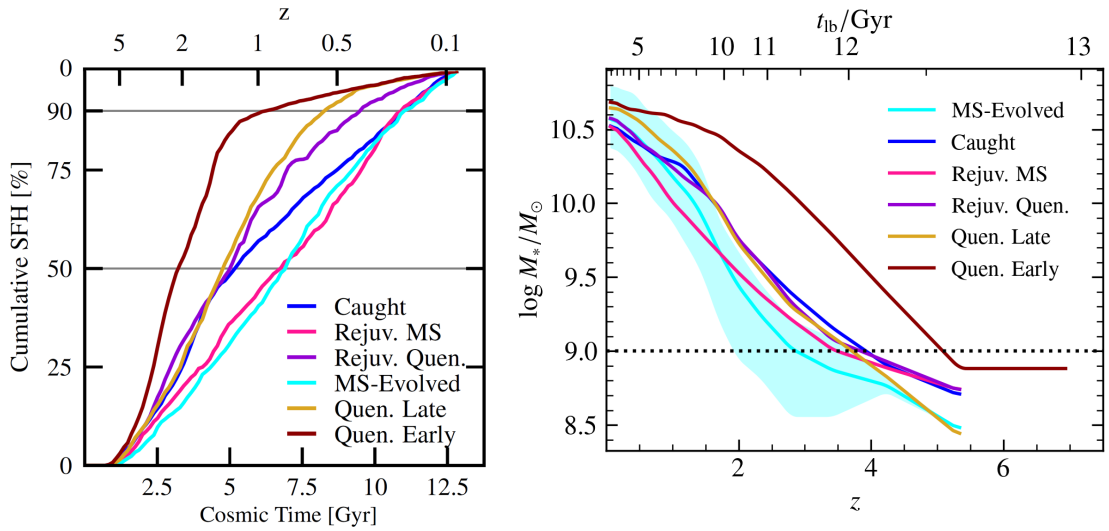


Figure 10.4. *Left:* Figure 6 by Fortuné et al., (subm.), showing the median cumulative star formation history for galaxies of each class as a function of cosmic time. *Right:* The median stellar mass against redshift for each class.

to note the relatively low rate of mergers for those early quenched galaxies, which may instead be quenched through other, internal means (Kimmig et al., 2025b).

We then turn to the final question of this work, which is once more in context of the results we presented in chapter 8. Given the rapid growth of galaxies on the SFMS derived there, we expect the main sequence-evolved galaxies defined here to either be more massive at $z = 0$, which cannot be the case because of the mass constraints applied to all galaxies, or to have formed at later times compared to the galaxies in the other classes. We therefore plot the stellar mass growth for Milky Way-mass galaxies as a cumulative star formation history (left, figure 6 by Fortuné et al., subm.) and as a total stellar mass (right) in Fig. 10.4.

The main sequence-evolved galaxies indeed end up forming the latest, both in terms of their absolute stellar mass and relative fraction to their $z = 0$ stellar mass. They cross a threshold of $M_* = 1 \times 10^{10} M_\odot$ on average at $z = 3$, which together with their final mass of $M_* \approx 10^{10.5} M_\odot$ correspond to a mean SFR of ≈ 0.2 dex below the SFMS, as derived by Kimmig et al. (in prep., see Fig. B.2). This value is well within the ± 0.5 dex bounds used by Fortuné et al. (2025) to define the classes. By contrast, the earliest growing classes are also those which are quiescent by $z = 0$. Interestingly, the rejuvenated main sequence class of galaxies grows in a similar way to the main sequence-evolved galaxies, beginning a bit earlier and flattening toward $z = 0$ but otherwise growing at comparable rates. This is likely because the cycles of sub- and super-main sequence star formation rates of different galaxies are combined into a median growth here, which then on average roughly follows that of the SFMS. Consequently, we find here excellent agreement between the behavior of simulated galaxies and our mathematical model presented in chapter 8.

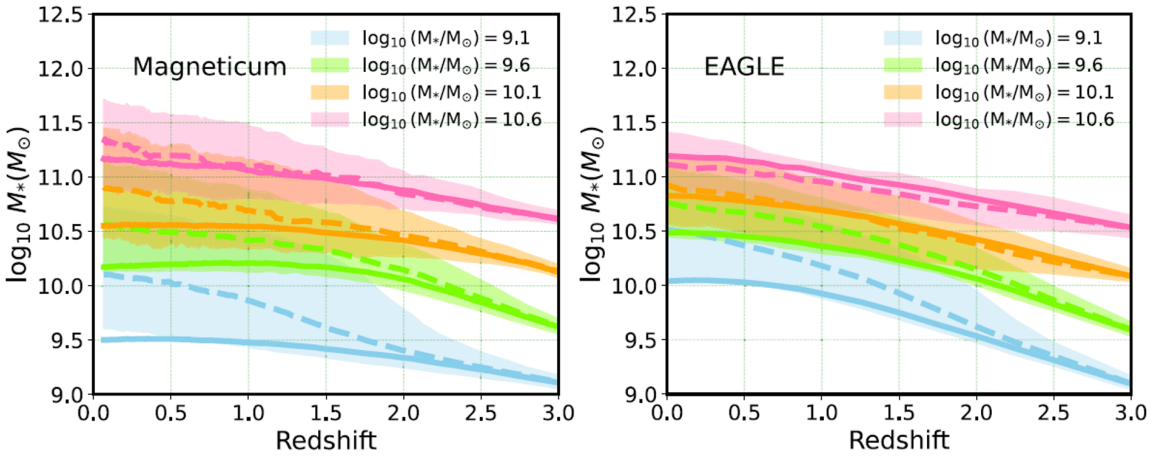


Figure 10.5. Figure adapted from Fig. 6 of Gao et al. (2026), showing the mass evolution of $z \approx 3$ galaxies in four different mass bins (colors) in simulations from the *Magneticum Pathfinder* (*left*) and EAGLE (*right*) suites. The solid (dashed) lines are the evolution based on constant number density (median number density), with the 20th to 80th percentiles shown as shaded bands.

10.2 The Impact of a Galaxies' Environment at Cosmic Noon in Predicting its Present-Day Stellar Mass

This Section summarizes findings from the publication by Gao et al. (incl. Kimmig), 2026, MNRAS 545, 2172, for which I am the third author and provided the Magneticum simulation data.

Beyond characterizing the growth of galaxies based on their star formation histories (Fortuné et al., 2025), which can be achieved for example through accurate measurement of stellar chemical abundances (see chapter 9), we have already discussed in chapter 8 the approach of connecting progenitors and descendants by assuming they remain at a constant number density through cosmic time (see also van Dokkum et al., 2013; Papovich et al., 2015). In the work by Gao et al. (2026), we used the *Magneticum Pathfinder* Box4/uhr simulation in addition to the EAGLE Ref-L0100N1504 simulation (Crain et al., 2015; Schaye et al., 2015) to test this hypothesis of whether a given galaxy observed at higher redshifts (here chosen to be $z = 3$) on average grows in stellar mass as would be expected if it remained at the same number density.

We show the key result by Gao et al. (2026) in Fig. 10.5, their figure 6, where the stellar mass is plotted against redshift in the case of constant number densities (solid lines) as well as when taking simulated galaxies directly from the simulations at $z = 3$ and tracing them down until $z = 0$ (dashed lines with shaded regions). It is immediately apparent that for both simulations these lines diverge for all galaxies except the most massive ones (pink and orange), with lower mass galaxies consistently growing more in stellar mass than expected from the constant number density argument.

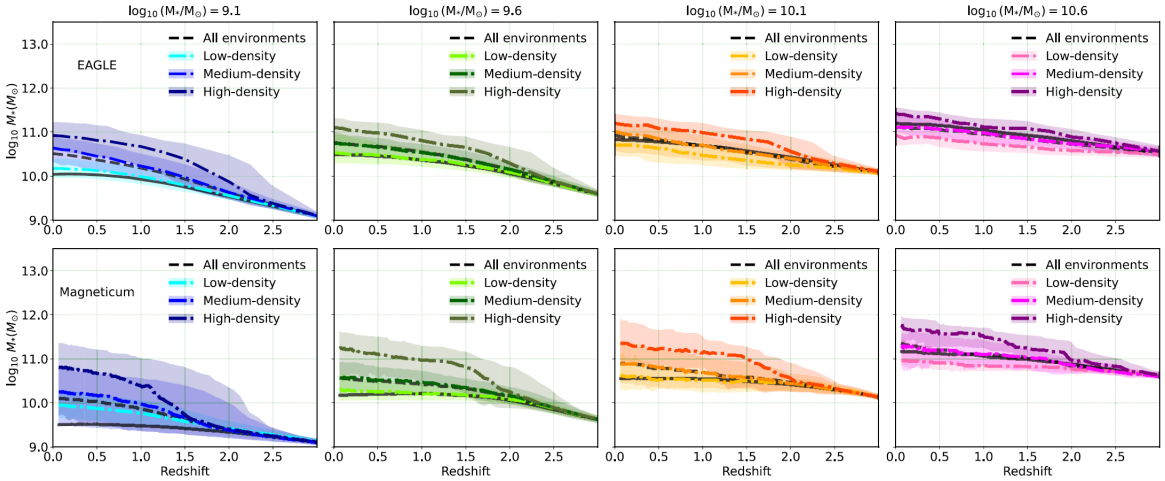


Figure 10.6. This Figure was published as Fig. 7 of Gao et al. (2026), and shows the evolution in stellar mass based on the assumption of a constant number density (solid lines) versus the true evolution within the simulation from the EAGLE (*top*) and *Magneticum Pathfinder* (*top row*) suites, split by their $z = 3$ stellar mass going from the lowest (*left*) to highest (*right*) mass bin.

As can be seen from the shaded bands, there is a considerable range in the stellar mass growth of individual galaxies in both simulations. Gao et al. (2026) consider therefore whether this behavior can be linked to the differing environments of the galaxies at $z = 3$, and thus predicted. We explore this idea even further in chapter 14, while showing here in Fig. 10.6 the main results by Gao et al. (2026).

We find there that the environment can be used to predict the evolution across all mass ranges, with the greatest split occurring for the low mass galaxies (left column). There, using environmental tracers as defined by Gao et al. (2026) results in differences of up to an order in magnitude of the final $z = 0$ stellar mass. This indicates that the constant number density argument holds true when taking high redshift galaxies which are either of low to intermediate stellar mass residing in underdense environments, or when taking the highest stellar mass galaxies that reside in medium density environments. In all other cases, and in particular for any galaxy residing in a high density environment, the true stellar mass growth with far outpaces that expected from a constant number density.

This critically highlights the need to incorporate the environment when trying to connect galaxies through cosmic time, as even common alternatives like assuming constant number density (van Dokkum et al., 2013; Papovich et al., 2015) fail to capture the true underlying behavior. We show in chapter 14 that this results holds true even when going beyond the galaxies, which may be impacted by the implemented baryonic physics within the simulations, and consider there the growth of their host dark matter halos, showing that these, too, diverge from typical expectations, but can be improved by accounting for the environment.

A broad and ample road, whose dust is gold
And pavement stars, as stars to thee appear
Seen in the Galaxie, that Milky Way
Which nightly as a circling zone thou seest
Powdered with stars.

John Milton, *Paradise lost*, Book 7, verse 577–581, 1667

11

Substructures as a Dynamical Clock for Galaxy Clusters

This chapter is part of the publication Kimmig et al., 2023, ApJ 949, 92, with the remainder of that publication being part of my Master's Thesis work.

Substructures are known to be good tracers for the dynamical states and recent accretion histories of the most massive collapsed structures in the Universe, galaxy clusters. Observations find extremely massive substructures in some clusters, especially Abell 2744. We identify a simulated Abell 2744 counterpart that not only has eight substructures of similar mass fractions but also exhibits similar features in the hot gas component. This cluster formed only recently through a major merger together with at least 6 massive minor merger events since $z = 1$, where prior the most massive component had a mass of less than $1 \times 10^{14} M_{\odot}$. We show that the mass fraction of all substructures and of the eighth substructure separately are excellent tracers for the dynamical state and assembly history for all galaxy cluster mass ranges, with high fractions indicating merger events within the last 2 Gyr.

11.1 Introduction

Galaxy clusters come in many different flavors: from relaxed clusters with smooth hot X-ray halos and a clearly identifiable brightest cluster galaxy (BCG), like Abell 383 (e.g., Allen et al., 2008), to highly disturbed systems with detectable shock fronts and multiple massive galaxies, like Abell 2744 (e.g., Jauzac et al., 2016) or MACS J0416.1-2403 (e.g., Grillo et al.,

2015). Their dynamical states are commonly linked to their recent accretion history, and are thought to reflect the state of their cosmic environment given that they mark the nodes of the collapsing cosmic web.

Galaxy cluster substructures are some of the best indicators to provide insights into both the dynamical state (e.g., De Lucia et al., 2004; Neto et al., 2007; Biffi et al., 2016) and the accretion history (e.g., Jiang & van den Bosch, 2016) of their host galaxy clusters, as well as providing a test for potential dark matter variants (Bhattacharyya et al., 2021) and cosmological parameters (e.g., Ragagnin et al., 2021). Recent gravitational lensing obervations of galaxy cluster substructures have posed challenges to the ΛCDM paradigm, due to discrepancies found between the observations and cosmological simulations: The observed substructure masses are found to be larger (e.g., Jauzac et al., 2016; Schwinn et al., 2017), especially in the central regions (Grillo et al., 2015), and they appear more concentrated (e.g., Meneghetti et al., 2020; Ragagnin et al., 2022). While the differing concentration is not resolved purely from the inclusion of baryonic physics (Munari et al., 2016), it has been discussed to arise from the exact included baryonic subgrid physics in simulations (Bahé, 2021). The higher observed masses, in turn, are thought to possibly arise from projection effects, albeit this has so far only been tested using dark matter only simulations (Mao et al., 2018; Schwinn et al., 2018). Therefore, to enable future joint investigations employing both hydrodynamical simulations and gravitational lensing observations, it is necessary to understand the relationship between the intrinsic, three-dimensional substructure identification from simulations and the projected substructure masses, which we will analyze in this study.

An excellent testing ground for this endeavor is provided by the particularly extreme case of galaxy cluster Abell 2744 at $z = 0.308$, with eight substructure masses measured by Jauzac et al. (2016) to all contain masses in excess of $5 \times 10^{13} M_{\odot}$ within 150 kpc apertures. In addition, the substructures are all located in close proximity within a sphere with a radius of 1 Mpc. This cluster has also been mapped in X-ray and radio bands, detecting both strong shock fronts (e.g., Owers et al., 2011; Eckert et al., 2015) in combination with radio relics (e.g., Giovannini et al., 1999; Eckert et al., 2016; Rajpurohit et al., 2021). All these detection have been interpreted as the results of at least one massive recent merger event (e.g., Kempner & David, 2004; Boschin et al., 2006), if not even multiple merger events (e.g., Merten et al., 2011). As part of the Hubble Frontier Field program (Lotz et al., 2017), Abell 2744 is one of the best studied and deepest imaged galaxy clusters, with multiple studies on its strong and weak lensing properties (e.g., Jauzac et al., 2016; Mahler et al., 2018; Bird & Goldberg, 2018). In addition, Abell 2744 is part of the GLASS-JWST program (Treu et al., 2022) and as such more detailed studies on its properties are to be expected soon, especially with regard to strong lensing (Bergamini et al., 2022).

The existence of multiple massive substructures inside a galaxy cluster is thought to be connected to recent merging activity. This is for example discussed by (Jauzac et al., 2016) for the case of the galaxy cluster Abell 2744 which is especially well known for its multiple massive substructures. Therefore, we will test this hypothesis in the following by

first reproducing Abell 2744 from the simulations and then tracking its formation pathways. Furthermore, we then broaden the analysis to our full cluster sample, aiming to encode the information hidden in these substructures.

We employ here the *Magneticum Pathfinder Box2b/hr* simulation (Dolag et al., 2025), and more specifically snapshot 31 at $z = 0.252$, comparable with the observed redshift of Abell 2744 $z = 0.308$. The simulation is run with a modified version of the smoothed particle hydrodynamics code GADGET-2 (Springel, 2005), with improvements discussed further by Teklu et al. (2015) and Dolag et al. (2025). From that simulation, we select four bins in virial mass summarized in Tab. 11.1.

For each selected galaxy cluster, we determine the mass fraction in substructures in two ways. The first is to take the three-dimensional masses of each subhalo identified by the substructure finder SUBFIND (Springel et al., 2001b; Dolag et al., 2009), and divide that by the cluster virial mass, $f_{\rm sub} = \sum M_{\rm sub,i}/M_{\rm vir}$. For the second, we determine the mass in projection by working with a projected map of the total mass (baryons plus dark matter) with pixel sizes of 2 kpc. We mask the pixels within apertures of size $r_{\rm ap}$ around the centers of substructures identified by SUBFIND, where $r_{\rm ap,\,giants} = 150$ kpc and the aperture for clusters of the other mass bins is scaled according to their virial radius $r_{\rm ap,\,i} = r_{\rm ap,\,giants} \cdot R_{\rm vir,i}/R_{\rm vir,\,giants}$. By fitting an Einasto (1965) profile to the resulting masked map, we determine the contribution of the main halo. We further subtract the mass added in from the mean background density $\rho_{\rm mean}$ by projecting the map out to a depth of $r_{\rm z} = \pm 5$ Mpc.

This finally gives the substructure mass fraction in projection as $f_{\rm cyl} = \sum M_{\rm cyl,i}/M_{\rm vir}$, with

$$M_{\rm cyl,i} \equiv M_{\rm ap,i} - [\rho_{\rm Ein,fit}(d_{\rm i}) + \rho_{\rm mean}] \cdot \pi r_{\rm ap}^2 \cdot r_{\rm z}, \tag{11.1}$$

where $M_{\rm ap,i}$ is the summed mass of all pixels within the aperture of substructure i, $\rho_{\rm mean}$ is the background density at the cluster redshift, $\pi r_{\rm ap}^2 \cdot r_{\rm z}$ the volume of the projected cylinder and $\rho_{\rm Ein,fit}(d_{\rm i})$ the main halo density at the center of the aperture.

Table 11.1. Overview of the relevant parameters for each mass bins used. Each mass bin is scaled relative to the "giants" according to their relative mean virial mass. The stellar mass cut used throughout is $M_{*,\rm cut}$, and the projection depth is $r_{\rm z} \approx 5 \cdot r_{\rm vir}$.

	Giants	Medium	Small	Tiny
$f_{\rm m,scale}$	1	0.381	0.152	0.076
$r_{\rm tot}$ [Mpc]	1.3	0.942	0.694	0.551
$r_{\rm ap}$ [kpc]	150.0	109	80.1	63.6
$r_{\rm conv}$[kpc]	25.0	18.1	13.4	10.6
$r_{\rm pix}$ [kpc]	2.0	1.45	1.07	0.848
$M_{*,\rm cut}$ [$10^{10} M_\odot$]	4.0	1.524	0.609	0.5

11.2 Results

11.2.1 The Case of Abell 2744

Using gravitational lensing measurements, Jauzac et al. (2016) found extremely large masses inside substructures for the galaxy cluster Abell 2744, significantly more than can be found within simulations (Schwinn et al., 2017). Using dark-matter only simulations, Mao et al. (2018) and Schwinn et al. (2018) present evidence that the discrepancy is caused by projection effects. Here, we will use, for the first time, a fully baryonic hydrodynamic cosmological simulation to identify Abell 2744 counterparts, applying the method outlined by Kimmig et al. (2023).

The eight substructures found by Jauzac et al. (2016) within Abell 2744 are not only very massive but also in close proximity within 1 Mpc. They find that the eighth most massive substructure still has a mass of $M_{\mathrm{cyl},8} = 5 \times 10^{13} M_{\odot}$ within an aperture of $r_{\mathrm{ap}} = 150\,\mathrm{kpc}$ (see Tab. 11.2). When compared to their measurement of the total mass within a radius $r_{\mathrm{tot}} = 1.3\,\mathrm{Mpc}$, $M_{\mathrm{tot}} = 2.3 \times 10^{15} M_{\odot}$, this is still equal to around 2.17%. Using the method from Kimmig et al. (2023), we find a total of 58 projections of galaxy clusters from the "giants" mass bin which manage to reproduce eight extremely massive substructures with a mass fraction $M_{\mathrm{cyl}}/M_{\mathrm{tot}} > 2.17\%$. Note that M_{tot} is defined here as the total projected mass within 1.3 Mpc to be comparable to the results by Jauzac et al. (2016).

The case which best reproduced the measurements for Abell 2744 is a projection of galaxy cluster number 20 from the "giants". The central $(2\,\mathrm{Mpc})^2$ region of the best projection is shown in Fig. 11.1. As seen on the top left, the eight most massive substructures (black circles) all lie close to the center (black x) and follow a strongly elongated distribution. For comparison the stellar surface density (bottom left) as well as a mock image in the r-band (bottom right) are shown. The black numbers are sorted by the mass of the substructures. Their mass as a fraction of M_{tot} is shown on the top right, with the values for this projection denoted as red crosses while the eight substructures observed in Abell 2744 by Jauzac et al. (2016) are shown as cyan diamonds. We find an exceedingly similar flat distribution of substructure mass fractions aside from the most massive one, in excellent agreement with the observations. This agreement can also be seen from the mass fractions of the individual substructures as shown in Tab. 11.2.

While this is the best fitting projection, it is not the only one, as can be seen from the shaded areas for each substructure in the upper right panel of Fig. 11.1: Underlayed in blue is the distribution of substructure masses for all 200 orientations of galaxy cluster 20, with the size of the bulge corresponding to the relative frequency of each value. The overall spread between orientations (blue vertical lines) is sizable. It can be concluded that while the extreme mass distribution within Abell 2744 is reproducible it represents an outlier, with very high substructure mass fractions for the fifth to eighth substructures.

This means that the masses observed in Abell 2744 are reproducible within simulations also when including baryons, and arise from projection effects. The impact from projection

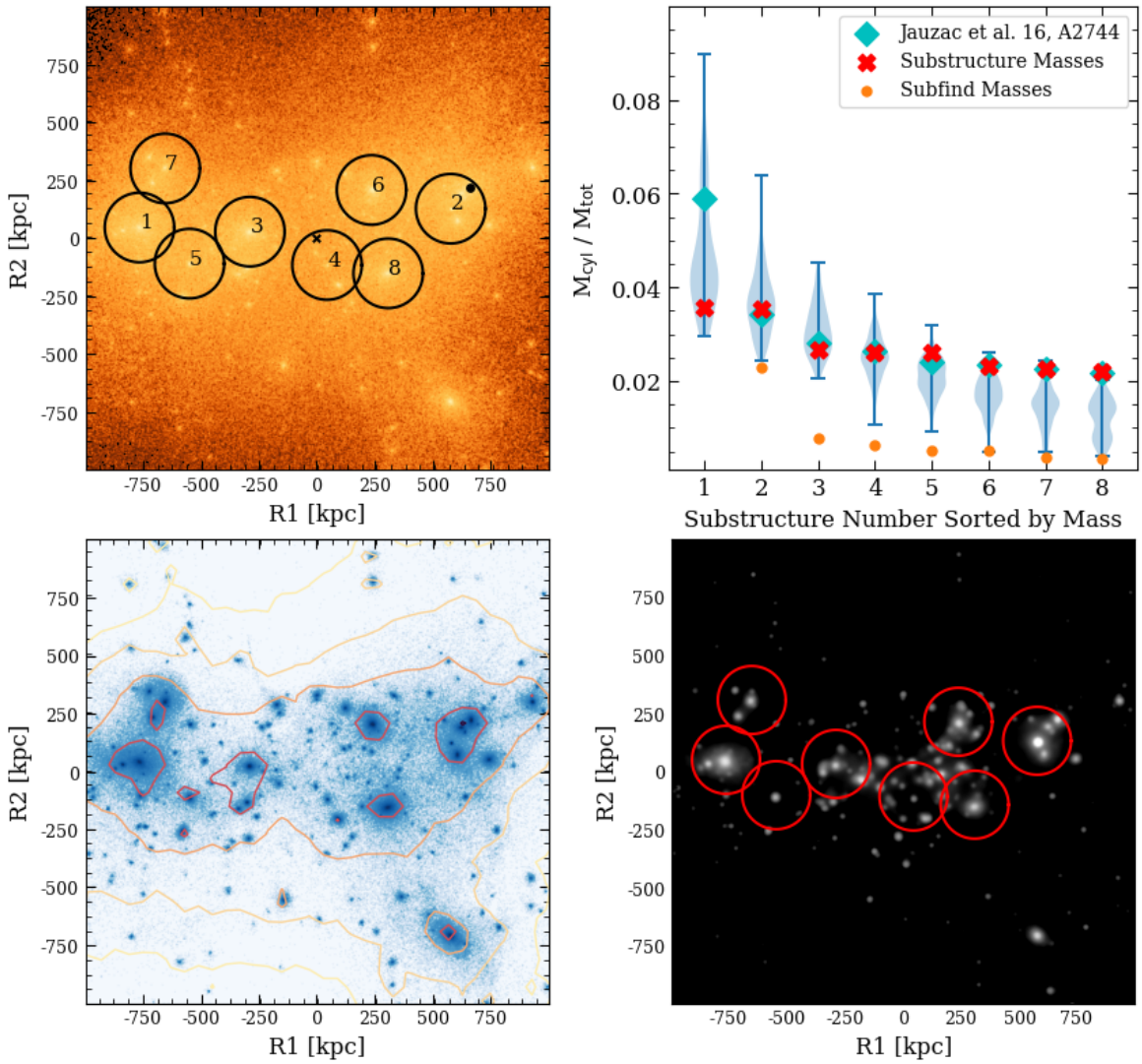


Figure 11.1. *Top left:* Surface mass density map of the central $(2\,\mathrm{Mpc})^2$ region of galaxy cluster 20 of the "giants" for the best projection found overall, centered on the projected center-of-mass (black cross) with the SubFind cluster center indicated as a black dot. The redshift is $z = 0.252$. The eight most massive substructures are shown as black circles numbered decreasing with mass. The colorbar range is $-3.7 < \log_{10}(\Sigma[10^{10} M_\odot]) < 0.1$. *Top right:* The substructure masses as a fraction of the total mass for the best projection (red crosses) as compared to those in Abell 2744 (blue diamonds) determined by Jauzac et al. (2016). Underlayed in blue is the total distribution of masses for all 200 random projections of the galaxy cluster, with the width of the shaded area denoting their relative frequency. The subhalo masses from SubFind (orange dots) are given as a fraction of the M_{tot} for the best projection. *Bottom left:* Same as *top left* but for the stars, with isodensity contours from the total mass map overlayed. $-6 < \log_{10}(\Sigma[10^{10} M_\odot]) < -1$. *Bottom right:* Mock image in the r-band as seen from $z = 0$ down to limiting magnitude of 25 mag, generated via the method from Martin et al. (2022). The red circles denote the eight most massive identified substructures.

becomes especially clear when considering the orange points in the upper right panel of Fig. 11.1. These mark the subhalo mass-fractions as determined by SubFind, i.e., when only counting the matter to the structure that is really bound to it. In this case only the first and second subhalo have a mass fraction comparable to the *eighth* substructure within Abell 2744, with all other subhalos lying far below. The mass fraction of the first subhalo lies

much higher outside of the plotted range as it is the main halo and thus assigned all bound mass of the galaxy cluster not within other subhalos. This clearly highlights the difficulty in comparing substructures obtained from simulation algorithms and observations, not just accounting for projection effects but also for the lack of possibility to separate bound from unbound structures in observations.

As outlined by Jauzac et al. (2016), one of the eight measured substructures, W_{bis}, is most likely a background source. When excluding the potential background source W_{bis}, the number of projections of galaxy clusters from the "giants" mass bin with seven substructures of mass $M_{cyl}/M_{tot} > 2.17\%$ rises to 108. However, the projections made here go out to a depth of $r_z \approx 5 \cdot r_{vir}$. We can instead require all the substructures to not be background sources by projecting out only to a depth of $1 \cdot r_{vir}$. Therefore, we repeated the study for 200 orientations of the cluster which provided the best reproduction of Abell 2744, namely galaxy cluster 20. We find in this case 15 projections with seven substructures of mass $M_{cyl}/M_{tot} > 2.17\%$ (and even 2 with eight). We conclude that Abell 2744 is still well reproducible by galaxy cluster 20, even if only substructures inside the galaxy cluster virial radius are considered.

Note that the reported virial radius and mass of Abell 2744 by Schwinn et al. (2017) are approximated by the radius enclosing 200 times the critical density, $r_{200} = 2.8\,\mathrm{Mpc}$ and $M_{200} = 3.3 \times 10^{15} M_\odot$. They are larger than the corresponding values for example cluster 20 of $r_{200} = 2.0\,\mathrm{Mpc}$ and $M_{200} = 1.1 \times 10^{15} M_\odot$. For the best projection in particular, $M_{tot} = 1.03 \times 10^{15} M_\odot$ for cluster 20 while $M_{tot} = 2.3 \times 10^{15} M_\odot$ for Abell 2744. It stands to reason that a larger simulation volume containing even more massive clusters would also be able to reproduce Abell 2744 with comparable absolute substructure masses. This is supported also by the fact that galaxy clusters of a total mass comparable to Abell 2744 are found in the larger volume of the *Magneticum Pathfinder* simulation suite (see Fig. 15 of Remus et al., 2023), however, the resolution of that simulation is too low for a substructure study as performed in this work.

Note further that we selected galaxy cluster 20 at $z = 0.252$ to better match the state of post-core passage claimed for Abell 2744. As we discuss in more detail in the following, at $z = 0.29$ cluster 20 is in the middle of the first passage of the most massive merger. As the true state of Abell 2744 is most likely matched by the configuration in between the two

Table 11.2. The eight substructure masses determined within 150 kpc apertures for a projection of galaxy cluster 20 of the "giants" as well as Abell 2744, with values for the latter as determined by Jauzac et al. (2016).

	1	2	3	4	5	6	7	8
ID	Core	NW	S3	N	S4	S2	W_{bis}	S1
	Mass fraction [%]							
A2744	5.9	3.4	2.8	2.7	2.4	2.3	2.3	2.2
Cl20	3.6	3.5	2.6	2.6	2.6	2.3	2.2	2.2
	Total masses of structures [$10^{13} M_\odot$]							
A2744	13.55	7.9	6.5	6.1	5.5	5.4	5.2	5.0
Cl20	3.7	3.7	2.7	2.7	2.7	2.4	2.3	2.3

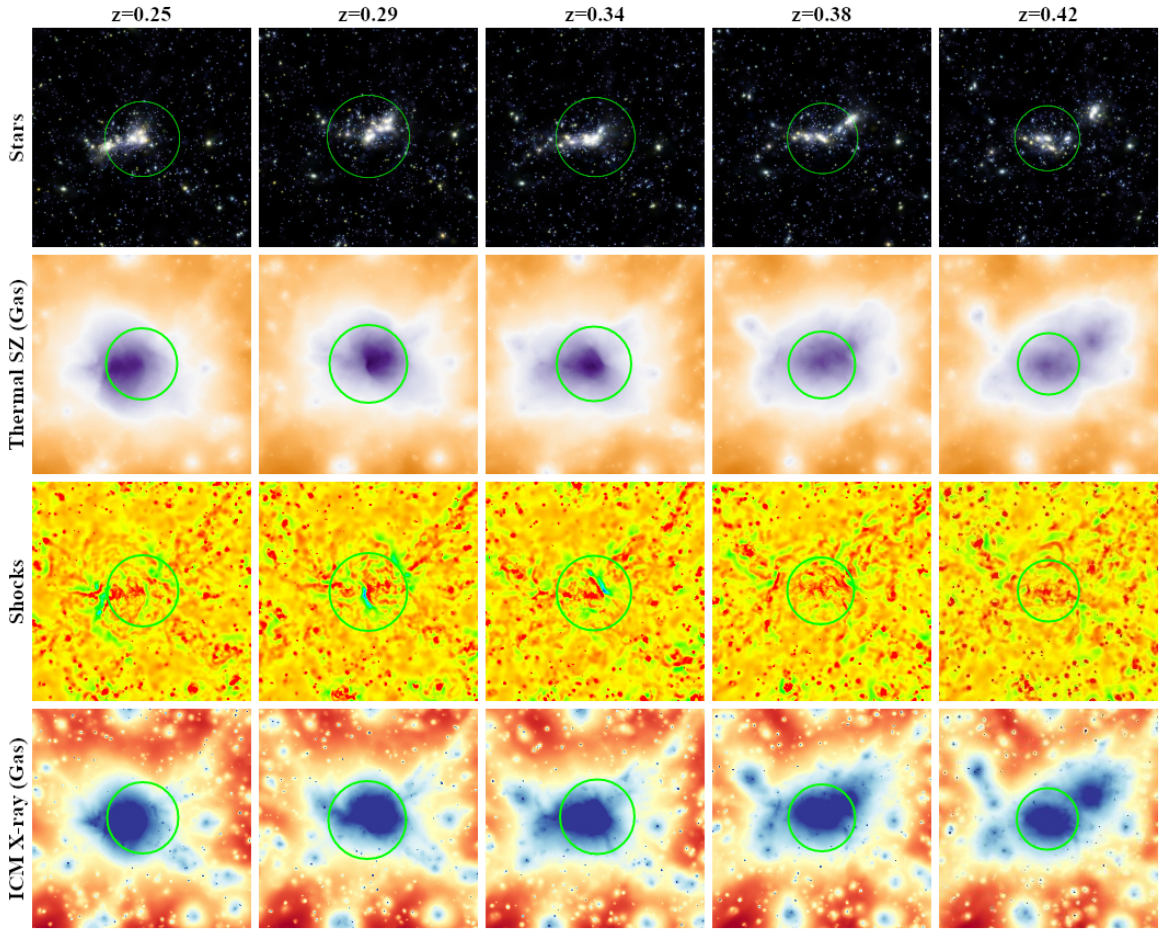


Figure 11.2. Redshift evolution of cluster 20 of the "giants", the Abell 2744 counterpart, with the different columns showing the different redshifts as indicated in the column titles. In all panels, the green circle marks the R_{500} radius of the cluster as calculated from the 3D mass distribution at each redshift. For scaling, at $z = 0$ this corresponds to $R_{500} = 1.94$Mpc. *Top row:* Stellar components. *Second row:* Map of the thermal SZ-effect, shown as Compton-X maps, with color according to the thermal pressure from low (orange) to high (violet). *Third row:* Shocks calculated from the Compton-X maps, with shocks in green or even blue if strongly compressed. *Bottom row:* X-ray emission from the hot gas component, from low (red) to bright (dark blue).

simulation snapshots, we have chosen the snapshot farther in the post-core passage phase. We do not expect a large difference when using the other as there is no significant additional matter infall between the two snapshots (as shown in Figs. 11.2 and 11.3).

The similarities in the substructure masses found for galaxy cluster 20 of the "giants" to Abell 2744 motivate a closer look at their origin. Fig. 11.2 shows the evolution of galaxy cluster 20 from $z = 0.42$ (right column) to $z = 0.25$ (left column), in maps depicting the stars, thermal SZ emission from the gas, the corresponding shocks, and finally the X-ray emission (top to bottom row). The images are centered on the deepest point of the potential at each time while the green circle denotes r_{500}.

In the stellar maps we see that galaxy cluster 20 is the result of a recent major merger with a mass ratio of 1:1.4. The initial two clusters are visually distinct for $z = 0.42$, where one is centrally located and the other to the upper right immediately outside r_{500} (henceforth cluster

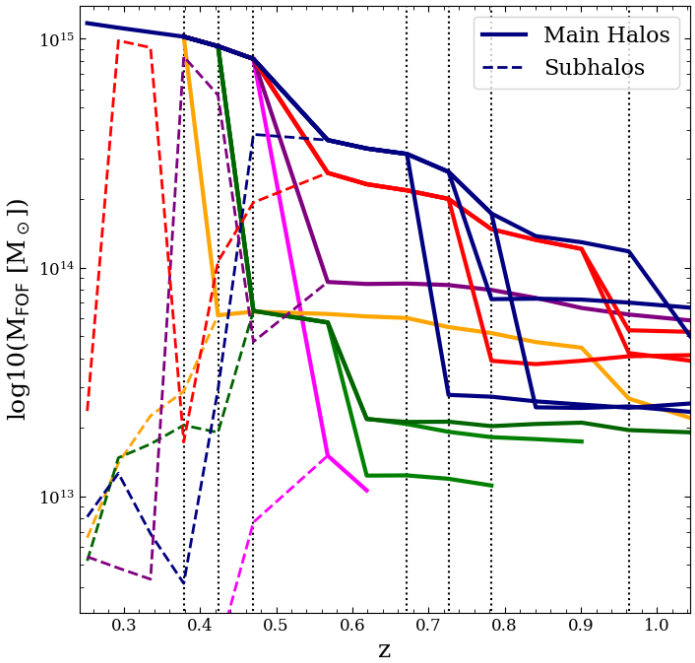


Figure 11.3. Merger history of Abell 2744 counterpart cluster 20 of the "giants", with main halos (solid) and their respective subhalos after infall (dashed lines). Subhalo masses are the summed mass of all bound particles. Only main halos with masses $M_{\rm FOF} \geq 1 \times 10^{13} M_\odot$ are shown. Branches belonging to the two components A and B of the major merger are in blue and red, respectively.

"A" and "B"). B has been on an infalling trajectory since $z = 0.67$ but has just reached a distance of $r_{3d} = 1.68$ Mpc at $z = 0.42$. Even though it is already within the $r_{200} = 2.15$ Mpc of cluster A at this time SubFind still assigns it a mass of $M_{\rm sub,B} = 1.1 \times 10^{14} M_\odot$. Moving forward in time, cluster B falls within r_{500} of A at $z = 0.38$, such that a significant portion of its mass is now assigned to cluster A, with $M_{\rm sub,B}$ dropping to $1.7 \times 10^{13} M_\odot$. This coincides with a connection of regions of high X-ray emission from the hot gas halos as can be seen in the bottom row, going from two distinct peaks to one.

Moving to $z = 0.34$, the nearly radial infall of cluster B triggers a strongly peaked shock (see third row of Fig. 11.2) to the immediate upper right of the cluster center of cluster A. As cluster B reemerges toward the bottom left at $z = 0.29$ and then continues left until $z = 0.25$, the shock front is pushed along. This is in excellent agreement with observations of shock fronts observed in Abell 2744 in X-ray with Chandra by Owers et al. (2011), coinciding with radio relics (Eckert et al., 2016; Rajpurohit et al., 2021). These shock fronts have been interpreted to result from a post core passage major merger with a resulting shock front toward the South-East (see also Kempner & David, 2004; Boschin et al., 2006), exhibiting much the same characteristics found here for galaxy cluster 20.

Following the evolution of cluster 20 further back in time as shown in Fig. 11.3, we find that it actually only assembled to a mass above $M_{\rm FOF} \geq 1 \times 10^{14} M_\odot$ at about $z \approx 0.96$. It is the result of multiple group merger events happening simultaneously: between $z = 0.62$ and $z = 0.42$, four halos with masses above group mass (i.e., $M_{\rm FOF} \geq 1 \times 10^{13} M_\odot$) are accreted onto the main halo A in addition to cluster B, with mass ratios relative to cluster A at the time

of merging of about 1:4, 1:6, 1:6, and 1:24. Note here that, different than for galaxies, a 1:24 merger is still a massive merger event in case of galaxy clusters. This is because the 1:24 merger is a group being accreted onto the cluster which, by itself, already harbors several galaxies and a hot gaseous halo. This supports claims from observations that Abell 2744 actually not only originated from a single major merger but rather several ongoing multiple merger events (e.g., Merten et al., 2011; Rajpurohit et al., 2021). Indeed, we find that of the total growth in mass from $z = 0.67$ to $z = 0.25$ 58% comes from mergers with halos of mass larger than $1 \times 10^{13} M_{\odot}$. This means that for the case of cluster 20 a significant amount of the mass of the cluster is pre-processed in groups.

Finally, the lower row of Fig. 11.2 clearly shows that cluster 20 is fed through four filaments, especially well visible at $z = 0.29$ and $z = 0.34$. This supports the idea that the multiple filaments observed by Eckert et al. (2015) in the hot gas map constructed for Abell 2744 using XMM-Newton data could be depicting four feeding filaments surrounding the cluster. All this gives further evidence that cluster 20 from the *Magneticum* simulation indeed resembles Abell 2744. We conclude that Abell 2744 is indeed a rare case of a violently assembling galaxy cluster, sitting at a node in the cosmic web that only recently started to collapse from multiple different directions.

11.2.2 Accretion and Dynamical State

Given the flat distribution of the mass fractions of the substructures for both Abell 2744 and our cluster 20 (see upper right panel of Fig. 11.1, the mass fraction of the eighth substructure is still rather large. As we have seen, our best matching cluster to Abell 2744, cluster 20, is highly dynamical active and dominated by recent multiple accretion events. Thus, the question arises how well the mass fraction of the eighth substructure would be in tracing the recent assembly history of a cluster, independent of the galaxy cluster mass.

To this end, we calculate for each cluster in our four cluster mass bins the median mass fraction of the eighth substructure from all projections, f_8. The first column of Fig. 11.4 depicts the mass accretion histories of the galaxy clusters of the "giants", "medium", and "small" cluster mass bins, respectively. More explicit, the mass fraction of the final cluster mass (at $z = 0.252$) is shown as a function of redshift. All individual clusters are shown as gray lines, with the three clusters with the highest f_8 for each cluster mass bin shown in blue, and those three with the lowest f_8 marked in red.

As can be seen immediately, for all cluster mass bins the clusters with the lowest f_8 show relatively flat recent accretion histories. This means that only small amounts of mass are accreted in at least the last 2 Gyr, while all clusters with the highest f_8 have accreted at least half of their mass in the last 2 to 3 Gyr. More specific, for the "giants" we find that the three galaxy clusters with the highest f_8 have gained around 55 to 68% of their final mass starting from $z \approx 0.47$ (equaling around 2 Gyr). This is significantly enhanced recent accretion activity compared to 17 to 31% for those with the lowest f_8. This shows that the relative mass of the eighth substructure is a good indicator for the amount of accretion in the

last 2 Gyr, as large values in f_8 can only be reached through recent large mass infall with a high likelyhood for a major merger event.

Given that the mass fraction of the eighth substructure is in first order an arbitrary choice, we also tested the correlation between the recent mass accretion history with the mass fractions of the fourth, fifth, and sixteenth substructure mass fractions f_4, f_5, and f_{16}. While the split is surprisingly the clearest for the eighth substructure fraction f_8, both f_4 and f_5 give similarly good results, while the signal vanishes when using the sixteenth substructure mass fraction. We also inspected the properties found for the second most massive substructure, however, the connection to the mass history was less clear. This indicates that a single merger in the recent accretion history of a cluster leading to a single massive remaining substructure does not necessarily trace a violent multiple merger dominated mass accretion history but is simply an occurring event for any cluster (see Ragagnin et al., 2019, for more details on the mass ratio of the second most massive substructure and the so-called fossilness parameter).

To avoid picking a single substructure to trace the mass accretion history, one can also use the total mass fraction contained within substructures $f_{\rm cyl}$ as a tracer for the dynamical state of a galaxy cluster. Previous studies found that higher $f_{\rm cyl}$ indicate a dynamically active galaxy cluster (De Lucia et al., 2004; Neto et al., 2007; Biffi et al., 2016). This is because once a subhalo falls into a larger halos influence, it begins being disrupted by processes such as ram-pressure and tidal stripping. As the accretion of new subhalos is slower than the disruption at lower redshifts (Jiang & van den Bosch, 2016), this leads to a net reduction of $f_{\rm cyl}$ with time and consequently a higher $f_{\rm cyl}$ correlates with a more recent formation time as described by Jiang & van den Bosch (2017).

While using $f_{\rm cyl}$ is not as efficient as f_8 in identifying the extremes of the dynamically active or passive clusters, we find it to be an overall excellent tracer for the recent mass accretion history. To more closely quantify the relation between final substructure mass and the mass accretion history, we select three redshifts as indicated by the vertical black lines in the left panels of Fig. 11.4. We then plot the mass fractions of the final mass of the clusters at these redshifts as a function of the final substructure mass fraction $f_{\rm cyl}$ in the three right columns of Fig. 11.4.

For the first at $z = 0.34$ all clusters have only accreted little mass, with a negligible dependence on $f_{\rm cyl}$. This can also be seen from the shallow slope m of the best-fit line (black dash-dotted) given in the legend. Going further back to $z = 0.47$, however, shows a steep trend toward decreasing mass fraction with increasing $f_{\rm cyl}$. This means that galaxy clusters exhibiting high substructure masses are indicative of a large amount of recent (within 2 Gyr) mass accretion. This trend persists (although with a more shallow slope) out to $z = 0.67$, with a comparable scatter as indicated by the residual of the fit (given as rs).

The same correlation between the total mass fraction in substructures $f_{\rm cyl}$ and the cluster mass accretion history can be found for all galaxy cluster mass bins as shown in Fig. 11.4 ("giants": upper row, "medium": middle row, and "small": bottom row), with two notable exceptions. First, the less massive galaxy clusters already show a noticeable slope at $z = 0.34$, though this is likely due to none of the clusters of the "giants" having accreted as high a mass

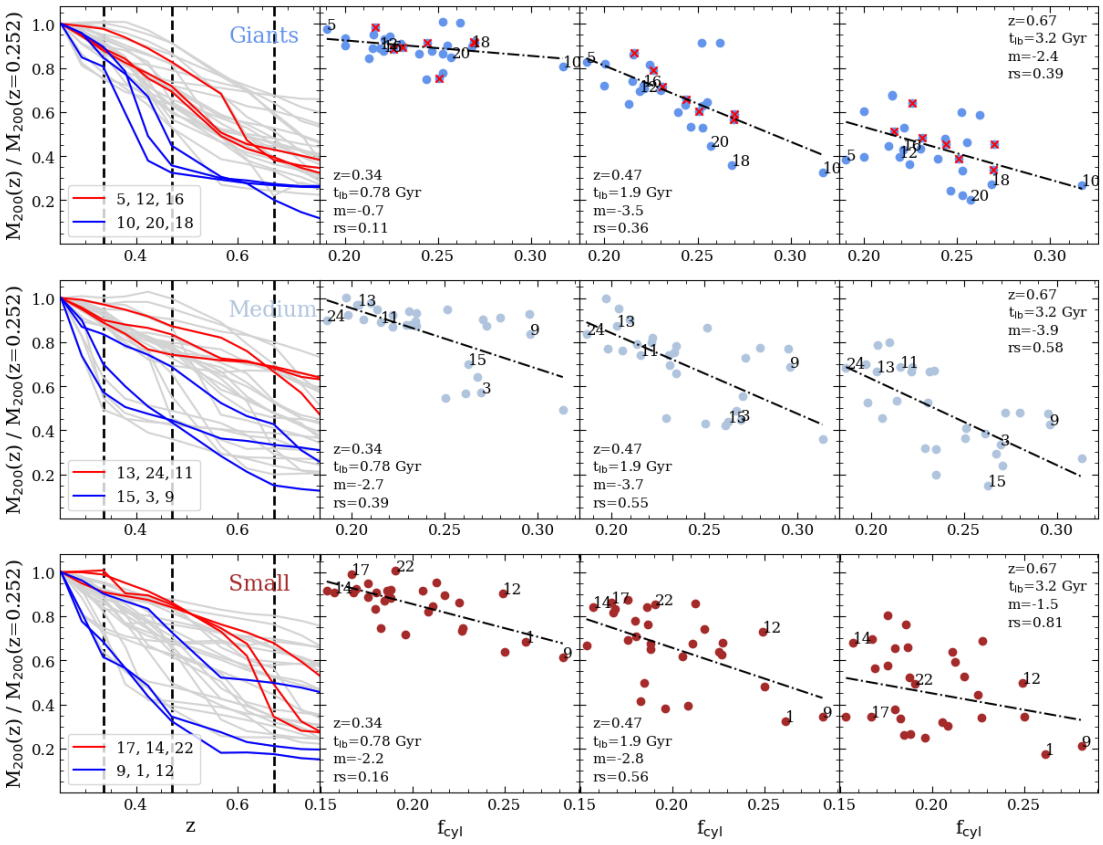


Figure 11.4. The mass history of the galaxy clusters of the "giants" to the "small" mass bins (top to bottom row) as a function of redshift (*first column*). The three galaxy clusters with the highest (lowest) f_8 are highlighted in blue (red), with their numbers given in the legend, and the three vertical black lines indicate three redshifts ($z = 0.34, 0.47, 0.67$). For each the mass fraction of the final mass of the clusters is depicted as a function of $f_{\rm cyl}$ (*second to fourth column*), and the black dash-dotted line is the best fit to the points. The slope m and residual rs of the fit are given in the legend. $t_{\rm lb}$ is the lookback time from the final redshift $z = 0.252$. Numbers indicate the six highlighted clusters, while the red crosses for the "giants" indicate galaxy clusters which were classified as protoclusters at $z = 4$ by Remus et al. (2023).

fraction within the same period. Secondly, the scatter in the relation is higher at $z = 0.67$ for the "medium" and "small" galaxy clusters compared to the "giants", as can be seen from the fit residual. Nonetheless, we still find a downwards slope present. It follows that the final substructure mass fraction measured in projection $f_{\rm cyl}$ is still a tracer for the mass accretion history, even out to a lookback time of $t_{\rm lb} = 3.2\,$Gyr. This time period is larger than the mass-loss timescale of subhalos as given by Jiang & van den Bosch (2017) for dark matter only halos, which may indicate that the presence of baryons allows the signal to persist for longer. We conclude that a large substructure mass fraction $f_{\rm cyl}$ is an excellent tracer for a large amount of accretion within the last 2 Gyr and can be indicative of recent major merger events. Furthermore, large values of $f_{\rm cyl}$ hint at more merger events happening at even earlier times, without the corresponding stellar cores of these structures being disrupted.

Additionally, the red crosses in Fig. 11.4 at all three redshifts of the "giants" indicate galaxy clusters which were classified as protoclusters at $z = 4.2$ by Remus et al. (2023). These are galaxy clusters for which their progenitor had assembled at least a mass of $M_{\rm vir} \geq 1 \times 10^{13} M_\odot$ already at $z = 4.2$, i.e., they are nodes that started collapsing early-on. Interestingly, fulfilling

various conditions to be a protocluster at high redshifts (for example having a high star-formation rate, high number of substructures or being very massive) is found here not to correlate either with a particularly high or low resulting substructure mass fraction $f_{\rm cyl}$, nor with noticeable deviations from the best-fit lines. Instead, those clusters that started collapsing early behave here comparably to those which did not yet start to collapse and build up into a protocluster at $z \approx 4$.

This clearly indicates that neither the mass nor the activity of assembly (i.e., the substructure mass fraction $f_{\rm cyl}$) observed at low redshifts is an indicator for the cluster having assembled a significant amount of its mass already at high redshifts. In fact, this is in agreement with our results for cluster 20, the Abell 2744 analogue, that we found to have assembled only recently below $z = 1$ even though it is one of the most massive galaxy clusters in our simulation volume. Furthermore, only about 25% of our most massive galaxy clusters are identified as protoclusters at redshifts of $z \approx 4$. Nevertheless, we do find one trend for the seven protoclusters present in out sample: the four protoclusters selected by their high number of substructures at $z \approx 4$ are also those which result in a higher $f_{\rm cyl}$ compared to the other three selected by mass or star-formation rate. This could indicate that these particular clusters sit at big nodes of the cosmic web, building up into future super clusters, however, we note that the sample here is of low significance due to the small number of clusters.

11.2.3 Substructures and Centershift

Another parameter which according to the literature correlates to the dynamical state of a galaxy cluster is the centershift s. It is defined as the distance between the point of lowest potential (highest density) to the center-of-mass (Biffi et al., 2016). As with $f_{\rm cyl}$, a higher centershift s indicates a dynamically active galaxy cluster, and the absolute value is typically divided by the virial radius to allow for comparisons between galaxy clusters of varying masses and sizes. Generally, thresholds of $f > 0.1$ and $s > 0.07$ are defined to be indicative of dynamical activity (Neto et al., 2007). However, the large differences between the total substructure mass fraction in projection $f_{\rm cyl}$ and the total subhalo mass fraction in three-dimensions $f_{\rm sub}$ found by Kimmig et al. (2023) cause problems when consistently classifying the dynamical state in observations and simulations. Thus, in the following we will investigate the importance of projection effects and the neglect of a binding criterion as used in three-dimensional substructure identifications for using f and s as tracers of dynamical activity.

Fig. 11.5 shows in the first two rows the median projected values of f and s as a function of their three-dimensional values, with the thresholds for dynamical activity from Neto et al. (2007) given as dashed lines. Although we find a trend to increasing $f_{\rm cyl}$ with increasing $f_{\rm sub}$ on the top row, the projected $f_{\rm cyl}$ all lie above the threshold even when their $f_{\rm sub}$ are lower than the threshold. This would necessitate either an increased threshold in projection or a decreased threshold in three dimensions to agree when predicting dynamical activity.

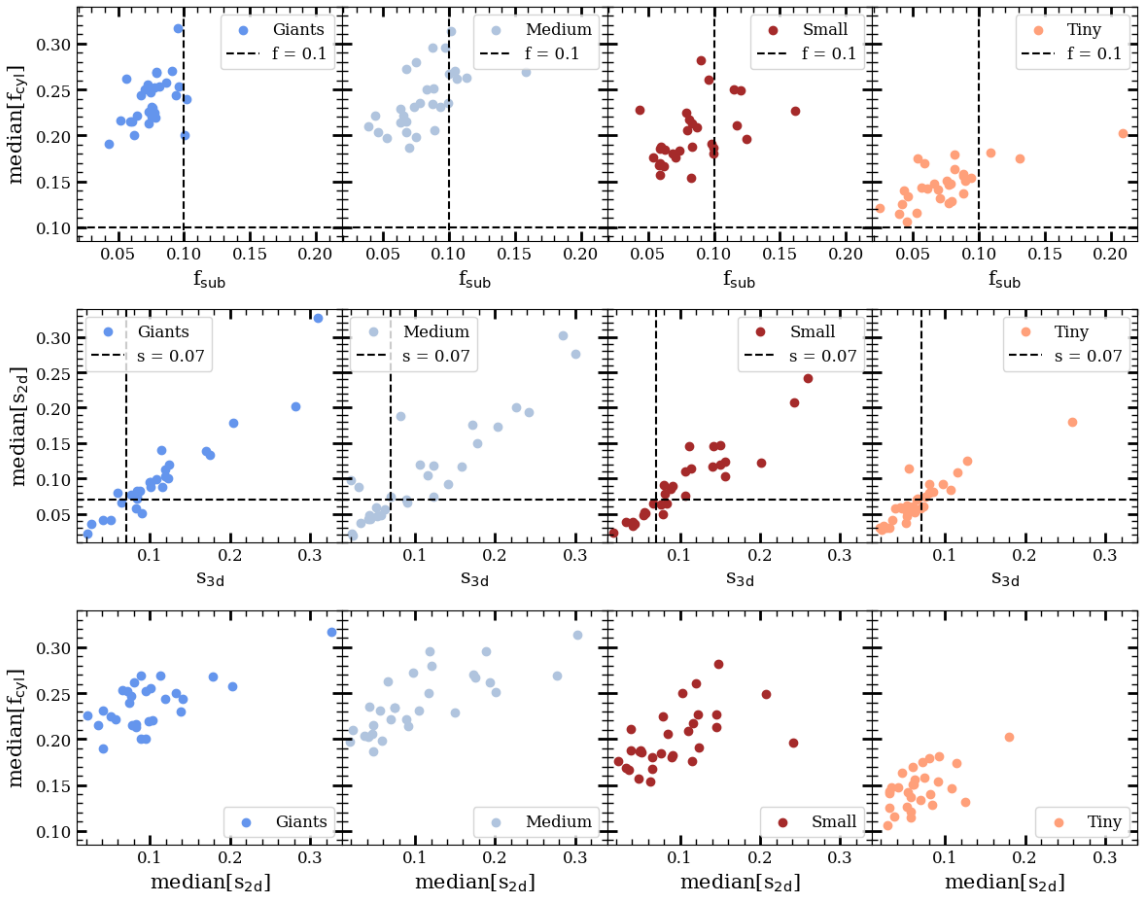


Figure 11.5. Median projected values of f (*top row*) and s (*middle row*) over the 200 random projections for each galaxy cluster as a function of their three-dimensional values, as well as the relation between projected f and s (*bottom row*). The dashed lines denote typical thresholds, with higher values indicative of a dynamically active galaxy cluster.

Conversely, the centershift is found to agree well between projection and three dimensions. Overall, the number of clusters whose dynamical state would be classified the same between two to three dimensions is found here to be 18 of 116 when using f as a tracer, compared to 103 of 116 when using s (or around 15.6% versus 88.8%).

Given that the centershift is a consistent determinant for the dynamical state independent of whether it is measured from projections in observations or intrinsically from simulations, the question is how well it correlates with f_{cyl}. We indeed find a good agreement in that high centershift corresponds to high substructure masses, as shown in the bottom row of Fig. 11.5, though there exists a noticeable scatter.

Nonetheless, the found correlation prompts the question of the impact of a high centershift on *individual* substructure masses for a given projection. To this end, the projections of the galaxy clusters within the giants mass bin are split into four groups based on their centershift. Then, the resulting fractional projected substructure masses $f_{\mathrm{x}} = M_{\mathrm{cyl}}/M_{\mathrm{tot}}$ are depicted in Fig. 11.6 as a function of the most massive bound subhalo mass fraction $M_{\mathrm{sub}}/M_{\mathrm{tot}}$ within their aperture. The colors denote the different ranks of the substructures, from f_1 the first substructure shown in purple to the eighth most massive substructure f_8 shown in pink.

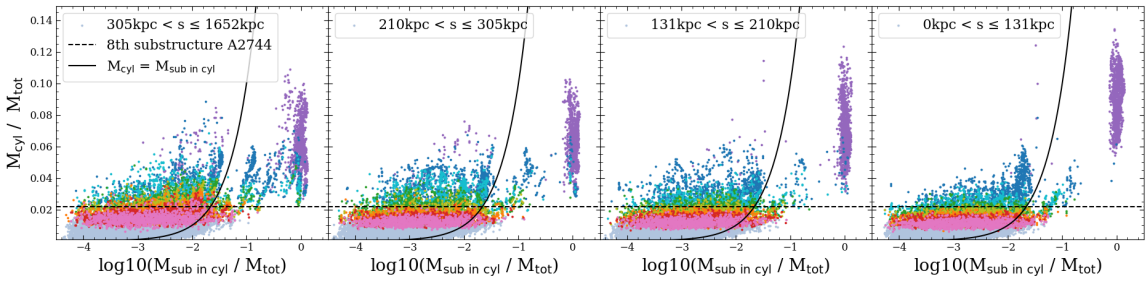


Figure 11.6. The substructure mass divided by the total mass within 1.3 Mpc in projected as a function of the most massive bound subhalo mass M_s within their aperture. The projections are split into quartiles by their centershift (each containing 1450), going from *left* to *right* as highest to lowest with borders as given in the legends. Within each projection, the first to eighth most massive substructures are colored as purple, blue, cyan, green, olive, orange, red and pink, with all others colored gray. The horizontal black line denotes the mass fraction of the eighth substructure of Abell 2744, such that all pink points which lie above it belong to a projection with a comparable substructure mass distribution. This is the case for $(57, 1, 0, 0)$ projections when going from left to right. The black dashed curve denotes equality between projected and bound mass.

We find the mass fractions f_1 of the first substructures to generally increase with decreasing centershift while the mass fractions of the second to eighth substructure decrease. For high centershifts s there are multiple cases where the most massive substructure (purple) lies at a low value of M_s (on the order of $1\% \cdot M_{tot}$). This is exceedingly rare for low centershifts s, where instead the most massive substructure also typically lies at the deepest point of the potential (thus containing the SubFind center of the cluster).

The horizontal black lines in Fig. 11.6 denotes the mass fraction f_8 of the eighth substructure of Abell 2744. For the lowest centershift bin there are only 23 of 1450 projections with a fifth substructure (olive) where the substructure mass fraction f_5 lies above this black line. Not a single sixth substructure reaches a mass fraction comparable to the eighth substructure mass fraction of Abell 2744. For the highest centershift bin, this occurs more frequently even for the eighth substructure (pink), with 57 of 1450 projections having an eighth substructure with a mass fraction f_8 larger or comparable to Abell 2744. There is only one projection with an eighth substructure mass fraction f_8 above the line which does not lie in the bin of highest centershift, and it instead lies in the bin with second highest. We conclude that multiple massive substructures can only be found in non-relaxed clusters with a large centershift, even if in return a large centershift does not necessarily indicate a large number of massive substructures. This is because a single major merger which is not yet relaxed can also lead to a large centershift, but may result in only two massive substructures.

We thus find that a high centershift enhances the likelihood to find a larger number of massive substructures. This can be understood when considering the relation of the line-of-sight to the feeding filaments or to the axis of a recent major merger. For the galaxy clusters where there is a dominant such axis, if one were to look straight along it the substructures would appear clumped together and thus result in a lower centershift. This would also reduce the number of very massive substructures as multiple of them may be projected into

single apertures. Conversely, orientations looking at the axis perpendicularly will see a string of individual substructures sitting within a strongly elongated halo. This allows for a higher number of apertures with extreme masses, while the center of these mass clumps is somewhere in between, shifted strongly compared to the potential minimum which will be inside the most massive of these substructures. Indeed, Eckert et al. (2015) find indications that the merger axis for Abell 2744 is perpendicular to the line-of-sight, comparable to what we find here for galaxy cluster 20 of the "giants" as discussed in Sec. 11.2.1.

11.3 Summary and Conclusion

In this study we compared substructure mass distributions of simulated galaxy clusters to those observed with gravitational lensing. Some of the observed galaxy clusters, especially Abell 2744, exhibit such massive substructures that these were discussed to possibly be in tension with results from cosmological ΛCDM simulations. So far, previous studies have tried to solve the tension using dark matter only simulations. Here, for the first time, we used a fully hydrodynamical cosmological simulation to search for Abell 2744 counterparts and study the substructure mass functions of galaxy clusters in projection.

To be able to compare the most massive structures in the known Universe, a large volume simulation with proper resolution is required. To this end, we used the *Box2b/hr* of the hydrodynamical cosmological simulation suite *Magneticum Pathfinder*, one of the largest baryonic simulations currently available covering a volume of $(909\,\mathrm{cMpc})^3$. In this simulation volume, at $z = 0.252$ there are 29 galaxy clusters with masses above $M_{\mathrm{FOF}} \geq 10^{15} M_{\odot}$. Galaxies are resolved down to stellar masses $M_{*} \geq 5 \times 10^{9} M_{\odot}$ when requiring halos to contain at least 100 stellar particles. While having more than 500 of such resolved member galaxies in the most massive cluster, this large dynamical range allows us to study galaxy cluster substructure properties down to $M_{\mathrm{vir}} \geq 10^{14} M_{\odot}$ with large significance.

We find that:

- we can successfully reproduce the substructure mass fractions observed within cluster Abell 2744 by Jauzac et al. (2016). Our best reproduction of the substructure mass fractions of Abell 2744 occurs for a galaxy cluster that just recently underwent a massive major merger event with a merger ratio of 1:1.4, in addition to several minor merger events with mass ratios of 1:4, 1:6, and 1:24. We find that the appearance of multiple large substructures is a direct consequence of such recent multiple merger accretion events.
- furthermore, our simulated counterpart of Abell 2744 exhibits strong noticeable shock fronts resulting from the post core passage major merger, in line with observations of strong shock fronts detected in Abell 2744 (e.g., Owers et al., 2011; Rajpurohit et al., 2021). In addition, we find that the simulated counterpart of Abell 2744 is fed through four main filaments, again in agreement with observations (Eckert et al., 2015).

- in general, a large total substructure mass fraction correlates to a larger amount of recently accreted mass and the dynamical state of the cluster, in agreement with previous works by Neto et al. (2007); Jiang & van den Bosch (2017). For the galaxy clusters with $M_{\rm vir} \geq 2\times10^{14} M_{\odot}$ this correlation persists even out to 3.2 Gyr, though it becomes quite scattered for the lower mass clusters. This clearly indicates that the appearance of multiple massive substructures, independent of the host cluster mass, is a good tracer for (multiple) massive merger events occurring within the last 3.2 Gyr, not yet long enough ago to completely disrupt the substructures due to stripping and dynamical friction processes in the cluster environment. This timescale is longer than what was previously found from dark matter only simulations, showing that the deeper potential wells generated due to the presence of the baryons fosters the longer survival times of the satellite galaxies (see also Bahé et al., 2019, for satellite galaxy survival timescales). Ultimately, this increases the time window of the appearance of large substructures and therefore allows for more extreme configurations of total substructure mass fractions in hydrodynamical simulations compared to dark matter only ones.
- galaxy clusters whose eighth most massive substructures have the highest (lowest) mass fractions out of our sample have gained a large (low) percentage of their mass within the last 2 Gyr, allowing for insight into the dynamical state and recent accretion history of the galaxy cluster without the requirement of having measured all substructure masses.
- the mass of the observed galaxy cluster is not necessarily a guarantee that a significant fraction of the current cluster has been assembling already at high redshift, in agreement with results from protocluster evolution pathways by Remus et al. (2023). Instead, we find some of the most massive galaxy clusters to have reached masses above $1\times10^{14} M_{\odot}$ only recently, below $z = 1$, clearly demonstrating that some of the most massive nodes in the cosmic web have been assembled in very complex ways, being the result of larger numbers of smaller systems merging together on comparatively shorter timescales. Multiple massive substructures might be a good indicator for such nodes, however, the present sample of massive galaxy clusters is too small to provide statistically representative conclusions on that matter.
- the necessary condition for finding a large number of massive substructure masses is a high centershift. This means that the galaxy cluster must be dynamically active *as well as* observed from a projection angle where the substructures are distributed largely perpendicular to the line-of-sight. Such in-plane geometry then also fosters the detectable appearance of other indications of dynamically strongly disturbed systems like the presence of radio relics.

We conclude that, given the importance of galaxy cluster substructures for quantifying the clusters dynamical state as well as for constraining models of dark matter (Bhattacharyya et al., 2021), it is of great importance to consider in detail the impact of projection effects when comparing measurements to cosmological simulations. The findings here further demonstrate that the total substructure mass fraction $f_{\rm cyl}$, even when measured in projection,



indicates dynamically active galaxy clusters and still correlates well with the mass accretion history of the cluster.

Finally, we have shown that we can successfully reproduce not just the substructure mass fractions but also other properties of the extreme galaxy cluster Abell 2744 in the hydrodynamical cosmological *Magneticum Pathfinder* simulation within the ΛCDM framework, demonstrating that there is no tension between ΛCDM and the existence of such massive substructures. Instead, we showed that such special galaxy clusters are rather interesting in terms of their accretion histories, and that they could be tracing special nodes of particularly late assembly in the cosmic web which, however, remains to be further analyzed in future studies.

Est via sublimis caelo manifesta sereno:
lactea nomen habet candore notabilis ipso;

Publius Ovidius Naso, *Metamorphoses* Book 1, Verse 168–169, circa 1–8

12

Intra-Cluster Light as a Dynamical Clock for Galaxy Clusters: Insights from the Magneticum, IllustrisTNG, Hydrangea, and Horizon-AGN Simulations

This chapter was published as Kimmig et al., 2025, A&A 700, 95.

As the most massive nodes of the cosmic web, galaxy clusters represent the best probes of structure formation. Over time, they grow by accreting and disrupting satellite galaxies, adding those stars to the brightest cluster galaxy (BCG) and the intra-cluster light (ICL). However, the formation pathways of different galaxy clusters can vary significantly. To inform upcoming large surveys, we aim to identify observables that can distinguish galaxy cluster formation pathways. Using four different hydrodynamical simulations, Magneticum, TNG100 of IllustrisTNG, Horizon-AGN, and Hydrangea, we study how the fraction of stellar mass in the BCG and ICL ($f_{\mathrm{ICL+BCG}}$) relates to the galaxy cluster mass assembly history. For all simulations, $f_{\mathrm{ICL+BCG}}$ is the best tracer for the time at which the cluster has accumulated 50% of its mass (z_{form}), performing better than other typical dynamical tracers, such as the subhalo mass fraction, the halo mass, and the position offset of the cluster mass barycenter to the BCG. More relaxed clusters have higher $f_{\mathrm{ICL+BCG}}$, in rare cases up to 90% of all stellar mass, while dynamically active clusters have lower fractions, down to 20%, which we find to be independent of the exact implemented baryonic physics. We determine the average increase in $f_{\mathrm{ICL+BCG}}$ from stripping and mergers to be between 3-4% per Gyr. $f_{\mathrm{ICL+BCG}}$

is tightly traced by the stellar mass ratio between the BCG and both the second (M12) and fourth (M14) most massive cluster galaxy. The average galaxy cluster has assembled half of its halo mass by $z_{\rm form} = 0.67$ (about 6 Gyr ago), though individual histories vary significantly from $z_{\rm form} = 0.06$ to $z_{\rm form} = 1.77$ (0.8 to 10 Gyr ago). As all four cosmological simulations consistently find that $f_{\rm ICL+BCG}$ is an excellent tracer of the cluster dynamical state, upcoming surveys can leverage measurements of $f_{\rm ICL+BCG}$ to statistically quantify the assembly of the most massive structures through cosmic time.

12.1 Introduction

Galaxy clusters are the most massive bound, virialized structures in the observable Universe, representing less than one percent of its volume but on the order of 5-10% of the total mass (Libeskind et al., 2018). Understanding their formation is akin to understanding all of cosmic structure formation, as they represent the final stage in bottom-up ΛCDM cosmology (e.g., Chon et al., 2015; Seidel et al., 2024). As clusters assemble mass from the cosmic web, which is dominated by dark matter, they simultaneously also assemble luminous matter in the form of galaxies (which then become satellite galaxies), and build up a significant amount of stellar mass both in the brightest cluster galaxy (BCG) and in a diffuse stellar component commonly referred to as the intra-cluster light (ICL; Montes 2022). A typical estimation is that each of the three components amounts to approximately one third of the total stellar mass hosted within a cluster (Dolag et al., 2010), but individual values between clusters for the ICL range from about 10% (e.g., Zibetti et al., 2005) to 35% (e.g., Gonzalez et al., 2007; Spavone et al., 2020; Ragusa et al., 2023; Kluge et al., 2024; Spavone et al., 2024). Similar fractions are also reported at higher redshifts of $z = 0.3 - 0.4$, varying from about 10% (e.g., Montes & Trujillo, 2018) to 30% (e.g., Furnell et al., 2021). Variations of ICL fractions measured directly via flux are even larger, from 3% (Jiménez-Teja et al., 2018) to 30% (Jiménez-Teja et al., 2021, 2023, 2024). Simulations find similarly diverse pictures, with the ICL containing more (Dolag et al., 2010) or less (Brown et al., 2024) stellar mass compared to the BCG, likely depending on varying definitions of where the BCG ends and the ICL starts, something which is still under debate (see Brough et al., 2024, for an overview on different methods). However, independent of the exact definition, the diffuse ICL accounts for a significant amount of the stellar mass in galaxy clusters, but is simultaneously the component which is most difficult to measure due to its low surface brightness nature (e.g., Murante et al., 2004; Montes, 2022).

From cosmological simulations several pathways are known that contribute to the formation and growth of the ICL (e.g., Brown et al., 2024; Bilata-Woldeyes et al., 2025), including ex-situ origin of the stars as well as in-situ star formation (e.g., Puchwein et al., 2010; Ahvazi et al., 2024). The ex-situ pathways include stars that are formed in other structures and then assembled through pre-processing (e.g., Mihos, 2004; Mihos et al., 2005; Contini et al., 2014), minor and major mergers (e.g., Monaco et al., 2006; Murante et al., 2007; Contini et al., 2014), the stripping of intermediate or massive satellite galaxies (e.g., Rudick et al., 2006, 2009, 2011; Contini et al., 2014, 2018; Chun et al., 2024), as well as from disrupting



dwarfs (e.g., Conroy et al., 2007; Giallongo et al., 2014). It is becoming clear from simulations (e.g., Brown et al., 2024), models (e.g., Fu et al., 2024) and observations (e.g., Spavone et al., 2017, 2020; Kluge et al., 2024; Zhang et al., 2024; Spavone et al., 2024; Golden-Marx et al., 2025) that the most dominant contribution to the stellar component of clusters is of an ex-situ nature and originates mostly from stellar stripping and mergers. Which of these is the more important is still debated, with evidence provided for stripping (e.g., Contini et al., 2014) as well as for merging (e.g., Murante et al., 2007; Montenegro-Taborda et al., 2023). It is further unclear if the dominant component of the ICL was formed within a single structure (i.e., galaxy) and then directly stripped within the cluster halo, or if, as found by Joo et al. (2024), the majority had already been pre-processed by another structure (galaxy or group) which only afterwards then fell into the cluster (Mihos, 2004; Mihos et al., 2017). Additionally, the efficiency of the stripping of satellites to build up the ICL may be both halo mass (Bahé et al., 2019; Contini et al., 2024a) and resolution dependent (Martin et al., 2024). However, in all cases it is clear that the ICL of galaxy clusters originates primarily from ex-situ accretion.

All other cluster stars are within the BCGs, which represent the most massive galaxies in the Universe. They predominantly grow through mergers, evidence for which is found both in models (e.g., Khochfar & Burkert, 2003; De Lucia & Blaizot, 2007) and from observations (e.g., Brough et al., 2011; Oliva-Altamirano et al., 2014; Edwards et al., 2024). The cores of these BCGs are often extremely old (e.g., Oliva-Altamirano et al., 2015; Edwards et al., 2020; Santucci et al., 2020), and for early forming clusters their BCGs are typically the first galaxies to collapse on very short timescales (e.g., Rennehan et al., 2020; Remus et al., 2023). However, some of the observed BCGs also show ongoing star formation, perhaps most extreme in the Phoenix cluster (Reefe et al., 2025), but also on a lower level in our neighborhood (Donahue et al., 2015; Tremblay et al., 2015), or indications of episodes of star formation shown in populations of stars with younger ages (Mittal et al., 2015; Edwards et al., 2024), hinting at either recent ongoing merging events or even gas accretion or cooling from the hot halo. Nonetheless, compared to the outskirts and the ICL, the BCGs are generally older and more metal rich (e.g., Montes & Trujillo, 2014; Oliva-Altamirano et al., 2015; Edwards et al., 2016; Montes & Trujillo, 2018; Edwards et al., 2020), which suggests that the BCGs form earlier and the ICL was accreted more recently (Montes et al., 2021).

While these overall trends are well established, separating the ICL component from the BCG is an as of yet open topic. Generally, it has been established that there are two kinematically distinct stellar components in galaxy clusters (Dolag et al., 2010; Bender et al., 2015; Longobardi et al., 2015; Remus et al., 2017a; Marini et al., 2024), which can be used to separate the central galaxy of a cluster from the surrounding ICL. Similarly, the radial luminosity profiles of galaxy clusters typically show two or sometimes even more components, which would suggest different origins for the stars belonging to each (Iodice et al., 2016; Spavone et al., 2017; Kluge et al., 2020; Spavone et al., 2020; Montes et al., 2021; Ragusa et al., 2023; Ahad et al., 2023, among others). In principle, the transition between the innermost component and the others could be used to split the ICL and BCG.

Furthermore, surface brightness cuts can be applied (e.g., Feldmeier et al., 2004; Burke et al., 2015; Montes & Trujillo, 2018; Martínez-Lombilla et al., 2023), or also non-parametric measures (e.g., Martínez-Lombilla et al., 2023). There are more methods (e.g., Ellien et al., 2021), as discussed in more detail by Brough et al. (2024), but unfortunately, these methods do not agree on the separation between the ICL and the BCG even when applied to the same galaxy clusters (Remus et al., 2017a; Remus & Forbes, 2022; Brough et al., 2024). Indeed, difficulties in quantifying the ICL between different methods were already presented by Rudick et al. (2011), who found increased ICL fractions when including the current velocity or past accretion history of individual particles as opposed to just surface brightness.

Nonetheless, both the BCG and ICL components are clearly dominated by ex-situ growth, building up through accretion events throughout a galaxy cluster's lifetime. Consequently, galaxy clusters are in a unique position, as they represent the extreme end of the highest ex-situ fractions (e.g., Rodriguez-Gomez et al., 2016; Dubois et al., 2016; Pillepich et al., 2018a; Davison et al., 2020; Remus & Forbes, 2022; Martin et al., 2022). This has a few interesting implications for determining the current dynamical state of galaxy clusters as well as predicting their past mass accretion history.

Firstly, with little in-situ formation of stars, the total stellar mass instead grows along with the accreted dark matter that dominates the total mass budget. So long as there are no large variances in the structure being assembled from cluster to cluster, this implies a self-similar scaling relation for their total stellar mass to halo mass. Indeed, both observations (Budzynski et al., 2014; Kravtsov et al., 2018) as well as simulations (Bahé et al., 2017; Pillepich et al., 2018a) have found slopes near unity for the total stellar to halo mass.

Secondly, given a self-similar budget of total stellar mass, this would imply that the distribution of this mass into the components of central galaxy (BCG), stellar halos (ICL) and satellite galaxies should depend on the individual formation pathway of the galaxy cluster, as stripping and merging processes all require time to transform the assembled satellite galaxies into the BCG and ICL component. Taking the crossing time as a proxy for the dynamical timescale, this results in satellite disruption on the order of $1 - 2$ Gyr (Jiang & van den Bosch, 2016; Contreras-Santos et al., 2022; Haggar et al., 2024), though this may be halo mass dependent (Bahé et al., 2019).

By contrast, the time-scale of the accretion of new mass onto the galaxy cluster as a whole is on the order of $M/\dot{M} \approx 10$ Gyr (McBride et al., 2009; Jiang & van den Bosch, 2017). This results in a picture where on average additional satellite galaxies are accreted more slowly than the mass in existing ones is disrupted. Consequently, the amount of mass in the cluster satellites should act as a dynamical clock, as already suggested by Dolag et al. (2010) based on galaxy clusters selected from the simulation of a local-Universe analogue. Additional credence for this idea was recently provided from models by Contini et al. (2023, 2024b), showing that clusters with higher concentrations, i.e., dynamically older clusters, have larger fractions of ICL. Similar results were also found from The Three Hundred Simulations (Contreras-Santos et al., 2024) and the Horizon Run-5 simulation (Yoo et al., 2024).

Furthermore, there is evidence from observations that the distribution of mass between the ICL and BCG versus the satellites does not depend simply on the total mass of the galaxy cluster. Both Kluge et al. (2021) and Ragusa et al. (2023) do not find any correlation between the observed fraction of the ICL and cluster mass, despite using different methods of ICL measurement, and both report a large scatter in the fractions. A trend is also observed between ICL fraction and the fraction of early type galaxies in nearby groups and clusters, with the ICL fraction being on average larger in those environments dominated by early-type galaxies (e.g., Aguerri et al., 2006; Da Rocha et al., 2008; Ragusa et al., 2021, 2022, 2023; Spavone et al., 2020, 2024). Even in more massive systems at higher redshifts, Montes & Trujillo (2018) noted that the most relaxed cluster in their sample of 6 (at $0.3 < z < 0.55$) has a higher fraction of ICL compared to the other clusters. Intriguingly, Jiménez-Teja et al. (2018) find at $0.2 < z < 0.4$ evidence for higher ICL fractions in the bluer bands of merging clusters compared to redder bands, indicating that these trends may further depend on the exact wavelengths used to measure the fractions. Nevertheless, all observations hint at a connection between the fraction of ICL and the dynamical state of clusters, in agreement with the theoretical considerations.

Interpreting this link is made more difficult by the variety of definitions of the dynamical state. Established parameters include the center shift, meaning the distance between the center of mass and the point of the deepest potential $s = \Delta_r / R_{200c}$ (e.g., Mann & Ebeling, 2012; Biffi et al., 2016; Cui et al., 2017; Roberts et al., 2018; Zenteno et al., 2020; Contreras-Santos et al., 2022), the total mass contained in subhalos f_{sub} (e.g., Neto et al., 2007; Jiang & van den Bosch, 2017; Cui et al., 2018), or the virial ratio $\eta = (2T - E_s)/|W|$, given by the total kinetic T, potential W, and surface pressure energy E_s (e.g., Shaw et al., 2006; Cui et al., 2017; Haggar et al., 2024). This list has expanded significantly in recent years to include, among others, the mass difference between the BCG and the second most massive galaxy (M12) (e.g., Jones et al., 2003; Ragagnin et al., 2017; Raouf et al., 2019; Casas et al., 2024), the offset between the central galaxy and the luminosity center of the total structure s_{stars} (e.g., Raouf et al., 2019), the fraction of total mass contained in the eighth most massive substructure of the cluster f_8 (Kimmig et al., 2023), and the formation redshift z_{form}, defined as the time when the galaxy cluster first reached 50% of its final $z = 0$ mass (e.g., Haggar et al., 2020; Contreras-Santos et al., 2022). For a more in depth overview see the work by Haggar et al. (2024).

However, many of these definitions require multi-wavelength observations to measure (center shift is often defined in the X-ray (Biffi et al., 2016; Zenteno et al., 2020), while the magnitude gap explicitly depends on the chosen band), while others such as f_{sub} require gravitational lensing (e.g., Jauzac et al., 2016) which may suffer from projection effects (Schwinn et al., 2018; Mao et al., 2018; Kimmig et al., 2023). Additionally, as shown by Haggar et al. (2024), different parameters may be measuring different types of cluster dynamical state. Regardless, it is of great importance to better quantify and understand the dynamical states of galaxy clusters, as there are indications of links to the properties of their galaxy populations (Aldás et al., 2023; Brambila et al., 2023; Véliz Astudillo et al., 2024).

With several facilities capable of probing the low-surface brightness regime that are either ongoing, such as *Euclid* (Laureijs et al., 2011; Kluge et al., 2024) or upcoming, for example Roman (Montes et al., 2023) or Vera Rubin Observatory's Legacy Survey of Space and Time (LSST, see Ivezić et al., 2019; Brough et al., 2020), as well as with improved methods (Canepa et al., 2025), it is of increasing importance to have a tool capable of inferring dynamical states for the expected large number of galaxy clusters.

In this work we utilize three large hydrodynamical cosmological simulation suites, namely Magneticum Pathfinder (Teklu et al., 2015, Dolag et al., in prep), IllustrisTNG (Nelson et al., 2019a), and Horizon-AGN (Dubois et al., 2014), as well as the cosmological hydrodynamical zoom-in simulation set of galaxy clusters Hydrangea (Bahé et al., 2017; Barnes et al., 2017), to investigate the connection between the ICL/BCG and the dynamical age of galaxy clusters. Of these, we focus in particular on the Magneticum simulations, as they have a statistically meaningful number of galaxy clusters over the full mass range from $M_{\rm vir} = 10^{14} M_{\odot}$ to $M_{\rm vir} = 2 \times 10^{15} M_{\odot}$ (for a statistical error $\sigma \propto \sqrt{N}$ we have a signal-to-noise ratio of $N/\sqrt{N} \approx 30$). However, to confirm that all predicted trends are independent of resolution or included physics, we compare with the other three simulations which have a higher particle resolution. This set of four simulations has already been shown by Brough et al. (2024) to produce similar fractions of ICL when observational techniques are run on self consistently-generated mock images.

In Sec. 12.2 the four different simulations are introduced. Sec. 12.3 discusses the evolution of the ICL+BCG fraction with time and their connection to the dynamical state of clusters. Furthermore, the average disruption rates of satellites is calculated. Finally, in Sec. 12.4 the results are summarized and discussed. Throughout this work, we assume the native cosmology of each of the simulations as described in Section 12.2.

12.2 Simulations

This study is performed using three different hydrodynamical cosmological simulation suites, Box2 hr of the Magneticum Pathfinder suite, TNG100 of the IllustrisTNG suite, Horizon-AGN, as well as the Hydrangea zoom-in simulation suite, which vary in their included physics, resolutions and box volumes. As we aim to quantify the connection between cluster mass assembly and the fraction of stellar mass in the BCG and ICL, we require a statistically significant number of clusters to cover a sufficient diversity in assembly histories. To this end, we focus in particular on the Magneticum Pathfinder simulations which provide the largest simulation volume and thus the highest number of clusters by $z = 0$, reaching 886 galaxy clusters of $M_{200c} \geq 10^{14} M_{\odot}$ for the Box2 hr simulation.

The other two uniform-volume simulations have a higher resolution but significantly fewer galaxy clusters, with 14 of $M_{200c} > 10^{14} M_{\odot}$ for both TNG100 and Horizon-AGN. The Hydrangea zoom-in simulations meanwhile have 46 such galaxy clusters. The set of simulations used for this work has already been shown in the previous study by Brough et al. (2024) to provide galaxy clusters with comparable properties in terms of their ICL and



BCG when applying the same criteria, providing reasonable ground for a further comparison. Following the approach introduced in that work, we will also calculate all quantities used in this study in the exact same way for all simulations, as described below.

The clusters for Horizon-AGN and TNG100 are equivalent to those selected by Brough et al. (2024). For Hydrangea we use all available 46 clusters, while for Magneticum Pathfinder Box2 hr we include most of the 886 total clusters by $z = 0$, removing a few clusters with assembly histories which break before $z = 3$ to ensure the same number of structures are followed at every point in time. Our final sample thus consists of 14, 14, 46 and 868 galaxy clusters with $M_{200c} \geq 10^{14} M_{\odot}$ from Horizon-AGN, TNG100, Hydrangea and Magneticum Pathfinder Box2 hr, respectively. The details of these four cosmological hydrodynamical simulations are described in more detail by Brough et al. (2024). Here, we provide only a brief summary and refer the reader to that work for more details, especially to the extensive Table A1 comparing the different simulation properties.

For a comparison between the different simulations, Fig. 12.1 shows the number of stellar particles that the typical progenitor galaxy building up the ICL, which is about Milky-Way (MW) mass, $M_{\rm vir}^{\rm MW} = 1 \times 10^{12} M_{\odot}$ and $M_{*}^{\rm MW} = 5 \times 10^{10} M_{\odot}$ (Contini et al., 2014; Brown et al., 2024), would have given the simulation stellar particle resolution, as a function of the range of halo masses covered by the simulations. The upper bound is given by the maximum mass of a halo at $z = 0$, while the lower bound is given by the mass of 1000 DM particles. This clearly demonstrates the reason for using both the large Magneticum Box2 hr volume (blue) in combination with the smaller but higher resolution simulations of TNG100 (purple), Horizon-AGN (gold), and Hydrangea (orange), as the former is required for covering the galaxy clusters in a statistical manner, while the latter are better resolved but lack sample size for a statistical approach.

12.2.1 Magneticum Pathfinder

For the majority of this work we focus on a set of clusters from the Magneticum Pathfinder[1] hydrodynamical cosmological simulations, a suite of 6 different simulation volumes with three different resolution levels. For this work, we use in particular Box2 hr, the simulation that has a large volume of $(352\text{cMpc}/h)^3$, with particle masses for dark matter of $m_{\rm dm} = 9.8 \times 10^8 M_{\odot}$ and for gas of $m_{\rm gas} = 2 \times 10^8 M_{\odot}$. Because gas particles can spawn up to four generations of stellar particles, the mass resolution in the stellar component is a factor four higher, with masses of $m_{*} \approx m_{\rm gas}/4 \approx 5 \times 10^7 M_{\odot}$, allowing for galaxies of $M_{*} \geq 10^{10} M_{\odot}$ to be sufficiently resolved with 200 stellar particles. Box2 hr harbors a significant number of clusters by $z = 0$, with 886 galaxy clusters of $M_{200c} \geq 10^{14} M_{\odot}$. The properties of the galaxy clusters from this particular simulation have already been used to study the dynamics of the ICL and BCG components by Remus et al. (2017a), and their galaxy populations have been investigated and compared to observations by Lotz et al. (2019, 2021).

[1] www.magneticum.org

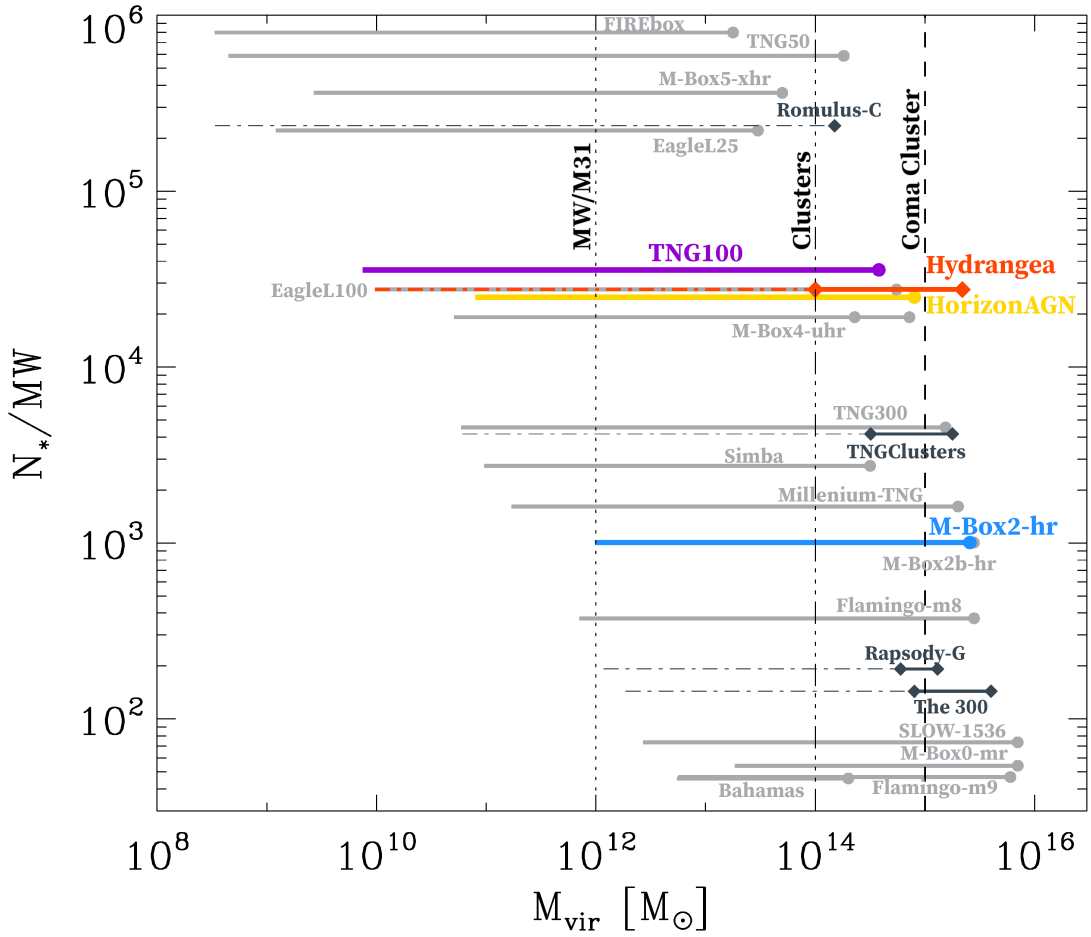


Figure 12.1. The number of stellar particles equating to the Milky Way-like (MW) stellar mass versus the halo mass covered by the simulation. The simulations used for this study are shown in color, with Magneticum Box2 hr shown in blue, TNG100 shown in purple, Horizon-AGN shown in gold, and Hydrangea shown in orange. Other commonly known simulations are shown in gray. Full box cosmological simulations are in light gray, with $M_{\rm vir,max}(z = 0)$ indicated by a filled circle while the line goes down to the resolution limit of 1000 dark matter particles. Zoom-in simulations are plotted in dark gray, going from the most massive halo in the set (diamond) down to the same 1000 dark matter particle limit (dashed thin line). Vertical dotted lines mark the MW halo mass, the $10^{14} M_\odot$ mass threshold used to define clusters, and the Coma cluster mass. Full box simulation suites shown are: Magneticum Pathfinder (Dolag et al., 2025), IllustrisTNG (Nelson et al., 2019b), Horizon-AGN (Dubois et al., 2014), SLOW (Dolag et al., 2023; Seidel et al., 2024), EAGLE (Schaye et al., 2015), Flamingo (Schaye et al., 2023), Millenium-TNG (Pakmor et al., 2023), and Bahamas (McCarthy et al., 2017). Zoom-in simulation suites shown are: Hydrangea (Bahé et al., 2017), Romulus-C (Tremmel et al., 2019), TNG-Clusters (Nelson et al., 2024), Rapsody-G (Hahn et al., 2017), and The300 Project (Cui et al., 2018).

The softening lengths for the particle types are $\epsilon_{\rm dm} = \epsilon_{\rm gas} = 5.3$ kpc and $\epsilon_* = 2.84$ kpc, while the assumed cosmology is given by WMAP-7 (Komatsu et al., 2011), with $h = 0.704$, $\Omega_m = 0.272$, $\Omega_b = 0.0451$, $\Omega_\lambda = 0.728$, $\sigma_8 = 0.809$ and $n_s = 0.963$. The simulation was performed with a modified version of GADGET-2 (Springel, 2005), with upgrades covering the smoothed particle hydrodynamics (SPH), thermal conduction (Dolag et al., 2005b) and artificial viscosity (Dolag et al., 2004), among others (Donnert et al., 2013; Beck et al., 2016).

The implementation of the baryonic physics is described in more detail by Teklu et al. (2015). We identify galaxies and galaxy clusters using the structure finder SUBFIND (Springel et al., 2001b; Dolag et al., 2009).

12.2.2 IllustrisTNG

The Next Generation Illustris[2] simulations (IllustrisTNG) are a suite of cosmological hydrodynamical simulations, of which we use the intermediate-sized medium-resolution volume called TNG100 (Marinacci et al., 2018; Naiman et al., 2018; Nelson et al., 2018; Pillepich et al., 2018a; Springel et al., 2018). The simulation has a volume of $(75\mathrm{cMpc}/h)^3$, and particle masses of $m_{\mathrm{dm}} = 7.5 \times 10^6 M_\odot$ for the dark matter and $m_{*,\mathrm{gas}} = 1.4 \times 10^6 M_\odot$ for the stellar and gas masses. This results in galaxies of $M_* \geq 10^{10} M_\odot$ to be highly resolved with around 7000 stellar particles. At $z = 0$, the simulation includes 14 galaxy clusters with masses of $M_{200\mathrm{c}} \geq 10^{14} M_\odot$. Many previous works have considered both the total stellar content (e.g., Pillepich et al., 2018a) as well as galaxy populations (e.g., Stevens et al., 2019; Donnari et al., 2021) of the simulation galaxy clusters.

For the particle species, the softening lengths are $\epsilon_{\mathrm{dm}} = \epsilon_* = 0.74$ kpc, while the spatial resolution of the gas cell is adaptive and is better at higher densities. The assumed cosmology is given by the Planck results (Planck Collaboration et al., 2016), with $h = 0.6774$, $\Omega_m = 0.3089$, $\Omega_b = 0.0486$, $\Omega_\lambda = 0.6911$, $\sigma_8 = 0.8159$ and $n_s = 0.9667$. The simulation was performed with the moving-mesh code AREPO (Springel, 2010), with updates as described by Pillepich et al. (2018b,a). Galaxies and galaxy clusters are identified via the structure finder SUBFIND (Springel et al., 2001b; Dolag et al., 2009).

12.2.3 Horizon-AGN

Horizon-AGN (Dubois et al., 2014) is a cosmological hydrodynamical simulation with a volume of $(100\mathrm{cMpc}/h)^3$, a dark matter particle resolution of $m_{\mathrm{dm}} = 8 \times 10^7 M_\odot$, and a stellar particle resolution of $m_* = 2 \times 10^6 M_\odot$. This results in galaxies of $M_* \geq 10^{10} M_\odot$ being well resolved with approximately 5000 stellar particles. At $z = 0$, the simulation includes 14 galaxy clusters with masses above $M_{200\mathrm{c}} \geq 10^{14} M_\odot$. Prior work has been done on the build up of the ICL (Brown et al., 2024), and the shape (Okabe et al., 2018), spin (Choi et al., 2018) and star formation histories of cluster galaxies (Jeon et al., 2022).

The assumed cosmology is given by WMAP-7 (Komatsu et al., 2011), as for Magneticum (i.e., $h = 0.704$, $\Omega_m = 0.272$, $\Omega_b = 0.045$, $\Omega_\lambda = 0.728$, $\sigma_8 = 0.81$ and $n_s = 0.967$). The simulation was performed using the adaptive mesh refinement (AMR)-based Eulerian hydrodynamics code RAMSES (Teyssier, 2002). Since the simulation was performed with a grid code, the initially-uniform 1024^3 cell gas grid is refined according to a quasi-Lagrangian criterion, with the smallest cell sizes fixed at 1 physical kpc. For mode details on the technical implementations, see Dubois et al. (2014). We identify galaxies and clusters using

[2] www.tng-project.org

the AdaptaHOP structure finder (Tweed et al., 2009) performed separately on the stars and DM. Structures are identified on the basis of local particle density with no unbinding procedure preformed. Structures and substructures are assembled from the groups created by linking particles with densities greater than 178 and 80 times the total matter density for stars and DM respectively according to their closest local density maxima. AdaptaHOP then links structures based on saddle points in the density field.

12.2.4 Hydrangea

Hydrangea (Bahé et al., 2017, see also Barnes et al. 2017) is a suite of 24 cosmological hydrodynamical zoom-in simulations of massive galaxy clusters using a variant of the EAGLE simulation model (Schaye et al., 2015). The parent simulation has a volume of $(2252\,\mathrm{cMpc}/h)^3$. The particle resolutions of the Hydrangea clusters are $m_{\mathrm{dm}} = 9.7 \times 10^6 M_\odot$ for dark matter, and $m_{\mathrm{gas},*} \approx 1.8 \times 10^6 M_\odot$, for gas and stars, respectively. This results in galaxies of $M_* \geq 10^{10} M_\odot$ to be well resolved with $\gtrsim 6000$ stellar particles. Softening lengths are $\epsilon_{\mathrm{dm}} = \epsilon_{\mathrm{gas}} = \epsilon_* = 0.7$ kpc, while the assumed cosmology is given by the Planck results (Planck Collaboration et al., 2014), with $h = 0.6777$, $\Omega_m = 0.307$, $\Omega_b = 0.04825$, $\Omega_\lambda = 0.693$, $\sigma_8 = 0.8288$ and $n_s = 0.9611$.

While the parent simulation contains $> 10^5$ galaxy clusters, the Hydrangea set of zoom-in simulations contains 54 galaxy clusters with masses above $M_{200\mathrm{c}} \geq 10^{14} M_\odot$. We here use a subsample of 46 clusters, with masses of $14 \leq \log_{10}(M_{200\mathrm{c}}\,[\mathrm{M}_\odot]) < 15.4$, thus expanding on the set used by Brough et al. (2024). Previous works have shown that the stellar mass function of cluster galaxies in Hydrangea agrees well with observations, both at $z \approx 0$ (Bahé et al., 2017) and $z \sim 1$ (Ahad et al., 2021). Although star formation in satellites is very efficiently quenched, DM stripping leads to a ≈1 dex positive offset of the stellar-to-halo mass relation from the field (Bahé et al., 2017). As shown by Bahé et al. (2019), only a few per cent of satellite galaxies accreted after $z \approx 2$ are fully disrupted. Nevertheless, the simulations predict a substantial ICL component that accounts for ∼ 20% of the total stellar mass even on group scales (Ahad et al., 2023, see also Brough et al. 2024).

The sub-grid parameters are the same as for the 50 Mpc 'AGNdT9' simulation of the EAGLE suite, which differs from the 'Reference' model as used for the 100 Mpc EAGLE simulation in the AGN heating temperature increment ΔT and viscosity parameter C_{visc} (Schaye et al., 2015). The simulations were performed with a significantly modified version of the SPH code GADGET-3 (last described by Springel 2005). Major updates include the 'Anarchy' pressure-entropy SPH scheme (Schaller et al., 2015) as well as subgrid physics models for reionization, gas cooling, star formation, metal enrichment, and stellar and AGN feedback (Schaye et al., 2015, see also Crain et al. 2015). As for TNG100 and Magneticum, we identify galaxies and galaxy clusters via the structure finder SUBFIND (Springel et al., 2001b; Dolag et al., 2009).

12.2.5 Property Definitions

Throughout this work, we define our quantities within the radius enclosing 200 times the critical density, R_{200c}. Halo mass is then given as the total mass in that radius, M_{200c}. The total stellar mass $M_{*,\mathrm{tot}}$ is the sum of all stellar mass in R_{200c}, while the ICL+BCG stellar mass $M_{*,\mathrm{ICL+BCG}}$ is the sum of all stellar mass within R_{200c} that is assigned to the central subhalo of the cluster, i.e., excluding mass in satellites. The ratio between the stellar mass in the ICL+BCG to total is given as $f_{\mathrm{ICL+BCG}} = M_{*,\mathrm{ICL+BCG}}/M_{*,\mathrm{tot}}$, and is by definition smaller than unity. Similarly, mass ratios to satellite galaxies are determined for satellites whose positions lie within R_{200c} of the cluster center as given by the BCG.

12.3 Results

As the main goal of this study is to understand to what extent the ICL and the BCG can be used as tracers for the evolution of galaxy clusters, we will first investigate the cluster populations with respect to their evolution before we connect them to the ICL and BCG properties. This also provides the basis for comparisons between the different simulations. Unless otherwise noted, we define the halo mass as M_{200c}, which is the total mass within a sphere of mean density of 200 times the critical density.

12.3.1 Populations of Galaxy Clusters

Galaxy clusters come in a variety of shapes and sizes, with the usual definition spanning over an order of magnitude in mass from $M_{200c} \geq 10^{14} M_\odot$ to $> 10^{15} M_\odot$. Their differences result from the different assembly histories, with some assembling a majority of their mass already early in the Universe (e.g., Sorce et al., 2020; Remus et al., 2023), while others have only recently undergone major mergers, such as the Coma cluster (e.g., Burns et al., 1994; Sanders et al., 2013; Seidel et al., 2024) or the Abell 2744 cluster (e.g., Owers et al., 2011; Kimmig et al., 2023).

Fig. 12.2 shows r-band mock images of 20 example galaxy clusters ranging from $M_{200c} = 1 \times 10^{14} M_\odot$ to $M_{200c} \approx 1.5 \times 10^{15} M_\odot$. The clusters are ordered to have increasing M_{200c} from left to right, with clusters in the same column having the same M_{200c}. The rows go from the highest to the lowest BCG mass (top to bottom), where, as motivated by Brough et al. (2024), we use $M_{*,100\mathrm{kpc}}$, defined as the stellar mass within 100kpc, excluding satellites. For each cluster, we show the projected image of radius R_{200c} out to a depth of $3 \cdot R_{200c}$. As can be seen immediately, the clusters show a larger amount of diffuse light with increasing halo mass (i.e., from left to right). However, it is also clear that in the galaxy clusters with the highest BCG masses (top row) have relatively less stellar mass (and therefore luminosity) in the satellites. This implies more recent merging activity for those clusters with lower BCG masses, which is indeed what we find. The galaxy clusters in the bottom rows commonly host two massive galaxies that would make the definition of a single BCG difficult.

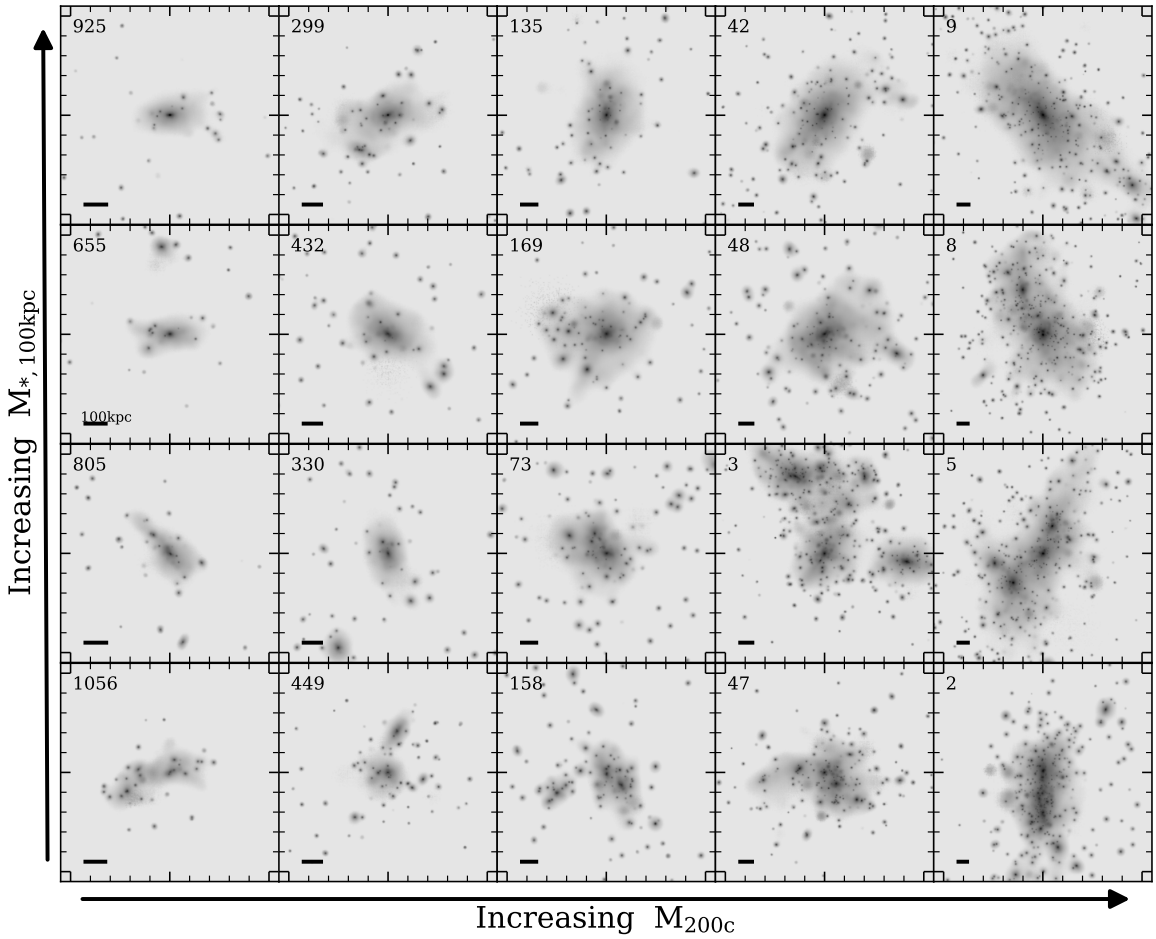


Figure 12.2. r-band mock images of example galaxy clusters from the Magneticum Box2 hr simulation in a random projection, with increasing mass from left to right and cluster IDs indicated in the top left. Clusters in the left column have about $M_{200c} = 1 \times 10^{14} M_{\odot}$, with clusters on the right having $M_{200c} > 1 \times 10^{15} M_{\odot}$. From top to bottom we plot galaxy clusters with decreasing BCG stellar mass (within 100 kpc, excising satellites) within a narrow bin of cluster halo mass. Each panel shows the full R_{200c} size of the cluster, with the black line in the bottom left of each panel marking the effective length of 100 kpc while the axes ticks are in units of $0.2 r_{200c}$.

As structure merges into the growing cluster, it brings with it a majority of its mass in the form of dark matter, as well as baryons in the form of stars and gas. Depending on the nature of the orbit of the merging galaxies, not all of the stars may reach into the deepest parts of the galaxy cluster potential (Karademir et al., 2019), resulting in a range of stellar masses for the central BCG. This is also the origin for the scatter in the stellar mass-halo mass relation that we show in the left panel of Fig. 12.3, with a range of around 0.7 dex in $M_{*,100kpc}$ at a given halo mass. Note that this scatter is entirely driven by the central BCG+ICL mass, as we exclude any contributions from satellites. For our set of example clusters in Fig. 12.2, they range in $M_{*,100kpc}/M_{200c}$ from 3.4% for cluster ID 925 (top left) to 0.5% for cluster ID 158 (bottom of the third column). Because the higher resolved simulations TNG100, Hydrangea and Horizon-AGN (purple, orange and gold) show a similar scatter in the left panel of Fig. 12.3, we can conclude this to be inherent in the way mass accretes onto the galaxy clusters. Finally, as also noted by Brough et al. (2024), all simulations reproduce

the underlying BCG-halo mass relation (e.g., Brough et al., 2008; Lidman et al., 2012), though there are some differences. Magneticum and Horizon-AGN tend toward higher stellar masses at equivalent halo mass relative to Hydrangea and TNG100. Crucially, however, the slopes of the $M_* - M_{\rm halo}$ relation are similar.

To see that this scatter is not due to large fluctuations in the halo mass, which may be driven by recently infalling structure which resides far away from the BCG, we can instead plot $M_{*,100\rm kpc}$ against M_{500c} (middle panel of Fig. 12.3). We find that the range in stellar masses at a given M_{500c} is still significant, and comparable for Magneticum Box2 hr to that found for TNG100. This scatter also matches the ±0.13 dex found by Pillepich et al. (2018a) for TNG300, the larger volume box of the IllustrisTNG suite, with the same galaxy formation model of TNG100. When comparing to individual galaxy cluster observations by DeMaio et al. (2018) and Kravtsov et al. (2018), we find that the simulations tend toward higher stellar masses compared to the observations. We note that we have rescaled all masses to a common h, and that observations at $z > 0.2$ are plotted in light-gray, which may at least in part be a cause of the differences. The size of the offset may also be mass dependent, where observational measurements for larger clusters could be biased towards lower masses as compared to the simulations (Kravtsov et al., 2018).

In light of recent findings by Popesso et al. (2024), who find Magneticum best reproduces the observed hot gas mass fractions in galaxy clusters, it is interesting to note that Magneticum lies at the highest stellar masses. This may imply the need for even stronger feedback, to neither overproduce the amount of stars nor the amount of hot gas in clusters. Alternatively, given that observations at high redshifts are finding significantly enhanced number densities of quenched galaxies compared to most cosmological simulations (Carnall et al., 2023a; Valentino et al., 2023), this may instead indicate the need for an earlier onset of significant AGN feedback (Kimmig et al., 2025b).

Notably, the scatter found in the simulations in Fig. 12.3 is also seen between the individual observations. To see there persists such a variety also for the total stellar content of galaxy clusters, we plot in the right panel of Fig. 12.3 the total stellar mass in the cluster $M_{*,\rm tot}$ (BCG+ICL+Satellites) against M_{500c}. We find a significant reduction in the scatter for all simulations, as well as closer agreement to observations of individual galaxy clusters by Andreon (2012); Laganá et al. (2013); Gonzalez et al. (2013); Kravtsov et al. (2018); Sartoris et al. (2020). As slopes of the $M_{*,\rm tot}$-M_{500c} relation, the simulations find 0.96 ± 0.02, 0.86 ± 0.05, 0.84 ± 0.07 and 1.13± for Magneticum, Hydrangea, Horizon-AGN and TNG100, respectively, where it is of note that Pillepich et al. (2018a) find a less steep 0.84 for TNG300. These slopes are comparable to those found by observations, with 0.52 ± 0.04, 1.05 ± 0.05 and 0.69 ± 0.9 found by Gonzalez et al. (2013), Budzynski et al. (2014) and Kravtsov et al. (2018). This could imply either that the larger relative stellar masses in the BCGs found in the simulations result from faster stripping of the satellites, or that the process of masking the satellites in observations also removes a significant amount of stars belonging to the diffuse ICL. Further investigation into this is needed in a more detailed comparison with observations, which will be the focus of a follow-up study to this work.

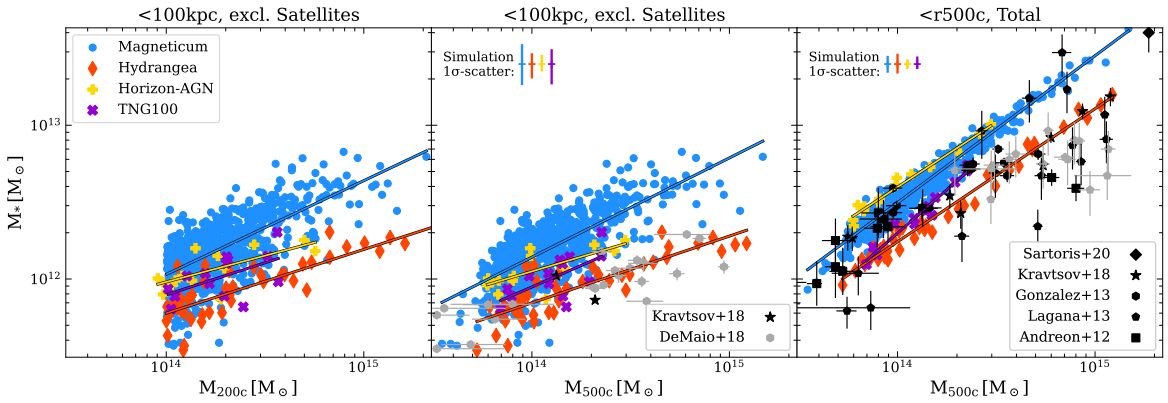


Figure 12.3. *Left:* Stellar mass of the central BCG within 100 kpc versus the total halo mass M_{200c} for the four simulations, scaled to a common h. Magneticum is plotted in blue, IllustrisTNG in purple, Hydrangea in orange and Horizon-AGN in gold. *Center:* The same stellar mass plotted against the halo mass as given by M_{500c}. Also plotted are observations by DeMaio et al. (2018) and Kravtsov et al. (2018). *Right:* The total stellar mass (BCG, ICL and satellites) against M_{500c} for the simulations, as well as observations by Andreon (2012); Laganá et al. (2013); Gonzalez et al. (2013); Budzynski et al. (2014); Kravtsov et al. (2018); Sartoris et al. (2020).

It is interesting to note, aside from TNG and Budzynski et al. (2014), the slope of the $M_{*,\mathrm{tot}}$-M_{500c} relation lies below that of self-similarity (slope of 1). As we expect the great majority of the stellar mass at the cluster scale to be accreted (e.g., Pillepich et al., 2018a; Remus & Forbes, 2022), this may indicate that satellites in smaller clusters of $M_{500c} = 10^{14} M_{\odot}$ possess ongoing star formation (e.g., Brown et al., 2024), while the more massive clusters are relatively more efficient in suppressing their satellite galaxies' star formation. This is consistent with the findings by Lotz et al. (2019), that gas is stripped more quickly in more massive clusters. Alternatively, the infalling regions for lower mass clusters may on average include galaxies that were more efficient at converting gas into stars, so which are potentially earlier formed when the baryon conversion efficiency was higher (Boylan-Kolchin, 2023; Turner et al., 2025), as compared to more massive clusters.

We further note that there are considerable differences between individual observations of total stellar versus halo mass. Halo masses based on X-ray gas using hydrostatic assumptions suffer from hydrostatic mass bias (Nelson et al., 2014) while weak-lensing measurements are impacted by weak lensing bias (Grandis et al., 2024). Stellar masses are impacted by uncertain mass-to-light ratios due to the not well known low-mass slope of the initial mass function, as well as a degeneracy between age and metallicity when stellar populations are inferred using broad-band colors (Swindle et al., 2011; Leauthaud et al., 2012).

12.3.2 Defining Cluster Dynamical State

Given the large scatter in BCG masses at a given halo mass, we now turn to consider how clusters grow. This means both their average total mass assembly, as well as how much of their stellar mass is already stripped/merged into the BCG or ICL relative to the total amount present.

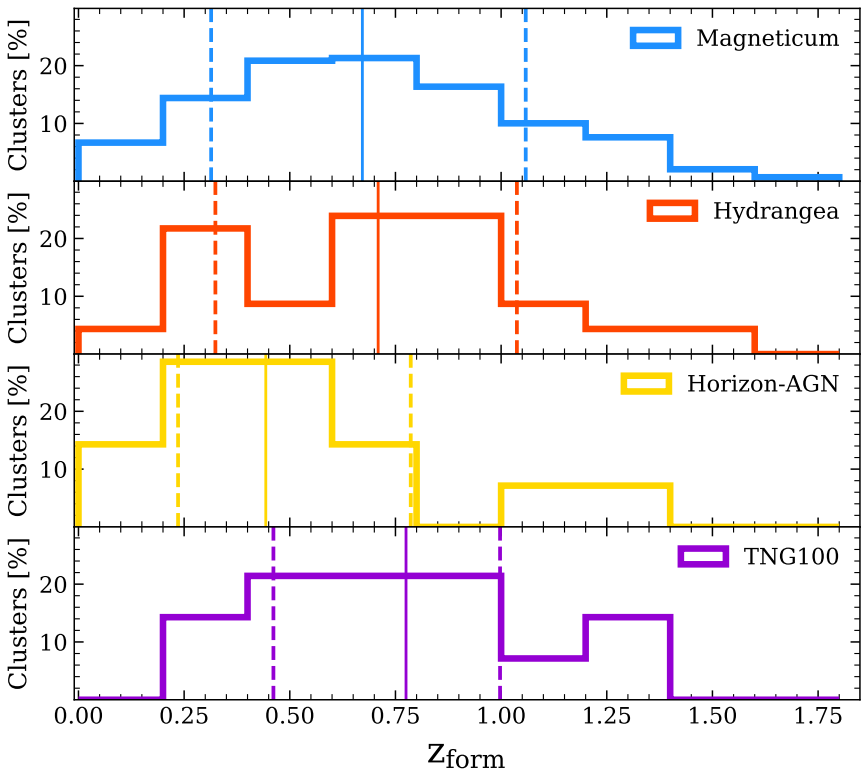


Figure 12.4. Histograms of the formation redshifts for all clusters from Magneticum Box2 hr (blue), Hydrangea (orange), Horizon-AGN (gold), and TNG100 (purple), going from top to bottom. Median (solid) and 1-σ bounds (dashed) are indicates as vertical lines.

To do so, we first require a proxy of the mass assembly history. We chose here the formation redshift $z_{\rm form}$, which is defined as the redshift when the galaxy cluster first reached half of its final halo mass $M_{\rm 200c}$ at $z = 0$. A higher $z_{\rm form}$ means an earlier formation and thus higher degree of relaxation of the galaxy cluster relative to those with lower $z_{\rm form}$. This is a definition commonly used in the literature (e.g., Boylan-Kolchin et al., 2009; Power et al., 2012, among others). We note that by using $z_{\rm form}$, we care particularly about the galaxy clusters dynamical evolution through cosmic time and the question of whether a given cluster lived in an early or late collapsing node, and care less about the most recent merging activity. Different definitions of the dynamical state or relaxedness of a galaxy cluster may be better traced by other parameters (Haggar et al., 2024), such as the X-ray center shift, given that the hydrodynamical gas component is stripped and relaxes on faster timescales than the dispersionless stars and dark matter. A more thorough look of which parameters are best suited across different timescales is needed, though it is beyond the scope of this study.

Fig. 12.4 shows the distribution of the formation redshift $z_{\rm form}$ for all clusters from the Magneticum simulations (blue) and the other three simulations. For the large number of Magneticum Box2 hr clusters, we find that the average galaxy cluster assembled half of its mass by a redshift of $z_{\rm form} \approx 0.67$, or just over 6 Gyr ago. This is in agreement with previous results for large cosmological dark matter only simulations, where Power et al. (2012) find average formation redshifts of $z_{\rm form} \approx 0.7$ for clusters of about $M_{\rm vir} = 10^{14} M_{\odot}$, and of $z_{\rm form} \approx 0.45$ for clusters of about $M_{\rm vir} = 10^{15} M_{\odot}$. Similar results are also reported for the

Millennium and Millennium-II simulations by Boylan-Kolchin et al. (2009), although these values are slightly older than what is predicted from the Press-Schechter Theorem (see Power et al., 2012).

The range of formation redshifts found for clusters from Magneticum reaches from formation redshifts as early as $z_{\rm form} = 1.8$ to as late as $z_{\rm form} = 0.06$. The other simulations used in this work also find a large spread in the formation redshift of their galaxy clusters, despite the lower number statistics of TNG100, Horizon-AGN and Hydrangea, as shown in Fig. 12.4. The average formation redshift between the samples varies slightly, with the Horizon-AGN clusters being the youngest at $\langle z_{\rm form}^{\rm Horizon} \rangle = 0.44$, both Magneticum and Hydrangea at similar formation times with $\langle z_{\rm form}^{\rm Magneticum} \rangle = 0.67$ and $\langle z_{\rm form}^{\rm Hydrangea} \rangle = 0.71$, while TNG100 has the earliest forming clusters at $\langle z_{\rm form}^{\rm TNG} \rangle = 0.78$.

We note that both TNG100 and Horizon-AGN lack clusters with $z_{\rm form} > 1.4$, as well as show a tighter spread. This is likely because they are simulations of about 100 Mpc boxlength and thus lack the largest modes of the initial power spectrum of the density fluctuations (e.g., Remus et al., 2023). As the Magneticum Box2 hr is a factor 3 larger in box-length, this equates to a factor of 27 in volume, and thus it includes not only significantly more galaxy clusters, but also more of the larger modes that can collapse earlier, leading to a larger variety in formation times.

The Hydrangea clusters, meanwhile, are drawn from a very large cosmological parent box of 3200 pMpc boxlength and thus show a similar spread that includes both the earliest and latest forming galaxy clusters. It is interesting that their selection, requiring them to be in relative isolation (no more massive halo within 30 pMpc or $20 R_{\rm 200c}$, whatever is larger), does not seem to imprint in the formation redshifts, unlike what may be typically assumed for more isolated nodes in the cosmic web (see also Remus et al., 2023; Seidel et al., 2024, for more details on this effect of early formation and starvation). Overall, Fig. 12.4 demonstrates the large variety in formation histories for galaxy clusters, making it a non-trivial problem to distinguish those from observations.

12.3.3 The Fraction of ICL+BCG and Cluster Dynamical State

To get a better understanding of how the mass of these galaxy clusters is assembled, we plot in the upper panels of Fig. 12.5 the amount of halo mass $M_{\rm 200c}(z)$ present in the galaxy clusters of the large Magneticum sample through time, relative to their final halo masses $M_{\rm 200c}(z = 0)$. The black line shows the median growth of all clusters, with the dark and light gray shades marking the 1σ- and 2σ-bounds.

The overall spread in the histories increases the farther back we look, with the 1σ-bounds reaching 0.5 dex (or a factor of 3 in range) by $z = 1$. On one hand, it is remarkable that the relative growth over the last nearly 8 Gyr remains on average within a factor of 3 for a large sample of clusters that spans well over an order of magnitude in mass at $z = 0$. On the other hand, by a redshift of $z = 1.5$ the range of typical progenitors for a $M_{\rm 200c} = 10^{14} M_\odot$ cluster already goes from large galaxies $M_{\rm 200c} \approx 7 \cdot 10^{12} M_\odot$ up to intermediate groups

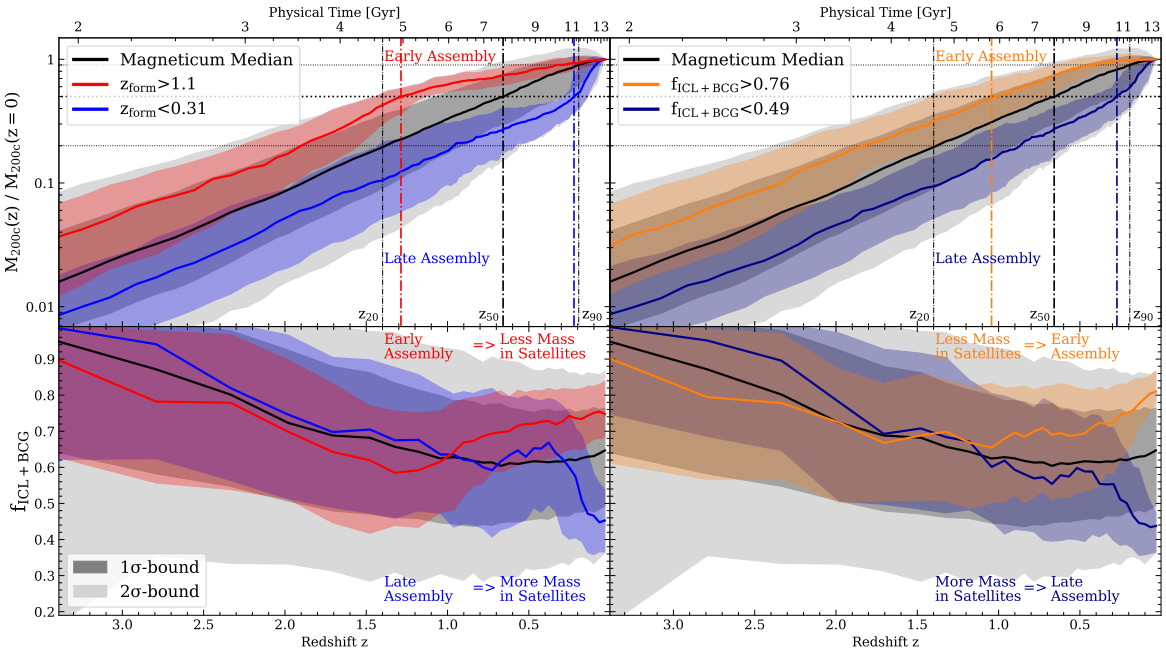


Figure 12.5. *Upper row:* Evolution of the halo mass $M_{200,c}$ with redshift z for all clusters in the Magneticum Box2 hr simulation, normalized to the final mass $M_{200,c}(z = 0)$. The black line shows the median, with the dark shaded area marking the 1σ-bounds and the light shaded area marking the 2σ-bounds. The colored lines and their 1σ-bounds show the evolution of a subset of clusters split by their formation redshift (*left*) or their $f_{\mathrm{ICL+BCG}}$ (*right*) as given in the legend. Black dash-dotted vertical lines mark the redshifts at which the average cluster has accumulated 20%, 50%, and 90% of its total mass (horizontal black lines), marked by z_{20}, z_{50}, and z_{90}, respectively. Note that z_{50} is what we define as formation redshift of a cluster. *Lower row*: Evolution of $f_{\mathrm{ICL+BCG}}$ with redshift z. As in the upper panel, the black line marks the average evolution of all clusters from Magneticum, with the gray shaded areas showing the 1σ- and 2σ-bounds. The colored lines and regions show the median and 1σ-bounds for the same subsets of galaxy clusters.

$M_{200c} \approx 3 \cdot 10^{13} M_{\odot}$. Additionally, we note that only the clusters in the upper 2σ-bound actually retain up to 10% of their halo mass down to $z = 3$, which would place them in the typical range of what is considered a protocluster with $M_{200c} > 1 \cdot 10^{13} M_{\odot}$ (Remus et al., 2023).

To emphasize this point even further, in the upper panel of Fig. 12.5 we split the total sample (black) into two subsets, those with z_{form} in the upper/lower 1σ-range of the total distribution (red/blue), with the exact cutoff shown in the legend. This results in around 140 clusters for each group. By construction, this results in the largest possible split between the formation redshifts of each group, with those assembling early (red) already reaching 50% of their final halo mass at $z \approx 1.4$ (vertical red line), while the late assembling clusters do so only by $z \approx 0.2$ (vertical blue line). Interestingly, even though the groups are split based on z_{form}, they are still largely separate at $z > 2$, indicating that clusters in either group inhabit fundamentally different assembling nodes through cosmic time. This raises the question if there is an observable that could be used to differentiate such starkly diverging histories.

Based on Fig. 12.3, we know that there is a range in the amount of mass already present in the BCG or ICL in comparison to the total stellar mass, where the range at a given halo mass is much more constrained. This is indicative of the mass transfer from satellite galaxies to the BCG or ICL as time passes, due to stripping, merging or other dynamical disruption events.

Therefore, we ask the question whether the mass assembly history of a galaxy cluster can be traced through the fraction of stellar mass contained in the BCG and ICL relative to the total stellar mass, $f_{\rm ICL+BCG}$. We choose this definition instead of only the BCG or the ICL for two reasons. First, there is no clean definition of how to split the ICL from the BCG, as discussed in depth in the literature (see Brough et al., 2024, and discussion therein), with strong disagreement between the kinematic selection and the surface brightness selection methods (see Remus et al., 2017a, for a direct comparison). Second, the distribution of stars through different stripping and merging events strongly depends on the orbit of the satellite that is disrupted or merged (Karademir et al., 2019) with the BCG, and as such there are second order effects when considering just the BCG or just the ICL beyond the tracing of dynamical timescales. Finally, though there appear to be two kinematically distinct components in clusters (Remus et al., 2017a; Marini et al., 2024), these need not also be physically separate.

We first consider how $f_{\rm ICL+BCG}$ evolves with time, plotted in the lower left panel of Fig. 12.5. The median of the Magneticum clusters is shown as a black solid line and the 1σ and 2σ bounds as dark and light shaded areas, respectively. Overall, $f_{\rm ICL+BCG}$ decreases with redshift up to $z \approx 0.6$, after which it shows a slight increase again. This increase at later times is interesting when we consider the expectations from the assembly history of dark matter only simulations, where at later times the disruption of substructure occurs on faster timescales ($\approx$ 1 Gyr) than the accretion of new matter (around 10 Gyr according to Jiang & van den Bosch, 2017). In this context, we thus expect an increase in $f_{\rm ICL+BCG}$ as more stars are disrupted than new galaxies are accreted. The lowest average value of $f_{\rm ICL+BCG}$ is reached at the time when the average cluster has assembled 50% of its mass. This implies that along the history of a galaxy cluster, the time when it has the highest fraction of stellar mass in satellites is when it reaches an intermediate group mass, which we discuss in more detail in Sec. 12.3.6.

The lower left panel of Fig. 12.5 also shows the evolution of $f_{\rm ICL+BCG}$ for the two subsets split by their $z_{\rm form}$, where we find a clear difference in their evolution. The early assembling clusters (red) reach their lowest $f_{\rm ICL+BCG}$ at $z = 1.3$, which is comparable to their median $z_{\rm form} = 1.25$. After this point they grow much slower, taking around 8 Gyrs to assemble the remaining half of their final mass, nearly half of which is spent on the final 10%. Over this same time their $f_{\rm ICL+BCG}$ steadily increases up to $f_{\rm ICL+BCG} = 74\%$ by $z = 0$, as the clusters grow very slowly with sufficient time to strip and disrupt any accreted satellites. By contrast, the late assembling clusters' $f_{\rm ICL+BCG}$ (blue line in the bottom left panel of Fig. 12.5) behaves much like the total sample of clusters up until $z = 0.3$, at which point the late assembling clusters sharply drop in $f_{\rm ICL+BCG}$, down to $f_{\rm ICL+BCG} = 0.45$ by $z = 0$. This coincides with

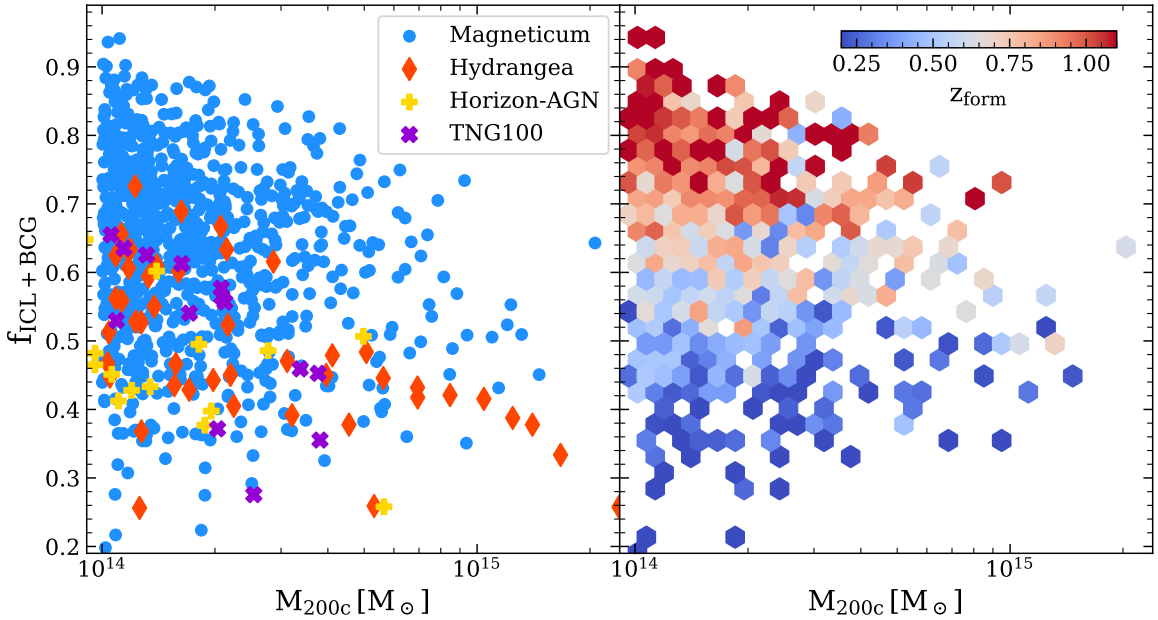


Figure 12.6. *Left panel:* The fraction of stellar mass within R_{200c} that is not bound to satellites but instead in the BCG or ICL, $f_{ICL+BCG}$, against the halo mass M_{200c}, for the Magneticum (blue), IllustrisTNG (purple), Horizon-AGN (gold) and Hydrangea (orange) clusters. *Right panel:* Same as the left panel but for the Magneticum galaxy clusters only, colored by the cluster formation redshift z_{form}. Colors as indicated in the legend.

the timeframe where they experience strong total mass growth, more than doubling their halo mass over a time of just around 2 Gyrs.

To confirm the implied anti-correlation between accretion events and $f_{ICL+BCG}$, we also split the sample of clusters based on their $f_{ICL+BCG}$ at $z = 0$. The two groups of around 140 galaxy clusters with the highest/lowest $f_{ICL+BCG}$ are shown in the right panels of Fig. 12.5. We find remarkably similar behavior to when we used the formation redshift to split the clusters, where a high/low $f_{ICL+BCG}$ directly implies an earlier/later assembly. What is of particular note is how significantly their mass assembly histories differ, with the 1σ-bounds of the two sets of clusters only overlapping at $z = 2$. This means that a measurement of $f_{ICL+BCG}$ allows us to differentiate the cluster's mass assembly history over the last 10 Gyrs. Generally, whenever another halo merges into the cluster, $f_{ICL+BCG}$ drops as the number of satellite galaxies is increased significantly. After the merger, as long as the cluster stays undisturbed, it starts to disrupt and merge the satellite galaxies, thereby adding the mass to the ICL and the BCG while the cluster is relaxing its dynamical state. However, as we are considering the stellar component which lies in the deepest parts of the satellites' potential wells, this process is imprinted over long timescales of up to 10 Gyrs.

12.3.4 Halo Mass (In-)Dependence

To test whether there is a systematic trend with galaxy cluster mass, we plot $f_{ICL+BCG}$ against halo mass M_{200c} in the left panel of Fig. 12.6. First, we find no clear correlation between the two parameters for any of the simulations. There is a slight tendency of the very most

massive clusters with $M_{200c} \approx 10^{15} M_\odot$ toward lower $f_{ICL+BCG}$, matching the observed trend (Montes, 2022). This is because these clusters generally have formed more recently due to the bottom-up structure formation for a ΛCDM cosmology, and thus had less time to strip their satellites' stars. However, it is unclear if the simulation volumes probed here are simply too small to house the extreme outlier cases of very early forming galaxy clusters with masses in excess of $M_{200c} > 10^{15} M_\odot$, which may then exhibit higher $f_{ICL+BCG}$, or if those do not form rapidly enough to be seen by $z = 0$.

We note that we find differences in the absolute values of $f_{ICL+BCG}$ between the simulations, with a median $f_{ICL+BCG} = 0.65$, 0.47, 0.46 and 0.55 for Magneticum, Hydrangea, Horizon-AGN and TNG100. On one hand, this may be caused by differences in the implemented subgrid physics, where Popesso et al. (2024) find that Magneticum best reproduces observed cluster gas properties among a set of simulations including IllustrisTNG and EAGLE, but in return produce overly massive central galaxies. On the other hand, the lower resolution of Magneticum could result in a lack of low-mass satellites in galaxy clusters, as they are stripped/disrupted too quickly because of their low particle numbers, which would increase $f_{ICL+BCG}$. Indeed, galaxies of $M_* < 10^{10} M_\odot$ are the progenitors of around 20% of the ICL+BCG stellar mass (Brown et al., 2024). However, as we will show in the following, this does not change the quantitative correlations found between the observables we consider.

When we color the points by the galaxy cluster formation redshift z_{form} in the right panel of Fig. 12.6, we find a clear color gradient. At a given halo mass M_{200c}, there is a direct correlation between $f_{ICL+BCG}$ and z_{form}, where galaxy clusters at the highest (lowest) $f_{ICL+BCG}$ have formed the earliest (latest). This provides strong credence to the idea that $f_{ICL+BCG}$ can indeed be used as a dynamical clock for the formation of galaxy clusters. We also see this for the different higher-resolved simulations, where, on average, the older galaxy cluster from both TNG100 and Hydrangea (Fig. 12.4) have higher $f_{ICL+BCG}$ than the younger Horizon-AGN clusters (left panel of Fig. 12.6).

We test this claim in the upper panel of Fig. 12.7, plotting $f_{ICL+BCG}$ at $z = 0$ against the formation redshift z_{form} of each galaxy cluster from all four simulations. It is apparent that there is a positive correlation, one which is present across all simulations and is therefore stable against calibrations of the subgrid physics. A higher $f_{ICL+BCG}$ consistently implies an earlier formation redshift. We quantify this by the Pearson correlation coefficient, finding significant values of $p = 0.69$, $p = 0.72$, $p = 0.82$ and $p = 0.83$ for Magneticum, Hydrangea, Horizon-AGN and TNG100, respectively. We have tested and find similar correlation strengths for both the Spearman ($p > 0.68$) and Kendall rank coefficients ($p > 0.5$), which is to be expected given that there is not strong indication away from linearity between $f_{ICL+BCG}$ and z_{form}.

The lower two panels of Fig. 12.7 show two other common tracers of the dynamical state of galaxy clusters known from the literature, namely the gas center shift s_{gas} (middle panel) and the fraction of total mass (including DM) in subhalos f_{sub} (lower panel), for all simulations. The former is given by the distance offset between the location of the BCG (typically at the deepest point in the potential) and the barycenter of all gas within R_{200c}.

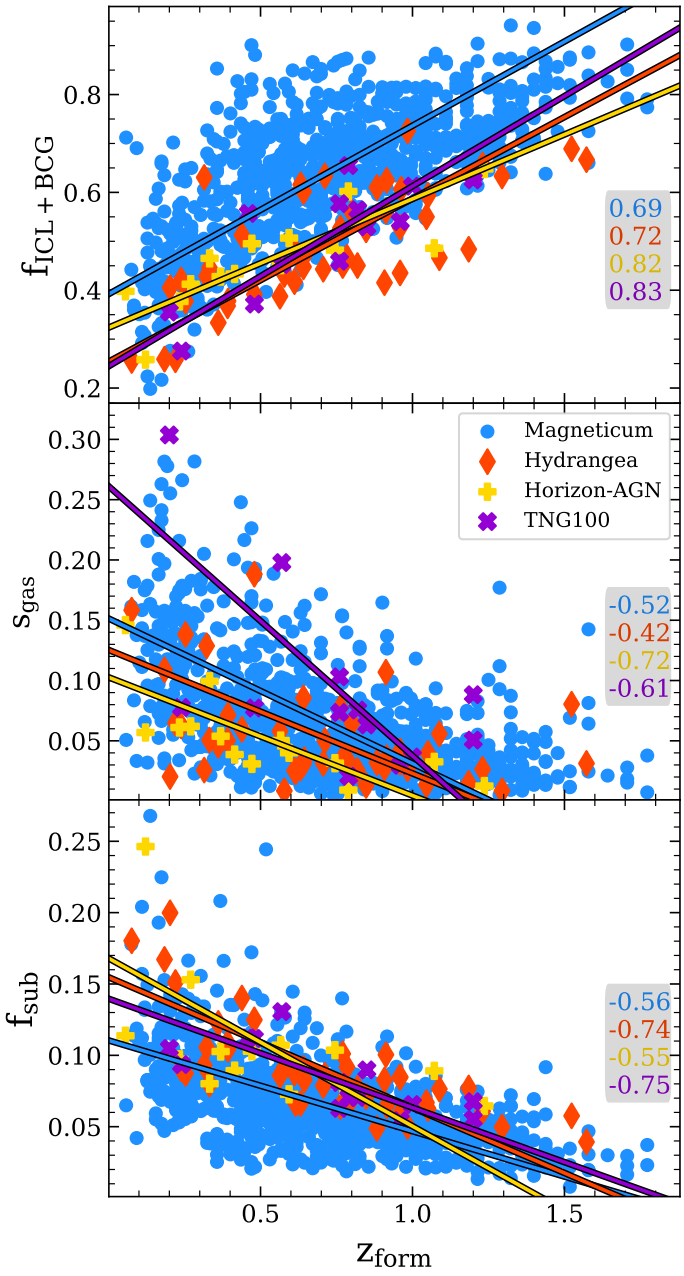


Figure 12.7. *Upper panel:* $f_{\mathrm{ICL+BCG}}$ versus formation redshift z_{form}, for the galaxy clusters from the Magneticum (blue), TNG100 (purple), Horizon-AGN (gold), and Hydrangea simulations (orange). The gray box displays the Pearson correlation coefficient for each simulation between $f_{\mathrm{ICL+BCG}}$ and z_{form}. The closer the absolute value is to unity, the tighter the correlation. We further include best fit lines for each simulation determined via the least squares method (colored lines). *Middle panel:* The center shift between the 3D gas barycenter and the location of the BCG (normalized by R_{200c}), plotted as a function of the formation redshift, with the colors the same as the upper panel. *Lower panel:* The fraction of the total halo mass mass which is in all subhalos f_{sub} (so excluding the central and diffuse halo) versus formation redshift, with colors as in the upper two panels.

We normalize this offset then by R_{200c}. Larger values thus indicate a strongly disturbed distribution of gas compared to the underlying dark matter halo, indicative of recent merging activity (e.g., Biffi et al., 2016; Zenteno et al., 2020; Kimmig et al., 2023).

Table 12.1. Fit parameters from the orthogonal distance regression for the relations between various parameters for all four simulations, where $f = f_{\mathrm{ICL+BCG}}$. We find the 1-σ error in predicting z_{form} from $f_{\mathrm{ICL+BCG}}$ to lie between ±0.16 and ±0.28, increasing with the sample size and considered mass range of the simulation.

	Magneticum		Hydrangea	
	A	B	A	B
$z_{\mathrm{form}} = A \cdot f + B$	2.90 ± 0.04	-1.14 ± 0.03	3.00 ± 0.12	-0.78 ± 0.06
$z_{\mathrm{form}} = A \cdot s_{\mathrm{gas}} + B$	-8.32 ± 0.06	1.26 ± 0.01	-9.76 ± 0.23	1.22 ± 0.02
$z_{\mathrm{form}} = A \cdot f_{\mathrm{sub}} + B$	-15.7 ± 0.1	1.7 ± 0.1	-10.9 ± 0.2	1.7 ± 0.1
$f = A \cdot \log_{10}(\mathrm{M12}) + B$	0.35 ± 0.02	0.37 ± 0.02	0.40 ± 0.12	0.26 ± 0.08
$f = A \cdot \log_{10}(\mathrm{M14}) + B$	0.44 ± 0.02	0.12 ± 0.02	0.47 ± 0.11	0.04 ± 0.11
$f = A \cdot \log_{10}(s_{\mathrm{stars}}) + B$	-0.40 ± 0.03	0.17 ± 0.04	-0.38 ± 0.18	0.02 ± 0.23
$f = A \cdot \log_{10}(\phi_{\mathrm{bcg}}) + B$	0.9 ± 0.1	-8.5 ± 0.9	1.7 ± 1.0	-17.3 ± 9.7
	Horizon-AGN		TNG100	
	A	B	A	B
$z_{\mathrm{form}} = A \cdot f + B$	3.80 ± 0.24	-1.23 ± 0.11	2.72 ± 0.19	-0.66 ± 0.10
$z_{\mathrm{form}} = A \cdot s_{\mathrm{gas}} + B$	-10.19 ± 0.28	1.05 ± 0.02	-4.47 ± 0.39	1.17 ± 0.05
$z_{\mathrm{form}} = A \cdot f_{\mathrm{sub}} + B$	-8.5 ± 0.5	1.4 ± 0.1	-13.1 ± 0.3	1.8 ± 0.1
$f = A \cdot \log_{10}(\mathrm{M12}) + B$	0.37 ± 0.16	0.19 ± 0.13	0.38 ± 0.15	0.27 ± 0.11
$f = A \cdot \log_{10}(\mathrm{M14}) + B$	0.45 ± 0.15	0.04 ± 0.14	0.50 ± 0.18	0.01 ± 0.19
$f = A \cdot \log_{10}(s_{\mathrm{stars}}) + B$	-0.24 ± 0.23	0.19 ± 0.26	-0.38 ± 0.31	0.10 ± 0.35
$f = A \cdot \log_{10}(\phi_{\mathrm{bcg}}) + B$	0.5 ± 0.3	-4.8 ± 3.1	1.5 ± 0.6	-15.4 ± 6.5

As expected from previous works, both s_{gas} and f_{sub} trace the formation redshift. However, we find for all simulations that $f_{\mathrm{ICL+BCG}}$ correlates tighter (or comparably well) with z_{form} compared to established dynamical state tracers, allowing for a better overall predictive power. We compile the best fit lines for each simulation for the formation redshift z_{form} as a function of $f_{\mathrm{ICL+BCG}}$, s_{gas} and f_{sub} in Table 12.1. We fit via orthogonal distance regression, which minimizes the errors in both directions, and provide the fit parameters in Table 12.1. For a discussion on the predictive power of the fit compared to least-squares fitting, we refer to the Appendix C.

12.3.5 Tracing ICL+BGC through Other Observables

As the ICL is difficult to observe even with the upcoming facilities, one question that remains is in how well the fraction of stars in the ICL plus BCG can be approximated by measuring other observables. In Fig. 12.8 we show four parameters that are generally easier to obtain than the stellar mass in the BCG and ICL itself. From left to right, we show the correlations between $f_{\mathrm{ICL+BCG}}$ and 1) the stellar mass ratio between the BCG and the second most massive galaxy within R_{200c} of the cluster, $\mathrm{M12} \equiv M_{*,\mathrm{BCG}}/M_{*,2^{\mathrm{nd}}}$, also termed the fossilness parameter (Tremaine & Richstone, 1977; Loh & Strauss, 2006; Ragagnin et al., 2017); 2) the stellar mass ratio between the BCG and the fourth most massive galaxy in the cluster, M14 (Golden-Marx & Miller, 2018); 3) the normalized offset $s_{\mathrm{stars}} = \Delta_r/R_{200c}$ between the barycenter of stellar mass of the cluster within R_{200c} and the position of the BCG, also known as the center shift (Mann & Ebeling, 2012; Biffi et al., 2016; Contreras-Santos et al., 2022);

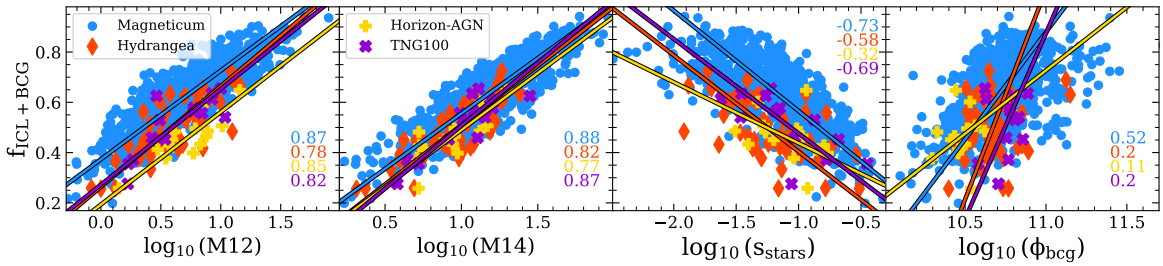


Figure 12.8. $f_{\mathrm{ICL+BCG}}$ versus different dynamical tracers, for all individual clusters from Magneticum Box2 (blue), TNG100 (purple), Horizon-AGN (gold), and Hydrangea (orange). The numbers in each panel indicate the Pearson correlation coefficient found for each relation and simulation (colors). We plot $f_{\mathrm{ICL+BCG}}$ against the stellar mass ratio of the BCG to the second (*left panel*) and fourth (*second panel*) most massive galaxy inside the cluster, counting the BCG. The *third panel* shows $f_{\mathrm{ICL+BCG}}$ as a function of the offset between the stellar barycenter and the BCG position $\mathrm{s_{stars}}$, while the *right panel* plots the fraction against the stellar potential $\phi_{\mathrm{stars}} = M_*/R_{*,\mathrm{half}}$ determined within $0.1 \cdot R_{200\mathrm{c}}$.

and 4) the quantity $\phi_{\mathrm{BCG}} = M_{*,\mathrm{BCG}}/R_{*,1/2,\mathrm{BCG}}$ in units of $M_\odot$/kpc, an approximation for the central stellar potential depth following Bluck et al. (2023), where we determine the stellar mass $M_{*,\mathrm{BCG}}$ and stellar half-mass radius $R_{*,1/2,\mathrm{BCG}}$ for the BCG within $0.1 \cdot R_{200\mathrm{c}}$.

Across all four simulations (Magneticum in blue, TNG100 in purple, Horizon-AGN in gold, and Hydrangea in orange) we consistently find that the correlation between $f_{\mathrm{ICL+BCG}}$ and the two stellar mass ratios (M12 and M14) is tightest, with remarkably little scatter. The Pearson correlation coefficients are shown in the figure, with all simulations finding $p \geq 0.7$. Interestingly, while there appears to be an offset between the simulations in the relation between $f_{\mathrm{ICL+BCG}}$ and M12, there is much less for the correlation between $f_{\mathrm{ICL+BCG}}$ and M14. This could imply that the fourth most massive galaxy is a more consistent representative of the overall stripping that occurred in the cluster, where the second most massive galaxy may be less affected. Nonetheless, we find that $f_{\mathrm{ICL+BCG}}$ may be well determined by both M12 and M14 for all simulations, with very similar slopes in the best fit lines for all, the values of which we provide in Table 12.1. When considering the relations of $f_{\mathrm{ICL+BCG}}$ to $\mathrm{s_{stars}}$ and in particular to ϕ_{BCG}, we find significantly increased scatter. For the latter, aside from Magneticum, the simulations find little to no correlation.

This means that good measurements of satellite stellar masses as well as the BCG (including, however, identifying cluster membership) are sufficient to tightly determine the overall fraction of stellar mass in the ICL and BCG $f_{\mathrm{ICL+BCG}}$. That fraction, in turn, well captures the mass assembly history of a galaxy cluster. Most significantly, we find this correlation to be stable against changes in the subgrid physics as well as the choice of structure finder. However, we note that when we test the partial correlation between z_{form} and both M12 and M14, we find that the underlying driver is their correlation with $f_{\mathrm{ICL+BCG}}$. Consequently, using the mass ratios to predict a cluster's z_{form} will generally add scatter compared to directly using $f_{\mathrm{ICL+BCG}}$. This point is further discussed in Appendix C.

We then broaden the spectrum of galaxy cluster parameters to also include a) the center shift of the gaseous component $\mathrm{s_{gas}}$, that is the offset between the BCG and the barycenter

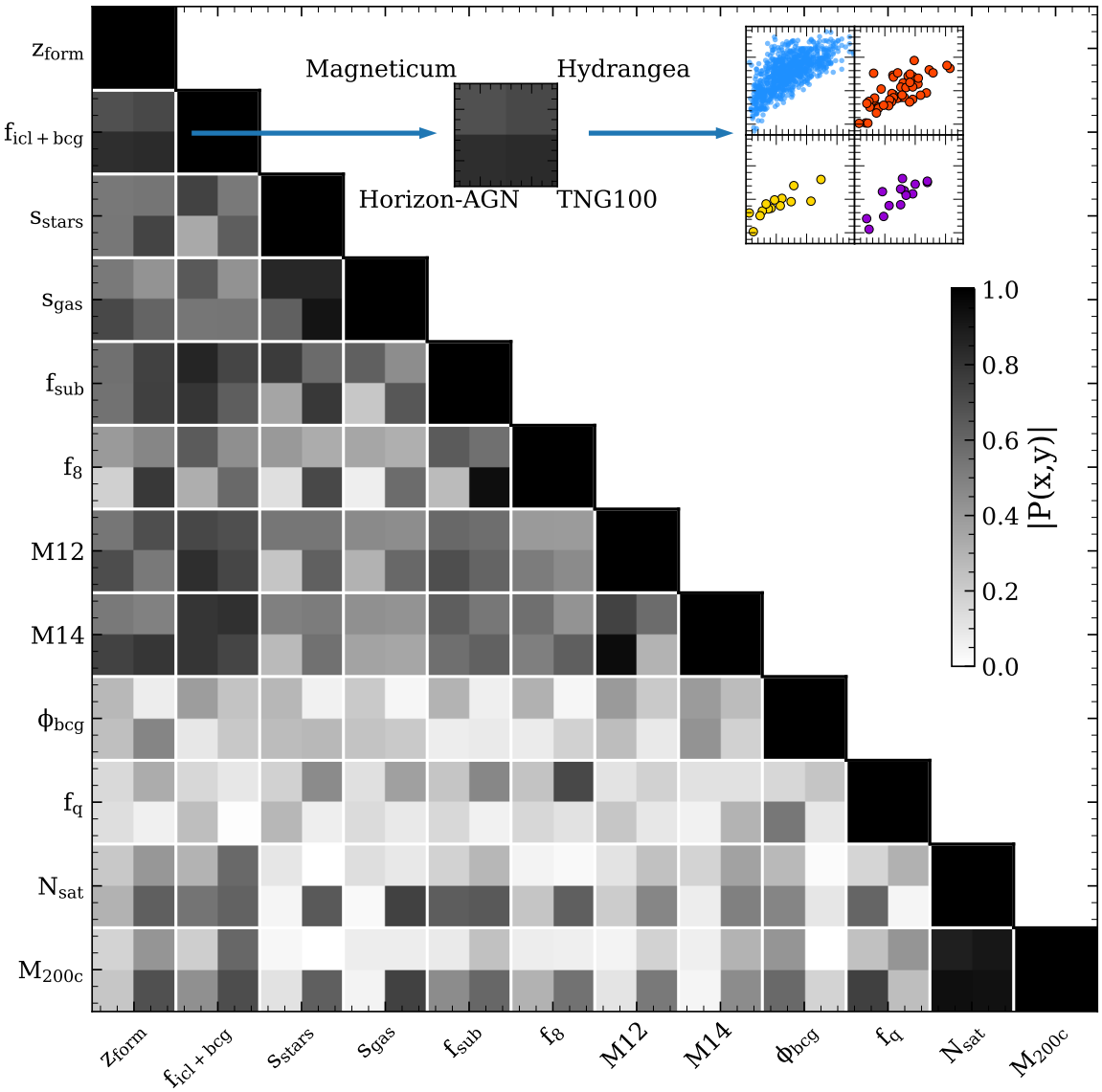


Figure 12.9. Full matrix of the correlation strength between different parameters, with darker colors indicating stronger correlations, for all four simulations as indicated at the respective tiles for each panel. From top to bottom and left to right are the same parameters, in the following order: formation redshift $z_{\rm form}$, the fraction of stellar mass within ICL plus BCG $f_{\rm ICL+BCG}$, the center shift between the stellar ($s_{\rm stars}$) or gas barycenter ($s_{\rm gas}$) and the BCG, the fraction of total mass within all substructures $f_{\rm sub}$ or within just the 8th most massive substructure f_8, the stellar mass ratio between the BCG and the second ($M12$) or fourth ($M14$) most massive galaxy in a cluster, the central stellar potential $\phi_{\rm BCG}$, the passive fraction $f_{\rm quench}$ of galaxies in the cluster with stellar masses above $1 \times 10^{10} M_\odot$ as well as their total number $N_{\rm sat}$, and the total halo mass $M_{\rm 200c}$. Note that black squares in the diagonal mark the self-correlation of the parameters and are thus all equal to one.

of the gas, closely mimicking the X-ray determined center shift (see Appendix C.2); b) the fraction of total mass contained in the 8th most massive substructure f_8 (see Kimmig et al., 2023, for more details), and both the total number (i.e., cluster richness) as well as passive fraction $f_{\rm quench}$ of cluster galaxies with $M_* > 10^{10} M_\odot$ (e.g., Aguerri et al., 2006). The full matrix of correlations between all these different tracers of the dynamical state of a cluster is shown in Fig. 12.9.



Fig. 12.9 is structured as follows: for a given parameter we determine the Pearson correlation strength with another parameter, doing this for every simulation separately to fill a two-by-two grid, with Magneticum in the upper left, Hydrangea in the upper right, Horizon-AGN in the lower left and finally TNG100 in the lower right. We color the cell based on the strength, going from white ($p = 0$, no correlation) to black ($p = 1$, one-to-one correlation). The upper inset of Fig. 12.9 illustrates this process for the case of a correlation between $f_{\mathrm{ICL+BCG}}$ versus z_{form}. Note that the full black squares in the top diagonal mark the relation between a parameter and itself, and are thus all fully black ($p = 1$).

The first column in Fig. 12.9 shows the correlation strength between the formation redshift z_{form} with all other parameters, for each of the simulations. We find that the overall strongest correlation exists for $f_{\mathrm{ICL+BCG}}$, aside from Hydrangea where f_{sub} performs negligibly better ($p = 0.74$ versus $p = 0.72$). Additionally, all simulations find that the mass ratios M12 and M14 are good tracers of z_{form}, which is explained by their strong correlation with $f_{\mathrm{ICL+BCG}}$ (see the second column of Fig. 12.9 or Fig. 12.8). $f_{\mathrm{ICL+BCG}}$ remains the true, tighter underlying correlation, however, as we discuss in Appendix C.

For all simulations, the number of satellite galaxies with stellar masses above $10^{10} M_{\odot}$, $N_{>10^{10}}$ correlates significantly with the total halo mass $M_{200\mathrm{c}}$, as expected. What is interesting is that the simulations do not find a significant correlation between the halo mass $M_{200\mathrm{c}}$ and the formation redshift z_{form}, aside from TNG100. For that simulation, however, $M_{200\mathrm{c}}$ also shows a notable correlation with $f_{\mathrm{ICL+BCG}}$, which may be the more fundamental link given that this is what the other three simulations find. Indeed, when we consider partial correlations, we find also for TNG100 that the correlation between z_{form} and $M_{200\mathrm{c}}$ practically vanishes when accounting for $f_{\mathrm{ICL+BCG}}$, as we discuss in Appendix C.

Thus, we conclude that the formation time of galaxy clusters, defined as the time when a cluster has assembled half of its present-day mass, is best traced through the amount of disruption suffered from the satellite component. This is best quantified by how much of the total stellar mass is bound to the full potential of the cluster, i.e., the BCG and the ICL, or in second order through the stellar mass ratios between the BCG and the most massive companion galaxies.

12.3.6 Evolution Through Cosmic Time

Finally, we want to understand the origin of the correlation between the stellar mass contained in the ICL plus BCG, and the formation redshift of galaxy clusters. As we are interested in the statistical behavior now, we will restrict the analysis in this last subsection to the Magneticum Box2 hr simulation only. To that end, we plot again the stellar-mass halo-mass relation in Fig. 12.10, but this time for all stars in $R_{200\mathrm{c}}$ (gray), as well as the subset of those stars which are not bound in satellites, and so belong to the BCG or ICL (colored). As already seen for all simulations in the right panel of Fig. 12.3, the total stellar mass is tightly increasing with halo mass, following a slope very close to 1.

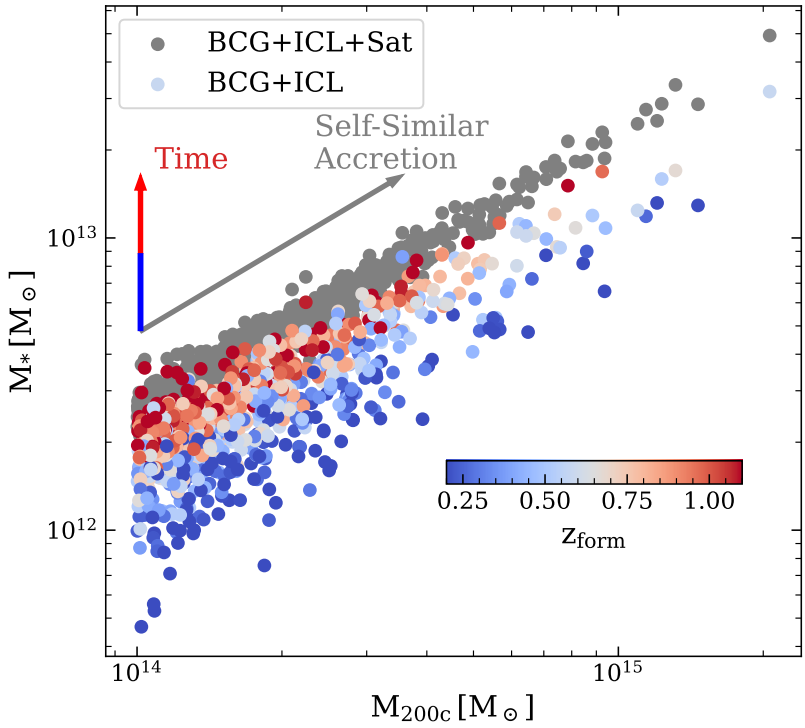


Figure 12.10. Stellar mass-halo mass relation for the Magneticum Box2 hr clusters. The gray points show the total stellar mass within R_{200c}, including the BCG, ICL and satellites. The colored symbols show the stellar mass of only the ICL and the BCG together, without including satellite galaxies. These points are colored according to the formation redshift of the cluster from older and more relaxed galaxy clusters (red) to younger, recently assembled clusters (blue).

On the other hand, the colored points which exclude the mass in satellites show a much larger scatter, with a slightly flatter slope. There is a clear color gradient driving this scatter, however, which is given by the formation redshift of the galaxy cluster. Clusters that have nearly all of their stellar mass in the BCG or ICL are consistently older and more relaxed, while clusters with lower BCG+ICL masses are more recently formed. As expected from Fig. 12.6, this is independent of halo mass. Consequently, if a cluster has time to disrupt and merge their satellite galaxies without being disturbed by additional merging, they will do so consistently across a full order of magnitude in halo mass. This demonstrates why $f_{\rm ICL+BCG}$ is such an effective clock for tracing the formation time, and mirrors prior results in the EAGLE simulations on the group mass scale by Matthee et al. (2017), as well as recent work with TNG300 when comparing to both the concentration of the halo and the formation time (Montenegro-Taborda et al., 2025).

We use this fact to split our sample of 868 galaxy clusters into two further groups. In ten equally log-spaced halo mass bins going from $M_{200c} = 10^{14} M_\odot$ to $M_{200c} = 5 \times 10^{14} M_\odot$ we select the 5 galaxy cluster with the highest/lowest $f_{\rm ICL+BCG}$. Using these two samples of 50 clusters each, which represent the extreme ends in $f_{\rm ICL+BCG}$ at a given halo mass, we trace the evolution in the distribution of stellar mass between the BCG (red), ICL (gold), second most massive satellite (violet) and the remaining satellites (blue) in Fig. 12.11. We choose here to define the split between BCG and ICL at $0.1 \times R_{200c}$, which allows the split to vary with the scale of the halo over time. For further definitions including a fixed aperture

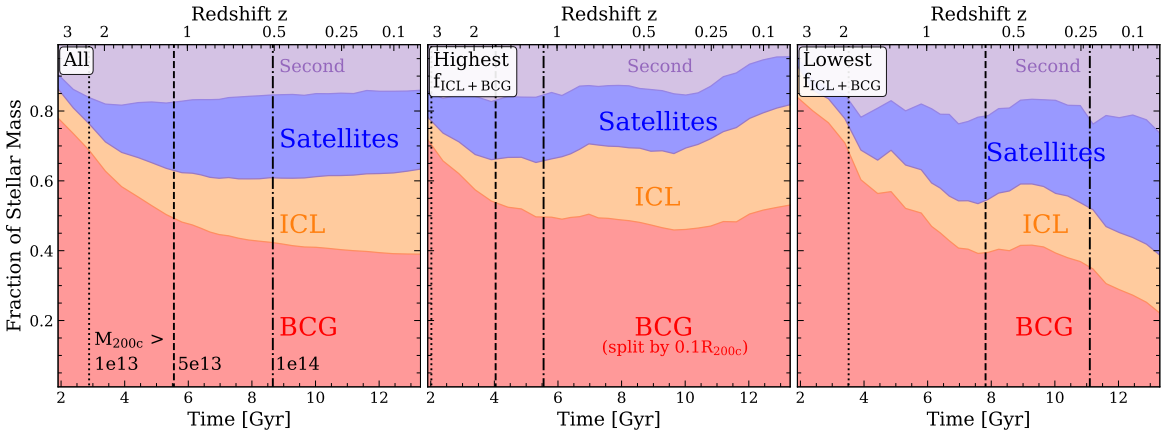


Figure 12.11. The fraction of the total stellar mass contained in the different components of the Magneticum Box2 hr galaxy clusters versus time, determined for all clusters (*left panel*) and for the 50 clusters with the highest (*central panel*) and the 50 clusters with the lowest $f_{\mathrm{ICL+BCG}}$ for their halo mass (*right panel*). The fraction of stellar mass contained within the BCG is shown in red, while the fraction in the ICL, the second most massive satellite, and all other satellites are plotted in gold, violet and blue, respectively. The black vertical lines mark the times when the median mass of each group of galaxy clusters is $M_{200,\mathrm{cri}} > 1 \times 10^{13} M_{\odot}$ (dotted), $M_{200,\mathrm{cri}} > 5 \times 10^{13} M_{\odot}$ (dashed), and $M_{200,\mathrm{cri}} > 1 \times 10^{14} M_{\odot}$ (dash-dotted). Note that here we split the BCG and ICL at $0.1 \times R_{200,\mathrm{cri}}$. For different definitions of the split between the ICL and the BCG, see Fig. C.4 in the Appendix.

cut, we refer to Fig. C.4 in the appendix, and simply note here that the qualitative results do not change strongly depending on the definition of the split.

First, we consider in the left panel of Fig. 12.11 the evolution in the components for all 868 clusters, and find that while the progenitors of the clusters were in the group mass regime ($z \approx 2$, given by the dotted vertical black line) the central galaxy dominated the overall stellar component, accounting for anywhere from 40% to 70%. As they grow from groups to clusters by $z = 0.5$ (dash-dotted line), the fraction of total stellar mass contained in satellites (second most massive plus others) increases, even while the amount of ICL increases too. This is because the BCG does not grow as quickly in stellar mass as satellites are accreted onto the cluster over this time. Upon reaching galaxy cluster masses, the BCG accounts for just 40% of total stellar mass, with the fraction in ICL rising to 20%. The second most massive galaxy at this point contains 15% of the galaxy cluster stellar mass, which is down from the group regime where it accounted for up to 20%. Consequently, as the overall contribution of satellites has increased this stellar mass is now distributed across a greater number of galaxies as opposed to being dominated by a single massive satellite. Finally, by $z = 0$, the fraction in ICL has continued rising to 25%, this time drawing from both the BCG as well as the satellites, following a rate of growth comparable to that found by Rudick et al. (2011). This is reasonable as it becomes more difficult for less massive infalling satellites to penetrate deeply into the growing galaxy cluster potential, and they are instead stripped already farther out (Lotz et al., 2019).

When we consider the subset of galaxy clusters with the highest $f_{\mathrm{ICL+BCG}}$, we find generally similar behavior. The crucial difference is that these processes occur much earlier,

as their progenitors are already groups at $z = 3$ and would thus fulfill the definition of what is typically considered a protocluster (Remus et al., 2023). By $z = 1$, they are already galaxy clusters, though with some differences to what we found for the total sample. They are more dominated by their BCG, which contains around half of the stellar mass (versus 40%), at the cost of both the ICL at 15% (versus 20%) and the satellites at 35% (versus 40%). This means at the moment these early forming clusters reach halo masses $M_{200c} > 10^{14} M_{\odot}$, they are already more centrally concentrated compared to the average clusters. Down to $z = 0$ their BCGs actually *increase* in stellar mass fraction (up to 53%), as does their ICL (up to 30%). This is because they strip, disrupt or merge with a significant portion of their satellites, given the nearly 6 Gyr time they have to do so, and by $z = 0$ their second most massive satellite barely accounts for 5% of the total stellar mass.

Finally, for the sample of clusters with the lowest $f_{\mathrm{ICL+BCG}}$, we note first that although they reach group masses at a similar time to the total sample (at $z = 1.9$ vs $z = 2.3$), they stagnate significantly afterwards. By $z = 0.5$, when the average galaxy cluster progenitor has reached halo masses $M_{200c} > 10^{14} M_{\odot}$, the progenitors of clusters with the lowest $f_{\mathrm{ICL+BCG}}$ are barely above massive groups. Indeed, it takes another nearly 2 Gyr of additional time until they reach galaxy cluster mass. At that time their BCG accounts for just 35% of the total stellar mass, while their ICL is about 15%. Indeed, their satellites already dominate the overall stellar mass at nearly half, which only increases toward $z = 0$ and ends at around 60% of their total stellar mass bound in satellites. The second most massive satellite is at a comparable stellar mass fraction to the BCG, at 25%. We therefore see here how differing mass assembly histories also result in a different *distribution* of mass within the final $z = 0$ structure.

12.3.7 Rate of Satellite Shredding

Thus, one interesting question which arises is how fast a cluster can disrupt its satellites to add their mass to the ICL+BCG. To this end, we consider how the halo mass and $f_{\mathrm{ICL+BCG}}$ change together over a characteristic time T. We choose $T = 1$ Gyr as it is approximately equal to the typical crossing time of our galaxy clusters (Jiang & van den Bosch, 2016; Contreras-Santos et al., 2022; Haggar et al., 2024), though we have tested that our conclusions do not strongly depend on varying the timescale between $T = 0.5$ Gyr to $T = 2$ Gyr. Defining t1 as the starting point and t2 as the end of the window, then

$$\delta M_{200c} \equiv \frac{\Delta M_{200c}}{M_{200c,t2}} = \frac{M_{200c,t2} - M_{200c,t1}}{M_{200c,t2}}, \tag{12.1}$$

$$\Delta f_{\mathrm{ICL+BCG}} \equiv f_{\mathrm{ICL+BCG,t2}} - f_{\mathrm{ICL+BCG,t1}}. \tag{12.2}$$

In Fig. 12.12 we plot $\Delta f_{\mathrm{ICL+BCG}}$ against δM_{200c} based on the assembly histories of our 868 galaxy clusters. The columns show the relation at $z > 0.8$ (left), $0.8 > z > 0.2$ (center) and $z < 0.2$ (right), based on the redshift at the end of the time window t2. We



further split the sample based on the halo mass at the time t2, plotting all clusters' assembly histories (top row), or only those clusters where the main progenitor has a halo mass of a small group $1 \times 10^{13} M_\odot \leq M_{200c} < 5 \times 10^{13} M_\odot$ (second row), massive group $5 \times 10^{13} M_\odot \leq M_{200c} < 1 \times 10^{14} M_\odot$ (third row), or is already a cluster $1 \times 10^{14} M_\odot \leq M_{200c}$ (bottom row). We plot the median and 1σ-bounds (solid and dashed thick black lines), as well as the horizontal and vertical lines corresponding to a net change of zero in either mass or $f_{\mathrm{ICL+BCG}}$.

Beginning with the top row, we find a negative dependence of $\Delta f_{\mathrm{ICL+BCG}}$ on δM_{200c}. When the halo mass decreases, $\delta M_{200c} < 0$, then $\Delta f_{\mathrm{ICL+BCG}}$ is most positive, which means that $f_{\mathrm{ICL+BCG}}$ most strongly increases. This may be the result of either a fly-by or a merger. For the former, a structure had previously entered the halo, bringing with it also stellar mass, and has then exited again. Because both halo and satellite stellar mass are removed, $\delta M_{200c} < 0$ and $\Delta f_{\mathrm{ICL+BCG}} > 0$. For the latter, this is a consequence of the definition of M_{200c}. As a structure begins to merge, increasingly more mass of the infalling satellite lies within the radial definition of R_{200c}, until a peak M_{200c} is reached that is approximately the sum of both structures total mass. However, if it is massive enough, the infalling structure does not instantly merge, instead continuing on its orbit until it reaches the apocenter. At this point, a portion of its mass may again lie outside of R_{200c}, thus decreasing M_{200c} (and increasing $f_{\mathrm{ICL+BCG}}$ as satellite stellar mass is moved outside of the cluster extent).

When the halo mass does not change over $T = 1$ Gyr, $\delta M_{200c} = 0$, then $\Delta f_{\mathrm{ICL+BCG}} \approx 4\%$. Thus, if left alone these systems increase the fraction of the total stellar mass contained within the BCG and ICL over time, consistent with the picture of stripping and merging. Finally, when $\delta M_{200c} > 0$, so when the halo grows, then $\Delta f_{\mathrm{ICL+BCG}}$ is either close to zero or negative. During large accretion events involving significant total mass, the fraction of the stellar mass in satellites therefore also increases (so $f_{\mathrm{ICL+BCG}}$ decreases).

What is remarkable is that the median line of this behavior remains consistent both across time (left to right columns) as well as between structures of different masses (top to bottom rows). This may indicate that there is an average response between the distribution of the stellar mass and the growth (or lack thereof) of the halo mass of the structure. Generally, as can be seen from the color indicating the number of systems, most lie in the low right quadrant where they are experiencing slight growth in halo mass while $f_{\mathrm{ICL+BCG}}$ decreases as they continue to accrete more satellites over time.

We can define the average change in $f_{\mathrm{ICL+BCG}}$ when a structure does not grow ($\delta M_{200c} = 0$) as the "shredding rate", and indicate this value in the panels of Fig. 12.12. We find that for galaxy groups $\Delta f_{\mathrm{ICL+BCG}} \approx 4\%$, while galaxy clusters lie slightly lower at 3% to 4% per Gyr. Therefore, as long as there is no new material being accreted, the stellar mass in the ICL+BCG will increase by around 4% of the galaxy cluster total stellar mass. Slower disruption rates of galaxies in clusters compared to groups were also found by Bahé et al. (2019), consistent with our findings here. We note that there is a relatively large scatter for individual clusters, as the actual rate of course depends on various factors. If the cluster is already strongly dominated by the BCG and ICL, then the remaining galaxies may be on more circular orbits that are stripped less quickly, while a cluster post major merger may suddenly and significantly

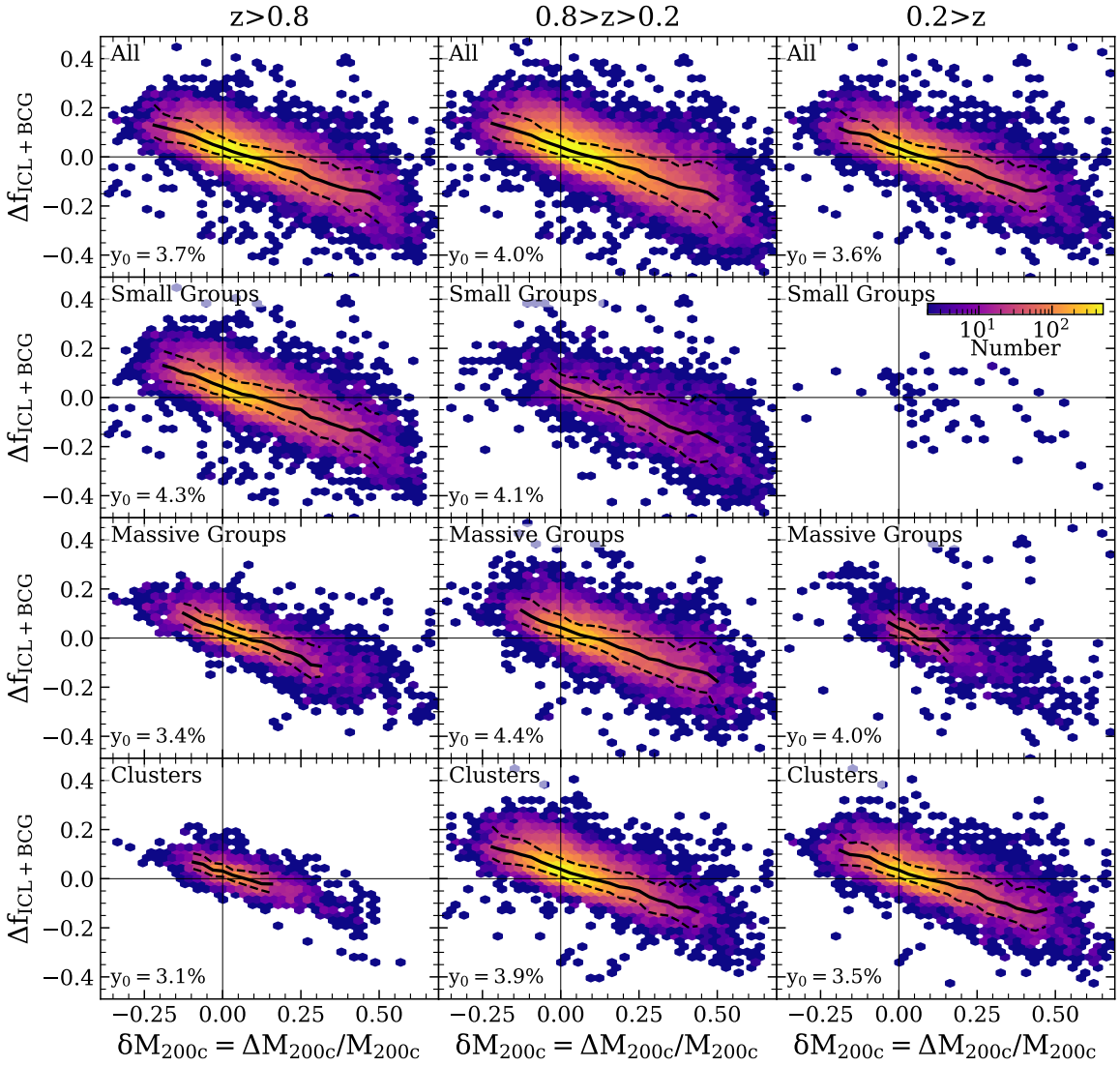


Figure 12.12. The absolute change in $f_{ICL+BCG}$ versus the relative change in mass δM_{200c} as determined over a period of $T = 1$ Gyr for the Magneticum clusters. Columns from left to right split the sample into redshift bins, while the rows separate the clusters based on their current mass, going from all clusters in the top row to small and massive groups and finally clusters on the bottom row. The median line and 1σ-bounds are plotted in black, while the thin vertical and horizontal black lines show the location of zero change in either $f_{ICL+BCG}$ or cluster mass. y_0 indicated in each panel is the median change in $f_{ICL+BCG}$ for halos where the total mass did not change, $\delta M_{200c} = 0$.

increase its $f_{ICL+BCG}$ when the two constituent BCGs merge. Indeed, Fig. 12.12 shows that there are also clusters at $z < 0.2$ which increase $f_{ICL+BCG}$ by 20% while $\delta M_{200c} = 0$, which likely has to do with the orbits, masses, compactness and velocity of the satellite population.

12.4 Summary and Conclusions

To inform the upcoming large surveys of galaxy clusters, which will provide a plethora of data on the largest forming structures throughout time, we have analyzed here the build up of the BCG and the ICL through four separate simulations. We have studied the connection between the fraction of the stellar mass in the ICL+BCG of clusters, $f_{ICL+BCG}$, and their

formation histories, following up on initial ideas presented by Brough et al. (2024), and show that this fraction acts as a dynamical clock for galaxy clusters. We primarily employed Box2 hr of the Magneticum Pathfinder hydrodynamical simulation suite (Dolag et al., in prep), a simulation with a box volume of $(352\mathrm{cMpc}/h)^3$ and 886 galaxy clusters with halo masses $M_{200c} > 10^{14} M_{\odot}$. We complemented this statistical sample with a smaller sample of higher resolved galaxy clusters from the TNG100 (Pillepich et al., 2018a) and Horizon-AGN (Dubois et al., 2014) simulations (14 clusters each), as well as from the Hydrangea suite of zoom-in cluster simulations (Bahé et al., 2017, 46 clusters), to verify that the results found for Magneticum are independent of the resolution, numerical details, or subgrid physics prescriptions.

Defining the formation redshift z_{form} of galaxy clusters as the redshift when the cluster first assembled 50% of its $z = 0$ halo mass, we find that clusters in Magenticum Box2 hr have on average assembled only recently with $\langle z_{\mathrm{form}}^{\mathrm{Box2}} \rangle = 0.67$, in agreement with previous studies (e.g., Boylan-Kolchin et al., 2009; Power et al., 2012), but that some clusters already assembled as early as $z_{\mathrm{form}} = 1.8$. This is consistent with the non-linearity in the growth of individual clusters compared to their statistical average and is matched nicely by linear growth theory (see also Remus et al. 2023 and Kimmig et al., in prep.).

Here, it is of special interest to note that there is a difference in cluster formation times, with the (on average) latest forming clusters in Horizon-AGN at $\langle z_{\mathrm{form}}^{\mathrm{Horizon}} \rangle = 0.44$, Magneticum and Hydrangea are similar at $\langle z_{\mathrm{form}}^{\mathrm{Magneticum}} \rangle = 0.67$ and $\langle z_{\mathrm{form}}^{\mathrm{Hydrangea}} \rangle = 0.71$, while TNG100 has the earliest forming clusters at $\langle z_{\mathrm{form}}^{\mathrm{TNG}} \rangle = 0.78$. However, all simulations cover a similar range in formation redshifts (Fig. 12.4), so that we can meaningfully compare the higher resolved simulations of TNG100, Horizon-AGN and Hydrangea to the larger sample of clusters in Magneticum Box2 hr.

We find that the formation time of a galaxy cluster z_{form} is tightly traced by $f_{\mathrm{ICL+BCG}}$, so the fraction of total stellar mass within the ICL+BCG (Fig. 12.7). We show this follows because the stripping/merging of stellar mass bound in satellite galaxies into the central potential of a galaxy cluster is proportional to how long a cluster has been left undisturbed (Fig. 12.12). More relaxed clusters have higher fractions of $f_{\mathrm{ICL+BCG}}$, with values up to 90%, while recent accretion can (temporarily) push the fraction down to as low as 20% (Fig. 12.6).

This process is also the origin for the scatter in the BCG stellar mass-halo mass relation (Fig. 12.3). Galaxy clusters at the upper end in stellar mass have formed much earlier and are thus both more compact and had more time to disrupt and strip their satellite populations (Fig. 12.10), supporting observational works that find this scatter to correlate with dynamical tracers such as M14 (Golden-Marx & Miller, 2018; Golden-Marx et al., 2025). If left undisturbed, that is to say without growing their halo mass, galaxy clusters will gradually disrupt their satellite population, stripping most or all of their mass even if a small core may survive. We calculate an average rate for this "shredding" at between 3% and 4% of the total stellar mass in the cluster per Gyr (Fig. 12.12).

We considered two other common tracers of the dynamical state, namely the fraction of total mass (including DM) in the galaxy cluster's subhalos, f_{sub}, and the gas center shift s_{gas},

defined as the offset between the 3D gas barycenter and the BCG position. Across all four simulations, $f_{\rm ICL+BCG}$ best traces $z_{\rm form}$ (Fig. 12.7). This is likely because different dynamical tracers trace different dynamical times, as shown by Haggar et al. (2024). In the future, a more detailed investigation in the timescales involved for the gas (X-ray centershift) and dark matter stripping ($f_{\rm sub}$) is necessary to understand when to use which tracer, to inform the new and upcoming measurements from multiple instruments that will significantly improve the set of observed galaxy clusters, such as *Euclid* (Laureijs et al., 2011; Kluge et al., 2024), Roman (Montes et al., 2023) and Rubin/LSST (Ivezić et al., 2019; Brough et al., 2020). However, that is beyond the scope of this work. Instead, we provide here fitting functions to predict the formation redshift $z_{\rm form}$ of observed galaxy clusters from measurements of $f_{\rm ICL+BCG}$ (Table 12.1).

We show that $f_{\rm ICL+BCG}$, which is difficult to measure because of the low-surface brightness of the outer ICL, can best be approximated by the stellar mass ratio between the BCG and the second or fourth most massive galaxy, M12 or M14 (Fig. 12.8), in agreement with Golden-Marx et al. (2025). Furthermore, all four simulations agree remarkably well on the presented relations, even though they are tuned to reproduce different relations, with Magneticum in particular focused on the hot gas component (Popesso et al., 2024). This is likely because the processes of stripping and merging for the stellar component of galaxy clusters is driven by gravity, which is treated equivalently between the simulations. We provide fitting functions from each simulation to estimate $f_{\rm ICL+BCG}$ based on M12, M14, the stellar barycenter offset $s_{\rm stars}$ and the ratio of BCG stellar mass to half mass radius $\phi_{\rm stars}$ (Table 12.1). Finally, we determine that, although M12 and M14 well trace $z_{\rm form}$ for all simulations, the underlying driver of the correlation is $f_{\rm ICL+BCG}$ (Fig. 12.9). Accurate measurements of the low-surface brightness ICL of galaxy clusters are thus necessary to best predict galaxy cluster assembly.

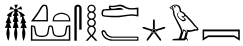
We conclude that the assembly histories of galaxy clusters are varied and complex, but that their present-day properties hold the key to disentangling their evolution. With the increasing number of massive galaxies observed by *JWST*, finding a means to robustly connect the largest cosmic structures through time is becoming increasingly necessary. This study finds that the distribution of the stellar component of these clusters, quantified either via the fraction of the total stellar mass in the ICL+BCG $f_{\rm ICL+BCG}$ or alternatively the stellar mass ratios of the BCG to the second or fourth most massive galaxy in the cluster, M12 or M14, is a crucial tool to predict whether a cluster originates from an early or late collapsing node of the cosmic web. Therefore, despite the difficulty of measuring this low-surface brightness feature of galaxy clusters, it is of great importance as the field of galaxy cluster research moves into the next phase with statistically significant samples from our observed Universe.

Data Availability

The Magneticum Pathfinder simulation data are available at
https://c2papcosmosim.uc.lrz.de/ (Ragagnin et al., 2017), with larger data sets on request.



The Hydrangea simulation data are publicly available at
https://ftp.strw.leidenuniv.nl/bahe/Hydrangea/.
The Horizon-AGN data used in this work can be obtained upon request from
https://www.horizon-simulation.org/data.html.
The IllustrisTNG data used in this work are publicly available at
http://www.tng-project.org.



Pyramid Texts, late Old Kingdom, circa 2400–2300 BCE

13

Intra-Cluster Light as a Dynamical Clock for Galaxy Clusters II: Insights from the SLOW/LowerDecks simulations

This chapter will be submitted to A&A as Kimmig et al., 2026.

13.1 Introduction

Galaxy clusters represent the largest bound structures in the Universe, amassing hundreds of galaxies within a single dark matter halo. Beyond merely assembling their constituent galaxies, however, the galaxy populations of clusters have consistently been found to diverge from those found in the field. They are older, redder, and more elliptical (e.g., Dressler, 1980; Postman & Geller, 1984; Goto et al., 2003). As of yet, it remains unclear whether these differences are predominantly caused by interactions of the galaxy with the host cluster, or whether they already manifested themselves in the galaxy population prior to infall into the cluster, with for example massive ellipticals themselves showing only a weak environmental dependence on their properties (Thomas et al., 2010), and quenched fractions remaining elevated out to five virial radii from the cluster center (McGee et al., 2009; Haines et al., 2015).

Determining the environmental impact of clusters is muddled by the large range in dynamical states that galaxy clusters are observed to be in, ranging from very old, relaxed

systems to those that are in the process of undergoing a major merger. In merging systems the typical projected phasespace diagnostics used to identify the infall times of galaxies (Rhee et al., 2017) are muddled as the original galaxy populations of both systems overlap (Çakır et al., 2025), and even identifying the brightest cluster galaxy becomes uncertain. Indeed, there are indications that in the latter case the merger itself may be driving a resurgence in star formation in the constituent galaxies (Bekki et al., 2010; Çakır et al., 2025).

With the advent of next generation facilities such as *Euclid* (Laureijs et al., 2011; Kluge et al., 2024), Roman (Montes et al., 2023) and Rubin/LSST (Ivezić et al., 2019; Brough et al., 2020), the set of available data for galaxy clusters both locally and out to higher redshifts is set to undergo a critical transformation in the coming years. Thus, to isolate the impact of the cluster environment on galaxies and leverage the upcoming data, it is necessary to first determine the state of assembly for a wide range in galaxy clusters.

As galaxy clusters grow bottom-up through the merging of smaller halos (Press & Schechter, 1974; Seidel et al., 2024), these bring along their dark matter, gas and stars. The stars and dark matter remain bound to the infalling galaxies for a while because they are collisionless, undergoing tidal interactions with the larger host galaxy cluster which over time strip or merge their mass with the central brightest cluster galaxy (BCG) or the diffuse intracluster light (ICL) (e.g., Gunn & Gott, 1972; Mihos, 2004; Contini et al., 2014; Bahé et al., 2019). Consequently, the distribution of stellar mass between the BCG and ICL versus the amount that remains bounds in satellite galaxies has been proposed as a viable way to determine the assembly time of the galaxy cluster itself (Dolag et al., 2010; Kimmig et al., 2025a). Furthermore, dynamically evolved clusters are known to host more massive BCGs, already having merged with a greater number of their satellites (Ahad et al., 2025).

Beyond the stellar component, the hot ($\approx 10^8$K), low-density ($\approx 10^{-3}$atoms/cm^3) gas of the intracluster medium (ICM) also brightly emits light in the X-ray regime due to thermal bremsstrahlung, with luminosities of 10^{43-45}ergs/sec (Sarazin, 1988). In merging systems the ICM of both clusters collides, leading to X-ray emission that is disturbed from spherical symmetry, becoming less concentrated (Santos et al., 2008), more asymmetric (Yuan & Han, 2020) and with local substructures (Weißmann et al., 2013). Due to the collisionless nature of the stars, the location of the BCG is additionally expected to be offset from the peak of the X-ray emission (Kolokotronis et al., 2001; Zenteno et al., 2020).

In this work we address the question of galaxy cluster dynamical state through a set of 26 simulated galaxy clusters from the new state-of-the-art Lower Decks simulation suite (Seidel et al., in prep.), built on the successful framework of the SLOW simulations (Dolag et al., 2023; Hernández-Martínez et al., 2024; Seidel et al., 2024). These simulations are unique in that they are run from constrained initial conditions to reproduce the local large scale structure, allowing direct comparisons to observed clusters in our neighborhood. We consider tracers from the 3D distribution of stars, gas and dark matter, following up on the work by Kimmig et al. (2025a), as well as four dynamical tracers determined directly from mock X-ray images via the code SMAC (Dolag et al., 2005a). We introduce the Lower Decks simulations in Sec. 13.2 and the dynamical parameters and mock images in Sec. 13.3. We



then show our results on the dynamical state of these systems in Sec. 13.4, before concluding in Sec. 13.5.

13.2 Simulations

We employ the Lower Decks set of zoom-in simulations (Seidel et al., in prep.), a set of 26 matched local galaxy clusters drawn from the SLOW simulations (Dolag et al., 2023; Hernández-Martínez et al., 2024; Seidel et al., 2024). These simulations build on the successful framework of the Magneticum Pathfinder model (Dolag et al., 2025), which is a based on a modified version of the smoothed particle hydrodynamics (SPH) code GADGET-2 (Springel, 2005) that includes updates such as a low-viscosity scheme to track turbulence (Dolag et al., 2005b; Beck et al., 2016), in addition to artificial viscosity (Dolag et al., 2004) and others (Donnert et al., 2013; Teklu et al., 2015). Of particular note is that they employ a density field derived via the peculiar velocities from surveys such as CosmicFlows-2 (Tully et al., 2013) to construct constrained ΛCDM initial conditions, as discussed in more detail by Sorce (2018). This provides a large scale density field that is derived from observations and thus produces observational counterparts.

The simulations assume a ΛCDM cosmological model with a total matter and baryon density of $\Omega_m = 0.307115$ and $\Omega_{\rm baryon} = 0.0480217$, a Hubble constant of $H_0 = 67.77$km/s/Mpc, the normalization of the power spectrum as $\sigma_8 = 0.829$ and with a slope of the primordial fluctuation spectra of $n = 0.961$ (Planck Collaboration et al., 2014). They were run at a particularly high resolution capable of well resolving galaxies down to $M_* = 10^9 M_\odot$, with particle masses of $m_{\rm dm} = 5.7 \times 10^7 M_\odot$, $m_{\rm gas} = 1.0 \times 10^7 M_\odot$ and $m_* = 2.5 \times 10^6 M_\odot$. This places it well in the upper right region of Fig. 12.1, with cluster masses of $M_{200c} = 2 \times 10^{15} M_\odot$ and 10^4 stellar particles per Milky Way mass galaxy, making it ideally suited to analyze the ICL and BCG components. Galaxies and galaxies clusters are themselves identified via the structure finder SUBFIND (Springel et al., 2001b; Dolag et al., 2009).

We use the set of 26 matched galaxies clusters from Lower Decks v1 (Seidel et al., in prep.) spread across 15 individual zoom-in simulations. The masses and redshifts of the observed galaxy clusters for which we have simulated counterparts are given in Table 13.1. We include the virial mass $M_{\rm vir}$, as well as the mass $M_{\Delta c}$ given by the total mass within a sphere that encloses a mean density of Δ times the critical density of the Universe ρ_c. In particular, we include the cases of $\Delta = 200$ and $\Delta = 500$.

13.3 Dynamical State Parameters and Mock Images

We consider here three dynamical parameters covering the stellar, gas and dark matter components used by Kimmig et al. (2025a), as well as four dynamical parameters based on the X-ray maps of our simulated clusters generated via the code SMAC (Dolag et al., 2005a).

Table 13.1. This table lists relevant properties of observed galaxy clusters with matched Lower Decks equivalents. $z_{\rm CMB}$ is obtained from the NASA/IPAC Extragalactic Database (NED) as the redshift corrected to the reference frame defined by the 3K cosmic microwave background (CMB), as is the cluster distance relative to the CMB, $D_{\rm CMB}$. The virial mass $M_{\rm vir}$ and radius $R_{\rm vir}$ are taken from Girardi et al. (1998). $M_{500}^{\rm SZ}$ comes from observations using the Sunyaev-Zeldovich (SZ) effect (Sunyaev & Zeldovich, 1970), gathered from Table 2 by Hernández-Martínez et al. (2024) and extended by data obtained from the SZ cluster database. The halo masses M_{200c} are taken from X-ray measurements by Reiprich & Böhringer (2002) recalculated from h_{50} to h_{100}.

Cluster-ID	$z_{\rm CMB}$	$D_{\rm CMB}$	$M_{\rm vir}$ $[10^{14} M_\odot]$	$R_{\rm vir}$ [Mpc]/h	M_{200c} $[10^{14} M_\odot]$	M_{500c} $[M_\odot]$	$f_{\rm ICL+BCG}$
Virgo	0.00546	24.13 ± 1.73	$2.04^{+0.28}_{-0.21}$	1.26	—	4.76 ± 0.55	—
A 85	0.0543	240.32 ± 16.88	$9.88^{+2.25}_{-1.68}$	1.94	$5.40^{+0.56}_{-0.52}$	4.90 ± 0.21	0.325
A S 373 (Fornax)	0.00444	19.65 ± 1.38	$0.31^{+0.07}_{-0.07}$	0.62	$0.71^{+0.18}_{-0.14}$	—	0.65 ± 0.2
A 426 (Perseus)	0.0167	73.68 ± 5.30	$9.08^{+2.13}_{-1.52}$	2.05	$5.40^{+0.23}_{-0.21}$	—	0.38 ± 0.6
A 496	0.0329	145.27 ± 10.21	$3.20^{+1.04}_{-0.95}$	1.37	$2.18^{+0.09}_{-0.09}$	2.74 ± 0.17	—
A 1060 (Hydra)	0.0135	59.85 ± 4.27	$0.75^{+0.51}_{-0.29}$	1.22	$2.12^{+0.28}_{-0.24}$	—	—
A 1367	0.0230	101.62 ± 7.23	$4.94^{+1.02}_{-0.94}$	1.60	$2.85^{+0.32}_{-0.28}$	1.76 ± 0.14	0.359
A 1656 (Coma)	0.0249	110.07 ± 7.72	$4.97^{+0.68}_{-0.57}$	1.64	$9.69^{+1.04}_{-0.99}$	5.29 ± 0.20	0.488
A 1736	0.0461	203.88 ± 14.41	$6.51^{+1.22}_{-0.99}$	1.71	$1.89^{+1.21}_{-.67}$	2.95 ± 0.27	—
A 1795	0.0635	280.71 ± 19.70	$5.86^{+1.33}_{-1.22}$	1.67	$7.70^{+1.59}_{-1.46}$	4.54 ± 0.21	0.215
A 2029	0.0793	350.74 ± 24.61	$6.82^{+2.40}_{-2.30}$	2.33	$9.40^{+1.70}_{-1.59}$	6.82 ± 0.24	0.550
A 2147	0.0369	163.30 ± 11.49	—	—	$2.42^{+0.82}_{-0.52}$	2.469 ± 0.8	0.328
A 2151 (Hercules)	0.0368	162.60 ± 11.42	$5.64^{+1.45}_{-1.15}$	1.50	$1.21^{+0.09}_{-0.09}$	—	0.262
A 2152	0.0445	196.63 ± 13.80	—	—	—	—	0.260
A 2197	0.0304	134.46 ± 9.45	$3.57^{+0.81}_{-0.78}$	1.22	—	—	—
A 2199	0.0304	134.40 ± 9.44	$5.71^{+1.56}_{-1.21}$	1.60	$3.37^{+0.26}_{-0.26}$	2.87 ± 0.13	0.436
A 2256	0.0581	256.92 ± 18.05	$23.12^{+3.95}_{-3.43}$	2.70	$10.91^{+2.04}_{-1.77}$	6.34 ± 0.18	0.139
A 3391	0.0543	240.17 ± 16.97	$3.61^{+2.20}_{-1.35}$	1.33	$4.21^{+1.07}_{-.91}$	2.04 ± 0.18	—
A 3526 (Centaurus)	0.0114	50.19 ± 3.65	$6.97^{+1.22}_{-1.25}$	1.58	$1.89^{+0.12}_{-0.09}$	1.23 ± 0.11	—
A 3558	0.0493	218.05 ± 15.29	$11.54^{+1.02}_{-0.91}$	1.95	$4.32^{+0.56}_{-0.52}$	4.41 ± 0.27	—
A 3559	0.0482	212.91 ± 14.96	$1.27^{+0.46}_{-0.29}$	0.91	—	—	—
A 3560	0.0501	221.47 ± 15.54	—	—	$1.80^{+0.65}_{-0.48}$	—	—
A 3571	0.0399	176.48 ± 12.54	$8.17^{+2.40}_{-2.19}$	2.09	$6.66^{+0.45}_{-0.43}$	4.67 ± 0.21	—
A 3651	0.0596	263.41 ± 18.53	$3.92^{+0.82}_{-0.75}$	1.25	—	3.24 ± 0.20	—
A 3667	0.0549	242.67 ± 17.06	$11.75^{+1.60}_{-1.26}$	1.94	$5.60^{+0.88}_{-0.83}$	5.77 ± 0.24	—
AWM 7	0.0166	73.49 ± 5.75	$5.77^{+1.80}_{-1.50}$	1.73	$3.04^{+0.31}_{-0.26}$	1.96 ± 0.15	0.627

As a direct tracer of the assembly time of the galaxy cluster, we use the formation redshift z_{50}, which is the redshift when the main progenitor of the galaxy cluster first reached 50% of its final halo mass M_{200c}.

The three tracers also employed by Kimmig et al. (2025a) are 1) the fraction of total stellar mass within R_{200c} that is bound to the BCG or ICL (i.e., not to satellite galaxies), $f_{\rm ICL+BCG} = (M_{*,\rm ICL} + M_{*,\rm BCG})/M_{*,200c}$, 2) the fraction of the total mass (including dark matter) within the same radius that is bound within satellite galaxies $f_{\rm sub} = \sum_i m_{\rm sub,i}/M_{200c}$, and finally 3) the 3D spatial offset between the gas barycenter and the BCG, normalized by R_{200c}, $s_{\rm gas} = |\vec{x}_{\rm gas} - \vec{x}_{\rm BCG}|/R_{200c}$. By definition, all three parameters range from 0 to 1, with a relaxed dynamical state corresponding to a high $f_{\rm ICL+BCG}$ and low $f_{\rm sub}$ and $s_{\rm gas}$.

For the X-ray properties, we consider those by Yuan et al. (2022) which they applied consistently to a set of 1308 X-ray images of XMM-Newton archival data. To this end, we generate for each of our 26 local clusters a mock X-ray image via SMAC (Dolag et al., 2005a)

in the band of 0.5 – 5keV, further excluding all cold gas particles with temperatures below 0.5keV. We project each cluster as seen from the best fitting Milky Way position within the SLOW parent simulation (Dolag et al., 2023). We place each cluster at the observed redshift and produce an image of 2048×2048 pixels spanning $\pm R_{200c}$, with a fixed depth of ±5Mpc. As the clusters range in mass and size, our pixels range in physical extent from 0.6kpc to 2.4kpc.

The first parameter is the centroid shift w, which has been used extensively in the literature to distinguish merging and relaxed clusters (e.g., Kolokotronis et al., 2001; Biffi et al., 2016; Zenteno et al., 2020). We begin by first smoothing our images with a gaussian kernel of fixed physical size $\sigma = 20$kpc to smooth out brightness peaks, and then identify the brightest pixel as the peak $\vec{x}_{\rm peak}$. We then perform the shrinking sphere method (Power et al., 2003), iteratively determining the next barycenter $\vec{x}_n$ within the aperture $R_{\rm ap,n} = R_{\rm ap,n-1} \cdot (1 - f_{\rm shrink})$ centered on the previous barycenter $\vec{x}_{n-1}$. We start with $\vec{x}_0 = \vec{x}_{\rm peak}$ and an aperture of $R_{\rm ap,0} = R_{500c}$, and shrink by $f_{\rm shrink} = 5\%$ per iteration, terminating when $R_{\rm ap,n} = 100$kpc or there are less than 1000 pixels left within the aperture, whichever occurs first.

This gives a sequence of centers $\vec{x}_n$ and thus offsets $\Delta_n = |\vec{x}_n - \vec{x}_{\rm peak}|$, with the centroid shift then defined as

$$w = \sqrt{\frac{1}{N-1}\sum_{i=0}^{N}[\Delta_i - \langle\Delta\rangle]^2} \cdot \frac{1}{R_{\rm ap,0}} = \frac{\mathrm{s}(\Delta_i)}{R_{\rm ap,0}}, \tag{13.1}$$

which is just the corrected standard deviation of the vector of offsets Δ_i normalized by the initial aperture size $R_{\rm ap,0}$. A smaller w indicates a smoother X-ray distribution and thus more relaxed cluster (Biffi et al., 2016; Yuan et al., 2022). We define our X-ray center as the final barycenter $\vec{x}_{\rm cent} = \vec{x}_N$, and determine the other dynamical tracers centered around this pixel.

The second parameter is the concentration index $c_{\rm SB}$ defined by Santos et al. (2008) as

$$c_{\rm SB} = \frac{F_{\rm core}}{F_{\rm tot}} = \frac{\sum_{R<R_{\rm core}} f(x_i, y_i)}{\sum_{R<R_{\rm outer}} f(x_i, y_i)}, \tag{13.2}$$

with $f(x_i, y_i)$ being the brightness of the pixel at (x_i, y_i). This parameter indicates how strongly concentrated the X-ray luminosity of a given cluster is, with more relaxed clusters having a longer time to build up a centrally concentrated ICM and thus more peaked X-ray distribution (Yuan et al., 2022). We choose here $R_{\rm core} = 100$kpc and $R_{\rm outer} = 500$kpc.

As clusters merge their two gaseous components collide and overlap, leading to substructures and local fluctuations in the X-ray images (Mann & Ebeling, 2012). To characterize these local fluctuations, the map can be split into angular slices via a two-dimensional multipole expansion, alternately adding and subtracting the X-ray surface brightness of all pixels in each slice (Buote & Tsai, 1995). If the distribution is smooth, i.e., the cluster is relaxed, the amount of light in the added and subtracted slices should be about equal, while disturbed clusters would have an excess.

To quantify this more explicitly, the multipole expansion of the two-dimensional gravitational potential $\psi(R, \phi)$ has the form

$$\psi(R, \phi) = -2G \left[a_0 \ln \frac{1}{R} + \sum_{m=1}^{\infty} \frac{1}{mR^m} \left(a_m \cos(m\phi) + b_m \sin(m\phi) \right) \right], \tag{13.3}$$

with G the gravitational constant and with the moments

$$a_m = \int_{r \leq R_{\rm ap}} f(x_i, y_i) \cdot R_i^m \cos(m\phi_i) \, \mathrm{d}x_i \mathrm{d}y_i, \tag{13.4}$$

$$b_m = \int_{r \leq R_{\rm ap}} f(x_i, y_i) \cdot R_i^m \sin(m\phi_i) \, \mathrm{d}x_i \mathrm{d}y_i, \tag{13.5}$$

where R_i is the distance of the pixel $(x_i, y_i) = (R_i, \phi_i)$ to the cluster center $\vec{x}_{\rm cent}$ and $R_{\rm ap}$ a chosen aperture size. Integrating the potential ψ_m over ϕ yields zero for all moments $m \geq 1$ (Buote & Tsai, 1995), such that they instead consider the integral of the magnitude of each term, so

$$P_{\rm m} = \frac{1}{2\pi} \int_0^{2\pi} \psi_m(R_{\rm ap}, \phi) \, \psi_m(R_{\rm ap}, \phi) \, \mathrm{d}\phi. \tag{13.6}$$

This is the definition of the power P_m within $R_{\rm ap}$ of terms of the order m, and they derive,

$$P_0 = [a_0 \ln(R_{\rm ap})]^2, \qquad \text{for m} = 0, \tag{13.7}$$

$$P_{m>0} = \frac{1}{2m^2 R_{\rm ap}^{2m}} (a_m^2 + b_m^2) \qquad \text{for m} > 0. \tag{13.8}$$

In this expansion $m = 0$ corresponds to the monopole, $m = 1, 2 \ldots$ are the dipole, quadrupole and so on. With increasing order m the scale that the power P_m is sensitive to becomes smaller, so lower values of m are preferred to quantify the whole cluster dynamical state. Furthermore, as even orders $m = 2, 4 \ldots$ are sensitive both to bimodality but also ellipticity (Weißmann et al., 2013), P_3 represents the smallest moment that unambiguously indicates substructure within the ICM (Buote & Tsai, 1995; Jeltema et al., 2005). This power is usually normalized by the monopole P_0 to better compare between clusters of different masses, resulting in the power ratio P_3/P_0.

Finally, we also determine the morphological parameter δ introduced by Yuan & Han (2020). We begin by first fitting an ellipse to the light distribution within an aperture of $R_{\rm ap} = R_{500c}$ centered on $\vec{x}_{\rm cent}$ following the method by Valenzuela et al. (2024). Essentially, we determine the second moment of the mass (or in this case, X-ray surface brightness) distribution tensor $\mathbf{M}$, with entries

$$M_{n,n'} = \sum_{R_i < R_{\rm ap}} f(x_i, y_i) \, R_{i,n} \, R_{i,n'}, \tag{13.9}$$

where $f(x_i, y_i)$ is the surface brightness of pixel (x_i, y_i), $\vec{R}_i$ is the pixel's vector to the X-ray center and its components are $R_{i,n}$ (being the nth component of pixel i). Then the square



roots of the eigenvalue ratios of $\mathbf{M}$ give the ellipse's axis ratio as $q = \sqrt{\lambda_2/\lambda_1} = b/a$ (with half-axis lengths $a \geq b$). With the fitted ellipse, we can define the ellipticity $\epsilon = 1 - q$ as well as the elliptical radius

$$r_{\rm ell}^2 = x_{\rm ell}^2 + \frac{y_{\rm ell}^2}{q^2}. \tag{13.10}$$

We then generate an X-ray surface brightness profile $f(r_{\rm ell})$ by binning each pixel via its elliptical radius into 50 log-spaced bins from 10kpc to $R_{\rm ap} = R_{\rm 500c}$. Note that the value of each bin is given as the median of the surface brightnesses $f(x_i, y_i)$ of all pixels in the bin, so as to avoid any single pixels outshining the rest, and we further use the smoothed X-ray map. By then also assigning each bin an error σ as the standard deviation of the surface brightnesses $f(x_i, y_i)$ of all pixels in the bin, we can then perform a weighted least-squares fit with a $\beta-$model (Cavaliere & Fusco-Femiano, 1978) as,

$$F_{SB}(R) = F_0 \left[1 + \left(\frac{R}{R_c}\right)^2\right]^{-3\beta+1/2}, \tag{13.11}$$

with a core radius R_c, normalization F_0, and the asymptotic radial falloff of the ICM in the outskirts given by $r^{-3\beta}$ (Mohr et al., 1999). This allows us to determine the profile parameter

$$\kappa = \frac{1+\epsilon}{\beta} \tag{13.12}$$

as defined by Yuan & Han (2020).

Finally, we calculate the asymmetry factor α given as the sum of squared differences between pixel pairs (x_i, y_i) and (x_i', y_i') symmetric with respect to the cluster center pixel $\vec{x}_{\rm cent}$, normalized by the sum of the square of each individual pixel's surface brightness, so

$$\alpha = \frac{\sum_i \left[f(x_i, y_i) - f(x_i', y_i')\right]^2}{\sum_i [f(x_i, y_i)]^2}. \tag{13.13}$$

Together, these define the morphology index δ as

$$\delta = 0.68 \log_{10}(\alpha) + 0.73\kappa + 0.21, \tag{13.14}$$

where a low δ indicates a relaxed cluster as it equates to both a low asymmetry α as well as a low κ or equivalently high β (i.e., a steeper outer profile indicating stronger central peaked-ness).

13.4 Results

We present here the dynamical states of our 26 simulated equivalents to local galaxy clusters. As the simulations allow for the full phasespace information, as well as tracing of their assembly history, we can determine both observable properties such as the fraction of stellar

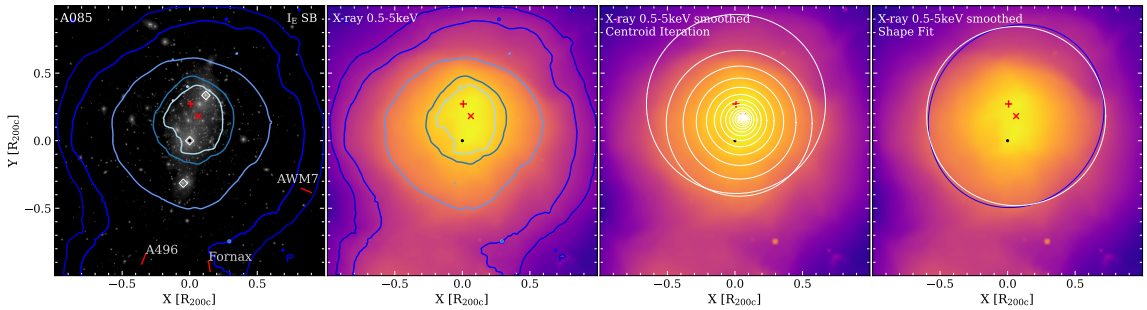


Figure 13.1. *Left:* Mock image in the *Euclid* band I_E produced via SMAC (Dolag et al., 2005a) of a simulated equivalent to the Abell 085 galaxy cluster. Contours enclose 99.9% (dark blue) to 50% (white) of the total X-ray surface brightness in the 0.5 – 5keV band, while red lines indicate the directions the three nearest other matched local clusters, in this case being Abell 496, Fornax and AWM7. *Center left:* X-ray surface brightness map. *Center right:* X-ray surface brightness smoothed with a gaussian kernel of 20kpc size. From this map we calculate the pixel with the highest absolute luminosity (red plus), and around that pixel determine the center (red cross) via iteratively shrinking spheres (Power et al., 2003) indicated by the white circles. For this cluster the peak and center are both offset from each other and the BCG position (black diamond). *Right:* The fit to the smoothed map for the ellipticity following the method by Valenzuela et al. (2024), showing the resulting ellipse (blue line).

mass contained in the ICL and BCG, or the smoothness and shape of the X-ray halo, in addition to unobservable properties such as the redshift when half of the galaxy cluster final halo mass was first assembled.

13.4.1 Simulated Counterparts

To illustrate our dynamical tracers defined in Sec. 13.3, we briefly discuss the example of our equivalent to Abell 085. We plot in Fig. 13.1 from left to right the mocked stellar light in the *Euclid* band I_E, the X-ray surface brightness in the band from 0.5 to 5 keV, both of which are produced via the code SMAC (Dolag et al., 2005a), and then in the third and fourth panel the smoothed version of the X-ray map after convolving it with a gaussian kernel of 20 kpc size. The orientation is projected as seen from the best-fit center of the SLOW parent simulation, which is thus as it would be seen from the position of the Milky Way galaxy (Dolag et al., 2023).

From the stellar light it is apparent that our simulated Abell 085 is a system with two BCGs, indicating recent merger activity (Haggar et al., 2024; Kimmig et al., 2025a). Indeed, when we determine in 3D the sum of stellar mass within the BCG and ICL as a fraction of the total stellar mass, we get a value of only $f_{\rm ICL+BCG} = 0.365$, which means that a majority of the stellar mass is contained in the satellites.

Simultaneously, both the X-ray peak (red plus), given by the brightest pixel in the smoothed map, as well as the X-ray centroid (red cross), given by a shrinking sphere method (Power et al., 2003) performed starting on the X-ray peak with initial radius of R_{500c} and shrinking factor of 5% (see the white circles in panel 3 of Fig. 13.1), are offset from the position of the BCG (black diamond) and from each other. This disturbed X-ray morphology and resulting large center shift w is known to also be an indicator of recent merging activity (Biffi et al.,

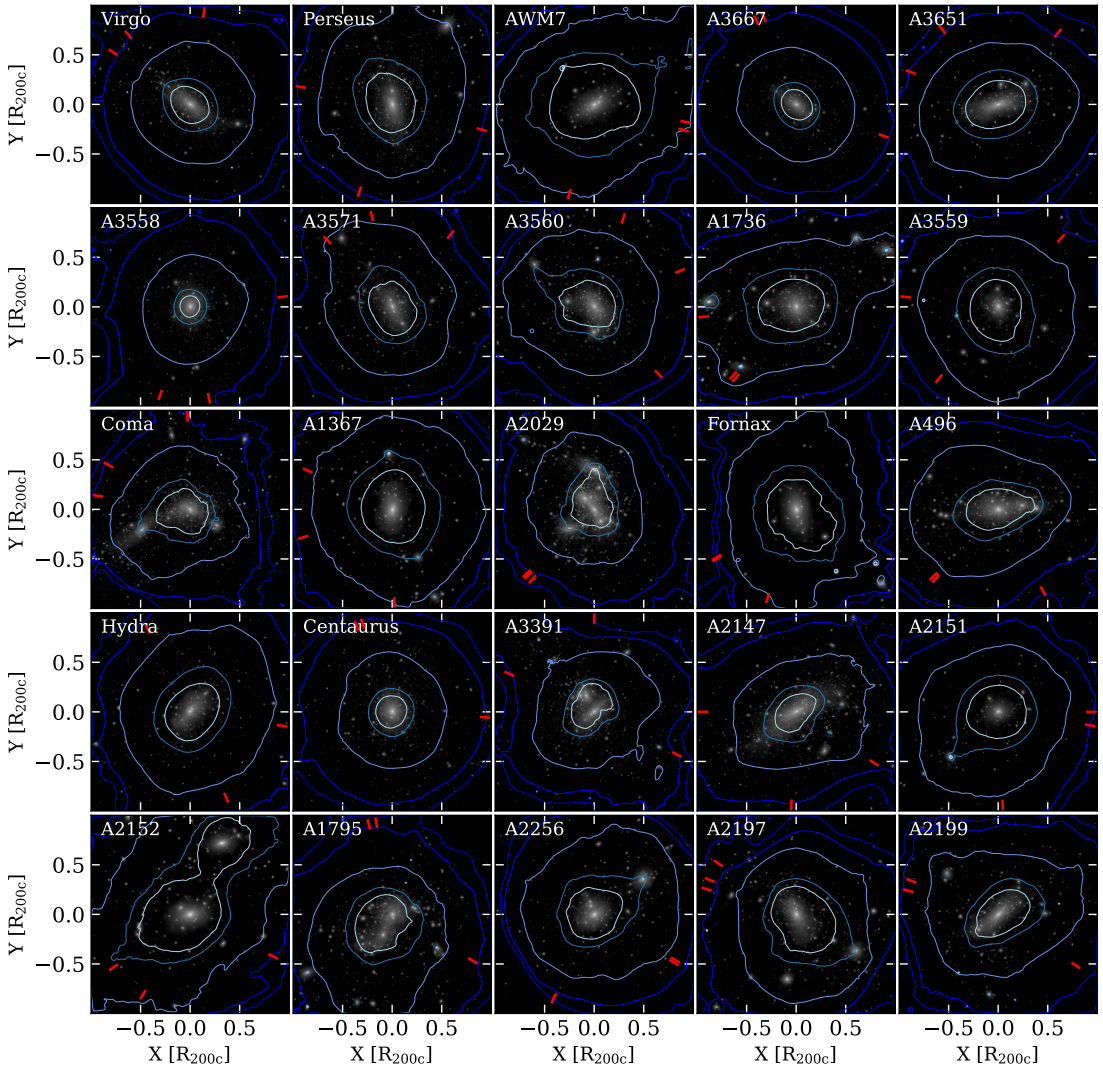


Figure 13.2. Mock images of our local matched galaxy cluster sample in the EUCLID band I_E produced via SMAC (Dolag et al., 2005a). Contours enclose 99.9% (dark blue) to 50% (white) of the total X-ray luminosity in the 0.5 − 5keV band, while red lines indicate the directions of the nearest three other matched local clusters.

2016; Haggar et al., 2024). Interestingly, the large-scale shape of the X-ray halo remains quite circular, as can be seen from the fitted ellipse in the right panel (blue line, following the method from Valenzuela et al.) with very low ellipticity of $\epsilon = 0.08$, well below the average of our sample of $\epsilon = 0.19$. The morphology parameter of $\delta = -0.09$ is also very low relative to the rest of our sample, even though this system has in fact undergone a recent major merger, as we discuss later in more detail.

A weak-lensing analysis performed on the observed Abell 085 has revealed that it too is undergoing a 1:2 merging event, with the southern subcluster having $M_{200c} = (1.23 \pm 0.52) \times 10^{14} M_\odot$, but which has not yet disturbed the X-ray (Kim et al., 2025), indicating it is on first passage. It is thus reasonable to assume that our region has collapsed somewhat faster than the observed equivalent and we are seeing a later stage of the merger when the two BCGs are already within R_{500c} of each other. Indeed, our simulated Abell 085 is about 20% more massive in M_{500c} than the observed one, as we discuss in more detail in Sec. 13.4.2.

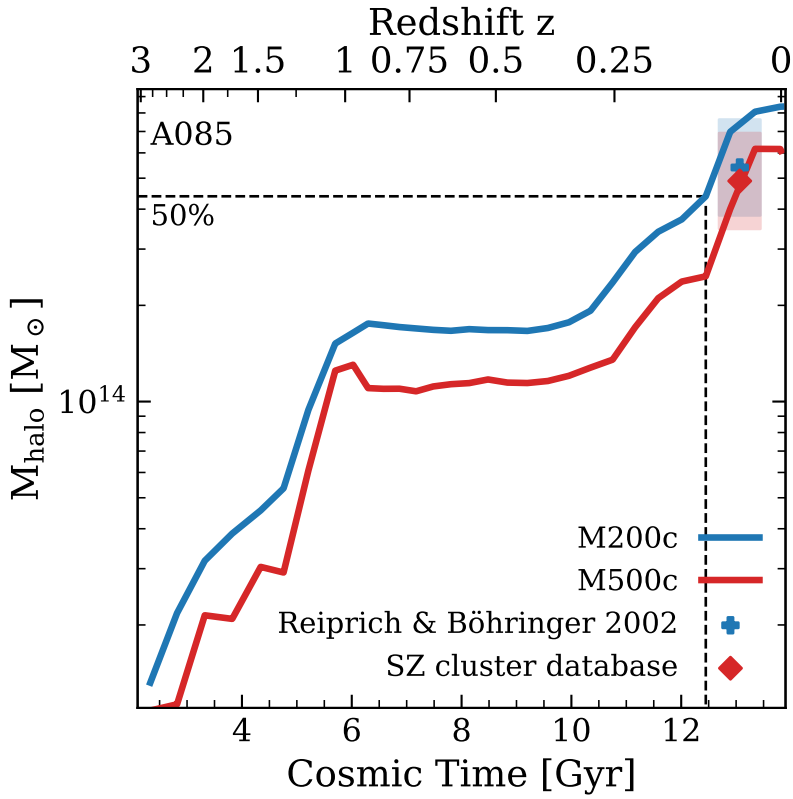


Figure 13.3. The mass assembly history of our simulated equivalent to Abell 085 as a function of cosmic time for both M_{200c} and M_{500c} (blue and red lines). The formation redshift z_{50}, defined as the time when it reached half of its final M_{200c} mass, is indicated by the black dashed lines. We plot also the observed masses M_{200c} (blue plus) from Reiprich & Böhringer (2002) and M_{500c} (red diamond) from the SZ cluster database.

We show the mock stellar light map with X-ray contours as in the left panel of Fig. 13.1 for all other 25 simulated clusters in Fig. 13.2. They span a range of clusters from those that appear highly relaxed with a single massive BCG and smooth X-ray contours such as the Abell 3558 equivalent, all the way to major mergers like the one for Abell 085 already discussed and clusters with noticeably elongated X-ray profiles and two BCGs such as Abell 3391.

13.4.2 The Mass Assembly Histories of Local Galaxy Clusters

Having seen the diversity in galaxy clusters, we consider now how they assembled their mass. Again we illustrate first the case of Abell 085 in Fig. 13.3, where we plot the halo masses M_{200c} (blue line) and M_{500c} (red line) of the simulated equivalent as a function of cosmic time (or equivalently redshift, upper axis). We see that the main progenitor underwent rapid growth to reach cluster mass $M_{200c} > 10^{14} M_\odot$ already by $z > 1$, before stagnating for nearly six gigayears. Consequently, it has only recently undergone its final phase of merging, reaching half its final mass only by $z_{50} = 0.1$ or just over one gigayear ago, comparable to the typical crossing time of the galaxy cluster itself (Jiang & van den Bosch, 2016; Contreras-Santos et al., 2022; Haggar et al., 2024).

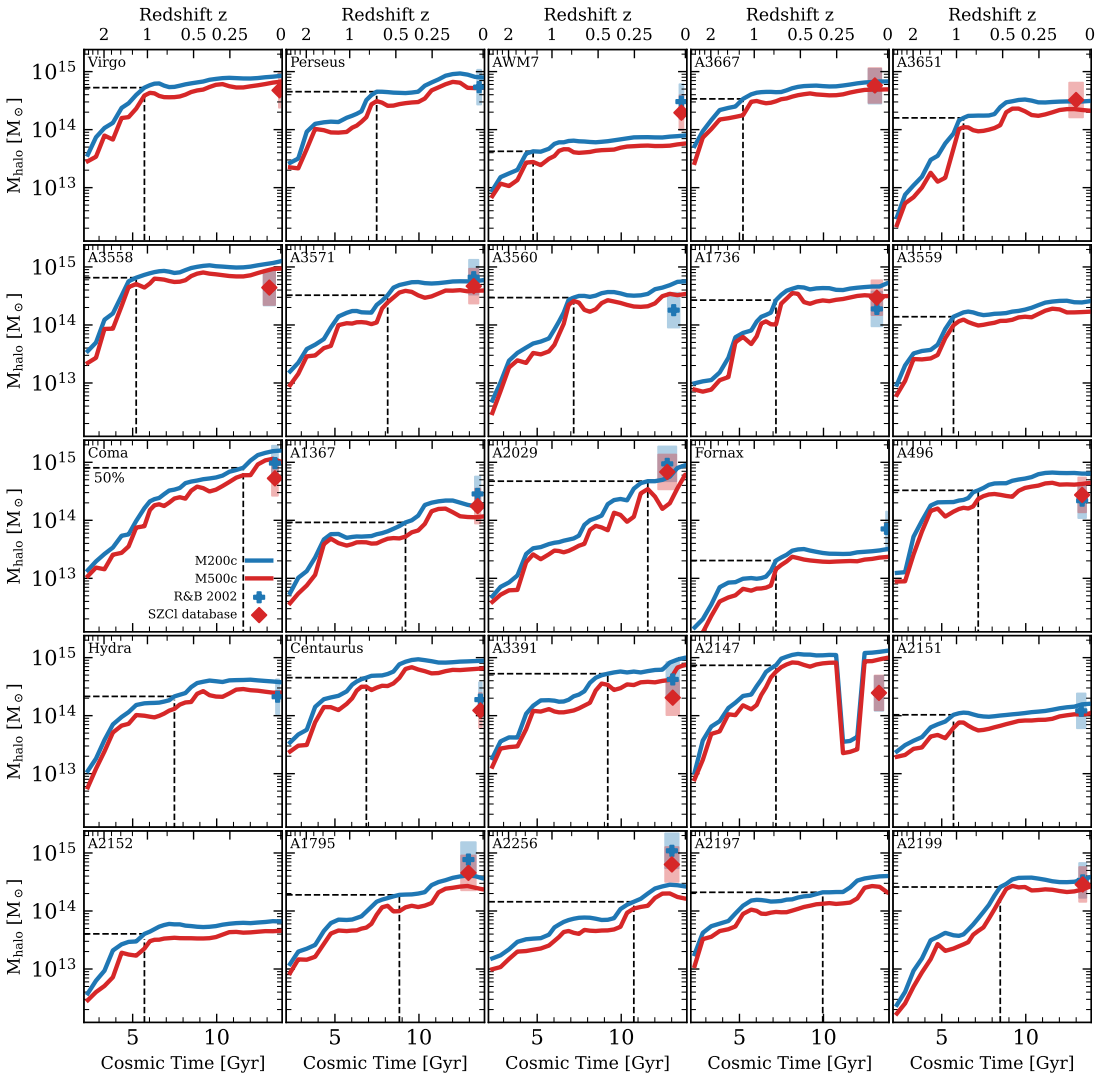


Figure 13.4. The mass assembly histories of our local galaxy cluster simulated equivalents as a function of cosmic time, for both M_{200c} and M_{500c} (blue and red lines). The redshift when a cluster reached half its final M_{200c} mass is indicated by the black dashed lines. Where available, we plot also the observed masses M_{200c} (blue plus) from Reiprich & Böhringer (2002) and M_{500c} (red diamond) from the SZ cluster database.

We plot also the observed masses of Abell 085, with M_{200c} from Reiprich & Böhringer (2002) as a blue plus and M_{500c} from the SZ cluster database[1] as a red diamond. We also plot as shaded regions a range of factor 2 in mass to indicate the uncertainty in the systematics of derived cluster masses (Biffi et al., 2016; Lebeau et al., 2024), comparable to that derived by Ferragamo et al. (2022) for MACS J0647.7+7015 between the hydrostatic and lensing mass estimates. The width of the shaded region is given by half their lookback time, as the farther away they are the less stringent our constraints from the peculiar velocity field become (Dolag et al., 2023), thus making the exact timing of our match more uncertain.

We plot the assembly histories for the remaining 25 clusters in Fig. 13.4, and find that the apparent diversity in dynamical states seen from the mock images is indeed indicative of the underlying range in assembly histories. Our simulated Abell 3558 has indeed assembled

[1] http://szcluster-db.ias.u-psud.fr/sitools/client-user/SZCLUSTER_DATABASE/project-index.html

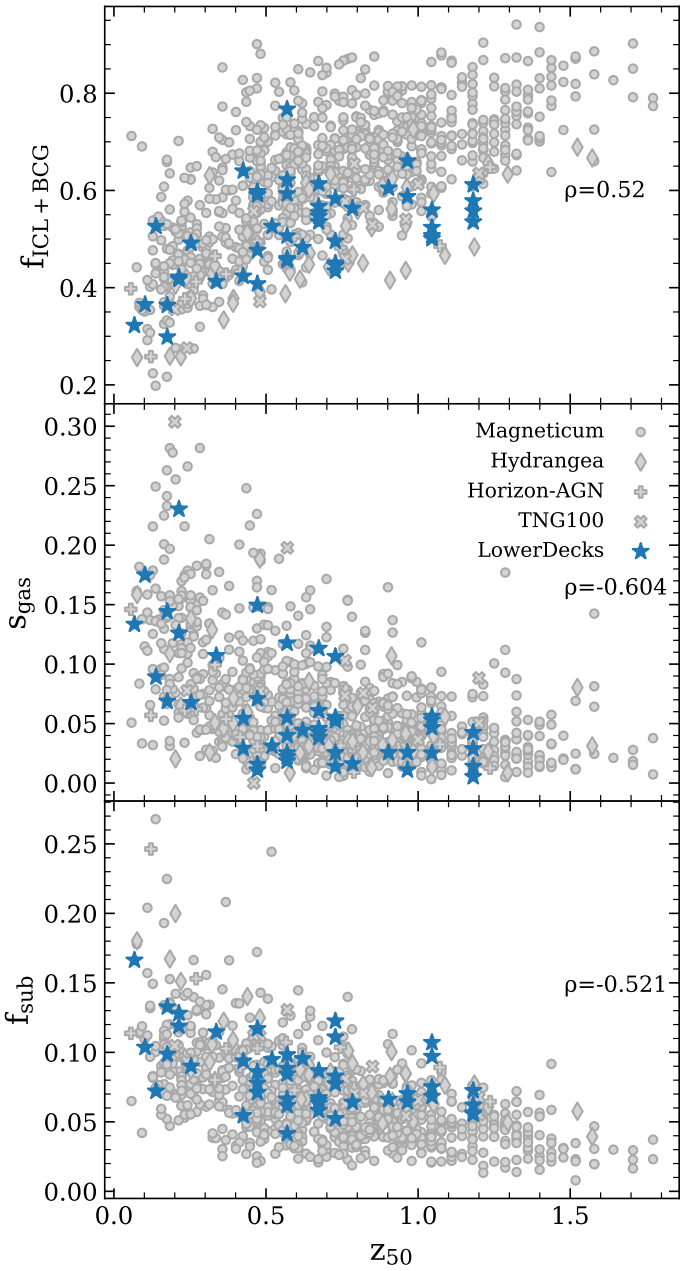


Figure 13.5. *Upper panel:* The fraction of stellar mass in the ICL and BCG, $f_{\mathrm{ICL+BCG}}$, as a function of the formation redshift z_{50} for the Lower Decks clusters (blue diamonds) as well as the compilation of galaxy clusters from the Magneticum (circles), TNG100 (crosses), Horizon-AGN (pluses), and Hydrangea simulations (diamonds) given by Kimmig et al. (2025a). ρ is the Pearson correlation coefficient determined for the Lower Decks clusters, where an absolute value closer to unity indicates a tighter correlation. *Middle panel:* The gas center shift s_{gas} as a function of the z_{50}, with markers as in the upper panel. The center shift s_{gas} is defined here as the offset between the 3D gas barycenter and the location of the BCG, normalized by R_{200c}. *Lower panel:* The fraction of the total halo mass mass contained in all subhalos f_{sub} as a function of z_{50}.

most of its mass already by $z > 1$, making it one of the oldest and most relaxed clusters in our set, while our simulated Abell 2029 equivalent has only recently undergone a major merger, much like Abell 085.

As shown by Kimmig et al. (2025a), the dynamical state of a cluster is strongly imprinted in its stellar distribution. To test whether this remains true for the Lower Decks clusters, we

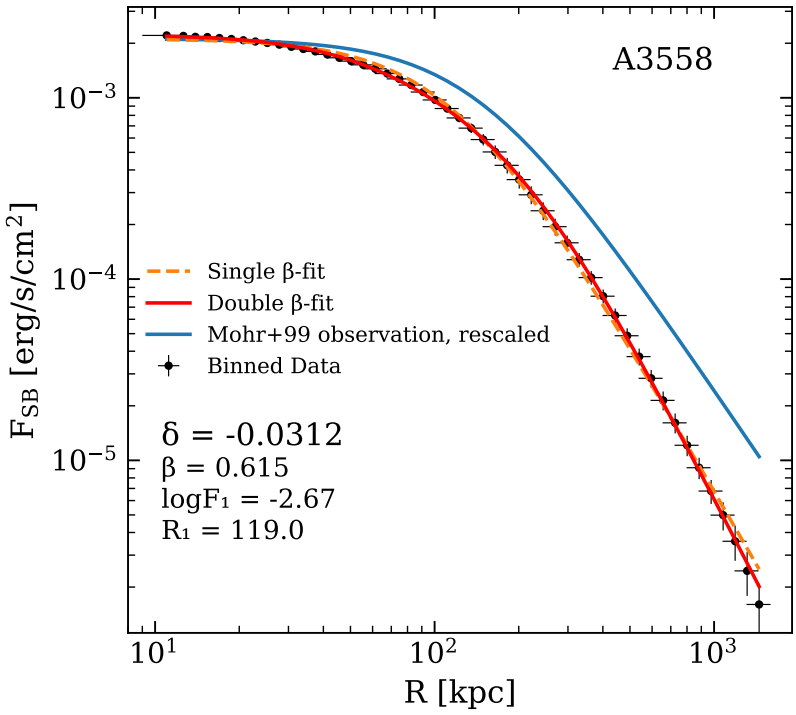


Figure 13.6. X-ray surface brightness profile for the Lower Decks Abell 3558 (black points) with a best fit single and double-β profile (orange and red lines). We additionally provide the fit parameters for the single-β fit as it well describes the profile, and plot also the rescaled single-β fit made by Mohr et al. (1999) on the observed Abell 3558.

plot for our 26 simulated clusters three of their considered dynamical tracers as function of the formation redshift z_{50} in Fig. 13.5. From top to bottom the tracers are the fraction of total stellar mass contained within the ICL and BCG, $f_{\rm ICL+BCG}$, the offset $s_{\rm gas}$ of the 3D gas barycenter and the BCG (normalized by $R_{\rm 200c}$), and the fraction of total halo mass $M_{\rm 200c}$ contained within all subhalos $f_{\rm sub}$.

The simulated clusters from Lower Decks follow the same relations as found by Kimmig et al. (2025a) for simulated cluster from the Magneticum (circles), TNG100 (crosses), Horizon-AGN (pluses), and Hydrangea simulations (diamonds). A more recent assembly thus correlates with a lower $f_{\rm ICL+BCG}$ and higher $s_{\rm gas}$ and $f_{\rm sub}$, all of which are significant correlations as can be seen from the Pearson correlation coefficients provided in Fig. 13.5. It is interesting to note that our clusters lie tower the lower edge in $f_{\rm ICL+BCG}$ and upper end in $f_{\rm sub}$, which is likely a result of their high resolution. Indeed, the other set of zoom-in simulated clusters with comparable particle mass resolution and halo masses, namely the Hydrangea clusters, lie very near to our Lower Decks galaxy clusters.

13.4.3 The X-ray Dynamical State of Local Galaxy Clusters

Having seen that the Lower Decks galaxy clusters follow the same correlations found by Kimmig et al. (2025a), we consider here in addition four dynamical tracers derived directly from the X-ray maps, namely the centroid shift w, the power ratio P_3/P_0, the concentration $c_{\rm SB}$ and the morphology index δ. To determine the latter, we must first fit a β profile to the

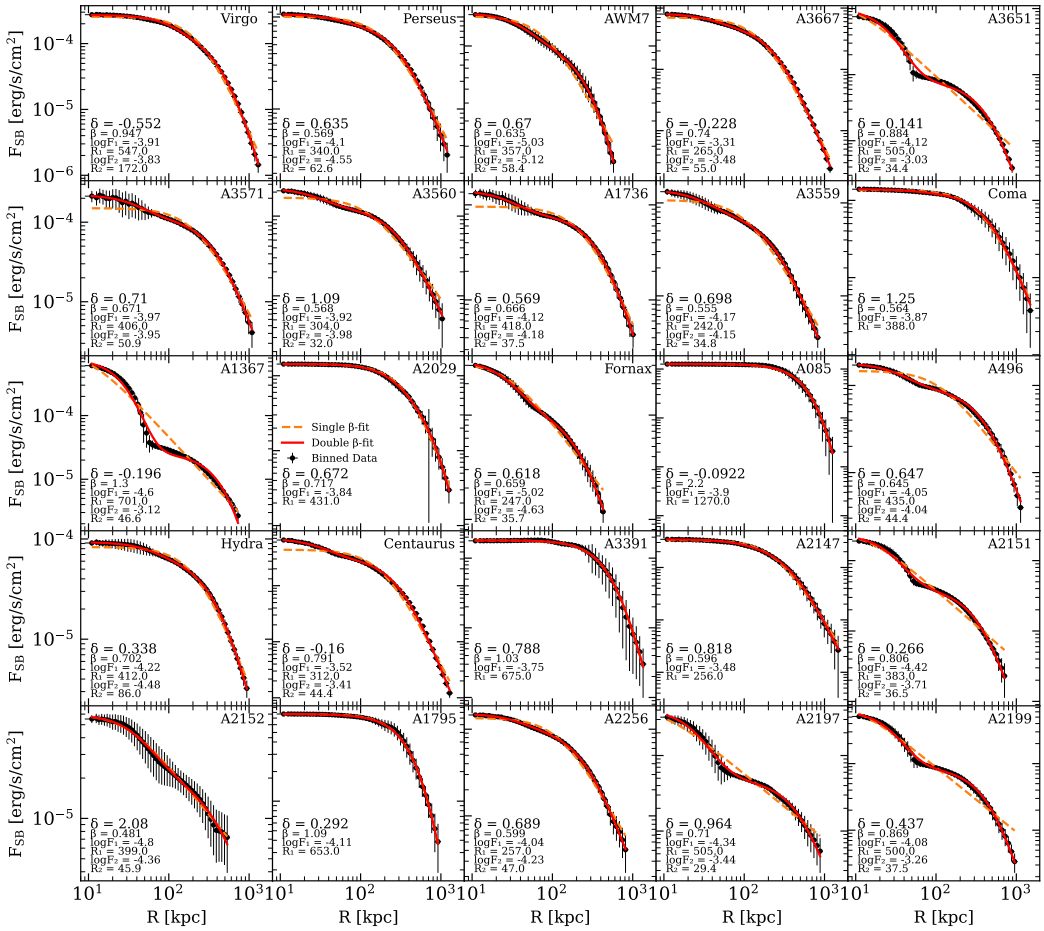


Figure 13.7. X-ray surface brightness profiles for the remaining 25 Lower Decks galaxy clusters (black points) with a best fit single and double-β profile (orange and red lines). We provide the fit parameters for the type of profile that fit best, preferring the single-β when it is sufficient to describe the galaxy cluster (χ^2 near unity).

X-ray surface brightness profiles. We plot such a fit to the simulated Abell 3558 equivalent in Fig. 13.6, with the data points and their errors plotted as black points. We fit both a single and double-β profile, where in the latter case we keep a fixed β across both profiles. A double-β profile can be necessary in cases where there is a central excess in X-ray surface brightness (Mohr et al., 1999).

We find that for the simulated Abell 3558 the single β-fit is sufficient to fit the profile shape, and thus show only those fit parameters in the plot. The simulated cluster is quite centrally concentrated and compact, with a correspondingly low morphology index δ indicating it is relaxed. Our fit ends up being quite close to the fit by Mohr et al. (1999) to the observed Abell 3558, where they find R_c = 143kpc and β = 0.548, albeit being somewhat flatter and more extended. We have included it as a blue line, rescaled to our central surface brightness to be more directly comparable (as the Lower Decks Abell 3558 is more massive, see Fig. 13.4).

In Fig. 13.7 we plot the X-ray surface brightness profiles in the same manner for the remaining 25 Lower Decks galaxy clusters. We find that many are well fit by a single-β profile, even in cases of obvious and strong ongoing mergers such as Abell 085. Indeed, the resulting δ is quite low relative to our overall sample. Interestingly, profiles with large

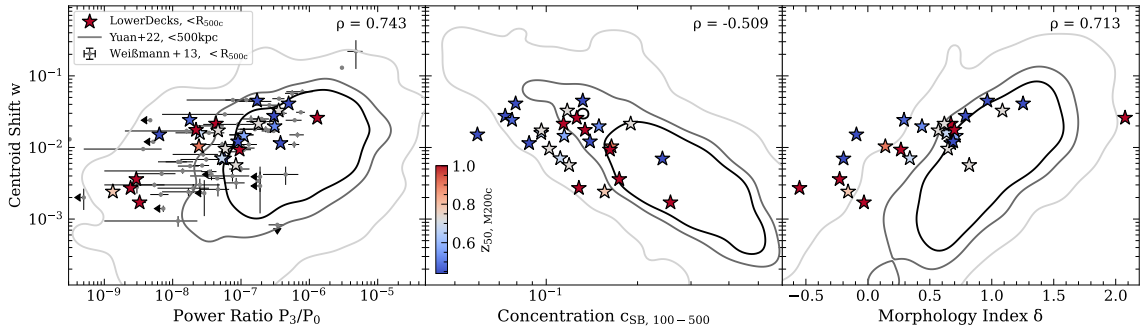


Figure 13.8. Centroid shift w of the 26 Lower Decks galaxy clusters plotted as a function of power ratio P_3/P_0 (*left*), concentration c_{SB} (*center*), and morphology index δ (*right*). Points are colored by the formation redshift z_{50}, and we provide the Pearson correlation coefficient ρ in the upper right corner of each panel. We further plot observational data by Weißmann et al. (2013) and Yuan et al. (2022), where for the latter we convert their sample of clusters into contours containing 95%, 68% and 50% of all points (light, medium and dark gray).

variations in the map (and correspondingly large errors in the binned data) all belong to clusters with among the highest values for their morphological index δ, indicating recent merging activity. However, we find no correlation with the need or lack thereof for a double-β profile based on the morphological index, aside from double-β fits having more extreme values of δ.

Finally, then, we compare the various X-ray dynamical state parameters against each other in Fig. 13.8. We note that the concentration c_{SB} is determined as the ratio in total brightness between a fixed core $R_{\mathrm{core}} = 100\mathrm{kpc}$ and outer aperture $R_{\mathrm{outer}} = 500\mathrm{kpc}$, while all other dynamical tracers are determined within an aperture of $R_{\mathrm{ap}} = R_{500\mathrm{c}}$.

We find all four tracers to correlate significantly with each other (Pearson correlation coefficient of at least $\rho = 0.5$). Furthermore, we find them all to correlate to varying degrees also with the underlying assembly time, in this case chosen as the formation redshift z_{50} of the clusters (colorbar), with Pearson correlation coefficients to z_{50} of $\rho = -0.42, -0.36, 0.5,$ and -0.14 for the centroid shift w, power ratio P_3/P_0, concentration c_{SB}, and morphology index δ. This means that for the Lower Decks clusters the concentration is the best tracer of the assembly time.

For comparison we include also the observational data by Weißmann et al. (2013) and Yuan et al. (2022), finding that the Lower Decks generally well follow the observational trends. Our simulated clusters appear to lie at generally lower values of δ relative to the observed clusters by Yuan et al. (2022), which we find to be because our clusters tend to be more symmetric than theirs, i.e., have a lower α (and thus lower δ, see Eq. 13.14). This may be due to differences in smoothing, pixel size or aperture size, as their fixed cut of $R_{\mathrm{ap}} = 500\mathrm{kpc}$ is below our $R_{\mathrm{ap}} = R_{500\mathrm{c}}$ for all but one of our clusters, meaning they determine the asymmetry in a more central region than we do.

13.5 Conclusion

We have performed an analysis of the dynamical states of 26 galaxy clusters drawn from the new state-of-the-art Lower Decks zoom-in simulations, which feature constrained initial conditions to reproduce our own local environment and the clusters therein (Dolag et al., 2023; Hernández-Martínez et al., 2024; Seidel et al., 2024). In particular, we consider the ability of various dynamical tracers to predict the galaxy cluster formation redshift z_{50}, which is the time when the main progenitor of the cluster first had assembled half of its final halo mass M_{200c}.

Comparing with the relations to z_{50} found by Kimmig et al. (2025a) for the Magneticum Pathfinder, Hydrangea, Horizon-AGN and IllustrisTNG-100 simulations, we find that Lower Decks galaxy clusters well match their results. We confirm a tight correlation between z_{50} and the fraction of the stellar mass in the ICL and BCG $f_{\mathrm{ICL+BCG}}$, as well as the gas center shift s_{gas} and total mass fraction within satellites f_{sub}. As in particular $f_{\mathrm{ICL+BCG}}$ can be determined observationally (Brough et al., 2024) this will allow future large-scale surveys such as *Euclid* (Laureijs et al., 2011; Kluge et al., 2024), Roman (Montes et al., 2023) and Rubin/LSST (Ivezić et al., 2019; Brough et al., 2020) to quantify the assembly time of a statistical set of galaxy clusters.

We then consider also four dynamical tracers determined directly from X-ray surface brightness maps, namely the centroid shift w (e.g., Neto et al., 2007; Biffi et al., 2016), the power ratio P_3/P_0 (Buote & Tsai, 1995), the concentration c_{SB} (Santos et al., 2008), and the morphology index δ (Yuan & Han, 2020). All parameters correlate significantly with each other for the Lower Decks galaxy clusters, and closely follow the observed trends by Weißmann et al. (2013) and Yuan et al. (2022). We find that the best X-ray tracer for predicting the formation redshift z_{50} is the concentration, with the centroid shift coming in second.

Die Sterne sind klug, sie halten mit Fug
Von unserer Erde sich ferne;
Am Himmelszelt, als Lichter der Welt,
Stehn ewig sicher die Sterne.

Heinrich Heine, *Neue Gedichte: Kluge Sterne*, 1852

14

A Whale of a Time: Cluster Evolution from Cosmic Dawn to Present Day

This chapter is a compilation of contributions to IAU proceedings, a paper to which I contributed, and additional research that is planned to be published as an independent paper in the future as Kimmig et al.

14.1 Introduction

As discussed in chapter 13, the largest bound structures in our Universe, galaxy clusters, are observed to be in various states of assembly. From those that are essentially comprised of a single, massive central brightest cluster galaxy (BCG) such as for the Abell 1835 galaxy cluster (Govoni et al., 2009), to those that have only recently undergone a major merger and thus still host what can be considered two BCGs like in Coma (Colless & Dunn, 1996; Neumann et al., 2003) or the Bullet cluster (Markevitch et al., 2002).

Understanding how clusters grow and evolve through cosmic time is crucial to uncovering the impact of the environment on galaxy formation. With ongoing attempts to identify the early phases of galaxy cluster formation, the so-called protocluster phase (Dannerbauer et al., 2014; Muldrew et al., 2015), it is becoming increasingly relevant to understand whether the assumptions about how the most massive structures can be linearly connected hold true (Sunyaev & Zeldovich, 1972), or whether nonlinearities in structure growth may pose significant challenges (Borzyszkowski et al., 2017). Indeed, the similarities of massive

ellipticals between the field and cluster environments implies that in both cases they grew early and rapidly to reach high stellar masses. However, where the latter then became the central galaxy within a massive galaxy cluster, the other type starved, becoming field ellipticals by $z = 0$.

The difficulty in connecting structures across cosmic time has been illustrated already for example by Remus et al. (2023). They used typical definitions used in observations to identify protocluster structures at high redshift, such as the number of satellites or the mass of the BCG, and applied them to the Magneticum simulations. This allowed them to trace the descendants of those structures, finding that while some did end up among the most massive clusters at $z = 0$, none became the most massive overall and some barely even made it into the range of cluster masses $M_{\rm vir} \geq 1 \times 10^{14} M_\odot$. Similarly, Kimmig et al. (2023) used the large-volume cosmological simulation Magneticum Pathfinder Box2b/hr to identify a simulated match in the to the Abell 2744 galaxy cluster, and demonstrated that it formed through a quad merger of smaller halos, rapidly rising from one of thousands to one of the twenty most massive clusters in the entire simulation volume.

This work expands on the foundations laid by Borzyszkowski et al. (2017); Remus et al. (2023); Kimmig et al. (2023), and others by 1) extending the sample of traced halos to larger numbers within a large-volume cosmological simulation and 2) considering which tracers, if any, link the cosmic structures through cosmic time. Throughout this chapter, we employ the Magneticum Pathfinder Box2/hr simulation (Dolag et al., 2025; Kimmig et al., 2025a), which we briefly introduce in Sec. 14.2. We then cover recent work to be submitted on the difficulty of connecting cosmic structure through time, and how that may be resolved by including the environment as a tracer, in Sec. 14.3 and Sec. 14.4. Sec. 14.5 was partially published as an IAU proceedings, and provides the view on connecting structure as seen from $z = 0$. We emphasize the relevance of the dynamical state and growth of clusters on the properties of their galaxy populations by highlighting the results found by Çakır et al. (2025) in Sec. 14.6, before concluding in Sec. 14.7.

14.2 The Magneticum Pathfinder Box2/hr Simulation

Throughout this chapter we mostly employ the power of the Box2/hr simulation from the Magneticum Pathfinder suite (Teklu et al., 2015; Dolag et al., 2025), which is particularly useful because of its large volume of $(500\,\mathrm{Mpc})^3$, thus hosting among the most massive structures possible in a ΛCDM Universe (Press & Schechter, 1974; Remus et al., 2023), while retaining enough resolution in stellar mass to identify early structures of $M_* = 1 \times 10^9 M_\odot$ (around 20 stellar particles) as well as in time to trace their evolution smoothly down to $z = 0$ (with 144 outputs spaced in around 100 Myr intervals). Structure is identified via SUBFIND (Springel et al., 2001b; Dolag et al., 2009), and linked together through time via merger trees based on L-BaseTree (Springel et al., 2005c).

The Box2/hr simulation was performed assuming the WMAP-7 cosmology (Komatsu et al., 2011), where $h = 0.704$, $\Omega_m = 0.272$, $\Omega_b = 0.0451$, $\Omega_\lambda = 0.728$, $\sigma_8 = 0.809$ and

$n_s = 0.963$. It was run with a modified version of the smoothed particle hydrodynamics (SPH) code GADGET-2 (Springel, 2005), with various improvements to the hydrodynamics (Dolag et al., 2004; Donnert et al., 2013; Beck et al., 2016) as discussed in greater detail by Dolag et al. (2025).

14.3 The Non-linear Growth of Massive Structures

As an illustrative example, we begin here by drawing two galaxy clusters from the Lower Decks set of zoom-in simulations (Seidel et al., in prep.) that we introduced in chapter 13. As is apparent from Fig. 13.4 therein, the Lower Decks Coma and Virgo clusters follow very different mass assembly histories, with Coma having assembled very recently (reaching 50% of its final halo mass M_{200c} only by $z_{50} = 0.18$) while Virgo has been massive already for a while ($z_{50} = 1.04$) with little recent assembly whatsoever.

We plot the evolution of halos within a fixed comoving volume for both Coma (first) and Virgo (second) in the upper two rows of Fig. 14.1. Halos which end up falling into the Coma or Virgo clusters by $z = 0$ are plotted in blue, with the main and second most massive progenitor being red and orange, while other halos in the environment are plotted in gray. The point sizes increase with the mass of the halos.

As is apparent already by $z = 4$ (first panel), the Coma protocluster region, i.e., the region that eventually collapses into the final galaxy cluster, is significantly more extended. Constituent halos spread across a projected area of $(30 \times 25)\text{cMpc}^2$ for Coma and $(25 \times 15)\text{cMpc}^2$ for Virgo, so half the extend. In the case of Coma, these regions collapse into various subnodes spread across a sheet, while for Virgo they cluster tightly together already early, and thus merge into the main progenitor structure early as well. It is also apparent that the region surrounding Coma contains many other massive structures, while Virgo is comparably poor.

This different type of assembly can be seen when we consider the histogramm of halo masses in the region in the lower two rows of Fig. 14.1. The masses of halos that eventually end up in Coma and Virgo are plotted in blue. Where the Coma region grows a great number of lower mass halos that only very late assemble into its final structure, the Virgo region has a comparably lower number of low mass halos but instead rapidly grows into one dominant halo. It reaches the mass of a galaxy cluster $M_{200c} \geq 1 \times 10^{14} M_\odot$ by $z = 2$ (third panel), where the most massive progenitor of Coma has only reached $M_{200c} < 2.5 \times 10^{13} M_\odot$. Comparing both with the average distribution of progenitors for all massive clusters ($M_{200c} \geq 5 \times 10^{14} M_\odot$) in the Magneticum Box2/hr simulation (black line), we see that Coma and Virgo are indeed both outlier in the amount of low mass halos, with the former lying well above and the latter well below the expected amount.

Given this particularly late assembly of the Coma galaxy cluster, it is apparent that such systems by their nature will be difficult to capture from measuring the masses of single objects. Their protocluster regions are explicitly characterized by the overabundance in number, as opposed to in individual masses. However, it stands to reason that at least protocluster

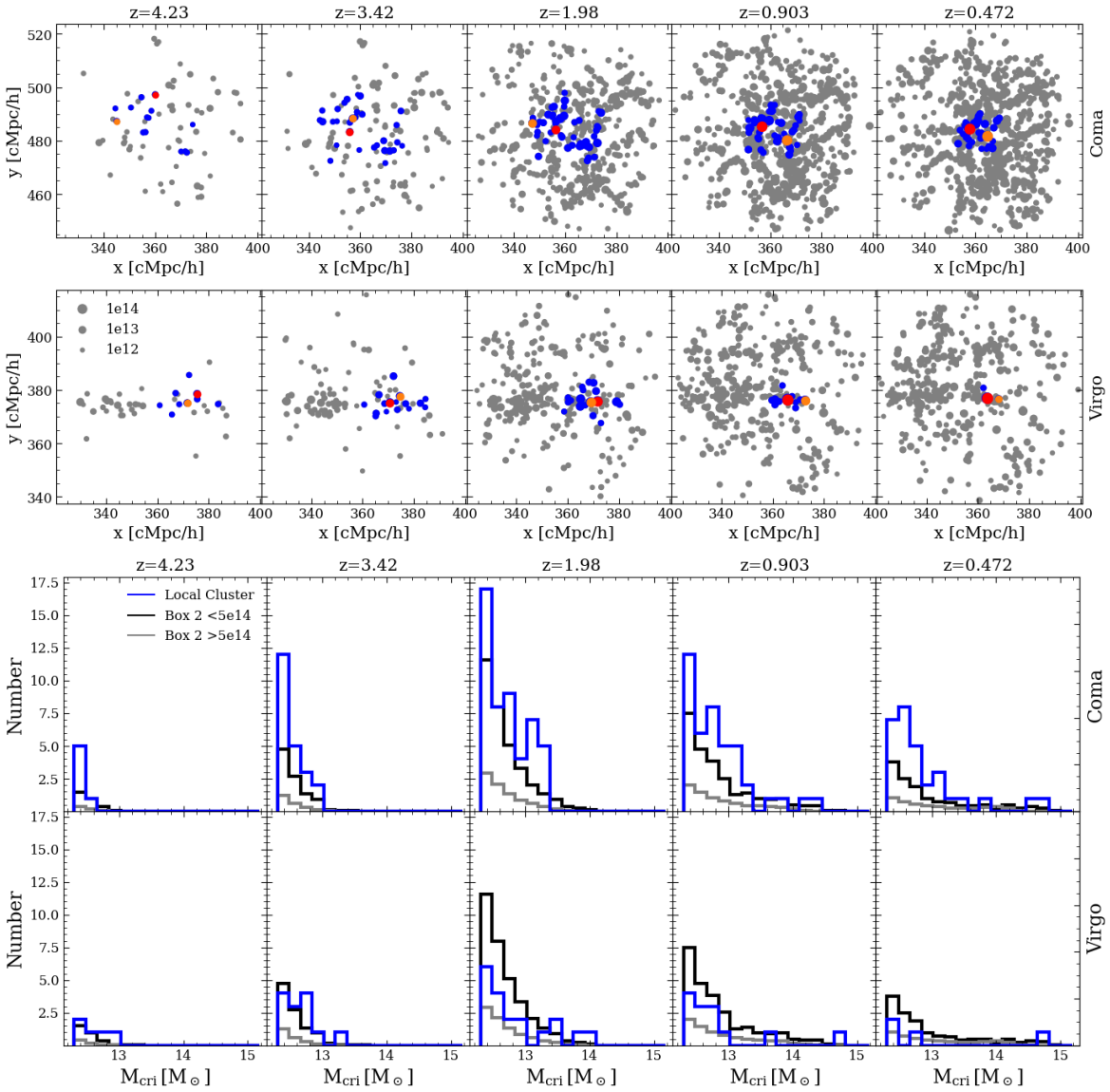


Figure 14.1. The *upper two rows* show the emergence of halos in a fixed comoving volume within the Coma and Virgo zoom-in simulations of the Lower Decks suite (Seidel et al., in prep.) going from the early protocluster phase at $z = 4.2$ (*left column*) to more recently at $z = 0.5$ (*right column*). Point sizes increase with halo mass M_{200c}, with blue points being those halos that merge into either Coma or Virgo by $z = 0$, while the main progenitor and the second most massive progenitor are plotted in red and orange, respectively. The *lower two rows* show for the same redshifts the evolution in the histogram of progenitor halo masses for Coma and Virgo (blue lines), as well as for all Magneticum Box2 galaxy clusters with masses of $M_{200c} < 5 \times 10^{14} M_\odot$ (black) and $M_{200c} > 5 \times 10^{14} M_\odot$ (gray).

regions belonging to Virgo-like galaxy clusters can be well identified at high redshifts, as they rapidly grew to host single massive outliers. To test this hypothesis, we now switch into the Magneticum Pathfinder Box2/hr simulation volume, and plot the evolution in halo mass for a set of galaxies selected by their halo masses at high redshift $z \geq 4$ in Fig. 14.2.

In the left panel, we plot the resulting halo mass evolution with varied halo mass cutoffs at fixed redshift $z = 4$, using a 0.1 dex range around $M_{200c} = 1 \times 10^{12} M_\odot$ (pink), $5 \times 10^{12} M_\odot$ (cyan) and $1 \times 10^{13} M_\odot$ (purple). We find that more massive halos do on average end up

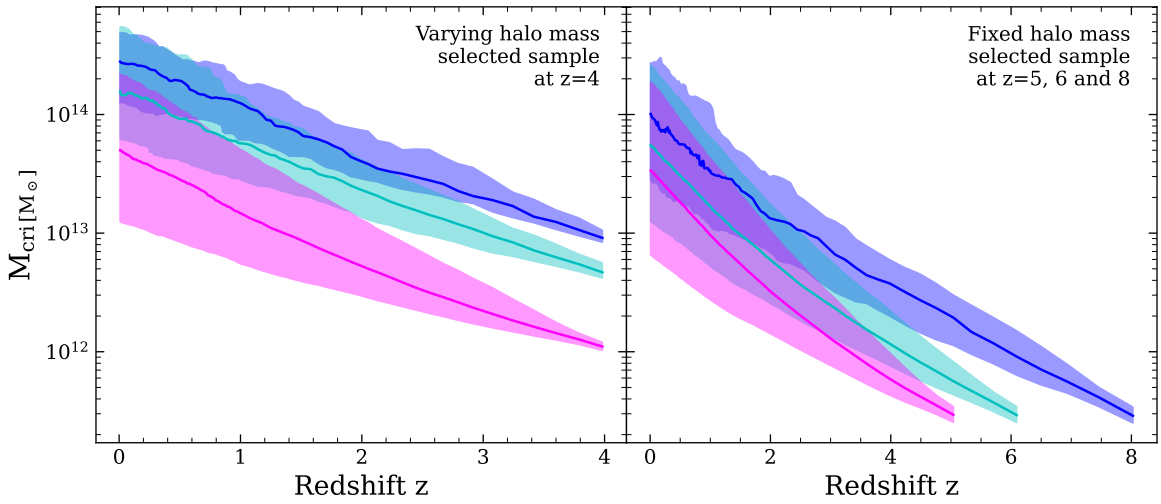


Figure 14.2. Evolution in halo mass M_{200c} for central galaxies selected at $z = 4$ with varying halo masses (*left panel*) of $M_{200c} = 1 \times 10^{12} M_\odot$ (pink), $5 \times 10^{12} M_\odot$ (cyan) and $1 \times 10^{13} M_\odot$ (purple), or selected at a fixed halo mass $M_{200c} = 3 \times 10^{11} M_\odot$ (*right panel*) at varying redshifts $z = 5$ (pink), $z = 6$ (cyan) and $z = 8$ (purple). Plotted are the median (solid lines) and 1σ-ranges (shaded regions).

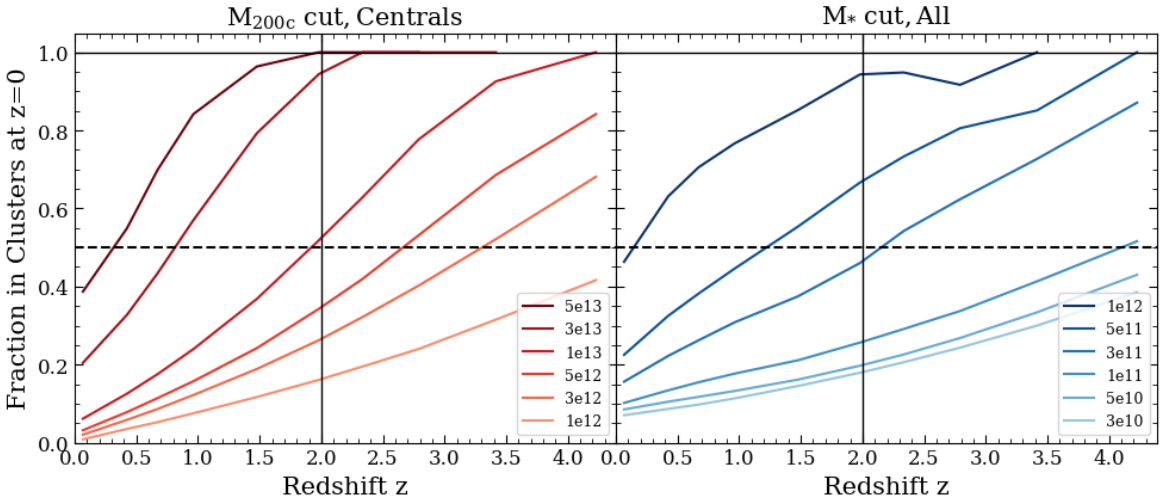


Figure 14.3. Fraction of galaxies which end up in a galaxy cluster by $z = 0$ when selecting them from $z = 4$ to $z = 0.1$ by their halo mass (*left*, including only centrals) or their stellar mass (*right*, including also satellites). We include increasing threshold masses (lighter to darker colors).

becoming more massive by $z = 0$ (blue versus cyan and pink solid lines). However, their 1σ-bounds significantly overlap, implying that this does not necessarily hold true for individual objects. Indeed, nearly 40% of all halos in the cyan selection become more massive than the least massive object in the blue selection, even though it began with a mass an order of magnitude larger. We find an even more significant overlap when we instead vary the selected redshift with a fixed halo mass selection of 0.1 dex around $M_{200c} = 3 \times 10^{11} M_\odot$ in the right panel of Fig. 14.2.

Instead of seeking to guarantee that a given high-redshift structure will end up more massive than another, we can instead explicitly try to identify protocluster structures, that is

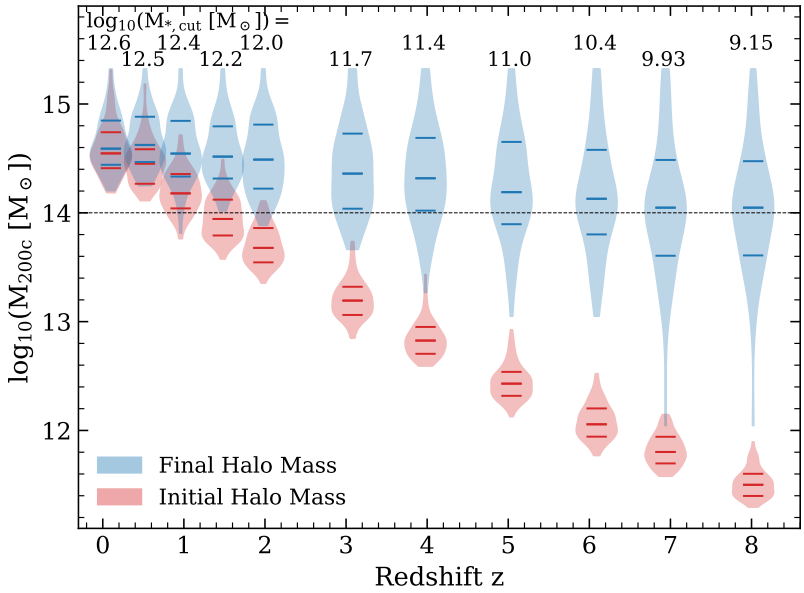


Figure 14.4. Distribution of initial (red) and final (blue) halo masses M_{200c} for the 100 most massive central galaxies at each redshift z. The numbers above the violins denote the stellar mass cut that this selection effectively equates to, while the horizontal dashed black line lies at $M_{200c} = 1 \times 10^{14} M_\odot$. Within each violin, the three horizontal colored line are the 20%, 50% and 80% quantiles.

to say, galaxies which will end up in a galaxy cluster by $z = 0$. This is done in Fig. 14.3, both for an observationally more difficult cut in halo mass (left panel) as well as a cut in stellar mass (right panel, which includes also satellite galaxies). We find that increasing the threshold mass (lighter to darker colors) for both kinds of mass cut also increases the fraction that belonged to a true protocluster region. However, any fixed cut rapidly decreases in its usefulness with decreasing redshift, requiring ever larger cuts to identify protocluster regions. This makes the identification very sensitive to the particular cosmology and hydrodynamics included in our simulation, where ideally it should be resilient to variations in either of those areas.

It is worthwhile to consider that fixed stellar or halo mass cuts may be showing this behavior because they include a greater number of objects just above the mass cut, because of the steep drop in number density at the high mass end of the galaxy mass function (Press & Schechter, 1974). Indeed, the most extreme halo mass cuts appear to guarantee cluster membership by $z = 0$ in Fig. 14.3. To test this possible explanation more thoroughly, we plot in Fig. 14.4 the initial (red violins) and final halo masses (blue violins) of the 100 most massive central galaxies for each given redshift on the x-axis. Presumably, this would capture the most dominant rapidly growing regions within the entire simulation volume, thus also the progenitors of Virgo-like galaxy clusters.

When we look at redshifts of $z \geq 6$, we instead find that just over 50% of those galaxies actually end up within a galaxy cluster by redshift $z = 0$ (lie above the dotted line denoting a halo mass of $M_{200c} \geq 1 \times 10^{14} M_\odot$). While this becomes better by $z = 3$, with 80% becoming clusters, the stellar mass cut has grown to around $M_* \geq 5^{11} M_\odot$, corresponding to host halos

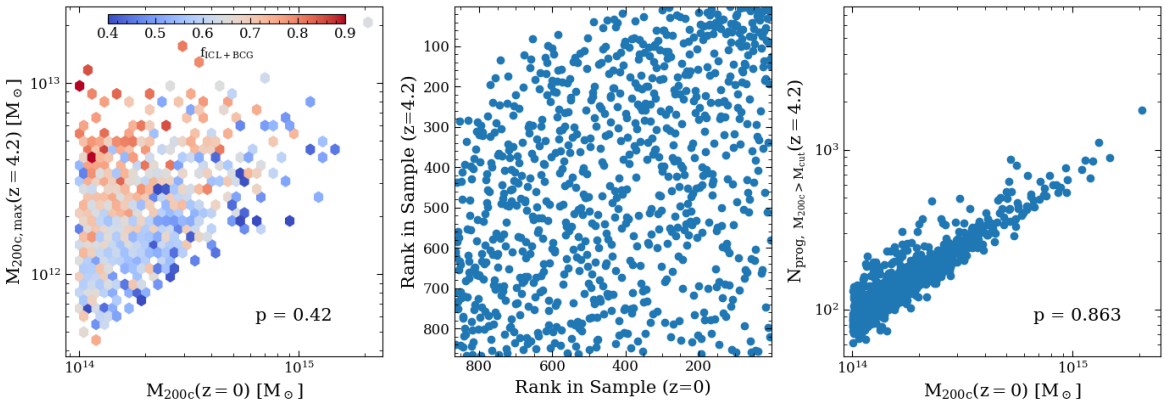


Figure 14.5. *Left:* The halo mass M_{200c} of $z = 0$ galaxy clusters plotted against the halo mass of their most massive progenitor at $z = 4.2$ and colored by $f_{ICL+BCG}$. *Center:* The rank order of their $z = 4.2$ and $z = 0$ masses, ranging from 1 (the most massive in our sample) to 863 (the least massive). *Right:* Number of progenitors at $z = 4.2$ with $M_{200c} \geq 5 \times 10^{10} M_\odot$ for each cluster plotted against its $z = 0$ halo mass.

that are already of group mass and above. And even still, 20% of these systems do not grow to be a cluster by $z = 0$. That leaves us with a new question: is it possible at all to identify protocluster regions, including also those with Coma-like assembly histories, not just Virgo-like.

14.4 The Power of Environment

To address this question, we turn toward the environment of our protocluster regions. We demonstrated with Fig. 14.1 that, while the region of Coma lacks a single outlier, it is significant in the number of massive galaxies. This is true also for Virgo, which has comparably less, but still shows an enhanced amount relative to a random region within the box. Therefore, we consider here the set of 863 galaxy clusters previously analyzed by Kimmig et al. (2025a). They found that these systems could be distinguished in their assembly by analyzing the $z = 0$ fraction of total stellar mass which has already been stripped or merged into the intracluster light (ICL) or brightest cluster galaxy (BCG), $f_{ICL+BCG}$.

When we plot the halo mass M_{200c} of the most massive halo among all progenitors for each galaxy cluster against their final $z = 0$ halo masses in the left panel of Fig. 14.5, we find only a weak correlation (Pearson correlation coefficient of $\rho = 0.42$). The most massive clusters ($M_{200c} > 1 \times 10^{15} M_\odot$) do end up having at least one massive progenitor ($M_{200c}(z = 4.2) > 1 \times 10^{12} M_\odot$) among their protocluster regions, but there are clusters which are much less massive at $z = 0$ with more massive progenitors. We color the points by their $f_{ICL+BCG}$ at $z = 0$, and find that for equal halo mass those with higher $f_{ICL+BCG}$ (redder color) did indeed assemble more rapidly, and thus had a more massive progenitor.

This result puts our findings in Sec. 14.3 into context, namely that Virgo-like protocluster regions can be directly identified as belonging to clusters with an elevated present day $f_{ICL+BCG}$. This distinguishing ability of a $z = 0$ observable is non-trivial, as we see in the

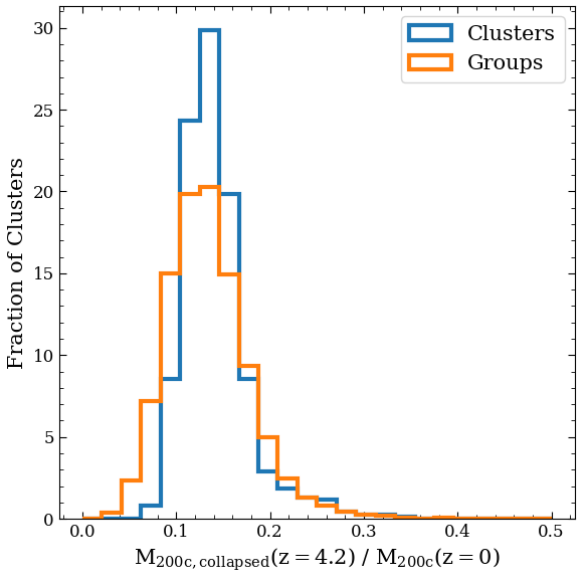


Figure 14.6. Distribution of fraction of the final $z = 0$ mass that has already collapsed into progenitor halos of $M_{200c} \geq 5 \times 10^{10} M_\odot$ by $z = 4.2$, both for $z = 0$ galaxy clusters (blue) and groups (orange).

second panel of Fig. 14.5. There we plot the mass rank for our clusters and their most massive progenitors, finding there to be little to no correlation. This means that the most massive cluster today did not necessarily have the most massive progenitor, and vice versa.

However, as we show in the right panel of Fig. 14.5, it is possible to far more tightly connect the protocluster region with the final mass of the galaxy cluster. This is done by counting for each cluster the number of progenitors at $z = 4.2$ with a halo mass $M_{200c} \geq 5 \times 10^{10} M_\odot$. Consequently, we can identify protocluster regions precisely by the fact that they are regions, which host a great number of assembling halos even if they do not always host one particularly massive one.

That this correlation is so tight (Pearson correlation coefficient $\rho = 0.86$) is somewhat surprising given that the total amount of mass that has already collapsed into halos by $z = 4.2$ is only about 15% of the final galaxy cluster mass, as we show in Fig. 14.6. However, we find this collapse fraction to be nearly identical for galaxy groups, meaning that the collapsed progenitors at $z = 4.2$ of the most massive structures (galaxy groups and clusters) tend to represent a consistent fraction of their final structure. It is because of this self-similar behavior of ΛCDM halos (Press & Schechter, 1974; Mo et al., 2010) that distinguishing the progenitor regions of a galaxy group of $M_{200c} = 1 \times 10^{13} M_\odot$, a regular galaxy cluster of $M_{200c} = 1 \times 10^{14} M_\odot$, and a massive cluster of $M_{200c} = 1 \times 10^{15} M_\odot$ is possible.

Based on these findings, we propose here an alternative definition to distinguish true protocluster regions from other regions of early collapse but later starvation. In Fig. 14.7, we plot the integrated stellar mass as a function of the aperture size R for galaxies which end up within a galaxy cluster by $z = 0$ (red) versus those which do not (blue). We plot the median (solid line) and 1σ-bounds (shaded regions). While there is an overlap, it is evident that galaxies in true protocluster regions are surrounded by more stellar mass on the scale

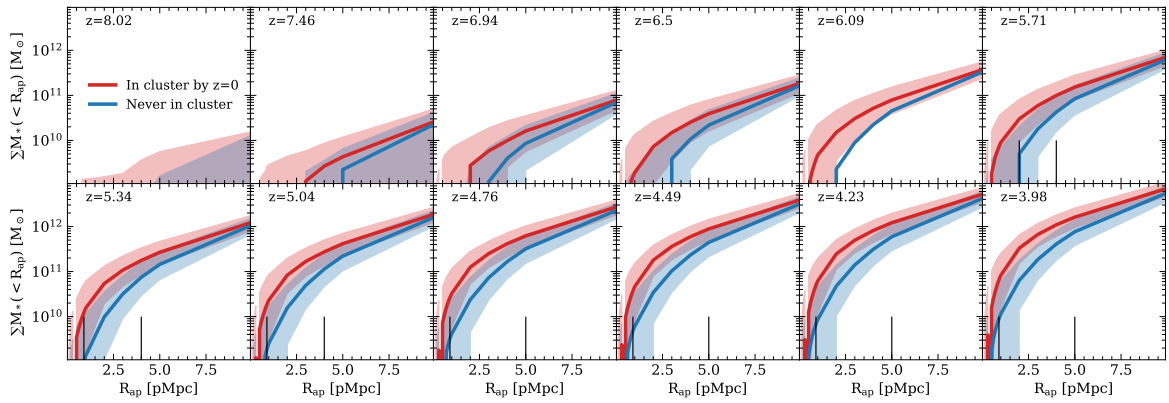


Figure 14.7. The integrated stellar mass as a function of the aperture size R for early galaxies ($M_* \geq 1 \times 10^9 M_\odot$) at redshifts $z = 8$ (*upper left*) to $z = 4$ (*lower right*). Colors distinguish galaxies which are within a true protocluster region (red, end up in a galaxy cluster by $z = 0$) from those that are not (blue). Black vertical lines denote the regions where neither 1σ-bound overlaps with the other median.

of $R = 2$ pMpc to 5 pMpc (being significantly different in regions between the vertical black lines). Upcoming space missions with a correspondingly large field of view will be able to map regions of this extent and thus finally allow us to distinguish what is and what is not a protocluster (Inoue et al., 2022; Harikane et al., 2022a).

14.5 Looking Back from $z = 0$

This section is part of the IAU proceedings for symposium 369 by Remus & Kimmig.

This study expands on the findings by Remus et al. (2023) and Kimmig et al. (2025a) on the formation and evolution of the most massive structures through cosmic time. Using a cosmological simulation of 500cMpc boxlength, we demonstrate that the progenitors of present day galaxy clusters are not always the most massive structures at every redshift, and at $z = 4.2$ are on average 0.2dex less massive than the most massive protoclusters, which we confirm to be less efficient at suppressing their star formation than $z = 0$ halos of the same mass.

14.5.1 Introduction

The formation and evolution of the most massive galaxies, the brightest cluster galaxies (BCGs), has been a longstanding subject of research, with the common census that they have formed early in so-called protocluster structures, while their recent formation was dominated by accretion and merging of other galaxies (e.g., Brown et al., 2024). In this picture, structures grow hierarchically, and intuitively this leads to the assumption that what has been massive in the past is also among the most massive structures at present day, i.e., that early massive galaxies become present day BCGs. As it is not possible to observe the evolution of structures, we employ cosmological simulations to study this connection in detail. However, there is

a caveat to this approach: to study the formation of the most massive galaxy clusters in a statistical manner, extremely large volumes need to be simulated to incorporate the massive nodes of the cosmic web (e.g., Remus et al., 2023), but with enough resolution to capture the high-redshift progenitors of such clusters in a phase of their life when they were barely Milky-Way mass galaxies. Only very few simulation suites sufficient to this task exist to date (e.g., Dolag et al., 2025) as they are extremely computationally expensive. One such simulation suite is the Magneticum Pathfinder simulations, which covers the largest range in box volumes and resolutions to date (Dolag et al., 2025). Using such simulations, Remus et al. (2023) and Onions et al. (2025) showed that, while the overall growth of structures is hierarchical, individual structures do not grow linearly, and that the most massive structures at high redshifts do not necessarily evolve into the most massive structures at present day. In fact, simulating the Universe to a redshift of $z = -0.99$, Seidel et al. (2024) showed that this cosmic disconnect continues into the future, with some of the most massive structures at present-day, such as the Virgo galaxy cluster, decoupling from the assembly of the cosmic web and starving much earlier than others.

We use the Magneticum Pathfinder suite of simulations, covering box volumes from $(2688\mathrm{Mpc/h})^3$ down to $(18\mathrm{Mpc/h})^3$, and a resolution range from $m_{\mathrm{dm}} = 1.8 \cdot 10^{10}$ to $m_{\mathrm{dm}} = 1.9 \cdot 10^{6}$, that are described in detail by Dolag et al. (2025) and Teklu et al. (2015). In this study, we employ two simulations, namely Box2 hr and Box3 uhr. The former has a simulation volume of $(352\mathrm{Mpc/h})^3$ with dark matter and stellar particle masses of $m_{\mathrm{dm}} = 6.9 \cdot 10^{8}\mathrm{M}_{\odot}/\mathrm{h}$, and $m_* \approx 1/4^{\mathrm{th}} m_{\mathrm{gas}} \approx 3.5 \cdot 10^{7}\mathrm{M}_{\odot}/\mathrm{h}$, respectively, while the latter has a volume of $(128\mathrm{Mpc/h})^3$ and $m_{\mathrm{dm}} = 3.6 \cdot 10^{7}\mathrm{M}_{\odot}/\mathrm{h}$ and $m_* \approx 1.8 \cdot 10^{6}\mathrm{M}_{\odot}/\mathrm{h}$. Both use WMAP-7 parameters, with $h = 0.704$, $\Omega_m = 0.272$, $\Omega_b = 0.0451$, $\Omega_\lambda = 0.728$, and $\sigma_8 = 0.809$.

14.5.2 The Most Massive Structures

We begin by considering how the most massive structures grow through cosmic time, using here the larger Box2 hr. First, we select the 868 most massive clusters at $z = 0$, comparable to the set used by Kimmig et al. (2025a), and trace their primary progenitors up to $z = 4.5$, plotting the distribution of their halo masses M_{200c} throughout cosmic time as blue half-violins in the left panel of Fig. 14.8. We also plot the 868 most massive structures at every redshift, i.e., not dependent on their final $z = 0$ mass, as orange half-violins. We find that, as we go farther back in time, the galaxy cluster progenitors represent an increasingly small fraction of the most massive structures. The range of progenitor masses starkly increases up to three orders of magnitude, with the extreme cases of progenitors spanning from galaxies smaller than the Milky Way up to small groups already formed by $z = 4.5$. The mean progenitor of a $z = 0$ galaxy cluster is over 0.2dex (60%) less massive than the most massive structures at early times. This demonstrates that the most massive structures at $z = 4.5$ do not necessarily become clusters, nor do clusters necessarily have the most massive progenitors, supporting the findings by Remus et al. (2023); Kimmig et al. (2023) and Onions et al. (2025).

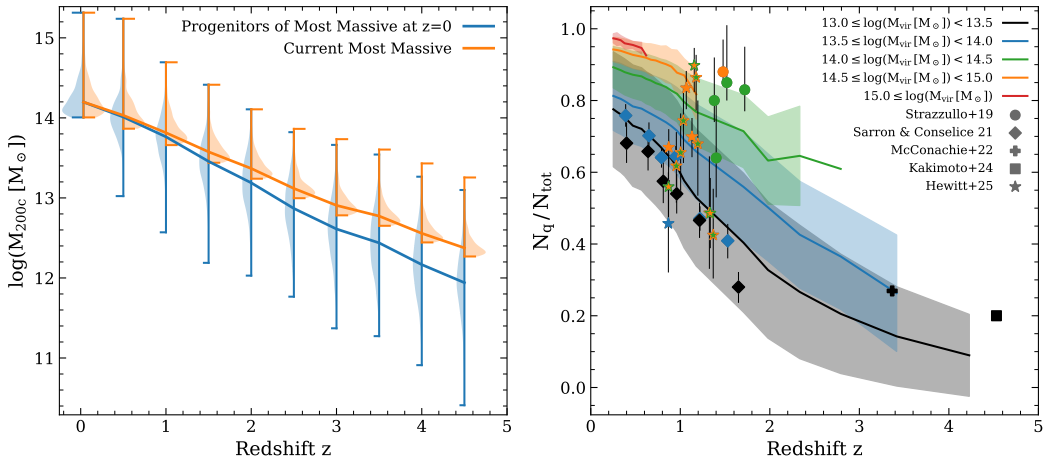


Figure 14.8. *Left panel:* Virial mass against redshift for structures from the Magneticum Pathfinder simulation Box2. We plot in orange the 868 most massive structures at each redshift bin are shown, while in blue the halo mass distribution of the progenitors of the 868 most massive galaxy clusters at $z = 0$ are depicted. We find that the progenitors of the $z = 0$ galaxy clusters are not the most massive structures at higher redshifts. This disconnect between the current and previous most massive structures was already discussed by Remus et al. (2023) and is shown here in a more concise manner. *Right panel:* The fraction of quiescent galaxies with stellar masses above $M_* > 1 \times 10^{10} M_\odot$ against redshift from the Magneticum Pathfinder simulation, with halos of different virial masses colored as given in the legend. The symbols mark different observations, with the colors marking the halo mass of the observed groups and clusters. This is an updated version of a figure presented by Remus et al. (2023), where in addition to observations by Sarron & Conselice (2021), Strazzullo et al. (2019), and McConachie et al. (2022) now also the observation of the protocluster by Kakimoto et al. (2024) is shown as well as data points for the GoGreen survey galaxy clusters adapted from Hewitt et al. (2025). For those clusters, symbols with a different colored border than the filled part mark cases where the given halo mass within the error bars spans two of our chosen halo mass bins.

We also consider the implications for the galaxies forming in these environments, by determining the fraction of quiescent galaxies within halos of group mass and above. This fraction is plotted for five halo mass bins in the right panel of Fig. 14.8 against redshift, in an updated version of a figure presented by Remus et al. (2023) including now also a large number of galaxy clusters at $z > 1$ from the GoGreen survey adapted from Hewitt et al. (2025), and in particular also a protocluster at $z > 4$ observed by Kakimoto et al. (2024). These additions further strengthen the point already made by Remus et al. (2023), that higher mass halos/higher density environments host a greater fraction of quiescent galaxies across all redshifts, but crucially also that halos of a given mass increase their quiescent fraction with time. The earliest protoclusters, which represent the highest density environments of their time, thus still host low quenched fractions, both when compared to current day galaxy clusters (which are higher mass) as well as when comparing to present day galaxy groups. However, the large scatter in the observational comparison samples clearly highlights the need for a more detailed comparison study in the future, accounting for stellar mass and radial cuts, and in particular the dynamical state of the clusters, which has been shown by

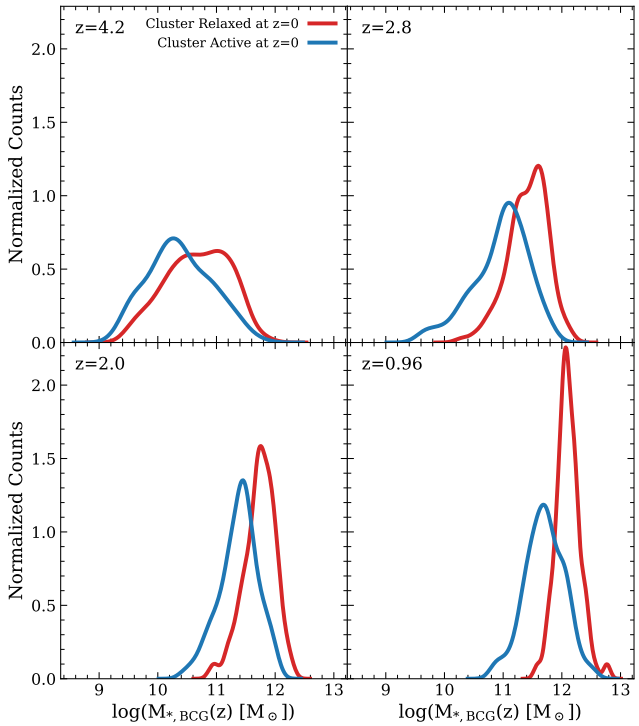


Figure 14.9. Distribution of the stellar masses of the BCGs of galaxy clusters selected at $z = 0$ from the Magneticum Pathfinder simulations Box2 split into relaxed (red) and actively merging (blue) clusters following Kimmig et al. (2025a). The four panels show the stellar masses these BCGs had at four different redshifts, from $z \approx 4$ (upper left) to $z \approx 1$ (lower right).

Kimmig et al. (2025a) to strongly impact the galaxy populations and which we next consider in more detail.

14.5.3 Consequences for Stellar Mass

Building on this cosmic structure disconnect through time, we finally test if the dynamical state of galaxy clusters at $z = 0$ imprints in differing stellar masses through their evolution. We use 868 galaxy clusters from Box2 hr and chose the 140 most and least relaxed clusters, as quantified by Kimmig et al. (2025a). We find that at $z = 1$ their brightest cluster galaxies already show strong differences (right set of panels in Fig. 14.9), with relaxed clusters at $z = 0$ (red) hosting more massive BCGs in their progenitors at $z \approx 1$. Interestingly, however, this difference was already present in their progenitors as early as $z = 4.2$, albeit less strongly. This shows that the most relaxed clusters formed their BCGs earlier than less relaxed clusters, but also that present-day relaxed clusters are more likely to already have a massive protocluster phase at cosmic dawn than present-day active clusters.

14.5.4 Summary and Conclusions

We find a clear disconnect between the most massive structures at cosmic dawn, cosmic noon, and present-day, with the most massive structures at high redshift not necessarily evolving into the most massive structures at low redshift and vice versa. The imprint of this

disconnect can be found in several aspects: the massive quenched galaxies seen at cosmic dawn now with JWST are not necessarily the progenitors of present-day BCGs. They can end as relic galaxies, become accreted onto a more massive galaxy, or even rejuvenate (Remus & Kimmig, 2025). Looking backward from $z = 0$, the relaxation status of a galaxy cluster can shed light onto the formation time (Kimmig et al., 2025a), with more relaxed cluster BCGs already having assembled a significant amount of mass at cosmic noon as compared to active cluster BCGs. While we find the fraction of quenched galaxies to increase through cosmic time for a given halo mass, we also expect an impact of these diverse formation pathways on the quenched fraction of galaxy clusters, possibly responsible for the large scatter seen in observations and simulations, however, this remains to be tested in more detail in the future.

14.6 The Impact of Dynamical State on the Star Forming Galaxy Population in Galaxy Clusters

This Section summarizes findings from the publication by Çakır et al. (incl. Kimmig), 2025, PASA 42, 163, for which I am the third author and provided the Magneticum simulation data.

Having seen the difficulties (in Sec. 14.3 and Sec. 14.5) and possible solutions (in Sec. 14.4) for how to connect the growth of the most massive structures through cosmic time, we highlight here a result from the work by Çakır et al. (2025) as an example why the assembly of these structures is significant. We there employed the Magneticum Pathfinder Box2/hr simulation to analyze the galaxy populations of the 55 earliest and 55 latest assembling galaxy clusters, as determined from the formation redshift z_{50} when the most massive progenitor first assembled 50% of the final galaxy cluster mass.

Plotting the projected phase space distributions of the star forming galaxies (SFG) in relaxed and merging galaxy clusters in the upper left and right panels of Fig. 14.10, we found significant differences. Merging systems host SFGs far into the centers of their phase space at low radii and projected velocities, which are thus expected to have fallen in early (Rhee et al., 2017). Given how rapidly SFGs quench in clusters when passing through the center regions (Lotz et al., 2019), it is more likely that these were instead in the outskirts of one of the merging clusters but now appear to be near the new BCG. What cannot be driven by a simple overlaying of the two phasespace distributions of the merging systems is the fraction of SFGs, however.

If both merging clusters started out with the same low fraction of SFGs as the relaxed clusters exhibit (lower left panel in Fig. 14.10), overlaying them on each other would not change anything. However, Çakır et al. (2025) find a noticeable increase in SFGs both within the cluster ($R < R_{200c}$) as well as in the outskirts. This means that either merging clusters already exhibited higher fractions of SFGs prior to merging, or the merger itself enhanced the SFRs of some galaxies enough for them to cross over the threshold (Bekki et al., 2010).

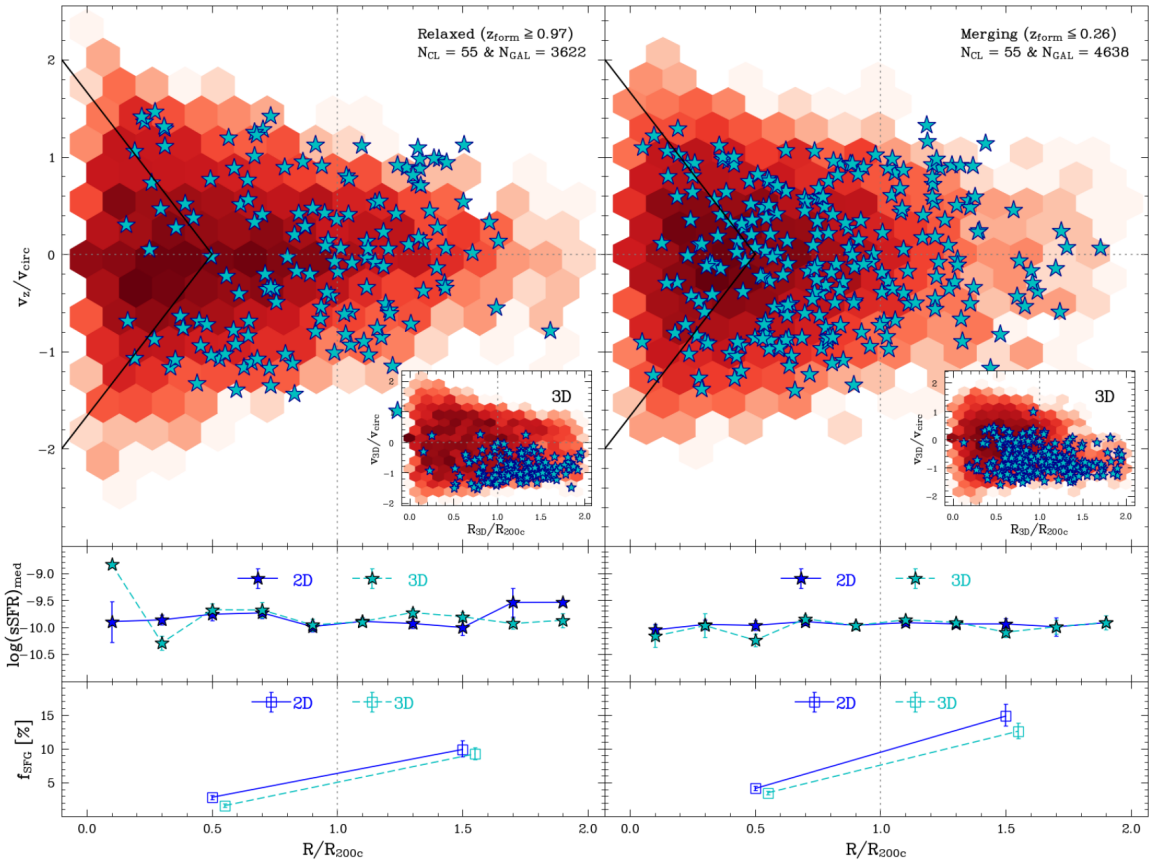


Figure 14.10. This figure was published as Fig. 10 by Çakır et al. (2025). It shows the projected (and 3D, see the inlet) phase space distribution of galaxies within relaxed (*upper left*) and merging (*upper right*) galaxy clusters from the Magneticum Pathfinder Box2/hr simulation, with star forming galaxies plotted as blue stars. The *center* panels show the median specific star formation rates of all galaxies as a function of projected (blue) and 3D radius (cyan), while the *lower* panels show the fraction of star forming galaxies.

In both cases, it is apparent that the dynamical state of the galaxy cluster plays a role in the galaxy populations star formation rates.

14.7 Conclusion

We have presented here an overview of various works on how to connect the growth of the most massive structures through cosmic time. Expanding on prior work by Borzyszkowski et al. (2017); Remus et al. (2023) and Kimmig et al. (2023), we have traced simulated halos both forward and backward in time, leveraging the large Magneticum Box2/hr simulation of 500 cMpc sidelength. We find that the differing types of assembly histories of galaxy clusters manifest within their initial density field, with Coma-like clusters collapsing first into many substructures across a plane while Virgo-like clusters collapse more rapidly into a single halo.

We show that looking for single individual massive galaxies does not capture this underlying density field of the cluster infall region, as of the top 100 most massive such systems in our simulation at redshifts $z \geq 6$, only 50% end in clusters by $z = 0$ (rising to 80% for

the 100 most massive galaxies at $z \geq 3$). Instead, we demonstrate that measuring a massive galaxies environment is a far greater predictor for its future growth, with significant (1σ) deviations of the integrated stellar mass surrounding galaxies that end up in a cluster versus those that do not, with the largest differences on scales of 2 pMpc to 5 pMpc. This matches results by Remus et al. (2023), who similarly found that using the BCG mass in protocluster candidates is less efficient than using the number of satellites. A large field of view, such as that planned for GREX-PLUS (Inoue et al., 2022; Harikane et al., 2022a), is thus crucial to distinguish protocluster environments at high redshifts $z \geq 3$.

Finally, we highlight the results by Çakır et al. (2025), who find an impact on the galaxy populations between relaxed and dynamically active galaxy clusters. This shows that identifying the dynamical state of galaxy clusters is crucial for upcoming large survey such as *Euclid* (Laureijs et al., 2011; Kluge et al., 2024), Roman (Montes et al., 2023) and Rubin/LSST (Ivezić et al., 2019; Brough et al., 2020). It is through tracers such as the fraction of total stellar mass that is within the ICL and BCG, $f_{\mathrm{ICL+BCG}}$, that the formation histories of galaxy clusters can be determined (Kimmig et al., 2025a). We show that this tracer at $z = 0$ is powerful enough to distinguish the most massive progenitors up to $z = 4$, despite the range in progenitor masses reaching over an order in magnitude.

Koia rā! Kua whetūrangitia koutou kei aku rau kahu rangi!

Maori Saying

15 Summary and Conclusion

How structure in our Universe forms and evolves has been one of humanity's most fundamental questions, and over the last century, our tools in this endeavor have advanced rapidly. Throughout this work we made use of one of the most advanced tools, namely fully hydrodynamic cosmological simulations, and primarily those from the *Magneticum Pathfinder* suite (Dolag et al., 2025). We also employed the *LOWER DECKS* suite (Seidel et al., in prep.) based on the *SLOW* simulation (Dolag et al., 2023), in addition to the EAGLE (Schaye et al., 2015), Horizon-AGN (Dubois et al., 2014), Hydrangea (Bahé et al., 2017), IllustrisTNG (Pillepich et al., 2018b), and the new MagneticumDAWN simulations (Kimmig et al., in prep.). This work was further complemented by semi-empirical models and theory.

These tools were used in concert to address three primary questions.

- How do the first galaxies form?
- How can we connect galaxies at present day with their progenitors at earlier times?
- How do the densest environments, clusters of galaxies, evolve through cosmic time?

Here we summarize the results for each question individually in Sec. 15.1, Sec. 15.2, and Sec. 15.3, before concluding with final thoughts on the field of structure formation, cosmological simulations, and the future in Sec. 15.4.

15.1 How do the First Galaxies form?

We began by demonstrating that the *Magneticum Pathfinder* Box3/uhr simulation, unlike many others, is capable of reproducing the observed number densities of massive quenched galaxies at cosmic dawn. These quenched galaxies undergo a process we term "rapid starburst quenching", where the galaxies form though a particularly isotropic infall (Kimmig et al.,

2025b). This infall produces high central gas densities that feed both a rapid star formation (on the timescale of just 100 million years, comparable to observations for example by Carnall et al., 2023b; Kakimoto et al., 2024; de Graaff et al., 2024a) and the central supermassive black hole. The combination of gas depletion by star formation and gas ejection from the combined stellar and AGN feedback, as well as the fact that these galaxies lie in local underdensities relative to star forming galaxies of the same stellar mass, results in the rapid quenching of star formation within these galaxies.

Indeed, we show that the long-term future of the star formation within any galaxy is determined far more by its environment (i.e., by how much more fuel it can draw on) than by its internal properties (stellar or black hole mass). Nonetheless, the emergence of the first quenched galaxies is still strongly dependent on being able to feed the central black holes quickly enough, which we find to be a key advantage of the dual accretion model by Steinborn et al. (2015). Modern simulation will need to account separately for the different accretion rates from the cold and hot gas surrounding the first galaxies if they wish to reproduce the observed early quenched galaxies.

Because of the short timeline for the formation of their stars, we find early massive quenched galaxies to have enhanced abundance in the α-element oxygen relative to iron, $[\mathrm{O/Fe}] \approx 0.14$, indicative of enrichment primarily through faster acting supernovae Type II (Kobayashi, 2025). Their gas is also significantly enriched in metals through the rapid star formation before being expelled, thereby enriching their surroundings with metal-rich gas. Furthermore, the quenching process does not alter their stellar kinematic properties, with both fast and slow rotating quenched galaxies already emerging within the first billion years. This prediction has since been confirmed by spectroscopic observations (Forrest et al., 2025, incl. Kimmig).

We further showed that early massive quenched galaxies can actually undergo rejuvenation cycles of their star formation owing to the abundance of cold gas in their surroundings (Remus & Kimmig, 2025). A third of the fully quenched galaxies at $z = 3.42$ stay fully quenched, a third has some small-scale rejuvenation, while the last third can reach star formation rates comparable to those of the star forming main sequence of galaxies by $z = 2$. It is therefore more apt to consider the abundantly observed quenched galaxies at cosmic dawn as "quiescent" (i.e., temporarily quenched), rather than quenched. Indeed, newer observations have found approximately the same number density of recently quenched galaxies at $z = 4$ and $z = 2$ (Nanayakkara et al., 2025; Merlin et al., 2025, incl. Kimmig). If these $z = 4$ recently quenched galaxies did not rejuvenate, the number of longer term "red-and-dead" galaxies would increase over the same time period, which is not found to be the case (Merlin et al., 2025, incl. Kimmig).

Finally, we explored the emergence of massive disk galaxies, which are now also being observed at $z \geq 3$ (e.g., Jain & Wadadekar, 2025; Rowland et al., 2024; Umehata et al., 2025b; Shapley et al., 2025; Wang et al., 2025; Xiao et al., 2025), and found them to occur both in over- and underdense regions. Indeed, there appears to be a surprisingly weak environmental dependence of the galaxy morphology, with the morphology-density relation



(Dressler, 1980) not yet in place at $z > 3$. We conclude therefore that the formation of the first galaxies is characterized both by the ubiquitous high gas fractions in galaxies and the lack of filaments, which leads to more isotropic modes of collapse. These two key differences to lower redshift galaxy formation and evolution are fundamentally the reason why current models and simulations have been struggling to capture the diversity of properties now observed with the JWST.

15.2 How Can We Connect Galaxies at Present Day with Their Progenitors at Earlier Times?

Turning to the question of how to connect galaxies at present day with their early Universe progenitors, we considered first the curious "failed-galaxy" type of ultra diffuse galaxies (UDGs, van Dokkum et al., 2015) observed at present day (Forbes & Gannon, 2024). These galaxies have only around one hundredth of the stellar mass of the Milky Way galaxy, but boast comparable stellar sizes and dark matter masses. In the work by Gannon, Kimmig, et al. (2025), we noted that plausible progenitors of these galaxies at higher redshifts ($z \approx 2$) are characterized by a particularly high angular momentum in both their gas and dark matter, which leads to flatter, more cored density profiles as well as a later assembly compared to galaxies of similar halo mass. This may also lead to more clumpy star formation farther out, increasing the stellar sizes and reducing stellar metallicities, in accordance with observations (Buzzo et al., 2022; Ferré-Mateu et al., 2023).

Moving on to the star formation histories of galaxies, we constructed a model (Kimmig, to be subm., a) to determine the evolution of galaxies that remain on the observed star forming main sequence (Popesso et al., 2023). We show that this assumption is sufficient to reproduce the mean of the present-day stellar mass–age relation (Mattolini et al., 2025), and naturally results in the downsizing effect, where more massive galaxies have more bursty and peaked star formation histories (Thomas et al., 2010). Comparing the results of the model to the observed star formation history of the Milky Way (Haywood et al., 2016), as well as the expected stellar growth over time when assuming equal number density arguments (van Dokkum et al., 2013; Papovich et al., 2015), we find that the Milky Way must have undergone a phase of rapid star formation at early times that was well above the star formation main sequence of that time (making the progenitor a starburst galaxy), while between $z = 1$ and $z = 0.5$ the star formation rate was low enough to potentially be considered quiescent. Even though it has kept a constant star formation rate, it today lies on or near the star forming main sequence only because the overall star formation rates have decreased (Popesso et al., 2023).

We further explore the question of whether the number density arguments by van Dokkum et al. (2013) and Papovich et al. (2015) are even applicable, finding them to predict different stellar growth than found in the two state-of-the-art cosmological hydrodynamical simulations of*Magneticum Pathfinder* and EAGLE (Gao et al., 2026, incl. Kimmig). Indeed, we show that the star formation histories of actual galaxies generally do not follow a simple growth

along the star forming main sequence, after which they either quench or do not, and instead undergo cycles in their star formation (Fortuné et al., 2025, incl. Kimmig), much like what we found happened to the early quenched galaxies (Remus & Kimmig, 2025). Current observations of galaxies at intermediate redshifts are now also finding indications of star formation rejuvenation, i.e., cycles of on and off star formation (Muñoz López et al., 2025).

Given this complexity in formation histories, we drew on the lessons learned from observations of stars in the Milky Way galaxy to consider whether chemical abundances in the stellar populations of galaxies can be used to predict their assembly time, among other properties. We find that the ratio of α-elements (in particular oxygen) to iron can tightly predict the assembly time of galaxies, so long as the stellar mass from ex-situ sources (i.e., merging) is not significant. We further find that the rapid rise in the fraction of metals locked in stars formed from gas enriched by Type Ia supernovae, where early galaxies are enriched almost entirely by supernovae Type II, plateaus around $z = 1$.

Both of those results stem from the different conditions of the star forming regions in high redshift versus low redshift galaxies. The higher central densities at earlier times allow both a more rapid formation of stars, but also enables these galaxies to retain the same gas and cycle it multiple times. It is therefore possible for the first galaxies to grow in a massive starburst to near solar metallicites, without having much contribution in metals from supernovae Type Ia or AGB stars. This leads to the strong differences in chemical abundances of early and late forming galaxies, which is how their star formation histories may be distinguished.

Finally, using new yield tables for supernovae Type II (Nomoto et al., 2013), we identify a simulated counterpart to the Milky Way in terms of its chemical abundances (e.g., Gaia Collaboration et al., 2023; Imig et al., 2023). The stars of this simulated galaxy show a clear bimodal distribution in the [O/Fe] versus [Fe/H] plane, which we find to be the result of a two-phase formation (Chiappini et al., 1997; Grisoni et al., 2017), rather than radial migration (Sellwood & Binney, 2002; Schönrich & Binney, 2009). Importantly, we find that our counterpart has been quenched since $z \approx 1.5$, which means that as long as the star formation occurs over timescales long enough to incorporate significant enrichment from the supernovae Type Ia, bimodal distribution can arise. Overall, the tool of stellar chemical abundances shows great promise in disentangling the histories of individual galaxies, even beyond our Milky Way, a goal that is becoming increasingly important as we recognize that prior, simpler assumptions of the shapes of star formation histories do not hold in general.

15.3 How do the Densest Environments, Clusters of Galaxies, Evolve through Cosmic Time?

Finally, we considered the evolution not only of individual galaxies, but also the environments within which they reside. Indeed, the role of the environment must change through cosmic time, as we already noted that for example the morphology-density relation in not yet in place at $z > 3$. To this end, we sought to identify and differentiate true protocluster regions (i.e.,



those that actually become galaxy clusters by $z = 0$) from those that only momentarily are the most massive structures before starving at later times.

We first discussed a simulated counterpart to the observed Abell 2744 galaxy cluster, and showed that it is a particularly good example for a cluster that has strongly risen in the ranks of the most massive systems over a very short period of time (Kimmig et al., 2023). Going a step further and drawing on over 1000 simulated systems from four cosmological simulations, we demonstrated that the assembly histories of individual galaxy clusters consistently exhibit a large diversity (Kimmig et al., 2025a). Making simple linear connections of the most massive systems at the earliest and latest times is thus prone to significant errors (Remus et al., 2023). We find this to be the case irrespective of whether the baryonic or total mass content is used to compare structures.

To remedy this, we used the fact that the diffuse stellar body (intracluster light, ICL) is built up through the very mergers that are responsible for shaking up the rank order of structures, and that consequently the fraction of all stellar light which is within the ICL and the central brightest cluster galaxy ($f_{\mathrm{ICL+BCG}}$) should correlate with the assembly time of the galaxy cluster itself. Drawing on the power of four differently tuned cosmological simulations, we demonstrate that the correlation between $f_{\mathrm{ICL+BCG}}$ and the cluster assembly time emerges remarkably similarly for all simulations (Kimmig et al., 2025a). We determine this to be the case because the amount of time that a cluster is left undisturbed is directly proportional to the growth in stripped/merged stellar mass in the ICL and BCG.

We further compare the predictive power of the tracer $f_{\mathrm{ICL+BCG}}$ to other common tracers, both those derived from the dark matter distribution and especially the X-ray halo of the hot intracluster medium, which has been commonly used in the past (Biffi et al., 2016). We find that, while other tracers also work to predict the cluster assembly, $f_{\mathrm{ICL+BCG}}$ is the overall strongest predictor (Kimmig, to be subm., b). Thus, future surveys may therefore use the low-surface brightness regime to better constrain the assembly of mass in our Universe, and we provide fitting functions to this effect (Kimmig et al., 2025a).

As for being able to distinguish the protocluster regions, we show that the only reliable tracer is the integrated mass within regions of considerable extent ($\approx 10\,\mathrm{cMpc}$). This is because local overdensities can give rise to single large structures, which may host massive galaxies or a hot, dense gas halo, but which cannot yet be guaranteed to grow into galaxy clusters by $z = 0$. A guaranteed identification of a protocluster region at $z > 3$ can only be found when going out far enough to cover a significant fraction ($\approx 20\%$) of the eventual $z = 0$ mass of the galaxy cluster itself.

15.4 Final Thoughts and the Future

The last decade has brought forth incredible advances in the field of astronomy, from expanding our range of observations to include the very first galaxies, all the way to the refinement of stellar and AGN feedback in modern cosmological simulations, which now manage to repro-

duce a diverse range of galaxies. These advances have often been driven by the unexpected, the outliers, the scatter in the relation where we understand the mean but not the unique.

I hope that this work has provided an overview of the diverse questions that new discoveries and observations have prompted over the last few years, as well as some answers on the formation of the first galaxies, star formation cycles, our Milky Way and the assembly of galaxy clusters. Exciting advances are being made every day, with plenty of fundamental processes in the formation of galaxies yet to be understood. Any one of these may very well prove to have far-reaching implications, such as the possibility of a time-dependent initial mass function (perhaps driven by a change in the typical density, metallicity, and virial parameter of star forming gas through cosmic time) or the formation of globular clusters, which are yet to emerge self-consistently within any large-volume cosmological simulations, but which must (based on their ages and present day numbers) represent a sizable fraction of the early star formation in our Universe. As such, I look forward to the new approaches, the novel ideas and unexpected observations that are yet to come.

A

Radial Profiles for High-Redshift Quenched Galaxies

This is the Appendix to the publication by Kimmig et al., 2025, ApJ 979, 15, presented in Chap. 3.

To understand the process of quenching in more detail, we consider the traced central galaxies at $z = 5.34$ to $z = 2.79$ (prior and post quenching). We reduce the sample to the 1027 non-quenched and 25 quenched galaxies which are centrals through the whole process (to avoid including interactions with a host halo). To understand if there is a difference in the distribution of mass prior to or during the quenching process, we determine for each galaxy at a given redshift the density profiles for the stars, dark matter, and cold ($T \leq 10^4 K$) and hot ($T > 10^4 K$) gas.

To remove variations in absolute density or radius, we normalize every profile to the galaxy's local density (baryonic and dark matter) at the virial radius as $\rho_i' \equiv \rho_i / \rho_{\rm tot}(r_{\rm vir})$. For all quenched galaxies, we then determine the mean density at a given radial bin r as the median of all profiles' normalized density $\overline{\rho}_i'(r) = \text{median}(\rho_i'(r))$. We then do the same for the non-quenched galaxies. This allows us to quantify the *shape* of the profiles of different components of the quenched versus non-quenched galaxies.

Fig. A.1 shows the evolution of these normalized profiles at all four snapshot redshifts from $z = 5.34$ to $z = 2.79$. The stellar profiles (top row) are largely identical between quenched and non-quenched centrals. A notable exception is that immediately prior and post quenching the quenched centrals show a noticeably enhanced central stellar density (see inlets in the two middle panels), with only the least dense of them reaching values comparable

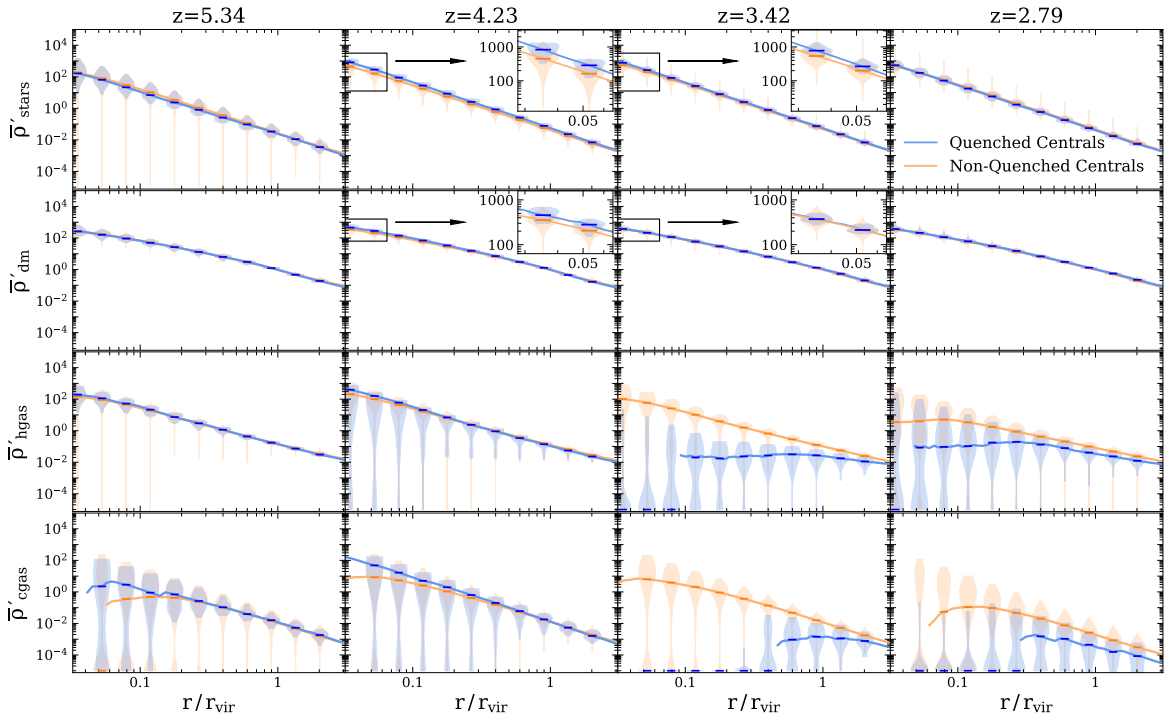


Figure A.1. Stacked and normalized density profiles, going from *top* to *bottom* as stars, dark matter, hot gas and cold gas. Lines are the medians for non-quenched (sand) and quenched (blue) central galaxies, while violins show the full distribution of the respective galaxy samples. The width of the bulge corresponds to the fraction of galaxies with that value. Columns go from $z = 5.34$ to $z = 2.79$. The inlets zoom in on the central densities for stars and dark matter immediately prior to ($z = 4.23$) and post quenching ($z = 3.42$).

to the non-quenched median. This means that their stellar profiles are more peaked toward the center, which may be a result of the isotropic collapse (see Fig. 3.10) more efficiently funneling gas to the center as opposed to distributing it into more of a gas disk. By $z = 2.79$ there is no more difference between the quenched and non-quenched centrals, most likely because the central stellar core has expanded and flattened the central density.

Interestingly, the dark matter of the quenched centrals (second row in Fig. A.1) shows a similar behavior of enhanced central density prior to quenching at $z = 4.32$, which we attribute again to the more isotropic collapse onto the center. However, unlike for the stars this signal is gone already by $z = 3.42$. This may be caused by the rapid stellar burst which happens right up until quenching (and thus also after $z = 4.32$), as the gas from which the stars form can effectively remove angular momentum and cool further to the center. For the dark matter, any non-isotropic accretion will flatten out the central density as it lacks the ability to remove angular momentum. Alternatively, this could be an indication for feedback-induced halo expansion as discussed for example by Dutton et al. (2016), Peirani et al. (2017), and Harris et al. (2020). At any rate it is quite striking to see a difference in the shape of the dark matter profiles of the quenched centrals prior to quenching, providing a clear hint at the differing modes of accretion.

For the hot (third) and cold gas (fourth row) the behavior is relatively comparable between non-quenched and quenched up to $z = 4.32$. While the quenched galaxies gas is peaked

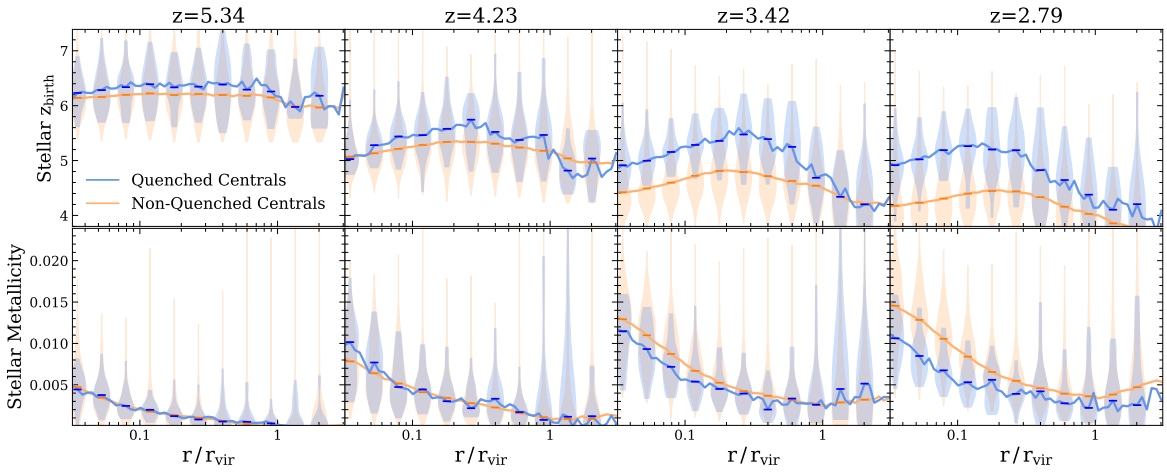


Figure A.2. Stacked quenched (blue) versus non-quenched (sand) radial profiles of median stellar $z_{\rm birth}$ (*top*) and metallicity (*bottom*) for different redshifts (columns).

slightly more to the center, the distribution shown by the violins indicates that this signal is not significant. Given the enhanced central stellar density, this may indicate that large amounts of the inflowing gas are rapidly converted, thus not leading to enhanced *gas* but instead *stellar* densities.

At the time when the galaxies are identified as quenched ($z = 3.42$), the gas has been nearly entirely ejected, matching the behavior seen in Fig. 3.6 and Fig. 3.7. While there are some quenched galaxies with remaining hot gas in the center of the halo approximately corresponding to the size of the galaxy $< 0.1\,r_{vir}$ or around 7 kpc, the median quenched galaxy has none. For the cold gas, however, every single quenched galaxy has fully removed it out to beyond $0.3\,r_{vir}$, and even up to the virial radius the density is well reduced compared to the non-quenched sample. By $z = 2.79$ gas is already flowing back into the quenched galaxies, indicative of the different conditions relative to low redshift. Most of this gas is, however, hot, potentially because it was shocked by colliding with the outflowing gas from the rapid starburst quenching prior.

Given the difference in the rapidity of the starburst which was imprinted in the metal species (see Fig. 3.8), we further consider in Fig. A.2 if there is a difference in the stellar ages (top row, given by the formation redshift) or stellar metallicites (summed mass of all metals divided by the hydrogen mass) of the quenched galaxies. We find that prior to quenching the stars of the non-quenched galaxies are generally younger farther out than their quenched counterparts, while at the center ($< 0.03\,r_{vir}$ or around 1.5 kpc) the median ages are identical. Although the differences are not very large, they may indicate a slight difference in the amount of active star formation farther away from the center.

As the quenched galaxies cease their star formation, the central ages increase significantly compared to the non-quenched galaxies. This effect does not hold true farther out within the halo, indicating that while they have gone quiescent they are still accreting surrounding stars which are young and potentially being formed in satellite galaxies. We thus do not

find high-redshift galaxies, which have older cores, to also house an older stellar envelope compared to their star forming counterparts.

For the total metallicity (bottom row) the quenched centrals again are nearly identical to the non-quenched sample prior to quenching. They show a minor increase in central metallicity, but it is not significant. Post-quenching we find that, although the quenching process has significantly enhanced their alpha element abundance (see Fig. 3.8) the total metallicity is comparable or slightly lower than that of the non-quenched samples. This difference becomes significant by $z = 2.79$, although again the halo stars at $r \approx 1\, r_{vir}$ show no differences.

B

Model Parameter Study for the Mass Evolution on the Main Sequence

This is the Appendix to the publication to be submitted by Kimmig et al., presented in Chap. 8.

B.1 Impact of the model parameters

As throughout this work we considered one setup of a main sequence evolution model with a timestep size of the iteration process of $\delta t = 100\,\mathrm{Myr}$, it is worth discussing how alternative choices would alter our results. We consider the impact of the timestep size by modelling main sequence-evolved galaxies with progenitors of $\mathrm{M}_* = 1 \times 10^8 \mathrm{M}_\odot$ seeded between $z = 0.5$ to $z = 6$ in 150 equal bins in cosmic time, equivalent to steps of 50 Myr. As a metric, we determine the deviation in final stellar mass relative to a model run with $\delta t = 5\,\mathrm{Myr}$. For timestep sizes of $\delta t = 10, 100, 200$, and 1000 Myr, the median absolute deviation is $0.0015, 0.027, 0.053$ and $0.207\,\mathrm{dex}$ ($0.35\%, 6.4\%, 13\%$ and 61%), while the maximum difference in stellar mass for any progenitor is $0.003, 0.053, 0.102$ and $0.39\,\mathrm{dex}$ ($0.7\%, 13\%, 27\%$ and 140%). The ratio in final stellar mass is dependent on when the progenitor is seeded, with shorter timebins resulting in increasingly larger final masses for increasingly earlier seeding. We attribute this to the fact that the SFR increases with the stellar mass, so updating the mass to higher values more frequently results in a net increase overall. This difference would likely be more stark if the SFMS itself was not rapidly sinking,

such that more frequent updates can, in particular at later times, effectively decrease the SFR and thus final stellar mass.

Further of note is the case where the SFR may vary around the value dictated by the SFMS and the model galaxy stellar mass. We find that adding a lognormal scatter in SFR, $\log \mathrm{SFR}(\mathrm{M}_*, t) = \log \mathrm{SFR}_{\mathrm{SFMS}}(\mathrm{M}_*, t) + \Delta_{\mathrm{SFMS}}$ with Δ_{SFMS} drawn from a normal distribution of variance $\sigma(\Delta_{\mathrm{SFMS}}) > 0$, necessarily results in larger stellar masses. This can be understood when considering that scattering 0.2dex above the SFMS SFR results in more net produced stellar mass than subsequently lying 0.2dex below the SFMS value looses (60% more vs 40% less). By that same consideration, the net stellar mass gain relative to purely main sequence-evolved galaxies increases with increasing scatter.

It is for the above reason that we have preferred here to work with fixed logarithmic separations from the SFMS, $\Delta_{\mathrm{SFMS}} = const$. We have confirmed that applying a fixed Δ_{SFMS} does not significantly increase the impact of our choice of timesteps. For our maximum $\Delta_{\mathrm{SFMS}} = +0.5$dex, the median absolute difference in final stellar mass between $\delta t = 5\,\mathrm{Myr}$ and our choice $\delta t = 100\,\mathrm{Myr}$ is 0.46 dex (11%) while the maximum difference is 0.47 dex (11.5%). For any negative Δ_{SFMS} the variation in stellar masses for different timebins actually decreases, as model galaxies reach very low sSFRs earlier, which do not significantly alter their stellar mass any more, regardless of timestep.

In summary, we find the median absolute deviation in the stellar masses of our modeled galaxies for a time step size of up to $\delta t = 100\,\mathrm{Myr}$ to be around 0.027 dex, or $\approx 7\%$, when compared to the stellar masses determined with $\delta t = 5\,\mathrm{Myr}$. We therefore conclude that our choice of timestep size $\delta t = 100\,\mathrm{Myr}$ does not significantly impact our presented results. In addition, it is worth mentioning that observed star formation rates from various tracers themselves trace different timescales, shorter ($\approx 10\,\mathrm{Myr}$) for Hα and longer ($\approx 100\,\mathrm{Myr}$) for FUV and NUV bands (Kennicutt & Evans, 2012).

B.2 Main sequence star formation history fits

As discussed for the bottom panel of Fig. 8.2, we fit gaussians to the specific star formation histories of our model galaxies seeded between $z = 0.5$ and $z = 6$, which were fully evolved along the SFMS. We found there remarkable agreement in the trend of earlier peaks for more massive galaxies when compared to ETGs from SDSS and ATLAS^{3D}. In Fig. B.1 we also consider the width of the gaussian fit, σ_{SFH}, as a function of the final stellar mass. We find for SFMS evolved galaxies that those which end up being more massive exhibit more shorter and more peaked SFHs, as also found by Thomas et al. (2010) for SDSS ETGs. Notably, however, their SFHs are quite a bit more peaked, which is to be expected, as they can have quenched. This quenching cuts the SFHs short compared to our SFMS galaxies, and thus reaches a level of peaked-ness that we by design cannot reproduce. It is still interesting to note the same mass trend as found for ETGs also appears within SFMS evolved galaxies.

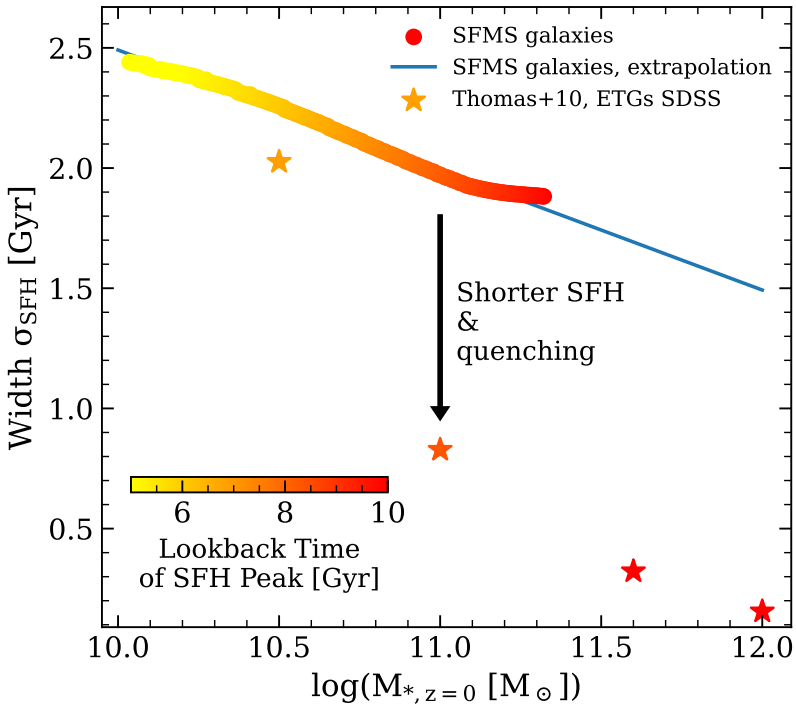


Figure B.1. The width $\sigma_{\rm SFH}$ of a gaussian fit to the specific star formation rate history of galaxies that evolved fully along the SFMS (shown in the top panel of Fig. 8.2), colored by the lookback time of the peak of the gaussian. Plotted are only models where the progenitor galaxy accounts for less than 1% of the final mass.

B.3 Connecting present day galaxies and their progenitors

We provide in Fig. B.2 the relation between progenitor stellar mass and final $z = 0$ stellar mass for galaxies that evolved on or at some fixed separation in log-space, $\Delta_{\rm SFMS}$, from the SFMS. These are as in the right panel of Fig. 8.4, with the color showing the fixed separation being either above (blue) or below (red) the SFMS SFR while the solid black lines going from top to bottom highlight $\Delta_{\rm SFMS} = 0.3, 0.1, 0, -0.1$, and -0.3 dex. The dashed black line is the expected connection between the $z = 0$ descendant and $z \geq 1$ progenitor galaxies obtained from the galaxy stellar mass function by Weaver et al. (2023) by matching equal comoving number densities across those redshifts. There is no line for $z = 5$ as the galaxy stellar mass function is not monotonically decreasing there, resulting in two stellar masses having the same number density.

We see that for early progenitors ($z = 6$, top left) the number density evolution would match expectations from the main sequence. That is to say, if we take galaxies of $M_* = 1\times10^{10}M_\odot$ at $z = 6$, the $z = 0$ mass of equivalent number density is $M_* = 3\times10^{11}M_\odot$, which is essentially identical to the expected mass if those galaxies had evolved along the SFMS until $z = 0$. This remains true at lower redshifts (down to $z = 1$) for the case of high mass progenitors $M_* > 1\times10^{10}M_\odot$, meaning that their number densities follow expectations from in-situ SFMS evolution. This is noteworthy as these massive galaxies are known to evolve secularly through mergers, which therefore must bring in a comparable amount of stellar mass to that which would have been produced in-situ if they had remained along the SFMS. For lower

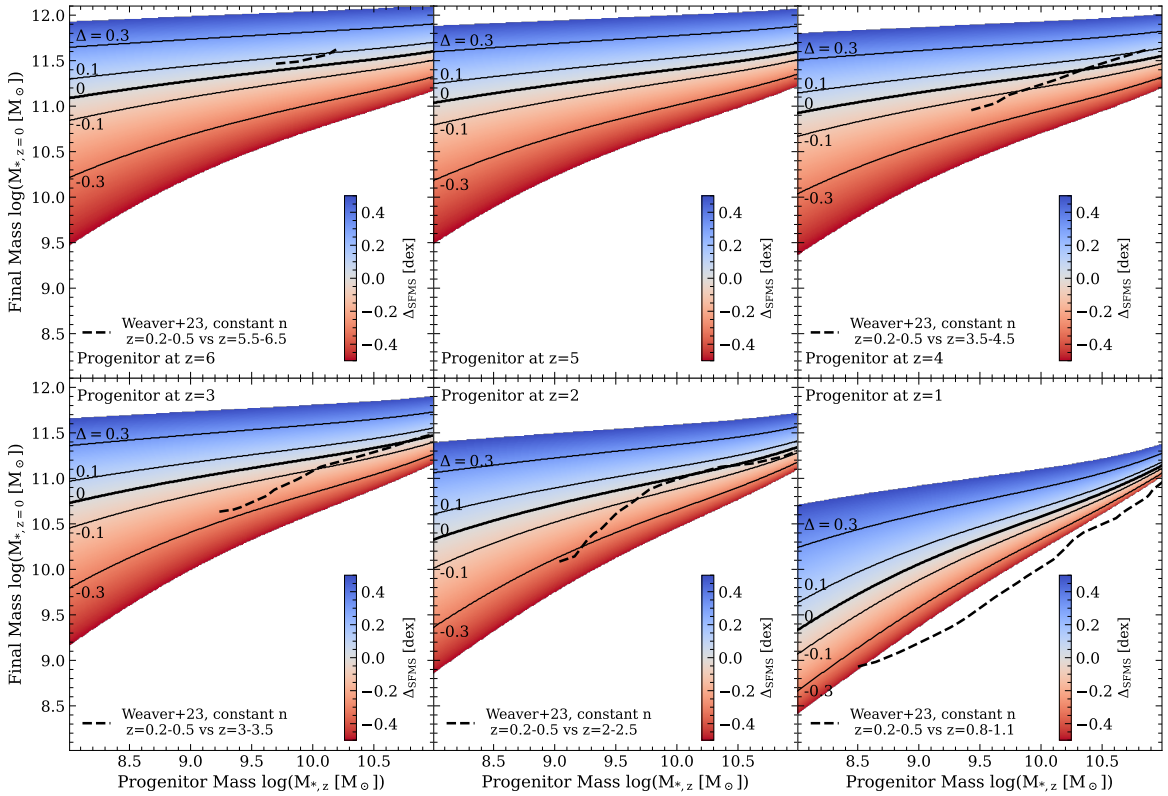


Figure B.2. As for the right panel of Fig. 8.4, the present day galaxy stellar masses $M_{*,z=0}$ relative to the stellar masses of their progenitor galaxies at redshifts $z = 6$ (**top left**) to $z = 1$ (**bottom right**). The color indicates the logarithmic separation from the SFMS, with blue being galaxies which evolved with SFRs consistently above the SFMS while red denotes galaxies which were consistently below. The dashed lines give the expected connection between present and past galaxy stellar masses under the assumption that their cosmic number density has remained constant, where we use the galaxy stellar mass function determined by Weaver et al. (2023) for the matching. There is no line for $z = 5$ as the galaxy stellar mas function is not monotonically decreasing there, leading to different galaxy stellar masses with identical number densities.

mass progenitor galaxies, instead, the $z = 0$ descendants of equal comoving number density are less massive than expected from a SFMS evolution. This means that they must have spent some amount of time well below the SFMS $\Delta_{\mathrm{SFMS}} = -0.3$.

C

Correlations and Definitions for ICL and BCG Quantities in Simulations

This is the Appendix to the publication by Kimmig et al., 2025, A&A 700, 95, presented in Chap. 12.

C.1 Partial Correlations and Fitting

Given that in Fig. 12.7 we find $f_{\mathrm{ICL+BCG}}$ to tightly trace with the cluster formation redshift z_{form}, it is of relevance if this correlation is driven by some other parameter that provides the link. To test the true driver of the relation to z_{form}, we calculate the partial correlation to $f_{\mathrm{ICL+BCG}}$ while accounting for all other parameters considered in this study individually. The partial correlation between two parameters x and y, accounting for z, is determined by fitting two linear regressions: between x and z as well as y and z. The residuals in x and y of these fits are thus corrected for any possible correlation with z, and the Pearson correlation coefficient of these residuals is defined as the partial correlation coefficient, which we plot in Fig. C.1. In all cases and for all simulations, the correlation between z_{form} and $f_{\mathrm{ICL+BCG}}$ remains significantly in place. Indeed, aside from f_{sub} for Hydrangea, the correlation of any parameter (from magnitude gap to center shift to halo mass) with z_{form} is less significant once accounting for that parameters correlation with $f_{\mathrm{ICL+BCG}}$. While it is possible that there is another underlying driver which best determines a galaxy cluster's formation redshift, of all the parameters discussed in this study, $f_{\mathrm{ICL+BCG}}$ is the strongest.

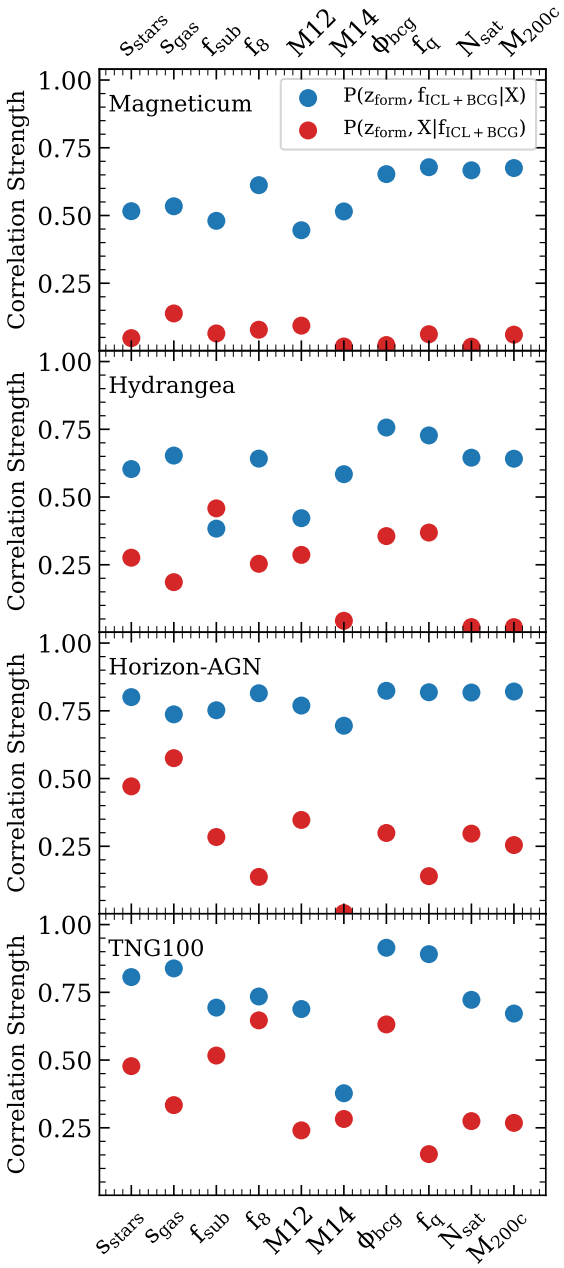


Figure C.1. Partial correlation of $z_{\rm form}$ with $f_{\rm ICL+BCG}$, accounting for other parameters X (blue), or between $z_{\rm form}$ and X, accounting for $f_{\rm ICL+BCG}$ (red), for all four simulations (panels).

This correlation allows us to define a fitting function, using $f_{\rm ICL+BCG}$ to predict $z_{\rm form}$, as discussed for Fig. 12.7. In the top row of Fig. C.2 we show the best fit lines between $z_{\rm form}$ and $f_{\rm ICL+BCG}$, as well as to $s_{\rm gas}$ and $f_{\rm sub}$, by using either the least-squares method, reducing the errors in either the x (red) or y-direction (blue), as well as using orthogonal distance regression (black, ODR), where both axes are weighted equally over the full range of their data. Using these best fit lines, we calculate the predicted formation redshift $z_{\rm form,prediction}$ and plot the cumulative distribution in absolute offset between the prediction and true $z_{\rm form}$ in the bottom row of Fig. C.2. The average 1σ-error is given by the vertical colored lines.

We find that the least-squares fit in the direction of x to y produces the overall tightest predictions, as expected because it minimizes precisely this error. ODR performs nearly as

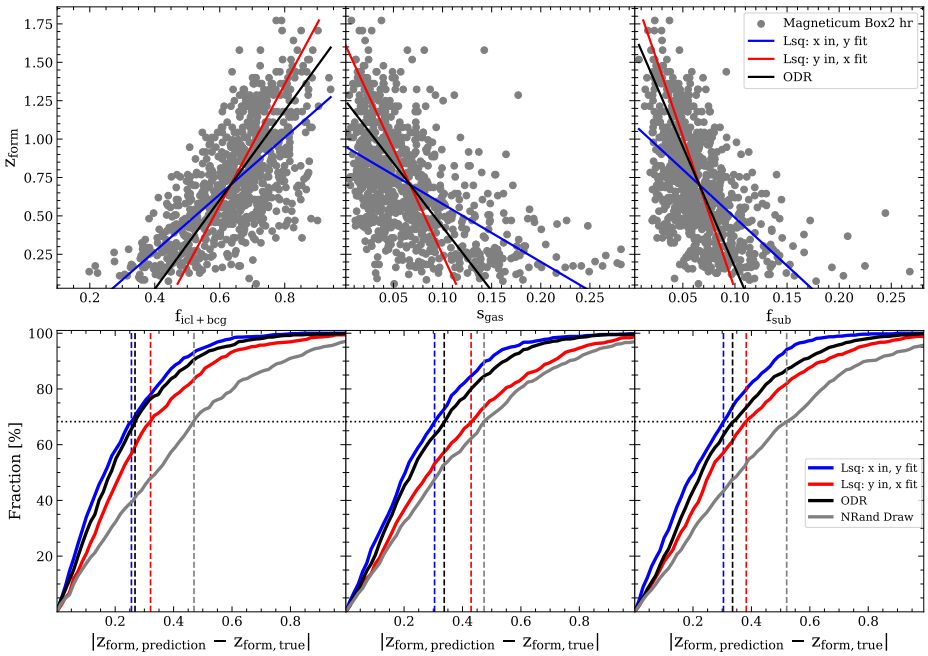


Figure C.2. *Top row:* The Magneticum data as in Fig. 12.7, with the axes swapped. Solid lines show the best fits using either the least-squares method, fitting toward x (red) or y (blue), as well as the best fit using orthogonal distance regression (black). *Bottom row:* The cumulative histogram of the absolute offset between the predicted versus actual formation redshifts for the three best fit lines, as well as when drawing randomly from a normal distribution of formation redshifts with the mean and standard deviation calculated from the total sample of clusters (gray). The 1σ-bounds (68.27%) are shown as colored vertical lines.

well in all cases, and additionally accounts for errors in the x-direction. As such, we chose ODR when calculating the best fit parameters defined in Table 12.1. We note that of all three dynamical tracers, $f_{\mathrm{ICL+BCG}}$ performs the best in predicting z_{form}, with a 1σ-error of around ± 0.25. While this is not insignificant, it is still remarkable that the time when a galaxy cluster had first assembled half of its present day total mass is imprinted into the current stellar distribution of mass to the point of being able to predict that time with just a 30% error on average (given the median $z_{\mathrm{form}} = 0.67$). The greatest deviations occur for galaxy clusters which assembled very recently (low z_{form}) but which already have merged most of that stellar mass into the BCG or ICL (high $f_{\mathrm{ICL+BCG}}$). For these cases, we find that it can be useful to consider other dynamical tracers as well, as often the center shift in the gas or stars still shows that there was a recent merger, even if the overall stars have already become bound to the central halo.

C.2 Definitions for Center Shift and BCG vs ICL

There are different options when defining a center shift, the offset between what represents the deepest point of the potential, traced either via the BCG or peak in the X-ray surface brightness, and the larger scale barycenter, either of the stellar mass, light, gas mass or X-ray luminosity. We chose for our comparison the BCG as the first point, and then determined

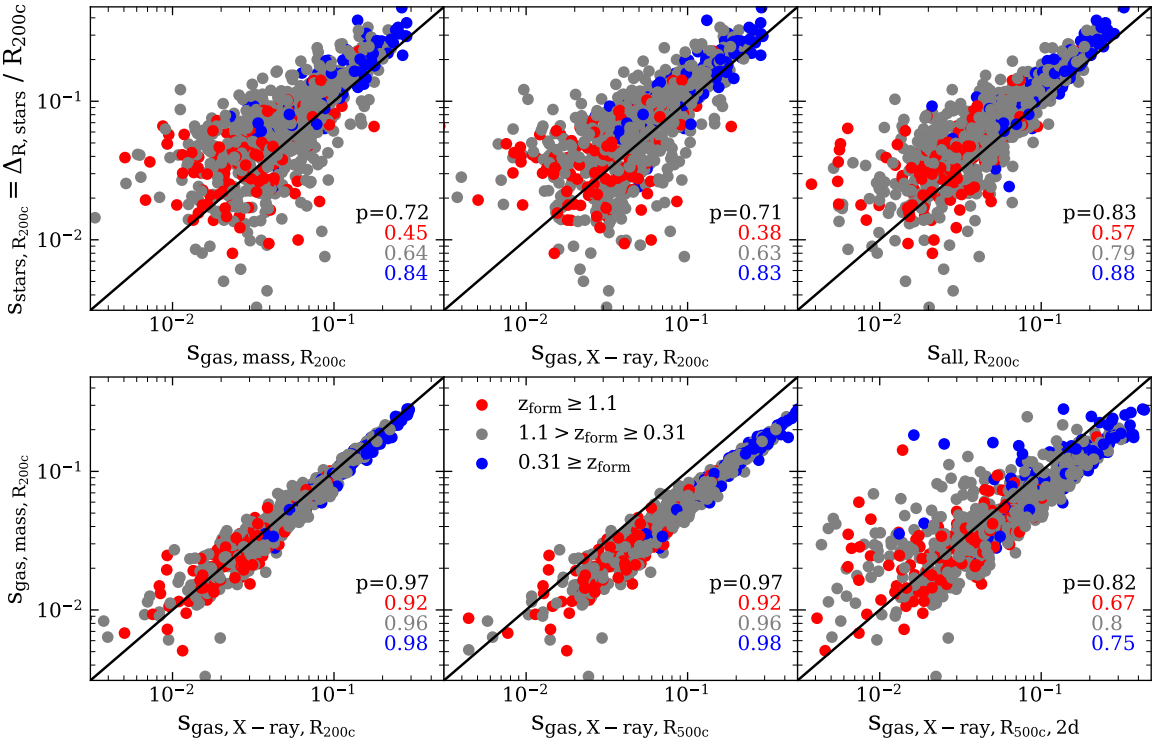


Figure C.3. Comparison of various center shift definitions for the Magneticum galaxy clusters. Coloring indicates whether the galaxy cluster has a formation redshift in the upper (red), middle (gray), or lower third (blue) of the total sample, as given in the legend.

the offset relative to the three-dimensional barycenter of the stellar (s_{stars}) or gas mass (s_{gas}). Here we consider the impact of alternative definitions, plotted in Fig. C.3. To distinguish the different center shifts, we add additional quantifiers in particular to the gas, such as the radius considered (R_{200c} or R_{500c}), whether we take the barycenter of the mass or X-ray luminosity, and finally if we determine it in projection (2d). We calculate the X-ray luminosity of individual gas particles via their mass M and temperature T, and approximate the electron density by assuming hydrogen and helium to be fully ionized ($n_e = n_{e,H} + n_{e,He}$), to get the luminosity in the range of $E_1 = 0.5$ to $E_2 = 2$ keV via:

$$L \propto n_e \cdot M \cdot \sqrt{T} \cdot \left(\exp\left(\frac{-E_2}{k_B \cdot T}\right) - \exp\left(\frac{-E_2}{k_B \cdot T}\right) \right).$$

The top row of Fig. C.3 shows the stellar center shift s_{stars} as a function of the gas mass center shift $s_{gas,m,R200c}$, the X-ray luminosity $s_{gas,X-ray,r200c}$, and the total barycenter $s_{all,R200c}$. We find the agreement between the center shifts to be very tight, with Pearson correlation coefficients in excess of $p = 0.7$. The stellar center shift apparently best correlated with the total mass center shift, which is likely because the mass is dominated by dark matter which, like the stellar particles, is dispersionless. Additionally, we color the points by the galaxy cluster formation redshift, with the upper third of the earliest forming clusters in red, the middle third in gray, and finally those clusters most recently formed in blue (with the formation redshift cuts used given in the legend). The colored values are the Pearson

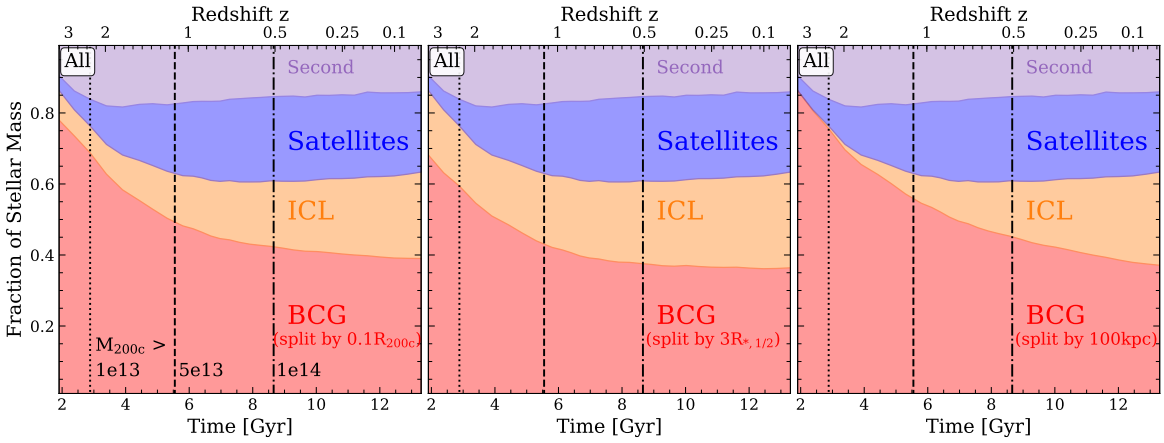


Figure C.4. Same as Fig. 4.10 for the Magneticum galaxy clusters using three different definitions of the split between ICL and BCG. *Left panel:* Same as the left panel of Fig. 4.10, with a split between BCG and ICL at $0.1 \cdot R_{200,\mathrm{cri}}$. *Central panel:* BCG and ICL split at $3 \cdot R_{*,1/2}$, with $R_{*,1/2}$ the stellar half mass radius. *Right panel:* BCG and ICL split at a fixed aperture of 100kpc.

correlation coefficients for their respective third, where we find that the agreement among the different types of center shift is always by far tightest for the most recently formed clusters. We attribute this to the fact that differences in the smaller center shift of a very relaxed, early formed cluster are inherently more spurious.

The second row of Fig. C.3 plots the gas mass center shift $s_{\mathrm{gas,m,r200c}}$ versus the X-ray center shift, determined in the same $r_{200\mathrm{c}}$ (left, $s_{\mathrm{gas,X-ray,r200c}}$), or within $r_{500\mathrm{c}}$ either in three-dimensions (center, $s_{\mathrm{gas,X-ray,r500c}}$) or projected along the z-axis (left, $s_{\mathrm{gas,X-ray,r500c,2d}}$). We find the gas mass center shift to trace that of the X-ray luminosity remarkably well, even when considering regions farther in or in projection. This is surprisingly true even for the earliest forming clusters (red).

Finally, we also consider differing definitions of where to split the BCG and ICL components used to trace their evolution in Fig. C.4. We show three different definitions for direct comparison. In the left panel, $r_{\mathrm{cut}} = 0.1 \cdot R_{200\mathrm{c}}$ is used as in Fig. 4.10, which cuts based on the size of the overall halo. The middle panel separates the BCG and the ICL based on the distribution of the central galaxy stars, namely $r_{\mathrm{cut}} = 3 \cdot R_{*,1/2}$, where $R_{*,1/2}$ is the radius which contains 50% of the central stellar component within $10\%R_{\mathrm{vir}}$. This is particularly interesting when comparing to recent observations by Joo & Jee (2023) who report little evolution in the ICL fraction with redshift. They find $f_{\mathrm{ICL}} \approx 14\%$ already at $z > 1$, which matches the values we find for the split at $r_{\mathrm{cut}} = 3 \cdot R_{*,1/2}$ at that redshift. This raises the question of whether the radial luminosity profiles at higher redshifts result in a split radius between BCG and ICL that moves increasingly inwards, a process which may be driven by increasingly centrally compact objects at these redshifts (Kimmig et al., 2025b; Ito et al., 2024), consequently resulting in a flat evolution in f_{ICL}. If instead we split by a fixed aperture, as shown in the right panel of Fig. C.4, we find that at high redshifts practically all of the non-satellite stellar mass in the cluster would be considered part of the BCG. Overall, the fixed aperture and halo based cuts are most similar in terms of the later evolution of galaxy clusters.

References

Adams N. J., Conselice C. J., Ferreira L., Austin D., Trussler J. A. A., Juodžbalis I., Wilkins S. M., Caruana J., Dayal P., Verma A., & Vijayan A. P.: *Discovery and properties of ultra-high redshift galaxies (9 < z < 12) in the JWST ERO SMACS 0723 Field.* MNRAS **518**, 4755 (2023)

Aguerri J. A. L., Castro-Rodríguez N., Napolitano N., Arnaboldi M., & Gerhard O.: *Diffuse light in Hickson compact groups: the dynamically young system HCG 44.* A&A **457**, 771 (2006)

Ahad S. L., Bahé Y. M., Hoekstra H., van der Burg R. F. J., & Muzzin A.: *The stellar mass function and evolution of the density profile of galaxy clusters from the Hydrangea simulations at 0 < z < 1.5.* MNRAS **504**, 1999 (2021)

Ahad S. L., Bahé Y. M., & Hoekstra H.: *How to interpret measurements of diffuse light in stacked observations of groups and clusters of galaxies.* MNRAS **518**, 3685 (2023)

Ahad S. L., Reid R., Mpetha C. T., Taylor J. E., Hildebrandt H., Hudson M. J., Chambers K. C., de Boer T., Guerrini S., Guinot A., et al.: *Cluster properties as a function of dynamical state in the DESI Legacy x UNIONS surveys.* arXiv e-prints, arXiv:2512 (2025)

Ahvazi N., Sales L. V., Navarro J. F., Benson A., Boselli A., & D'Souza R.: *Star formation beyond galaxies: widespread in-situ formation of intra-cluster stars.* The Open Journal of Astrophysics **7**, 111 (2024)

Aldás F., Zenteno A., Gómez F. A., Hernandez-Lang D., Carrasco E. R., Vega-Martínez C. A., & Nilo Castellón J. L.: *Clash of Titans: the impact of cluster mergers in the galaxy cluster red sequence.* MNRAS **525**, 1769 (2023)

Allen S. W., Rapetti D. A., Schmidt R. W., Ebeling H., Morris R. G., & Fabian A. C.: *Improved constraints on dark energy from Chandra X-ray observations of the largest relaxed galaxy clusters.* MNRAS **383**, 879 (2008)

Allen S. W., Evrard A. E., & Mantz A. B.: *Cosmological Parameters from Observations of Galaxy Clusters.* ARA&A **49**, 409 (2011)

Amorisco N. C.: *On feathers, bifurcations and shells: the dynamics of tidal streams across the mass scale.* MNRAS **450**, 575 (2015)

Andalman Z. L., Teyssier R., & Dekel A.: *On the origin of the high star formation efficiency in massive galaxies at Cosmic Dawn.* MNRAS **540**, 3350 (2025)

Andreon S.: *A low-scatter survey-based mass proxy for clusters of galaxies.* A&A **548**, A83 (2012)

Angulo R. E., Springel V., White S. D. M., Jenkins A., Baugh C. M., & Frenk C. S.: *Scaling relations for galaxy clusters in the Millennium-XXL simulation.* MNRAS **426**, 2046 (2012)

Antwi-Danso J., Papovich C., Esdaile J., Nanayakkara T., Glazebrook K., Hutchison T. A., Whitaker K. E., Marsan Z. C., Diaz R. J., Marchesini D., et al.: *The FENIKS Survey: Spectroscopic Confirmation of Massive Quiescent Galaxies at z ∼3-5.* arXiv e-prints, arXiv:2307 (2023)

Aragón-Calvo M. A., van de Weygaert R., & Jones B. J. T.: *Multiscale phenomenology of the cosmic web.* MNRAS **408**, 2163 (2010)

Argudo-Fernández M., Duarte Puertas S., & Verley S.: *Fundamental relation in isolated galaxies, pairs, and triplets in the local Universe.* A&A **695**, A256 (2025)

Arrabal Haro P., Dickinson M., Finkelstein S. L., Kartaltepe J. S., Donnan C. T., Burgarella D., Carnall A., Cullen F., Dunlop J. S., Fernández V., et al.: *Confirmation and refutation of very luminous galaxies in the early universe.* arXiv e-prints, arXiv:2303 (2023)

Bagley M. B., Pirzkal N., Finkelstein S. L., Papovich C., Berg D. A., Lotz J. M., Leung G. C. K., Ferguson H. C., Koekemoer A. M., Dickinson M., et al.: *The Next Generation Deep Extragalactic Exploratory Public (NGDEEP) Survey.* ApJ **965**, L6 (2024)

Bahé Y. M., Barnes D. J., Dalla Vecchia C., Kay S. T., White S. D. M., McCarthy I. G., Schaye J., Bower R. G., Crain R. A., Theuns T., et al.: *The Hydrangea simulations: galaxy formation in and around massive clusters.* MNRAS **470**, 4186 (2017)

Bahé Y. M., Schaye J., Barnes D. J., Dalla Vecchia C., Kay S. T., Bower R. G., Hoekstra H., McGee S. L., & Theuns T.: *Disruption of satellite galaxies in simulated groups and clusters: the roles of accretion time, baryons, and pre-processing.* MNRAS **485**, 2287 (2019)

Bahé Y. M.: *Strongly lensed cluster substructures are not in tension with ΛCDM.* MNRAS **505**, 1458 (2021)

Baker W. M., Tacchella S., Johnson B. D., Nelson E., Suess K. A., D'Eugenio F., Curti M., de Graaff A., Ji Z., Maiolino R., et al.: *A core in a star-forming disc as evidence of inside-out growth in the early Universe.* Nature Astronomy **9**, 141 (2025a)

Baker W. M., Valentino F., Lagos C. d. P., Ito K., Jespersen C. K., Gottumukkala R., Hjorth J., Langeroodi D., & Sedgewick A.: *Exploring over 700 massive quiescent galaxies at z = 2-7: Demographics and stellar mass functions.* A&A **702**, A270 (2025b)

Baldry I. K., Glazebrook K., Brinkmann J., Ivezić Ž., Lupton R. H., Nichol R. C., & Szalay A. S.: *Quantifying the Bimodal Color-Magnitude Distribution of Galaxies.* ApJ **600**, 681 (2004)

Baldwin J. A., Phillips M. M., & Terlevich R.: *Classification parameters for the emission-line spectra of extragalactic objects.* PASP **93**, 5 (1981)

Barnes D. J., Kay S. T., Bahé Y. M., Dalla Vecchia C., McCarthy I. G., Schaye J., Bower R. G., Jenkins A., Thomas P. A., Schaller M., et al.: *The Cluster-EAGLE project: global properties of simulated clusters with resolved galaxies.* MNRAS **471**, 1088 (2017)

Barnes J. E.: *Encounters of Disk/Halo Galaxies.* ApJ **331**, 699 (1988)

Barnes J. E.: *Transformations of Galaxies. I. Mergers of Equal-Mass Stellar Disks.* ApJ **393**, 484 (1992)

Barnes J. E. & Hernquist L.: *Transformations of Galaxies. II. Gasdynamics in Merging Disk Galaxies.* ApJ **471**, 115 (1996)

Barnes J. & Hut P.: *A hierarchical O(N log N) force-calculation algorithm.* Nature **324**, 446 (1986)

Barone T. M., D'Eugenio F., Colless M., Scott N., van de Sande J., Bland-Hawthorn J., Brough S., Bryant J. J., Cortese L., Croom S. M., et al.: *The SAMI Galaxy Survey: Gravitational Potential and Surface Density Drive Stellar Populations. I. Early-type Galaxies.* ApJ **856**, 64 (2018)

Beck A. M., Murante G., Arth A., Remus R.-S., Teklu A. F., Donnert J. M. F., Planelles S., Beck M. C., Förster P., Imgrund M., et al.: *An improved SPH scheme for cosmological simulations.* MNRAS **455**, 2110 (2016)

Behroozi P. S., Wechsler R. H., & Conroy C.: *The Average Star Formation Histories of Galaxies in Dark Matter Halos from $z = 0$-8.* ApJ **770**, 57 (2013)

Behroozi P. & Silk J.: *The most massive galaxies and black holes allowed by ΛCDM.* MNRAS **477**, 5382 (2018)

Bekki K., Owers M. S., & Couch W. J.: *Synchronized Formation of Starburst and Post-starburst Galaxies in Merging Clusters of Galaxies.* ApJ **718**, L27 (2010)

Bell E. F., Naab T., McIntosh D. H., Somerville R. S., Caldwell J. A. R., Barden M., Wolf C., Rix H.-W., Beckwith S. V., Borch A., et al.: *Dry Mergers in GEMS: The Dynamical Evolution of Massive Early-Type Galaxies.* ApJ **640**, 241 (2006)

Belli S., Newman A. B., & Ellis R. S.: *MOSFIRE Spectroscopy of Quiescent Galaxies at 1.5 $< z <$ 2.5. II. Star Formation Histories and Galaxy Quenching.* ApJ **874**, 17 (2019)

Belli S., Park M., Davies R. L., Mendel J. T., Johnson B. D., Conroy C., Benton C., Bugiani L., Emami R., Leja J., et al.: *Massive and Multiphase Gas Outflow in a Quenching Galaxy at z=2.445.* arXiv e-prints, arXiv:2308 (2023)

Belokurov V., Erkal D., Evans N. W., Koposov S. E., & Deason A. J.: *Co-formation of the disc and the stellar halo.* MNRAS **478**, 611 (2018)

Belokurov V. & Kravtsov A.: *From dawn till disc: Milky Way's turbulent youth revealed by the APOGEE+Gaia data.* MNRAS **514**, 689 (2022)

Bender R., Kormendy J., Cornell M. E., & Fisher D. B.: *Structure and Formation of cD Galaxies: NGC 6166 in ABELL 2199.* ApJ **807**, 56 (2015)

Benson A. J., Bower R. G., Frenk C. S., Lacey C. G., Baugh C. M., & Cole S.: *What Shapes the Luminosity Function of Galaxies?* ApJ **599**, 38 (2003)

Bergamini P., Acebron A., Grillo C., Rosati P., Caminha G. B., Mercurio A., Vanzella E., Angora G., Brammer G., Meneghetti M., & Nonino M.: *New high-precision strong lensing modeling of Abell 2744. Preparing for JWST observations.* arXiv e-prints, arXiv:2207 (2022)

Bethe H. A.: *Energy Production in Stars.* Physical Review **55**, 434 (1939)

Bezanson R., van Dokkum P. G., Tal T., Marchesini D., Kriek M., Franx M., & Coppi P.: *The Relation Between Compact, Quiescent High-redshift Galaxies and Massive Nearby Elliptical Galaxies: Evidence for Hierarchical, Inside-Out Growth.* ApJ **697**, 1290 (2009)

Bezanson R., Labbe I., Whitaker K. E., Leja J., Price S. H., Franx M., Brammer G., Marchesini D., Zitrin A., Wang B., et al.: *The JWST UNCOVER Treasury Survey: Ultradeep NIRSpec and NIRCam Observations before the Epoch of Reionization.* ApJ **974**, 92 (2024)

Bhattacharyya S., Adhikari S., Banerjee A., More S., Kumar A., Nadler E. O., & Chatterjee S.: *The Signatures of Self-Interacting Dark Matter and Subhalo Disruption on Cluster Substructure.* arXiv e-prints, arXiv:2106 (2021)

Biffi V., Borgani S., Murante G., Rasia E., Planelles S., Granato G. L., Ragone-Figueroa C., Beck A. M., Gaspari M., & Dolag K.: *On the Nature of Hydrostatic Equilibrium in Galaxy Clusters.* ApJ **827**, 112 (2016)

Bilata-Woldeyes B., Perea J. D., & Solanes J. M.: *Growth of Ex-situ Diffuse Intragroup Light in Simulated Galaxy Groups.* arXiv e-prints, arXiv:2502 (2025)

Binney J. & Tabor G.: *Evolving cooling flows.* MNRAS **276**, 663 (1995)

Bird J. P. & Goldberg D. M.: *Flexion in Abell 2744.* MNRAS **476**, 1198 (2018)

Birnboim Y. & Dekel A.: *Virial shocks in galactic haloes?* MNRAS **345**, 349 (2003)

Blaizot J., Guiderdoni B., Devriendt J. E. G., Bouchet F. R., Hatton S. J., & Stoehr F.: *GALICS- III. Properties of Lyman-break galaxies at a redshift of 3.* MNRAS **352**, 571 (2004)

Bland-Hawthorn J., Sutherland R., & Webster D.: *Ultrafaint Dwarf Galaxies—the Lowest-mass Relics from Before Reionization.* ApJ **807**, 154 (2015)

Bland-Hawthorn J. & Gerhard O.: *The Galaxy in Context: Structural, Kinematic, and Integrated Properties.* ARA&A **54**, 529 (2016)

Bluck A. F. L., Mendel J. T., Ellison S. L., Patton D. R., Simard L., Henriques B. M. B., Torrey P., Teimoorinia H., Moreno J., & Starkenburg E.: *The impact of galactic properties and environment on the quenching of central and satellite galaxies: a comparison between SDSS, Illustris and L-Galaxies.* MNRAS **462**, 2559 (2016)

Bluck A. F. L., Piotrowska J. M., & Maiolino R.: *The Fundamental Signature of Star Formation Quenching from AGN Feedback: A Critical Dependence of Quiescence on Supermassive Black Hole Mass, Not Accretion Rate.* ApJ **944**, 108 (2023)

Bluck A. F. L., Conselice C. J., Ormerod K., Piotrowska J. M., Adams N., Austin D., Caruana J., Duncan K. J., Ferreira L., Goubert P., et al.: *Galaxy Quenching at the High Redshift Frontier: A Fundamental Test of Cosmological Models in the Early Universe with JWST-CEERS.* ApJ **961**, 163 (2024)

Blumenthal G. R., Faber S. M., Primack J. R., & Rees M. J.: *Formation of galaxies and large-scale structure with cold dark matter.* Nature **311**, 517 (1984)

Blumenthal G. R., Faber S. M., Flores R., & Primack J. R.: *Contraction of Dark Matter Galactic Halos Due to Baryonic Infall.* ApJ **301**, 27 (1986)

Bois M., Emsellem E., Bournaud F., Alatalo K., Blitz L., Bureau M., Cappellari M., Davies R. L., Davis T. A., de Zeeuw P. T., et al.: *The ATLAS^{3D} project - VI. Simulations of binary galaxy mergers and the link with fast rotators, slow rotators and kinematically distinct cores.* MNRAS **416**, 1654 (2011)

Bondi H. & Hoyle F.: *On the mechanism of accretion by stars.* MNRAS **104**, 273 (1944)

Bondi H.: *On spherically symmetrical accretion.* MNRAS **112**, 195 (1952)

Borzyszkowski M., Porciani C., Romano-Díaz E., & Garaldi E.: *ZOMG - I. How the cosmic web inhibits halo growth and generates assembly bias.* MNRAS **469**, 594 (2017)

Boschin W., Girardi M., Spolaor M., & Barrena R.: *Internal dynamics of the radio halo cluster Abell 2744.* A&A **449**, 461 (2006)

Böss L. M., Steinwandel U. P., Dolag K., & Lesch H.: *CRESCENDO: an on-the-fly Fokker-Planck solver for spectral cosmic rays in cosmological simulations.* MNRAS **519**, 548 (2023)

Bouché N., Dekel A., Genzel R., Genel S., Cresci G., Förster Schreiber N. M., Shapiro K. L., Davies R. I., & Tacconi L.: *The Impact of Cold Gas Accretion Above a Mass Floor on Galaxy Scaling Relations.* ApJ **718**, 1001 (2010)

Bournaud F., Jog C. J., & Combes F.: *Multiple minor mergers: formation of elliptical galaxies and constraints for the growth of spiral disks.* A&A **476**, 1179 (2007)

Bouwens R., González-López J., Aravena M., Decarli R., Novak M., Stefanon M., Walter F., Boogaard L., Carilli C., Dudzevičiūtė U., et al.: *The ALMA Spectroscopic Survey Large Program: The Infrared Excess of z = 1.5-10 UV-selected Galaxies and the Implied High-redshift Star Formation History.* ApJ **902**, 112 (2020)

Bower R. G., Benson A. J., Malbon R., Helly J. C., Frenk C. S., Baugh C. M., Cole S., & Lacey C. G.: *Breaking the hierarchy of galaxy formation.* MNRAS **370**, 645 (2006)

Boylan-Kolchin M., Springel V., White S. D. M., Jenkins A., & Lemson G.: *Resolving cosmic structure formation with the Millennium-II Simulation.* MNRAS **398**, 1150 (2009)

Boylan-Kolchin M.: *Stress testing ΛCDM with high-redshift galaxy candidates.* Nature Astronomy **7**, 731 (2023)

Brambila D., Lopes P. A. A., Ribeiro A. L. B., & Cortesi A.: *Examining transitional galaxies to understand the role of clusters and their dynamical status in galaxy quenching.* MNRAS **523**, 785 (2023)

Brammer G. B., Whitaker K. E., van Dokkum P. G., Marchesini D., Franx M., Kriek M., Labbé I., Lee K.-S., Muzzin A., Quadri R. F., et al.: *The Number Density and Mass Density of Star-forming and Quiescent Galaxies at 0.4 <= z <= 2.2.* ApJ **739**, 24 (2011)

Brinchmann J., Charlot S., White S. D. M., Tremonti C., Kauffmann G., Heckman T., & Brinkmann J.: *The physical properties of star-forming galaxies in the low-redshift Universe.* MNRAS **351**, 1151 (2004)

Brough S., Couch W. J., Collins C. A., Jarrett T., Burke D. J., & Mann R. G.: *The luminosity-halo mass relation for brightest cluster galaxies.* MNRAS **385**, L103 (2008)

Brough S., Tran K. V., Sharp R. G., von der Linden A., & Couch W. J.: *Spatial kinematics of Brightest Cluster Galaxies and their close companions from Integral Field Unit spectroscopy.* MNRAS **414**, L80 (2011)

Brough S., van de Sande J., Owers M. S., d'Eugenio F., Sharp R., Cortese L., Scott N., Croom S. M., Bassett R., Bekki K., et al.: *The SAMI Galaxy Survey: Mass as the Driver of the Kinematic Morphology-Density Relation in Clusters.* ApJ **844**, 59 (2017)

Brough S., Collins C., Demarco R., Ferguson H. C., Galaz G., Holwerda B., Martinez-Lombilla C., Mihos C., & Montes M.: *The Vera Rubin Observatory Legacy Survey of*

Space and Time and the Low Surface Brightness Universe. arXiv e-prints, arXiv:2001 (2020)

Brough S., Ahad S. L., Bahé Y. M., Ellien A., Gonzalez A. H., Jiménez-Teja Y., Kimmig L. C., Martin G., Martínez-Lombilla C., Montes M., et al.: *Preparing for low surface brightness science with the Vera C. Rubin Observatory: a comparison of observable and simulated intracluster light fractions.* MNRAS **528**, 771 (2024)

Brown H. J., Martin G., Pearce F. R., Hatch N. A., Bahé Y. M., & Dubois Y.: *Assembly of the intracluster light in the HORIZON-AGN simulation.* MNRAS **534**, 431 (2024)

Bruzual G. & Charlot S.: *Stellar population synthesis at the resolution of 2003.* MNRAS **344**, 1000 (2003)

Bryan G. L. & Norman M. L.: *Statistical Properties of X-Ray Clusters: Analytic and Numerical Comparisons.* ApJ **495**, 80 (1998)

Budzynski J. M., Koposov S. E., McCarthy I. G., & Belokurov V.: *The similarity of the stellar mass fractions of galaxy groups and clusters.* MNRAS **437**, 1362 (2014)

Buitrago F., Trujillo I., Conselice C. J., & Häußler B.: *Early-type galaxies have been the predominant morphological class for massive galaxies since only $z \sim 1$.* MNRAS **428**, 1460 (2013)

Bullock J. S., Dekel A., Kolatt T. S., Kravtsov A. V., Klypin A. A., Porciani C., & Primack J. R.: *A Universal Angular Momentum Profile for Galactic Halos.* ApJ **555**, 240 (2001)

Buote D. A. & Tsai J. C.: *Quantifying the Morphologies and Dynamical Evolution of Galaxy Clusters. I. The Method.* ApJ **452**, 522 (1995)

Burke C., Hilton M., & Collins C.: *Coevolution of brightest cluster galaxies and intracluster light using CLASH.* MNRAS **449**, 2353 (2015)

Burkert A.: *A bathtub model for the star-forming interstellar medium.* Mem. Soc. Astron. Italiana **88**, 533 (2017)

Burkert A. & Forbes D. A.: *High-precision Dark Halo Virial Masses from Globular Cluster Numbers: Implications for Globular Cluster Formation and Galaxy Assembly.* AJ **159**, 56 (2020)

Burns J. O., Roettiger K., Ledlow M., & Klypin A.: *The Coma Cluster after Lunch: Has a Galaxy Group Passed through the Cluster Core?* ApJ **427**, L87 (1994)

Busso M., Gallino R., & Wasserburg G. J.: *Nucleosynthesis in Asymptotic Giant Branch Stars: Relevance for Galactic Enrichment and Solar System Formation.* ARA&A **37**, 239 (1999)

Buzzo M. L., Forbes D. A., Brodie J. P., Romanowsky A. J., Cluver M. E., Jarrett T. H., Laine S., Couch W. J., Gannon J. S., Ferré-Mateu A., & Okabe N.: *The stellar populations of quiescent ultra-diffuse galaxies from optical to mid-infrared spectral energy distribution fitting.* MNRAS **517**, 2231 (2022)

Cameron A. G. W.: *Abundances of the Elements in the Solar System.* Space Sci. Rev. **15**, 121 (1973)

Canepa L., Brough S., Lanusse F., Montes M., & Hatch N.: *Measuring the Intracluster Light Fraction with Machine Learning.* ApJ **980**, 245 (2025)

Cappellari M. & Copin Y.: *Adaptive spatial binning of integral-field spectroscopic data using Voronoi tessellations.* MNRAS **342**, 345 (2003)

Carnall A. C., McLure R. J., Dunlop J. S., & Davé R.: *Inferring the star formation histories of massive quiescent galaxies with BAGPIPES: evidence for multiple quenching mechanisms.* MNRAS **480**, 4379 (2018)

Carnall A. C., Walker S., McLure R. J., Dunlop J. S., McLeod D. J., Cullen F., Wild V., Amorin R., Bolzonella M., Castellano M., et al.: *Timing the earliest quenching events with a robust sample of massive quiescent galaxies at 2 < z < 5.* MNRAS **496**, 695 (2020)

Carnall A. C., McLeod D. J., McLure R. J., Dunlop J. S., Begley R., Cullen F., Donnan C. T., Hamadouche M. L., Jewell S. M., Jones E. W., et al.: *A surprising abundance of massive quiescent galaxies at 3 < z < 5 in the first data from JWST CEERS.* MNRAS **520**, 3974 (2023a)

Carnall A. C., McLure R. J., Dunlop J. S., McLeod D. J., Wild V., Cullen F., Magee D., Begley R., Cimatti A., Donnan C. T., et al.: *A massive quiescent galaxy at redshift 4.658.* Nature **619**, 716 (2023b)

Carnall A. C., Cullen F., McLure R. J., McLeod D. J., Begley R., Donnan C. T., Dunlop J. S., Shapley A. E., Rowlands K., Almaini O., et al.: *The JWST EXCELS survey: Too much, too young, too fast? Ultra-massive quiescent galaxies at 3 < z < 5.* arXiv e-prints, arXiv:2405 (2024)

Casas M. C., Putnam K., Mantz A. B., Allen S. W., & Somboonpanyakul T.: *Optical Photometric Indicators of Galaxy Cluster Relaxation.* ApJ **967**, 14 (2024)

Cautun M., van de Weygaert R., & Jones B. J. T.: *NEXUS: tracing the cosmic web connection.* MNRAS **429**, 1286 (2013)

Cavaliere A. & Fusco-Femiano R.: *The Distribution of Hot Gas in Clusters of Galaxies.* A&A **70**, 677 (1978)

Çakır O., Owers M., Kimmig L., Nulsen P., Pak M., Quattropani G., & Couch W.: *The impact of cluster mergers on galaxy properties.* PASA **42**, e163 (2025)

Cen R.: *A Hydrodynamic Approach to Cosmology: Methodology.* ApJS **78**, 341 (1992)

Cervantes-Sodi B., Hernandez X., & Park C.: *Clues on the origin of galactic angular momentum from looking at galaxy pairs.* MNRAS **402**, 1807 (2010)

Ceverino D., Nakazato Y., Yoshida N., Klessen R. S., & Glover S. C. O.: *Redshift-dependent galaxy formation efficiency at $z = 5$ - 13 in the FirstLight Simulations.* A&A **689**, A244 (2024)

Chabrier G.: *The Galactic Disk Mass Budget. I. Stellar Mass Function and Density.* ApJ **554**, 1274 (2001)

Chabrier G.: *Galactic Stellar and Substellar Initial Mass Function.* PASP **115**, 763 (2003)

Chaikin E., Schaye J., Schaller M., Benítez-Llambay A., Nobels F. S. J., & Ploeckinger S.: *A thermal-kinetic subgrid model for supernova feedback in simulations of galaxy formation.* MNRAS **523**, 3709 (2023)

Chandra V., Semenov V. A., Rix H.-W., Conroy C., Bonaca A., Naidu R. P., Andrae R., Li J., & Hernquist L.: *The Three-phase Evolution of the Milky Way.* ApJ **972**, 112 (2024)

Chandrasekhar S.: *Stochastic Problems in Physics and Astronomy.* Reviews of Modern Physics **15**, 1 (1943)

Chandro-Gómez Á., Lagos C. d. P., Power C., Baker W. M., Benítez-Llambay A., Chaikin E., Chittenden H. G., Correa C., Frenk C. S., Huško F., et al.: *Unveiling the properties and origin of massive quenched galaxies at $z \geq 2$ in the COLIBRE hydrodynamical simulations.* arXiv e-prints, arXiv:2512 (2025)

Chauke P., van der Wel A., Pacifici C., Bezanson R., Wu P.-F., Gallazzi A., Straatman C., Franx M., Barišić I., Bell E. F., et al.: *Rejuvenation in $z \sim 0.8$ Quiescent Galaxies in LEGA-C.* ApJ **877**, 48 (2019)

Chelouche D.: *The Case for Standard Irradiated Accretion Disks in Active Galactic Nuclei.* ApJ **772**, 9 (2013)

Chevance M., Krumholz M. R., McLeod A. F., Ostriker E. C., Rosolowsky E. W., & Sternberg A.: *The Life and Times of Giant Molecular Clouds.* In: Inutsuka S., Aikawa Y., Muto T., Tomida K., & Tamura M. (eds.): *Protostars and Planets VII.* Astronomical Society of the Pacific Conference Series **534**, 1 (2023)

Chiappini C., Matteucci F., & Gratton R.: *The Chemical Evolution of the Galaxy: The Two-Infall Model.* ApJ **477**, 765 (1997)

Chiba M. & Beers T. C.: *Kinematics of Metal-poor Stars in the Galaxy. III. Formation of the Stellar Halo and Thick Disk as Revealed from a Large Sample of Nonkinematically Selected Stars.* AJ **119**, 2843 (2000)

Chittenden H. G., Glazebrook K., Nanayakkara T., Kawinwanichakij L., Lagos C., Kimmig L., & Remus R.-S.: *On the unique evolutionary mechanisms of massive quiescent galaxies in the epoch of reionisation.* arXiv e-prints, arXiv:2504 (2025)

Choi H., Yi S. K., Dubois Y., Kimm T., Devriendt J. E. G., & Pichon C.: *Early-type Galaxy Spin Evolution in the Horizon-AGN Simulation.* ApJ **856**, 114 (2018)

Chon G., Böhringer H., & Zaroubi S.: *On the definition of superclusters.* A&A **575**, L14 (2015)

Chun K., Shin J., Ko J., Smith R., & Yoo J.: *Formation Channels of Diffuse Lights in Groups and Clusters over Time.* ApJ **969**, 142 (2024)

Churazov E., Sunyaev R., Forman W., & Böhringer H.: *Cooling flows as a calorimeter of active galactic nucleus mechanical power.* MNRAS **332**, 729 (2002)

Churazov E., Sazonov S., Sunyaev R., Forman W., Jones C., & Böhringer H.: *Supermassive black holes in elliptical galaxies: switching from very bright to very dim.* MNRAS **363**, L91 (2005)

Chworowsky K., Finkelstein S. L., Spilker J. S., Leung G. C. K., Bagley M. B., Casey C. M., Gronwall C., Jogee S., Larson R. L., Papovich C., et al.: *ALMA 1.1mm Observations of a Conservative Sample of High Redshift Massive Quiescent Galaxies in SHELA.* arXiv e-prints, arXiv:2305 (2023)

Cole S. & Lacey C.: *The structure of dark matter haloes in hierarchical clustering models.* MNRAS **281**, 716 (1996)

Cole S., Lacey C. G., Baugh C. M., & Frenk C. S.: *Hierarchical galaxy formation.* MNRAS **319**, 168 (2000)

Colina L., Crespo Gómez A., Álvarez-Márquez J., Bik A., Walter F., Boogaard L., Labiano A., Peissker F., Pérez-González P., Östlin G., et al.: *Uncovering the stellar structure of the dusty star-forming galaxy GN20 at $z = 4.055$ with MIRI/JWST.* A&A **673**, L6 (2023)

Colless M. & Dunn A. M.: *Structure and Dynamics of the Coma Cluster.* ApJ **458**, 435 (1996)

Combes F.: *AGN feedback and its quenching efficiency.* Frontiers in Astronomy and Space Sciences **4**, 10 (2017)

Comerón S., Trujillo I., Cappellari M., Buitrago F., Garduño L. E., Zaragoza-Cardiel J., Zinchenko I. A., Lara-López M. A., Ferré-Mateu A., & Dib S.: *The massive relic galaxy NGC 1277 is dark matter deficient. From dynamical models of integral-field stellar kinematics out to five effective radii.* A&A **675**, A143 (2023)

Conroy C., Wechsler R. H., & Kravtsov A. V.: *The Hierarchical Build-Up of Massive Galaxies and the Intracluster Light since $z = 1$.* ApJ **668**, 826 (2007)

Conroy C., Weinberg D. H., Naidu R. P., Buck T., Johnson J. W., Cargile P., Bonaca A., Caldwell N., Chandra V., Han J. J., et al.: *Birth of the Galactic Disk Revealed by the H3 Survey.* arXiv e-prints, arXiv:2204 (2022)

Conselice C. J.: *The Evolution of Galaxy Structure Over Cosmic Time.* ARA&A **52**, 291 (2014)

Contini E., De Lucia G., Villalobos Á., & Borgani S.: *On the formation and physical properties of the intracluster light in hierarchical galaxy formation models.* MNRAS **437**, 3787 (2014)

Contini E., Yi S. K., & Kang X.: *The different growth pathways of brightest cluster galaxies and intracluster light.* MNRAS **479**, 932 (2018)

Contini E., Jeon S., Rhee J., Han S., & Yi S. K.: *The Intracluster Light and its Link with the Dynamical State of the Host Group/Cluster: the Role of the Halo Concentration.* arXiv e-prints, arXiv:2310 (2023)

Contini E., Rhee J., Han S., Jeon S., & Yi S. K.: *The Connection between the Intracluster Light and its Host Halo: Formation Time and Contribution from Different Channels.* AJ **167**, 7 (2024a)

Contini E., Yi S. K., & Jeon S.: *Brightest Cluster Galaxies and the Intracluster Light.* arXiv e-prints, arXiv:2404 (2024b)

Contreras-Santos A., Knebe A., Pearce F., Haggar R., Gray M., Cui W., Yepes G., De Petris M., De Luca F., Power C., et al.: *The three hundred project: galaxy cluster mergers and their impact on the stellar component of brightest cluster galaxies.* MNRAS **511**, 2897 (2022)

Contreras-Santos A., Knebe A., Cui W., Alonso Asensio I., Dalla Vecchia C., Cañas R., Haggar R., Mostoghiu Paun R. A., Pearce F. R., & Rasia E.: *Characterising the intracluster light in The Three Hundred simulations.* A&A **683**, A59 (2024)

Corbelli E., Thilker D., Zibetti S., Giovanardi C., & Salucci P.: *Dynamical signatures of a ΛCDM-halo and the distribution of the baryons in M 33.* A&A **572**, A23 (2014)

Cortese L., Fogarty L. M. R., Bekki K., van de Sande J., Couch W., Catinella B., Colless M., Obreschkow D., Taranu D., Tescari E., et al.: *The SAMI Galaxy Survey: the link between angular momentum and optical morphology.* MNRAS **463**, 170 (2016)

Costantin L., Pérez-González P. G., Guo Y., Buttitta C., Jogee S., Bagley M. B., Barro G., Kartaltepe J. S., Koekemoer A. M., Cabello C., et al.: *A Milky Way-like barred spiral galaxy at a redshift of 3.* Nature **623**, 499 (2023)

Crain R. A., Schaye J., Bower R. G., Furlong M., Schaller M., Theuns T., Dalla Vecchia C., Frenk C. S., McCarthy I. G., Helly J. C., et al.: *The EAGLE simulations of galaxy formation: calibration of subgrid physics and model variations.* MNRAS **450**, 1937 (2015)

Croom S. M., Lawrence J. S., Bland-Hawthorn J., Bryant J. J., Fogarty L., Richards S., Goodwin M., Farrell T., Miziarski S., Heald R., et al.: *The Sydney-AAO Multi-object Integral field spectrograph.* MNRAS **421**, 872 (2012)

Croton D. J., Springel V., White S. D. M., De Lucia G., Frenk C. S., Gao L., Jenkins A., Kauffmann G., Navarro J. F., & Yoshida N.: *The many lives of active galactic nuclei: cooling flows, black holes and the luminosities and colours of galaxies.* MNRAS **365**, 11 (2006)

Cui W., Power C., Borgani S., Knebe A., Lewis G. F., Murante G., & Poole G. B.: *On the dynamical state of galaxy clusters: insights from cosmological simulations - II.* MNRAS **464**, 2502 (2017)

Cui W., Knebe A., Yepes G., Pearce F., Power C., Dave R., Arth A., Borgani S., Dolag K., Elahi P., et al.: *The Three Hundred project: a large catalogue of theoretically modelled galaxy clusters for cosmological and astrophysical applications.* MNRAS **480**, 2898 (2018)

Curti M., Maiolino R., Curtis-Lake E., Chevallard J., Carniani S., D'Eugenio F., Looser T. J., Scholtz J., Charlot S., Cameron A., et al.: *JADES: Insights into the low-mass end of the mass-metallicity-SFR relation at 3 < z < 10 from deep JWST/NIRSpec spectroscopy.* A&A **684**, A75 (2024)

Curtis-Lake E., Carniani S., Cameron A., Charlot S., Jakobsen P., Maiolino R., Bunker A., Witstok J., Smit R., Chevallard J., et al.: *Spectroscopic confirmation of four metal-poor galaxies at z = 10.3-13.2.* Nature Astronomy **7**, 622 (2023)

Da Rocha C., Ziegler B. L., & Mendes de Oliveira C.: *Intragroup diffuse light in compact groups of galaxies - II. HCG 15, 35 and 51.* MNRAS **388**, 1433 (2008)

Daddi E., Renzini A., Pirzkal N., Cimatti A., Malhotra S., Stiavelli M., Xu C., Pasquali A., Rhoads J. E., Brusa M., et al.: *Passively Evolving Early-Type Galaxies at 1.4 <∼z <∼2.5 in the Hubble Ultra Deep Field.* ApJ **626**, 680 (2005)

Damiano A., Valentini M., Borgani S., Tornatore L., Murante G., Ragagnin A., Ragone-Figueroa C., & Dolag K.: *Dynamical friction and the evolution of black holes in cosmological simulations: A new implementation in OpenGadget3.* A&A **692**, A81 (2024)

Danieli S., van Dokkum P., Trujillo-Gomez S., Kruijssen J. M. D., Romanowsky A. J., Carlsten S., Shen Z., Li J., Abraham R., Brodie J., et al.: *NGC 5846-UDG1: A Galaxy Formed Mostly by Star Formation in Massive, Extremely Dense Clumps of Gas.* ApJL **927**, L28 (2022)

Dannerbauer H., Kurk J. D., De Breuck C., Wylezalek D., Santos J. S., Koyama Y., Seymour N., Tanaka M., Hatch N., Altieri B., et al.: *An excess of dusty starbursts related to the Spiderweb galaxy.* A&A **570**, A55 (2014)

Davé R., Anglés-Alcázar D., Narayanan D., Li Q., Rafieferantsoa M. H., & Appleby S.: *SIMBA: Cosmological simulations with black hole growth and feedback.* MNRAS **486**, 2827 (2019)

Davis S. W. & Laor A.: *The Radiative Efficiency of Accretion Flows in Individual Active Galactic Nuclei.* ApJ **728**, 98 (2011)

Davison T. A., Norris M. A., Pfeffer J. L., Davies J. J., & Crain R. A.: *An EAGLE's view of ex situ galaxy growth.* MNRAS **497**, 81 (2020)

de Graaff A., Rix H.-W., Carniani S., Suess K. A., Charlot S., Curtis-Lake E., Arribas S., Baker W. M., Boyett K., Bunker A. J., et al.: *Ionised gas kinematics and dynamical masses of $z \gtrsim 6$ galaxies from JADES/NIRSpec high-resolution spectroscopy.* A&A **684**, A87 (2024a)

de Graaff A., Setton D. J., Brammer G., Cutler S., Suess K. A., Labbe I., Leja J., Weibel A., Maseda M. V., Whitaker K. E., et al.: *Efficient formation of a massive quiescent galaxy at redshift 4.9.* arXiv e-prints, arXiv:2404 (2024b)

De Lucia G., Kauffmann G., Springel V., White S. D. M., Lanzoni B., Stoehr F., Tormen G., & Yoshida N.: *Substructures in cold dark matter haloes.* MNRAS **348**, 333 (2004)

De Lucia G. & Blaizot J.: *The hierarchical formation of the brightest cluster galaxies.* MNRAS **375**, 2 (2007)

De Lucia G., Fontanot F., Xie L., & Hirschmann M.: *Tracing the quenching journey across cosmic time.* A&A **687**, A68 (2024)

de Vaucouleurs G.: *Recherches sur les Nebuleuses Extragalactiques.* Annales d'Astrophysique **11**, 247 (1948)

Dehnen W. & Aly H.: *Improving convergence in smoothed particle hydrodynamics simulations without pairing instability.* MNRAS **425**, 1068 (2012)

Dekel A. & Silk J.: *The Origin of Dwarf Galaxies, Cold Dark Matter, and Biased Galaxy Formation.* ApJ **303**, 39 (1986)

Dekel A. & Birnboim Y.: *Galaxy bimodality due to cold flows and shock heating.* MNRAS **368**, 2 (2006)

Dekel A. & Cox T. J.: *The dissipative merger progenitors of elliptical galaxies.* MNRAS **370**, 1445 (2006)

Dekel A. & Birnboim Y.: *Gravitational quenching in massive galaxies and clusters by clumpy accretion.* MNRAS **383**, 119 (2008)

DeMaio T., Gonzalez A. H., Zabludoff A., Zaritsky D., Connor T., Donahue M., & Mulchaey J. S.: *Lost but not forgotten: intracluster light in galaxy groups and clusters.* MNRAS **474**, 3009 (2018)

Desprez G., Martis N. S., Asada Y., Sawicki M., Willott C. J., Muzzin A., Abraham R. G., Bradač M., Brammer G., Estrada-Carpenter V., et al.: *ΛCDM not dead yet: massive high-z Balmer break galaxies are less common than previously reported.* arXiv e-prints, arXiv:2310 (2023)

D'Eugenio F., Pérez-González P. G., Maiolino R., Scholtz J., Perna M., Circosta C., Übler H., Arribas S., Böker T., Bunker A. J., et al.: *A fast-rotator post-starburst galaxy quenched by supermassive black-hole feedback at $z = 3$.* Nature Astronomy **8**, 1443 (2024)

Di Cintio A., Brook C. B., Dutton A. A., Macciò A. V., Obreja A., & Dekel A.: *NIHAO - XI. Formation of ultra-diffuse galaxies by outflows.* MNRAS **466**, L1 (2017)

Di Teodoro E. M., Posti L., Ogle P. M., Fall S. M., & Jarrett T.: *Rotation curves and scaling relations of extremely massive spiral galaxies.* MNRAS **507**, 5820 (2021)

Ding X., Onoue M., Silverman J. D., Matsuoka Y., Izumi T., Strauss M. A., Jahnke K., Phillips C. L., Li J., Volonteri M., et al.: *Detection of stellar light from quasar host galaxies at redshifts above 6.* arXiv e-prints, arXiv:2211 (2022)

Dolag K., Jubelgas M., Springel V., Borgani S., & Rasia E.: *Thermal Conduction in Simulated Galaxy Clusters.* ApJ **606**, L97 (2004)

Dolag K., Hansen F. K., Roncarelli M., & Moscardini L.: *The imprints of local superclusters on the Sunyaev-Zel'dovich signals and their detectability with Planck.* MNRAS **363**, 29 (2005a)

Dolag K., Vazza F., Brunetti G., & Tormen G.: *Turbulent gas motions in galaxy cluster simulations: the role of smoothed particle hydrodynamics viscosity.* MNRAS **364**, 753 (2005b)

Dolag K., Bykov A. M., & Diaferio A.: *Non-Thermal Processes in Cosmological Simulations.* Space Sci. Rev. **134**, 311 (2008)

Dolag K., Borgani S., Murante G., & Springel V.: *Substructures in hydrodynamical cluster simulations.* MNRAS **399**, 497 (2009)

Dolag K., Murante G., & Borgani S.: *Dynamical difference between the cD galaxy and the diffuse, stellar component in simulated galaxy clusters.* MNRAS **405**, 1544 (2010)

Dolag K., Sorce J. G., Pilipenko S., Hernández-Martínez E., Valentini M., Gottlöber S., Aghanim N., & Khabibullin I.: *Simulating the LOcal Web (SLOW). I. Anomalies in the local density field.* A&A **677**, A169 (2023)

Dolag K., Remus R.-S., Valenzuela L. M., Kimmig L. C., Seidel B., Fortune S., Stoiber J., Ivleva A., Hoffmann T., Biffi V., et al.: *Encyclopedia Magneticum: Scaling Relations from Cosmic Dawn to Present Day.* arXiv e-prints, arXiv:2504 (2025)

Dome T., Tacchella S., Fialkov A., Dekel A., Ginzburg O., Lapiner S., & Looser T. J.: *Mini-Quenching of High-Redshift Galaxies by Bursty Star Formation.* arXiv e-prints, arXiv:2305 (2023)

Donahue M., Connor T., Fogarty K., Li Y., Voit G. M., Postman M., Koekemoer A., Moustakas J., Bradley L., & Ford H.: *Ultraviolet Morphology and Unobscured UV Star Formation Rates of CLASH Brightest Cluster Galaxies.* ApJ **805**, 177 (2015)

Donnan C. T., McLeod D. J., Dunlop J. S., McLure R. J., Carnall A. C., Begley R., Cullen F., Hamadouche M. L., Bowler R. A. A., Magee D., et al.: *The evolution of the galaxy UV luminosity function at redshifts $z \simeq 8$ - 15 from deep JWST and ground-based near-infrared imaging.* MNRAS **518**, 6011 (2023)

Donnari M., Pillepich A., Nelson D., Marinacci F., Vogelsberger M., & Hernquist L.: *Quenched fractions in the IllustrisTNG simulations: comparison with observations and other theoretical models.* MNRAS **506**, 4760 (2021)

Donnert J., Dolag K., Brunetti G., & Cassano R.: *Rise and fall of radio haloes in simulated merging galaxy clusters.* MNRAS **429**, 3564 (2013)

Dressler A.: *Galaxy morphology in rich clusters: implications for the formation and evolution of galaxies.* ApJ **236**, 351 (1980)

D'Silva J. C. J., Driver S. P., Lagos C. D. P., Robotham A. S. G., Bellstedt S., Davies L. J. M., Thorne J. E., Bland-Hawthorn J., Bravo M., Holwerda B., et al.: *GAMA/DEVILS: cosmic star formation and AGN activity over 12.5 billion years.* MNRAS **524**, 1448 (2023a)

D'Silva J. C. J., Lagos C. D. P., Davies L. J. M., Lovell C. C., & Vijayan A. P.: *Unveiling the main sequence of galaxies at $z \geq 5$ with the JWST: predictions from simulations.* MNRAS **518**, 456 (2023b)

Dubois Y., Pichon C., Welker C., Le Borgne D., Devriendt J., Laigle C., Codis S., Pogosyan D., Arnouts S., Benabed K., et al.: *Dancing in the dark: galactic properties trace spin swings along the cosmic web.* MNRAS **444**, 1453 (2014)

Dubois Y., Peirani S., Pichon C., Devriendt J., Gavazzi R., Welker C., & Volonteri M.: *The HORIZON-AGN simulation: morphological diversity of galaxies promoted by AGN feedback.* MNRAS **463**, 3948 (2016)

Duncan K., Conselice C. J., Mortlock A., Hartley W. G., Guo Y., Ferguson H. C., Davé R., Lu Y., Ownsworth J., Ashby M. L. N., et al.: *The mass evolution of the first galaxies: stellar mass functions and star formation rates at 4 < z < 7 in the CANDELS GOODS-South field.* MNRAS **444**, 2960 (2014)

Durkalec A., Le Fèvre O., de la Torre S., Pollo A., Cassata P., Garilli B., Le Brun V., Lemaux B. C., Maccagni D., Pentericci L., et al.: *Stellar mass to halo mass relation from galaxy clustering in VUDS: a high star formation efficiency at z ≈ 3.* A&A **576**, L7 (2015)

Dutton A. A., Macciò A. V., Dekel A., Wang L., Stinson G., Obreja A., Di Cintio A., Brook C., Buck T., & Kang X.: *NIHAO IX: the role of gas inflows and outflows in driving the contraction and expansion of cold dark matter haloes.* MNRAS **461**, 2658 (2016)

Eckert D., Jauzac M., Shan H., Kneib J.-P., Erben T., Israel H., Jullo E., Klein M., Massey R., Richard J., & Tchernin C.: *Warm-hot baryons comprise 5-10 per cent of filaments in the cosmic web.* Nature **528**, 105 (2015)

Eckert D., Jauzac M., Vazza F., Owers M. S., Kneib J. P., Tchernin C., Intema H., & Knowles K.: *A shock front at the radio relic of Abell 2744.* MNRAS **461**, 1302 (2016)

Eddington A. S.: *The Internal Constitution of the Stars.* (1926)

Edwards L. O. V., Alpert H. S., Trierweiler I. L., Abraham T., & Beizer V. G.: *Stellar populations of BCGs, close companions and intracluster light in Abell 85, Abell 2457 and IIZw108.* MNRAS **461**, 230 (2016)

Edwards L. O. V., Salinas M., Stanley S., Holguin West P. E., Trierweiler I., Alpert H., Coelho P., Koppaka S., Tremblay G. R., Martel H., & Li Y.: *Clocking the formation of today's largest galaxies: wide field integral spectroscopy of brightest cluster galaxies and their surroundings.* MNRAS **491**, 2617 (2020)

Edwards L. O. V., Hamel K. A. S. J., Shy J. C., Hernandez J., Holguin Luna P., Higgins D. J., Chawla T., Gavidia A., & Cole S.: *Stellar populations and merger rates of brightest cluster galaxies a billion years ago: SDSS MaNGA IFU spectroscopy.* MNRAS **530**, 3924 (2024)

Efstathiou G. & Jones B. J. T.: *Angular momentum and the formation of galaxies by gravitational instability.* Comments on Astrophysics **8**, 169 (1980)

Eggen O. J., Lynden-Bell D., & Sandage A. R.: *Evidence from the motions of old stars that the Galaxy collapsed.* ApJ **136**, 748 (1962)

Einasto J.: *On the Construction of a Composite Model for the Galaxy and on the Determination of the System of Galactic Parameters.* Trudy Astrofizicheskogo Instituta Alma-Ata **5**, 87 (1965)

Eisenstein D. J. & Hu W.: *Baryonic Features in the Matter Transfer Function.* ApJ **496**, 605 (1998)

Eisenstein D. J., Willott C., Alberts S., Arribas S., Bonaventura N., Bunker A. J., Cameron A. J., Carniani S., Charlot S., Curtis-Lake E., et al.: *Overview of the JWST Advanced Deep Extragalactic Survey (JADES).* arXiv e-prints, arXiv:2306 (2023)

Ellien A., Slezak E., Martinet N., Durret F., Adami C., Gavazzi R., Rabaça C. R., Da Rocha C., & Epitácio Pereira D. N.: *DAWIS: a detection algorithm with wavelets for intracluster light studies.* A&A **649**, A38 (2021)

Ellison S. L., Wilkinson S., Woo J., Leung H.-H., Wild V., Bickley R. W., Patton D. R., Quai S., & Gwyn S.: *Galaxy mergers can rapidly shut down star formation.* MNRAS **517**, L92 (2022)

Emsellem E., Cappellari M., Krajnović D., van de Ven G., Bacon R., Bureau M., Davies R. L., de Zeeuw P. T., Falcón-Barroso J., Kuntschner H., et al.: *The SAURON project - IX. A kinematic classification for early-type galaxies.* MNRAS **379**, 401 (2007)

Emsellem E., Cappellari M., Krajnović D., Alatalo K., Blitz L., Bois M., Bournaud F., Bureau M., Davies R. L., Davis T. A., et al.: *The ATLAS^{3D} project - III. A census of the stellar angular momentum within the effective radius of early-type galaxies: unveiling the distribution of fast and slow rotators.* MNRAS **414**, 888 (2011)

Endsley R., Stark D. P., Whitler L., Topping M. W., Johnson B. D., Robertson B., Tacchella S., Alberts S., Baker W. M., Bhatawdekar R., et al.: *The Star-forming and Ionizing Properties of Dwarf z∼6-9 Galaxies in JADES: Insights on Bursty Star Formation and Ionized Bubble Growth.* arXiv e-prints, arXiv:2306 (2023)

Escala I., Gilbert K. M., Kirby E. N., Wojno J., Cunningham E. C., & Guhathakurta P.: *Elemental Abundances in M31: A Comparative Analysis of Alpha and Iron Element Abundances in the the Outer Disk, Giant Stellar Stream, and Inner Halo of M31.* ApJ **889**, 177 (2020)

Faber S. M.: *Variations in Spectral-Energy Distributions and Absorption-Line Strengths among Elliptical Galaxies.* ApJ **179**, 731 (1973)

Faber S. M. & Gallagher J. S.: *Masses and mass-to-light ratios of galaxies.* ARA&A **17**, 135 (1979)

Fabian A. C.: *Observational Evidence of Active Galactic Nuclei Feedback.* ARA&A **50**, 455 (2012)

Fabjan D., Borgani S., Tornatore L., Saro A., Murante G., & Dolag K.: *Simulating the effect of active galactic nuclei feedback on the metal enrichment of galaxy clusters.* MNRAS **401**, 1670 (2010)

Falcón-Barroso J., Lyubenova M., & van de Ven G.: *Angular Momentum across the Hubble sequence from the CALIFA survey.* In: Cappellari M. & Courteau S. (eds.): *Galaxy Masses as Constraints of Formation Models.* **311**, 78 (2015)

Fall S. M.: *Dissipation, merging and the rotation of galaxies.* Nature **281**, 200 (1979)

Fall S. M. & Efstathiou G.: *Formation and rotation of disc galaxies with haloes.* MNRAS **193**, 189 (1980)

Fall S. M. & Romanowsky A. J.: *Angular Momentum and Galaxy Formation Revisited: Effects of Variable Mass-to-light Ratios.* ApJ **769**, L26 (2013)

Fan X., Bañados E., & Simcoe R. A.: *Quasars and the Intergalactic Medium at Cosmic Dawn.* ARA&A **61**, 373 (2023)

Farina E. P., Schindler J.-T., Walter F., Bañados E., Davies F. B., Decarli R., Eilers A.-C., Fan X., Hennawi J. F., Mazzucchelli C., et al.: *The X-shooter/ALMA Sample of Quasars in the Epoch of Reionization. II. Black Hole Masses, Eddington Ratios, and the Formation of the First Quasars.* ApJ **941**, 106 (2022)

Faucher-Giguère C.-A.: *A cosmic UV/X-ray background model update.* MNRAS **493**, 1614 (2020)

Feldmann R. & Mayer L.: *The Argo simulation - I. Quenching of massive galaxies at high redshift as a result of cosmological starvation.* MNRAS **446**, 1939 (2015)

Feldmeier J. J., Mihos J. C., Morrison H. L., Harding P., Kaib N., & Dubinski J.: *Deep CCD Surface Photometry of Galaxy Clusters. II. Searching for Intracluster Starlight in Non-cD clusters.* ApJ **609**, 617 (2004)

Ferland G. J., Korista K. T., Verner D. A., Ferguson J. W., Kingdon J. B., & Verner E. M.: *CLOUDY 90: Numerical Simulation of Plasmas and Their Spectra.* PASP **110**, 761 (1998)

Ferragamo A., Macías-Pérez J. F., Pelgrims V., Ruppin F., De Petris M., Mayet F., Muñoz-Echeverría M., Perotto L., & Pointecouteau E.: *Comparison of hydrostatic and lensing cluster mass estimates: A pilot study in MACS J0647.7+7015.* A&A **661**, A65 (2022)

Ferré-Mateu A., Gannon J. S., Forbes D. A., Buzzo M. L., Romanowsky A. J., & Brodie J.: *The star formation histories of quiescent ultra-diffuse galaxies and their dependence on environment and globular cluster richness.* MNRAS (2023)

Finkelstein S. L., Ryan J., Russell E., Papovich C., Dickinson M., Song M., Somerville R. S., Ferguson H. C., Salmon B., Giavalisco M., Koekemoer A. M., et al.: *The Evolution of the Galaxy Rest-frame Ultraviolet Luminosity Function over the First Two Billion Years.* ApJ **810**, 71 (2015)

Finkelstein S. L., Leung G. C. K., Bagley M. B., Dickinson M., Ferguson H. C., Papovich C., Akins H. B., Arrabal Haro P., Davé R., Dekel A., et al.: *The Complete CEERS Early Universe Galaxy Sample: A Surprisingly Slow Evolution of the Space Density of Bright Galaxies at $z \sim 8.5$–14.5.* ApJ **969**, L2 (2024)

Finkelstein S. L., Bagley M. B., Arrabal Haro P., Dickinson M., Ferguson H. C., Kartaltepe J. S., Kocevski D. D., Koekemoer A. M., Lotz J. M., Papovich C., et al.: *The Cosmic Evolution Early Release Science Survey (CEERS).* ApJ **983**, L4 (2025)

Forbes D. A., Alabi A., Romanowsky A. J., Brodie J. P., & Arimoto N.: *Globular clusters in Coma cluster ultra-diffuse galaxies (UDGs): evidence for two types of UDG?* MNRAS **492**, 4874 (2020)

Forbes D. A. & Gannon J.: *Do ultra diffuse galaxies with rich globular clusters systems have overly massive haloes?* MNRAS **528**, 608 (2024)

Forrest B., Marsan Z. C., Annunziatella M., Wilson G., Muzzin A., Marchesini D., Cooper M. C., Chan J. C. C., McConachie I., Gomez P., et al.: *The Massive Ancient Galaxies at $z > 3$ NEar-infrared (MAGAZ3NE) Survey: Confirmation of Extremely Rapid Star Formation and Quenching Timescales for Massive Galaxies in the Early Universe.* ApJ **903**, 47 (2020)

Forrest B., Cooper M. C., Muzzin A., Wilson G., Marchesini D., McConachie I., Gomez P., Annunziatella M., Marsan Z. C., Braspenning J., et al.: *MAGAZ3NE: Massive, Extremely Dusty Galaxies at $z \sim 2$ Lead to Photometric Overestimation of Number Densities of the Most Massive Galaxies at $3 < z < 4$.* arXiv e-prints, arXiv:2404 (2024)

Forrest B., Muzzin A., Marchesini D., Pan R., Ozden N., Antwi-Danso J., Chang W., Cooper M. C., Edward A. H., Gomez P., et al.: *A massive, evolved slow-rotating galaxy in the early Universe.* arXiv e-prints, arXiv:2508 (2025)

Fortuné S., Remus R.-S., Kimmig L. C., Burkert A., & Dolag K.: *Die Hard: The On-Off-Cycle of Galaxies on the Star Formation Main Sequence.* arXiv e-prints, arXiv:2503 (2025)

Franx M., van Dokkum P. G., Förster Schreiber N. M., Wuyts S., Labbé I., & Toft S.: *Structure and Star Formation in Galaxies out to $z = 3$: Evidence for Surface Density Dependent Evolution and Upsizing.* ApJ **688**, 770 (2008)

Freeman K. & Bland-Hawthorn J.: *The New Galaxy: Signatures of Its Formation.* ARA&A **40**, 487 (2002)

Fu H., Shankar F., Ayromlou M., Koutsouridou I., Cattaneo A., Bertemes C., Bellstedt S., Martín-Navarro I., Leja J., Allevato V., et al.: *Unveiling the (in)consistencies among the galaxy stellar mass function, star formation histories, satellite abundances, and intracluster light from a semi-empirical perspective.* MNRAS **532**, 177 (2024)

Fudamoto Y., Oesch P. A., Schouws S., Stefanon M., Smit R., Bouwens R. J., Bowler R. A. A., Endsley R., Gonzalez V., Inami H., et al.: *Normal, dust-obscured galaxies in the epoch of reionization.* Nature **597**, 489 (2021)

Fudamoto Y., Inoue A. K., & Sugahara Y.: *Red Spiral Galaxies at Cosmic Noon Unveiled in the First JWST Image.* ApJ **938**, L24 (2022)

Fuhrmann K.: *Nearby stars of the Galactic disk and halo.* A&A **338**, 161 (1998)

Furnell K. E., Collins C. A., Kelvin L. S., Baldry I. K., James P. A., Manolopoulou M., Mann R. G., Giles P. A., Bermeo A., Hilton M., et al.: *The growth of intracluster light in XCS-HSC galaxy clusters from 0.1 < z < 0.5.* MNRAS **502**, 2419 (2021)

Gabor J. M. & Davé R.: *Hot gas in massive haloes drives both mass quenching and environment quenching.* MNRAS **447**, 374 (2015)

Gaia Collaboration, Vallenari A., Brown A. G. A., Prusti T., de Bruijne J. H. J., Arenou F., Babusiaux C., Biermann M., Creevey O. L., Ducourant C., et al.: *Gaia Data Release 3. Summary of the content and survey properties.* A&A **674**, A1 (2023)

Gannon J. S., Buzzo M. L., Ferré-Mateu A., Forbes D. A., Brodie J. P., & Romanowsky A. J.: *Keck spectroscopy of NGC 1052-DF9: stellar populations in the context of the NGC 1052 group.* MNRAS **524**, 2624 (2023)

Gannon J. S., Kimmig L. C., Forbes D. A., Brodie J. P., Valenzuela L. M., Remus R.-S., Pfeffer J. L., & Dolag K.: *Analysis of Galaxies at the Extremes: Failed Galaxy Progenitors in the MAGNETICUM Simulations.* The Open Journal of Astrophysics **8**, E150 (2025)

Gao T., Mendel J. T., Kimmig L. C., Lagos C. d. P., Remus R.-S., Wisnioski E., & Grasha K.: *The influence of external environment at cosmic noon on the subsequent evolution of galaxy stellar mass.* MNRAS **545**, staf2172 (2026)

Gaspari M., Ruszkowski M., & Oh S. P.: *Chaotic cold accretion on to black holes.* MNRAS **432**, 3401 (2013)

Genzel R., Tacconi L. J., Gracia-Carpio J., Sternberg A., Cooper M. C., Shapiro K., Bolatto A., Bouché N., Bournaud F., Burkert A., et al.: *A study of the gas-star formation relation over cosmic time.* MNRAS **407**, 2091 (2010)

Giallongo E., Menci N., Grazian A., Gallozzi S., Castellano M., Fiore F., Fontana A., Pentericci L., Boutsia K., Paris D., et al.: *Diffuse Optical Intracluster Light as a Measure of Stellar Tidal Stripping: The Cluster CL0024+17 at z ∼0.4 Observed at the Large Binocular Telescope.* ApJ **781**, 24 (2014)

Gingold R. A. & Monaghan J. J.: *Smoothed particle hydrodynamics: theory and application to non-spherical stars.* MNRAS **181**, 375 (1977)

Giovannini G., Tordi M., & Feretti L.: *Radio halo and relic candidates from the NRAO VLA Sky Survey.* New A **4**, 141 (1999)

Girardi M., Giuricin G., Mardirossian F., Mezzetti M., & Boschin W.: *Optical Mass Estimates of Galaxy Clusters.* ApJ **505**, 74 (1998)

Glazebrook K., Nanayakkara T., Schreiber C., Lagos C., Kawinwanichakij L., Jacobs C., Chittenden H., Brammer G., Kacprzak G. G., Labbe I., et al.: *An extraordinarily massive galaxy that formed its stars at zrsim*11. arXiv e-prints, arXiv:2308 (2023)

Gogarten S. M., Dalcanton J. J., Williams B. F., Roškar R., Holtzman J., Seth A. C., Dolphin A., Weisz D., Cole A., Debattista V. P., et al.: *The Advanced Camera for Surveys Nearby Galaxy Survey Treasury. V. Radial Star Formation History of NGC 300.* ApJ **712**, 858 (2010)

Golden-Marx J. B. & Miller C. J.: *The Impact of Environment on the Stellar Mass-Halo Mass Relation.* ApJ **860**, 2 (2018)

Golden-Marx J. B., Zhang Y., Ogando R. L. C., Yanny B., da Silva Pereira M. E., Hilton M., Aguena M., Allam S., Andrade-Oliveira F., Bacon D., et al.: *The hierarchical growth of bright central galaxies and intracluster light as traced by the magnitude gap.* MNRAS **538**, 622 (2025)

Gómez-Guijarro C., Elbaz D., Xiao M., Kokorev V. I., Magdis G. E., Magnelli B., Daddi E., Valentino F., Sargent M. T., Dickinson M., et al.: *GOODS-ALMA 2.0: Starbursts in the main sequence reveal compact star formation regulating galaxy evolution prequenching.* A&A **659**, A196 (2022)

Gonzalez A. H., Zaritsky D., & Zabludoff A. I.: *A Census of Baryons in Galaxy Clusters and Groups.* ApJ **666**, 147 (2007)

Gonzalez A. H., Sivanandam S., Zabludoff A. I., & Zaritsky D.: *Galaxy Cluster Baryon Fractions Revisited.* ApJ **778**, 14 (2013)

Goto T., Yamauchi C., Fujita Y., Okamura S., Sekiguchi M., Smail I., Bernardi M., & Gomez P. L.: *The morphology-density relation in the Sloan Digital Sky Survey.* MNRAS **346**, 601 (2003)

Gould K. M. L., Brammer G., Valentino F., Whitaker K. E., Weaver J. R., Lagos C. d. P., Rizzo F., Franco M., Hsieh B.-C., Ilbert O., et al.: *COSMOS2020: Exploring the Dawn of Quenching for Massive Galaxies at 3 < z < 5 with a New Color-selection Method.* AJ **165**, 248 (2023)

Govoni F., Murgia M., Markevitch M., Feretti L., Giovannini G., Taylor G. B., & Carretti E.: *A search for diffuse radio emission in the relaxed, cool-core galaxy clusters A1068, A1413, A1650, A1835, A2029, and Ophiuchus.* A&A **499**, 371 (2009)

Grandis S., Ghirardini V., Bocquet S., Garrel C., Mohr J. J., Liu A., Kluge M., Kimmig L., Reiprich T. H., Alarcon A., et al.: *The SRG/eROSITA All-Sky Survey. Dark Energy Survey*

year 3 weak gravitational lensing by eRASS1 selected galaxy clusters. A&A **687**, A178 (2024)

Graur O.: *The ancient Egyptian personification of the Milky Way as the Sky Goddess Nut: an astronomical and cross-cultural analysis.* Journal of Astronomical History and Heritage **27**, 28 (2024)

Greggio L. & Renzini A.: *The binary model for type I supernovae - Theoretical rates.* A&A **118**, 217 (1983)

Grillo C., Suyu S. H., Rosati P., Mercurio A., Balestra I., Munari E., Nonino M., Caminha G. B., Lombardi M., De Lucia G., et al.: *CLASH-VLT: Insights on the Mass Substructures in the Frontier Fields Cluster MACS J0416.1-2403 through Accurate Strong Lens Modeling.* ApJ **800**, 38 (2015)

Grisoni V., Spitoni E., Matteucci F., Recio-Blanco A., de Laverny P., Hayden M., Mikolaitis Ŝ., & Worley C. C.: *The AMBRE project: chemical evolution models for the Milky Way thick and thin discs.* MNRAS **472**, 3637 (2017)

Grudić M. Y., Guszejnov D., Hopkins P. F., Offner S. S. R., & Faucher-Giguère C.-A.: *STARFORGE: Towards a comprehensive numerical model of star cluster formation and feedback.* MNRAS **506**, 2199 (2021)

Gunn J. E. & Gott J. R., III: *On the Infall of Matter Into Clusters of Galaxies and Some Effects on Their Evolution.* ApJ **176**, 1 (1972)

Haardt F. & Madau P.: *Modelling the UV/X-ray cosmic background with CUBA.* In: Neumann D. M. & Tran J. T. V. (eds.): *Clusters of Galaxies and the High Redshift Universe Observed in X-rays.* 64 (2001)

Haardt F. & Madau P.: *Radiative Transfer in a Clumpy Universe. IV. New Synthesis Models of the Cosmic UV/X-Ray Background.* ApJ **746**, 125 (2012)

Haggar R., Gray M. E., Pearce F. R., Knebe A., Cui W., Mostoghiu R., & Yepes G.: *The Three Hundred project: backsplash galaxies in simulations of clusters.* MNRAS **492**, 6074 (2020)

Haggar R., De Luca F., De Petris M., Sazonova E., Taylor J. E., Knebe A., Gray M. E., Pearce F. R., Contreras-Santos A., Cui W., et al.: *Reconsidering the dynamical states of galaxy clusters using PCA and UMAP.* MNRAS **532**, 1031 (2024)

Hahn O., Martizzi D., Wu H.-Y., Evrard A. E., Teyssier R., & Wechsler R. H.: *rhapsody-g simulations - I. The cool cores, hot gas and stellar content of massive galaxy clusters.* MNRAS **470**, 166 (2017)

Haines C. P., Pereira M. J., Smith G. P., Egami E., Babul A., Finoguenov A., Ziparo F., McGee S. L., Rawle T. D., Okabe N., & Moran S. M.: *LoCuSS: The Slow Quenching of Star Formation in Cluster Galaxies and the Need for Pre-processing.* ApJ **806**, 101 (2015)

Hamadouche M. L., Whitaker K. E., Valentino F., Antwi-Danso J., Ito K., Beverage A., Zhu P., Brammer G., Kokorev V., de Lucia G., et al.: *DeepDive: Tracing the early quenching pathways of massive quiescent galaxies at $z > 3$ from their star-formation histories and chemical abundances.* arXiv e-prints, arXiv:2602 (2026)

Harikane Y., Inoue A. K., Mawatari K., Hashimoto T., Yamanaka S., Fudamoto Y., Matsuo H., Tamura Y., Dayal P., Yung L. Y. A., et al.: *A Search for H-Dropout Lyman Break Galaxies at z 12-16.* ApJ **929**, 1 (2022a)

Harikane Y., Ono Y., Ouchi M., Liu C., Sawicki M., Shibuya T., Behroozi P. S., He W., Shimasaku K., Arnouts S., et al.: *GOLDRUSH. IV. Luminosity Functions and Clustering Revealed with 4,000,000 Galaxies at z 2-7: Galaxy-AGN Transition, Star Formation Efficiency, and Implication for Evolution at z > 10.* ApJS **259**, 20 (2022b)

Harikane Y., Nakajima K., Ouchi M., Umeda H., Isobe Y., Ono Y., Xu Y., & Zhang Y.: *Pure Spectroscopic Constraints on UV Luminosity Functions and Cosmic Star Formation History From 25 Galaxies at $z_{\rm spec} = 8.61 - 13.20$ Confirmed with JWST/NIRSpec.* arXiv e-prints, arXiv:2304 (2023a)

Harikane Y., Ouchi M., Oguri M., Ono Y., Nakajima K., Isobe Y., Umeda H., Mawatari K., & Zhang Y.: *A Comprehensive Study of Galaxies at $z = 9$–16 Found in the Early JWST Data: Ultraviolet Luminosity Functions and Cosmic Star Formation History at the Pre-reionization Epoch.* ApJS **265**, 5 (2023b)

Harikane Y., Zhang Y., Nakajima K., Ouchi M., Isobe Y., Ono Y., Hatano S., Xu Y., & Umeda H.: *JWST/NIRSpec First Census of Broad-Line AGNs at z = 4–7: Detection of 10 Faint AGNs with M_BH∼10^6-10^7 M_sun and Their Host Galaxy Properties.* arXiv e-prints, arXiv:2303 (2023c)

Harris W. E., Remus R.-S., Harris G. L. H., & Babyk I. V.: *Measuring Dark Matter in Galaxies: The Mass Fraction within Five Effective Radii.* ApJ **905**, 28 (2020)

Hartley A. I., Nelson E. J., Suess K. A., Garcia A. M., Park M., Hernquist L., Bezanson R., Nevin R., Pillepich A., Schechter A. L., et al.: *The first quiescent galaxies in TNG300.* MNRAS **522**, 3138 (2023)

Harvey T., Conselice C. J., Adams N. J., Austin D., Juodžbalis I., Trussler J., Li Q., Ormerod K., Ferreira L., Lovell C. C., et al.: *EPOCHS. IV. SED Modeling Assumptions and Their Impact on the Stellar Mass Function at $6.5 \leq z \leq 13.5$ Using PEARLS and Public JWST Observations.* ApJ **978**, 89 (2025)

Hasselquist S., Hayes C. R., Lian J., Weinberg D. H., Zasowski G., Horta D., Beaton R., Feuillet D. K., Garro E. R., Gallart C., et al.: *APOGEE Chemical Abundance Patterns of the Massive Milky Way Satellites.* ApJ **923**, 172 (2021)

Hayden M. R., Bovy J., Holtzman J. A., Nidever D. L., Bird J. C., Weinberg D. H., Andrews B. H., Majewski S. R., Allende Prieto C., Anders F., et al.: *Chemical Cartography with APOGEE: Metallicity Distribution Functions and the Chemical Structure of the Milky Way Disk.* ApJ **808**, 132 (2015)

Haywood M., Lehnert M. D., Di Matteo P., Snaith O., Schultheis M., Katz D., & Gómez A.: *When the Milky Way turned off the lights: APOGEE provides evidence of star formation quenching in our Galaxy.* A&A **589**, A66 (2016)

Helmi A., Babusiaux C., Koppelman H. H., Massari D., Veljanoski J., & Brown A. G. A.: *The merger that led to the formation of the Milky Way's inner stellar halo and thick disk.* Nature **563**, 85 (2018)

Hernández-Martínez E., Dolag K., Seidel B., Sorce J. G., Aghanim N., Pilipenko S., Gottlöber S., Lebeau T., & Valentini M.: *Simulating the LOcal Web (SLOW). II. Properties of local galaxy clusters.* A&A **687**, A253 (2024)

Herwig F.: *Evolution of Asymptotic Giant Branch Stars.* ARA&A **43**, 435 (2005)

Hewitt G., Sarron F., Balogh M. L., Rudnick G., Bahé Y., Baxter D. C., Castignani G., Cerulo P., Cooper M. C., Demarco R., et al.: *Distinct origins of environmentally quenched galaxies in the core and outer virialized regions of massive clusters at $0.8 < z < 1.5$.* MNRAS **541**, 409 (2025)

Hilton M., Hasselfield M., Sifón C., Baker A. J., Barrientos L. F., Battaglia N., Bond J. R., Crichton D., Das S., Devlin M. J., et al.: *The Atacama Cosmology Telescope: the stellar content of galaxy clusters selected using the Sunyaev-Zel'dovich effect.* MNRAS **435**, 3469 (2013)

Hilz M., Naab T., Ostriker J. P., Thomas J., Burkert A., & Jesseit R.: *Relaxation and stripping - The evolution of sizes, dispersions and dark matter fractions in major and minor mergers of elliptical galaxies.* MNRAS **425**, 3119 (2012)

Hirschmann M., Dolag K., Saro A., Bachmann L., Borgani S., & Burkert A.: *Cosmological simulations of black hole growth: AGN luminosities and downsizing.* MNRAS **442**, 2304 (2014)

Hockney R. W. & Eastwood J. W.: *Computer Simulation Using Particles.* (1981)

Holmberg E.: *A photographic photometry of extragalactic nebulae.* Meddelanden fran Lunds Astronomiska Observatorium Serie II **136**, 1 (1958)

Hopkins P. F., Kereš D., Oñorbe J., Faucher-Giguère C.-A., Quataert E., Murray N., & Bullock J. S.: *Galaxies on FIRE (Feedback In Realistic Environments): stellar feedback explains cosmologically inefficient star formation.* MNRAS **445**, 581 (2014)

Hopkins P. F.: *A new class of accurate, mesh-free hydrodynamic simulation methods.* MNRAS **450**, 53 (2015)

Hopkins P. F., Grudic M. Y., Su K.-Y., Wellons S., Angles-Alcazar D., Steinwandel U. P., Guszejnov D., Murray N., Faucher-Giguere C.-A., Quataert E., & Keres D.: *FORGE'd in FIRE: Resolving the End of Star Formation and Structure of AGN Accretion Disks from Cosmological Initial Conditions.* The Open Journal of Astrophysics **7**, 18 (2024)

Hopkins P. F.: *Cosmic Rays on Galaxy Scales: Progress and Pitfalls for CR-MHD Dynamical Models.* arXiv e-prints, arXiv:2509 (2025)

Hoshi A., Yamada T., Kokubo M., Matsuoka Y., & Nagao T.: *The Relationship of Supermassive Black Holes and Host Galaxies at $z < 4$ in the Deep Optical Variability-selected Active Galactic Nuclei Sample in the COSMOS Field.* ApJ **969**, 11 (2024)

Houston T., Croton D. J., & Sinha M.: *Using the star-forming main sequence to explore quiescent galaxies across cosmic time.* MNRAS **522**, L11 (2023)

Hoyle F. & Lyttleton R. A.: *The effect of interstellar matter on climatic variation.* Proceedings of the Cambridge Philosophical Society **35**, 405 (1939)

Hubble E. P.: *A general study of diffuse galactic nebulae.* ApJ **56**, 162 (1922)

Hubble E. P.: *Extragalactic nebulae.* ApJ **64**, 321 (1926)

Huertas-Company M., Iyer K. G., Angeloudi E., Bagley M. B., Finkelstein S. L., Kartaltepe J., McGrath E. J., Sarmiento R., Vega-Ferrero J., Arrabal Haro P., et al.: *Galaxy morphology from $z \sim 6$ through the lens of JWST.* A&A **685**, A48 (2024)

Huertas-Company M., Shuntov M., Dong Y., Walmsley M., Ilbert O., McCracken H. J., Akins H. B., Allen N., Casey C. M., Costantin L., et al.: *COSMOS-Web: The emergence of the Hubble Sequence.* arXiv e-prints, arXiv:2502 (2025)

Ilbert O., McCracken H. J., Le Fèvre O., Capak P., Dunlop J., Karim A., Renzini M. A., Caputi K., Boissier S., Arnouts S., et al.: *Mass assembly in quiescent and star-forming galaxies since $z \approx 4$ from UltraVISTA.* A&A **556**, A55 (2013)

Ilbert O., Arnouts S., Le Floc'h E., Aussel H., Bethermin M., Capak P., Hsieh B.-C., Kajisawa M., Karim A., Le Fèvre O., et al.: *Evolution of the specific star formation rate function at $z< 1.4$ Dissecting the mass-SFR plane in COSMOS and GOODS.* A&A **579**, A2 (2015)

Imig J., Price C., Holtzman J. A., Stone-Martinez A., Majewski S. R., Weinberg D. H., Johnson J. A., Allende Prieto C., Beaton R. L., Beers T. C., et al.: *A Tale of Two Disks: Mapping the Milky Way with the Final Data Release of APOGEE.* ApJ **954**, 124 (2023)

Inoue A. K., Kaneda H., Yamada T., Harikane Y., Ishihara D., Kodama T., Komiyama Y., Moriya T., Motohara K., Nomura H., et al.: *GREX-PLUS: galaxy reionization explorer and planetary universe spectrometer.* In: Coyle L. E., Matsuura S., & Perrin M. D. (eds.): *Space Telescopes and Instrumentation 2022: Optical, Infrared, and Millimeter Wave.* Society of Photo-Optical Instrumentation Engineers (SPIE) Conference Series **12180**, 121801I (2022)

Iodice E., Capaccioli M., Grado A., Limatola L., Spavone M., Napolitano N. R., Paolillo M., Peletier R. F., Cantiello M., Lisker T., et al.: *The Fornax Deep Survey with VST. I. The Extended and Diffuse Stellar Halo of NGC 1399 out to 192 kpc.* ApJ **820**, 42 (2016)

Ito K., Tanaka M., Miyaji T., Ilbert O., Kauffmann O. B., Koekemoer A. M., Marchesi S., Shuntov M., Toft S., Valentino F., & Weaver J. R.: *COSMOS2020: Ubiquitous AGN Activity of Massive Quiescent Galaxies at $0 < z < 5$ Revealed by X-Ray and Radio Stacking.* ApJ **929**, 53 (2022)

Ito K., Valentino F., Brammer G., Faisst A. L., Gillman S., Gómez-Guijarro C., Gould K. M. L., Heintz K. E., Ilbert O., Jespersen C. K., et al.: *Size–Stellar Mass Relation and Morphology of Quiescent Galaxies at $z \geq 3$ in Public JWST Fields.* ApJ **964**, 192 (2024)

Ivezić Ž., Kahn S. M., Tyson J. A., Abel B., Acosta E., Allsman R., Alonso D., AlSayyad Y., Anderson S. F., Andrew J., et al.: *LSST: From Science Drivers to Reference Design and Anticipated Data Products.* ApJ **873**, 111 (2019)

Jain R. & Wadadekar Y.: *A grand-design spiral galaxy 1.5 billion years after the Big Bang with JWST.* A&A **703**, A96 (2025)

Jauzac M., Eckert D., Schwinn J., Harvey D., Baugh C. M., Robertson A., Bose S., Massey R., Owers M., Ebeling H., et al.: *The extraordinary amount of substructure in the Hubble Frontier Fields cluster Abell 2744.* MNRAS **463**, 3876 (2016)

Jeltema T. E., Canizares C. R., Bautz M. W., & Buote D. A.: *The Evolution of Structure in X-Ray Clusters of Galaxies.* ApJ **624**, 606 (2005)

Jeon J., Bromm V., Liu B., & Finkelstein S. L.: *Physical Pathways for JWST-observed Supermassive Black Holes in the Early Universe.* ApJ **979**, 127 (2025a)

Jeon J., Liu B., Bromm V., Fujimoto S., Taylor A. J., Kokorev V., Larson R. L., Chisholm J., Finkelstein S. L., & Kocevski D. D.: *Little Red Dots and their Progenitors from Direct Collapse Black Holes.* arXiv e-prints, arXiv:2508 (2025b)

Jeon S., Yi S. K., Dubois Y., Chung A., Devriendt J., Han S., Jackson R. A., Kimm T., Pichon C., & Rhee J.: *Star Formation History and Transition Epoch of Cluster Galaxies Based on the Horizon-AGN Simulation.* ApJ **941**, 5 (2022)

Jesseit R., Naab T., Peletier R. F., & Burkert A.: *2D kinematics of simulated disc merger remnants.* MNRAS **376**, 997 (2007)

Jesseit R., Cappellari M., Naab T., Emsellem E., & Burkert A.: *Specific angular momentum of disc merger remnants and the λ_R-parameter.* MNRAS **397**, 1202 (2009)

Jiang F. & van den Bosch F. C.: *Statistics of dark matter substructure - I. Model and universal fitting functions.* MNRAS **458**, 2848 (2016)

Jiang F. & van den Bosch F. C.: *Statistics of dark matter substructure - III. Halo-to-halo variance.* MNRAS **472**, 657 (2017)

Jiménez-Teja Y., Dupke R., Benítez N., Koekemoer A. M., Zitrin A., Umetsu K., Ziegler B. L., Frye B. L., Ford H., Bouwens R. J., et al.: *Unveiling the Dynamical State of Massive Clusters through the ICL Fraction.* ApJ **857**, 79 (2018)

Jiménez-Teja Y., Vílchez J. M., Dupke R. A., Lopes P. A. A., de Oliveira N. O. L., & Coe D.: *RELICS: ICL Analysis of the $z = 0.566$ Merging Cluster WHL J013719.8-08284.* ApJ **922**, 268 (2021)

Jiménez-Teja Y., Dupke R. A., Lopes P. A. A., & Vílchez J. M.: *Dissecting the RELICS cluster SPT-CLJ0615-5746 through intracluster light: Confirmation of the multiple merging state of the cluster formation.* A&A **676**, A39 (2023)

Jiménez-Teja Y., Dupke R. A., Lopes P. A. A., & Dimauro P.: *Evidence for a Redshifted Excess in the Intracluster Light Fractions of Merging Clusters at $z = 0.8$.* ApJ **960**, L7 (2024)

Jofré P., Heiter U., & Soubiran C.: *Accuracy and Precision of Industrial Stellar Abundances.* ARA&A **57**, 571 (2019)

Jones G. C., Maiolino R., D'Eugenio F., Arribas S., Bunker A. J., Charlot S., Perna M., Rodriguez del Pino B., Übler H., Böker T., et al.: *GA-NIFS: A smouldering disk galaxy undergoing ordered rotation at z=4.26.* arXiv e-prints, arXiv:2512 (2025)

Jones L. R., Ponman T. J., Horton A., Babul A., Ebeling H., & Burke D. J.: *The nature and space density of fossil groups of galaxies.* MNRAS **343**, 627 (2003)

Joo H. & Jee M. J.: *Intracluster light is already abundant at redshift beyond unity.* Nature **613**, 37 (2023)

Joo H., Jee M. J., Kim J., Lee J., Ko J., Park C., Shin J., Snaith O., Pichon C., Gibson B., & Kim Y.: *Tracing the Formation History of Intrahalo Light with Horizon Run 5.* arXiv e-prints, arXiv:2411 (2024)

Kakimoto T., Tanaka M., Onodera M., Shimakawa R., Wu P.-F., Gould K. M. L., Ito K., Jin S., Kubo M., Suzuki T. L., et al.: *A Massive Quiescent Galaxy in a Group Environment at $z = 4.53$.* ApJ **963**, 49 (2024)

Kannan R., Springel V., Hernquist L., Pakmor R., Delgado A. M., Hadzhiyska B., Hernández-Aguayo C., Barrera M., Ferlito F., Bose S., et al.: *The MillenniumTNG project: the galaxy population at $z \geq 8$.* MNRAS **524**, 2594 (2023)

Kant I.: *Allgemeine Naturgeschichte und Theorie des Himmels.* Petersen (1775)

Karademir G. S., Remus R.-S., Burkert A., Dolag K., Hoffmann T. L., Moster B. P., Steinwandel U. P., & Zhang J.: *The outer stellar halos of galaxies: how radial merger mass deposition, shells, and streams depend on infall-orbit configurations.* MNRAS **487**, 318 (2019)

Karakas A. I.: *Updated stellar yields from asymptotic giant branch models.* MNRAS **403**, 1413 (2010)

Kartaltepe J. S., Rose C., Vanderhoof B. N., McGrath E. J., Costantin L., Cox I. G., Yung L. Y. A., Kocevski D. D., Wuyts S., Ferguson H. C., et al.: *CEERS Key Paper. III. The Diversity of Galaxy Structure and Morphology at $z = 3$-9 with JWST.* ApJ **946**, L15 (2023)

Katz N.: *Dissipational Galaxy Formation. II. Effects of Star Formation.* ApJ **391**, 502 (1992)

Kauffmann G., Heckman T. M., White S. D. M., Charlot S., Tremonti C., Brinchmann J., Bruzual G., Peng E. W., Seibert M., Bernardi M., et al.: *Stellar masses and star formation histories for 10^5 galaxies from the Sloan Digital Sky Survey.* MNRAS **341**, 33 (2003)

Kempner J. C. & David L. P.: *A Chandra view of the multiple merger in Abell 2744.* MNRAS **349**, 385 (2004)

Kennicutt R. C., Jr.: *Star Formation in Galaxies Along the Hubble Sequence.* ARA&A **36**, 189 (1998a)

Kennicutt R. C., Jr.: *The Global Schmidt Law in Star-forming Galaxies.* ApJ **498**, 541 (1998b)

Kennicutt R. C. & Evans N. J.: *Star Formation in the Milky Way and Nearby Galaxies.* ARA&A **50**, 531 (2012)

Kewley L. J., Dopita M. A., Sutherland R. S., Heisler C. A., & Trevena J.: *Theoretical Modeling of Starburst Galaxies.* ApJ **556**, 121 (2001)

Kewley L. J. & Ellison S. L.: *Metallicity Calibrations and the Mass-Metallicity Relation for Star-forming Galaxies.* ApJ **681**, 1183 (2008)

Kewley L. J., Nicholls D. C., & Sutherland R. S.: *Understanding Galaxy Evolution Through Emission Lines.* ARA&A **57**, 511 (2019)

Khaire V. & Srianand R.: *New synthesis models of consistent extragalactic background light over cosmic time.* MNRAS **484**, 4174 (2019)

Khochfar S. & Burkert A.: *The Importance of Spheroidal and Mixed Mergers for Early-Type Galaxy Formation.* ApJ **597**, L117 (2003)

Khochfar S., Emsellem E., Serra P., Bois M., Alatalo K., Bacon R., Blitz L., Bournaud F., Bureau M., Cappellari M., et al.: *The ATLAS^{3D} project - VIII. Modelling the formation and evolution of fast and slow rotator early-type galaxies within ΛCDM.* MNRAS **417**, 845 (2011)

Kim S., HyeongHan K., Lee W., In Park J., Jee M. J., & Hwang H. S.: *Weak-Lensing Analysis of the Galaxy Cluster Abell 85: Constraints on the Merger Scenarios of Its Southern Subcluster.* arXiv e-prints, arXiv:2511 (2025)

Kimmig L. C., Remus R.-S., Dolag K., & Biffi V.: *The Hateful Eight: Connecting Massive Substructures in Galaxy Clusters like A2744 to Their Dynamical Assembly State Using the Magneticum Simulations.* ApJ **949**, 92 (2023)

Kimmig L. C., Brough S., Dolag K., Remus R.-S., Bahé Y. M., Martin G., Pillepich A., Hatch N., Montes M., Lammim Ahad S., et al.: *Intra-cluster light as a dynamical clock for galaxy clusters: Insights from the MAGNETICUM, IllustrisTNG, Hydrangea, and Horizon-AGN simulations.* A&A **700**, A95 (2025a)

Kimmig L. C., Remus R.-S., Seidel B., Valenzuela L. M., Dolag K., & Burkert A.: *Blowing Out the Candle: How to Quench Galaxies at High Redshift—An Ensemble of Rapid Starbursts, AGN Feedback, and Environment.* ApJ **979**, 15 (2025b)

Kluge M., Neureiter B., Riffeser A., Bender R., Goessl C., Hopp U., Schmidt M., Ries C., & Brosch N.: *Structure of Brightest Cluster Galaxies and Intracluster Light.* ApJS **247**, 43 (2020)

Kluge M., Bender R., Riffeser A., Goessl C., Hopp U., Schmidt M., & Ries C.: *Photometric Dissection of Intracluster Light and Its Correlations with Host Cluster Properties.* ApJS **252**, 27 (2021)

Kluge M., Hatch N. A., Montes M., Golden-Marx J. B., Gonzalez A. H., Cuillandre J. C., Bolzonella M., Lançon A., Laureijs R., Saifollahi T., et al.: *Euclid: Early Release Observations – The intracluster light and intracluster globular clusters of the Perseus cluster.* arXiv e-prints, arXiv:2405 (2024)

Kobayashi C., Karakas A. I., & Lugaro M.: *The Origin of Elements from Carbon to Uranium.* ApJ **900**, 179 (2020)

Kobayashi C.: *Nucleosynthesis and the chemical enrichment of galaxies.* arXiv e-prints, arXiv:2506 (2025)

Kolokotronis V., Basilakos S., Plionis M., & Georgantopoulos I.: *Searching for cluster substructure using APM and ROSAT data.* MNRAS **320**, 49 (2001)

Komatsu E., Smith K. M., Dunkley J., Bennett C. L., Gold B., Hinshaw G., Jarosik N., Larson D., Nolta M. R., & Page L.: *Seven-year Wilkinson Microwave Anisotropy Probe (WMAP) Observations: Cosmological Interpretation.* ApJS **192**, 18 (2011)

Kormendy J. & Ho L. C.: *Coevolution (Or Not) of Supermassive Black Holes and Host Galaxies.* ARA&A **51**, 511 (2013)

Kravtsov A. V., Vikhlinin A. A., & Meshcheryakov A. V.: *Stellar Mass—Halo Mass Relation and Star Formation Efficiency in High-Mass Halos.* Astronomy Letters **44**, 8 (2018)

Kroupa P., Tout C. A., & Gilmore G.: *The Distribution of Low-Mass Stars in the Galactic Disc.* MNRAS **262**, 545 (1993)

Kroupa P.: *On the variation of the initial mass function.* MNRAS **322**, 231 (2001)

Krumholz M. R.: *The big problems in star formation: The star formation rate, stellar clustering, and the initial mass function.* Phys. Rep. **539**, 49 (2014)

Kudritzki R.-P. & Puls J.: *Winds from Hot Stars.* ARA&A **38**, 613 (2000)

Kudritzki R.-P., Teklu A. F., Schulze F., Remus R.-S., Dolag K., Burkert A., & Zahid H. J.: *Galaxy Look-back Evolution Models: A Comparison with Magneticum Cosmological Simulations and Observations.* ApJ **910**, 87 (2021)

Kudritzki R.-P., Urbaneja M. A., Bresolin F., Macri L. M., Yuan W., Li S., Anand G. S., & Riess A. G.: *The Hubble Constant Anchor Galaxy NGC 4258: Metallicity and Distance from Blue Supergiants.* ApJ **977**, 217 (2024)

Kurinchi-Vendhan S., Farcy M., Hirschmann M., & Valentino F.: *On the origin of star-formation quenching in massive galaxies at zr sim3 in the cosmological simulations IllustrisTNG.* arXiv e-prints, arXiv:2310 (2023)

Kusakabe H., Shimasaku K., Ouchi M., Nakajima K., Goto R., Hashimoto T., Konno A., Harikane Y., Silverman J. D., & Capak P. L.: *The stellar mass, star formation rate and dark matter halo properties of LAEs at z ∼ 2.* PASJ **70**, 4 (2018)

Labbé I., van Dokkum P., Nelson E., Bezanson R., Suess K. A., Leja J., Brammer G., Whitaker K., Mathews E., Stefanon M., & Wang B.: *A population of red candidate massive galaxies 600 Myr after the Big Bang.* Nature **616**, 266 (2023)

Laganá T. F., Martinet N., Durret F., Lima Neto G. B., Maughan B., & Zhang Y. Y.: *A comprehensive picture of baryons in groups and clusters of galaxies.* A&A **555**, A66 (2013)

Lagos C. d. P., Emsellem E., van de Sande J., Harborne K. E., Cortese L., Davison T., Foster C., & Wright R. J.: *The diverse nature and formation paths of slow rotator galaxies in the EAGLE simulations.* MNRAS **509**, 4372 (2022)

Lagos C. d. P., Bravo M., Tobar R., Obreschkow D., Power C., Robotham A. S. G., Proctor K. L., Hansen S., Chandro-Gómez Á., & Carrivick J.: *Quenching massive galaxies across cosmic time with the semi-analytic model SHARK V2.0.* MNRAS **531**, 3551 (2024)

Lange R., Driver S. P., Robotham A. S. G., Kelvin L. S., Graham A. W., Alpaslan M., Andrews S. K., Baldry I. K., Bamford S., Bland-Hawthorn J., et al.: *Galaxy And Mass Assembly (GAMA): mass-size relations of $z < 0.1$ galaxies subdivided by Sérsic index, colour and morphology.* MNRAS **447**, 2603 (2015)

Laureijs R., Amiaux J., Arduini S., Augueres J. L., Brinchmann J., Cole R., Cropper M., Dabin C., Duvet L., Ealet A., et al.: *Euclid Definition Study Report.* arXiv e-prints, arXiv:1110 (2011)

Leauthaud A., George M. R., Behroozi P. S., Bundy K., Tinker J., Wechsler R. H., Conroy C., Finoguenov A., & Tanaka M.: *The Integrated Stellar Content of Dark Matter Halos.* ApJ **746**, 95 (2012)

Lebeau T., Sorce J. G., Aghanim N., Hernández-Martínez E., & Dolag K.: *Mass bias in clusters of galaxies: Projection effects on the case study of Virgo replica.* A&A **682**, A157 (2024)

Lee L. L., Förster Schreiber N. M., Herrera-Camus R., Liu D., Price S. H., Genzel R., Tacconi L. J., Lutz D., Davies R., Naab T., et al.: *The ALMA-CRISTAL survey: Resolved kinematic studies of main sequence star-forming galaxies at $4 < z < 6$.* A&A **701**, A260 (2025)

Leitner S. N. & Kravtsov A. V.: *Fuel Efficient Galaxies: Sustaining Star Formation with Stellar Mass Loss.* ApJ **734**, 48 (2011)

Leja J., Johnson B. D., Conroy C., van Dokkum P. G., & Byler N.: *Deriving Physical Properties from Broadband Photometry with Prospector: Description of the Model and a Demonstration of its Accuracy Using 129 Galaxies in the Local Universe.* ApJ **837**, 170 (2017)

Leja J., Speagle J. S., Johnson B. D., Conroy C., van Dokkum P., & Franx M.: *A New Census of the $0.2 < z < 3.0$ Universe. I. The Stellar Mass Function.* ApJ **893**, 111 (2020)

Lelli F., Zhang Z.-Y., Bisbas T. G., Lin L., Papadopoulos P., Schombert J. M., Di Teodoro E., Marasco A., & McGaugh S. S.: *Cold gas disks in main-sequence galaxies at cosmic noon: Low turbulence, flat rotation curves, and disk-halo degeneracy.* A&A **672**, A106 (2023)

Leslie S. K., Schinnerer E., Liu D., Magnelli B., Algera H., Karim A., Davidzon I., Gozaliasl G., Jiménez-Andrade E. F., Lang P., et al.: *The VLA-COSMOS 3 GHz Large Project: Evolution of Specific Star Formation Rates out to $z \sim 5$.* ApJ **899**, 58 (2020)

Leung H. W., Bovy J., Mackereth J. T., & Miglio A.: *A variational encoder-decoder approach to precise spectroscopic age estimation for large Galactic surveys.* MNRAS **522**, 4577 (2023)

Libeskind N. I., van de Weygaert R., Cautun M., Falck B., Tempel E., Abel T., Alpaslan M., Aragón-Calvo M. A., Forero-Romero J. E., Gonzalez R., et al.: *Tracing the cosmic web.* MNRAS **473**, 1195 (2018)

Liddel H. G. & Scott R.: *A Greek-English Lexicon.* Oxford University Press (1996)

Lidman C., Suherli J., Muzzin A., Wilson G., Demarco R., Brough S., Rettura A., Cox J., DeGroot A., Yee H. K. C., et al.: *Evidence for significant growth in the stellar mass of brightest cluster galaxies over the past 10 billion years.* MNRAS **427**, 550 (2012)

Lilly S. J., Carollo C. M., Pipino A., Renzini A., & Peng Y.: *Gas Regulation of Galaxies: The Evolution of the Cosmic Specific Star Formation Rate, the Metallicity-Mass-Star-formation Rate Relation, and the Stellar Content of Halos.* ApJ **772**, 119 (2013)

Lisenfeld U., Ogle P. M., Appleton P. N., Jarrett T. H., & Moncada-Cuadri B. M.: *Molecular gas in super spiral galaxies.* A&A **673**, A87 (2023)

Loh Y.-S. & Strauss M. A.: *The bright end of the luminosity function of red sequence galaxies.* MNRAS **366**, 373 (2006)

Long A. S., Antwi-Danso J., Lambrides E. L., Lovell C. C., de la Vega A., Valentino F., Zavala J. A., Casey C. M., Wilkins S. M., Yung L. Y. A., et al.: *Efficient NIRCam Selection of Quiescent Galaxies at $3 < z < 6$ in CEERS.* arXiv e-prints, arXiv:2305 (2023)

Longobardi A., Arnaboldi M., Gerhard O., & Hanuschik R.: *The outer regions of the giant Virgo galaxy M 87 Kinematic separation of stellar halo and intracluster light.* A&A **579**, A135 (2015)

Looser T. J., D'Eugenio F., Maiolino R., Witstok J., Sandles L., Curtis-Lake E., Chevallard J., Tacchella S., Johnson B. D., Baker W. M., et al.: *A recently quenched galaxy 700 million years after the Big Bang.* Nature **629**, 53 (2024)

Lotz J. M., Koekemoer A., Coe D., Grogin N., Capak P., Mack J., Anderson J., Avila R., Barker E. A., Borncamp D., et al.: *The Frontier Fields: Survey Design and Initial Results.* ApJ **837**, 97 (2017)

Lotz M., Remus R.-S., Dolag K., Biviano A., & Burkert A.: *Gone after one orbit: How cluster environments quench galaxies.* MNRAS **488**, 5370 (2019)

Lotz M., Dolag K., Remus R.-S., & Burkert A.: *Rise and fall of post-starburst galaxies in Magneticum Pathfinder.* MNRAS **506**, 4516 (2021)

Lovell C. C., Vijayan A. P., Thomas P. A., Wilkins S. M., Barnes D. J., Irodotou D., & Roper W.: *First Light And Reionization Epoch Simulations (FLARES) - I. Environmental dependence of high-redshift galaxy evolution.* MNRAS **500**, 2127 (2021)

Lovell C. C., Harrison I., Harikane Y., Tacchella S., & Wilkins S. M.: *Extreme value statistics of the halo and stellar mass distributions at high redshift: are JWST results in tension with ΛCDM?* MNRAS **518**, 2511 (2023a)

Lovell C. C., Roper W., Vijayan A. P., Seeyave L., Irodotou D., Wilkins S. M., Conselice C. J., Fortuni F., Kuusisto J. K., Merlin E., et al.: *First light and reionisation epoch simulations (FLARES) - VIII. The emergence of passive galaxies at $z \geq 5$.* MNRAS **525**, 5520 (2023b)

Lucy L. B.: *A numerical approach to the testing of the fission hypothesis.* AJ **82**, 1013 (1977)

Lustig P., Strazzullo V., Remus R.-S., D'Eugenio C., Daddi E., Burkert A., De Lucia G., Delvecchio I., Dolag K., Fontanot F., et al.: *Massive quiescent galaxies at z 3: A comparison of selection, stellar population, and structural properties with simulation predictions.* MNRAS **518**, 5953 (2023)

Lynden-Bell D.: *Statistical mechanics of violent relaxation in stellar systems.* MNRAS **136**, 101 (1967)

Mackereth J. T., Crain R. A., Schiavon R. P., Schaye J., Theuns T., & Schaller M.: *The origin of diverse α-element abundances in galaxy discs.* MNRAS **477**, 5072 (2018)

Madau P. & Dickinson M.: *Cosmic Star-Formation History.* ARA&A **52**, 415 (2014)

Mahler G., Richard J., Clément B., Lagattuta D., Schmidt K., Patrício V., Soucail G., Bacon R., Pello R., Bouwens R., et al.: *Strong-lensing analysis of A2744 with MUSE and Hubble Frontier Fields images.* MNRAS **473**, 663 (2018)

Maiolino R., Nagao T., Grazian A., Cocchia F., Marconi A., Mannucci F., Cimatti A., Pipino A., Ballero S., Calura F., et al.: *AMAZE. I. The evolution of the mass-metallicity relation at $z > 3$.* A&A **488**, 463 (2008)

Maiolino R., Scholtz J., Curtis-Lake E., Carniani S., Baker W., de Graaff A., Tacchella S., Übler H., D'Eugenio F., Witstok J., et al.: *JADES: The diverse population of infant black holes at $4 < z < 11$: Merging, tiny, poor, but mighty.* A&A **691**, A145 (2024)

Majewski S. R., Schiavon R. P., Frinchaboy P. M., Allende Prieto C., Barkhouser R., Bizyaev D., Blank B., Brunner S., Burton A., Carrera R., et al.: *The Apache Point Observatory Galactic Evolution Experiment (APOGEE).* AJ **154**, 94 (2017)

Man A. & Belli S.: *Star formation quenching in massive galaxies.* Nature Astronomy **2**, 695 (2018)

Mandelbaum R., Seljak U., Kauffmann G., Hirata C. M., & Brinkmann J.: *Galaxy halo masses and satellite fractions from galaxy-galaxy lensing in the Sloan Digital Sky Survey: stellar mass, luminosity, morphology and environment dependencies.* MNRAS **368**, 715 (2006)

Mann A. W. & Ebeling H.: *X-ray-optical classification of cluster mergers and the evolution of the cluster merger fraction.* MNRAS **420**, 2120 (2012)

Mao T.-X., Wang J., Frenk C. S., Gao L., Li R., Wang Q., Cao X., & Li M.: *Resolution of the apparent discrepancy between the number of massive subhaloes in Abell 2744 and* Λ*CDM.* MNRAS **478**, L34 (2018)

Marin-Gilabert T., Valentini M., Steinwandel U. P., & Dolag K.: *The role of physical and numerical viscosity in hydrodynamical instabilities.* MNRAS **517**, 5971 (2022)

Marinacci F., Vogelsberger M., Pakmor R., Torrey P., Springel V., Hernquist L., Nelson D., Weinberger R., Pillepich A., Naiman J., & Genel S.: *First results from the IllustrisTNG simulations: radio haloes and magnetic fields.* MNRAS **480**, 5113 (2018)

Marini I., Saro A., Borgani S., & Boi M.: *Inferring intrahalo light from stellar kinematics: A deep learning approach.* A&A **689**, A181 (2024)

Markevitch M., Gonzalez A. H., David L., Vikhlinin A., Murray S., Forman W., Jones C., & Tucker W.: *A Textbook Example of a Bow Shock in the Merging Galaxy Cluster 1E 0657-56.* ApJ **567**, L27 (2002)

Martell S. L., Sharma S., Buder S., Duong L., Schlesinger K. J., Simpson J., Lind K., Ness M., Marshall J. P., Asplund M., et al.: *The GALAH survey: observational overview and Gaia DR1 companion.* MNRAS **465**, 3203 (2017)

Martin G., Bazkiaei A. E., Spavone M., Iodice E., Mihos J. C., Montes M., Benavides J. A., Brough S., Carlin J. L., Collins C. A., et al.: *Preparing for low surface brightness science with the Vera C. Rubin Observatory: Characterization of tidal features from mock images.* MNRAS **513**, 1459 (2022)

Martin G., Pearce F. R., Hatch N. A., Contreras-Santos A., Knebe A., & Cui W.: *Stellar stripping efficiencies of satellites in numerical simulations: the effect of resolution, satellite properties, and numerical disruption.* MNRAS **535**, 2375 (2024)

Martín-Navarro I., Shankar F., & Mezcua M.: *Rejuvenation triggers nuclear activity in nearby galaxies.* MNRAS **513**, L10 (2022)

Martínez-Lombilla C., Brough S., Montes M., Baena-Gallé R., Akhlaghi M., Infante-Sainz R., Driver S. P., Holwerda B. W., Pimbblet K. A., & Robotham A. S. G.: *Galaxy And Mass Assembly (GAMA): extended intragroup light in a group at z = 0.2 from deep Hyper Suprime-Cam images.* MNRAS **518**, 1195 (2023)

Matthee J., Schaye J., Crain R. A., Schaller M., Bower R., & Theuns T.: *The origin of scatter in the stellar mass-halo mass relation of central galaxies in the EAGLE simulation.* MNRAS **465**, 2381 (2017)

Mattolini D., Zibetti S., Gallazzi A. R., Scholz-Diaz L., & Pratesi J.: *Re-assessing the stellar population scaling relations of the galaxies in the Local Universe.* arXiv e-prints, arXiv:2509 (2025)

McBride J., Fakhouri O., & Ma C.-P.: *Mass accretion rates and histories of dark matter haloes.* MNRAS **398**, 1858 (2009)

McCarthy I. G., Schaye J., Bird S., & Le Brun A. M. C.: *The BAHAMAS project: calibrated hydrodynamical simulations for large-scale structure cosmology.* MNRAS **465**, 2936 (2017)

McConachie I., Wilson G., Forrest B., Marsan Z. C., Muzzin A., Cooper M. C., Annunziatella M., Marchesini D., Chan J. C. C., Gomez P., et al.: *Spectroscopic Confirmation of a Protocluster at z = 3.37 with a High Fraction of Quiescent Galaxies.* ApJ **926**, 37 (2022)

McDermid R. M., Alatalo K., Blitz L., Bournaud F., Bureau M., Cappellari M., Crocker A. F., Davies R. L., Davis T. A., de Zeeuw P. T., et al.: *The ATLAS^{3D} Project - XXX. Star formation histories and stellar population scaling relations of early-type galaxies.* MNRAS **448**, 3484 (2015)

McGee S. L., Balogh M. L., Bower R. G., Font A. S., & McCarthy I. G.: *The accretion of galaxies into groups and clusters.* MNRAS **400**, 937 (2009)

McKee C. F. & Ostriker J. P.: *A theory of the interstellar medium: three components regulated by supernova explosions in an inhomogeneous substrate.* ApJ **218**, 148 (1977)

McMillan P. J.: *The mass distribution and gravitational potential of the Milky Way.* MNRAS **465**, 76 (2017)

McNamara B. R. & Nulsen P. E. J.: *Mechanical feedback from active galactic nuclei in galaxies, groups and clusters.* New Journal of Physics **14**, 055023 (2012)

Meneghetti M., Davoli G., Bergamini P., Rosati P., Natarajan P., Giocoli C., Caminha G. B., Metcalf R. B., Rasia E., Borgani S., et al.: *An excess of small-scale gravitational lenses observed in galaxy clusters.* Science **369**, 1347 (2020)

Mérida R. M., Gómez-Guijarro C., Pérez-González P. G., Sánchez-Blázquez P., Elbaz D., Franco M., Leroy L., Magdis G. E., Magnelli B., & Xiao M.: *Measuring the gas reservoirs in $10^8 < M_\star < 10^{11}$ $M_\odot$ galaxies at $1 \leq z \leq 3$.* A&A **686**, A64 (2024)

Merlin E., Chiosi C., Piovan L., Grassi T., Buonomo U., & La Barbera F.: *Formation and evolution of early-type galaxies - III. Dependence of the star formation history on the total mass and initial overdensity.* MNRAS **427**, 1530 (2012)

Merlin E., Fortuni F., Torelli M., Santini P., Castellano M., Fontana A., Grazian A., Pentericci L., Pilo S., & Schmidt K. B.: *Red and dead CANDELS: massive passive galaxies at the dawn of the Universe.* MNRAS **490**, 3309 (2019)

Merlin E., Fortuni F., Calabró A., Castellano M., Santini P., Fontana A., Kimmig L. C., Shankar F., Napolitano L., Koekemoer A. M., et al.: *Witnessing downsizing in the making: quiescent and breathing galaxies at the dawn of the Universe.* The Open Journal of Astrophysics **8**, E170 (2025)

Merten J., Coe D., Dupke R., Massey R., Zitrin A., Cypriano E. S., Okabe N., Frye B., Braglia F. G., Jiménez-Teja Y., et al.: *Creation of cosmic structure in the complex galaxy cluster merger Abell 2744.* MNRAS **417**, 333 (2011)

Mihos J. C.: *Interactions and Mergers of Cluster Galaxies.* In: Mulchaey J. S., Dressler A., & Oemler A. (eds.): *Clusters of Galaxies: Probes of Cosmological Structure and Galaxy Evolution.* 277 (2004)

Mihos J. C., Harding P., Feldmeier J., & Morrison H.: *Diffuse Light in the Virgo Cluster.* ApJ **631**, L41 (2005)

Mihos J. C., Harding P., Feldmeier J. J., Rudick C., Janowiecki S., Morrison H., Slater C., & Watkins A.: *The Burrell Schmidt Deep Virgo Survey: Tidal Debris, Galaxy Halos, and Diffuse Intracluster Light in the Virgo Cluster.* ApJ **834**, 16 (2017)

Mittal R., Whelan J. T., & Combes F.: *Constraining star formation rates in cool-core brightest cluster galaxies.* MNRAS **450**, 2564 (2015)

Mo H. J., Mao S., & White S. D. M.: *The formation of galactic discs.* MNRAS **295**, 319 (1998)

Mo H., van den Bosch F. C., & White S.: *Galaxy Formation and Evolution.* Cambridge University Press (2010)

Mohr J. J., Mathiesen B., & Evrard A. E.: *Properties of the Intracluster Medium in an Ensemble of Nearby Galaxy Clusters.* ApJ **517**, 627 (1999)

Monaco P., Murante G., Borgani S., & Fontanot F.: *Diffuse Stellar Component in Galaxy Clusters and the Evolution of the Most Massive Galaxies at $z<\sim 1$.* ApJ **652**, L89 (2006)

Monaghan J. J.: *Smoothed particle hydrodynamics.* ARA&A **30**, 543 (1992)

Montenegro-Taborda D., Rodriguez-Gomez V., Pillepich A., Avila-Reese V., Sales L. V., Rodríguez-Puebla A., & Hernquist L.: *The growth of brightest cluster galaxies in the TNG300 simulation: dissecting the contributions from mergers and in situ star formation.* MNRAS **521**, 800 (2023)

Montenegro-Taborda D., Avila-Reese V., Rodriguez-Gomez V., Manuwal A., & Cervantes-Sodi B.: *The stellar mass composition of galaxy clusters and dependencies on dark matter halo properties.* MNRAS **537**, 3954 (2025)

Montes M. & Trujillo I.: *Intracluster Light at the Frontier: A2744.* ApJ **794**, 137 (2014)

Montes M. & Trujillo I.: *Intracluster light at the Frontier - II. The Frontier Fields Clusters.* MNRAS **474**, 917 (2018)

Montes M.: *The intracluster light and its role in galaxy evolution in clusters.* arXiv e-prints, arXiv:1912 (2019)

Montes M., Brough S., Owers M. S., & Santucci G.: *The Buildup of the Intracluster Light of A85 as Seen by Subaru's Hyper Suprime-Cam.* ApJ **910**, 45 (2021)

Montes M.: *The faint light in groups and clusters of galaxies.* Nature Astronomy **6**, 308 (2022)

Montes M., Annibali F., Bellazzini M., Borlaff A. S., Brough S., Buitrago F., Chamba N., Collins C., Dell'Antonio I., Escala I., et al.: *Optimizing Roman's High Latitude Wide Area Survey for Low Surface Brightness Astronomy.* arXiv e-prints, arXiv:2306 (2023)

Morishita T., Mason C. A., Kreilgaard K. C., Trenti M., Treu T., Vulcani B., Zhang Y., Abdurro'uf, Alavi A., Atek H., et al.: *BEACON: JWST NIRCam Pure-parallel Imaging Survey. I. Survey Design and Initial Results.* ApJ **983**, 152 (2025)

Moster B. P., Naab T., & White S. D. M.: *Galactic star formation and accretion histories from matching galaxies to dark matter haloes.* MNRAS **428**, 3121 (2013)

Muñoz López C., Krajnović D., Epinat B., Urrutia T., Pessa I., Contini T., Nanayakkara T., Pharo J., Gonçalves T. S., Thi Thai T., & Bouché N. F.: *Multiple star-forming episodes of intermediate-redshift galaxies.* A&A **702**, A146 (2025)

Muñoz-Mateos J. C., Gil de Paz A., Boissier S., Zamorano J., Jarrett T., Gallego J., & Madore B. F.: *Specific Star Formation Rate Profiles in Nearby Spiral Galaxies: Quantifying the Inside-Out Formation of Disks.* ApJ **658**, 1006 (2007)

Muldrew S. I., Hatch N. A., & Cooke E. A.: *What are protoclusters? - Defining high-redshift galaxy clusters and protoclusters.* MNRAS **452**, 2528 (2015)

Munari E., Grillo C., De Lucia G., Biviano A., Annunziatella M., Borgani S., Lombardi M., Mercurio A., & Rosati P.: *Numerical Simulations Challenged on the Prediction of Massive Subhalo Abundance in Galaxy Clusters: The Case of Abell 2142.* ApJ **827**, L5 (2016)

Murante G., Arnaboldi M., Gerhard O., Borgani S., Cheng L. M., Diaferio A., Dolag K., Moscardini L., Tormen G., Tornatore L., & Tozzi P.: *The Diffuse Light in Simulations of Galaxy Clusters.* ApJ **607**, L83 (2004)

Murante G., Giovalli M., Gerhard O., Arnaboldi M., Borgani S., & Dolag K.: *The importance of mergers for the origin of intracluster stars in cosmological simulations of galaxy clusters.* MNRAS **377**, 2 (2007)

Muzzin A., Marchesini D., Stefanon M., Franx M., McCracken H. J., Milvang-Jensen B., Dunlop J. S., Fynbo J. P. U., Brammer G., Labbé I., & van Dokkum P. G.: *The Evolution of the Stellar Mass Functions of Star-forming and Quiescent Galaxies to $z = 4$ from the COSMOS/UltraVISTA Survey.* ApJ **777**, 18 (2013)

Naab T., Johansson P. H., & Ostriker J. P.: *Minor Mergers and the Size Evolution of Elliptical Galaxies.* ApJ **699**, L178 (2009)

Naab T., Oser L., Emsellem E., Cappellari M., Krajnović D., McDermid R. M., Alatalo K., Bayet E., Blitz L., Bois M., et al.: *The ATLAS^{3D} project - XXV. Two-dimensional kinematic analysis of simulated galaxies and the cosmological origin of fast and slow rotators.* MNRAS **444**, 3357 (2014)

Naidu R. P., Conroy C., Bonaca A., Johnson B. D., Ting Y.-S., Caldwell N., Zaritsky D., & Cargile P. A.: *Evidence from the H3 Survey That the Stellar Halo Is Entirely Comprised of Substructure.* ApJ **901**, 48 (2020)

Naidu R. P., Oesch P. A., Brammer G., Weibel A., Li Y., Matthee J., Chisolm J., Pollock C. L., Heintz K. E., Johnson B. D., et al.: *A Cosmic Miracle: A Remarkably Luminous Galaxy at zspec = 14.44 Confirmed with JWST.* The Open Journal of Astrophysics **9**, 56033 (2026)

Naiman J. P., Pillepich A., Springel V., Ramirez-Ruiz E., Torrey P., Vogelsberger M., Pakmor R., Nelson D., Marinacci F., Hernquist L., et al.: *First results from the IllustrisTNG simulations: a tale of two elements - chemical evolution of magnesium and europium.* MNRAS **477**, 1206 (2018)

Nanayakkara T., Glazebrook K., Jacobs C., Kawinwanichakij L., Schreiber C., Brammer G., Esdaile J., Kacprzak G. G., Labbe I., Lagos C., et al.: *A population of faint, old, and massive quiescent galaxies at 3 <z <4 revealed by JWST NIRSpec Spectroscopy.* Scientific Reports **14**, 3724 (2024)

Nanayakkara T., Glazebrook K., Schreiber C., Chittenden H., Brammer G., Esdaile J., Jacobs C., Kacprzak G. G., Kawinwanichakij L., Kimmig L. C., et al.: *The Formation*

Histories of Massive and Quiescent Galaxies in the 3 < z < 4.5 Universe. ApJ **981**, 78 (2025)

Navarro-Carrera R., Rinaldi P., Caputi K. I., Iani E., Kokorev V., & van Mierlo S. E.: *Constraints on the Faint End of the Galaxy Stellar Mass Function at z = 4-8 from Deep JWST Data.* ApJ **961**, 207 (2024)

Navarro J. F. & Steinmetz M.: *The Effects of a Photoionizing Ultraviolet Background on the Formation of Disk Galaxies.* ApJ **478**, 13 (1997)

Navarro J. F. & Steinmetz M.: *Dark Halo and Disk Galaxy Scaling Laws in Hierarchical Universes.* ApJ **538**, 477 (2000)

Nelson D., Pillepich A., Springel V., Weinberger R., Hernquist L., Pakmor R., Genel S., Torrey P., Vogelsberger M., Kauffmann G., et al.: *First results from the IllustrisTNG simulations: the galaxy colour bimodality.* MNRAS **475**, 624 (2018)

Nelson D., Pillepich A., Springel V., Pakmor R., Weinberger R., Genel S., Torrey P., Vogelsberger M., Marinacci F., & Hernquist L.: *First results from the TNG50 simulation: galactic outflows driven by supernovae and black hole feedback.* MNRAS **490**, 3234 (2019a)

Nelson D., Springel V., Pillepich A., Rodriguez-Gomez V., Torrey P., Genel S., Vogelsberger M., Pakmor R., Marinacci F., Weinberger R., et al.: *The IllustrisTNG simulations: public data release.* Computational Astrophysics and Cosmology **6**, 2 (2019b)

Nelson D., Pillepich A., Ayromlou M., Lee W., Lehle K., Rohr E., & Truong N.: *Introducing the TNG-Cluster simulation: Overview and the physical properties of the gaseous intracluster medium.* A&A **686**, A157 (2024)

Nelson E. J., Suess K. A., Bezanson R., Price S. H., van Dokkum P., Leja J., Wang B., Whitaker K. E., Labbé I., Barrufet L., et al.: *JWST Reveals a Population of Ultrared, Flattened Galaxies at 2 $\lesssim z \lesssim$ 6 Previously Missed by HST.* ApJ **948**, L18 (2023)

Nelson K., Lau E. T., Nagai D., Rudd D. H., & Yu L.: *Weighing Galaxy Clusters with Gas. II. On the Origin of Hydrostatic Mass Bias in ΛCDM Galaxy Clusters.* ApJ **782**, 107 (2014)

Neto A. F., Gao L., Bett P., Cole S., Navarro J. F., Frenk C. S., White S. D. M., Springel V., & Jenkins A.: *The statistics of Λ CDM halo concentrations.* MNRAS **381**, 1450 (2007)

Neumann D. M., Lumb D. H., Pratt G. W., & Briel U. G.: *The dynamical state of the Coma cluster with XMM-Newton.* A&A **400**, 811 (2003)

Newman A. B., Belli S., Ellis R. S., & Patel S. G.: *Resolving Quiescent Galaxies at $z \gtrsim 2$. II. Direct Measures of Rotational Support.* ApJ **862**, 126 (2018)

Ni Y., Di Matteo T., Bird S., Croft R., Feng Y., Chen N., Tremmel M., DeGraf C., & Li Y.: *The ASTRID simulation: the evolution of supermassive black holes.* MNRAS **513**, 670 (2022)

Nobels F. S. J., Schaye J., Schaller M., Ploeckinger S., Chaikin E., & Richings A. J.: *Tests of subgrid models for star formation using simulations of isolated disc galaxies.* MNRAS **532**, 3299 (2024)

Noeske K. G., Weiner B. J., Faber S. M., Papovich C., Koo D. C., Somerville R. S., Bundy K., Conselice C. J., Newman J. A., Schiminovich D., et al.: *Star Formation in AEGIS Field Galaxies since z=1.1: The Dominance of Gradually Declining Star Formation, and the Main Sequence of Star-forming Galaxies.* ApJ **660**, L43 (2007)

Nomoto K., Thielemann F.-K., & Yokoi K.: *Accreting white dwarf models for type I supernovae. III. Carbon deflagration supernovae.* ApJ **286**, 644 (1984)

Nomoto K., Kobayashi C., & Tominaga N.: *Nucleosynthesis in Stars and the Chemical Enrichment of Galaxies.* ARA&A **51**, 457 (2013)

Oesch P. A., Bouwens R. J., Illingworth G. D., Labbé I., & Stefanon M.: *The Dearth of $z \sim 10$ Galaxies in All HST Legacy Fields—The Rapid Evolution of the Galaxy Population in the First 500 Myr.* ApJ **855**, 105 (2018)

Oesch P. A., Brammer G., Naidu R. P., Bouwens R. J., Chisholm J., Illingworth G. D., Matthee J., Nelson E., Qin Y., Reddy N., et al.: *The JWST FRESCO survey: legacy NIRCam/grism spectroscopy and imaging in the two GOODS fields.* MNRAS **525**, 2864 (2023)

Ogle P. M., Jarrett T., Lanz L., Cluver M., Alatalo K., Appleton P. N., & Mazzarella J. M.: *A Break in Spiral Galaxy Scaling Relations at the Upper Limit of Galaxy Mass.* ApJ **884**, L11 (2019a)

Ogle P. M., Lanz L., Appleton P. N., Helou G., & Mazzarella J.: *A Catalog of the Most Optically Luminous Galaxies at $z < 0.3$: Super Spirals, Super Lenticulars, Super Post-mergers, and Giant Ellipticals.* ApJS **243**, 14 (2019b)

Okabe T., Nishimichi T., Oguri M., Peirani S., Kitayama T., Sasaki S., & Suto Y.: *Projected alignment of non-sphericities of stellar, gas, and dark matter distributions in galaxy clusters: analysis of the Horizon-AGN simulation.* MNRAS **478**, 1141 (2018)

O'Leary J. A., Moster B. P., Naab T., & Somerville R. S.: *EMERGE: empirical predictions of galaxy merger rates since $z \sim 6$.* MNRAS **501**, 3215 (2021)

Oliva-Altamirano P., Brough S., Lidman C., Couch W. J., Hopkins A. M., Colless M., Taylor E., Robotham A. S. G., Gunawardhana M. L. P., Ponman T., et al.: *Galaxy And Mass Assembly (GAMA): testing galaxy formation models through the most massive galaxies in the Universe.* MNRAS **440**, 762 (2014)

Oliva-Altamirano P., Brough S., Jimmy T., Kim-Vy, Couch W. J., McDermid R. M., Lidman C., von der Linden A., & Sharp R.: *The accretion histories of brightest cluster galaxies from their stellar population gradients.* MNRAS **449**, 3347 (2015)

Onions J., Pearce F., Knebe A., Gray M., Haggar R., Kuchner U., Contreras-Santos A., Yepes G., & Cui W.: *The life and times of dark matter haloes: what will I be when I grow up?* MNRAS **542**, 1477 (2025)

Oser L., Ostriker J. P., Naab T., Johansson P. H., & Burkert A.: *The Two Phases of Galaxy Formation.* ApJ **725**, 2312 (2010)

Owers M. S., Randall S. W., Nulsen P. E. J., Couch W. J., David L. P., & Kempner J. C.: *The Dissection of Abell 2744: A Rich Cluster Growing Through Major and Minor Mergers.* ApJ **728**, 27 (2011)

Pacucci F., Nguyen B., Carniani S., Maiolino R., & Fan X.: *JWST CEERS & JADES Active Galaxies at z = 4-7 Violate the Local $M_\bullet - M_\star$ Relation at $> 3\sigma$: Implications for Low-Mass Black Holes and Seeding Models.* arXiv e-prints, arXiv:2308 (2023)

Padovani P. & Matteucci F.: *Stellar Mass Loss in Elliptical Galaxies and the Fueling of Active Galactic Nuclei.* ApJ **416**, 26 (1993)

Pakmor R., Springel V., Coles J. P., Guillet T., Pfrommer C., Bose S., Barrera M., Delgado A. M., Ferlito F., Frenk C., et al.: *The MillenniumTNG Project: the hydrodynamical full physics simulation and a first look at its galaxy clusters.* MNRAS **524**, 2539 (2023)

Papovich C., Labbé I., Quadri R., Tilvi V., Behroozi P., Bell E. F., Glazebrook K., Spitler L., Straatman C. M. S., Tran K. V., et al.: *ZFOURGE/CANDELS: On the Evolution of M* Galaxy Progenitors from $z = 3$ to 0.5.* ApJ **803**, 26 (2015)

Park M., Belli S., Conroy C., Tacchella S., Leja J., Cutler S. E., Johnson B. D., Nelson E. J., & Emami R.: *Rapid Quenching of Galaxies at Cosmic Noon.* ApJ **953**, 119 (2023)

Pascalau R. G., D'Eugenio F., Tacchella S., Maiolino R., Cappellari M., Duan Q., Lagos C. d. P., Bunker A. J., Jones G. C., Scholtz J., et al.: *When relics were made: vigorous stellar rotation and low dark matter content in the massive ultra-compact galaxy GS-9209 at z=4.66.* arXiv e-prints, arXiv:2505 (2025)

Patel S. G., Kelson D. D., Williams R. J., Mulchaey J. S., Dressler A., McCarthy P. J., & Shectman S. A.: *The Stellar Mass-Halo Mass Relation for Low-mass X-Ray Groups At 0.5< z< 1 in the CDFS With CSI.* ApJ **799**, L17 (2015)

Pearson W. J., Wang L., Hurley P. D., Małek K., Buat V., Burgarella D., Farrah D., Oliver S. J., Smith D. J. B., & van der Tak F. F. S.: *Main sequence of star forming galaxies beyond the Herschel confusion limit.* A&A **615**, A146 (2018)

Peebles P. J. E.: *Origin of the Angular Momentum of Galaxies.* ApJ **155**, 393 (1969)

Peirani S., Dubois Y., Volonteri M., Devriendt J., Bundy K., Silk J., Pichon C., Kaviraj S., Gavazzi R., & Habouzit M.: *Density profile of dark matter haloes and galaxies in the HORIZON-AGN simulation: the impact of AGN feedback.* MNRAS **472**, 2153 (2017)

Peletier R. F., Falcón-Barroso J., Bacon R., Cappellari M., Davies R. L., de Zeeuw P. T., Emsellem E., Ganda K., Krajnović D., Kuntschner H., et al.: *The SAURON project - XI. Stellar populations from absorption-line strength maps of 24 early-type spirals.* MNRAS **379**, 445 (2007)

Pen U.-L.: *A High-Resolution Adaptive Moving Mesh Hydrodynamic Algorithm.* ApJS **115**, 19 (1998)

Peng E. W. & Lim S.: *A Rich Globular Cluster System in Dragonfly 17: Are Ultra-diffuse Galaxies Pure Stellar Halos?* ApJ **822**, L31 (2016)

Peng Y., Maiolino R., & Cochrane R.: *Strangulation as the primary mechanism for shutting down star formation in galaxies.* Nature **521**, 192 (2015)

Pérez-González P. G., Barro G., Annunziatella M., Costantin L., García-Argumánez Á., McGrath E. J., Mérida R. M., Zavala J. A., Arrabal Haro P., Bagley M. B., et al.: *CEERS Key Paper. IV. A Triality in the Nature of HST-dark Galaxies.* ApJ **946**, L16 (2023)

Pfeffer J., Janssens S. R., Buzzo M. L., Gannon J. S., Bastian N., Bekki K., Brodie J. P., Couch W. J., Crain R. A., Forbes D. A., et al.: *Origin of the correlation between stellar kinematics and globular cluster system richness in ultradiffuse galaxies.* MNRAS **529**, 4914 (2024)

Pillepich A., Nelson D., Hernquist L., Springel V., Pakmor R., Torrey P., Weinberger R., Genel S., Naiman J. P., Marinacci F., & Vogelsberger M.: *First results from the IllustrisTNG simulations: the stellar mass content of groups and clusters of galaxies.* MNRAS **475**, 648 (2018a)

Pillepich A., Springel V., Nelson D., Genel S., Naiman J., Pakmor R., Hernquist L., Torrey P., Vogelsberger M., Weinberger R., & Marinacci F.: *Simulating galaxy formation with the IllustrisTNG model.* MNRAS **473**, 4077 (2018b)

Piotrowska J. M., Bluck A. F. L., Maiolino R., & Peng Y.: *On the quenching of star formation in observed and simulated central galaxies: evidence for the role of integrated AGN feedback.* MNRAS **512**, 1052 (2022)

Planck Collaboration, Ade P. A. R., Aghanim N., Armitage-Caplan C., Arnaud M., Ashdown M., Atrio-Barandela F., Aumont J., Baccigalupi C., Banday A. J., et al.: *Planck 2013 results. XVI. Cosmological parameters.* A&A **571**, A16 (2014)

Planck Collaboration, Ade P. A. R., Aghanim N., Arnaud M., Ashdown M., Aumont J., Baccigalupi C., Banday A. J., Barreiro R. B., Bartlett J. G., et al.: *Planck 2015 results. XIII. Cosmological parameters.* A&A **594**, A13 (2016)

Ploeckinger S., Richings A. J., Schaye J., Trayford J. W., Schaller M., & Chaikin E.: *HYBRID-CHIMES: a model for radiative cooling and the abundances of ions and molecules in simulations of galaxy formation.* MNRAS **543**, 891 (2025)

Popesso P., Concas A., Cresci G., Belli S., Rodighiero G., Inami H., Dickinson M., Ilbert O., Pannella M., & Elbaz D.: *The main sequence of star-forming galaxies across cosmic times.* MNRAS **519**, 1526 (2023)

Popesso P., Marini I., Dolag K., Lamer G., Csizi B., Biffi V., Robothan A., Bravo M., Biviano A., Vladutesku-Zopp S., et al.: *Average X-ray properties of galaxy groups. From Milky Way-like halos to massive clusters.* arXiv e-prints, arXiv:2411 (2024)

Postman M. & Geller M. J.: *The morphology-density relation - The group connection.* ApJ **281**, 95 (1984)

Power C., Navarro J. F., Jenkins A., Frenk C. S., White S. D. M., Springel V., Stadel J., & Quinn T.: *The inner structure of ΛCDM haloes - I. A numerical convergence study.* MNRAS **338**, 14 (2003)

Power C., Knebe A., & Knollmann S. R.: *The dynamical state of dark matter haloes in cosmological simulations - I. Correlations with mass assembly history.* MNRAS **419**, 1576 (2012)

Press W. H. & Schechter P.: *Formation of Galaxies and Clusters of Galaxies by Self-Similar Gravitational Condensation.* ApJ **187**, 425 (1974)

Puchwein E., Springel V., Sijacki D., & Dolag K.: *Intracluster stars in simulations with active galactic nucleus feedback.* MNRAS **406**, 936 (2010)

Ragagnin A., Dolag K., Biffi V., Cadolle Bel M., Hammer N. J., Krukau A., Petkova M., & Steinborn D.: *A web portal for hydrodynamical, cosmological simulations.* Astronomy and Computing **20**, 52 (2017)

Ragagnin A., Dolag K., Moscardini L., Biviano A., & D'Onofrio M.: *Dependency of halo concentration on mass, redshift and fossilness in Magneticum hydrodynamic simulations.* MNRAS **486**, 4001 (2019)

Ragagnin A., Saro A., Singh P., & Dolag K.: *Cosmology dependence of halo masses and concentrations in hydrodynamic simulations.* MNRAS **500**, 5056 (2021)

Ragagnin A., Meneghetti M., Bassini L., Ragone-Figueroa C., Granato G. L., Despali G., Giocoli C., Granata G., Moscardini L., Bergamini P., et al.: *Galaxies in the central regions of simulated galaxy clusters.* A&A **665**, A16 (2022)

Ragusa R., Spavone M., Iodice E., Brough S., Raj M. A., Paolillo M., Cantiello M., Forbes D. A., La Marca A., D'Ago G., et al.: *VEGAS: A VST Early-type GAlaxy Survey. VI. Diffuse light in HCG 86 as seen from the ultra-deep VEGAS images.* A&A **651**, A39 (2021)

Ragusa R., Mirabile M., Spavone M., Cantiello M., Iodice E., La Marca A., Paolillo M., & Schipani P.: *The Intra-Group Baryons in the LEO I Pair From the VST Early-Type GAlaxy Survey.* Frontiers in Astronomy and Space Sciences **9**, 852810 (2022)

Ragusa R., Iodice E., Spavone M., Montes M., Forbes D. A., Brough S., Mirabile M., Cantiello M., Paolillo M., & Schipani P.: *Does the virial mass drive the intra-cluster light?. Relationship between the ICL and M_{vir} from VEGAS.* A&A **670**, L20 (2023)

Rajpurohit K., Vazza F., van Weeren R. J., Hoeft M., Brienza M., Bonnassieux E., Riseley C. J., Brunetti G., Bonafede A., Brüggen M., et al.: *Dissecting nonthermal emission in the complex multiple-merger galaxy cluster Abell 2744: Radio and X-ray analysis.* A&A **654**, A41 (2021)

Ramesh R., Nelson D., & Girichidis P.: *IllustrisTNG plus cosmic rays with a simple transport model: From dwarfs to L^* galaxies.* A&A **699**, A125 (2025)

Raouf M., Smith R., Khosroshahi H. G., Dariush A. A., Driver S., Ko J., & Hwang H. S.: *The Impact of the Dynamical State of Galaxy Groups on the Stellar Populations of Central Galaxies.* ApJ **887**, 264 (2019)

Reefe M., McDonald M., Chatzikos M., Seebeck J., Mushotzky R., Veilleux S., Allen S., Bayliss M., Calzadilla M., Canning R., et al.: *Cold Gas and Star Formation in the Phoenix Cluster with JWST.* arXiv e-prints, arXiv:2501 (2025)

Reiprich T. H. & Böhringer H.: *The Mass Function of an X-Ray Flux-limited Sample of Galaxy Clusters.* ApJ **567**, 716 (2002)

Remus R.-S., Dolag K., & Hoffmann T.: *The Outer Halos of Very Massive Galaxies: BCGs and their DSC in the Magneticum Simulations.* Galaxies **5**, 49 (2017a)

Remus R.-S., Dolag K., Naab T., Burkert A., Hirschmann M., Hoffmann T. L., & Johansson P. H.: *The co-evolution of total density profiles and central dark matter fractions in simulated early-type galaxies.* MNRAS **464**, 3742 (2017b)

Remus R.-S. & Forbes D. A.: *Accreted or Not Accreted? The Fraction of Accreted Mass in Galaxies from the Magneticum Simulations and Observations.* ApJ **935**, 37 (2022)

Remus R.-S., Dolag K., & Dannerbauer H.: *The Young and the Wild: What Happens to Protoclusters Forming at Redshift $z \approx 4$?* ApJ **950**, 191 (2023)

Remus R.-S. & Kimmig L. C.: *Relight the Candle: What Happens to High-redshift Massive Quenched Galaxies.* ApJ **982**, 30 (2025)

Rennehan D., Babul A., Hayward C. C., Bottrell C., Hani M. H., & Chapman S. C.: *Rapid early coeval star formation and assembly of the most-massive galaxies in the Universe.* MNRAS **493**, 4607 (2020)

Rey M. P., Pontzen A., Agertz O., Orkney M. D. A., Read J. I., & Rosdahl J.: *EDGE: from quiescent to gas-rich to star-forming low-mass dwarf galaxies.* MNRAS **497**, 1508 (2020)

Reyes R., Mandelbaum R., Gunn J. E., Nakajima R., Seljak U., & Hirata C. M.: *Optical-to-virial velocity ratios of local disc galaxies from combined kinematics and galaxy-galaxy lensing.* MNRAS **425**, 2610 (2012)

Rhee J., Smith R., Choi H., Yi S. K., Jaffé Y., Candlish G., & Sánchez-Jánssen R.: *Phase-space Analysis in the Group and Cluster Environment: Time Since Infall and Tidal Mass Loss.* ApJ **843**, 128 (2017)

Rieder S., van de Weygaert R., Cautun M., Beygu B., & Portegies Zwart S.: *Assembly of filamentary void galaxy configurations.* MNRAS **435**, 222 (2013)

Riess A. G., Yuan W., Macri L. M., Scolnic D., Brout D., Casertano S., Jones D. O., Murakami Y., Anand G. S., Breuval L., et al.: *A Comprehensive Measurement of the Local Value of the Hubble Constant with 1 km s^{-1} Mpc^{-1} Uncertainty from the Hubble Space Telescope and the SH0ES Team.* ApJ **934**, L7 (2022)

Rizzo F., Roman-Oliveira F., Fraternali F., Frickmann D., Valentino F., Brammer G., Zanella A., Kokorev V., Popping G., Whitaker K. E., et al.: *The ALMA-ALPAKA survey I: high-resolution CO and [CI] kinematics of star-forming galaxies at $z = 0.5$-3.5.* arXiv e-prints, arXiv:2303 (2023)

Roberts I. D., Parker L. C., & Hlavacek-Larrondo J.: *Connecting optical and X-ray tracers of galaxy cluster relaxation.* MNRAS **475**, 4704 (2018)

Robertson B., Bullock J. S., Cox T. J., Di Matteo T., Hernquist L., Springel V., & Yoshida N.: *A Merger-driven Scenario for Cosmological Disk Galaxy Formation.* ApJ **645**, 986 (2006)

Rodriguez-Gomez V., Pillepich A., Sales L. V., Genel S., Vogelsberger M., Zhu Q., Wellons S., Nelson D., Torrey P., Springel V., et al.: *The stellar mass assembly of galaxies in the Illustris simulation: growth by mergers and the spatial distribution of accreted stars.* MNRAS **458**, 2371 (2016)

Roman-Oliveira F., Fraternali F., & Rizzo F.: *Regular rotation and low turbulence in a diverse sample of z 4.5 galaxies observed with ALMA.* MNRAS **521**, 1045 (2023)

Romanowsky A. J. & Fall S. M.: *Angular Momentum and Galaxy Formation Revisited.* ApJS **203**, 17 (2012)

Rowland L. E., Hodge J., Bouwens R., Mancera Piña P. E., Hygate A., Algera H., Aravena M., Bowler R., da Cunha E., Dayal P., et al.: *REBELS-25: discovery of a dynamically cold disc galaxy at $z = 7.31$.* MNRAS **535**, 2068 (2024)

Rudick C. S., Mihos J. C., & McBride C.: *The Formation and Evolution of Intracluster Light.* ApJ **648**, 936 (2006)

Rudick C. S., Mihos J. C., Frey L. H., & McBride C. K.: *Tidal Streams of Intracluster Light.* ApJ **699**, 1518 (2009)

Rudick C. S., Mihos J. C., & McBride C. K.: *The Quantity of Intracluster Light: Comparing Theoretical and Observational Measurement Techniques using Simulated Clusters.* ApJ **732**, 48 (2011)

Sala L., Valentini M., Biffi V., & Dolag K.: *Supermassive black hole spin evolution in cosmological simulations with OPENGADGET3.* A&A **685**, A92 (2024)

Salmon B., Papovich C., Finkelstein S. L., Tilvi V., Finlator K., Behroozi P., Dahlen T., Davé R., Dekel A., Dickinson M., et al.: *The Relation between Star Formation Rate and Stellar Mass for Galaxies at 3.5 <= z <= 6.5 in CANDELS.* ApJ **799**, 183 (2015)

Salpeter E. E.: *The Luminosity Function and Stellar Evolution.* ApJ **121**, 161 (1955)

Sanders J. S., Fabian A. C., Churazov E., Schekochihin A. A., Simionescu A., Walker S. A., & Werner N.: *Linear Structures in the Core of the Coma Cluster of Galaxies.* Science **341**, 1365 (2013)

Santos J. S., Rosati P., Tozzi P., Böhringer H., Ettori S., & Bignamini A.: *Searching for cool core clusters at high redshift.* A&A **483**, 35 (2008)

Santucci G., Brough S., Scott N., Montes M., Owers M. S., van Sande J., Bland-Hawthorn J., Bryant J. J., Croom S. M., Ferreras I., et al.: *The SAMI Galaxy Survey: Stellar Population Gradients of Central Galaxies.* ApJ **896**, 75 (2020)

Sarazin C. L.: *X-ray emission from clusters of galaxies.* Cambridge University Press (1988)

Sarkar P. & Bharadwaj S.: *The Local Dimension: a method to quantify the Cosmic Web.* MNRAS **394**, L66 (2009)

Sarron F., Adami C., Durret F., & Laigle C.: *Pre-processing of galaxies in cosmic filaments around AMASCFI clusters in the CFHTLS.* A&A **632**, A49 (2019)

Sarron F. & Conselice C. J.: *DETECTIFz galaxy groups in the REFINE survey - I. Group detection and quenched fraction evolution at z < 2.5.* MNRAS **506**, 2136 (2021)

Sartoris B., Biviano A., Rosati P., Mercurio A., Grillo C., Ettori S., Nonino M., Umetsu K., Bergamini P., Caminha G. B., & Girardi M.: *CLASH-VLT: a full dynamical reconstruction of the mass profile of Abell S1063 from 1 kpc out to the virial radius.* A&A **637**, A34 (2020)

Schaller M., Frenk C. S., Bower R. G., Theuns T., Jenkins A., Schaye J., Crain R. A., Furlong M., Dalla Vecchia C., & McCarthy I. G.: *Baryon effects on the internal structure of ΛCDM haloes in the EAGLE simulations.* MNRAS **451**, 1247 (2015)

Schaye J., Crain R. A., Bower R. G., Furlong M., Schaller M., Theuns T., Dalla Vecchia C., Frenk C. S., McCarthy I. G., Helly J. C., et al.: *The EAGLE project: simulating the evolution and assembly of galaxies and their environments.* MNRAS **446**, 521 (2015)

Schaye J., Kugel R., Schaller M., Helly J. C., Braspenning J., Elbers W., McCarthy I. G., van Daalen M. P., Vandenbroucke B., Frenk C. S., et al.: *The FLAMINGO project: cosmological hydrodynamical simulations for large-scale structure and galaxy cluster surveys.* MNRAS **526**, 4978 (2023)

Schaye J., Chaikin E., Schaller M., Ploeckinger S., Huško F., McGibbon R., Trayford J. W., Benítez-Llambay A., Correa C., Frenk C. S., et al.: *The COLIBRE project: cosmological hydrodynamical simulations of galaxy formation and evolution.* arXiv e-prints, arXiv:2508 (2025)

Schmidt M.: *The Rate of Star Formation.* ApJ **129**, 243 (1959)

Schönrich R. & Binney J.: *Chemical evolution with radial mixing.* MNRAS **396**, 203 (2009)

Schreiber C., Glazebrook K., Nanayakkara T., Kacprzak G. G., Labbé I., Oesch P., Yuan T., Tran K. V., Papovich C., Spitler L., & Straatman C.: *Near infrared spectroscopy and star-formation histories of $3 \leq z \leq 4$ quiescent galaxies.* A&A **618**, A85 (2018)

Schulze F., Remus R.-S., Dolag K., Burkert A., Emsellem E., & van de Ven G.: *Kinematics of simulated galaxies - I. Connecting dynamical and morphological properties of early-type galaxies at different redshifts.* MNRAS **480**, 4636 (2018)

Schwinn J., Jauzac M., Baugh C. M., Bartelmann M., Eckert D., Harvey D., Natarajan P., & Massey R.: *Abell 2744: too much substructure for ΛCDM?* MNRAS **467**, 2913 (2017)

Schwinn J., Baugh C. M., Jauzac M., Bartelmann M., & Eckert D.: *Uncovering substructure with wavelets: proof of concept using Abell 2744.* MNRAS **481**, 4300 (2018)

Scott N., van de Sande J., Croom S. M., Groves B., Owers M. S., Poetrodjojo H., D'Eugenio F., Medling A. M., Barat D., Barone T. M., et al.: *The SAMI Galaxy Survey: Data Release Two with absorption-line physics value-added products.* MNRAS **481**, 2299 (2018)

Scoville N., Sheth K., Aussel H., Vanden Bout P., Capak P., Bongiorno A., Casey C. M., Murchikova L., Koda J., Álvarez-Márquez J., et al.: *ISM Masses and the Star formation Law at $Z = 1$ to 6: ALMA Observations of Dust Continuum in 145 Galaxies in the COSMOS Survey Field.* ApJ **820**, 83 (2016)

Seidel B. A., Dolag K., Remus R. S., Sorce J. G., Hernández-Martínez E., Khabibullin I., & Aghanim N.: *SLOW IV: Not all that is Close will Merge in the End. Superclusters and their Lagrangian collapse regions.* arXiv e-prints, arXiv:2412 (2024)

Seidel B. A., Remus R.-S., Valenzuela L. M., Kimmig L. C., & Dolag K.: *Go with the flow: The self-similar and non-linear behaviour of large-scale in- and outflows and the impact of accretion shocks from galaxies to galaxy clusters.* A&A **701**, A192 (2025)

Sellwood J. A. & Binney J. J.: *Radial mixing in galactic discs.* MNRAS **336**, 785 (2002)

Sérsic J. L.: *Influence of the atmospheric and instrumental dispersion on the brightness distribution in a galaxy.* Boletin de la Asociacion Argentina de Astronomia La Plata Argentina **6**, 41 (1963)

Sersic J. L.: *Atlas de Galaxias Australes.* Geologische Rundschau **55**, 342 (1968)

Shahidi A., Mobasher B., Nayyeri H., Hemmati S., Wiklind T., Chartab N., Dickinson M., Finkelstein S. L., Pacifici C., Papovich C., et al.: *Selection of Massive Evolved Galaxies at $3 \leq z \leq 4.5$ in the CANDELS Fields.* ApJ **897**, 44 (2020)

Shakura N. I. & Sunyaev R. A.: *Black holes in binary systems. Observational appearance.* A&A **24**, 337 (1973)

Shapley A. E., Sanders R. L., Topping M. W., Reddy N. A., Pahl A. J., Oesch P. A., Berg D. A., Bouwens R. J., Brammer G., Carnall A. C., et al.: *The AURORA Survey: An Extraordinarily Mature, Star-forming Galaxy at $z \sim 7$.* ApJ **981**, 167 (2025)

Shapley H. & Curtis H. D.: *The Scale of the Universe.* Bulletin of the National Research Council **2**, 171 (1921)

Shaw L. D., Weller J., Ostriker J. P., & Bode P.: *Statistics of Physical Properties of Dark Matter Clusters.* ApJ **646**, 815 (2006)

Silk J. & Rees M. J.: *Quasars and galaxy formation.* A&A **331**, L1 (1998)

Smith S.: *The Mass of the Virgo Cluster.* ApJ **83**, 23 (1936)

Snaith O., Haywood M., Di Matteo P., Lehnert M. D., Combes F., Katz D., & Gómez A.: *Reconstructing the star formation history of the Milky Way disc(s) from chemical abundances.* A&A **578**, A87 (2015)

Somerville R. S. & Davé R.: *Physical Models of Galaxy Formation in a Cosmological Framework.* ARA&A **53**, 51 (2015)

Song M., Finkelstein S. L., Ashby M. L. N., Grazian A., Lu Y., Papovich C., Salmon B., Somerville R. S., Dickinson M., Duncan K., et al.: *The Evolution of the Galaxy Stellar Mass Function at $z = 4$-8: A Steepening Low-mass-end Slope with Increasing Redshift.* ApJ **825**, 5 (2016)

Sorce J. G.: *Galaxy clusters in local Universe simulations without density constraints: a long uphill struggle.* MNRAS **478**, 5199 (2018)

Sorce J. G., Gottlöber S., & Yepes G.: *The past history of galaxy clusters told by their present neighbours.* MNRAS **496**, 5139 (2020)

Spavone M., Capaccioli M., Napolitano N. R., Iodice E., Grado A., Limatola L., Cooper A. P., Cantiello M., Forbes D. A., Paolillo M., & Schipani P.: *VEGAS: A VST Early-type GAlaxy Survey. II. Photometric study of giant ellipticals and their stellar halos.* A&A **603**, A38 (2017)

Spavone M., Iodice E., van de Ven G., Falcón-Barroso J., Raj M. A., Hilker M., Peletier R. P., Capaccioli M., Mieske S., Venhola A., et al.: *The Fornax Deep Survey with VST. VIII. Connecting the accretion history with the cluster density.* A&A **639**, A14 (2020)

Spavone M., Iodice E., Lohmann F. S., Arnaboldi M., Hilker M., La Marca A., Calvi R., Cantiello M., Corsini E. M., D'Ago G., et al.: *Galaxy populations in the Hydra I cluster from the VEGAS survey: III. The realm of low surface brightness features and intra-cluster light.* A&A **689**, A306 (2024)

Speagle J. S., Steinhardt C. L., Capak P. L., & Silverman J. D.: *A Highly Consistent Framework for the Evolution of the Star-Forming "Main Sequence" from z ~0-6.* ApJS **214**, 15 (2014)

Spiniello C., Tortora C., D'Ago G., Coccato L., La Barbera F., Ferré-Mateu A., Napolitano N. R., Spavone M., Scognamiglio D., Arnaboldi M., et al.: *INSPIRE: INvestigating Stellar Population In RElics. I. Survey presentation and pilot study.* A&A **646**, A28 (2021)

Spiniello C., D'Ago G., Coccato L., Hartke J., Tortora C., Ferré-Mateu A., Pulsoni C., Cappellari M., Maksymowicz-Maciata M., Arnaboldi M., et al.: *INSPIRE: INvestigating Stellar Population In RElics – V. Final Data Release: the first catalogue of relics outside the local Universe.* arXiv e-prints, arXiv:2309 (2023)

Springel V., White S. D. M., Tormen G., & Kauffmann G.: *Populating a cluster of galaxies – I. Results at $z = 0$.* MNRAS **328**, 726 (2001a)

Springel V., Yoshida N., & White S. D. M.: *GADGET: a code for collisionless and gasdynamical cosmological simulations.* New A **6**, 79 (2001b)

Springel V. & Hernquist L.: *Cosmological smoothed particle hydrodynamics simulations: a hybrid multiphase model for star formation.* MNRAS **339**, 289 (2003)

Springel V.: *The cosmological simulation code GADGET-2.* MNRAS **364**, 1105 (2005)

Springel V., Di Matteo T., & Hernquist L.: *Modelling feedback from stars and black holes in galaxy mergers.* MNRAS **361**, 776 (2005a)

Springel V., Di Matteo T., & Hernquist L.: *Black Holes in Galaxy Mergers: The Formation of Red Elliptical Galaxies.* ApJ **620**, L79 (2005b)

Springel V. & Hernquist L.: *Formation of a Spiral Galaxy in a Major Merger.* ApJ **622**, L9 (2005)

Springel V., White S. D. M., Jenkins A., Frenk C. S., Yoshida N., Gao L., Navarro J., Thacker R., Croton D., Helly J., et al.: *Simulations of the formation, evolution and clustering of galaxies and quasars.* Nature **435**, 629 (2005c)

Springel V.: *E pur si muove: Galilean-invariant cosmological hydrodynamical simulations on a moving mesh.* MNRAS **401**, 791 (2010)

Springel V., Pakmor R., Pillepich A., Weinberger R., Nelson D., Hernquist L., Vogelsberger M., Genel S., Torrey P., Marinacci F., & Naiman J.: *First results from the IllustrisTNG simulations: matter and galaxy clustering.* MNRAS **475**, 676 (2018)

Stefanon M., Bouwens R. J., Labbé I., Illingworth G. D., Gonzalez V., & Oesch P. A.: *Galaxy Stellar Mass Functions from z 10 to z 6 using the Deepest Spitzer/Infrared Array Camera Data: No Significant Evolution in the Stellar-to-halo Mass Ratio of Galaxies in the First Gigayear of Cosmic Time.* ApJ **922**, 29 (2021)

Steidel C. C., Giavalisco M., Pettini M., Dickinson M., & Adelberger K. L.: *Spectroscopic Confirmation of a Population of Normal Star-forming Galaxies at Redshifts $Z > 3$.* ApJ **462**, L17 (1996)

Steinborn L. K., Dolag K., Hirschmann M., Prieto M. A., & Remus R.-S.: *A refined sub-grid model for black hole accretion and AGN feedback in large cosmological simulations.* MNRAS **448**, 1504 (2015)

Steinmetz M., Zwitter T., Siebert A., Watson F. G., Freeman K. C., Munari U., Campbell R., Williams M., Seabroke G. M., Wyse R. F. G., et al.: *The Radial Velocity Experiment (RAVE): First Data Release.* AJ **132**, 1645 (2006)

Steinwandel U. P., Dolag K., Böss L. M., & Marin-Gilabert T.: *Toward Cosmological Simulations of the Magnetized Intracluster Medium with Resolved Coulomb Collision Scale.* ApJ **967**, 125 (2024)

Stevens A. R. H., Diemer B., Lagos C. d. P., Nelson D., Pillepich A., Brown T., Catinella B., Hernquist L., Weinberger R., Vogelsberger M., & Marinacci F.: *Atomic hydrogen in IllustrisTNG galaxies: the impact of environment parallelled with local 21-cm surveys.* MNRAS **483**, 5334 (2019)

Stevenson S. D., Carnall A. C., Leung H.-H., Taylor E., Cullen F., Dunlop J. S., McLeod D. J., McLure R. J., Begley R., Arellano-Córdova K. Z., et al.: *PRIMER and JADES reveal an abundance of massive quiescent galaxies at $2 < z < 5$.* MNRAS **545**, staf2087 (2026)

Stinson G. S., Brook C., Macciò A. V., Wadsley J., Quinn T. R., & Couchman H. M. P.: *Making Galaxies In a Cosmological Context: the need for early stellar feedback.* MNRAS **428**, 129 (2013)

Straatman C. M. S., Labbé I., Spitler L. R., Allen R., Altieri B., Brammer G. B., Dickinson M., van Dokkum P., Inami H., Glazebrook K., et al.: *A Substantial Population of Massive Quiescent Galaxies at z ∼4 from ZFOURGE.* ApJ **783**, L14 (2014)

Strazzullo V., Pannella M., Mohr J. J., Saro A., Ashby M. L. N., Bayliss M. B., Bocquet S., Bulbul E., Khullar G., Mantz A. B., et al.: *Galaxy populations in the most distant SPT-SZ clusters. I. Environmental quenching in massive clusters at 1.4 ≲ z ≲ 1.7.* A&A **622**, A117 (2019)

Sunyaev R. A. & Zeldovich Y. B.: *Small-Scale Fluctuations of Relic Radiation.* Ap&SS **7**, 3 (1970)

Sunyaev R. A. & Zeldovich Y. B.: *Formation of Clusters of Galaxies; Protocluster Fragmentation and Intergalactic Gas Heating.* A&A **20**, 189 (1972)

Swindle R., Gal R. R., La Barbera F., & de Carvalho R. R.: *SPIDER. V. Measuring Systematic Effects in Early-type Galaxy Stellar Masses from Photometric Spectral Energy Distribution Fitting.* AJ **142**, 118 (2011)

Tacchella S., Dekel A., Carollo C. M., Ceverino D., DeGraf C., Lapiner S., Mandelker N., & Primack J. R.: *Evolution of density profiles in high-z galaxies: compaction and quenching inside-out.* MNRAS **458**, 242 (2016)

Tacchella S., Diemer B., Hernquist L., Genel S., Marinacci F., Nelson D., Pillepich A., Rodriguez-Gomez V., Sales L. V., Springel V., & Vogelsberger M.: *Morphology and star formation in IllustrisTNG: the build-up of spheroids and discs.* MNRAS **487**, 5416 (2019)

Tacchella S., Conroy C., Faber S. M., Johnson B. D., Leja J., Barro G., Cunningham E. C., Deason A. J., Guhathakurta P., Guo Y., et al.: *Fast, Slow, Early, Late: Quenching Massive Galaxies at z ∼ 0.8.* ApJ **926**, 134 (2022a)

Tacchella S., Finkelstein S. L., Bagley M., Dickinson M., Ferguson H. C., Giavalisco M., Graziani L., Grogin N. A., Hathi N., Hutchison T. A., et al.: *On the Stellar Populations of Galaxies at z = 9-11: The Growth of Metals and Stellar Mass at Early Times.* ApJ **927**, 170 (2022b)

Tacchella S., Johnson B. D., Robertson B. E., Carniani S., D'Eugenio F., Kumari N., Maiolino R., Nelson E. J., Suess K. A., Übler H., et al.: *JWST NIRCam + NIRSpec: interstellar medium and stellar populations of young galaxies with rising star formation and evolving gas reservoirs.* MNRAS **522**, 6236 (2023)

Tadaki K.-i., Kodama T., Nelson E. J., Belli S., Förster Schreiber N. M., Genzel R., Hayashi M., Herrera-Camus R., Koyama Y., Lang P., et al.: *Rotating Starburst Cores in Massive Galaxies at z = 2.5.* ApJ **841**, L25 (2017)

Tanaka T. S., Shimasaku K., Tacchella S., Ando M., Ito K., Yesuf H. M., & Matsui S.: *HINOTORI I: The Nature of Rejuvenation Galaxies.* arXiv e-prints, arXiv:2307 (2023)

Teklu A. F., Remus R.-S., Dolag K., Beck A. M., Burkert A., Schmidt A. S., Schulze F., & Steinborn L. K.: *Connecting Angular Momentum and Galactic Dynamics: The Complex Interplay between Spin, Mass, and Morphology.* ApJ **812**, 29 (2015)

Teklu A., Kudritzki R.-P., Dolag K., Remus R.-S., & Kimmig L.: *On the Decline of Star Formation during the Evolution of Galaxies.* ApJ **954**, 182 (2023)

Teyssier R.: *Cosmological hydrodynamics with adaptive mesh refinement. A new high resolution code called RAMSES.* A&A **385**, 337 (2002)

Thielemann F.-K., Argast D., Brachwitz F., Hix W. R., Höflich P., Liebendörfer M., Martinez-Pinedo G., Mezzacappa A., Nomoto K., & Panov I.: *Supernova Nucleosynthesis and Galactic Evolution.* In: Hillebrandt W. & Leibundgut B. (eds.): *From Twilight to Highlight: The Physics of Supernovae.* 331 (2003)

Thomas D., Maraston C., Schawinski K., Sarzi M., & Silk J.: *Environment and self-regulation in galaxy formation.* MNRAS **404**, 1775 (2010)

Tinsley B. M.: *Galactic Evolution.* A&A **20**, 383 (1972)

Tollet É., Cattaneo A., Macciò A. V., Dutton A. A., & Kang X.: *NIHAO XIX: how supernova feedback shapes the galaxy baryon cycle.* MNRAS **485**, 2511 (2019)

Tomczak A. R., Quadri R. F., Tran K.-V. H., Labbé I., Straatman C. M. S., Papovich C., Glazebrook K., Allen R., Brammer G. B., Kacprzak G. G., et al.: *Galaxy Stellar Mass Functions from ZFOURGE/CANDELS: An Excess of Low-mass Galaxies since $z = 2$ and the Rapid Buildup of Quiescent Galaxies.* ApJ **783**, 85 (2014)

Toomre A. & Toomre J.: *Galactic Bridges and Tails.* ApJ **178**, 623 (1972)

Toomre A.: *Mergers and Some Consequences.* In: Tinsley B. M. & Larson R. B. G., D. Campbell (eds.): *Evolution of Galaxies and Stellar Populations.* 401 (1977)

Tornatore L., Borgani S., Matteucci F., Recchi S., & Tozzi P.: *Simulating the metal enrichment of the intracluster medium.* MNRAS **349**, L19 (2004)

Tornatore L., Borgani S., Dolag K., & Matteucci F.: *Chemical enrichment of galaxy clusters from hydrodynamical simulations.* MNRAS **382**, 1050 (2007)

Tozzi G., Maiolino R., Cresci G., Piotrowska J. M., Belfiore F., Curti M., Mannucci F., & Marconi A.: *Unveiling hidden active nuclei in MaNGA star-forming galaxies with He II λ4686 line emission.* MNRAS **521**, 1264 (2023)

Trager S. C., Worthey G., Faber S. M., Burstein D., & González J. J.: *Old Stellar Populations. VI. Absorption-Line Spectra of Galaxy Nuclei and Globular Clusters.* ApJS **116**, 1 (1998)

Trayford J. W., Schaye J., Correa C., Ploeckinger S., Richings A. J., Chaikin E., Schaller M., Benítez-Llambay A., Frenk C., & Huško F.: *Modelling the evolution and influence of dust in cosmological simulations that include the cold phase of the interstellar medium.* MNRAS **545**, staf2040 (2026)

Tremaine S. D. & Richstone D. O.: *A test of a statistical model for the luminosities of bright cluster galaxies.* ApJ **212**, 311 (1977)

Tremblay G. R., O'Dea C. P., Baum S. A., Mittal R., McDonald M. A., Combes F., Li Y., McNamara B. R., Bremer M. N., Clarke T. E., et al.: *Far-ultraviolet morphology of star-forming filaments in cool core brightest cluster galaxies.* MNRAS **451**, 3768 (2015)

Tremmel M., Quinn T. R., Ricarte A., Babul A., Chadayammuri U., Natarajan P., Nagai D., Pontzen A., & Volonteri M.: *Introducing ROMULUSC: a cosmological simulation of a galaxy cluster with an unprecedented resolution.* MNRAS **483**, 3336 (2019)

Treu T., Roberts-Borsani G., Bradac M., Brammer G., Fontana A., Henry A., Mason C., Morishita T., Pentericci L., Wang X., et al.: *The GLASS-JWST Early Release Science Program. I. Survey Design and Release Plans.* ApJ **935**, 110 (2022)

Trujillo I., Conselice C. J., Bundy K., Cooper M. C., Eisenhardt P., & Ellis R. S.: *Strong size evolution of the most massive galaxies since $z \sim 2$.* MNRAS **382**, 109 (2007)

Trussler J. A. A., Conselice C. J., Adams N., Austin D., Caruana J., Harvey T., Li Q., Lovell C. C., Seeyave L. T. C., Vijayan A. P., & Wilkins S. M.: *Like a candle in the wind: the embers of once aflame, now smouldering galaxies at $5 < z < 8$.* MNRAS **537**, 3662 (2025)

Tsukui T. & Iguchi S.: *Spiral morphology in an intensely star-forming disk galaxy more than 12 billion years ago.* Science **372**, 1201 (2021)

Tsukui T., Wisnioski E., Krumholz M. R., & Battisti A.: *Spatially resolved dust properties and quasar-galaxy decomposition of a hyper-luminous infrared galaxy at $z = 4.4$.* MNRAS **523**, 4654 (2023)

Tully R. B., Courtois H. M., Dolphin A. E., Fisher J. R., Héraudeau P., Jacobs B. A., Karachentsev I. D., Makarov D., Makarova L., Mitronova S., et al.: *Cosmicflows-2: The Data.* AJ **146**, 86 (2013)

Tumlinson J., Peeples M. S., & Werk J. K.: *The Circumgalactic Medium.* ARA&A **55**, 389 (2017)

Turner C., Tacchella S., D'Eugenio F., Carniani S., Curti M., Glazebrook K., Johnson B. D., Lim S., Looser T., Maiolino R., et al.: *Age-dating early quiescent galaxies: high star formation efficiency, but consistent with direct, higher-redshift observations.* MNRAS **537**, 1826 (2025)

Tweed D., Devriendt J., Blaizot J., Colombi S., & Slyz A.: *Building merger trees from cosmological N-body simulations. Towards improving galaxy formation models using subhaloes.* A&A **506**, 647 (2009)

Übler H., Maiolino R., Curtis-Lake E., Pérez-González P. G., Curti M., Perna M., Arribas S., Charlot S., Marshall M. A., D'Eugenio F., et al.: *GA-NIFS: A massive black hole in a low-metallicity AGN at $z \sim 5.55$ revealed by JWST/NIRSpec IFS.* A&A **677**, A145 (2023)

Umehata H., Kubo M., Smail I., Lehmer B. D., Monson E. B., Nakanishi K., & Matsuda Y.: *ADF22-WEB: ALMA and JWST (sub)kpc-scale views of dusty star-forming galaxies in a $z \approx 3$ proto-cluster.* arXiv e-prints, arXiv:2502 (2025a)

Umehata H., Steidel C. C., Smail I., Swinbank M., Monson E. B., Rosario D., Lehmer B. D., Nakanishi K., Kubo M., Iono D., et al.: *ADF22-WEB: A giant barred spiral starburst galaxy in the $z = 3.1$ SSA22 protocluster core.* PASJ **77**, 432 (2025b)

Urbano Stawinski S. M., Cooper M. C., Forrest B., Muzzin A., Marchesini D., Wilson G., Gomez P., McConachie I., Marsan Z. C., Annuziatella M., & Chang W.: *Spectroscopic Confirmation of an Ultra-Massive Galaxy in a Protocluster at $z \sim 4.9$.* The Open Journal of Astrophysics **7**, 46 (2024)

Valentini M. & Dolag K.: *Hydrodynamic methods and sub-resolution models for cosmological simulations.* arXiv e-prints, arXiv:2502 (2025)

Valentino F., Brammer G., Gould K. M. L., Kokorev V., Fujimoto S., Jespersen C. K., Vijayan A. P., Weaver J. R., Ito K., Tanaka M., et al.: *An Atlas of Color-selected Quiescent Galaxies at $z > 3$ in Public JWST Fields.* ApJ **947**, 20 (2023)

Valenzuela L. M., Remus R.-S., Dolag K., & Seidel B. A.: *Galaxy shapes in Magneticum: I. Connecting stellar and dark matter shapes to dynamical and morphological galaxy properties and the large-scale structure.* A&A **690**, A206 (2024)

Valenzuela L. M., Forbes D. A., & Remus R.-S.: *Globular cluster ages and their relation to high-redshift stellar cluster formation times from different globular cluster models.* MNRAS **537**, 306 (2025)

van de Sande J., Bland-Hawthorn J., Fogarty L. M. R., Cortese L., d'Eugenio F., Croom S. M., Scott N., Allen J. T., Brough S., Bryant J. J., et al.: *The SAMI Galaxy Survey: Revisiting Galaxy Classification through High-order Stellar Kinematics.* ApJ **835**, 104 (2017)

van de Sande J., Lagos C. D. P., Welker C., Bland-Hawthorn J., Schulze F., Remus R.-S., Bahé Y., Brough S., Bryant J. J., Cortese L., et al.: *The SAMI Galaxy Survey: comparing 3D spectroscopic observations with galaxies from cosmological hydrodynamical simulations.* MNRAS **484**, 869 (2019)

van de Sande J., Croom S. M., Bland-Hawthorn J., Cortese L., Scott N., Lagos C. D. P., D'Eugenio F., Bryant J. J., Brough S., Catinella B., et al.: *The SAMI galaxy survey: Mass and environment as independent drivers of galaxy dynamics.* MNRAS **508**, 2307 (2021)

van de Sande J., Fraser-McKelvie A., Fisher D. B., Martig M., Hayden M. R., & Geckos Survey Collaboration: *GECKOS: Turning galaxy evolution on its side with deep observations of edge-on galaxies.* In: Tabatabaei F., Barbuy B., & Ting Y.-S. (eds.): *Early Disk-Galaxy Formation from JWST to the Milky Way.* IAU Symposium **377**, 27 (2024)

van den Hoek L. B. & Groenewegen M. A. T.: *New theoretical yields of intermediate mass stars.* A&AS **123**, 305 (1997)

van der Burg R. F. J., Muzzin A., Hoekstra H., Wilson G., Lidman C., & Yee H. K. C.: *A census of stellar mass in ten massive haloes at z ∼1 from the GCLASS Survey.* A&A **561**, A79 (2014)

van der Wel A., Franx M., van Dokkum P. G., Skelton R. E., Momcheva I. G., Whitaker K. E., Brammer G. B., Bell E. F., Rix H. W., Wuyts S., et al.: *3D-HST+CANDELS: The Evolution of the Galaxy Size-Mass Distribution since z = 3.* ApJ **788**, 28 (2014)

van Dokkum P. G., Leja J., Nelson E. J., Patel S., Skelton R. E., Momcheva I., Brammer G., Whitaker K. E., Lundgren B., Fumagalli M., et al.: *The Assembly of Milky-Way-like Galaxies Since z ∼2.5.* ApJ **771**, L35 (2013)

van Dokkum P. G., Abraham R., Merritt A., Zhang J., Geha M., & Conroy C.: *Forty-seven Milky Way-sized, Extremely Diffuse Galaxies in the Coma Cluster.* ApJL **798**, L45 (2015)

van Dokkum P., Wasserman A., Danieli S., Abraham R., Brodie J., Conroy C., Forbes D. A., Martin C., Matuszewski M., Romanowsky A. J., & Villaume A.: *Spatially Resolved Stellar Kinematics of the Ultra-diffuse Galaxy Dragonfly 44. I. Observations, Kinematics, and Cold Dark Matter Halo Fits.* ApJ **880**, 91 (2019)

Vayner A., Zakamska N. L., Ishikawa Y., Sankar S., Wylezalek D., Rupke D. S. N., Veilleux S., Bertemes C., Barrera-Ballesteros J. K., Chen H.-W., et al.: *First results from the JWST Early Release Science Program Q3D: Powerful quasar-driven galactic scale outflow at* $z = 3$. arXiv e-prints, arXiv:2307 (2023)

Vazdekis A., Sánchez-Blázquez P., Falcón-Barroso J., Cenarro A. J., Beasley M. A., Cardiel N., Gorgas J., & Peletier R. F.: *Evolutionary stellar population synthesis with MILES - I. The base models and a new line index system.* MNRAS **404**, 1639 (2010)

Veilleux S., Liu W., Vayner A., Wylezalek D., Rupke D. S. N., Zakamska N. L., Ishikawa Y., Bertemes C., Barrera-Ballesteros J. K., Chen H.-W., et al.: *First Results from the JWST Early Release Science Program Q3D: The Warm Ionized Gas Outflow in z 1.6 Quasar XID 2028 and Its Impact on the Host Galaxy.* ApJ **953**, 56 (2023)

Véliz Astudillo S., Carrasco E. R., Nilo Castellón J. L., Zenteno A., & Cuevas H.: *The effect of dynamical states on galaxy clusters populations. I. Classification of dynamical states.* arXiv e-prints, arXiv:2408 (2024)

Vernstrom T., West J., Vazza F., Wittor D., Riseley C. J., & Heald G.: *Polarized accretion shocks from the cosmic web.* Science Advances **9**, eade7233 (2023)

Vogelsberger M., Marinacci F., Torrey P., & Puchwein E.: *Cosmological simulations of galaxy formation.* Nature Reviews Physics **2**, 42 (2020)

Waller W. H. & Hodge P. W.: *Galaxies and the cosmic frontier.* Harvard University Press (2003)

Wang B., Leja J., Atek H., Labbe I., Li Y., Bezanson R., Brammer G., Cutler S. E., Dayal P., Furtak L. J., et al.: *Quantifying the Effects of Known Unknowns on Inferred High-redshift Galaxy Properties: Burstiness, the IMF, and Nebular Physics.* (2023)

Wang W., Cantalupo S., Pensabene A., Galbiati M., Travascio A., Steidel C. C., Maseda M. V., Pezzulli G., de Beer S., Fossati M., et al.: *A giant disk galaxy two billion years after the Big Bang.* Nature Astronomy **9**, 710 (2025)

Weaver J. R., Kauffmann O. B., Ilbert O., McCracken H. J., Moneti A., Toft S., Brammer G., Shuntov M., Davidzon I., Hsieh B. C., et al.: *COSMOS2020: A Panchromatic View of the Universe to z∼10 from Two Complementary Catalogs.* ApJS **258**, 11 (2022)

Weaver J. R., Davidzon I., Toft S., Ilbert O., McCracken H. J., Gould K. M. L., Jespersen C. K., Steinhardt C., Lagos C. D. P., Capak P. L., et al.: *COSMOS2020: The galaxy stellar mass function. The assembly and star formation cessation of galaxies at 0.2< z ≤ 7.5.* A&A **677**, A184 (2023)

Weißmann A., Böhringer H., Šuhada R., & Ameglio S.: *Studying the properties of galaxy cluster morphology estimators.* A&A **549**, A19 (2013)

Weller E. J., Pacucci F., Ni Y., Hernquist L., & Park M.: *Discrepancies between JWST Observations and Simulations of Quenched Massive Galaxies at z > 3: A Comparative Study with IllustrisTNG and ASTRID.* ApJ **979**, 181 (2025)

Westcott L., Conselice C. J., Harvey T., Austin D., Adams N., Ferrari F., Ferreira L., Trussler J., Li Q., Rusakov V., et al.: *EPOCHS. XI. The Structure and Morphology of Galaxies in the Epoch of Reionization to z ∼ 12.5.* ApJ **983**, 121 (2025)

Whitaker K. E., van Dokkum P. G., Brammer G., & Franx M.: *The Star Formation Mass Sequence Out to z = 2.5.* ApJ **754**, L29 (2012)

White S. D. M. & Rees M. J.: *Core condensation in heavy halos: a two-stage theory for galaxy formation and clustering.* MNRAS **183**, 341 (1978)

Wiersma R. P. C., Schaye J., & Smith B. D.: *The effect of photoionization on the cooling rates of enriched, astrophysical plasmas.* MNRAS **393**, 99 (2009)

Wild V., Almaini O., Dunlop J., Simpson C., Rowlands K., Bowler R., Maltby D., & McLure R.: *The evolution of post-starburst galaxies from z=2 to 0.5.* MNRAS **463**, 832 (2016)

Williams B. F., Dalcanton J. J., Dolphin A. E., Holtzman J., & Sarajedini A.: *The Detection of Inside-Out Disk Growth in M33.* ApJ **695**, L15 (2009)

Wolf M.: *Die Klassifizierung der kleinen Nebelflecken.* Publikationen des Astrophysikalischen Instituts Koenigstuhl-Heidelberg **3**, 109 (1908)

Woosley S. E. & Weaver T. A.: *The Evolution and Explosion of Massive Stars. II. Explosive Hydrodynamics and Nucleosynthesis.* ApJS **101**, 181 (1995)

Wylezalek D., Flores A. M., Zakamska N. L., Greene J. E., & Riffel R. A.: *Ionized gas outflow signatures in SDSS-IV MaNGA active galactic nuclei.* MNRAS **492**, 4680 (2020)

Xiang M. & Rix H.-W.: *A time-resolved picture of our Milky Way's early formation history.* Nature **603**, 599 (2022)

Xiao M., Williams C. C., Oesch P. A., Elbaz D., Dessauges-Zavadsky M., Marques-Chaves R., Bing L., Ji Z., Weibel A., Bezanson R., et al.: *PANORAMIC: Discovery of an ultra-massive grand-design spiral galaxy at z ∼ 5.2.* A&A **696**, A156 (2025)

Yagi M., Koda J., Komiyama Y., & Yamanoi H.: *Catalog of Ultra-diffuse Galaxies in the Coma Clusters from Subaru Imaging Data.* ApJS **225**, 11 (2016)

Yang L., Kartaltepe J. S., Franco M., Ding X., Achenbach M. J., Arango-Toro R. C., Casey C. M., Drakos N. E., Faisst A. L., Gillman S., et al.: *COSMOS-Web: Unraveling the Evolution of Galaxy Size and Related Properties at 2 < z < 10.* ApJS **281**, 68 (2025)

Yi S. K., Yoon S. J., Kaviraj S., Deharveng J. M., Rich R. M., Salim S., Boselli A., Lee Y. W., Ree C. H., Sohn Y. J., et al.: *Galaxy Evolution Explorer Ultraviolet Color-Magnitude Relations and Evidence of Recent Star Formation in Early-Type Galaxies.* ApJ **619**, L111 (2005)

Yoo J., Park C., Sabiu C. G., Singh A., Ko J., Lee J., Pichon C., Jee M. J., Gibson B. K., Snaith O., et al.: *Spatial Distribution of Intracluster Light versus Dark Matter in Horizon Run 5.* ApJ **965**, 145 (2024)

York D. G., Adelman J., Anderson J. E., Jr., Anderson S. F., Annis J., Bahcall N. A., Bakken J. A., Barkhouser R., Bastian S., Berman E., et al.: *The Sloan Digital Sky Survey: Technical Summary.* AJ **120**, 1579 (2000)

Yuan Z. S. & Han J. L.: *Dynamical state for 964 galaxy clusters from Chandra X-ray images.* MNRAS **497**, 5485 (2020)

Yuan Z. S., Han J. L., & Wen Z. L.: *Dynamical state of galaxy clusters evaluated from X-ray images.* MNRAS **513**, 3013 (2022)

Zel'dovich Y. B.: *Gravitational instability: An approximate theory for large density perturbations.* A&A **5**, 84 (1970)

Zenteno A., Hernández-Lang D., Klein M., Vergara Cervantes C., Hollowood D. L., Bhargava S., Palmese A., Strazzullo V., Romer A. K., Mohr J. J., et al.: *A joint SZ-X-ray-optical analysis of the dynamical state of 288 massive galaxy clusters.* MNRAS **495**, 705 (2020)

Zhang J., Li Y., Leja J., Whitaker K. E., Nersesian A., Bezanson R., & van der Wel A.: *A Simple Spectroscopic Technique to Identify Rejuvenating Galaxies.* ApJ **952**, 6 (2023)

Zhang Y., Golden-Marx J. B., Ogando R. L. C., Yanny B., Rykoff E. S., Allam S., Aguena M., Bacon D., Bocquet S., Brooks D., et al.: *Dark Energy Survey Year 6 results: Intra-cluster light from redshift 0.2 to 0.5.* MNRAS **531**, 510 (2024)

Zibetti S., White S. D. M., Schneider D. P., & Brinkmann J.: *Intergalactic stars in z˜ 0.25 galaxy clusters: systematic properties from stacking of Sloan Digital Sky Survey imaging data.* MNRAS **358**, 949 (2005)

Zinger E., Dekel A., Kravtsov A. V., & Nagai D.: *Quenching of Satellite Galaxies at the Outskirts of Galaxy Clusters.* arXiv e-prints, arXiv:1610 (2016)

Zinger E., Pillepich A., Nelson D., Weinberger R., Pakmor R., Springel V., Hernquist L., Marinacci F., & Vogelsberger M.: *Ejective and preventative: the IllustrisTNG black hole feedback and its effects on the thermodynamics of the gas within and around galaxies.* MNRAS **499**, 768 (2020)

Zwicky F.: *Die Rotverschiebung von extragalaktischen Nebeln.* Helvetica Physica Acta **6**, 110 (1933)

Quotations

Chapter 1

> See yonder, lo, the Galaxyë
> Which men clepeth the Milky Wey
> For hit is whyt
>
> *See yonder, lo, the Galaxy, which men call the Milky Way, since it is white*

Geoffrey Chaucer, *The House of Fame*, circa 1380

Chapter 2

> The fault, dear Brutus, is not in our stars,
> But in ourselves

William Shakespeare, *Julius Caesar*, circa 1599

Chapter 3

> παντὶ γάρ μοι δοκεῖ δῆλον ὅτι αὕτη [ἀστρονομίας] γε ἀναγκάζει ψυχὴν εἰς τὸ ἄνω ὁρᾶν καὶ ἀπὸ τῶν ἐνθένδε ἐκεῖσε ἄγει.
>
> *For every one, as I think, must see that astronomy compels the soul to look upwards and leads us from this world to another.*

Plato, *The Republic*, Book VII, circa 375 BCE

Chapter 4

Preso dall'operazione del lume del Sole, il quale, mentre attrae quei vapori o riscalda quella pianta, gli attrae e la riscalda in modo, come se altro non avesse che fare; anzi nel maturar quel grappolo d'uva, anzi pur quel grapello solo, vi si applica che piu efficacemente applicar non vi si potrebbe quando il termine di tutti i suoi affari fusse la sola maturazione di quel grano.

For when the sun draws up some vapors here, or warms a plant there, it draws these and warms this as if it had nothing else to do. Even in ripening a bunch of grapes, or perhaps just a single grape, it applies itself so effectively that it could not do more even if the goal of all its affairs were just the ripening of this one grape.

Galileo Galilei, *Dialogo sopra i due massimi sistemi del mondo*, 1632

Chapter 5

Sól þat né vissi hvar hon sali átti,
stjörnur þat né vissu hvar þær staði áttu,
Máni þat né vissi hvat hann megins átti.

The sun knew not where should be his palaces;
The moon knew not where would be her home.
The stars knew not where would be their station.

Völuspá, *Codex Regius*, Ancient Norse poem, circa 1270

Chapter 6

Wenn eine solche Welt von Fixsternen [wie die Milchstraße] in einem so unermesslichen Abstand . . . angeschaut wird, so wird dieselbe unter einem kleinen Winkel als ein mit schwachem Lichte erleuchtetes Räumchen erscheinen, dessen Figur zirkelrund sein wird, wenn seine Fläche sich dem Auge gerade zu darbietet, und elliptisch, wenn es von der Seite gesehen wird.

If such a world of fixed stars [like the Milky Way] is seen at such an immeasurable distance . . . , then this world will appear in a small angle as a tiny and weakly lit area, with a circular shape if its plane is oriented directly in the line of sight and elliptical if it is viewed from the side.

Immanuel Kant, *Allgemeine Naturgeschichte und Theorie des Himmels, erster Theil*, 1755

Chapter 7

> First, it is allowed ... by all modern Philosophers, that the Sun and Stars are all of the same or like Nature; consequently, that the Stars are all Suns, and that the Sun himself is a Star.

Thomas Wright, *An Original Theory or New Hypothesis of the Universe, 6th Letter*, 1750

Chapter 8

> Περισκοπεῖν ἄστρων δρόμους ὥσπερ συμπεριθέοντα καὶ τὰς τῶν στοιχείων εἰς ἄλληλα μεταβολὰς συνεχῶς ἐννοεῖν: ἀποκαθαίρουσι γὰρ αἱ τούτων φαντασίαι τὸν ῥύπον τοῦ χαμαὶ βίου.
>
> *Watch the stars in their courses as one that runneth about with them therein; and think constantly upon the reciprocal changes of the elements, for thoughts on these things cleanse away the mire of our earthly life.*

Marcus Aurelius, *Meditationes*, circa 161–180

Chapter 9

> Veritatem inquirenti, semel in vita de omnibus, quantum fieri potest, esse dubitandum.
>
> *To seek truth, it is necessary that at least once in your life you doubt, as far as possible, all things.*

Rene Descartes, *Principles of Philosophy*, 1644.

Chapter 10

> 天の川　流れてぞありし　夏の月
>
> *The Milky Way*
> *it flowed away*
> *the summer moon.*

Matsuo Bashō, circa 1660–1694

Chapter 11

> A broad and ample road, whose dust is gold
> And pavement stars, as stars to thee appear
> Seen in the Galaxie, that Milky Way
> Which nightly as a circling zone thou seest
> Powdered with stars.

John Milton, *Paradise lost*, Book 7, verse 577–581, 1667

Chapter 12

Est via sublimis caelo manifesta sereno:
lactea nomen habet candore notabilis ipso;

There is a high track, seen when the sky is clear:
Milky [Way] is its name, known for its whiteness.

Publius Ovidius Naso, *Metamorphosis Book. 1, Verse 168–169*, circa 1–8

Chapter 13



Suspected Egyptian name for the Milky Way, with competing translations "path of sailing stars" or "beaten path of stars".

Pyramid Texts, late Old Kingdom, circa 2400–2300 BCE
from Graur (2024)

Chapter 14

Die Sterne sind klug, sie halten mit Fug
Von unserer Erde sich ferne;
Am Himmelszelt, als Lichter der Welt,
Stehn ewig sicher die Sterne.

The stars are more wise, and keep in the skies,
And hold the earth at a distance;
They shed their light in the heavens so bright,
In safe and endless existence.

Heinrich Heine, *Neue Gedichte: Kluge Sterne*, 1852

Chapter 15

Koia rā! Kua whetūrangitia koutou kei
aku rau kahu rangi!

It is that! You have become stars, amongst myriads of celestial garments!

Maori Saying, *Matariki Handbook*, matariki.twoa.ac.nz

Acknowledgments

The writing of this thesis has been a fascinating endeavor, as it encompasses multiple years of learning and doing science. It further represents the closing of one chapter and the opening of another, and far more importantly would not have been possible without the many fantastic people around me. As such, I would like to extend my gratitude to those who have supported me along the way.

First and foremost I would like to thank Klaus Dolag for many things, but highlight here the frequent discussions, the great input, the freedom to pursue the topics that I found personally interesting, as well as the invaluable advice which I carry with me to my next step in academia. Thank you.

I would like to thank Andreas Burkert for the intriguing ideas and uncanny ability to point at parts of the question that are worth exploring further, as well as the support of my collaborative efforts around the world.

Next, I would like to thank Rhea-Silvia Remus for the creativity, joy and inspiration that helped pave the path forward, even when the code was not behaving as it should. I repeat myself, but thank you for being you. Additionally, I am very grateful to Lucas Valenzuela for the many years of delving into science together, and look forward to continuing that into the future.

I would like to thank the Dragons team as a whole, which has been a great, warm place to pursue my science. I hope to see many of you at future conferences.

I would then like to thank my family for the unwavering support and love over what at this point can be called decades, without whom the successes of these last few years would not have been possible in this form. I cherish you all very much. Finally, I would like to thank Julian Thewes, for being ready at all times with humor, advice, and a train ticket in hand.

Selbstständigkeitserklärung

Hiermit erkläre ich, die vorliegende Arbeit selbstständig verfasst zu haben und keine anderen als die in der Arbeit angegebenen Quellen und Hilfsmittel benutzt zu haben.

München, [18.02.2026]

_____

Lucas Cameron Kimmig